Dinâmica e origem dos asteroides de alta inclinação

Texto sistematizado de parte dos trabalhos de pesquisa realizados após a obtenção do título de doutor. Apresentado ao Departamento de Matemática da UNESP, Campus de Guaratinguetá, como parte dos requisistos para obtenção do título de Livre Docência.

Valerio Carruba

6 de agosto de 2013

To my Ladies:
Andrea
Amelie
Yasmine

Agradecimentos

Agradeço a minha família na Itália por todo o carinho e o afeto recebidos e por ter me sustentado por muitos anos na minha excêntrica busca de uma carriera científica do outro lado do mundo.

Agradeço a minha família no Brasil, minha esposa Andréa, meus sogros e nossas "filhas peludas", Amelie e Yasmim, para todo o carinho com o qual foi recebido, e o suporte a minha atividade de pesquisa neste país.

Agradeço aos meus orientadores na Itália, EUA e Brasil, os Drs. Angioletta Coradini, Joseph A. Burns, Sylvio Ferraz-Mello, e Tadashi Yokoyama, para terem orientado meus primeiros passos no mundo da pesquisa científica.

Agradeço aos meus colaboradores Angioletta Coradini, William Bottke, David Nesvoný, Phil. D. Nicholson, Fernando Roig, Tatiana Michtchenko, e Damya Souami por terem sido fontes de inspiração para muitos trabalhos científicos.

Agradeço às agências financiadoras, FAPESP e CNPq, por terem financiados meus trabalhos de pesquisa desde que cheguei ao Brasil, e por terem acreditado no meu futuro como pesquisador na área de dinâmica de asteroides neste país.

Agradeço à UNESP e ao Grupo de Dinâmica Orbital e Planetologia da UNESP por terem me acolhido aqui em Guaratinguetá.

Agradeço ao Departamento de Matemática da UNESP, campus de Guaratinguetá, e em particular ao prof. Dr. Galeno José de Sena por todo o apoio que tem me dado e pela ajuda em organizar este concurso.

Agradeço à todos que, direta ou mesmo indiretamente, contribuíram para o meu crescimento dentro da carreira acadêmica.

Sumário

1 Introdução **4**

2 Famílias de asteroides no espaço das frequências próprias $(n, g, g + s)$ **7**

3 Famílias de asteroides em outros espaços de frequências **23**

4 Famílias dinâmicas na região de Phocaea **40**

5 Erosão dinâmica de grupos de asteroides na região da família de Phocaea **56**

6 O arquipelago de ilhas de estabilidade no cinturão central de alta inclinação **73**

7 Erosão dinâmica de grupos de asteroides na região da família de Pallas **96**

8 A família de Tina **108**

9 Famílias dinâmicas no cinturão externo **121**

10 A distribuição "Emmenthal" dos asteroides de alta inclinação **143**

11 Difusão caótica nas regiões das famílias de Pallas e Euphrosyne **157**

12 Um método multi-variado para a determinaçaõ de famílias de asteroides **169**

13 Considerações finais **192**

1

Introdução

Asteroides de alta inclinação são definidos em Gil-Hutton (2006) como os corpos com $sin(i) > 0.3$. Outros autores definem os corpos de alta inclinação como os asteroides com valores de inclinação maior que a inclinação da ressonância secular ν_6 por correspondentes valores de semi-eixo maior [1] A inclinação de um objeto é associada ao momento angular (h) de um corpo, e a sua componente z (h_z) com respeito a um sistema de referência associado, por exemplo, ao plano invariante do Sistema Solar e a direção ortogonal a este plano, por meio da relação:

$$h_z = h \cdot cosI. \tag{1.1}$$

Segue, portanto, que para mudar a inclinação de um objeto é necessário mudar o seu momento angular, o que implica mecanismos como encontros próximos com objetos massivos, colisões, etc. No cinturão atual, tais mecânismos não conseguem mudar facilmente a inclinação de um objeto abaixo da ressonância ν_6 para valores de i acima dela. Objetos que evolvem para a região da ressonância ν_6 são instáveis com tempos-escalas máximos de 10 Myr (Gladman et al. 1992). Os asteroides que têm órbitas de alta inclinação podem, portanto, ser vestígios de fases iniciais da evoluçao orbital do Sistema Solar, e manter informações sobre esta fase primordial. Comprender a distribuição orbital e as características físicas deste objetos é portanto importante para nossa compreensão da evolução do Sistema

[1] Ressonâncias seculares ocorrem quando existe uma comensurabilidade entre as frequências (e os períodos) de precessão do argumento do pericentro ou da longitude do nó ascendente (g e s, respetivamente) do asteroide e do planeta. A ressonância ν_6 seria equivalente à comensurabilidade $g - g_6$.

Solar como um todo.

Nessa dissertação, revisitarei trabalhos que publiquei nos últimos seis anos sobre asteroides em várias regiões do cinturão principal. Por razões dinâmicas, as ressonâncias de movimento médio J4:-1A, J3:-1A, J5:-2A, e 2J:-1A dividem o cinturão principal em cinco regiões: a region dos asteroides Hungaria ($a < a_{J4:-1A}$), o cinturão interno ($a_{J4:-1A} < a < a_{J3:-1A}$), o cinturão central ($a_{J3:-1A} < a < a_{J5:-2A}$), o cinturão externo ($a_{J5:-2A} < a < a_{J2:-1A}$), e a região dos asteroides de tipo Cybele ($a > a_{J2:-1A}$). Outros asteroides se encontram em ressonâncias estáveis de movimento médio com Júpiter, como os asteroides Trojanos, os Hilda, e os Thule, mas não são considerados como parte do cinturão principal. Desde o fim da fase de migração planetaria os asteroides evoluiram colisionalmente. Depois da colisão entre dois córpos, fragmentos foram espalhados formando famílias, que são reagrupamentos de asteroides no espaço dos elementos próprios que tem caracteristicas físicas semelhantes. Sendo que as velocidades de ejeção dos fragmentos são da ordem de m/s, e as velocidades orbitais dos asteroides são da ordem de km/s, objetos membros de famílias não são espalhados para longe. As caracteristicas do impacto definem as velocidades típicas de ejeção dos membros de uma família, e determinam o quanto os fragmentos distam do corpo princípal em termos de elementos próprios. Os elementos próprios $a, e, sin(i)$, contrariamente aos elementos osculadores que variam com o tempo, são constantes em tempo-escala de milhões de anos e podem ser computados a partir dos elementos osculadores por meio de teorias analíticas (Milani e Knežević 1994) ou método númericos (Knežević e Milani 2003).

Mas até os elementos próprios mudam com o passar do tempo: efeitos não gravitacionais como os efeitos Yarkovsky (associado com a reemissão de luz solar da superfície do asteroide, que muda prevalentemente o semi-eixo maior da órbita, e cuja entidade depende de vários parâmetros como o albedo Bond, a emissividade, a capacidades e condutividade térmica das superfícies, a densidade média e superficial, etc.) e YORP (associado com os torques que superfícies não esféricas exercem sobre o eixo de rotação de asteroides, e que muda o período e a obliquidade do eixo de rotação de um asteroide, e portanto a entidade do efeito Yarkovsky, que depende destes parâmetros), desvios causados por encontros próximos com planetas ou asteroides massivos, interação com a rede local de ressonâncias de movimento médio e seculares, colisões de alta e baixa energia, mudam o valor

dos elementos próprios de asteroides desde da formação de uma família, rendendo a determinação do campo de ejeção originário mais difícil com o passar do tempo, e, em alguns casos, espalhando as famílias até um ponto onde a identificação fica impossível (evaporação das famílias de asteróides).

Nos artigos que irei apresentar, tentei, entre outras coisas, introduzir ferramentas novas para a identificação de famílias de asteróides. Tentei estudar a evolução dinâmica de membros de algumas famílias, com uma atenção especial para as famílias que interagem com ressonâncias seculares, e revisar nosso conhecimento sobre as propriedades físicas destes objetos. Trata-se, na minha opinião, de uma área de pesquisa bem viva e intrigante, com muitas perguntas ainda à serem respondidas.

Começamos esta análise dos asteróides de alta inclinação introduzindo métodos de determinação de famílias dinâmicas de asteroides em espaço de frequências próprias, que serão aplicados depois nesta região do cinturão principal.

2

Famílias de asteroides no espaço das frequências próprias $(n, g, g + s)$

O enfoque desta dissertação é sobre asteroides de alta inclinação, mas no estudo destes objetos foram utilizadas técnicas como o método das frequências próprias para identificar famílias de asteroides. Nesta sessão iremos discutir deste método, e da suas utilidade em estudar difusão de asteroides em ressonâncias seculares, lineares e não.

Famílias de asteroides são usualmente identificadas como agrupamentos no espaço dos elementos próprios $(a, e, sin(i))$ (semi-eixo maior, excentricidade e seno da inclinação do plano orbital). A distância entre dois objetos é medida neste espaço usando uma relação métrica. A métrica mais comumente usada é aquela introduzida por Zappalá et al. (1990), onde:

$$d = na\sqrt{k_1(\frac{\Delta a}{a})^2 + k_2(\Delta e)^2 + k_3(\Delta sin(i))^2}. \tag{2.1}$$

n é o movimento médio do asteroide, Δx e a diferença em a, e, and $sin(i)$; e k_1, k_2, k_3 são fatores de ponderação, definidos como $k_1 = 5/4$, $k_2 = 2$, $k_3 = 2$ em Zappalá et al. (1990, 1995). Se um objeto estiver a uma distância menor de um valor dado (distância de "cutoff") do primeiro corpo considerado, assume-se que este objeto é um membro da família, e a procedimento é repetido até não encontrar novos membros. Uma possível limitação deste método é que, desde a formação da família de asteroides, os seus membros mudaram suas órbitas e os valores dos seus elementos próprios por

causa de uma série de mecânismos, como a interação com ressonâncias de movimento médio e seculares, efeitos não gravitacionais como os efeitos Yarkovsky e YORP, encontros próximos com asteroides massivos, colisões de baixa energia, etc. Em particular, asteroides que evoluíram dentro de ressonâncias seculares por causa do efeito Yarkovsky podem ter se afastados do atual centro da família e não serem mais reconhecíveis como membros da família. Ressonâncias seculares lineares acontecem quando existe uma comensurabilidade entre as frequências de precessão do argumento do pericentro g ou longitude do nodo ascendente s do asteroide e de um planeta, como no caso das ressonâncias $\nu_5 = g - g_5$, $\nu_6 = g - g_6$, e $\nu_{16} = s - s_6$ (os suffixos 5 e 6 identificam as frequencias de Jupiter e Saturno, respetivamente). Ressonâncias seculares não lineares são combinações de ordem maior de ressonâncias lineares, como no caso das ressonâncias da série $z_k = k \cdot \nu_6 + \nu_{16} = k \cdot (g - g_6) + s - s_6, k = 1, 2, 3, ...$ Um asteroide que tenha migrado na ressonância z_1 fora de uma família não seria reconhecível como membro no espaço dos elementos próprios $(a, e, sin(i))$, especialmente considerando a complicada estrutura tridimensional das ressonâncias seculares no espaço dos elemento próprios. Mas, considerado que esta ressonância aparece como uma linha horizontal no plano $(g, g + s)$, e que asteroides dentro desta ressonância conservam o valor das frequência próprias $g + s = g_6 + s_6 = 1.898$ arcsec/yr, ele poderia ser ainda identificado como membro de uma família identificado no espaço das frequências próprias $(n, g, g + s)$. Em Carruba and Michtchenko (2007) introduzimos uma nova métrica de distância neste espaço definida como:

$$f = \sqrt{h_1 \left(\frac{\Delta n}{h_0}\right)^2 + h_2(\Delta g)^2 + h_3(\Delta(g+s))^2}, \tag{2.2}$$

onde h_0 é um fator de normalização com dimensões de 1 grau/arcsec, e $h_1 = h_2 = h_3 = 1$, e identificamos quatro das maiores famílias de asteroides neste espaço de frequências: as famílias de Vesta, Eunomia, Eos, e Koronis. Muitos objetos de tipo V e K, usualmente associados às família de Vesta e Eos, e hoje com órbitas fora da região ocupada para estas famílias, foram identificados com este método como membros das famílias no espaço das frequências. A possível evolução dinâmica destes objetos fora das famílias para as órbitas atuais por meio de evolução fora sucessivamente confirmada em outros trabalhos.

A seguir apresentamos o artigo, que foi publicado em Astronomy and Astrophysics em 2007, volume 475, pp. 1145-1158.

A&A 475, 1145–1158 (2007)
DOI: 10.1051/0004-6361:20077689

Astronomy & Astrophysics

A frequency approach to identifying asteroid families

V. Carruba[1] and T. A. Michtchenko[2]

[1] IPD, UNIVAP, São José dos Campos, SP, 12244-000, Brazil
e-mail: valerio@univap.br
[2] IAG, USP, São Paulo, SP, 05508-900, Brazil
e-mail: tatiana@astro.iag.usp.br

Received 20 April 2007/ Accepted 17 August 2007

ABSTRACT

Context. Secular resonances usually have a complicated three-dimensional structure in $a - e - i$ (or $a - e - \sin(i)$) space, which is not easily represented in a two-dimensional projection. As a consequence, the classic approach to identifying asteroid families fails in some cases to identify objects that have migrated in such resonances because of the Yarkovsky effect.
Aims. We propose an alternative approach by identifying asteroid families in the proper frequency domain $(n, g, g + s)$ rather than in the proper element domain $(a, e, \sin(i))$.
Methods. We applied the HCM method in the proper frequency domain $(n, g, g + s)$ to identify four of the largest asteroid families: Vesta, Eunomia, Eos, and Koronis. We compared our results with those obtained with the classical method. In addition, we applied the extended metrics in the domain of asteroid colors in both proper element and frequency domains.
Results. The frequency approach to determining families is an excellent tool for (i) more easily identifying the effect of nonlinear secular resonances on families and (ii) connecting to the family of origin objects that have migrated via the interplay of the Yarkovsky effect and nonlinear secular resonances.

Key words. minor planets, asteroids – celestial mechanics

1. Introduction

Asteroid families are groups of minor planets sharing a common collisional origin. Since the work of Hirayama (1918), it has been noticed that clusters of objects appear when the proper orbital elements of asteroids (proper semi-major axis a, eccentricity e, and inclination i[1]) are plotted in the $a - e$ or $a - \sin(i)$ planes. Zappalà et al. (1990) introduced the hierarchical clustering method (HCM hereafter) to identify neighbors in proper element space and separate asteroid families from objects in the background. This method has been successively used by several authors (Zappalà et al. 1993; Bendjoya & Zappalà 2002; Nesvorný et al. 2005, just to quote some of the works on the subject), and it is currently one of the most used tools for determining asteroid families[2].

However, many long-lasting dynamical effects can modify the orbits of members of asteroid families after the collisional event that originated them. Contrary to what was believed in the early 90s, asteroid proper elements can be significantly modified due to collisional evolution (O'Brien & Greenberg 2005), thermal effects such as the Yarkovsky and YORP effects (Vokrouhlický 1999; Vokrouhlický & Čapek 2002), repeated close encounters with massive asteroids (Carruba et al. 2003, 2007a), capture into mean-motion and secular resonances (Gladman et al. 1997), and the interplay of any of these mechanisms.

In particular, nonlinear secular resonances have recently assumed a significant role in asteroid dynamics. Secular resonances are commensurabilities among the frequencies of variation in the longitudes of perihelion, or in the longitudes of nodes or in both of an asteroid and the planets. Several groups (Bottke et al. 2001, for the Koronis family; Vokrouhlický et al. 2002, 2006, for the Eos family; Carruba et al. 2005, 2007a,b, for several V-type asteroids outside the Vesta and Eunomia families, among others) have demonstrated that the interplay of the Yarkovsky effect and nonlinear secular resonances has sculpted the shape of observed families and it is responsible for the diffusion of family members that today are no longer recognizable as such when methods like the classical HCM are used.

Nonlinear secular resonances usually have complicated three-dimensional structures in the proper $a - e - \sin(i)$ space, and are not easily represented in a two-dimensional projection (see Sect. 2). As a consequence, the classical Zappalà approach in some cases fails to identify objects that have migrated in such

[1] Unlike osculating orbital elements, which respond to short-period perturbations, proper elements determined via analytical (Milani & Knežević 1994) or numerical (Knežević, 2002) methods are nearly constant over long-time spans.

[2] We must make a distinction between the original family and the family determined with the classical HCM and other methods described in this article. When the asteroid family was formed, their members were thrown in a region already populated by other objects, sometimes having different superficial compositions. Also, the orbits of some of the family members evolved due to the several gravitational and non-gravitational effects described in the article. Therefore, when applying methods such as the HCM, we find clusters of objects in the current proper element or frequency space that may or may not have the same origin. Also, these methods may miss some of the asteroids that evolved farther away from the family core. When using the word family we will usually refer to the agglomeration of objects found with the methods described in this article, keeping in mind that the relationship of these clusters with the original agglomeration of objects created in the collisional event is generally a very complicated one.

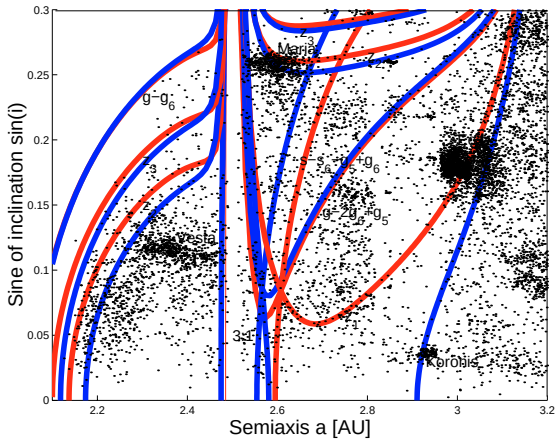

Fig. 1. The location of the main secular resonances in the asteroid belt. The secular resonances obtained for the fixed value 0.10 of the proper eccentricity are superimposed to the proper elements a and $\sin(i)$ of the asteroids with proper e within the range of ±0.025 of the central value. The names indicate the main asteroid families in the region. The red lines display the locations of the resonances at the lower edge, while the blue curves show the same at the upper edge. See Figs. 7, 8 and 9 of Milani & Knežević (1994) for more details.

resonances because of the Yarkovsky effect as family members, and, more generally, makes understanding the dynamics involving secular resonances more difficult than it should be.

We believe this problem may be overcome if we analyze asteroid families in the space of proper asteroid frequencies (n, g, s), where n is the asteroid mean-motion and g, s are the asteroid secular frequencies of the pericenter and node, respectively[3]. Indeed, the complicated three-dimensional structure of secular resonances may be more easily represented in the proper $(g, g+s)$ plane, where secular resonances appear as vertical (resonances of pericenter), horizontal (resonances that contain the $(g+s)$ combination), and inclined lines (resonances of node and other linear combinations of pericenter and node), forming the so-called "Arnold web" of resonances. In this paper we show that, by applying the HCM procedure in such a space, we may compensate for some dynamical effects of diffusion that were missed by the classical Zappalà (1990) approach.

This work is divided as follows: in the second section we see how the main belt appears in frequency space. In the third section we discuss the HCM method originally proposed by Zappalà (1990), introduce a metrics to apply the HCM in frequency space, and discuss the role that asteroid colors play in identifying asteroid families via the "extended metrics" of Bus & Binzel (2002), and its extension to the new HCM in frequency space. In the fourth section we apply our method to four asteroid families, namely Eos, Koronis, Eunomia, and Vesta, and compare the results to those obtained with the classical methods. Finally, we present our conclusions in the fifth section.

2. The main belt seen in frequency space

Secular resonances are commensurabilities that involve the frequencies of the asteroid longitude of perihelion g, node s and the fundamental frequencies of planetary theories $g_i = \dot{\varpi}_i$ and

[3] We used synthetic proper elements and frequencies obtained numerically and publically available at the AstDyS site `http://hamilton.dm.unipi.it/cgi-bin/astdys/astibo`. The reason for using the numerically obtained proper elements rather than analytical ones will be explained in Sect. 3.2.

Table 1. The values of the planetary frequencies (in ″/yr) used in this article.

Name	Freq. [″/yr]
g_5	4.257
g_6	28.243
g_7	3.093
g_8	0.673
s_6	–26.345
s_7	–2.996
s_8	–0.693

$s_i = \dot{\Omega}_i$, where i is a suffix that indicates the planets (5 for Jupiter, 6, for Saturn, etc.). The frequencies associated with such resonances have to satisfy the relationship

$$p \cdot g + q \cdot s + \sum_i (p_i \cdot g_i + q_i \cdot s_i) = 0, \quad (1)$$

where the integers p, q, p_i, q_i have to fulfill the D'Alembert rules of permissible arguments: the sum of the coefficients must be zero and the sum of coefficients of nodal longitudes frequencies must be even. The critical combinations (1) that involve only the frequency of the asteroid perihelion are often referred to as "pericenter resonances" and those with only frequency of the asteroid node as "node resonances".

The relevance of the sequence of resonances $z_k = k(g - g_6) + (s - s_6)$ ($k = 1, 2, 3$, etc.) was first investigated by Milani & Knežević (1992, 1994) and later confirmed by Vokrouhlický et al. (2002, 2006a,b), Carruba et al. (2007b) for the z_1 resonance, and by Carruba et al. (2005, 2007b) for the z_2 resonance. In contrast to mean-motion resonances, secular resonances usually have complicated three-dimensional structures in the proper $a - e - \sin(i)$ space and are not easily represented in a plane. Figure 1 displays the locations of the z_k resonances, of the pericenter resonance $g - 2g_6 + g_5$, and of the node resonance $s - s_6 - g_5 + g_6$ computed for proper $e = 0.10$ (the two curves refer to resonances computed for values of e to within ±0.025 of the central values) with the program frek.f of Milani & Knežević (1994)[4] using the values of planetary frequencies listed in Table 1. The location and shape of the secular resonances change significantly for different values of the proper e, making it hard to visualize how asteroid families members may interact with such resonances.

The reason for this behavior is that the secular resonances are not separable in the (a, e, i) space; that is, the position of a resonance depends on all three elements. To overcome this problem, we project asteroids in different space, that of the proper frequencies (n, g, s), where the mean-motion and secular resonances are separable. According to nonlinear perturbation theories, the proper frequencies are functions of the proper elements and the transformation from proper elements to proper frequencies is one-to-one if the Kolgomorov's non-degeneracy condition is satisfied (see Ferraz-Mello 2007). In this space, mean-motion resonances mostly depend on the proper frequency n, while secular resonances depend only on the proper (g, s) frequencies and appear as lines in such a plane. Figure 2 displays

[4] The analytic approach used by Milani & Knežević (1994) may fail in some cases to predict the accurate location of some of the nonlinear secular resonances, especially near powerful mean-motion resonances, where the values of proper g are significantly affected. While determining the exact location of those resonances is a task better dealt by numerical methods (Carruba et al. 2007b), we believe that this approach is justified for illustrative purposes.

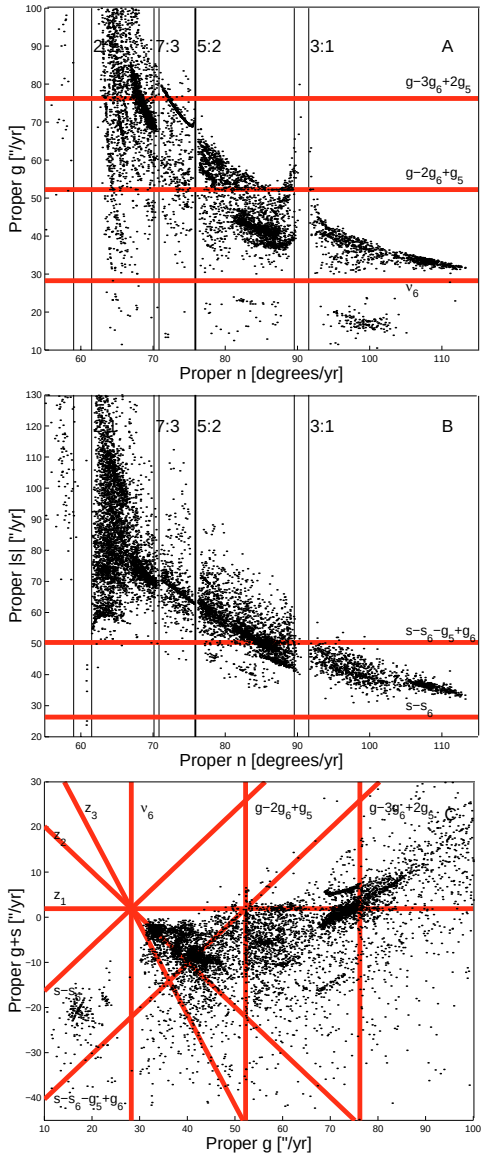

Fig. 2. Projection in the proper (n, g) (panel **A)**), $(n, |s|)$ (panel **B)**), and $(g, g + s)$ (panel **C)**) planes of all main belt asteroids with absolute magnitude H lower than 13. In panels **A)** and **B)**, vertical lines display the locations of mean-motion resonances, while horizontal lines show the positions of secular resonances of pericenter and node, respectively. See the text for a discussion of the meaning of the lines in panel **C)**.

the location in the (n, g), $(n, |s|)$, and $(g, g + s)$ planes of the asteroids with available numerical elements and absolute magnitudes lower than 13.

We start by analyzing the projection in the (n, g) plane. According to the third Kepler law, the proper motions are proportional to the semi-major axes to the power of –3/2. Therefore, higher values of n correspond to lower values of a. Generally, the evolution of proper g as a function of n tends to follow a line of negative slope, but the values of g are strongly affected by powerful mean-motion resonances such as the 3:1, the 5:2, and the 2:1 resonances with Jupiter (vertical lines in Fig. 2, panel A). As can be seen in panel A of Fig. 2 the values of proper g tend to increase near powerful mean-motion resonances, especially near the 3:1 and 2:1. This is explained by the appearance of small divisors of the form $(kn - ln_j)$ (where k and l are integers) in the expression of proper g computed with the analytical perturbation theory of Milani & Knežević (1994). The effect is also present for the case of the s frequency (see also Knežević et al. 1991), although it is less evident. The behavior of g near powerful mean-motion resonances introduces some difficulties in the asteroid families determination via frequency analysis and will be discussed in more detail in Sect. 3.2 and in Appendix B.

The (n, g) plane is the ideal plane for plotting the location of mean-motion and pericenter resonances. In panel A of Fig. 2 the vertical lines display the main two-body mean-motion resonances with Jupiter and the horizontal lines display the location of four pericenter resonances. The $g - g_6$ resonance (known as ν_6) is one of the most powerful resonances in the main belt, and it is very efficient in removing any captured asteroid in a short time. The $g - 2g_6 + g_5$ and the $g - 3g_6 + 2g_5$ are two resonances of pericenter. Milani & Knežević (1994) have shown that these resonances have the strongest effect on the stability of asteroid proper elements. The reader may want to compare the simple shape of the $g - 2g_6 + g_5$ resonance in the (n, g) plane, computed for all possible values of the asteroid eccentricity, with the complicated shape of the resonance in the $a - \sin(i)$ plane (Fig. 1), computed for a small range proper e values. From the comparison, the advantages of using frequency planes are obvious.

We should also point out that secular resonances involving the g_5 frequency usually present a multiplet structure with the g_7 fundamental frequency. This is due to the fact that the difference between g_5 and g_7 is less than 1.1 ″/yr, which Milani & Knežević (1994) set as the limit for resolving two near secular resonances in proper element space. The values of these two frequencies are so close because the perihelia of Jupiter and Uranus are in fact anti-aligned: $\varpi_5 - \varpi_7$ oscillates around 180° with a period of 1.1 Myr (Milani & Nobili 1984). This explains why several nonlinear secular resonances that we observe in the main belt are overlapping. For simplicity, in this work we will only list the resonance involving the jovian frequency when referring to a secular resonance involving the g_5 frequency, such as the $g - 2g_6 + g_5$. We assume that the reader is aware that nearby resonances involving Uranus frequency g_7, such as the $g - 2g_6 + g_7$, $g - 2g_6 + 2g_5 - g_7$, etc., are also present in the region.

Figure 2B shows a projection of the main belt asteroids in the $(n - |s|)$ plane. The proper s frequency is always negative and has a slope as a function of n that is almost opposite to that of g. Thus, following the approach of Knežević et al. (1991) we plot the absolute value of the proper frequency s for graphical purposes. As in Fig. 2A, we show the location of the main mean-motion resonances (vertical lines) and of the most powerful secular resonances of node (horizontal lines). In contrast to the case of proper g, the values of proper s are not strongly affected by nearby mean-motion resonances, but roughly follow an inclined line until reaching the 2:1 resonance.

Finally, Fig. 2C shows a projection of the main belts asteroids in the $(g, g + s)$ plane. Because the slope of g with respect to n is almost opposite that of s with respect to n, this representation allows displaying main belt population as parallel to the x-axis. In this figure, vertical lines display the locations of perihelion resonances, horizontal lines show resonances that contain the $g + s$ combination, and inclined lines display the location of node resonances and resonances involving other linear combinations of g and s. An interesting thing that can be observed in Fig. 2C is that all the z_k, the ν_6, and the $s - s_6$ resonances pass through the point with coordinates $g = 28.243$ ″/yr and $g + s = 1.898$ ″/yr. This is caused because at this point $g = g_6$ and $g + s = g_6 + s_6$, and the resonant arguments of all these resonances are simultaneously equal to zero. The location in the proper elements space of this point corresponds to a strongly

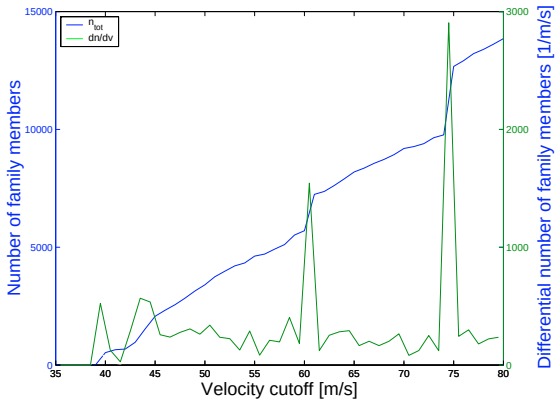

Fig. 3. The number of Eunomia family members (in blue) and the differential number of family members (in green) as a function of the velocity cutoff used in Eq. (2). For $v_{\rm cutoff} = 40$ m/s, the first family members are found, while for $v_{\rm cutoff} = 61$ m/s the family coalesces with other nearby families such as the Adeona family. For $v_{\rm cutoff} = 74$ m/s, the family coalesces with the local background. In this work we assume that $v_{\rm cutoff} = 55$ m/s can be a reasonable value for determining the family.

unstable domain inside the ν_6 resonance, at the intersection with the $s - s_6$ resonance, and is free of real objects populations.

3. The hierarchical clustering method in frequency and color spaces

In this section we present various methods, published and original, of determining asteroid families. We start by revising the classical HCM of Zappalà (1990).

3.1. The classical hierarchical clustering method

As can be seen in Fig. 1, asteroid proper elements are clustered in some cases in small regions of space. Following the Zappalà (1990) approach, asteroid families are identified with the following procedure: given an individual asteroid the distance between this object and the other one is computed. If the distance is less than a threshold limit ($d_{\rm cutoff}$), the new object is added to the list. The procedure is repeated until no new family member is found.

A critical point in this procedure is related to the choice of a reasonable metric in the three-dimensional element space. In Zappalà et al. (1990), the distance is defined as

$$d = na\sqrt{k_1(\Delta a/a)^2 + k_2(\Delta e)^2 + k_3(\Delta \sin(i))^2}, \quad (2)$$

where n is the asteroid mean motion; Δx the difference in proper a, e, and $\sin(i)$; and k_1, k_2, k_3 are weighting factors, defined as $k_1 = 5/4$, $k_2 = 2$, $k_3 = 2$ in Zappalà et al. (1990). Other choices of weighting factors are possible and yield similar results.

The reason for the choice of the value of the weighting factors resides in how Zappalà et al. (1990) modeled the distance in proper element space (see Appendix A). Their idea was essentially to preserve what at the time was believed to be the pristine ejection velocity field of asteroid families. When dealing with distances in the frequency space, we believe a similar approach to the one used by Zappalà et al. (1990) can no longer be used: first, because we now know that the current orbits of members of asteroid families do not reflect the original ejection velocity field, but have probably been modified by several effects (Yarkovsky and YORP effect, diffusion in mean-motion and secular resonances, and the repeated effect of close encounters with massive asteroids, etc.), especially for old families. And second contrary to what was believed in 1990, we now know that the asteroid semi-major axis is one of the quantities that has undergone the largest variation since the families' formations. Another approach must be found, and will be discussed in the following sections.

Another problem with the classical HCM is the choice of the velocity cutoff. There is no a priori value that can be set, and the velocity cutoff is usually a function of the number of asteroids present in the local background, which also depends on the number of asteroids available in the constantly updated database of asteroid proper elements of Milani & Knežević (1994). The typical procedure is to find the family for several values of the velocity cutoff, until the family coalesces with the local background, enclosing members of other known asteroid families; then a value that is 90% of this critical value is used, so as not to include too many asteroids not necessarily linked with the family.

To illustrate this procedure, we applied this method to the Eunomia family and our results are shown in Fig. 3, where we found that $v_{\rm cutoff} = 55$ m/s is a reasonable choice for the cutoff. For differential number of family members, we mean the number of family members that are added to the family when the cutoff is increased by a fixed quantity (step); for the case of Fig. 3 we used a step of 1 m/s. A metric that includes the proper frequencies would have to work with different values of the cutoff, and a procedure similar to the one discussed here for the Eunomia family should be applied to this extended metric as well.

3.2. The hierarchical clustering method in the frequency space

As discussed in the previous section, the space of proper frequencies n, g, s is the most adequate for identifying secular resonances. A natural question that therefore arises is why not to search for asteroid families in such a space. For this purpose, we need to find an appropriate metric in the frequency space, evaluating the typical distances in frequencies between neighbors in the region of known asteroid families. We applied the classical HCM to various asteroid members of large asteroid families, such as Vesta, Eunomia, Koronis, etc, and computed the differences in proper elements and proper frequencies for their neighbors. Figure 4 shows the histograms of such differences when the classical HCM is applied to (15) Eunomia with a cutoff of 160 m/s. If we measure n in degree/yr and g and s in ″/yr, typical differences for neighbors in families all have the same order of magnitude of 0.05 degrees or ″ per year.

Since the differences in proper n, g, and $g + s$ all have the same order of magnitude, we may define the metric as

$$d_2 = \sqrt{h_1\left(\frac{\Delta n}{h_0}\right)^2 + h_2(\Delta g)^2 + h_3(\Delta(g+s))^2}, \quad (3)$$

where h_0 is a normalization factor of dimension 1 degree/″, and the simplest choice for the h_i ($i = 1, 3$) weights is to take them all equal to 1. The distance in frequency space then has the units of ″/yr. We tested other values of the h_i coefficients (in the range 0.5–5.0), obtaining similar results.

A problem that might arise by using Eq. (3) is that it might identify artificial clusters near secular resonances. These artificial clumps are formed because the ≃2–10 Myr averaging procedure used by Milani & Knežević (2003), to numerically determine the g, n, and s frequencies bring all objects into the center

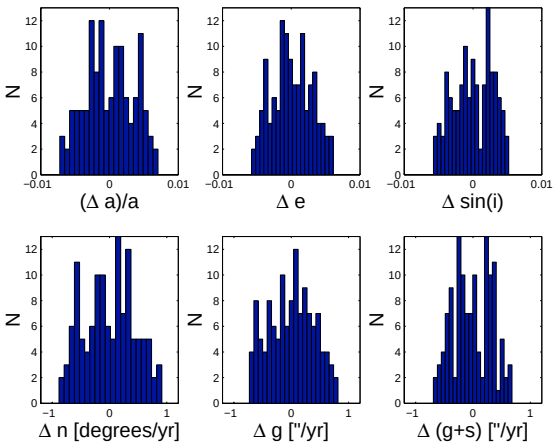

Fig. 4. The changes in proper elements $(\Delta a)/a, \Delta e, \Delta \sin(i)$ (*top panels*) and proper frequencies $\Delta n, \Delta g, \Delta s$ (*bottom panels*) for neighbors of (15) Eunomia computed with the classical HCM and a cutoff of 160 m/s. Results are similar for other asteroids in different regions of the asteroid belt. Note how the changes in proper frequencies all have the same order of magnitude of 0.05 degrees or $''$ per year.

(zero-degrees of libration) of the resonance and produce artificially dense clusters (see Fig. 4 of Milani & Knežević 2003, and discussion therein). An example of this effect might be seen on the right side of Fig. 1, where a little clump of data points near the $g-2g_6+g_5$ resonance is observed. Any new clump or family identified with the frequency approach should therefore be tested by using the classical HCM or other methods, and an analysis of the dynamics in the region should be performed, before the new family can be accepted as such.

Another limitation of the metric given in Eq. (3) is that it fails to recognize as family members objects very close to powerful mean-motion resonances, where the behavior of g as a function of n diverges from a linear one. In the neighborhood of such resonances, asteroids that are close in the proper element space may be very distant in frequency space. A way to partly circumvent this difficulty is to introduce a metric of proper elements and frequencies. This metric, which will be discussed in the Appendix B, may connect some of the critical asteroids that a pure frequency metric may fail to connect. In some cases, however, the change in g is so steep that even this five-dimensional metric fails to connect asteroids across powerful mean-motion resonances. Also, the five-dimensional metric may fail to recognize family members that have drifted far away from the family in proper element space, while we shall see in Sect. 4 that the frequency metric is a powerful tool for detecting asteroids that were captured in nonlinear secular resonances. For simplicity, we decided to solely use the frequency metric and to discuss its limitations on a case to case basis. We believe that losing some peripheral objects is an acceptable price to pay in order to gain the powerful insights on the dynamical evolution of families that the frequency metric allows. But we acknowledged this is a problem yet to be solved.

Finally, Bus & Binzel (2002) introduced a method to take asteroid colors into account in the family determination. We will discuss this method and its extension to a frequency space in the next subsection.

3.3. The role of colors

The Sloan Digital Sky Survey Moving Object Catalog, hereafter SDSS MOC3 lists astrometric and photometric data for asteroids observed by the 2.5-m Sloan telescope located at Apache Point Observatory, in Sunspot, New Mexico. To date (3rd release), the survey has determined the positions, brightness, and five-color CCD photometry of 204 305 moving objects (Ivezić et al., 2001). The 67 636 unique moving objects detected by the survey (i.e., about 28% of the total) have been matched (Jurić et al. 2002) to known asteroids listed in the ASTORB file (Bowell et al. 1994). The flux reflected by the detected objects was measured almost simultaneously in five bands (measurements in two successive bands were separated in time by 72 s) with effective wavelengths 3557 angstrom (u band), 4825 angstrom (g band), 6261 angstrom (r band), 7672 angstrom (i band), and 9097 angstrom (z band), and with 0.1–0.3-μm band widths (Fukugita et al. 1996).

This data has been used recently by Nesvorný et al. (2004) to classify asteroids according to their taxonomic types and to determine asteroids families in the space of proper elements and colors simultaneously. Bus & Binzel (2002) introduced the following extended metrics in this space:

$$d_3 = \sqrt{d^2 + C_{PC}[(\delta PC_1)^2 + (\delta PC_2)^2]}. \quad (4)$$

Where d is given by Eq. (2), PC_1 and PC_2 are the two first principal components (we determined them using the approach described in Roig & Gil-Hutton (2006), $\delta PC_i = |PC_i(1) - PC_i(2)|$ with $i = 1, 2$, and C_{PC} is a numerical factor, usually set equal to 10^6, if v is measured in m/s (values in a range between 10^4 and 10^8 were tested by the authors without significantly changing the robustness of the results).

We applied this extended metric to the several asteroid families, and the results will be discussed in the next section. As in Nesvorný et al. (2004), we found that, while the extended HCM method in itself does not provide robust concentrations in the extended proper element and color space that could help in identifying new families, the method is excellent to identify family "halos", i.e., populations of peripheral family members that were not joined with the rest of the family with the standard HCM method. In Carruba et al. (2007b) we applied this method to the Eunomia family and found a halo of objects connecting this family with two objects suspected and confirmed to be of the V taxonomic type. This was very helpful for determining the possible origin of these two asteroids.

Following Bus & Binzel (2002) we also define a metrics of colors and frequency in the form:

$$d_4 = \sqrt{(d_2)^2 + D_{PC}[(\delta PC_1)^2 + (\delta PC_2)^2]}, \quad (5)$$

where D_{PC} is a numerical factor, that we empirically set equal to 200, so as to give comparable results for the typical differences in proper frequencies and the typical differences in principal components. Other values in the range 10–1000 were also tested, without significantly changing the robustness of the results. A discussion of the application of this method to various asteroid families will be given in the next section.

4. An application to selected asteroid families

In the next subsections we apply our methods to four asteroid families: Eos, Koronis, Eunomia, and Vesta. While we used our new method to re-derive the major families in the main belt, we prefer to only show families known in the literature to have strong interactions with nonlinear secular resonances, so as to emphasize the advantages of using the new method. In general, we concentrate on the comparison of families obtained with

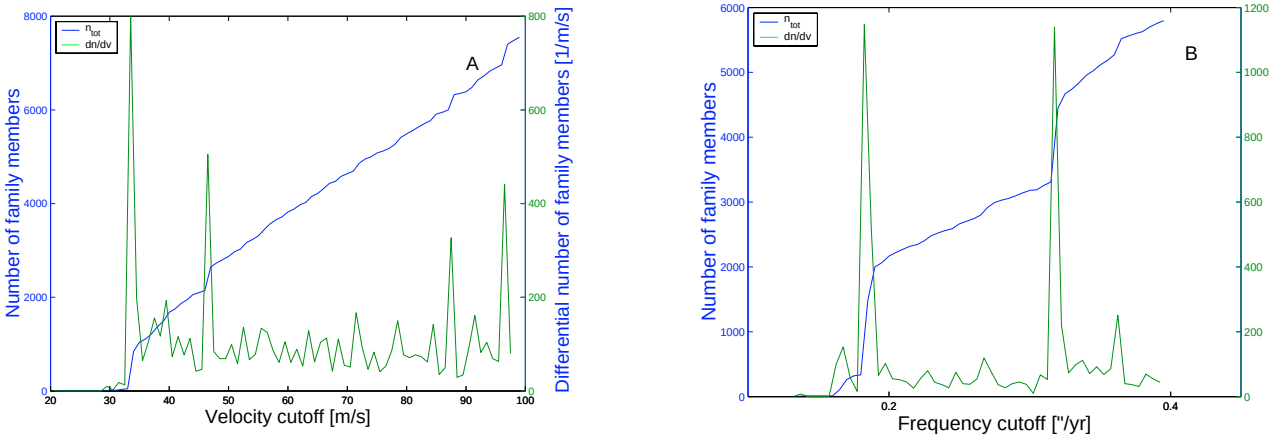

Fig. 5. The number of Eos family members and the differential number as a function of the velocity (*left panel*) and frequency (*right panel*) cutoff.

the classical HCM (Eq. (2)) and the frequency metric (Eq. (3)). Results obtained by using the color metrics (Eqs. (4), (5) will be discussed briefly at the end of the four sub-sections.

We will start by analyzing families in the outer main belt and proceed in the inward direction.

4.1. The outer belt

4.1.1. (221) Eos

The Eos asteroid family is the third most populous, after Themis and Koronis, and its dynamics have been the subject of a thorough recent study by Vokrouhlický et al. (2006). Most of its members belong to the characteristic K spectral type. The family is bounded by the 7/3 mean-motion resonance with Jupiter. It is crossed by the 9/4 mean-motion resonance, and strongly interacts with the z_1 nonlinear secular resonance. We start by determining the family with the classical and frequency method and by revising the distribution of mean-motion resonance in the region.

At a velocity cutoff of 34 m/s, the classical family starts to agglomerate neighbors of (221) Eos (Fig. 5), at 47 m/s the family connects to asteroids beyond the 9/4 resonance with Jupiter, and at 87 m/s the family coalesces with the near Veritas family. To be consistent with the choice made by Vokrouhlický et al. (2006), we choose a velocity cutoff of 62 m/s. The first neighbors of (221) Eos in frequency space are found at a frequency cutoff of 0.165 ″/yr. At a frequency of 0.320 ″/yr, the family connects to asteroids beyond the 9/4 resonance. Finally, for a cutoff of 0.365 ″/yr, the family merges with the nearby Veritas family. We choose a cutoff of 0.36 ″/yr to define the family in frequency space. Figure 6A displays the locations in the proper $g, g+s$ plane of the family member obtained with the two methods. The tail of asteroids obtained with the classical method at very high values of g is formed by asteroids that are close to the 2:1 mean-motion resonance. Due to the strong perturbations in proper g caused by this resonance, the frequency method fails to recognize these bodies as family members (see Appendix B).

The next step is to identify the location in the proper $a-\sin(i)$ plane of the main two-body and three-body resonances. We report the location of the 7/3, 9/4, 13/6 two-body resonances with Jupiter and of the $3J-2S-1A$ in Fig. 6. We then identify all nonlinear secular resonances involving the frequencies of the planets from Jupiter to Uranus up to order 6 and display their location in the proper $(g, g+s)$ plane (see Fig. 6A, where the order of a secular resonance is defined as the sum of the absolute values of the p, q, p_i, q_i coefficients in Eq. (1)). We find that three secular resonances have the strongest impact on the long-term stability of asteroid proper elements: the z_1 resonance (or $(s-s_6)+(g-g_6)$), the $g-(-2g_5+3g_6)$ resonance, and the $(s-s_6)-2(g_5-g_6)$ resonances. Apart from harmonics of these resonances involving combinations of the g_5 and g_7 frequencies, other weaker resonances (such as the $s-3s_6+2s_7$, $(s-2s_6+s_7)-(g_5-g_6)$, and the $(s-s_7)+(g-g_7)$ and their harmonics) are also present but generally play a minor role. These results agree with Vokrouhlický et al. (2006).

To accurately draw the center of the nonlinear secular resonances in the $a-\sin(i)$ and $(a-e)$ planes, we adopted the following procedures. For each resonance we identify all asteroids in the range around the resonance frequency (±0.3 ″/yr from the central value) that have values of proper $\sin(i)$ ($a-e$ projection) or e ($a-\sin(i)$ projection) compatible with those of the family, or, in some cases, with those of the peculiar feature (for example a tail, like for the case of asteroids in the $(s-s_6)-2(g_5-g_6)$) we were studying in the particular case. We then best-fit a polynomial curve to those objects and identify the center of the resonances with this curve. We discuss this procedure in more detail for each of the resonance we are going to study.

Figure 6B shows an $a-\sin(i)$ projection of the Eos classical and frequency families (for brevity, we do not show an $a-e$ and $e-\sin(i)$ projection of the Eos family, since the $a-\sin(i)$ plane is the most interesting one). As in Vokhrouhlický et al. (2006), we find that the z_1 resonance (computed for $e=0.08$) plays a major role in shaping the Eos family. The tail of objects at $a\simeq 3.05$ and $\sin(i)\simeq 0.2$ identified by the classical methods as members that drifted via the Yarkovsky force in the z_1 are also found with the new approach. The new metric, however, allows us to identify a stream of objects leaving the Eos family toward lower values of $\sin(i)$ via the $g-2g_5+3g_6$ and the $(s-s_6)-2(g_5-g_6)$ resonances that the classical method failed to recognize as family members. Other streams of objects leaving the family are associated to harmonics of these two resonances involving the g_7 frequency, such as $g+3g_6-2g_7$, the $(s-s_6)-2(g_7-g_6)$ or other possible combinations of g_5 and g_7. We believe the identification of these secular resonances as possible pathways for dynamical diffusion, obtained without performing extensive numerical simulations of the asteroid orbital evolution, is one of the most important result of our method.

Another interesting result found with the frequency metrics regards four asteroids, (20845) 2000 UY102, (21211) 1994 PP36, (33780) 1999 RU171, and (62948) 2000 VE32, currently

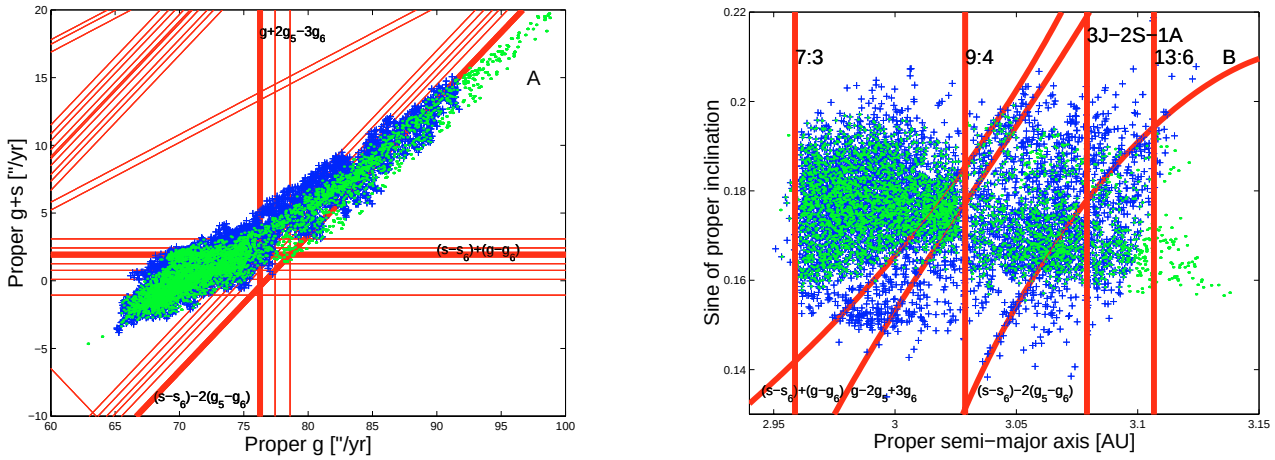

Fig. 6. A $(g, g + s)$ and $(a, \sin(i))$ projection of the Eos family obtained with the classical HCM (green dots), and with the frequency HCM (blue crosses). Secular resonances shown in $(a, \sin(i))$ planes are identified by thicker lines in the $(g, g+s)$ plane (we have identified all secular resonances of order up to 6).

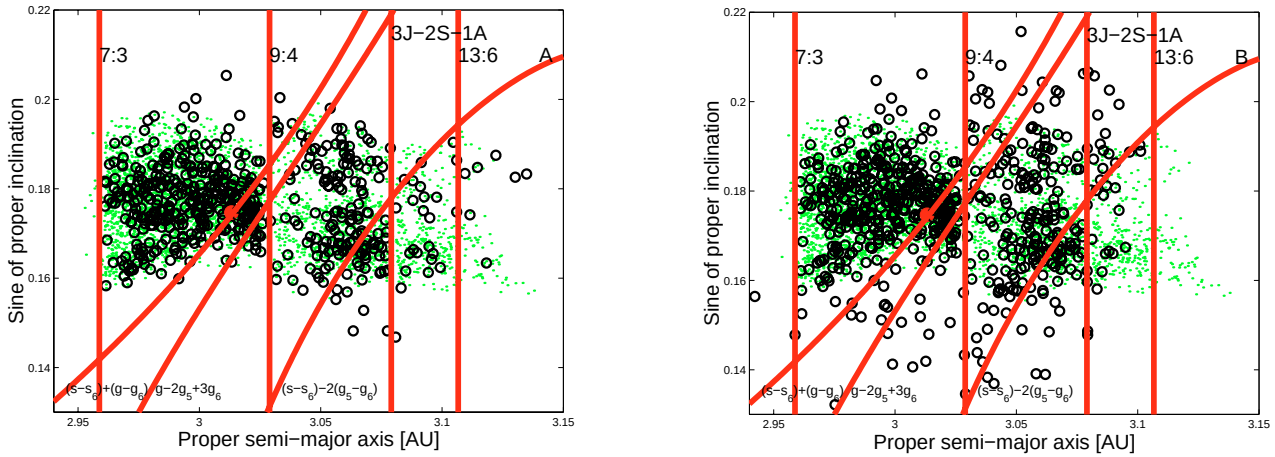

Fig. 7. An $a - \sin(i)$ projection of the members of the Eos family found with the classical approach (green dots), with the metric of colors and proper elements (black circles, *left panel*) and with the metric of color and frequencies, (black circles, *right panel*). The full large red dot displays the location of (320) Katharina. The other symbols have the same meaning as those in Fig. 6B.

inside the z_1 resonance and at low values of proper e and $\sin(i)$. Vokrouhlický et al. (2006) hypothesized that those objects were former members of the Eos family that diffused to their current position due to the interplay of the Yarkovsky effect and the z_1 resonance. To investigate this hypothesis, they were observed by some of the Vokhrouhlický et al. (2006) authors so as to confirm their taxonomic compatibility with Eos family members[5]. We find that these four asteroids are identified as Eos members by the frequency method, thereby confirming the usefulness of performing an analysis of families in the frequency space.

We also identified the Eos family in the spaces of proper elements and colors (Eq. (4)) and of proper frequencies and colors (Eq. (5)). As the first member for the family, we chose the lowest numbered object in the dynamical family that was also present in the SDSS catalog: (320) Katharina (Carruba et al. 2007b). We repeated the analysis of the dependence of the number of families members on the cutoffs and we chose to work with a cutoff of 189 m/s (metric of colors and proper elements) and of 1.78 ″/yr (metric of colors and frequencies), respectively.

[5] The first three objects have a T spectral type and are compatible with Eos family membership, while the fourth was most likely an interloper.

While the family in the color and proper element space essentially follows the same orbital distribution of the family obtained with the classical approach, a very interesting result regarding the metric of colors and frequencies is that it recognizes objects that drifted in the z_1, $g - 2g_5 + 3g_6$ and $(s - s_6) - 2(g_5 - g_6)$ resonances toward lower values of proper $\sin(i)$ as family members.

Also, while the metric of color and frequencies identifies all features already identified by the frequency metric, the advantage of the frequency metric is that it is not limited to the asteroids currently present in the SDSS catalog, thereby identifying a larger number of family members than the metrics of color. It is evident in Fig. 7 that many objects identified by the frequency metric as family members were not in the SDSS catalog, and did not appear in the "color" families. We believe this argument clearly shows the advantage of frequency metrics: while some of the evolutionary features of asteroid families could be identified using methods already in the literature, such as the metric of Bus & Binzel (2002), only families obtained in frequency space can give a more complete picture of the family dynamical evolution. We clarify this point further with the analysis of the other three families we focused on.

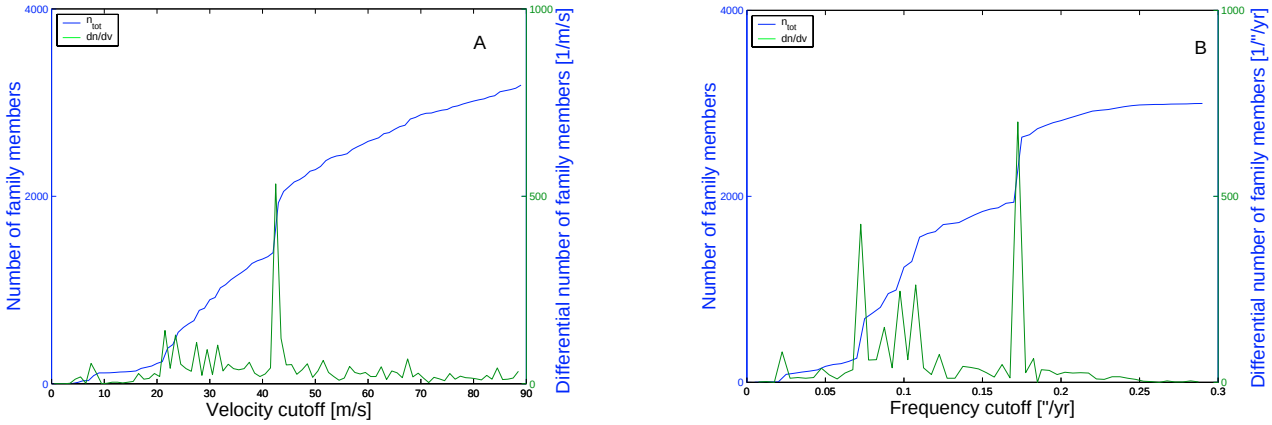

Fig. 8. The number of Koronis family members and the differential number as a function of the velocity (*left panel*) and frequency (*right panel*) cutoff.

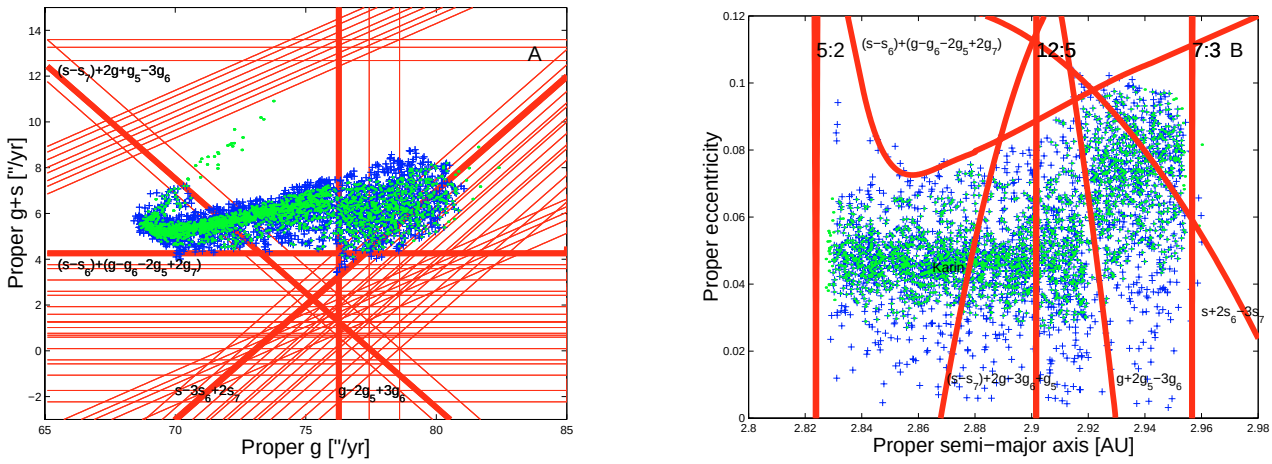

Fig. 9. A $(g, g+s)$ and $(a-e)$ projections of the Koronis family obtained with the classical HCM (green dots) and with the frequency HCM (blue crosses). The Karin cluster is shown at $a \simeq 2.865$ AU.

4.1.2. (158) Koronis

As for the Eos family, we start by identifying the Koronis family with the classical and the frequency metrics. Figure 8 displays the number of Koronis family members and the differential number as a function of the velocity (left panel) and frequency (right panel) cutoff. For $v_{\rm cutoff} = 43$ m/s, the family found with the classical method connects to the asteroids beyond the $g + 2g_5 - 3g_6$ secular resonance, as already found by Bottke et al. (2001), while the family connects to asteroids beyond the 7:3 mean-motion resonance with Jupiter for $v_{\rm cutoff} > 60$ m/s. To be consistent with the family used by Bottke et al. (2001), we choose a cutoff of 56 m/s. The right panel of Fig. 8 displays the number of Koronis family members as a function of the frequency cutoff. For $\nu_{\rm cutoff} = 0.075$ ″/yr, the first nucleus of the family is found. Around $\nu_{\rm cutoff} = 0.100$ ″/yr, a series of secondary features inside the Koronis families start to be identified, including the Karin cluster of Nesvorný and Bottke (2004). For $\nu_{\rm cutoff} = 0.175$ ″/yr, the family connects with asteroids beyond the $g + 2g_5 - 3g_6$ secular resonance, and the family is essentially saturated for values of $\nu_{\rm cutoff} > 0.250$ ″/yr, i.e., increasing the cutoff to values of $\nu_{\rm cutoff} = 0.300$ ″/yr only causes the family to grow by six new members. For this reason, we choose to work with the family defined by $\nu_{\rm cutoff} = 0.250$ ″/yr. The classical family so determined is in agreement with that found by Bottke et al. (2001).

The Koronis family is bounded by the 5:2 and 7:3 mean-motion resonances with Jupiter, is crossed by the 12:5 resonance, and has a strong interaction with the $g - 2g_5 + 3g_6$ secular resonance (Bottke et al. 2001). The most striking feature of the Koronis family is visible in a $a - e$ projection: asteroids beyond the $g - 2g_5 + 3g_6$ secular resonance have their eccentricity significantly enhanced by the passage through the resonance, thus giving the family a characteristic bi-modal shape (see Fig. 9; for brevity we do not show an $a - \sin(i)$ projection of this family).

We identified all nonlinear secular resonances up to order 8. We needed to go to a higher order to clarify what caused some of the observed features in the proper element distribution of the frequency family. Figure 9A displays the usual $(g, g+s)$ projection. Apart from the $g - 2g_5 + 3g_6$ secular resonance (and the usual harmonics involving combinations of g_5 and g_7), we identified three other resonances responsible for diffusing members of the family: the $s - 3s_6 + 2s_7$, the $(s-s_7) + 2g + g_5 - 3g_6$ and the $(s-s_6)+(g-g_6+2g_5-2g_7)$ resonances. The last one is a harmonic of the powerful z_1 secular resonance. Figure 9B displays an $a-e$ projection of the family, with the location of these resonances computed for the inclination of (158) Koronis. Asteroids that diffused to lower values of proper e did so mostly by interacting with the $g-2g_5+3g_6$ and $(s-s_7)+2g+g_5-3g_6$ secular resonances or their harmonics. The upper side of the frequency family appears to be nicely bounded by the $(s - s_6) + (g - g_6 + 2g_5 - 2g_7)$ secular resonances. It was already known that asteroid families

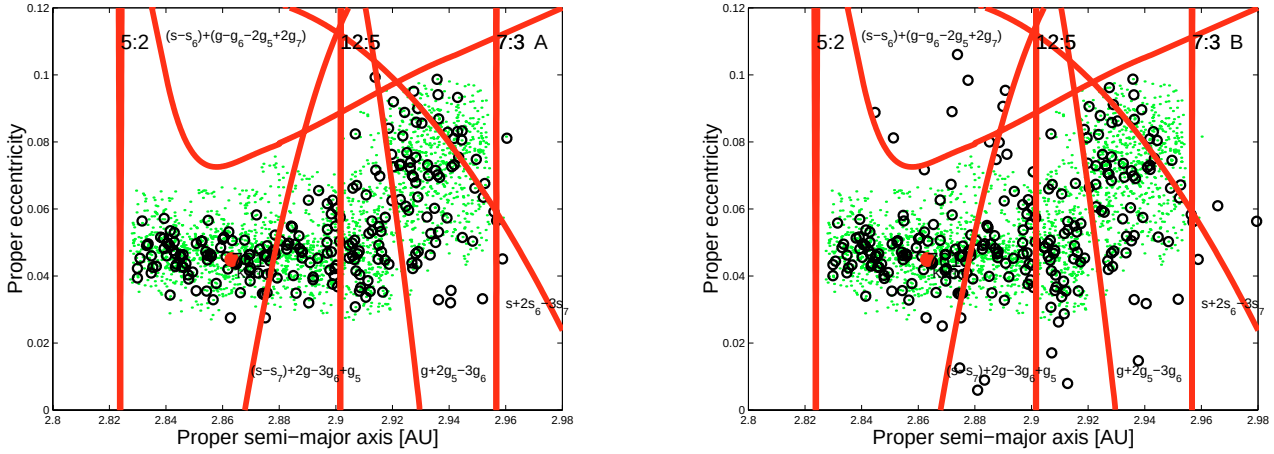

Fig. 10. An $a - \sin(i)$ projection of the members of the Koronis family found with the classical approach (green dots), with the metric of colors and proper elements (black circles, *left panel*), and with the metric of color and frequencies (black circles, *right panel*). The full large red dot displays the location of (761) Brendelia. The other symbols have the same meaning as those in Fig. 6B.

were bounded by mean-motion resonances; our results for the Koronis and for the Eunomia families suggest that asteroid families are also bounded by nonlinear secular resonances.

We also performed an analysis of the Koronis family with the color metrics. The metric of color and elements (Fig. 10, left panel) did not reveal new information. We chose the lowest numbered asteroid in the dynamical family that is also present in the SDSS catalog, (761) Brendelia, and determined the family for various values of the velocity cutoff. For a cutoff of 198 m/s, the family coalesced with the local background, and for lower cutoffs family members essentially followed the same $(a - e)$ distribution of the members of the Zappalà classical family.

Regarding the metric of color and frequencies, results confirm those of the metric of frequency. The family merged with the local background for a frequency cutoff of 1.82 ″/yr, so we chose to work with a cutoff of 1.78 ″/yr. Apart from a few objects at high eccentricity above the $(s - s_6) + (g - g_6 + 2g_5 - 2g_7)$ resonance not found with the frequency metric, all other objects were already present in the list found with Eq. (3).

4.2. The middle Belt

4.2.1. (15) Eunomia

The Eunomia family is one of the largest families in the middle belt. It is bounded on the right side by the 8:3 mean-motion resonance, but its limit on the left side is not so easily defined when the classical HCM is used. We applied both the classical and the frequency HCMs to this family. Figure 3 shows how the number of member varies as a function of the velocity cutoff, while Fig. 11 show the same as a function of the frequency cutoff. Finally, Fig. 12 displays $(g, g + s)$ and $(a - \sin(i))$ projection of the Eunomia family obtained with both methods.

As can be seen in Fig. 12, the frequency HCM manages to recognize asteroids that drifted in nonlinear secular resonances and that the classical HCM does not recognize as family members. In particular, the left side of the Eunomia family is now strongly bounded by the $(g-g_7)+2(s-s_6)$ (and $g-g_5)+2(s-s_6)$) resonances. Farther on the left, for lower values of a, the influence of the near 3:1 mean-motion resonance with Jupiter causes a sudden increase in the values of proper g (see Fig. 2), which also causes an overlap of several secular resonances such as the z_1, the $g - (2g_5 - g_6)$, etc. to occur. We believe that this might be

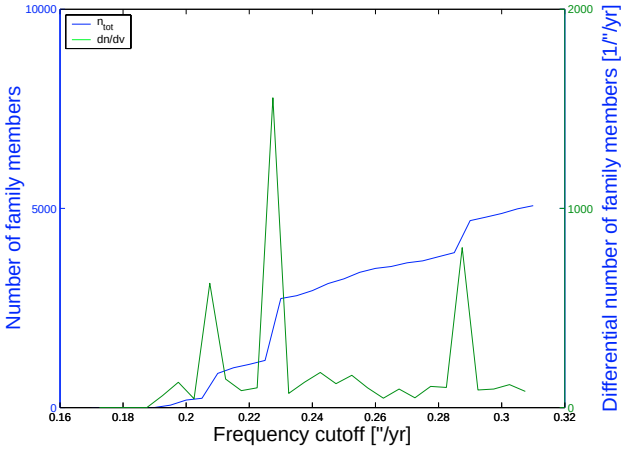

Fig. 11. The number of Eunomia family members (in blue) and the differential number of family members (in red) as a function of the frequency cutoff used in Eq. (3). For $f_{\rm cutoff}$ = 0.21 ″/yr, the first family members are found, while for $f_{\rm cutoff}$ = 0.310 ″/yr the family coalesces into the local background. The secondary peak at $f_{\rm cutoff}$ = 0.285 ″/yr is associated with the coalescence of secondary features inside the Eunomia family. In this work we use a frequency cutoff of 0.275 ″/yr.

one of the causes for the large-scale instabilities near the boundaries of the 3:1 resonance, which was first studied by Guillens et al. (2002).

The frequency HCM also allowed us to detect a tail of asteroids that drifted in the $(s - s_6) - (g_5 - g_6)$ resonance. Recently, Carruba et al. (2007b) has hypothesized that (21238) 1995 WV7 and (40521) 1999 RL95, two newly identified V-type objects (Hammergren et al. 2006; Roig et al. 2007) might be explained in the framework of migration from the near Eunomia family via Yarkovsky diffusion in secular resonances. While most of the members of the Eunomia family are S-type asteroids, it has been observed (Nathues et al. 2005) that (15) Eunomia is the remnant of a differentiated or partially differentiated body whose originally pyroxene-enriched crust layer was lost either in the collision that originated the Eunomia family or in a preceding collision (Carruba et al. 2007). We believe the presence of this tail of newly found Eunomia members in the $(s - s_6) - (g_5 - g_6)$

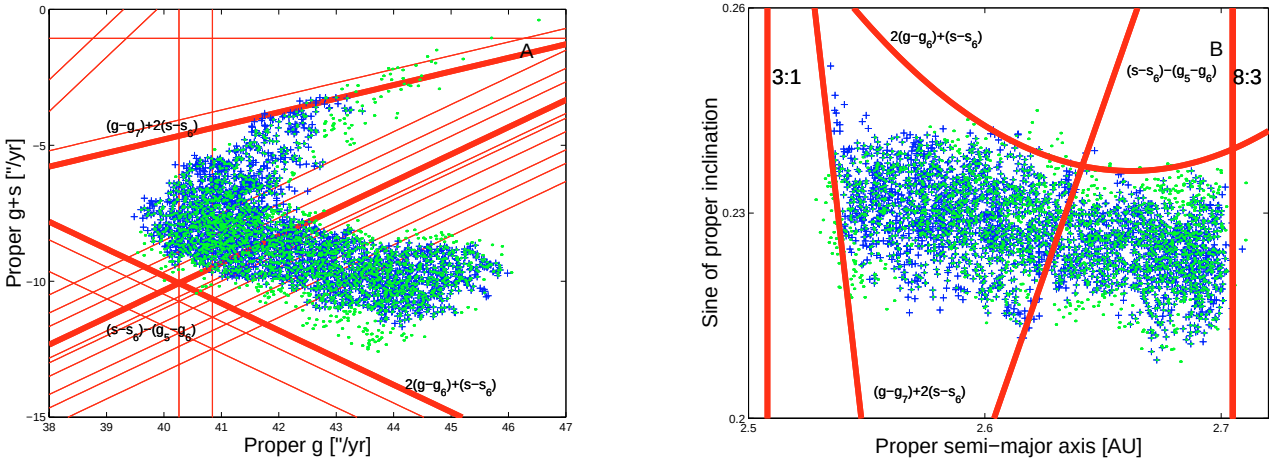

Fig. 12. A $(g, g + s)$, and $(a - i)$ projection of the Eunomia family obtained with the classical HCM (green dots) and of that obtained with the frequency HCM (blue crosses). Note that the objects that diffused in the secular resonances of perihelia and node, such as $(g - g_7) + 2(s - s_6)$, and of node, such as $(s - s_6) - (g_5 - g_6)$, are only identified by the frequency HCM as family members. The family is bounded by the 8:3 mean-motion resonance on the right and by the $(g - g_5) + 2(s - s_6)$ and $(g - g_7) + 2(s - s_6)$ resonances on the left.

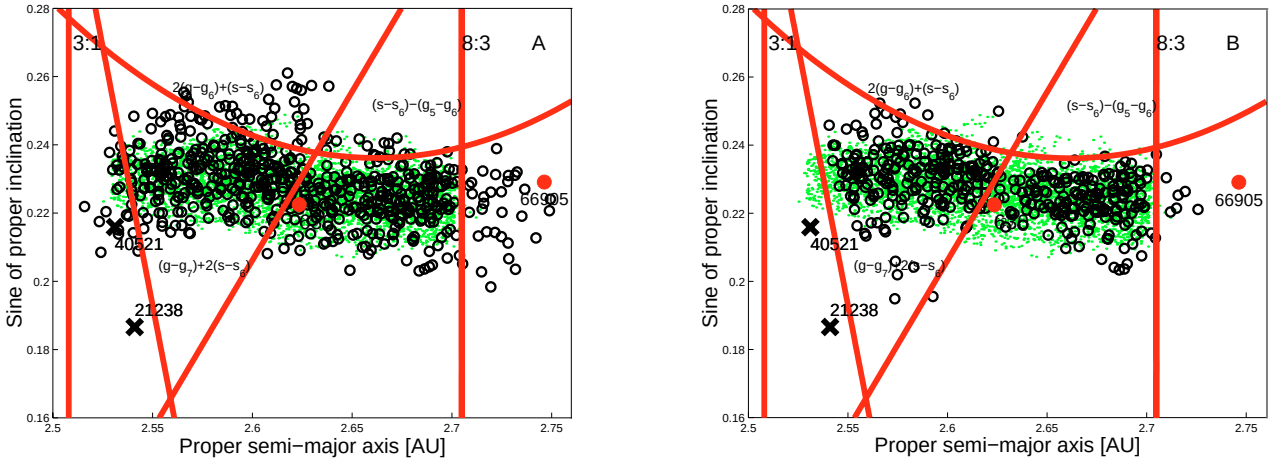

Fig. 13. The $a - i$ projection of (21238) and (40521) (black ×), and of a V-type candidate identified by Roig & Gil-Hutton (2006), (66905), large red dot, of members of the Eunomia dynamical family computed with a cutoff of 55 m/s (small green dots), and of members of the Eunomia family in the extended space of proper elements and colors, with a cutoff of 229 m/s (black circles, *left panel*). and of members of the family in the extended space of proper frequencies and colors, with a cutoff of 1.1 ″/yr (black circles, *right panel*). The full red dot at $a \simeq 2.62$ AU displays the location of (630) Euphemia. The other lines have the same meaning as in Fig. 12B.

resonance further confirms the hypothesis of (21238) 1995 WV7 being one of the last surviving fragments of the long-lost crust of the parent body of (15) Eunomia (Carruba et al. 2007).

Finally, the upper side of the Eunomia family seems to be defined by the influence of the strong z_2 $(2(g - g_6) + (s - s_6))$ resonance. The frequency HCM allowed us to detect a tail of asteroids that drifted in such resonance until reaching higher values of $\sin(i)$.

We also performed an analysis of the Eunomia family with the color metrics. We chose (630) Euphemia as the lowest numbered asteroid in the dynamical family also present in the SDSS catalog and determined the family with a velocity cutoff of 231 m/s and a frequency cutoff of 1.1 ″/yr (beyond that, the family coalesced with the nearby Maria family).

The family found with the metric of color and frequencies confirmed the important role played by the $(s - s_6) - (g_5 - g_6)$ resonance, as also found in Carruba et al. (2007). The metrics of color also identified a few objects that diffused in the z_2 resonance and were not found with other methods.

4.3. The inner belt

4.3.1. (4) Vesta

We start by determining the Vesta family with the classical and with the frequency approaches. Figure 14 shows the number and differential number of family members as a function of the velocity and frequency cutoffs.

The Vesta family in proper elements space coalesces with the background for a cutoff of 74 m/s and in frequency space for a frequency of 0.135 ″/yr. We therefore choose to use cutoffs of 68 m/s and of 0.134 ″/yr, respectively. As can be seen in Fig. 15, the frequency method does not connect asteroids to the family beyond values of $g \simeq 41.6$ ″/yr. This is due to the influence of the near 3:1 mean-motion resonance with Jupiter, which causes a steep increase in the variation of g with respect to n. We discuss a possible way to partially solve this problem in the Appendix B.

The next step is to determine the location of the main mean-motion resonances in the region. The Vesta family is bounded by the powerful 3:1 and 7:2 mean-motion resonances with Jupiter and is crossed by the 1:2 resonance with Mars. Among the

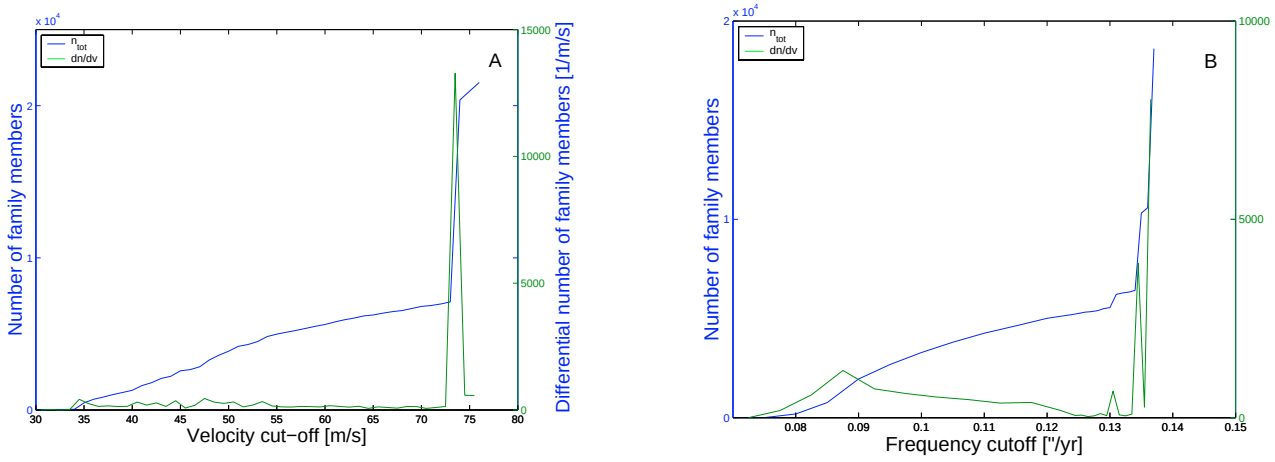

Fig. 14. The number of Vesta family members and the differential number as a function of the velocity (*left panel*) and frequency (*right panel*) cutoff.

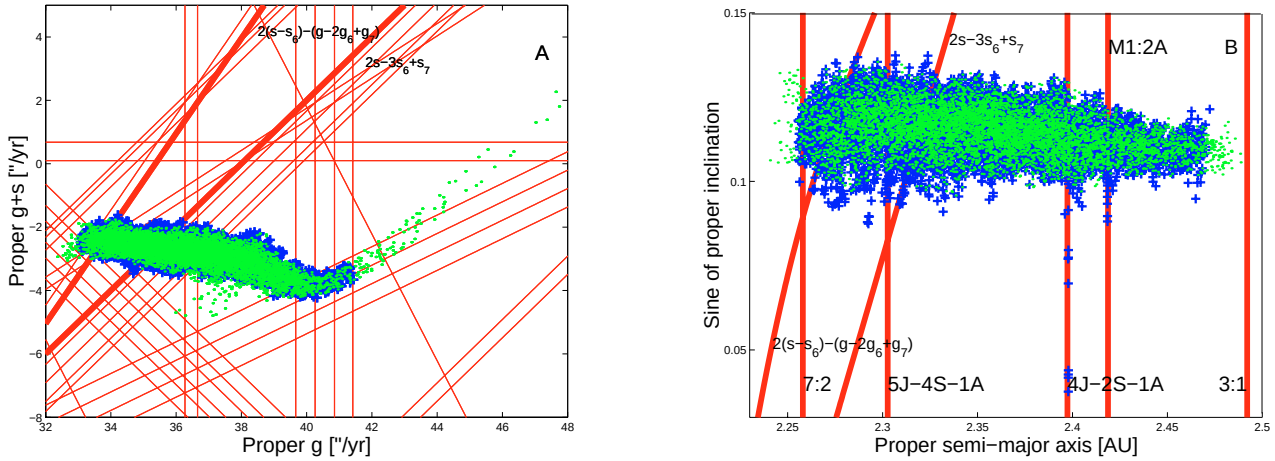

Fig. 15. A $(g, g + s)$ and $(a - \sin(i))$ projections of the Vesta family obtained with the classical HCM (green dots) and obtained with the frequency HCM (blue crosses).

three-body resonances, the 5J-4S-1A and the 4J-2S-1A are known to play significant dynamical roles (Carruba et al. 2005).

The role of secular resonances in the dynamics of members of the Vesta family is generally minor when compared to that of mean-motion resonances. Apart from two resonances, the $2s - 3s_6 + s_7$ and the $2(s - s_6) - (g - 2g_6 + g_7)$ and their harmonics involving the g_5 and g_7 frequencies, nonlinear secular resonances do not generally perturb the family members significantly. In this case, however, the frequency approach to family determination is very important for identifying the effect of diffusion via mean-motion resonances. The $a - \sin(i)$ projection of the Vesta classical and frequency families displayed in the right panel of Fig. 15 shows how the frequency approach was able to identify objects that migrated in the $4J-2S-1A$ and the $1M:2A$ mean-motion resonances toward lower values of proper $\sin(i)$ as family members. Since most of the V-type asteroids (asteroids with the same spectral type of most of the Vesta family members for which a spectral classification is available) outside the Vesta family are actually found at lower values of proper $\sin(i)$ than the family, we believe our method provides a possible explanation for the origin of some of these objects, without the need to perform a time-costly simulation with symplectic integrators.

Also, we found that the family obtained in the frequency space includes three of the V-type asteroids outside the classical family (3536) Schleicher, (4977) Rauthgundis, and (7148) Reinholdbien), and ten objects identified by Roig and Gil-Hutton (2006) as having SDSS albedos compatible with a V-type spectral classification: (6563) Steinheim, (7484) Dogo Onsen, (14323) 1979 MV1, (19809) Nancyowen, (35718) 1999 FE34, (53950) 2000 GX56, (56381) 2000 EN43, (61068) 2000 LR6, (64311) 2001 UQ32, and (103401) 2000 AW130. We believe that the fact that our approach to family determination detects fugitives from asteroid families directly is an important validation of our method.

We also performed an analysis of the Vesta family with the color metrics. We pick (1979) Sakharov as the lowest numbered asteroid in the dynamical family also present in the SDSS catalog, and determine the family for various values of the velocity and frequency cutoffs. We chose to work with a velocity cutoff of 217 m/s and with a frequency cutoff of 0.86 ″/yr. The families coalesced with the local background for cutoffs of 218 m/s and 0.87 ″/yr, respectively.

Apart from a few isolated objects, mostly beyond the 7:2 resonance and along the 5J-4S-1A, the metrics of colors did not provide any significant new information on the orbital diffusion of Vesta family members. It is interesting to notice that the families in frequency space coalesced with the background mostly at values of low sin(i) ($\sin(i) < 0.1$) and low $a < 2.3$ AU, following the two strong secular resonances in the region $(2s - 3s_6 + s_7$ and $2(s - s_6) - (g - 2g_6 + g_7))$.

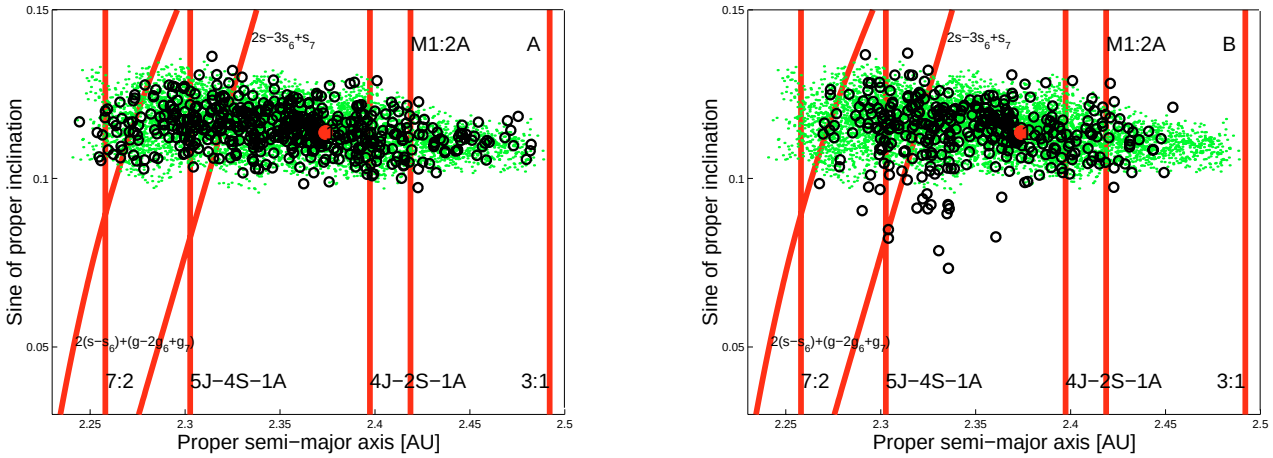

Fig. 16. An $a - \sin(i)$ projection of the members of the Vesta family found with the classical approach (green dots), with the metric of colors and proper elements (black circles, *left panel*), and with the metric of color and frequencies, (black circles, *right panel*). The full large red dot displays the location of (1979) Sakharov. The other symbols have the same meaning as in Fig. 6B.

5. Conclusions

In this work we obtained asteroid families from a different perspective than the one used traditionally. Since several papers in the last years have shown the importance that secular resonances have played in shaping the orbits of members of asteroid families, we decided to analyze asteroid families in proper frequency space, where the complicated three-dimensional structure of secular resonances may be more easily represented. For this purpose, we did the following:

- We introduced a distance metric in the proper frequency space $(n, g, g + s)$.
- Following the approach of Bus & Binzel (2002), we extended the metric of asteroid colors and proper elements to the frequency space.
- We applied the new approaches to identifying members of four of the largest asteroid families in the inner, middle, and outer belt namely Vesta, Eunomia, Eos, and Koronis.

One benefit of analyzing the dynamics in the $g, g + s$ plane is that secular resonances are very easily represented as lines in this plane, in contrast to the complicated three-dimensional structure that such resonances have in the $a, e, \sin(i)$ space. This makes this plane ideal for understanding the dynamical effects that secular resonances have produced on asteroid families.

The most striking result we obtained regards what Bus and Binzel (2002) defines as "halo objects", i.e., objects on the boundaries of the families that were not connected with the Zappalà (1990, 1994) approach. The hierarchical clustering method in frequency space is a very efficient way to identify family members that migrated because of the interplay between the Yarkovsky effect and nonlinear secular resonances. Our analysis of the four asteroid families has confirmed results obtained previously through numerical simulations with symplectic integrators that included the Yarkovsky effect and, in some case, discovered new possible paths of migration. By identifying "halo objects", we believe that our method may be very useful for identifying possible targets for observational campaigns. Also, simulations with symplectic integrators to account for the diffusion of such objects may provide limits on asteroid families' ages (see also Carruba et al. 2005, 2007a,b).

Another interesting result regards the family boundaries. It was already known that asteroid families were bounded by powerful mean-motion resonances, but our analysis showed they are also bound by secular resonances such as the z_2 resonance for the Eunomia family and a harmonic of the z_1 resonance (the $(s - s_6) + (g - g_6 - 2g_5 + 2g_7)$ for the Koronis family. Also, the fact that in the region near powerful mean-motion resonances, such as the 2:1 and the 3:1, the values of g suffer a steep increase produces an overlapping of secular resonances in these regions. We believe this may be one of the causes of the instability of orbits observed by Guillens et al. (2002) in the proximity of the 3:1 resonance.

The steep behavior of g (and, in a less measure, of s) in these regions also causes a limitation to our approach. Our metric fails to connect objects near powerful mean-motion resonances. We show that other approaches, such as the metrics of frequencies and proper elements described in the Appendix B, may partially solve this problem, but at the price of losing objects that drifted far in secular or mean-motion resonances. Since, in this work, we were mostly interested in determining possible migration paths away from asteroid families, we only concentrated on the use of the metric of frequencies.

To conclude, while numerical simulations will always be needed to confirm the viability of the evolution of asteroids drifting away from families (Carruba et al. 2007b), we believe that the new approach to asteroid family identification provides a fast way to hypothesize about the diffusion mechanisms of former asteroid families' members. We consider this to be the major new result of this work.

Appendix A: The Zappalà metrics

The metrics described in Eq. (2) was originally devised by Zappalà et al. (1990) in order to most accurately preserve the alleged pristine ejection velocity field of asteroid families. At the time, it was believed that the current proper orbital element distribution of asteroid families reflected the ejection velocity field formed at the time of the catastrophic disruption of asteroid families.

Following Brouwer (1951) and Zappalà et al. (1984), if we neglect terms proportional to the eccentricity, the following relationship between change in proper elements and velocity at infinity holds:

$$2\Delta V_N/na = \Delta a/a,$$

$$\Delta V_R \sin(f)/na + 2\Delta V_N \cos(f)/na = \Delta e,$$

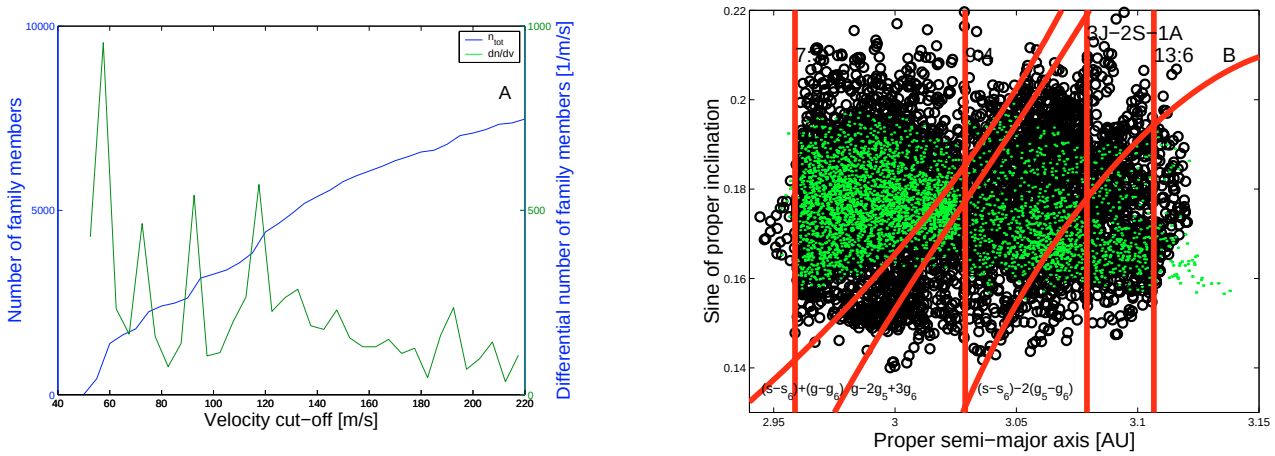

Fig. B.1. *Left panel*: the number and differential number of the Eos family found with the metric of proper elements and frequencies (Eq. (11)) as a function of the velocity cutoff. In the right panel we show an a – sin(i) projection of the members of the Eos family found with the classical approach (green dots), and with the metric of proper elements and frequencies (black circles).

$$\Delta V_W \cos(\omega + f)/na = \Delta i, \quad (6)$$

where a, e, i, ω, and f are the osculating semi-major axis, eccentricity, inclination, argument of perihelion, and true anomaly of the parent body, V_N, V_R, V_W are the components if the velocity at infinity in the along-track, radial, and out-of-plane directions, respectively (the other quantities have the same meaning as in Eq. (2)).

Even with f and $\omega + f$ unknown, if we choose a distance function in the proper element space in the form

$$\Delta V = na\sqrt{k_1(\Delta a/a)^2 + k_2(\Delta e)^2 + k_3(\Delta i)^2}, \quad (7)$$

with coefficients k_1, k_2, k_3 of order unity, the metric will give an order of magnitude estimate of the velocity increase causing separation of the two orbits.

By squaring Eq. (6), averaging over f and $f + \omega$, and then substituting in the Δ elements, Zappalà et al. (1990) obtained

$$\Delta v = \sqrt{x\langle\Delta V_N{}^2\rangle + y\langle\Delta V_R{}^2\rangle + z\langle\Delta V_W{}^2\rangle}, \quad (8)$$

with

$$x = (4k_1 + 2k_2), y = k_2/2, z = k_3/2. \quad (9)$$

As the authors noticed, there was no choice for the k_i (i = 1,2,3) coefficient that yielded $x = y = z = 1$. The choice of $k_1 = 5/4$, $k_2 = 2$, $k_3 = 2$ was made to give a greater weight to the ΔV_N component, and therefore to the proper semi-major axes that were known with higher accuracy than proper eccentricities and inclinations.

Appendix B: A metric of proper elements and frequencies

As discussed in Sect. 3.2, the frequency metric may fail to connect to the bulk of the family asteroid near very powerful mean-motion resonances. Recently, Nesvorný et al. (2006) and Nesvorný and Vokrouhlický (2006) have introduced a five dimensional metric to investigate the database of asteroid osculating orbital elements in order to identify very recent asteroid families. In their work, the authors used a metric of the form:

$$\left(\frac{d}{na}\right)^2 = k_1\left(\frac{\Delta a}{a}\right)^2 + k_2(\Delta e)^2 + k_3(\Delta\sin(i))^2 + k_\Omega(\Delta\Omega)^2 + k_\varpi(\Delta\varpi)^2, \quad (10)$$

where $\Delta\Omega$, $\Delta\varpi$ are the asteroid separations in longitude of the node and pericenter, respectively, and $k_\Omega = k_\varpi$ are factors ranging from 10^{-4} to 10^{-7} (the other symbols have the same meaning as in Eq. (2)). The authors used $k_\Omega = k_\varpi$ because the secular precession rates of Ω and ϖ are comparable across the main belt (Brouwer & Clemence 1961).

Following this example, to solve some of the shortcomings of a pure frequencies' metric, we introduced an extended metric of the form:

$$\left(\frac{d}{na}\right)^2 = k_1\left(\frac{\Delta a}{a}\right)^2 + k_2(\Delta e)^2 + k_3(\Delta\sin(i))^2 + k_{gs}((\Delta g)^2 + (\Delta s)^2), \quad (11)$$

with k_{gs} a factor going from 10^{-3} to 10^{-5}, with the best result given by $k_{gs} = 10^{-4}$. We applied this metric to the two families that are close to the 2:1 and 3:1 mean-motion resonances, and presented the problems related to the very steep increase in g near such resonances, when the frequency metric was applied: Eos and Vesta. Other approaches that we tried, such as metrics with logarithms of the distances in frequencies or metrics with normalized distances in frequencies (of the form $2(g_1 - g_2)/(g_1 + g_2)$, for example) did not produced satisfactory results. Generally, they produced families that rapidly coalesced into the local background.

Figure B.1 displays the number and differential number of Eos family members as a function of the velocity cutoff (left panel) and a a – sin(i) projection of the family. For $v_{\rm cutoff}$ = 190 m/s the Eos family coalesced with near families, so we choose to work with a cutoff of 185 m/s. The metric of color and frequencies identified almost all asteroids with a beyond the 13:6 mean-motion resonance with Jupiter and was able to catch most of the family members found by the metric of frequency. It did however failed to identify members at very low and very high sin(i) that drifted in one of the harmonics of the $(s - s_6) - 2(g_5 - g_6)$. While very minor for the Eos family, this is an effect that has been observed in higher proportions in other families, like the Vesta one.

Figure B.2 displays the number and differential number of Vesta family members as a function of the velocity cutoff (left panel) and a a – sin(i) projection of the family. We choose to work with a cutoff of 85 m/s, just below the value for which the family coalesced into the background.

As can be seen in the right panel of Fig. B.2, the metric of proper elements and frequencies actually did connected

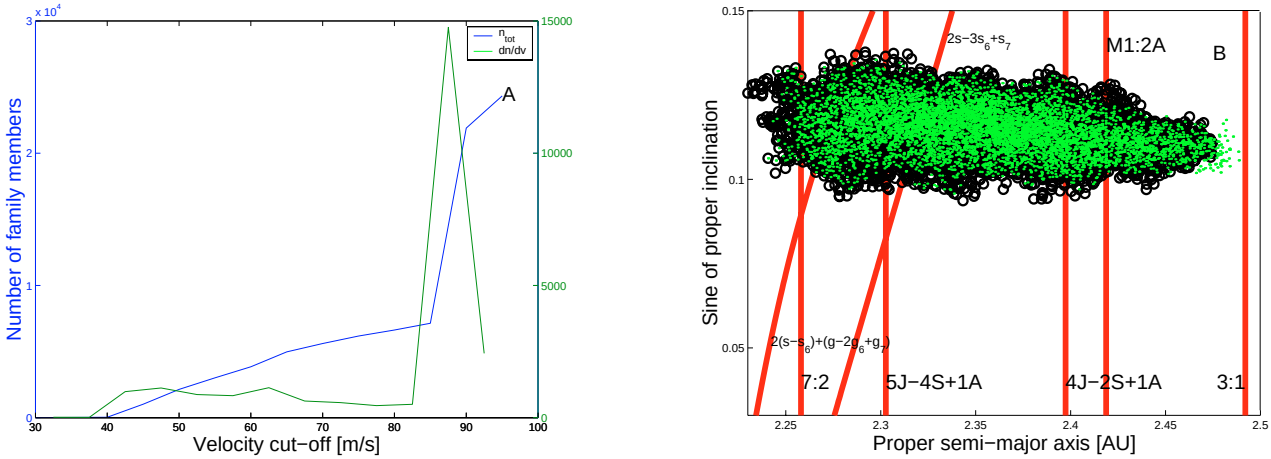

Fig. B.2. *Left panel*: the number and differential number of the Vesta family found with the metric of proper elements and frequencies (Eq. (11)) as a function of the velocity cutoff. In the right panel we show an $a - \sin(i)$ projection of the members of the Vesta family found with the classical approach (green dots) and with the metric of proper elements and frequencies (black circles).

almost all asteroids up to the neighborhood of the 3:1 resonance. But this was achieved at the cost of losing the asteroids found by the metric of frequencies, which migrated at lower values of proper $\sin(i)$, via the $2s - 3s_6 + s_7$ secular resonance, possibly the $4J - 2S - 1A$ three-body resonance, and other resonances (see Fig. 15B). Since in this work we were mostly interested in determining possible migration paths from asteroid families, we decided to mostly use the metric of frequencies and to accept its limitations near powerful mean-motion resonances.

Acknowledgements. We are grateful to David Vokrouhlický for his careful revision of our paper and for various helpful hints and suggestions. The authors would also like to thank the São Paulo State Science Foundation (FAPESP) and the Brazilian Research Council (CNPq), which supported this work via diverse grants and fellowships. The codes used for family determination are available upon request to the first author.

References

Bendjoya, P., & Zappalà, V. 2002, Asteroids III (Tucson: Univ. of Arizona Press), 613
Bottke, W. F., Vokrouhlický, D., Brož, M., Nesvorný, D., & Morbidelli, A. 2001, Science, 294, 1693
Bowell, E., Muinonen, K., & Wasserman, L. H. 1994, Asteroids III (Tucson: Univ. of Arizona Press), 477
Brouwer, D. 1951, Astron. J. 56, 9
Brouwer, D., & Clemence, G. M. 1961, Methods of Celestial Mechanics (New York: Academic)
Bus, J. S., & Binzel, R. P. 2002a, Icarus, 158, 106
Bus, J. S., & Binzel, R. P. 2002b, Icarus, 158, 146
Carruba, V., Burns, J., Ćuk, A., Bottke, W., & Nesvorný, D. 2003, Icarus, 162, 308
Carruba, V., Nesvorný, D., Burns, J. A., Ćuk, M., & Tsiganis, K. 2004, AJ, 128, 1899
Carruba, V., Michtchenko, T., Roig, F., Ferraz-Mello, S., & Nesvorný, D. 2005, A&A 441, 819
Carruba, V., Roig, F., Michtchenko, T., Ferraz-Mello, S., & Nesvorný, D. 2007a, A&A, 465, 315
Carruba, V., Michtchenko, T., & Lazzaro, D. 2007b, A&A, 473, 967
Ferraz-Mello, S. 2007, Canonical Perturbation Theories, Degenerate Systems and Resonances, ed. W. B. Burton, et al. (New York: Springer), 345, 88
Fukugita, M., Ichikawa, T., Gunn, J. E., et al. 1996, AJ, 111, 1748
Gladman, B. J., Migliorini, F., Morbidelli, A., et al. 1997, Science, 277, 197
Guillens, S.A., Vieira Martins, R., & Gomes, R. S. 2002, AJ, 124, 2322
Hammergren, M., Gyuk, G., & Puckett, A. 2006 [arXiv:astro-ph/0609420]
Hirayama, K. 1918, Astron. J. 31, 185
Ivezić Z., and 32 colleagues 2001, AJ, 122, 2749
Jurić M., and 15 colleagues 2002, AJ, 124, 1776
Knežević, Z., Milani, A., Farinella, P., Froeschlé Ch., & Froeschlé, C. 1991, Icarus, 93, 316
Knežević, Z., & Milani, A. 2000, Celest. Mech. Dyn. Astron., 78, 17
Milani, A., & Nobili, A. M. 1984, Nature 310, 753
Milani, A., & Knežević, Z. 1992, Icarus 98, 211
Milani, A., & Knežević, Z. 1994, Icarus 107, 219
Milani, A., & Knežević, Z. 2003, A&A 403, 1165
Nathues A., Mottola, S., Kaasalainen M., & Neukum, G. 2005, Icarus, 175, 452
Nesvorný, D., & Bottke, W., 2004, Icarus, 170, 324
Nesvorný, D., & Vokrouhlický, D. 2006, AJ, 132, 1950
Nesvorný, D., Jedicke, R., Whiteley, R. J., & Ivezić, Z. 2005, Icarus, 173, 132
Nesvorný, D., Vokrouhlický, D., & Bottke, W. F. 2006, Science, 312, 1490
O'Brien, D. P., & Greenberg, R. 2005, Icarus, 178, 179
Roig, F., & Gil-Hutton, R. 2006, Icarus, 183, 411
Roig, F., Nesvorný, D., Gil-Hutton, R., & Lazzaro, D. 2007, [arXiv:astro-ph/0707.1012]
Vokrouhlický D. 1999, A&A, 344, 362
Vokrouhlický D., & Brož, M. 2002, Modern Celestial Mechanics: from Theory to Applications, 467
Vokrouhlický D., & Čapek, D. 2002, Icarus, 159, 449
Vokrouhlický D., Brož, M., Morbidelli, A., et al. 2006a, Icarus, 182, 92
Vokrouhlický D., Brož, M., Bottke, W. F., Nesvorný, & Morbidelli, A. 2006b, Icarus, 183, 349
Zappalà V., Farinella, P., Knežević, Z., & Paolicchi, P. 1984, Icarus, 59, 261
Zappalà V., Cellino, A., Farinella, P., & Knežević, Z. 1990, AJ, 100, 2030
Zappalà, V., Bendjoya, Ph., Cellino, A., Farinella, P., & Froeschlè, C. 1995, Icarus, 116, 291

3

Famílias de asteroides em outros espaços de frequências

Em Carruba e Michtchenko (2007) introduzimos um novo método para a identificação de famílias no espaço das frequências próprias $(n, g, g + s)$. Este espaço, ideal para analizar ressonância lineares de pericentro (ou de tipo g, como a ressonância $\nu_6 = g - g_6$), e ressonâncias envolvendo combinações de frequências do tipo $g+s$, como a ressonância $z_1 = g-g_6+s-s_6$, não é o mais indicado para estudar outros tipos de ressonâncias. Por exemplo, a ressonância $\nu_{16} = s-s_6$ seria melhor representada no espaço (n, g, s), onde apareceria como uma linha horizontal, que no espaço $(n, g, g+s)$. Em Carruba e Michtchenko (2009) introduzimos novas métricas de distância óptimais para estudar ressonâncias dos tipos $2g-s, 3g-s, g-s, s$, and $2s$, e técnicas para regularizar a dependencia da frequencia g com respeito à frequencia n em proximidade de ressonâncias de movimento médio poderosas como a 3J:-1A. Estes novos métodos permitiram obter uma melhor representação da evolução de asteroides neste tipo de ressonâncias seculares, e permitiram identificar uma fração maior de asteroides ressonântes como membros das respetivas famílias.

A seguir apresentamos o artigo, que foi publicado em Astronomy and Astrophysics em 2009, volume 493, pp. 267-282.

A&A 493, 267–282 (2009)
DOI: 10.1051/0004-6361:200809852

Astronomy & Astrophysics

A frequency approach to identifying asteroid families

II. Families interacting with nonlinear secular resonances and low-order mean-motion resonances

V. Carruba[1] and T. A. Michtchenko[2]

[1] IPD, UNIVAP, São José dos Campos, SP, 12244-000, Brazil
e-mail: valerio@univap.br
[2] IAG, Universidade de São Paulo, São Paulo, 05508-900, Brazil
e-mail: tatiana@astro.iag.usp.br

Received 26 March 2008 / Accepted 18 September 2008

ABSTRACT

Aims. In an earlier paper we introduced a new method for determining asteroid families where families were identified in the proper frequency domain $(n, g, g+s)$ (where n is the mean-motion, and g and s are the secular frequencies of the longitude of pericenter and nodes, respectively), rather than in the proper element domain $(a, e, \sin(i))$ (semi-major axis, eccentricity, and inclination). Here we improve our techniques for reliably identifying members of families that interact with nonlinear secular resonances of argument other than g or $g+s$ and for asteroids near or in mean-motion resonant configurations.
Methods. We introduce several new distance metrics in the frequency space optimal for determining the diffusion in secular resonances of argument $2g-s$, $3g-s$, $g-s$, s, and $2s$. We also regularize the dependence of the g frequency as a function of the n frequency (Vesta family) or of the eccentricity e (Hansa family).
Results. Our new approaches allow us to recognize as family members objects that were lost with previous methods, while keeping the advantages of the Carruba & Michtchenko (2007, A&A, 475, 1145) approach. More important, an analysis in the frequency domain permits a deeper understanding of the dynamical evolution of asteroid families not always obtainable with an analysis in the proper element domain.

Key words. minor planets, asteroids – celestial mechanics

1. Introduction

In Carruba & Michtchenko (2007) we proposed an alternative approach to the classical Hierarchical Clustering Method (CHCM hereafter) to identifying asteroid families (Zappalà et al. 1990): rather than looking for clusters in the proper elements $(a-e-\sin(i))$ space (semi-major axis, eccentricity and inclination), we searched for families in the space of proper frequencies $(n, g, g+s)$ (where n is the asteroid mean-motion and g and s are the asteroid secular frequencies of the pericenter and node, respectively).

The advantages of this approach were numerous, among these: i) secular resonances are more easily identified in the $(n, g, g+s)$ plane, where they are separable, in contrast with the complicated three-dimensional structure that such resonances have in the $(a, e, \sin(i))$ space; ii) the hierarchical clustering method in the frequency domain (FHCM, hereafter) is a very efficient way to identify family members that diffused because of the interplay of the Yarkovsky and YORP effects and nonlinear secular resonances; and iii) our analysis showed that asteroids families are also bound by secular resonances such as the z_2 resonance for the Eunomia family, and a harmonic of the z_1 resonance (the $(s-s_6)+(g-g_6-2g_5+2g_7)$ resonance) for the Koronis family.

The Carruba & Michtchenko (2007) approach had however some limitations: i) the $(n.g, g+s)$ domain was ideal for studying families interacting with resonances involving the g or the $g+s$ frequencies, but was not the most efficient space to display the effect of resonances involving other combination of frequencies, such as the $k(g-g_6)+(s-s_6)$ resonances (z_k in the notation of Milani & Knežević 1994) for $k>1$, the $g-g_6-s-s_6$ resonance, or resonances of node of argument s or $2s$, and ii) the frequency of the pericenter precession g may not follow a linear trend as a function of n near low-order mean-motion resonances or may be negative (or retrograde) for asteroid locked in mean-motion resonant configuration.

In this work we extend our investigation of families in the frequency domain to these cases. In the first part of the article we investigate the case of families interacting with nonlinear secular resonances of arguments other than g and $g+s$. For this purpose, we introduce new appropiate representative planes and distance metrics that are more efficient to study the process of diffusion in such resonances. Our results show that these new metrics are in general up to 77% more efficient than either the classical approach or the "standard" metric in the $(n, g, g+s)$ domain in identifying asteroids that diffused in such secular resonances as family members.

In the second part of our article we study the region near low-order mean-motion resonances, which is quite interesting from a dynamical point of view. Because of the steep behavior of the g frequencies many nonlinear secular resonances overlap in the region. Understanding how to connect fugitives to their original dynamical family in this region could therefore be a quite interesting and important task. For this purpose we introduce a regularization procedure that allows us to extend families in regions where the behavior of the g frequency is not linear as a function of n. Our method allows us to identify as family members objects that drifted in the $g+g_5-2g_6$ and $2g+g_5-3g_6$ and that were not recognizable with other approaches. Finally, we consider the case of resonant asteroids, characterized by a retrograde frequency of pericenter precession g, such as the Hildas and some of the members of the Hansa family.

Article published by EDP Sciences

Our results show that it is possible to extend the family determination method in the frequency space to regions that were not covered by the Carruba & Michtchenko (2007) approach, while preserving all the advantages of this method. We will start by introducing numerical tools that will be useful to classify the nonlinear secular resonance that we are studying and to quantify the efficiency of our methods in identifying as family members objects that drifted in non linear secular resonances.

2. Families interacting with nonlinear secular resonances of arguments other than $g + s$

In this section we will discuss the case of families interacting with nonlinear secular resonances of argument other than $g + s$. Secular resonances involve commensurabilities between the secular frequencies of precession of the pericenter g or of the node s of the asteroid and of the planets. Linear secular resonances are direct equalities between the frequency of the asteroid and that of the planet. Very strong linear resonances of order 2 are the pericenter resonances $\nu_5 = g - g_5$, $\nu_6 = g - g_6$, and $\nu_7 = g - g_7$, and the node resonances $\nu_{16} = s - s_6$, $\nu_{17} = s - s_7$ (Williams & Faulkner 1981; Milani & Knežević 1994). Nonlinear secular resonances are commensurabilities of secular frequencies of higher order. The most accurate way to represent these resonances is in term of combinations of the linear resonances, so that the $2(g - g_6) + s - s_6$ resonant argument (or z_2, in the notation of Milani & Knežević 1994) becomes $2\nu_6 + \nu_{16}$, or that $2g + g_5 - 3g_6$ becomes $3\nu_6 - \nu_5$ (Michtchenko et al. 2008). Expressed in these terms, it becomes clearer why some resonances such as the z_2 have a stronger dynamical effect than other resonances of the same order that are higher order combination of the linear secular resonances. In this paper, however, we are interested in identifying families in the space of proper frequencies, and for this purpose it is easier to classify families in terms of the g and s frequencies. We will therefore still first give the name of the resonance as a function of g and s, and then provide the classification in terms of the linear resonances.

For the purpose of family identification, as in Carruba & Michtchenko (2007), we used a catalog of 172 043 synthetic proper elements and frequencies obtained numerically and publically available at the AstDys site, accessed on May 25th 2008. Families in the domain of proper elements are obtained with the standard metric of Zappalà et al. (1990, 1995), while families in the domain of proper frequencies were mostly obtained with the standard metric in the $(n, g, g + s)$ domain (Carruba & Michtchenko 2007, Eq. (3)). To obtain families interacting with resonances of argument other than $g + s$ we introduced a series of alternative distance metric in the $(n, g, 2g + s)$, $(n, g, 3g + s)$, $(n, g, g - s)$, (n, g, s), $(n, g, 2s)$ domains.

To compare the efficiency with which the new distance metrics connect objects in the nonlinear secular resonances with respect to the previous methods we introduce the following procedure.

1. We delimit a local background around the asteroid families under study. Morbidelli et al. (2003) define the local background limits via these equations:

$$\sin(i_{\min}) - 0.03 < \sin(i) < \sin(i_{\max}) + 0.03 \quad (1)$$

$$q_{\min} - 0.1 < q < q_{\max} + 0.1 \quad (2)$$

$$a_{\min} - 0.05 < a < a_{\max} + 0.05, \quad (3)$$

where the minimal and maximal values of i, q (pericenter distance), and a refer to the observed extreme values of the asteroid families. Table 3 reports the values of a, e, and $\sin(i)$ for the families that we studied in this paper. We defined the minimal and maximal value of e as the extreme values in the sample obtained with Eqs. (1)–(3).
2. We computed the number of objects in the local background currently inside the resonance of interest. We define the efficiency of our metrics in connecting these object to the family as the fraction of family members inside the resonance compared to the total number of object in the resonance in the local background.

We will discuss the efficiency of the new distance metrics in more detail in each of the next subsections. Here we just want to clarify that, by efficiency of our distance metrics, we just intend the ability of the new metrics to connect objects inside secular resonances to the asteroid family under study. As discussed in the first paper, the potential membership in a family of the asteroid so identified needs to be confirmed by an analysis of its size, and spectral type. Also the actual possibility of migration on timescales comparable to the estimated age of the family needs to be tested via numerical integration.

Finally, previous works (Zappalà et al. 1990, 1995) displayed (a, e), $(a, \sin(i))$, $(e, \sin(i))$, projections of asteroids in the local background of asteroid families. The number of asteroids in these projections furnished information on the local density of asteroids, and, indirectly, on the local dynamics (regions dynamically unstable because of the effect of mean-motion or secular resonances appeared locally deprieved of asteroids). The number of objects with known proper elements has however improved dramatically since the 90's, and directly plotting the position of asteroids in the local background may result in figures visually saturated. To overcome this problem and to quantitatively determine the local density of asteroids in the local background we computed the number of asteroids in grids of proper elements and frequencies. Following the approach of Michtchenko et al. (2008), we used steps of 0.008 AU in a, 0.008 in e, and 0.008 in $\sin(i)$. To eliminate the problems associated with projecting three-dimensional structure in 2D planes, binning and other effects that may introduce distortions in the density maps we also applied a median filter (Carruba et al. 2004, Appendix 1) to the density maps so obtained. The procedure was repeated until the percentage difference between the number of asteroids before and after the application of the median filter was less than 5%. We then plotted the color plot of the $\log_{10}$ of the number of asteroids per unit bin in the interval (0, 2.5) in each of the figures where we projected the asteroid families. We believe that this method allow us to keep the benefits of the old projection method of Zappalà et al. (1995), but extended for the much more numerous database of proper elements currently available.

Having introduced these tools, we start our discussion by considering families interacting with resonances of argument $2g + s$ (z_2-resonances).

2.1. 2g + s resonances

The series of the z_k (or $k \cdot \nu_6 + \nu_{16}$, where k is a small integer) resonances and its interaction with the Yarkovsky and YORP effects has been the subject of several recent studies (Vokrouhlický et al. 2006a,b,c; Carruba et al. 2005, 2007, among others). In Carruba & Michtchenko (2007) we concentrated our attention on the z_1 resonance (and its harmonics involving the g_7 frequency), of argument $g + s$. Here we extend our work by analyzing families that interact with the z_2 and z_3 (see next section) resonance. The z_2 and z_3 resonances are found in regions near the powerful

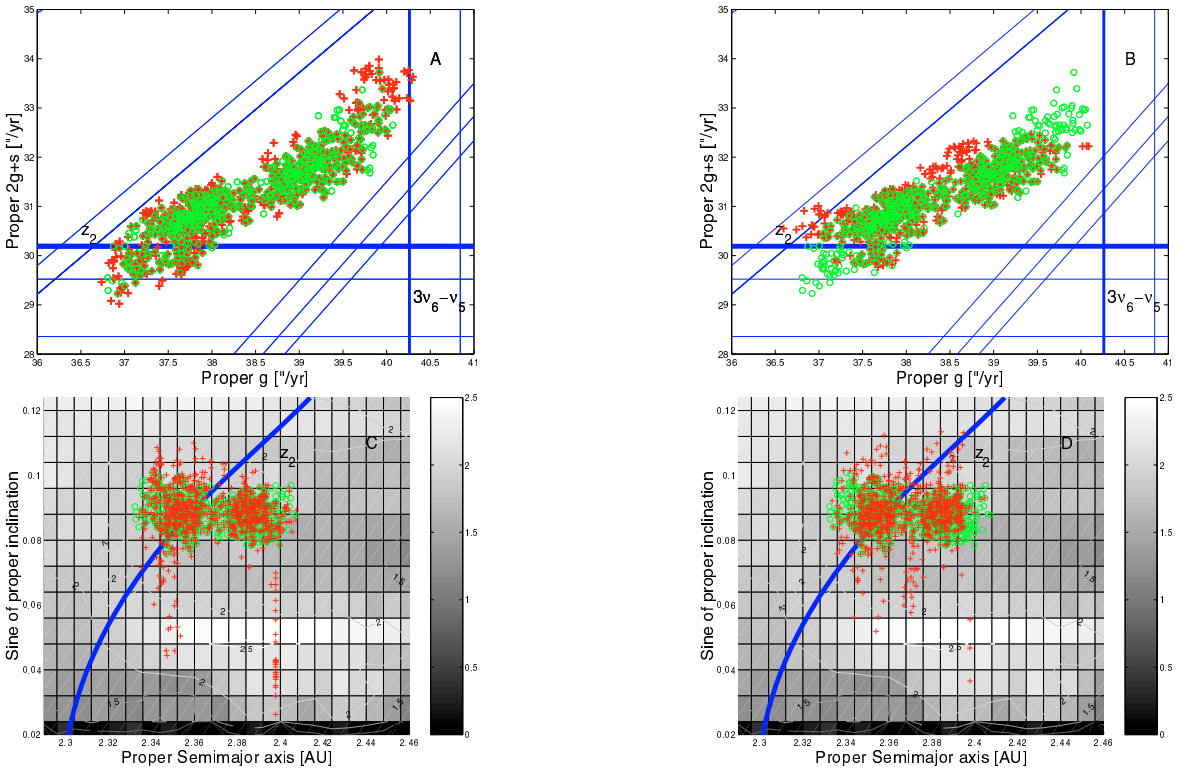

Fig. 1. A $(g, 2g + s)$ projection of the classical Erigone family (green circles and of the family obtained with the "standard" frequency metric (red crosses, panel **A)**), and the $(n, g, 2g + s)$ metric of Eq. (4) (red crosses, panel **B)**). Panels **C)** and **D)** display an $(a, \sin(i))$ projection of the same families, superimposed to a color and contour plot of the $\log_{10}$ of asteroid number in the local background per unit bin.

linear resonance ν_6. In particular, the higher the value of k, the nearer in proper element and frequency domain the resonance is to the ν_6. For $k > 3$ the z_k resonances overlap with the ν_6, and have no significant dynamical effect of their own (Michtchenko et al. 2008), that is why we do not consider z_4 and higher order resonances in this work.

Since the work of Milani & Knežević (1994) it is known that the old Flora family (current Baptistina and Belgica families, and other clumps in the region, Mothé-Diniz et al. 2005) strongly interacts with the z_2, and marginally interacts with the z_3 resonances. The former Flora family was therefore a very good candidate for an analysis in the frequency domain for what concerns these two resonances. Unfortunately, the region of Flora is characterized by a very high density of asteroids and secular resonances (Michtchenko et al. 2008), which makes an analysis of families in the frequency domain quite difficult (we will return on this subject in Sect. 2.4). Families found in the frequency domain in this region may very quickly converge with the local background, providing very little dynamical information.

To avoid the problems associated with the Flora region we turned our attention to another family strongly interacting with the z_2 secular resonance, (163) Erigone. This family has been the subject of a recent study of Vokrouhlický et al. (2006a). Based on results of Monte Carlo simulation of the Yarkovsky and YORP diffusion of family members in semimajor axis, Vokrouhlický et al. (2006a) estimated the age of the family in 240 Myr, with a 40% uncertainty. The central region of the family is crossed by the z_2 resonance, and its right border in the $(a, \sin(i))$ plane is defined by the $4J{:}-2S{:}-1A$ three-body resonance.

We determined the family using the CHCM and found that at a cutoff of 68 m/s (for larger values the family expands beyond the $4J{:}-2S{:}-1A$ resonance) 5.0% of its members (33 bodies out of 658 members) are inside the resonance. To best represent asteroids that drifted in the z_2 resonance, we introduce a $(g, 2g + s)$ representative plane and we determined the family in the frequency space with a metric of the form:

$$d_2 = \sqrt{h_1 \left(\frac{\Delta n}{h_0}\right)^2 + h_2(\Delta g)^2 + h_3(\Delta(2g + s))^2}, \quad (4)$$

(where h_0 is a normalization factor of dimension 1 degree/″, $h_1 = h_2 = h_3 = 1$; Δx, with $x = n, g, 2g + s$, represents the difference in x between two neighboring asteroids). We determined the family in frequency space with the FHCM and with the metric of Eq. (4), and found that the family is best defined at a cutoff of 0.181″/yr and 0.176″/yr, respectively. Figure 1 displays the $(g, 2g + s)$ projection of the two families (panels A and B). The thicker horizontal line shows the location of the z_2 resonance. Panels C and D of Fig. 1 display an $(a, \sin(i))$ projection of the two families, superimposed with a color plot of the $\log_{10}$ of the number of asteroids per unit bin in the local background, filtered five times with the median filter of Sect. 2. The thick blue line displays the location of the center of the z_2 resonance in the $(a, \sin(i))$ plane calculated with the analytical approach of Milani & Knežević (1994), in the $(a, \sin(i))$ interval covered by the family local background and for the mean value of eccentricity of the Erigone family (see Carruba et al. 2005, for a discussion of the limits of this approach, that it is used here only for illustrative purposes). In the local background of the classical Erigone family 2192 objects are currently inside the z_2 resonance. This large number of objects is caused by the fact that the local background of Erigone include the high density region of the former Flora family. Of these objects, 49 (2.2% of the total) were identified as family members by the standard metric, while 73 (3.3%

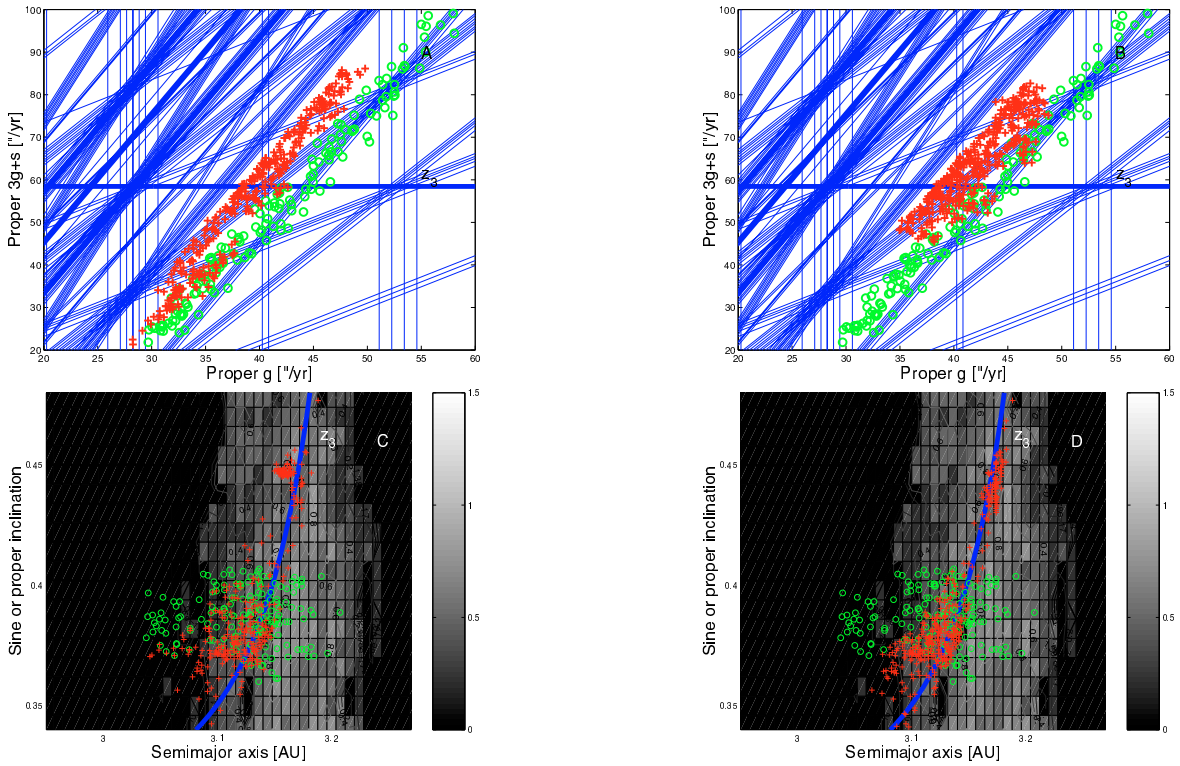

Fig. 2. A $(g, 3g + s)$ projection of the classical Elektra clump (green circles and of the family obtained with the "standard" frequency metric (red crosses, panel **A)**), and the $(n, g, 3g + s)$ metric of Eq. (5) (red crosses, panel **B)**). Panels **C)** and **D)** display an $(a, \sin(i))$ projection of the same families, superimposed to a color and contour plot of the $\log_{10}$ of asteroid number in the local background per unit bin.

of the total, 50% more than the metric in the $(n, g, g+s)$ domain) were identified by the $2g + s$ metric of Eq. (4).

Note how both the frequency and classical families interact with the pericenter resonance of argument $2g-3g_6+g_5$ ($3\nu_6-\nu_5$ in the notation of Michtchenko et al. 2008, approximately located at $a = 2.345$ AU), and its harmonics involving the g_7 frequency. The metric in the $(n, g, g + s)$ domain more efficiently identifies objects that drifted in the $4J{:}-2S{:}-1A$ resonance (for a discussion of the mechanism with which such metric identifies objects drifting in mean-motion resonance see Sect. 3.1), but the metric in the $(n, g, 2g+s)$ domain identifies more than 50% more objects that drifted in the z_2 secular resonance and depleted the central region of the Erigone family. We believe that the interplay of the Yarkovsky and YORP effect with the z_2 resonance could explain part of the lower density of objects observed in the central region of the Erigone family.

We summarized the results that we obtained in this section in Table 4. In view of its higher efficiency, we believe that the metric of Eq. (4) could be an useful tool to study the diffusion of family members in the z_2 secular resonance.

2.2. 3g + s resonances

The z_3 secular resonance occurs in regions very close in the proper element and frequency domains to the ν_6. Apart from clumps in the former Flora family region, which are quite difficult to analyze for reasons discussed in Sect. 2.1, we found a clump that is characterized by its interaction with the z_3 resonance: (130) Elektra. We determined the clump and found that it is best defined at a cutoff of 233 m/s. We then introduce a distance metric most apt to find neighbors inside the z_3 resonance, which has the form:

$$d_2 = \sqrt{h_1\left(\frac{\Delta n}{h_0}\right)^2 + h_2(\Delta g)^2 + h_3(\Delta(3g + s))^2}, \quad (5)$$

(where $h_1 = h_2 = h_3 = 1$). With the FHCM the clump was defined at a cutoff of 0.1365″/yr, while with the distance metric of Eq. (5) the clump was found with a cutoff of 1.22″/yr. Figure 2 displays the $(g, 3g + s)$ projection of the two families, with the ticker horizontal line showing the location of the z_3 resonance (note that (130) Elektra itself is currently inside the resonance). Other lines display the location of nonlinear secular resonance up to order eight (we plotted resonances up to this order to be consistent with the order of the z_3 resonance). Panels C and D of Fig. 2 display an $(a, \sin(i))$ projection of the two frequency families, superimposed with a color plot of the $\log_{10}$ of the number of asteroids per unit bin in the local background, filtered twice with the median filter. Since the Elektra clump is in a region with much lower density of asteroids than the other families that we are studying (with the exception of the Phocaea family), here we use a smaller range of values for the $\log_1 0$ of the number of asteroids per unit bin ([0, 1.5] with respect to the [0, 2.5] range used in the other cases). The thick blue line displays the location of the z_3 resonance in the $(a, \sin(i))$ plane computed with the same method of Sect. 2.1. Note how the clump obtained with the metric of Eq. (5) follows the center of the z_3 resonance (the location of the resonance center displayed in the figure is approximated and subject to the limitation of the analytical approach of Milani & Knežević 1994 near the ν_6 resonance; Carruba et al. 2005). In the local background of the Elektra clump 1755 objects are currently inside the z_3 resonance. Of these, 39 (2.2%) were idenitified with the CHCM, 85 (4.8%) with the FHCM, and

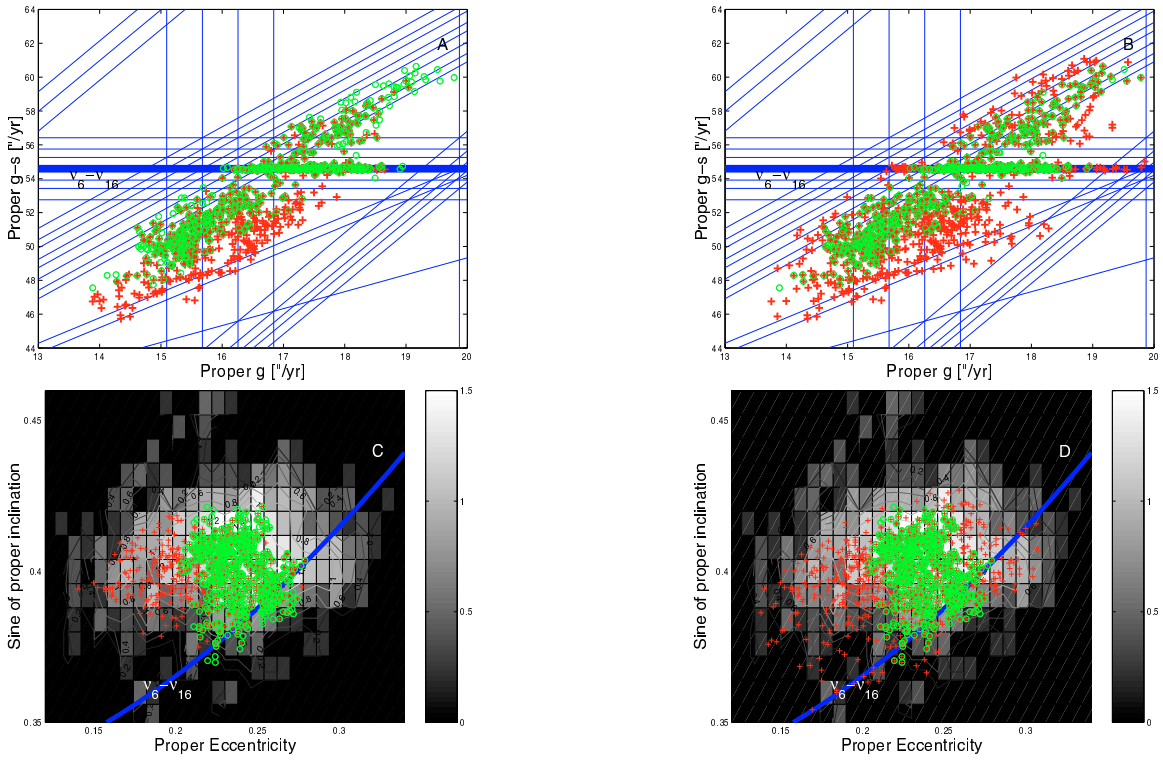

Fig. 3. A $(g, g-s)$ projection of the classical Phocaea family (green circles and of the family obtained with the "standard" frequency metric (red crosses, panel **A**)), and the $(n, g, g-s)$ metric of Eq. (6) (red crosses, panel **B**)). Panels **C**) and **D**) display an $(e, \sin(i))$ projection of the same families, superimposed to a color and contour plot of the $\log_{10}$ of asteroid number in the local background per unit bin.

137 (7.8%) with the distance metric of Eq. (5). Results are summarized in Table 4. In view of this results, we believe that the the distance metric of Eq. (5) could be an useful tool to study diffusion of family members in the z_3 secular resonance.

2.3. g – s resonances

The Phocaea asteroid family is a group of asteroids with a semi-major axis less than that of the 3:1 mean-motion resonance with Jupiter, a large inclination and a quite large eccentricity. It is also characterized by its interaction with the $g-s-g_6+s_6$ resonance, or $\nu_6-\nu_{16}$ (Knežević & Milani 2003). We determined the family using the CHCM, and found that at a cutoff of 134 m/s (for larger values of the cutoff the family merges with other families in the region such as Wood & Krylov (Gil-Hutton 2006), 16.4% of its members (96 bodies of 584 members) are inside the resonance. In view of its strong interaction with a $g-s$ secular resonance, we thought that the Phocaea family could be best represented in a $(g, g-s)$ plane, and determined it in the frequency space with a metric of the form:

$$d_2 = \sqrt{h_1\left(\frac{\Delta n}{h_0}\right)^2 + h_2(\Delta g)^2 + h_3(\Delta(g-s))^2}, \quad (6)$$

(where $h_1 = h_2 = h_3 = 1$) rather than with the "standard frequency metric" of Carruba & Michtchenko (2007). To test this hypothesis, we determined the family in the frequency space with both approaches. We found that the Phocaea family is best defined at a cutoff of 0.52″/yr with the standard frequency metric, and at 0.595″/yr with the metric of Eq. (6). Figure 3 displays the $(g, g-s)$ projection of the two families (panels A and B, respectively). The thicker horizontal line shows the location of the $g-s+g_6-s_6$ resonance, while the other horizontal lines display harmonics of the same resonance involving combinations of the g_5 and g_7 frequencies. For reference, an $(e, \sin(i))$ projection of the two family is also displayed in Fig. 3, panels C and D, superimposed with contour and color plot of the $\log_{10}$ of the number of asteroids per unit bin in the local background, filtered twice with the median filter. As for the case of the Elektra clump, here we use the smaller [0, 1.5] range for the values of the $\log_{10}$ of the number of asteroids per unit bin in the local background. The blue line displays the location of the center of the $\nu_6-\nu_{16}$ resonance computed with the analytical approach of Milani & Knežević (1994). Note how the Phocaea family is surrounded by regions with very little density of asteroids or none. The lack of bodies around the Phocaea family region is caused by the presence of the strong $7J::-2A$ mean-motion resonance with Jupiter, and by the ν_6, ν_5, and ν_{16} secular resonances (Knežević & Milani 2003).

In the local background of the classical Phocaea family 279 objects are currently inside the $\nu_6-\nu_{16}$ resonance. Of these 96 (34.4% of the total) were identified as family members by the standard frequency metric, while 133 (47.7% of the total) were identified by the $g-s$ metric of Eq. (6). Note how the standard metric obtained the same number of objects in the $g-s$ resonance than the classical approach, while the metric of Eq. (6) connected 38.5% more objects than both other methods. We summarized these results in Table 4. In view of this, we believe that the metric of Eq. (6) could be considered a useful tool to study diffusion in $g-s$ secular resonances.

2.4. s resonances

The Baptistina family has been the subject of a recent study by Bottke et al. (2007) where the authors suggested that the Chixculub impactor that produced the Cretaceous/Tertiary

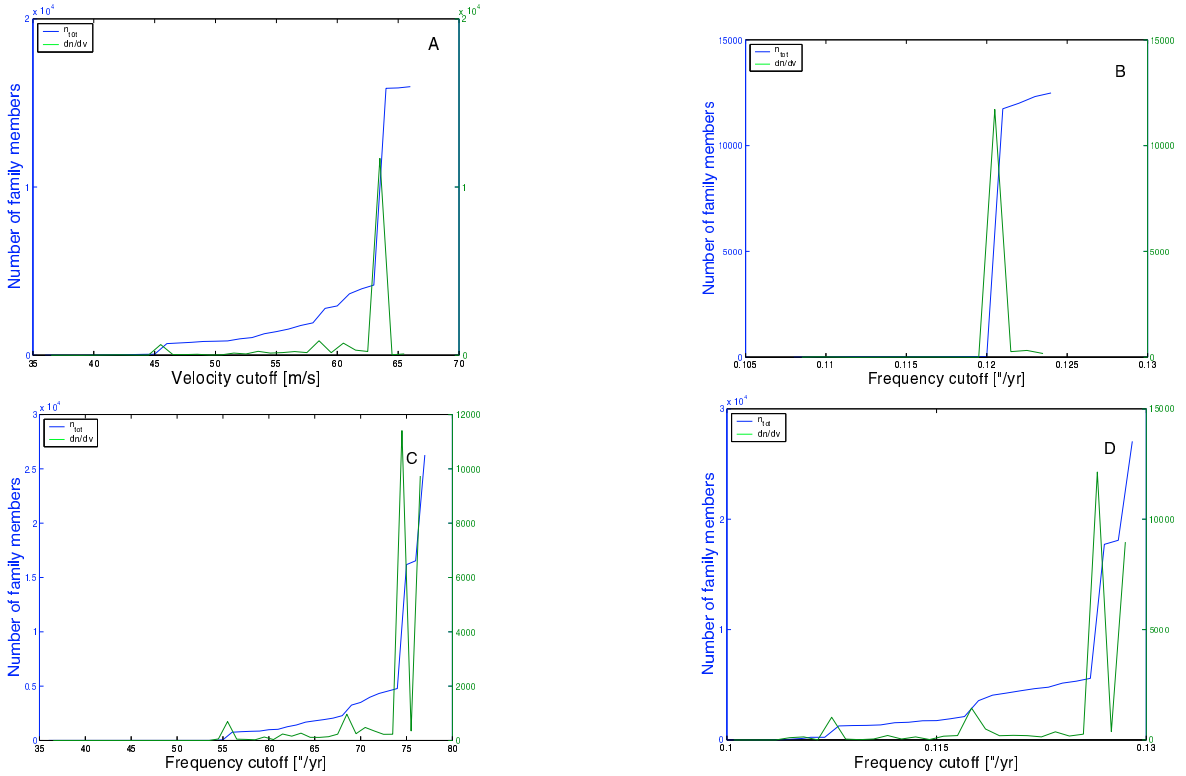

Fig. 4. The number of Baptistina members (in blue, *left* ordinate) and the differential number of family members (in green, *right* ordinate) as a function of the cutoffs, for the family found with the metric of proper elements (panel **A**)), the metric in the $(n, g, g+s)$ space (panel **B**)), the metric of proper elements and frequencies (panel **C**)), and the metric in the (n, g, s) domain.

(K/T) mass extinction event 65 Myr ago could have been a past member of the family that interacted with the $7J{:}{-}2A$ mean-motion resonance with Jupiter.

From the point of view of family determination, the Baptistina family is also a very interesting one. The Baptistina family is in the proximity of the powerful ν_6 secular resonance and it is crossed by the $2\nu_6 + \nu_{16}$ (or z_2, as in the notation of Milani & Knežević 1994[1]) secular resonance, which would make this family an ideal candidate for the use of the metric of Eq. (4). Unfortunately this family is in the region of the former Flora family which is characterized by a quite large density of asteroids and a by a dense web of secular and mean-motion resonances, many involving martian frequencies (Michtchenko et al. 2008), that make an analysis in the frequency domain quite difficult. Our analysis of the Baptistina family and other clumps formerly associated with the Flora family such as (219) Thusnelda, (650) Amalasuntha, (883) Matterania, and others with the FCHM and the metrics of Eqs. (4) and (5) display a typical behavior: the families connect to a few objects for small values of the frequency cutoff and then rapidly merge with the local background.

An example of this is given in Fig. 4 for the Baptistina family. If we determine the Baptistina family with the classical approach, it is defined for a velocity cutoff of 52 m/s (for larger values of the cutoff the families merges with other known clumps in the region), and the family has 973 members (Fig. 4, panel A, the left ordinate display the number of family members and the right ordinate the differencial number $\mathrm{d}n/\mathrm{d}v$ as a function of the cutoff). Note that the family rapidly increases in sizes for slightly larger values of the cutoff, and merges with the local background for a cutoff of 64 m/s. This problem is more dramatic if we use the frequency approach of Carruba & Michtchenko (2007): for a cutoff of less than 0.120″/yr the family has only 30 members, while it merges with the local background for larger values of the cutoff (Fig. 4, panel B).

Quite simply, it is not possible to obtain significant information about the dynamical evolution of the Baptistina family by using the FHCM. A natural question that arises is why the family can be determined in the proper element, but not in the frequency domain. To answer this question we study the dynamics in the region of the family. The Baptistina family is crossed by the $7J{:}{-}2A$ mean-motion resonance with Jupiter. For values of proper a smaller than that of the resonance, there is a region with a relatively high density of asteroids, all at relatively low distances in the $(g + s)$ dimension and having lower values of $\sin(i)$ than those of the classical Baptistina family members. For values of the frequency cutoff lower than 0.120″/yr the family in the frequency domain is confined to right side of the $7J{:}{-}2A$ in the $(a, \sin(i))$ plane. As soon as the frequency cutoff is increased, the family passes the barrier in frequency space presented by the $7J{:}{-}2A$ resonances and rapidly merge with the conspicuous population of low-inclination objects, jumping to 11 741 family members.

To further confirm this hypothesis, we performed the following numerical experiment: we computed the average value of distances in the g, s and $(g + s)$ spaces between each member of the Baptistina classical family and its neighbor in a radius of 150 m/s in the space of proper elements. In Fig. 5 we plotted the results as a function of the proper n of family members. As can be seen in the figure, changes in proper g and s follow a U-shaped curve with respect to the n-frequency (the actual dependence is inverse for the s frequency with respect to the g frequency, in the figure we plotted the absolute values of changes),

[1] (298) Baptistina itself is currently inside this resonance.

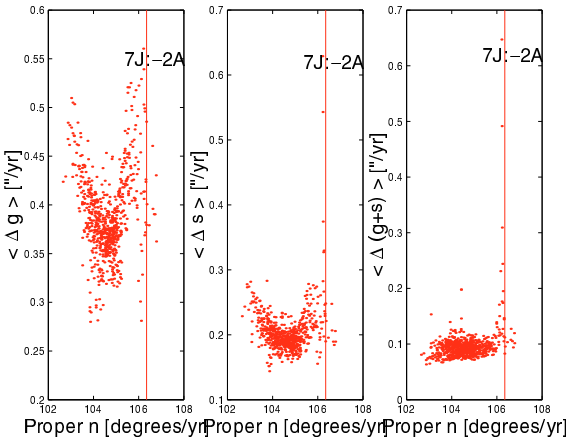

Fig. 5. The average values of changes in proper g, s, $(g+s)$ for asteroids to within 150 m/s of the central body, as a function of the body's n, for the members of the classical Baptistina family. Vertical lines display the position of the $7J{:}-2A$ mean-motion resonance with Jupiter.

while changes in the $g+s$ are very flat, with the exception of the region near the $7J{:}-2A$ resonances where they diverge. This may explain why the Baptistina family in the $(n, g, g+s)$ frequency space was not well-determined. Since distances in the $(g+s)$ space are very weakly dependent on n, and a significant increase in the cutoff is needed to pass the $7J{:}-2A$ frequency barrier, small changes in the cutoff after the barrier is passed lead to connect to the vast numbers of objects at low-i, as observed. Similar problems are observed not only for Baptistina, but also for other families and clumps in the region of the former Flora family, such as Thusnelda, Amalasuntha, and Matterania, among others.

While the FHCM is not very useful in this part of the belt, significant dynamical information can still be obtained using different approaches. One possibility is to use the metric of proper elements and frequencies introduced in Carruba & Michtchenko (2007), Eq. (11). Figure 4, panel C, displays the number of family members obtained with this method as a function of the velocity cutoff. This method allows us to cross the barrier represented by the $7J{:}-2A$ mean-motion resonance without creating giant families, but at the cost of partially losing information on family members that migrated in local secular resonances because of the Yarkovsky and YORP effects. Another possible approach could be to use a different metric in frequency space. Rather than to look in the $(n, g, g+s)$ space, we look for the Baptistina family in the (n, g, s) domain. Distances in s as a function of n are less flat than distances in $g+s$; families obtained in the (n, g, s) domain should therefore be more numerous as a function of the frequency cutoff than families obtained in the $(n, g, g+s)$ domain. We therefore introduce a metric of the form:

$$d = \sqrt{h_1\left(\frac{\Delta n}{h_0}\right)^2 + h_2(\Delta g)^2 + h_3(\Delta(s))^2}, \quad (7)$$

where $h_1 = h_2 = h_3 = 1$. We used this metric for determining the Baptistina family and we found that the family is well defined by a cutoff of 0.113″/yr, and contains 1597 family members at this cutoff (Fig. 4, panel D). Larger values of the cutoff results in families that conglomerate vast populations of low-i asteroids, and the family itself coalesces with the background for a cutoff of 0.127″/yr.

In Fig. 6 we show a $(g, |s|)$ (panel A, we use the absolute value of s for illustrative purposes) and $(a, \sin(i))$ (panel B) projections of the Baptistina family obtained with CHCM and the distance metric of Eq. (7). Superimposed to the the $(a, \sin(i))$ projection there is a color plot of the $\log_{10}$ of the number of asteroids per unit bin in the local background, filtered three times with the median filter. While for the value of the cutoff that was used we were not able to cross the $7J{:}-2A$ barrier, the method offered some considerable advantage. In particular, we identified tails of asteroids that possibly drifted in local node secular resonances (involving martian frequencies) such as the $\nu_{17} + \nu_4 + \nu_5 - 2\nu_6$ $((s - s_7) - g_5 + 2g_6 - g_4)$ resonance and harmonics involving the g_7 frequency. The thick blue line in Fig. 6, panel B, displays the location of this resonance in the $(a, \sin(i))$ plane computed with the same method of Sect. 2.1.

In the local background of the classical Baptistina family 3130 objects are currently inside the $\nu_{17} + \nu_4 + \nu_5 - 2\nu_6$. Of these, the CHCM identified 36 objects (1.2%) as family members, while the (n, g, s) metric of Eq. (7) identified 163 objects (5.2%). Results are summarized in Table 4. We believe that, considering the limitations imposed by the high density of asteroids and secular resonances in the former Flora family region, the metric of Eq. (7) was able to provide significant dynamical information on former Baptistina family members.

2.5. 2s resonances

The Vesta family has been the subject of several recent studies (Carruba et al. 2005, 2007; Carruba & Michtchenko 2007; Nesvorný et al. 2008). From a mineralogical point of view, the Vesta family is interesting because most of its members (including (4) Vesta itself) present a V-type spectrum, which is characterized by a moderately steep red slope shortwards of 0.7 μm and a deep absorption band longwards of 0.75 μm. This kind of spectra is associated with a basaltic composition (Bus 2002; Duffard et al. 2004). From the point of view of family identification in frequency space the Vesta family is also a very interesting one. In this section we will concentrate on its interaction with a resonance of argument $2s$, the $2s - 3s_6 + s_7$ ($3\nu_{16} - \nu_{17}$ in the Michtchenko et al. 2008, notation). In Sect. 3.1 we will treat the effect that the proximity of the $3J{:}1A$ resonance has on the values of the g frequencies.

We start by analyzing the family with the CHCM. The family coalesces with the local background at a cutoff of 68 m/s, so we decided to use a cutoff in the proper element space of 62 m/s (the difference with the cutoff used in Carruba & Michtchenko 2007 is caused by the larger number of asteroids currently available in the synthetic proper element database). Since in this section we are interested in analyzing how the family interacts with the $3\nu_{16} - \nu_{17}$ resonance, we represent the Vesta family in the $(g, 2s)$ and introduced a new distance metric of the form:

$$d_2 = \sqrt{h_1\left(\frac{\Delta n}{h_0}\right)^2 + h_2(\Delta g)^2 + h_3(\Delta(s))^2}, \quad (8)$$

(where $h_1 = h_2 = 1, h_3 = 2$). We determined the Vesta with the FHCM and the new distance metric. We found that the family is best defined at a cutoff of 0.115″/yr (again, the difference with the value of Carruba & Michtchenko 2007 is caused by the larger number of asteroids in the proper element database since the publication of that paper) in the $(n.g, g+s)$ domain, and of 150″/yr in the $(n, g, 2s)$ domain. Figure 7 displays the $(g, 2s)$ projection of the two families (panels A and B,

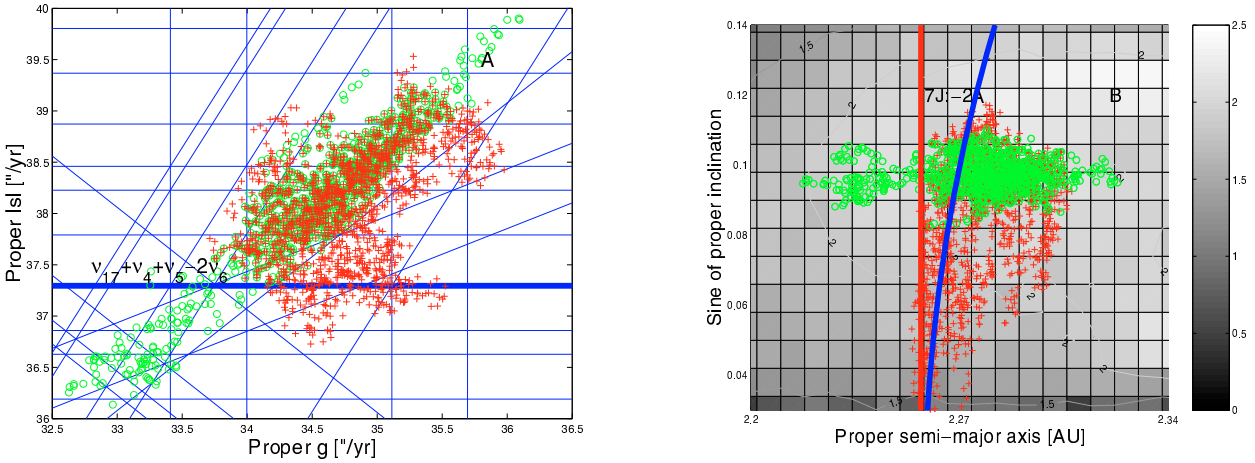

Fig. 6. A $(g, |s|)$ projection of the classical Baptistina family (green circles) and of the family obtained with the (n, g, s) metric of Eq. (7) (red crosses, panel **A)**). Panel **B)** displays an $(a, \sin(i))$ projection of the same families, superimposed to a color and contour plot of the $\log_{10}$ of the asteroid number in the local background per unit bin.

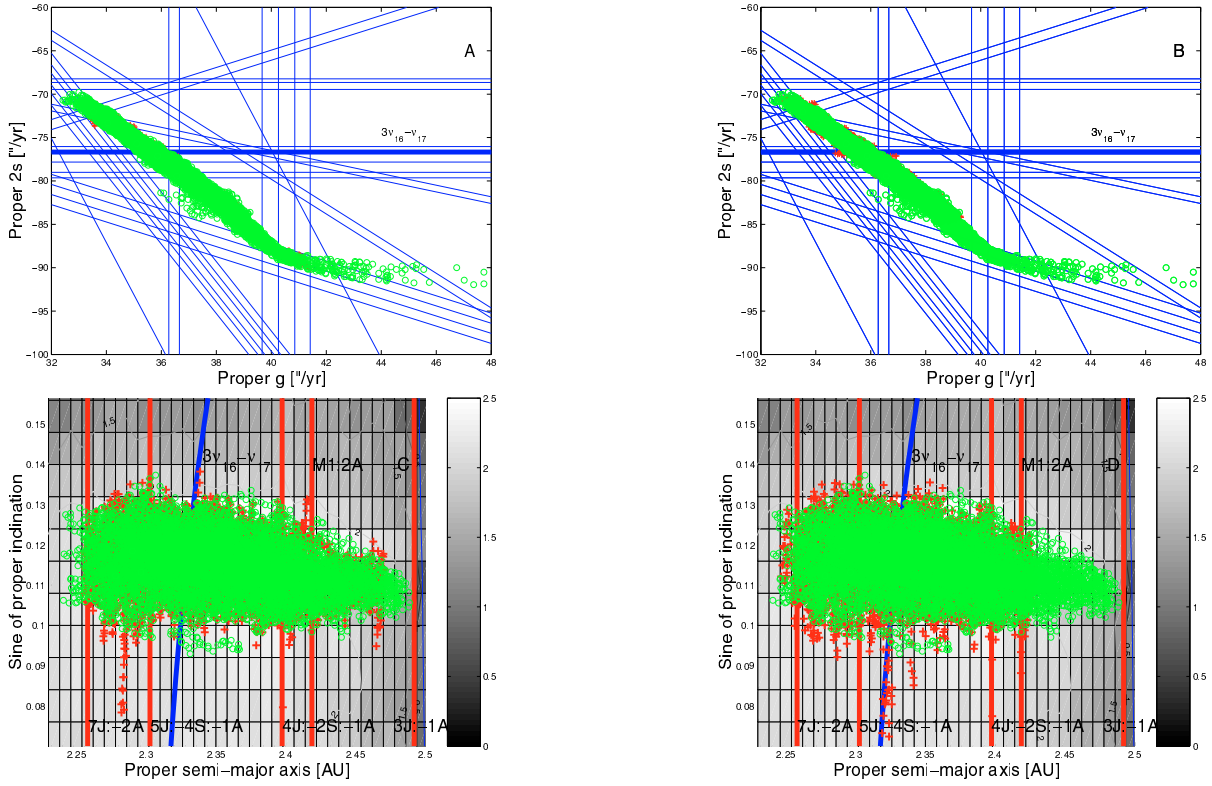

Fig. 7. A $(g, 2s)$ projection of the classical Vesta family (green circles and of the family obtained with the "standard" frequency metric (red crosses, panel **A)**), and the $(n, g, 2s)$ metric of Eq. (8) (red crosses, panel **B)**). Panels **C)** and **D)** display an $(a, \sin(i))$ projection of the same families, superimposed to a color and contour plot of the $\log_{10}$ of asteroid number in the local background per unit bin.

respectively). The thicker horizontal line shows the location of the $3\nu_{16} - \nu_{17}$ resonance. The diverging behavior of the values of g for $g > 41''/\text{yr}$ is caused by the perturbation of the g values induced by the proximity of the $3J{:}1A$ resonance. Techniques to study diffusion of asteroids in this regions will be discussed in Sect. 3.1. Panels C and D displays an $(a, \sin i(i))$ projection of the two families, superimposed with color plot of the $\log_{10}$ of the number of asteroids per unit bin in the local background, filtered three times with the median filter. The blue line displays the location of the $3\nu_{16} - \nu_{17}$ resonance computed with the analytical approach of Milani & Knežević (1994).

As can be seen in Fig. 7, panel D, the new distance metric was able to identify more objects that diffused from the Vesta family in the $3\nu_{16} - \nu_{17}$ resonance than the other two approaches. In particular, in the local background of the Vesta family we found 1106 asteroids inside the $3\nu_{16} - \nu_{17}$ resonance. Of these, 143 (12.9% of the total) were identified with the classical approach, 145 (13.1%) were identified by the FHCM, and 251 (22.7%) by the distance metric of Eq. (8) (we summarize these results in Table 4). We believe therefore that the distance metric of Eq. (8) could be an useful tool to study diffusion of family members in $2s$ resonances.

3. Families interacting with low-order mean-motion resonances

In the previous section we discussed the case of families interacting with nonlinear secular resonances, and we introduced new techniques to study the diffusion of family members in resonances of arguments other than g and $g + s$. In this section we focus our attention on families interacting with low-order mean-motion resonances such as the $2J{:}-1A$, $3J{:}-1A$, and $3J{:}-2A$. Such resonances can affect asteroidal frequencies in two ways: i) the frequency of pericenter precession g of asteroids near the resonant border may not follow a linear trend as a function of n, as is the case for some of the members of the Vesta family; and ii) it may be negative (retrograde precession) for asteroids locked in resonant configuration, as for the Hildas in the $3J{:}-2A$ and some members of the Hansa family which may be currently locked in the apocentric tail of the $3J{:}1A$ mean-motion resonance.

In this section we will study the problem of diffusion into secular resonances in regions affected by low-order mean-motion resonances. For this purpose, we will introduce new techniques for regulazing the behavior of the g frequency as a function of n (Vesta family) and e (Hansa family). We will start with the case of the Vesta family.

3.1. Families close to the border of low-order mean-motion resonances: the case of the Vesta family

The proximity of asteroids families to low-order mean-motion resonances may generate difficulties to the process of identifying asteroid families in the frequency domain. To study in more depth this phenomenon we turn our attention to the Vesta family, whose determination is affected by two of the most typical problems in asteroid family identification. The Vesta family is crossed by the 1:2 mean-motion resonance with Mars ($M1{:}2A$ hereafter) and its right border in proper a is quite close to the $3J{:}-1A$ resonance with Jupiter.

The $M1{:}2A$ resonance results in a barrier in frequency space that does not allow to connect asteroids in opposite sides of the resonance until a critical value of the cutoff is reached. Asteroids are connected to the family only for values of the frequency cutoff larger than $0.10''$/yr, but lower than the critical value of $0.12''$/yr, for which the family coalesces into the local background. In this case a value of the cutoff large enough to connect the family beyond the $M1{:}2A$ resonance but lower than the critical one existed. In other cases however, this might not be the case and mean-motion resonances may appear to act as a barrier for asteroid families found either in the frequency or in the element space.

Another effect of mean-motion resonances on family determination is that they significantly spreads the observed dynamical family in the proper e and $\sin(i)$ space. Figure 8 displays the behavior of the proper g (panel A) and $g + s$ (panel B) frequencies as a function of n in the region of the 1/2 mean motion resonance with Mars (black dots). As can be seen in the figure, the procedure that generates synthetic proper elements gives values of proper n (or, equivalently, of proper a) located at the center of libration of the mean-motion resonance. As a consequence, objects inside the resonance all have very close values of proper a and n, and the differences Δa and Δn between two neighbors are limited. Asteroids are identified as family members in the frequency domain via the distance metric:

$$d_2 = \sqrt{h_1 \left(\frac{\Delta n}{h_0}\right)^2 + h_2(\Delta g)^2 + h_3(\Delta(g+s))^2}, \quad (9)$$

where h_0 is a normalization factor of dimension 1 degree/$''$, and the simplest choice for the h_i ($i = 1,2,3$) weights is to take them all equal to 1 (Carruba & Michtchenko 2007). For the same value of the cutoff d_2, therefore asteroids in the resonance can be neighbors in the frequency space for larger changes in proper g and $g + s$. That is the reason why our metric was able to connect to family objects with significant differences in proper e and $\sin(i)$ with respect to the classical Vesta family (Fig. 15, panel B, Carruba & Michtchenko 2007)[2]: objects that are neighbors in the frequency domain may be relatively more distant in the proper element space, and viceversa. In particular, in the local background of the Vesta family there are 466 objects inside the $M1{:}2A$. Of these, 13 (2.8%) where identified as family members by the CHCM, while 23 (4.9%) where identified by the FHCM. The FHCM was 43.4% more efficient in connecting asteroids to the Vesta family than the CHCM.

The effect of the $3J{:}-1A$ mean-motion resonance with Jupiter on our method of asteroid family identification is subtler. As discussed in Carruba & Michtchenko (2007) the perturbing effect of the $3J{:}-1A$ mean-motion resonance on the g frequency does not allow us to connect asteroids in the proximity of this resonance to the rest of the dynamical family. This is shown in Fig. 9, panel A, where the green circles represent members of the classical Vesta family, the red crosses members of the family obtained with the frequency method (Carruba & Michtchenko 2007), and the black dots all the asteroids having proper e and $\sin(i)$ between the minimum and maximum values of the Vesta family. The horizontal green lines display the location of the strongest pericenter resonances in the region, and the vertical lines show the location of the $3J{:}-1A$ and $M1{:}2A$ mean-motion resonances border.

As can be seen in the figure, as soon as the g frequency starts to diverge from a linear behavior (this occurs roughly for $n <$ 93.0 degrees/yr) the frequency metric is no longer able to connect asteroids in the region with the rest of the dynamical family. A possible solution of this problem is to artificially extend the linear behavior of the g frequency as a function of n from the regular region to the perturbed region at $n < 93.0$ degrees/yr, so that asteroids in the proximity of the $3J{:}-1A$ resonance have assigned the value of the g frequency they should have had if the $3J{:}-1A$ resonance were not in the region. In this paper we call this procedure "regularization"[3].

For this purpose, we selected asteroids in the synthetic proper element database in $(e, \sin(i))$ box near Vesta, defined by the maximum and minimum values of e and $\sin(i)$ of members

[2] We should point out that the objects that show significant differences in proper e and $\sin(i)$ with respect to the mean values of Vesta family members are not necessarily family members, and could just be asteroids that happen to be just close in frequency space because of the perturbing effect of the mean-motion resonance on the proper n. The possibility that these objects are former family members that migrated always needs to be verified by other methods such as long-term numerical simulations with symplectic integrators, compositional analysis, etc.

[3] Here we use the term regularization with a different meaning than the one used in mathematics (solution of ill-posed inverse problems by introducing assumptions on the smoothness or the norm of the solution), or in quantum field theory (introduction of a regulator for dealing with infinite, divergent expressions). While this may be confusing for a reader familiar with other definitions of the term, we found that alternatives were even more confusing. For example, linearization in mathematics refers to finding the linear approximation to a function to a given point. Since the point we are using for linearizing the function is not the same for which we are computing the "regularized" value of the frequency, the term linearization was improperly used. For this reason, we opted for the term regularization.

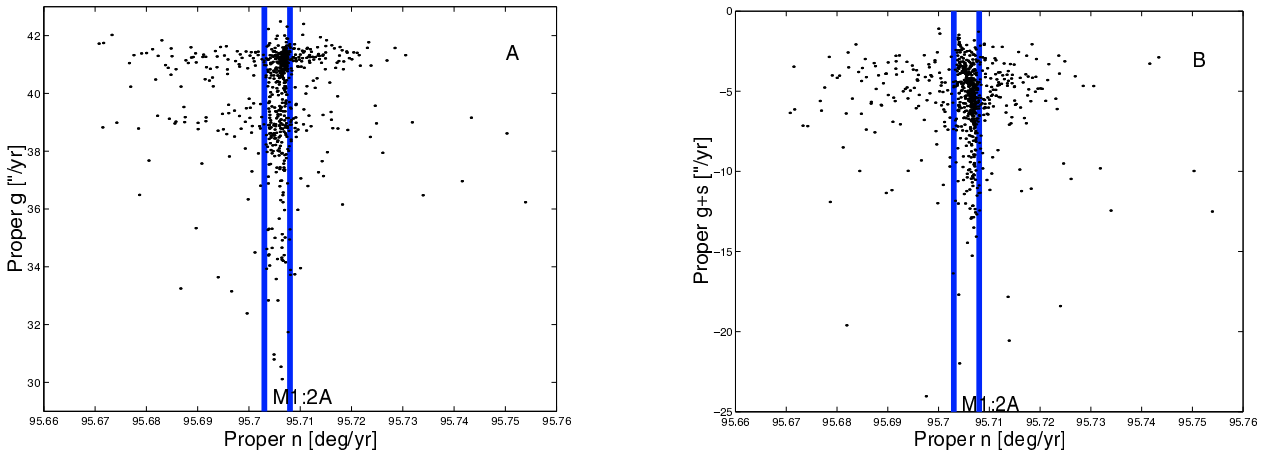

Fig. 8. The dependence of proper g and proper $g + s$ versus the proper n in the region of the $M1{:}2A$ mean-motion resonance. The vertical lines display the borders of the $M1{:}2A$ resonance.

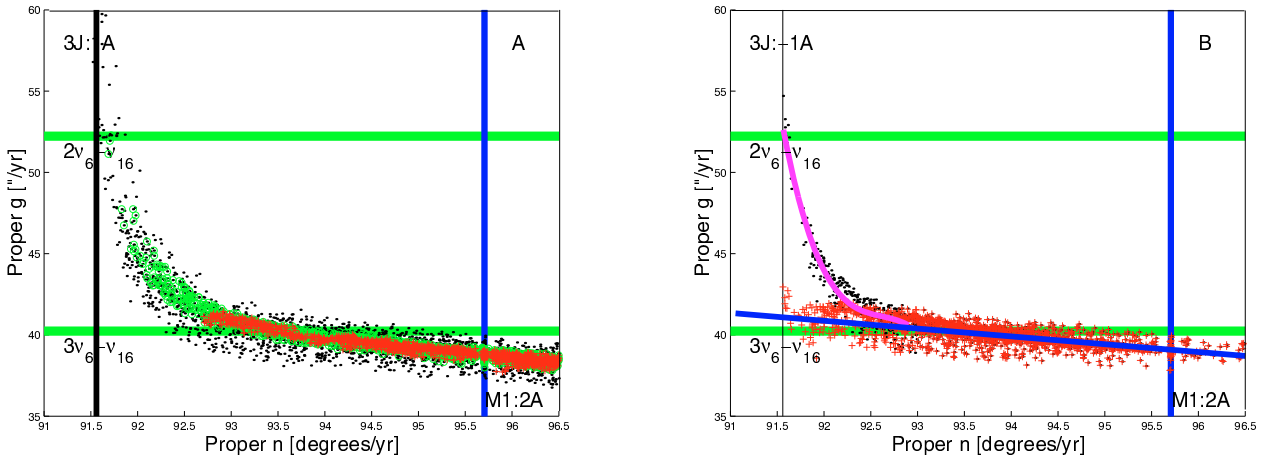

Fig. 9. *Left panel*: the behavior of proper g versus n in the region of the Vesta family. Black dots displays the (n, g) values of objects in the local background, as defined in Sect. 3.1, green circles refers to members of the classical family, and red crosses to members of the frequency family. *Right panel*: the regularized values of g as a function of n (red crosses), for s larger in the interval $[-45.00, -47.64]''$/yr.

of the classical family plus or minus 0.01, and in the n interval between 91.4 degrees/yr (to avoid to include asteroids inside the $3J{:}-1A$) and 96.5 degrees/yr (to avoid the perturbing effect of the $4J{:}-2S{:}-1A$ three-body resonance, which is just outside the range of n values shown in Fig. 9). Asteroids in this range are shown as black dots in Fig. 9, panel A. In order to regularize the behavior of asteroids with $n < 93$ degrees/yr (548 objects were found in this region in the $(e, \sin(i))$ box, in a range of s values between -47.64 and $-42.89''$/yr) we divided the asteroids in the Vesta family region in two samples characterized by values of s smaller than $-45.0''$/yr and larger than this value. This was done so as to have a sample of asteroids in both the perturbed and regular regions, such that the behavior of the perturbed asteroids could be simulated by the behavior of the regular ones in the same range of s values. We choose to use two intervals in order to have a statistically significant number of members (#>100)[4]. Once the two set of asteroids were obtained, we first best-fitted a line to the regular members in each s-interval, and a third-order polynomial curve in n for the g values of the corresponding asteroids in the perturbed region (higher order polynomial were tried to simulate the perturbed region without significantly improving the accuracy of the fit; see the Appendix for an analysis of the errors on g caused by this procedure). The values of the g frequencies of the asteroids in the perturbed region were finally regularized by using the equation:

$$g_r = g \cdot \frac{y_1}{y_2}, \tag{10}$$

where g_r is the regularized value of the g frequency, $y_1 = n \cdot p(1) + p(2)$, with $p(i)$ $(i = 1, 2)$ the linear and angular coefficient of the line that best-fit the regular asteroids, and n the asteroid mean-motion, and $y_2 = q(1) \cdot n^3 + q(2) \cdot n^2 + q(3) \cdot n + q(4)$, where the $q(i)$ $(i = 1, ..., 4)$ are the coefficient of the third-order polynomial that best-fit the g frequency in the perturbed domain. Values of the p and q coefficients for the two ranges of s values that we used are given in Table 1. The factor g/y_2 that multiplies the right side of Eq. (10) is a factor that quantifies how well the g value of the frequency is represented by the third-order polynomial that models the nonlinear regime of g in the (n, g) plane. This factor is equal to 1 for a perfect fit, is less than 1 for $g < y_2$ and more than 1 for $g > y_2$.

The right panel of Fig. 9 displays the results of this procedure for the asteroids in the region of the Vesta family with s in the interval $[-45.00, -47.64]''$/yr (results are similar for asteroids with s in the interval $[-42.89, -45.00]''$/yr, and are not

[4] Dividing the interval in s in three interval or more produced ensembles of asteroids with a not large enough number of members in each interval.

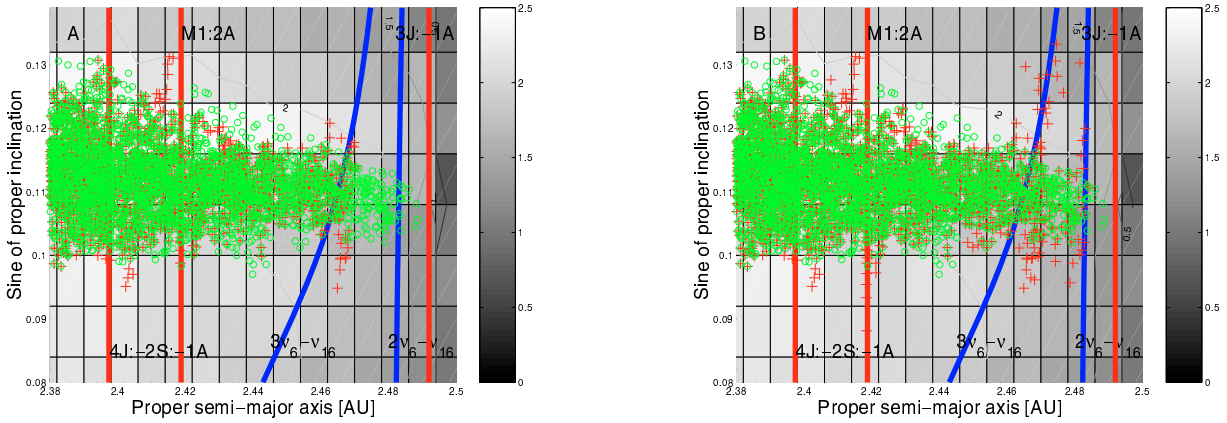

Fig. 10. An $(a, \sin(i))$ of the Vesta frequency family (red crosses, panel **A**)), of the regularized Vesta frequency family (red crosses, panel **B**)), and of the family obtained with the CHCM (green circles), in the region of the 3:1 mean-motion resonance. The thick blue lines display the location of the $2\nu_6 - \nu_5$ and $3\nu_6 - \nu_5$ secular resonances obtained with the analytical approach of Milani & Knežević (1994).

Table 1. Numerical values of the coefficients used to regularize g as a function of n for the Vesta family (s-intervals between −42.89 and −45.00″/yr, and between −45.00 and −47.64″/yr).

Coefficient	Vesta	Vesta
	$-42.89 < s < -45.00$ ″/yr	$-45.00 < s < -47.64$
$p(1)$ [″/degrees]	−0.4073	−0.4624
$p(2)$ [″/yr]	79.2635	83.7082
$q(1)$ [″yr^2/degrees^3]	−26.1652	−7.1026
$q(2)$ [″yr/degrees^2]	7.2563×10^3	1.9738×10^3
$q(3)$ [″/degrees]	-6.7080×10^5	-1.8284×10^5
$q(4)$ [″/yr]	2.0670×10^6	5.6457×10^6

shown for concisiness). The black dots display the real values of g, the inclined blue line is the line that best-fit asteroids in the regular region, and the magenta line is the third-order polynomial that best-fit the asteroid in the perturbed region. The red crosses are the regularized values of g. Note how they follow the line of extended linear behavior, with a spreadth caused by the g/y_2 factor in Eq. (10).

We replaced the regularized values of g in the catalog of asteroid synthetic proper elements and we used FHCM on this modified set of elements to re-obtain the Vesta family. For a cutoff of 0.120″/yr the family coalesced with the local background, so we chose to work with a cutoff of 0.119″/yr. With this cutoff we found 8413 members of the Vesta family. Figure 10 displays an $(a, \sin(i))$ projection of a part of the Vesta frequency family (red crosses, panel A), and of the regularized Vesta frequency family (red crosses, panel B) in the region near the $3J{:}-1A$ resonance ($a > 2.38$ AU). Superimposed we show a color plot of the $\log_{10}$ of the number of asteroid per unit bin in the local background of the Vesta family. The reader may also want to compare this figure with Fig. 15 in Carruba & Michtchenko (2007). With the new method we were able not only to retrieve most of the asteroids that were identified as family members with the CHCM, but also to identify tails of asteroids that drifted in some of the local three-body (such as the $9J{:}-7S{:}-2A$) and secular (such as the $2\nu_6-\nu_5$ ($g+g_5-2g_6$) and $3\nu_6-\nu_5$ ($2g+g_5-3g_6$)) resonances, not identified as family members by the classical method. In particular, we identified 2265 objects in the $3\nu_6-\nu_5$ resonance in the local background of the Vesta family. Of these, 83 (3.6% of the total) were identified by the CHCM, 44 (1.9%) by the FHCM, and 130 (5.7%) were identified by the regularized FHCM described in this section (note how in this case, because of the proximity of the $3J{:}-1A$ resonance and its effect on the g frequency, the CHCM identified more resonant objects than the unregularized FHCM). The advantages of this method are more evident for what concern the $2\nu_6-\nu_5$ resonance. There are 2839 objects inside this resonance in the local background. Here the CHCM and the FHCM identified none, while the regularized FHCM identified 5 objects (0.2%). By regularizing the values of g, we were able to retrieve 37% more objects that drifted in the $g+g_5-2g_6$) than with the CHCM, and we extended the Vesta family almost up to the border of the $3J{:}-1A$ resonance.

The procedure that we described in this section presents one disadvantage and several advantages. The disadvantage relates to the procedure itself, which is not easily generalizable. Each family in the proximity of mean-motion resonance presents a different situation and may need an ad hoc approach for the procedure of regularization of the g frequency as a function of n (but we believe that the procedure that we outlined here may serve as a basis for the study of other, similar cases). The advantages of this approach, however, in our opinion more than compensate for the disadvantages. Apart for the tails of asteroids that drifted in local mean-motion and secular resonances, that were not recognized as family members by the CHCM, the regularized FHCM that we introduce in this section provides a deeper understanding of the local dynamics, (i.e., the perturbing effect of the $3J{:}-1A$ resonance on the g frequency, the consequent overlapping of g resonances, etc.) which is not furnished by the CHCM. We believe that this alone is a very important benefit of this method, which we will discuss in more detail in the next sections.

3.2. Asteroid in resonant configurations with retrograde perihelion motion: the Hilda and Hansa families

Another effect that mean-motion resonances have on the precession frequency of the pericenter of asteroids happens for asteroids in resonant configurations. It is well known (Schubart 1988, 2007) that asteroids locked in the $3J{:}-2A$ mean-motion resonance with Jupiter (the so-called "Hildas"). Recently Brož & Vokrouhlický (2008) identified two collisional families, one associated with (153) Hilda, and one associated with (1911) Schubart, among the population of resonant asteroids. In this paper for convenience we will refer to the whole population of resonant asteroids as "Hildas") are characterized by retrograde precession frequency of the pericenter (negative

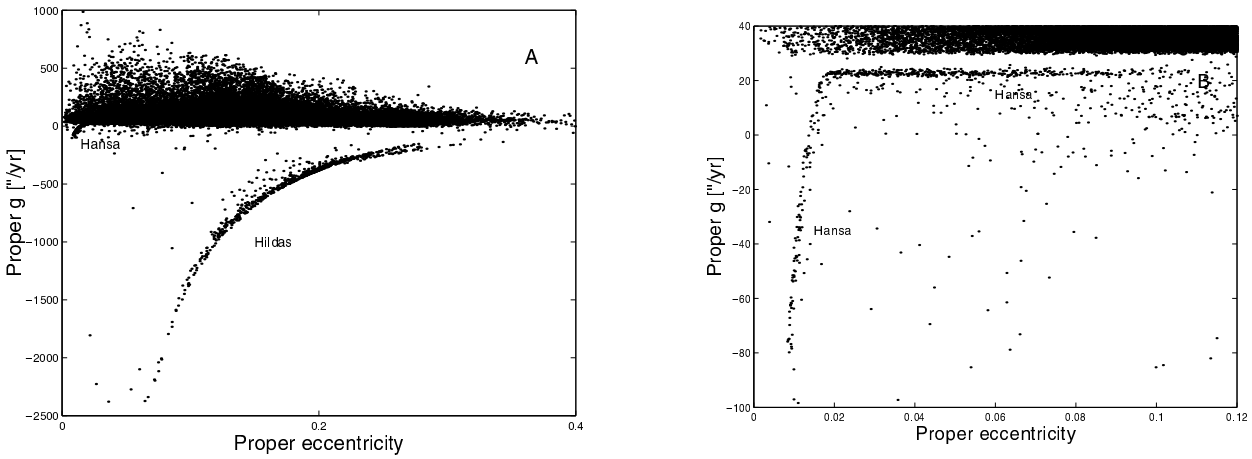

Fig. 11. Proper pericenter precession frequency g versus proper eccentricity for all asteroids in the main belt (panel **A**)) and for the region of the Hansa family (panel **B**)).

values of g). Since the precession frequency is higher for objects at low-eccentricities, an useful plane to show the dependence of g on e is the (e, g) plane. As can be seen in Fig. 11, panel A, there is a tail of asteroids at negative g whose precession frequency values are higher for smaller values of e. No Hilda is currently observed at an eccentricity smaller than 0.07.

While the case of the Hildas was well known, we found that this was not the only population of objects characterized by retrograde values of g. The Hansa family is a family at quite high inclination, quite low eccentricities, near the right side of the $3J{:}-1A$ mean-motion resonance with Jupiter. As can be seen in Fig. 11, panel B, members of the Hansa family with $e < 0.0179$ are also characterized by negative values of the pericenter precession frequencies. We believe this behavior can be explained if we consider the possibility that these objects could currently be inside the apocentrice tail of the $3J{:}-1A$ resonance.

Apocentric and pericentric orbits have been studied in the planar circular restricted three-body problem by Tsiganis et al. (2000) for the case of the $12J{:}7A$ resonance, and by Ferraz-Mello et al. (1998), that used a spatial asymmetric expansion of the disturbing function that included the effect of the Great Inequality of Jupiter's longitude for the case of the $2J{:}-1A$ resonance. Both these studies were conducted in the planar approximation, so that their results should be extrapolated to the case of a high-inclined family such as Hansa with a lot of caution. What it is generally observed is that in the planar circular restricted three-body problem (Sun-Jupiter-Asteroid) the family of nearly circular periodic resonant asteroidal orbits bifurcates at higher energies into a pericenter and apocenter branches, at lower and higher values of semimajor axis a, respectively (Tsiganis et al. 2000, Fig. 1). Basically, in the case of the $3J{:}-1A$ resonance, we would expect apocentric orbits to be circulating orbits of high energy whose equinoctial resonant elements $(e{*}\cos(3{*}\lambda_J{-}\lambda{-}2{*}\varpi), e{*}\sin(3{*}\lambda_J{-}\lambda{-}2{*}\varpi))$ (where $\varpi = \Omega{+}\omega$ and $\lambda = \varpi{+}M$) would be characterized by the interaction with the saddle point at $(0, 0)$. Contrary to normal circulating orbits, apocentric orbits would pass through the origin of the equinoctial orbital plane, while librating orbits would librate in one of the two libration islands of the $3J{:}-1A$ resonance.

We believe that a similar mechanism may be at play in this case, and that the Hansa family as found in Gil-Hutton (2006) using the CHCM may be actually made of two distinct components: one at $e > 0.0179$ that corresponds to most of the classical dynamical family and one at lower e, that is made up of objects currently in the apocentric tail of $3J{:}-1A$ resonance with Jupiter. To confirm this hyphothesis we perfomed a 20 000 yr integration of asteroids in both components of the Hansa family with Swift_whm.f, the integrator in the SWIFT package that uses the symplecting mapping of Wisdom & Holman (1991). We included all planets except Mercury and used a time-step of 20 days. Figure 12 displays the time series of the equinoctial resonant elements Fourier filtered so as to eliminate all frequencies with period lower than 1000 yr (Carruba et al. 2005) of two members of the Hansa family, an object in the high-e component ((40971) 1999 TY264, panel A), and an asteroid in the low-e component ((20517) Judycrystal, panel B). As can be seen in the figure, (20517) Judycrystal seems to display the behavior expected in a object in apocentric orbit, which could explain the retrograde values of its pericenter precession frequency. A similar behavior was observed in other objects in the low-e component of the Hansa family.

For what concern this paper, we believe that the study of the Hilda-type asteroid families goes beyond the purposes of this work, first because the proper elements of asteroids in the $3J{:}-2A$ mean-motion resonant configuration with Jupiter should more appropiately be obtained with analytical methods such in Miloni et al. (2005), or with ad hoc numerical procedure as in Schubart (1988), rather than with the general Knežević & Milani (2003) general numerical approach (we also refer the reader to Schubart 2007; and to Brož & Vokrouhlický 2008, for a more recent treatment of Hilda-type orbits).

The Hansa family has so far received much less attention. In the next section we will concentrate on the two components of the Hansa family, the low-e objects possibly in the apocentric tail of the $3J{:}-1A$ resonance with Jupiter and the others, at higher eccentricity, and discuss how the tecniques for family determination discussed in Sect. 3.1 can be extended to the case of this family.

3.2.1. The Hansa family

As discussed in the previous subsection, it is quite likely that the Hansa family as found by Gil-Hutton (2006) may be actually made of two well distinct components: a low-eccentricity component of asteroids possibly in apocentric $3J{:}1A$ resonant orbits, and an high-eccentricity component of asteroids not in resonant configuration. Understanding the true nature of the Hansa family is actually a very interesting field of research on its own.

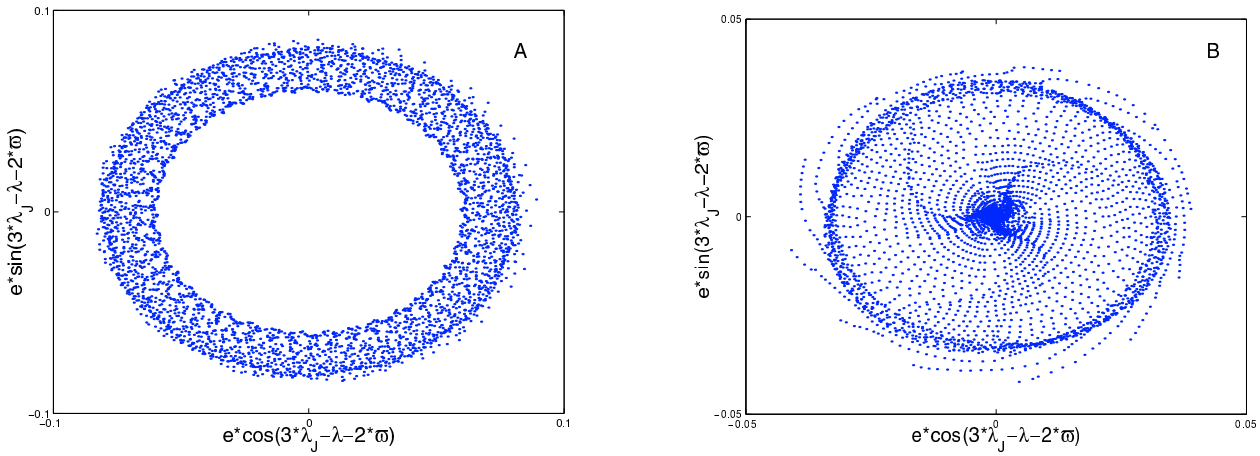

Fig. 12. A plot of $(e * \cos(3 * \lambda_J - \lambda - 2 * \varpi), e * \sin(3 * \lambda_J - \lambda - 2 * \varpi))$ for an asteroid in the high eccentricity component of the Hansa family ((40971) 1999 TY264, panel **A**)), and for an asteroid in the low eccentricity component of the Hansa family ((20517) Judycrystal, panel **B**)).

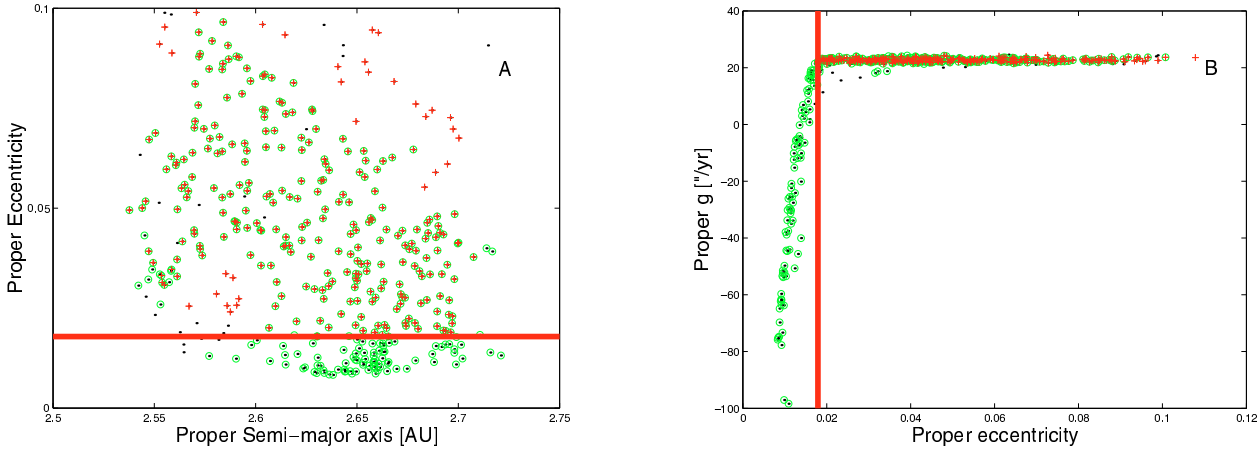

Fig. 13. An (a, e) (panel **A**)) and (e, g) (panel **B**)) projections of members of the Hansa family (green circles) found in proper element space and members of the family found in the frequency space (red crosses). The black dots show the locations of background asteroids in the region.

Here, however, we are mostly interested in introducing new techniques to determinying asteroid families. For this purpose, and as a numerical experiments, here we applied the regularization technique seen for the case of the Vesta family to the case of the Hansa family, but in the (e, g) space rather than in the (n, g) space.

Figure 13 (right panel) displays how the values of g depend on e for asteroids in the region of the Hansa family[5]. Note how for eccentricities of less than 0.0179 (vertical line) values of g significantly drop. Inevitably, this behavior of the g frequency creates problems to identifying the Hansa family in the frequency domain.

Since (480) Hansa itself is characterized by a significant high value of g, to identify the family in frequency space we used the lowest numbered object in the linear regime, (4880) Tovstorogov. We used a cutoff value in the frequency domain of 0.57″/yr (for larger values the family merged with the local background) and of 146 m/s in the proper element space. Projections of the two families in the (a, e) space plane, supermiposed with asteroids in the region of the Hansa family (black dots), are shown in Fig. 13, panel A. The horizontal (left panel) and vertical (right panel) lines display the limit value of e (0.0179) for which g drops. Note how objects with high absolute values of g and low e are recognized as family members by the classical approach, but not by the frequency method.

To try to overcome this problem we regularized the behavior of the g-frequency of asteroids at low eccentricities. For this purpose we employed a procedure similar to the one used for the Vesta family. We substituted the values of g with the regularized values g_r given by:

$$g_r = g \cdot \frac{y_1}{y_2} \tag{11}$$

where g_r is the regularized value of the g frequency, $y_1 = e \cdot p(1) + p(2)$, with $p(i)$ $(i = 1, 2)$ the linear and angular coefficient of the line that best-fit the regular asteroids, and n the asteroid mean-motion, and $y_2 = q(1) \cdot e^3 + q(2) \cdot e^2 + q(3) \cdot e + q(4)$, where the $q(i)$ $(i = 1, ..., 4)$ are the coefficient of the third-order polynomial that best-fit the g frequency in the perturbed domain. Values of the p and q coefficients for the two ranges of s values that we used are given in Table 2. Figure 14, right panel, displays the location of the regularized values of g_r with respect to e (green circles). The blue line is the line that best fit the data in the regular region, while the magenta line is the third-order polynomial that best-fit the data in the perturbed region. We applied this procedure to the asteroids in the local background having a value of g smaller than the minimum of those observed for the family in frequency space, and computed the new family for this

[5] Objects having values of e and $\sin(i)$ between the maximum and minimum of the classical Hansa family, and in the same range of semi-major axis.

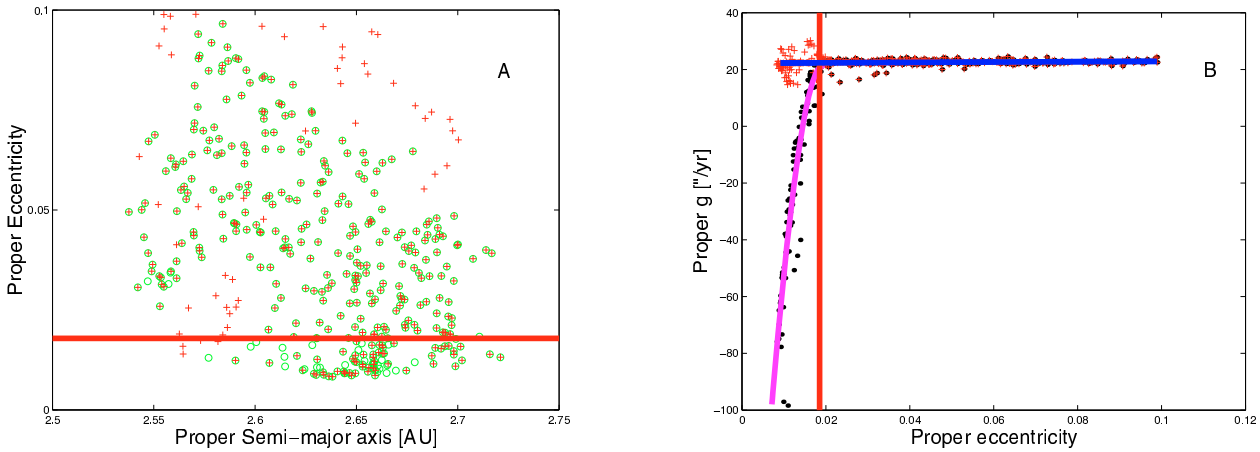

Fig. 14. An (a, e) (panel **A**)) and an (e, g) (panel **B**)) projections of the regularized Hansa family members (red crosses), superimposed to asteroids in the Hansa family region (black dots). The green circles are members of the classical family.

Table 2. Numerical values of the coefficients used to regularize g as a function of e for the Hansa family.

Coefficient	Numerical value
$p(1)$	6.4087
$p(2)$	22.2483
$q(1)$	-1.4938×10^7
$q(2)$	-1.1956×10^5
$q(3)$	2.1345×10^4
$q(4)$	−238.6464

modified set of proper frequencies. The family coalesced with the local background for a cutoff of 1.13″/yr, so we decided to work with a cutoff of 1.12″/yr.

The left panel of Fig. 14 shows an (a, e) projection of the regularized family (red asterisks), superimposed with the classical family. As can be seen in the figure, our method allows us to recognize as family members objects at very low-eccentricities that were lost otherwise, and also to connect object not recognized as members by other methods, such as the objects in the region centered at $a = 2.58$ AU and $e = 0.03$. We therefore believe that this procedure may therefore permit to overcome the problem presented by the perturbed behavior of the g frequency for apocentric $3J$:$1A$ resonant orbits.

4. Discussions

In this work we analyzed the cases of asteroid families interacting with secular resonances of argument other than g or $g + s$, or with low-order mean-motion resonances. Following the approach of Carruba & Michtchenko (2007), we obtained asteroid families in the proper frequency domain $(n, g, g + s)$ and in other domains most apt to describe the particular resonance that we were studying, and introduced techniques to "regularize" the behavior of the g frequency near mean-motion resonances. In particular, we did the following:

– We introduced several new representative planes and distance metrics for studying the case of diffusion of family members in resonances of argument other than g and $g + s$, such as the z_2, z_3, $\nu_6 - \nu_{16}$, $\nu_{17} + \nu_4 + \nu_5 - 2\nu_6$, and $3\nu_{16} - \nu_{17}$. Our new approaches (results are summarized in Table 4; the first column reports the family name and the second column the resonance argument, in the Michtchenko et al. 2008, notation) allows us to more efficiently track diffusion in such resonances by a 50% factor with respect to either families found in the proper element space or with the "standard distance metric" in frequency space of Carruba & Michtchenko (2007).
– We inquired why our method allows us to identify as family members objects currently inside mean-motion resonances that drifted far from the center of the family, as for objects inside the 1:2 resonance with Mars near the Vesta family.
– Introduced a new techniques to regularize the behavior of the g frequency as a function of the n frequency that allowed us to connect to the Vesta family objects near the left border of the 3:1 mean-motion resonance with Jupiter.
– Investigated the case of families characterized by a retrograde behavior of the g frequency, such as some members of the Hansa family and all the Hildas, and introduced a technique to regularize the behavior of the g frequency as a function of the eccentricity e.

Based on our experience, we believe that the cases we treated in this article should be fairly representative. Other possible resonant combinations, such as resonance of arguments $g+2s$, $g-2s$, $3s$ etc. have a minor effect on the stability of asteroid proper elements according to Milani & Knežević (1994) and were not treated in this paper. Approaches for treating such resonances can be easily derived from the examples that we provided in this paper. By regularizing the behavior of the g frequency as a function of n and e and introducing new distance metrics we were able to extend families in regions that were not accessible with the Carruba & Michtchenko (2007) approach, while keeping all the advantages of the recently published method (i.e., identifying objects that drifted in secular resonances due to the Yarkovsky and YORP effects as family members, simplicity in representing secular resonances etc.). More important, an analysis of asteroid families in the frequency domain may provide insight on the dynamical evolution of its members, in a way not always possible with the classical analysis in the proper element space. Examples of this include the evolution of members of the Erigone family in the z_2 resonance, the effect of the $\nu_6 - \nu_{16}$ resonance on the Phocaea family, and the role that the apocentric tail of the $3J$:$1A$ may have had in shaping the dynamics of 24.4% of the members of the Hansa family. The deeper understanding of the dynamics near asteroid families provided by an analysis in the frequency domain is, in our opinion, the most important new result of this work.

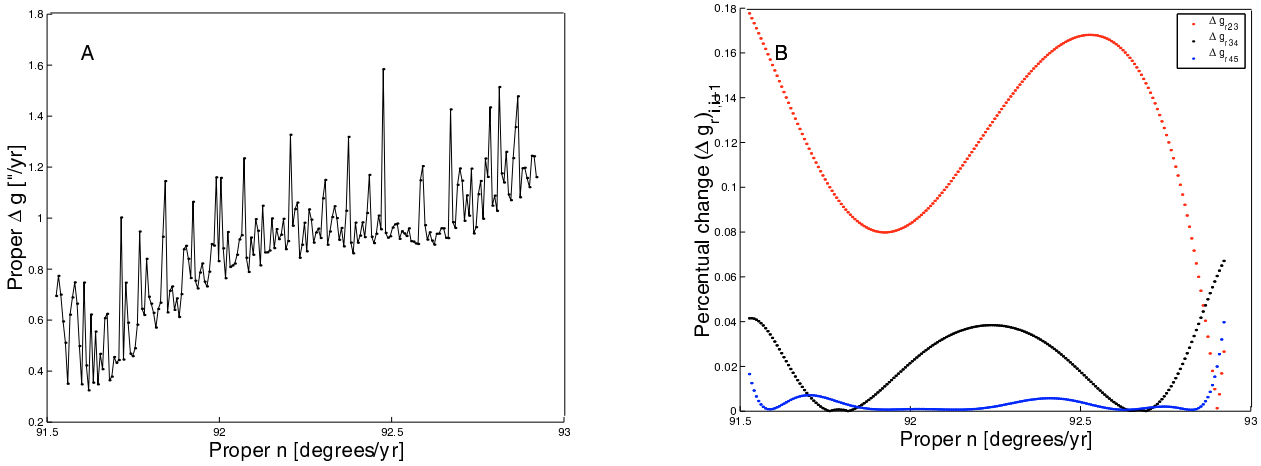

Fig. 15. Panel **A)**: Δg_r values obtained with Eq. (12) as a function of n for asteroids in the $3J{:}-1A$ perturbed region ($n < 93.0$) near the Vesta family for a third-order approximation of the $g(n)$ values in the region. Panel **B)**: a plot of the relative changes of the errors in g_r between different order approximation of $g(n)$.

Table 3. The limits in the $(a, e, \sin(i))$ domain of the local background for the families studied in this paper.

Family name	$a_{\min}$ [AU]	$a_{\max}$ [AU]	$e_{\min}$	$e_{\max}$	$\sin(i_{\min})$	$\sin(i_{\max})$
Erigone	2.28	2.46	0.04	0.32	0.05	0.13
Elektra	2.94	3.27	0.08	0.31	0.33	0.48
Phocaea	2.21	2.48	0.12	0.34	0.34	0.45
Baptistina	2.17	2.37	0.01	0.30	0.05	0.14
Vesta	2.19	2.54	0.00	0.30	0.06	0.17
Hansa	2.45	2.81	0.01	0.18	0.33	0.42

Table 4. Percentage of resonant asteroids in the local background identified as family members by the classical method (CHCM), the "standard" frequency method (FHCM), and the new distance metrics introduced in this article (AHCM).

Family name	Resonant argument	CHCM	FHCM	AHCM
Erigone	$2\nu_6 + \nu_{16}$	1.5	2.2	3.3
Elektra	$3\nu_6 + \nu_{16}$	2.2	4.8	7.8
Phocaea	$\nu_6 - \nu_{16}$	34.4	34.4	47.7
Baptistina	$\nu_{17} + \nu_4 + \nu_5 - 2\nu_6$	1.2	N/A	5.2
Vesta	$3\nu_{16} - \nu_{17}$	12.9	13.1	22.7
Vesta	$3\nu_6 - \nu_5$	3.6	1.9	5.7
Vesta	$2\nu_6 - \nu_5$	0.0	0.0	0.2

Acknowledgements. We thank the referee, David Vokrouhlický, for his comments and suggestions that helped to improve the original version of the paper. This work has been supported by the São Paulo State Science Foundation – FAPESP (grant 06/50005-5), and the Brazilian National Research Council – CNPq. The authors gratefully acknowledge the support of the Computation Center of the University of São Paulo (LCCA-USP), of the Astronomy Department of the IAG/USP, and of the Physics and Astronomy department of the IPD/UNIVAP for the use of their facilities.

Appendix A: Estimates of the errors on the regularized values of *g*

In Sect. 3.1 we introduced a technique to regularize the behavior of the g frequency as a function of n in the region near the $3J{:}-1A$ resonance, where $g(n)$ was approximated with a third-order polynomial. Here we try to quantify the errors on g_r caused by the application of Eq. (10) on the values of g and n of asteroids near the $3J{:}-1A$. For this purpose we make two assumptions:

- We use the RMS values of the g frequencies available at the AstDyS site as estimates of the errors on g.
- We neglect errors on n

The second assumption is in our opinion justified by the fact that rms values of n in the region of the Vesta family are a factor 10^{-4}–10^{-2} smaller than the rms of g. With these assumptions, we use Eq. (10) on a set of $(n, g \pm \Delta g)$ to obtain values of the regularized frequency g_r. Errors on g_r can be obtained using the standard propagation of errors formula, i.e.,

$$\Delta g_r = \Delta g \cdot \frac{y_1}{y_2} + g \cdot \frac{\Delta y_1}{y_2} + \frac{g y_1}{y_2} \Delta y_2, \tag{12}$$

where Δg is the rms value of g, Δy_1 is obtained using:

$$\Delta y_1 = n \cdot \Delta p(1) + \Delta p(2), \tag{13}$$

(where $\Delta p(1)$ and $\Delta p(2)$ are obtained using least-square formulas for the errors on the linear and angular coefficient of a line (Press et al. 1992); and Δy_2 is obtained numerically using a MATLAB routine (polyval.m) that uses the Cholesky factor of the Vandermonde matrix to obtain error estimates of the fitted g_r-values (Press et al. 1992).

Figure 15, panel A, displays Δg_r values obtained with Eq. (12) as a function of n for asteroids in the $3J{:}-1A$ perturbed region ($n < 93.0$) near the Vesta family for a third-order approximation of the $g(n)$ values in the region. We computed the errors also for a second, fourth, and fifth approximation of $g(n)$. Figure 15, panel B, is a semi-log plot of the relative changes of the errors in g_r between different order approximation of $g(n)$, defined as

$$\Delta g_{r\,i+1,i} = \frac{(\Delta g_r)_i - (\Delta g_r)_{i+1}}{(\Delta g_r)_i}, \tag{14}$$

with $i = 2$–4. As can be seen in the Fig. 15, panel A, errors on g_r are in a range between 0.3 and 1.6″/yr. Figure 15, panel B, shows that taking a third-order approximation improved the quality of our fit with respect to a third-order one by an average value of 14%. Using a fourth-order approximation would improve the value of the error by just 4%, and going to fifth-order would grant another 1%. The values of the $q(i)$ coefficients

for a fourth-order approximation are however rather large, and produce larger round-off errors in the estimate of the g_r values obtained with Eq. (10). In view of these considerations, we decided to adopt a third-order approximation of $g(n)$ in this work.

References

Bottke, W. F., Vokrouhlický, D., & Nesvorný, D. 2007, Nature, 449, 48
Bowell, E., Muinonen, K., & Wasserman, L. H. 1994, Asteroid, Comets and Meteorids III, ed. A. Milani, M. di Martino, & A. Cellino (Dordrecht: Kluwer), 477
Brož, M., & Vokrouhlický, D. 2008, MNRAS, in press
Bus, J. S., & Binzel, R. P. 2002a, Icarus, 158, 106
Bus, J. S., & Binzel, R. P. 2002b, Icarus, 158, 146
Carruba, V., & Michtchenko, T. 2007, A&A, 475, 1145
Carruba, V., Burns, J. A., Bottke, W., & Nesvorný, D. 2003, Icarus, 162, 308
Carruba, V., Nesvorný, D., Burns, J. A., Ć, M., & Tsiganis, K. 2004, AJ, 128, 1899
Carruba, V., Michtchenko, T., Roig, F., Ferraz-Mello, S., & Nesvorný, D. 2005, A&A, 441, 819
Carruba, V., Roig, F., Michtchenko, T., Ferraz-Mello, S., & Nesvorný, D. 2007, A&A, 465, 315
Duffard, R., Lazzaro, D., Licandro, J., et al. 2004, Icarus, 171, 120
Ferraz-Mello, S., Michtchenko, T. A., & Roig, F. 1998, AJ, 116, 1491
Gil-Hutton, R. 2006, Icarus, 183, 93
Guillens, S. A., Vieira Martins, R., & Gomes, R. S. 2002, AJ, 124, 2322
Knežević, Z., & Milani, A. 2000, Celest. Mech. Dyn. Astron., 78, 17
Knežević, Z., & Milani, A. 2003, A&A, 403, 1165
Lazzaro, D., Angeli, C. A., Carvano, J. M., et al. 2004, Icarus, 172, 179
McCord, T. B., Adams, J. B., & Johnson, T. V. 1970, Science, 168, 1445
Michtchenko, T. A., & Ferraz-Mello, S. 2002, Icarus, 149, 357
Michtchenko, T. A., Carruba, V., & Lazzaro, D. 2008, MNRAS, submitted
Milani, A., & Knežević, Z. 1994, Icarus, 107, 219
Milani, A., & Knežević, Z. 2003, A&A, 403, 1165
Miloni, O., Ferraz-Mello, S., & Beaugé, C. 2005, CeMDA, 92, 89
Morbidelli, A., & Vokrouhlický, D. 2003, Icarus, 163, 120
Morbidelli, A., Nesvorný, D., Bottke, W. F., et al. 2003, Icarus, 162, 328
Nesvorný, F., Roig, B., Gladman, D., et al. 2008, Icarus, 183, 85
Press, W. H., Vetterling, W. T., Teukolsky, S. A., & Flannery, B. P. 1992, Numerical Recipes in Fortran 77 (Cambridge University Press)
Šidlichovsky, M., & Nesvorný, D. 1997, Cel. Mech. Dyn. Astron., 65, 137
Schubart, J. 1998, Cel. Mech. Dyn. Astron., 43, 309
Schubart, J. 2007, Icarus, 188, 189
Tsiganis, K., Varvoglis, H., & Hadjidemetriou, J. D. 2000, Icarus, 146, 240
Vokrouhlický, D., Brož, M., Bottke, W. F., Nesvorný, D., & Morbidelli, A. 2006a, Icarus, 181, 118
Vokrouhlický, D., Brož, M., Morbidelli, A., et al. 2006b, Icarus, 182, 92
Vokrouhlický, D., Brož, M., Bottke, W. F., Nesvorný, D., & Morbidelli, A. 2006c, Icarus, 183, 349
Williams, J. G., & Faulkner, J. 1981, Icarus, 46, 390
Wisdom, J., & Holman, M. 1991, AJ, 102, 1528
Zappalà, V., Cellino, A., Farinella, P., & Knežević, Z. 1990, AJ, 100, 2030
Zappalà, V., Bendjoya, Ph., Cellino, A., Farinella, P., & Froeschlè, C. 1995, Icarus, 116, 291
Zellner, B., Tholen, D. J., & Tedesco, E. F. 1985, Icarus, 61, 355

4

Famílias dinâmicas na região de Phocaea

Com este artigo começou meu trabalho de análise dos asteroides de alta inclinação. A família dinâmica de Phocaea está contida em uma ilha de estabilidade entre as ressonâncias de movimento médio 4J:-1A e 3J:-1A em semi-eixo maior, e entre as ressonâncias seculares ν_6 e ν_5 em inclinação (Knežević and Milani 2003). O fato da família dinâmica estar em uma ilha de estabilidade coloca perguntas sobre a viabilidade da família como grupo colisional, e não como um conglomerado de objetos com órbitas semelhantes. Neste trabalho obtive grupos dinâmicos nos espaços dos elementos e das frequências próprias, revisei as propriedades taxonômicas, de albedo geométrica dos asteroides na região, obtive mapas dinâmicos, e estimativas preliminares das idades dos grupos identificados. A família de Phocaea aparentou ser uma possível família colisional de tipo espectral S, com uma idade de mais de 2.2 Byr, cujos membros de mais altos semi-eixo maior podem ter sido perdidos por causa da interação com a rede local de ressonâncias de movimento médio e seculares. De particular interesse foi a identificação do primeiro "clump" de objetos visível somente no espaço das frequências, o "clump" de (6246) Komurotoru, cuja evolução dinâmica foi investigada em um outro trabalho.

A seguir apresentamos o artigo, que foi publicado em Monthly Notices of the Royal Astronomical Society em 2009, volume 398, pp. 1512-1526.

Mon. Not. R. Astron. Soc. **398,** 1512–1526 (2009) doi:10.1111/j.1365-2966.2009.15220.x

An analysis of the region of the Phocaea dynamical family

V. Carruba[1,2]★

[1]*IPD, UNIVAP, São José dos Campos, SP, 12244-000, Brazil*
[2]*Department of Mathematics, UNESP, Guaratinguetá, SP, Brazil*

Accepted 2009 June 9. Received 2009 June 9; in original form 2009 March 10

ABSTRACT

In this work, I conduct a preliminary analysis of the Phocaea family region. I obtain families and clumps in the space of proper elements and proper frequencies, study the taxonomy of the asteroids for which this information is available, analyse the albedo and absolute magnitude distribution of objects in the area, obtain a preliminary estimate of the possible family age, study the cumulative size distribution and collision probabilities of asteroids in the region, the rotation rate distribution and obtain dynamical map of averaged elements and Lyapunov times for grids of objects in the area.

Among my results, I identified the first clump visible only in the frequency domain, the (6246) Komurotoru clump, obtained a higher limit for the possible age of the Phocaea family of 2.2 Byr, identified a class of Phocaea members on Mars-crossing orbits characterized by high Lyapunov times and showed that an apparently stable region on time-scales of 20 Myr near the ν_6 secular resonance is chaotic, possibly because of the overlapping of secular resonances in the region. The Phocaea dynamical group seems to be a real S-type collisional family, formed up to 2.2 Byr ago, whose members with a large semimajor axis have been dynamically eroded by the interaction with the local web of mean-motion and secular resonances. Studying the long-term stability of orbits in the chaotic regions and the stability of family and clumps identified in this work remain challenges for future works.

Key words: celestial mechanics – minor planets, asteroids.

1 INTRODUCTION

Among highly inclined asteroids [asteroids with $\sin(i) > 0.3$, for which the analytical theory used to obtain proper elements is not very accurate (Milani & Knežević (1994)], the asteroids in the region of the Phocaea family are characterized by a very interesting dynamics. The region of the Phocaea family is delimited by the 7J:-2A mean-motion resonance at low a, by the 3J:-1A resonance at high a and by the $\nu_6 = g - g_6$ (where g is the secular frequency of precession of the pericentre, and the suffix 6 refers to Saturn) secular resonance at low i (Knežević & Milani 2003). A region of shallow close encounters with Mars appears at $e > 0.3$, but deep close encounters with Mars are made impossible by the Kozai-class protection mechanism (Milani et al. 1989). The Phocaea family itself is characterized by its interaction with the $\nu_6 - \nu_{16}$ secular resonance [$(g - g_6) - (s - s_6)$, where s is the secular precession frequency of the asteroid node], and harmonics of this resonance are also present in the region. To better understand the interaction of the Phocaea family with the $(\nu_6 - \nu_{16})$ secular resonance, the family was recently obtained in the (n, g, $g - s$) frequency domain by Carruba & Michtchenko (2009). Other families and clumps in the region were recently identified by Foglia & Masi (2004) and Gil-Hutton (2006).

One of the open questions about the Phocaea family is if the dynamical family is real or an artefact created by the stable island region between secular and mean-motion resonances, and the zone of close encounters with Mars (Knežević & Milani 2003). For the purpose of answering this and other questions in this work, I first re-obtained dynamical families in the space of proper element and frequencies (Carruba & Michtchenko 2007, 2009), I studied the spectroscopical and Sloan Digital Sky Survey Moving Objects Catalogue, fourth release (SDSS-MOC4) data for the region, reviewed the current knowledge on geometric albedos and absolute magnitudes, obtained the Yarkovsky isolines, studied the cumulative distribution and collision probabilities of family members and the information on asteroid rotation rates, and the role that mean-motion and secular resonances have had in shaping the family.

I found that, with the exception of the family around (19536) (1999 JM4), formerly associated with the clump around (2860) Pasacentennium, the families and clumps found by Gil-Hutton (2006) are now substructures of the Phocaea family. I identified new clumps in a proper element and frequency space, and in particular I found the first 'frequency-only' clump around (6246) Komurotoru.

A preliminary analysis of Yarkovsky isolines shows that the family can be up to 2.2 Byr old. Dynamical maps of the region showed

★E-mail: valerio@univap.br

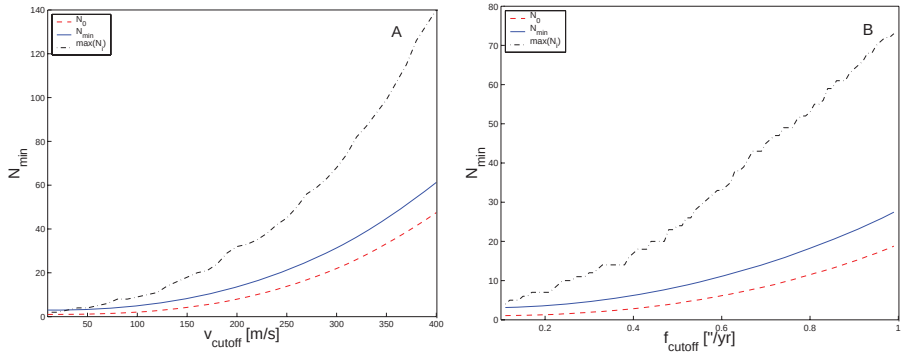

Figure 1. The average number N_0, $N_{\rm min}$ and the maximum number max (N_i) of asteroids as a function of the velocity cut-off (panel A), and of the frequency cut-off (panel B), for the asteroids in the region of the Phocaea family.

us that there exist regions that are dynamically stable on the timescales of the integration, but yet deprived of asteroids. Such regions, all characterized by very low values of Lyapunov times, are either associated with Mars-crossing orbits, or are near the border of the ν_6 secular resonance separatrix. Understanding the long-term stability of orbits in the chaotic regions and the stability of family and clumps identified in this work will be the subject of a next paper on this subject.

2 DYNAMICAL FAMILIES AND CLUMPS IN THE REGION

I start my analysis of the Phocaea family region by re-deriving classical and frequency families and clumps in the area. I identify the members of the dynamical families in the region using the classical hierarchical clustering method [CHCM; see Bendjoya & Zappalà 2002 and references therein], and the frequency hierarchical clustering method (FHCM; Carruba & Michtchenko 2007, 2009).[1]

In identifying asteroid families in the space of proper elements two parameters are fundamental: the cut-off distance at which the family members are defined (d_0) and the minimum number of objects N_{min} for a cluster to be considered significant. Beaugé & Roig (2001) define a nominal distance cut-off as the average minimum distance between all the neighbouring asteroids in the same region of the asteroid belt. The value of $N_{\rm min}$ is defined by Zappalà et al. (1995) as

$$N_{\rm min} = N_0 + 2\sqrt{N_0}, \tag{1}$$

where N_0 is the average number of orbits within a sphere of radius d_0 at every point of the proper element space. A cluster with a number of objects larger than this critical value is called a clump, while a family is a cluster with a number of members larger than $2.5 \times N_{\rm min}$. As we shall see in more detail in Section 8, the region of the Phocaea family is delimited by the 7J:-2A and 3J:-1A mean-motion resonances in proper a and by the ν_6 secular resonance at low inclination. Currently, 1736 objects are found in the AstDyS site in this region. The nominal distance velocity cut-off as defined in Beaugé & Roig (2001) is of 146.9 m s^{-1}, while Fig. 1 displays the average number N_0, $N_{\rm min}$ and the maximum number max (N_i) of asteroids as a function of the velocity cut-off, for asteroids in the region. The value of $N_{\rm min}$ corresponding at $d_0 = 146.9$ m s^{-1} is 8. As can be seen in Fig. 1, the fact that max (N_i) is not much larger than $N_{\rm min}$ may be a hint that the families dominate the local background of objects (see Section 6).

For what concerns the domain of proper frequencies, since the Phocaea group is characterized by its interaction with the $(g - s - g_6 + s_6)$ resonance, or $(\nu_6 - \nu_{16})$ (Knežević & Milani 2003, see also Section 8), following the approach of Carruba & Michtchenko (2009), I determined the family with a metric of the form

$$f = \sqrt{h_1 \left(\frac{\Delta n}{h_0}\right)^2 + h_2(\Delta g)^2 + h_3(\Delta(g-s))^2}, \tag{2}$$

(where $h_1 = h_2 = h_3 = 1$) rather than with the 'standard frequency metric' in the $(n, g, g + s)$ domain of Carruba & Michtchenko (2007). I determined the nominal frequency cut-off defined as the average minimum distance between all neighbouring asteroids in the $(n, g, g - s)$ domain, and I found a value of $f_0 = 0.525$ arcsec yr^{-1}. Fig. 1 (panel B) displays the average number N_0, $N_{\rm min}$ and the maximum number max (N_i) of asteroids as a function of the frequency cut-off defined by equation (2). The value of $N_{\rm min}$ corresponding at $f_0 = 0.525$ arcsec yr^{-1} is 26. As observed for the values of $N_{\rm min}$ and max (N_i) obtained in the proper element domain in the domain of frequencies, I still do not observe a much larger value of max N_i with respect to $N_{\rm min}$. Again, this may suggest that the local background of the Phocaea family is indeed dominated by the Phocaea family itself (see Section 6).

Since the Phocaea family is by far the most prominent family in the region, I started by using the CHCM for this family. Fig. 2 (panel A) displays the number of family members (left ordinate) and the differential number dn/dv (right ordinate) as a function of the velocity cut-off. The red vertical line displays the nominal cut-off according to Beaugé & Roig (2001). The numbers on the top of the peaks of differential asteroid numbers are related to the cluster of objects englobed by the Phocaea family. For $d_{\rm cut-off} = 110$ m s^{-1} the Phocaea family conglomerates with the (587) Hypsipyle cluster, at $d_{\rm cut-off} \simeq 130$ the Phocaea families annexed the former Gil-Hutton families associated with (1660) Wood and (5247) Krylov, at $d_{\rm cut-off} = 177$ m s^{-1} the family englobes the newly found family associated with (2860) Pasacentennium [a former clump in Gil-Hutton (2006)] and, finally, at $d_{\rm cut-off} = 198$ m s^{-1} the Phocaea family conglomerates with the last independent clump associated with (17628) 1996 FB5. For higher values of the cut-off, the family simply slowly expands annexing peripheral objects. This may suggest that the local background of the Phocaea family is dominated by the Phocaea family itself. I will come back to this subject in the following sections.

[1] I used synthetic proper elements and frequencies obtained numerically and is publically available at the AstDyS site http://hamilton.dm.unipi.it/cgi-bin/astdys/astibo, accessed on 2008 December 1.

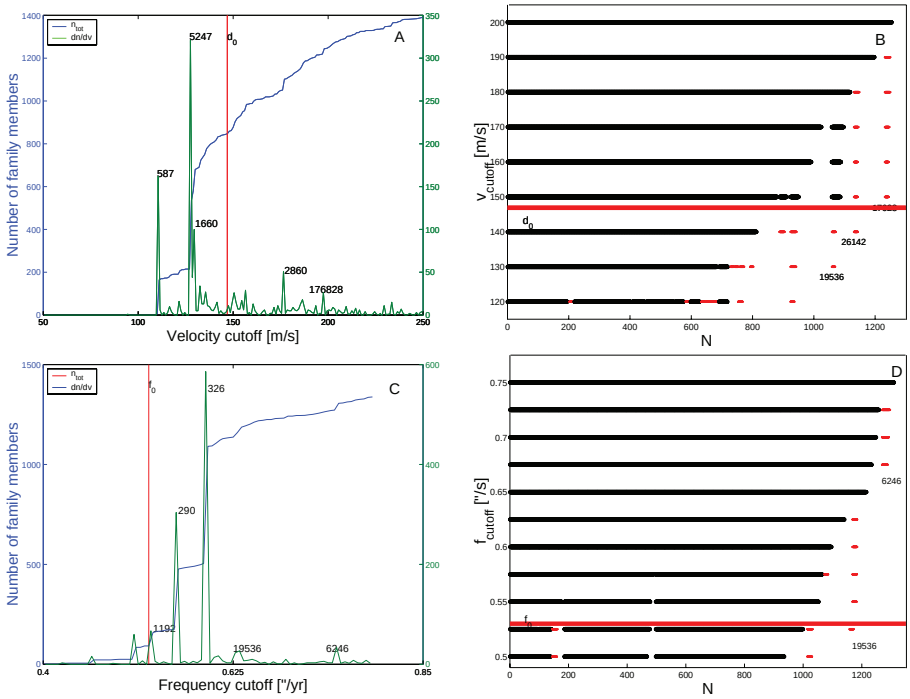

Figure 2. Panel A: the number and differential number of members of the classical Phocaea family as a function of the cut-off. The numbers on the peaks of the differential number of family members are related to the clusters that were englobed by the Phocaea family at higher velocity cut-offs. Panel B: a stalactite diagram of the Phocaea family region. Panels C and D: the same as panels A and B, but for the frequency groups.

To re-identify asteroid families, I also constructed a stalactite diagram in the traditional way defined by Zappalà et al. (1990) and Brož & Vokrouhlický (2008): I start with (25) Phocaea as the first central body and identify all the bodies associated with it at $d_{\rm cut-off} = 200$ m s^{-1}, a value for which no other independent cluster of asteroids was found in the Phocaea region. I then decrease the cut-off and identified the families and clumps among the asteroids not associated with (25) Phocaea. Fig. 2 (panel B) displays my results in the interval of cut-offs between 120 and 200 m s^{-1}. Full black squares are associated with families in the region, and empty black squares are associated with clumps, according to the limits displayed in Fig. 1. Table 1 reports the families and clumps that I identified in this work. The first column reports if it is a family or a clump (the suffix c stands for groups identified in the proper element domain, while f stands for the groups found in the frequency space), the second column reports the lowest numbered asteroid in the group, the third reports the number of objects associated with the group, the fourth reports the number of object with spectral classification and the fifth reports the number of objects with SDSS-MOC4 data (see Section 3).

Table 1. Families and clumps in the region of the Phocaea group.

Id	Name	N	$N_{\rm spec}$	$N_{\rm SDSS-MOC4}$
Family(c)	(25) Phocaea	988	26	98
Family(f)	(25) Phocaea	1137	29	102
Family(c)	(19536) (1999 JM4)	27	0	3
Clump(f)	(19536) (1999 JM4)	14	0	2
Clump(c)	(17628) (1996 FB5)	10	0	0
Clump(c)	(26142) (1994 PL1)	10	0	1
Clump(f)	(6246) Komurotoru	9	0	1

To find the groups I used the following criterion. The clusters should be observable for a cut-off equal to d_0 and the 'length of the stalactite' associated with the family should be at least of 20 per cent of d_0, i.e. $\simeq 30$ m s^{-1}. The last requirement was set so as to avoid to identify as families sub-clusters of the Phocaea family that are eventually not connected to the family because of a conservative choice of the velocity cut-off. Based on the analysis of Fig. 2 (panel A), I choose to work with a cut-off of 160 m s^{-1}, a value a bit larger than d_0 so as to include in the Phocaea family two small clusters [associated with (1963) Bezovec and (6487) Tonyspear]. With this choice of cut-off most of the Gil-Hutton families [such as the two families of (1660) Wood and (5247) Krylov] and clumps are now substructures of the Phocaea family. A new family associated with (19536) (1999 JM4) and two clumps associated with (17628) (1996 FB5) and (26142) (1994 PL1) were found in this work. The (19536) family picks the lower numbered asteroid (2860) Pasacentennium (former clump in Gil-Hutton 2006) at $v_{\rm cut-off} = 164$ m s^{-1}.

I then used the FHCM in the $(n, g, g - s)$ domain to identify members of the Phocaea dynamical family. Fig. 2 (panel C) displays the number of family members (left ordinate) and differential number $\mathrm{d}n/\mathrm{d}f$ (right ordinate) as a function of the frequency cut-off. The red vertical line displays the nominal frequency cut-off. The frequency family has only 92 members at the nominal frequency cut-off, and this fact may play against the possibility of using the nominal frequency cut-off for family determination in the frequency domain.

The numbers on the top of the peaks of differential asteroid numbers are related to the cluster of objects englobed by the Phocaea family at higher cut-offs. For $f_{\rm cut-off} = 0.530$ arcsec yr^{-1} the Phocaea family conglomerates with the (1192) Prisma cluster, at $f_{\rm cut-off} = 0.560$ arcsec yr^{-1} it merges with the (290) Bruna family, at $f_{\rm cut-off} = 0.595$ arcsec yr^{-1} it coalesces with the (326) Tamara family, at $f_{\rm cut-off} = 0.625$ arcsec yr^{-1} the family englobes the clump

associated with (19536) (1999 JM4), which is a family found in the proper element domain and, finally, at $f_{\rm cut-off} = 0.750$ arcsec yr^{-1} the family coalesces with the last clump, associated with (6246) Komurotoru, which is a clump only observed in the frequency domain. As observed for the classical family, there is no sudden fusion with the local background for higher values of the cut-off.

As done for the families in the proper element domain, I also constructed a stalactite diagram in the frequency domain. I follow a procedure similar to that described for the proper element groups, starting with a frequency cut-off of $f_{\rm cut-off} = 0.750$ arcsec yr^{-1}, for which no independent clump or family other than the Phocaea one could be identified in the region. Table 1 reports the families and clumps that were identified in the frequency domain. As observed in Fig. 2 (panel C), the value of the frequency cut-off needs to be at least larger than 0.595 arcsec yr^{-1}, or else the Phocaea family would be divided in two different groups. This value seems in agreement with that found in Carruba & Michtchenko (2009) for a smaller proper frequencies set. Information given by the stalactite diagram (Fig. 2, panel D) shows that the (19536) group, which was also identified in the proper element domain, is also distinguishable for $f_{\rm cut-off}$ larger than 0.525 arcsec yr^{-1} and smaller than 0.625 arcsec yr^{-1}. To obtain the larger possible sample of body in the Phocaea frequency family, I decided to work with a cut-off of 0.625 arcsec yr^{-1}.

An interesting feature observed at larger cut-offs is the clump around (6246) Komurotoru. This clump, which only coalesces with the Phocaea family for $f_{\rm cut-off} = 0.750$ arcsec yr^{-1}, is associated with the $(2\nu_6 - \nu_{16})$ resonance and is the first, to my knowledge, clump of object only detected in the frequency domain.[2] The clumps around (17628) and (26142), observed in the proper element domain, were not found in the proper frequency space.

To understand how the Phocaea family interacts with other families and clumps in the region, I also determined the local density of asteroids, following the approach of Carruba & Michtchenko (2009). Density maps will display regions characterized by strong mean-motion or secular resonances by a relatively low number of asteroids per unit bin. To quantitatively determine the local density of asteroids, I choose a region in the range of the a, e and $\sin(i)$ values of the local background for the Phocaea family as determined by Carruba & Michtchenko (2009). I computed the $\log_{10}$ of the number of asteroids per unit square in a 30 by 34 grid in a (starting at $a = 2.20$ au, with a step of 0.008 au) and e (starting at 0.08, with a step of 0.008). Results are shown in panel A of Fig. 3. Using similar procedures, I computed a density map of the Padua family region in the $(a - \sin(i))$ (Fig. 3, panel C), and $(g,\ g - s)$ (Fig. 3, panel E) planes. I choose to work with the $(g - s)$ plane because of the influence that the $(\nu_6 - \nu_{16})$ resonance exerts on the asteroids in the region (Carruba & Michtchenko 2009). Superimposed to the density maps I show projections of the Phocaea and (19536) families (as plus signs) and of the (17628) and (26142) clumps (as triangles, see also Table 1 for information on the families and clumps) obtained in the proper element domain. Since the number density of objects in this area is relatively low, I did not use the median filter described in Carruba et al. (2004) to smooth out the effects of three-dimensional projections in 2D planes, binning, etc.

[2] At a cut-off of 0.625 arcsec yr^{-1} the clump has nine members, which is slightly below the criterion used to identify clumps for this cut-off (11 members). Since the clump is robust at higher cut-offs, I decided to accept it at 0.625 arcsec yr^{-1} as well.

As already discussed in Carruba & Michtchenko (2009), note how the Phocaea family is surrounded by a region with a very low density of asteroids. The Phocaea family seems essentially to fill all the available space in the 'stable island' region between secular and mean-motion resonances. This might either suggest that the family is an artefact of the dynamics in the region, rather than be an actual collisional family, or that it is an actual family leaking members to the local web of powerful mean-motion and secular resonances. I will come back to the subject in Section 8. Also note how in the $(g,\ g - s)$ space several members of the family are aligned inside the $(\nu_6 - \nu_{16})$ resonance at $g - s = 54.588$ arcsec yr^{-1}. Since the family strongly interacts with a resonance of argument $(g - s)$, Carruba & Michtchenko (2009) suggested to look for families in the region in the $(n,\ g,\ g - s)$ domain.

For what concerns the frequency groups, in Fig. 3, I show $(a,\ e)$ (panel B), $(a,\ \sin(i))$ (panel D) and $(g,\ g - s)$ (panel F) projections of the frequency family and clumps, superimposed with the density map obtained for the classical case. Note how the frequency Phocaea family is much more extended along the $(\nu_6 - \nu_{16})$ resonance than the corresponding Phocaea classical family [see Fig. 3 (panel F), Fig. 3 (panel E) and the discussion in Carruba & Michtchenko (2009) for a quantitative estimate of the efficiency of the metric in the $(n, g, g - s)$ domain in obtaining members of families interacting with such resonances].

Also, note how the Komurotoru clump is essentially aligned with a strip at $\simeq 63$ arcsec yr^{-1} in the $(g - s)$ variable. In Section 8, I will show how this region is associated with the $(2\nu_6 - \nu_{16})$ secular resonance. In the following sections, I will further analyse the families obtained in the proper element and frequency domain in terms of compositional analysis.

3 THE COMPOSITIONAL ANALYSIS

As a preliminary step in the analysis of the Phocaea family, I reviewed the current knowledge about the taxonomical classification of members of the frequency Padua family. Using the data present in the three major photometric/spectroscopic surveys Eight-Colour Asteroid Analysis (ECAA; Zellner, Tholen & Tedesco 1985; Tholen 1989), Small Main Belt Spectroscopic Survey (SMASS; Xu et al. 1995; Bus & Binzel 2002a,b) and Small Solar System Objects Spectroscopic Survey (S3OS2; Lazzaro et al. 2004), I identified in the Phocaea family background (defined as in Carruba & Michtchenko 2009) four A-type, one L-type, 36 S-type, two X-type, four C-type and three D-T-type objects. Of these, 26 were members of the Phocaea classical family and seven were members of the Phocaea frequency family (but not of the classical one; vice versa there were four objects that were members of the classical family but not of the frequency one). Table 2 reports the asteroid identification, family status (c stands for the classical family, and f for the frequency one), geometric albedo, diameter and spectral class for the asteroids for which at least some of this information is available. Data on the albedo and asteroid diameters for which an error estimate was available was taken from Tedesco et al. (2002) (see also Section 3). Data on the albedo for which an error estimate is not available were from the Horizon web site (http://ssd.jpl.nasa.gov).

Carvano et al. (2001) analysed 31 objects in the Phocaea region (as well as 29 asteroids in the Hungaria group) and concluded that, despite the presence of a large C-type object in the family, (105) Artemis, the fact that the majority of asteroids was tightly concentrated in the region of the Phocaea family suggested that the family could be a real product of a collisional outbreak. Fig. 4 displays an $(a,\ e)$ (panel A), $(a,\ \sin(i))$, (panel B), $(e,\ \sin(i))$

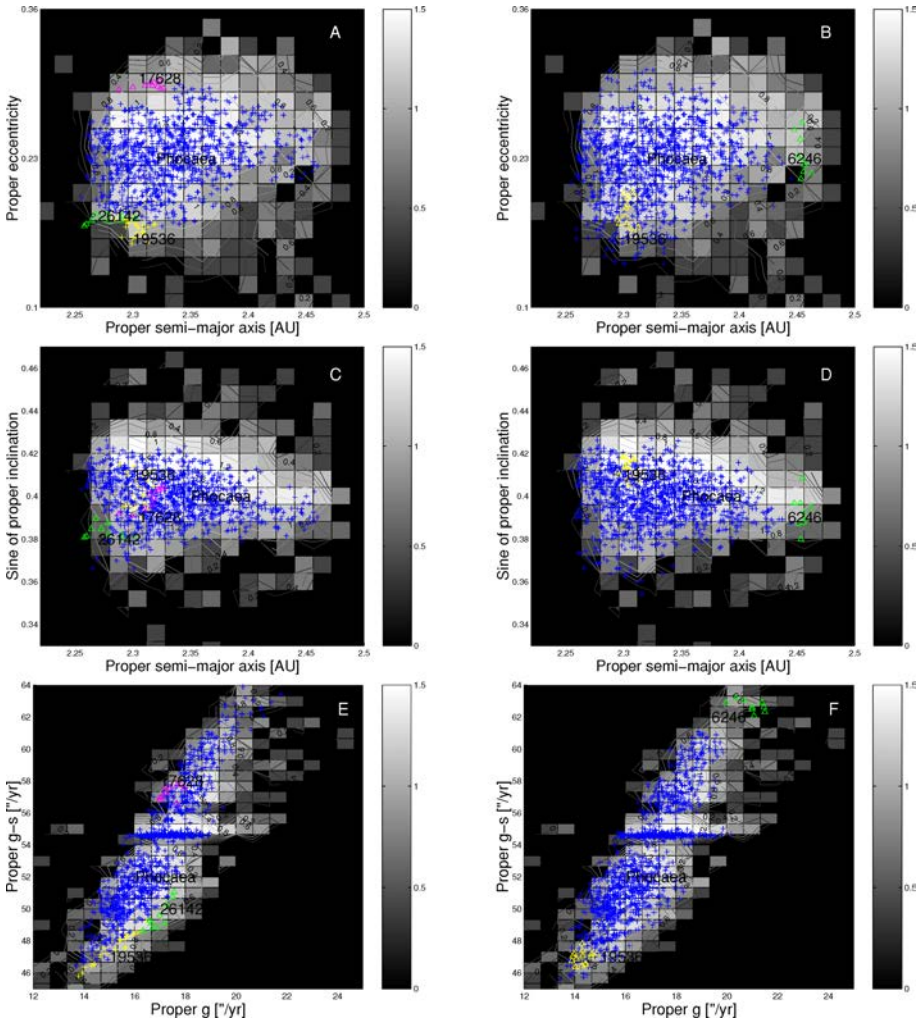

Figure 3. An $(a - e)$ (panel A), $(a - \sin(i))$ (panel C) and $(g, g - s)$ (panel E) projections of the families and clumps (see Table 1) in the region of the Phocaea family, obtained in the proper element domain. Panels B, D and F display the same, but for the groups obtained in the $(n, g, g - s)$ frequency domain.

(panel C) and $(g, g - s)$ (panel D) projections of the asteroids with a known spectroscopical classification, along with the members of the Phocaea frequency family (blue dots).

As can be seen in Fig. 4, and from the data of Table 2, all C-type asteroids in the region are not members of the Phocaea families, including (105) Artemis. Most of the S-type objects in the region were members of the Phocaea families, with six exception. There were only three members of the family with types other than S: (950) Ahrens (A-type, not incompatible with the mineralogy of an S-type family), (1318) Nerina (X-type) and (4666) Dietz (D-T type). The ratio of 9.1 per cent of objects with a spectral type different than the dominant one seems to be compatible with the expected ratio of interlopers for a family of the size of Phocaea (Migliorini et al. 1995, but the sample of objects with a known spectral type is still too small to reach a definitive conclusion).

For the purpose of extending the sample for which information on taxonomy is available, I turn my attention to the SDSS-MOC4 data. The SDSS MOC4 lists astrometric and photometric data for asteroids observed by the 2.5-m Sloan telescope located at Apache Point Observatory, in Sunspot, New Mexico. To date (fourth release), the survey has determined positions, brightness, and five-colour CCD photometry of 471 569 moving objects (Parker et al. 2008).

The flux reflected by the detected objects was measured almost simultaneously in five bands (measurements in two successive bands were separated in time by 72 s) with effective wavelengths 3557 Å (u band), 4825 Å (g band), 6261 Å (r band), 7672 Å (i band) and 9097 Å (z band), and with 0.1–0.3 μm band-widths (Fukugita et al. 1996). Here I follow the approach of Roig & Gil-Hutton (2006) to obtain principal components in the space of albedos F_u, F_g, F_i, F_z. Using the criteria introduced by Roig & Gil-Hutton (2006) to reject data with large errors, I obtain a data set of 18 178 objects with principal components data, 17 258 of which are related to numbered objects.

Once the two first principal components are found, the data can be used to classify asteroids according to their taxonomic types and to determine asteroid families in the space of proper elements and colours simultaneously. Bus & Binzel (2002a,b) and Nesvorný et al. (2005) introduced the following extended metrics in this space:

$$d_3 = \sqrt{d^2 + C_{\rm PC}[(\delta {\rm PC}_1)^2 + (\delta {\rm PC}_2)^2]}, \quad (3)$$

where d is the distance given by the standard metric of Zappalà et al. (1995), and $\rm PC_1$ and $\rm PC_2$ are the two first principal components. Carruba & Michtchenko (2007, equation 3) also introduced metrics of colours and frequencies in the $(n, g, g + s, {\rm PC}_1, {\rm PC}_2)$

Table 2. Asteroids in the Phocaea region with known spectral classification.

Number	Name	Family membership	Albedo	Diameter (km)	Spectral type
25	Phocaea	Phocaea c,f	(0.2310 ± 0.024)	(75.13 ± 3.6)	S
105	Artemis		(0.0465 ± 0.002)	(119.08 ± 2.8)	C
265	Anna		(0.1045 ± 0.033)	(23.66 ± 3.0)	X
273	Atropos		(0.1624 ± 0.015)	(29.27 ± 1.3)	L
323	Brucia	Phocaea c,f	(0.1765 ± 0.018)	(35.82 ± 1.7)	S
391	Ingeborg				S
502	Sigune	Phocaea c,f	(0.3405 ± 0.105)	(15.98 ± 2.0)	S
654	Zelinda		(0.0425 ± 0.003)	(127.40 ± 3.9)	C
914	Palisana		(0.0943 ± 0.004)	(76.61 ± 1.7)	C
950	Ahrensa	Phocaea f	(0.1793 ± 0.054)	(15.03 ± 1.8)	A
1090	Sumida				D-T
1108	Demeter		(0.0464 ± 0.008)	(25.61 ± 2.0)	C
1164	Kobolda	Phocaea c,f			S
1316	Kasan				A
1318	Nerina	Phocaea c,f	(0.1811 ± 0.017)	(13.02 ± 0.6)	X
1322	Coppernicus				S
1367	Nongoma	Phocaea c			S
1568	Aisleen	Phocaea c,f			S
1573	Vaisala	Phocaea f	(0.2226 ± 0.043)	(9.77 ± 0.8)	S
1575	Winifred	Phocaea c,f	0.2452	9.3	S
1591	Baize	Phocaea c,f	0.1056	18.7	S
1660	Wood	Phocaea c,f			S
1816	Liberia	Phocaea c,f			S
1883	Rimito	Phocaea c,f			S
2014	Vasilevskis	Phocaea c,f			S
2050	Francis	Phocaea f			S
2105	Gudy		(0.1078 ± 0.007)	(22.25 ± 0.7)	D-T
2430	Bruce Helin	Phocaea f			S
2791	Paradise				A
2965	Surikov				S
3267	Glo	Phocaea c,f	0.0607	13.6	S
3343	Nezdel				S
3388	Tsanghinchi	Phocaea c,f			S
3792	Preston	Phocaea f			S
3888	Hoyt	Phocaea c,f			S
3913	Chemin	Phocaea c,f			S
4103	Chahine		(0.3477 ± 0.027)	(12.97 ± 0.5)	A
4121	Carlin	Phocaea c,f	(0.4164 ± 0.086)	(6.82 ± 0.6)	S
4132	Bartok	Phocaea c,f	(0.3308 ± 0.039)	(10.5 ± 0.6)	S
4340	Dence				S
4511	Rembrandt	Phocaea c,f	(0.2861 ± 0.066)	(9.02 ± 0.9)	S
4533	Orth	Phocaea c,f			S
4666	Dietz	Phocaea f			D-T
4826	Wilhelms	Phocaea c,f			S
4995	Griffin	Phocaea c,f			S
5647	(1990 TZ)	Phocaea c	(0.4729 ± 0.072)	(10.62 ± 0.7)	S
6084	Bascom	Phocaea f			S
6560	Pravdo				S
6847	Kunz-Hallstein	Phocaea c,f			S
11548	Jerrylewis	Phocaea c			S

domain. Since in this work, I am interested in studying the interaction of asteroids with a resonance of argument $(g - s)$, it is more appropriate to use a metric in the $(n, g, g - s, \mathrm{PC}_1, \mathrm{PC}_2)$ domain of the form

$$d_4 = \sqrt{f^2 + D_{\mathrm{PC}}[(\Delta \mathrm{PC}_1)^2 + (\Delta \mathrm{PC}_2)^2]}, \quad (4)$$

where f is the distance metric in the frequency domain given by equation (2), and D_{PC} is a numerical factor, empirically set equal to 200 to give comparable results for the typical differences in proper frequencies and those in principal components.

Following the approach of Carruba & Michtchenko (2007), I selected an S-type asteroid in the Phocaea classical and frequency families also present in the 17 258 data base of numbered asteroids for which data on PC_1 and PC_2 are available: (4132) Bartok. A similar procedure was carried out for the families and clumps obtained in the proper element domain for which at least one member had principal component data. I found that for a cut-off of 380 $\mathrm{m\,s^{-1}}$ the (19 536) family coalesces with the Phocaea family, and therefore I decided to work with a cut-off of 375 $\mathrm{m\,s^{-1}}$. At this cut-off I found that the Phocaea family has 112 members, the (19 536) family has 11 members and the (26 142) clump has one member [no

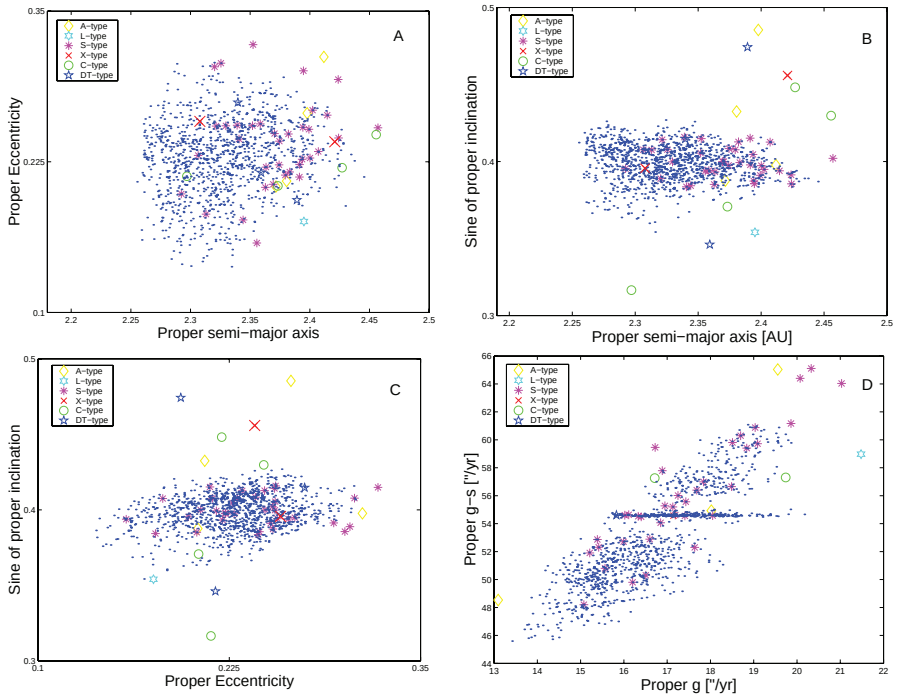

Figure 4. Taxonomic distribution of asteroids in the region of the Phocaea family.

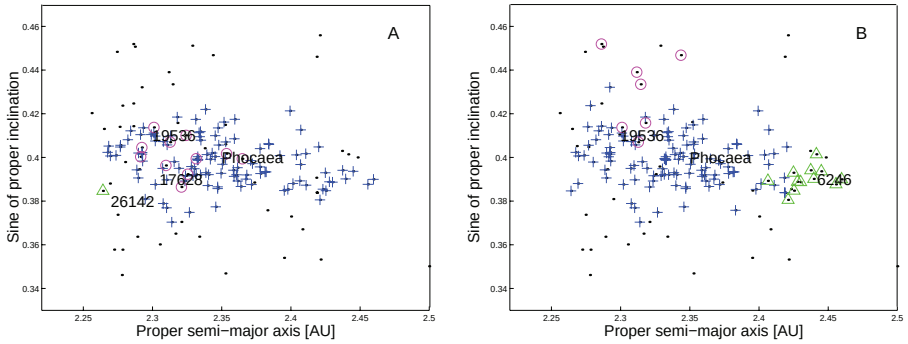

Figure 5. Panel A: an $(a, \sin(i))$ projection of the members of the Phocaea, (blue crosses), (19 536) (magenta circles) and (26 142) (green triangle) dynamical groups found in the space of proper element and principal components. Black dots display the location of asteroids in the SDSS-MOC4 data base in the region. Panel B: the same for members of the Phocaea (blue crosses), (19 536) (magenta circles) and (6246) (green triangles) found in the space of proper frequencies $(n, g, g - s)$ and principal components.

member with principal component data was found for the (17 628) clump].

Fig. 5 (panel A) displays a projection of the members of the Phocaea, (blue crosses), (19 536) (magenta circles) and (26 142) (green triangle) dynamical groups found in the space of proper element and principal components. Black dots display the location of asteroids in the SDSS-MOC4 data base in the region. As can be seen in the figure, the orbital distribution of the Phocaea family members found in the domain of proper elements and principal components follows quite closely the distribution of the family members in the space of proper elements (see Fig. 3, panel C).

I then obtained families and clumps in the domain of proper frequencies and principal components using equation (4). For a cut-off of 2.3 arcsec yr^{-1} the (6246) Kunamoto cluster merges with the Phocaea family, so I decided to work with a cut-off of 2.2 arcsec yr^{-1}. At this cut-off, the Phocaea family has 115 members, the (19 536) clumps have seven members and the (6246) clump has 12 members.

Fig. 5 (panel B) displays a projection of the members of the Phocaea, (blue crosses), (19 536) (magenta circles) and (6246) (green triangle) dynamical groups found in the space of proper frequencies and principal components. As can be seen in the figure, the orbital distribution of the Phocaea family members follows closely that of the family found in the space of proper frequencies (see Fig. 3, panel D). The 19 536 clump found in the domain of proper frequencies and principal components is, however, extended at higher $\sin(i)$ values with respect to the clump obtained in the space of proper frequencies only. The (6246) Kunamoto clump is extended at smaller values of the semimajor axis with respect to the one found in the space of proper frequencies only, and merges with the Phocaea family for slightly larger values of the frequency cut-off. In the next section, I will investigate the values of albedo and

absolute magnitudes for asteroids in the region that are available in the literature.

4 GEOMETRIC ALBEDOS AND ABSOLUTE MAGNITUDES

The cumulative size distribution of asteroid family members can be used to obtain important information about the collisional and orbital evolution of asteroid families (Vokrouhlický et al. 2006a,b,c). Estimates of the asteroid diameters can be obtained via the relationship

$$D = \frac{D_0}{\sqrt{p_V}} \times 10^{-0.2H}, \quad (5)$$

where $D_0 = 1329$ km, H is the asteroid absolute magnitude and p_V is the geometric albedo. To obtain reliable estimates of the diameters of asteroids, it is therefore important to first obtain good values of the asteroids geometric albedos and absolute magnitudes. For what concerns the asteroids albedos, I turn my attention to the work of Tedesco et al. (2002), which reported the values of geometric albedo (with their uncertainties) for 2226 bodies. Of these, I found 33 objects in the region of the local background of the Phocaea frequency family (Carruba & Michtchenko 2009), for which synthetic proper elements were also available. 11 of these objects belong to either the Phocaea classical or frequency families and have a reported spectral classification.

Fig. 6 (panel A) displays an (a, sin(i)) projection of the Phocaea frequency family (small blue dots) and of the 33 objects with albedos in the region. Asteroids with albedos lower than 0.10 (usually associated with C-type bodies) are displayed with small black dots, those with albedos between 0.10 and 0.25 (associated with S-type objects, Bus & Binzel 2002a,b) are shown with larger red dots, and asteroids with albedos larger than 0.25 are displayed with large full yellow dots. As can be seen in the figure, most of the objects with low albedos are found outside the family, and there is a concentration of the objects with an S-type compatible albedo in the region of the Phocaea family, so confirming the possible interpretation of the family as being the product of the disruption of a large S-type parent body. I however also observe some high-albedo objects that are associated with the family. This is more evident in Fig. 6 (panel B) where I show a histogram of the normalized number of objects in the albedo intervals 0.00–0.10 (C-type), 0.10–0.25 (S-type) and larger than 0.25, for all asteroids in the region (blue line) and just for the Phocaea families members (red line). While only a member of the Phocaea family has low albedo, there were five objects, all with diameters of 10 km or less, with albedo larger than the value usually associated with S-type bodies.

Taking the median value of the Phocaea member albedo, and using the standard deviation as a measure of its error, I found that the albedo values of the Phocaea members lie in the interval $p_V = (0.24 \pm 0.12)$. For what concerns the asteroids absolute magnitudes, Fig. 7 displays ($a - e$) (panel A), ($a - \sin(i)$) (panel B), ($e - \sin(i)$) (panel C) and (g, $g - s$) projections of the asteroids in the region of the Phocaea family. Small black dots display the locations of asteroids with $H > 12$, red full dots are associated with asteroids with $10 < H < 12$ and large yellow dots display the position of all objects with magnitude smaller than 10.

As can be seen in the figure, the distribution of bodies is not symmetrical about the semimajor axis, with respect to the centre of the family. There is an excess of objects at the lower semimajor axis with respect to the distribution at higher a. Three large C-type objects, (105) Artemis, (654) Zelinda and (914) Palisana are present in the region but are not connected to the Phocaea dynamical family, as discussed in the previous sections. The family of (25) Phocaea itself sits on the separatrix of the ($\nu_6 - \nu_{16}$) secular resonance. Medium-sized bodies are generally associated with the family. More information on the size distribution of the Phocaea family will be discussed in Section 6.

5 YARKOVSKY ISOLINES AND *C*-TARGET FUNCTION

Now that I have already revised the information on the literature on geometric albedos and absolute magnitude, I am equipped to start setting constraint on an age estimate for the Phocaea family. In Vokrouhlický et al. (2006a,b) the authors used the (a, H) distribution of asteroid families to determine their ages. In particular, the authors introduced a target function C defined as

$$0.2H = \log_{10}(\Delta a / C), \quad (6)$$

where $\Delta a = a - a_c$, and a_c is the 'central' value of the semimajor axis of the family members. The most appropriate definition of family centre relates to the concept of barycentre. I took

$$a_c = \sum_{i=1}^{n_{ast}} \frac{a \times M_i}{M_{tot}}, \quad (7)$$

where n_{ast} is the number of family members and M_i is the mass of each asteroid, estimated by assuming that all asteroids can be approximated as spheres, using a density of 2500 kg m^{-3}, typical of S-type objects, and a diameter obtained using equation (5). For

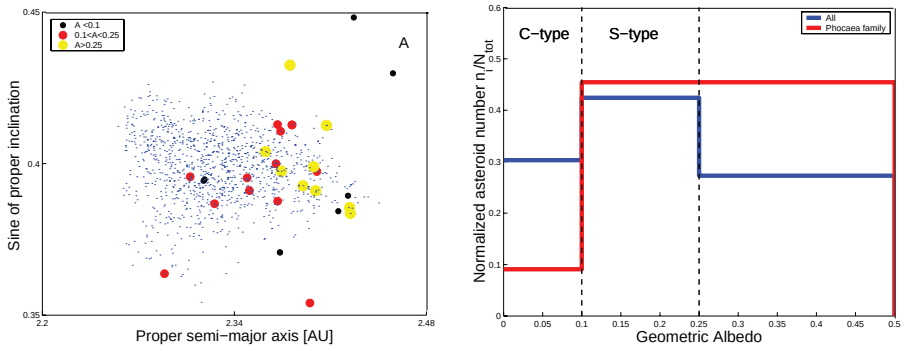

Figure 6. Panel A: an (a, sin(i)) projection of the orbital location of asteroids for which a value of the geometric albedo is available in the region of the Phocaea family. Panel B: histogram of the normalized number of objects per unit bins in the albedo intervals 0.00-0.10 (C-type), 0.10–0.25 (S-type) and larger than 0.25, for all asteroids in the region (blue line) and just for the Phocaea families members (red line).

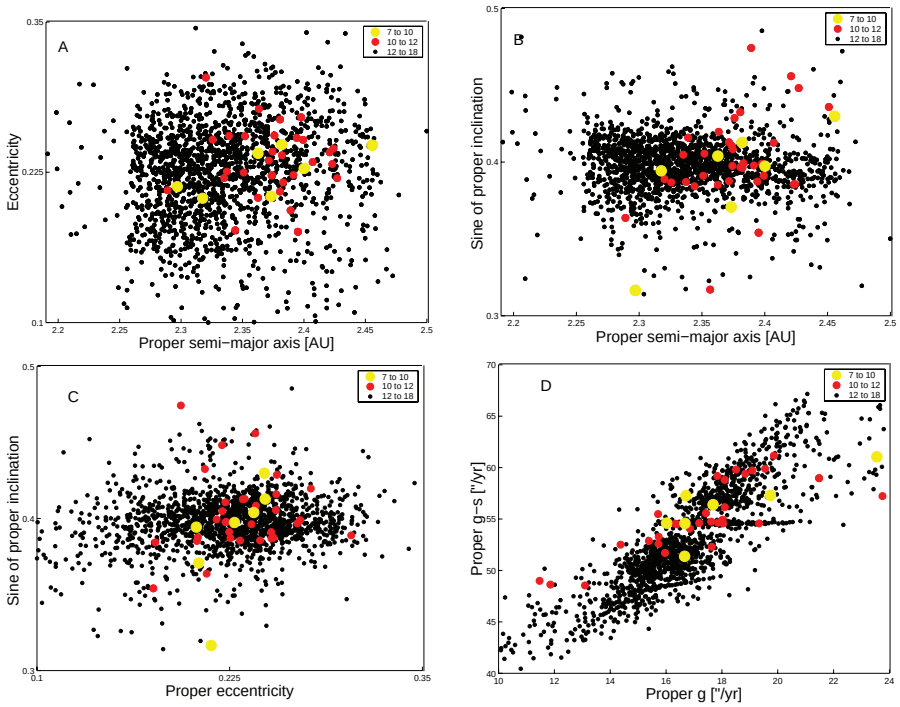

Figure 7. An $(a - e)$ (panel A), $(a - \sin(i))$ (panel B), $(e - \sin(i))$ (panel C), and $(g, g - s)$ projections of the asteroids in the region of the Phocaea family. Small black dots display the locations of asteroids with $H > 12$, red full dots are associated with asteroids with $10 < H < 12$ and large yellow dots display the position of all objects with magnitude smaller than 10.

asteroids for which the geometric albedo is not available, I used the average value of albedo for the Phocaea family, $p_V = 0.24$. Equations similar to equation (7) hold for e_c and i_c. With these approximations, I found that the total mass M_{tot} of the classical family is of the order of 2.35×10^{18} Kg, 34.7 per cent of which is contained in (25) Phocaea. The total mass of the frequency family is of the order of 2.88×10^{18} Kg, 28.3 per cent of which is contained in (25) Phocaea. The barycentre of the classical family is located at $a_c = 2.3851$ au, $e_c = 0.2373$ and $i_c = 23\overset{\circ}{.}8433$, while that of the frequency family is located at $a_c = 2.3497$ au, $e_c = 0.2151$ and $i_c = 23\overset{\circ}{.}3117$.[3] For what concerns the a_c value obtained for the frequency family, I notice that the frequency family is seriously depleted beyond higher values of a with respect to the M1:-2A resonance with Mars. As a consequence, the value of the family barycentre is displaced at lower a with respect to that of the classical family. For this reason, I choose to work essentially with the barycentre of the classical family.

As part of my preliminary analysis of the Phocaea family I show (a, H) and $(g - s, H)$ projections of the members of the frequency Phocaea family. Results are similar for the classical family. For what concerns the (a, H) projections, I also show the distance covered by the asteroids to diffuse from the centre of the family via the Yarkovsky effect, computed using the Vokrouhlický (1998) model of the diurnal version of the Yarkovsky effect, for spherical bodies and in the linear approximation for the heat conduction in a spherical, solid and rotating body illuminated by solar radiation. I used the following parameters to describe the Yarkovsky force: a value of thermal conductivity $K = 0.0001\ \mathrm{W\,m^{-1}\,K^{-1}}$, a specific heat capacity of $C_p = 680\ \mathrm{J\,kg^{-1}\,K^{-1}}$, a density of $2500\ \mathrm{g\,cm^{-3}}$, a surface density of $1500\ \mathrm{g\,cm^{-3}}$, a bond albedo of 0.11 and a geometric albedo of 0.24 (see Section 4 for a discussion on the geometric albedo data). With these parameters, using the barycentric value of the family a distribution a_c, and assuming a rotation period inversely proportional to the radius (Farinella, Vokrouhlický & Hartmann 1998), I obtained lines of maximal Yarkovsky drift for the Phocaea frequency (Fig. 8, panels A) members, for ages of 1500 and 2200 Myr. Since I am not considering the effect of the primordial ejection velocity field, this sets upper limits on the possible age of the family. My preliminary analysis seems to confirm the possibility that the Phocaea family is indeed a very old one. Also notice how both classical and frequency families (and more so for the frequency family) are depleted in members for values of the semimajor axis larger than the family barycentre. This is most likely caused by the local dynamics, and in particular by the direct and indirect effect of the strong ν_6 secular resonance. More information on the local dynamics can be found in Section 8.

Another interesting piece of information can be obtained by observing the $(g - s, H)$ projection of the frequency family (Fig. 8). Note that the central strip of the family members is locked in the $(\nu_6 - \nu_{16})$ secular resonance. Contrary to the case of the Padua family (Carruba 2009), however, only 112 members of the classical family (11.33 per cent of the total members) and 120 of the frequency family (10.55 per cent of the family total) are locked in this resonance (more than 75 per cent of the Padua family members were locked in the z_1 resonance). The fact that the majority of the members of the family are not in the resonant configuration is reflected by the fact that the family is characteristically dispersed in 'triangle diagrams'. The role of the $(\nu_6 - \nu_{16})$ secular resonance is therefore more limited for the case of the Phocaea family than the one played by the z_1 resonance for the Padua family. Finally, the lack of objects in the frequency family with values of $(g - s)$ higher than

[3] The mean values of the family semimajor axis, eccentricity and inclination are $a_c = 2.3348$ au, $e_c = 0.2328$ and $i_c = 23\overset{\circ}{.}5143$ for the classical family, and $a_c = 2.3284$ au, $e_c = 0.2280$ and $i_c = 23\overset{\circ}{.}4883$, for the frequency one.

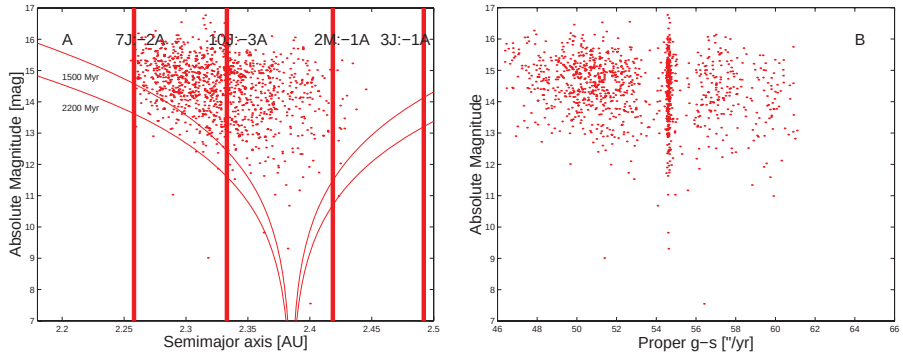

Figure 8. An (a, H) (panel A) and ($g + s$, H) (panel B) projection of the members of the frequency Phocaea family.

61.5 arcsec yr^{-1} is caused by the barrier in the frequency domain presented by the M1:-2A resonance with Mars (see Section 8).

The asymmetry between the population of objects at lower and higher a is also observed if we compute the C-target function.[4] Positive values of C are significantly depleted and I do not observe a peak at $C > 0$. I believe this asymmetry can be explained in terms of the local dynamics, as discussed above. More information on secular and mean-motion resonances in the region will be given in Section 8.

6 CUMULATIVE DISTRIBUTION AND COLLISION PROBABILITIES

The size distribution of asteroids is one of the most significant observational constraints on their history, and it is also one of the hardest quantities to determine because of strong selection effects (Parker et al. 2008). As a next step of my preliminary analysis of the Phocaea family, I compute the cumulative H distribution $N(<H)$ for the two Phocaea families, the classical (Fig. 9, panel A) and the frequency one (Fig. 9, panel B). As it is the case for several other families studied by Parker et al. (2008), the Phocaea family cumulative distribution seems to be best approximated by a 'broken' power law, for the two intervals in H between 12 and 14 and between 14 and 15. I found that for the classical family, the γ exponents that best fit the two intervals are 0.60 and 0.35, respectively, while for the frequency family I obtained values of γ of 0.53 and 0.32. The γ exponents found for the first interval are compatible with the 0.61 γ value for background population found by Parker et al. (2008) for the inner main belt, but the values found for the second intervals seem quite low and may indicate that there was a significant depletion in the population of smaller objects in the area.

In Fig. 9 (panels C and D), I show the dependence of the exponent of the cumulative H distribution $N(<H)$ as a function of the velocity and of the frequency cut-offs, found in the range of the absolute magnitude of H (12.5, 14.0) (red lines) and (14.0, 15.0) (blue lines). Vertical lines display the values of the cut-offs for which the Phocaea family englobes other families and clumps in the region (see Fig. 2, panels A and C). As can be seen in the figure, the cumulative exponents fluctuate when the Phocaea cluster englobes some of the minor group in the region and then practically reach a constant value for larger cut-offs. The fact that the exponents do not drop at very large cut-off, i.e. when the whole background zone becomes associated with the family (Vokrouhlický et al. 2006b), is caused by the fact that I obtained the Phocaea (and the other groups in the region) using a sample with only the asteroids in the Phocaea family local background (Carruba & Michtchenko 2009). Apparently the local background of the Phocaea family is actually dominated by Phocaea family members (plus the odd large C- and X-type asteroids; see Section 3). As soon as the Phocaea family reaches the dynamical limits of the stable island, it essentially stops to grow significantly, and so the cumulative exponents essentially stop varying.

One question that may arise at this point regards the possibility that the Phocaea family was created by a collision and it is therefore an actual family, rather than a dynamical group limited by the 'stable island' region. To start investigating the possible role that asteroids in different regions may have had in the collisional evolution of the Phocaea family, I used the approach of Greenberg (1982) for obtaining intrinsic collision probabilities of members of the Phocaea classical family with (25) Phocaea itself, an asteroid in the inner main belt, (8) Flora and an asteroid in the middle belt, (15) Eunomia.

Values of collision probabilities are actually in general higher for the interaction of asteroids with (8) Flora than with (25) Phocaea itself. The average value of P for collisions with (8) Flora was of 8.2×10^{-18} km^{-2} yr^{-1}, while that with (25) Phocaea was of 10.9×10^{-18} km^{-2} yr^{-1}. For comparison, the average value of P with (15) Eunomia was of 4.8×10^{-18} km^{-2} yr^{-1}, while the average probability of two main belt asteroid to collide is of 2.8×10^{-18} km^{-2} yr^{-1}. This simple test may indicate that collision with inner main belt, low-inclination objects may have certainly played a role in the collisional history of the Phocaea family, but a further, more in-depth, study is needed to clarify this point.

As an order of magnitude estimate for the age of the Phocaea family, let us assume a value of the collision probability of the impact of $a \simeq 10$ km size projectile of $P_i \simeq 10^{-17}$ km^{-2} yr^{-1}. The disruption of a parent body of 120–150 km would have a characteristic time-scale of

$$\tau \simeq \frac{1}{(P_i(R_t + R_p)^2)N_p)}, \tag{8}$$

where N_p is the number of projectiles in the main belt (between 5000 and 10 000 according to Bottke et al. 2005), R_t is the target radius (of the order of 60 km) and R_p is the projectile radius (of the order of 5 km). Assuming an optimistic value for the number of projectiles in the main belt, this supports a 2.4 Byr estimate for the collisional age of the Phocaea family, in agreement with the estimates obtained in Section 5.

[4] I computed the observed data $N_{\rm obs}(C)$ for the classical and frequency families, obtained by (C, $C + \Delta C$) binning with $\Delta C = 4.0 \times 10^{-6}$ and $a_{\rm c} = 2.3851$ au (the barycentre of the classical family).

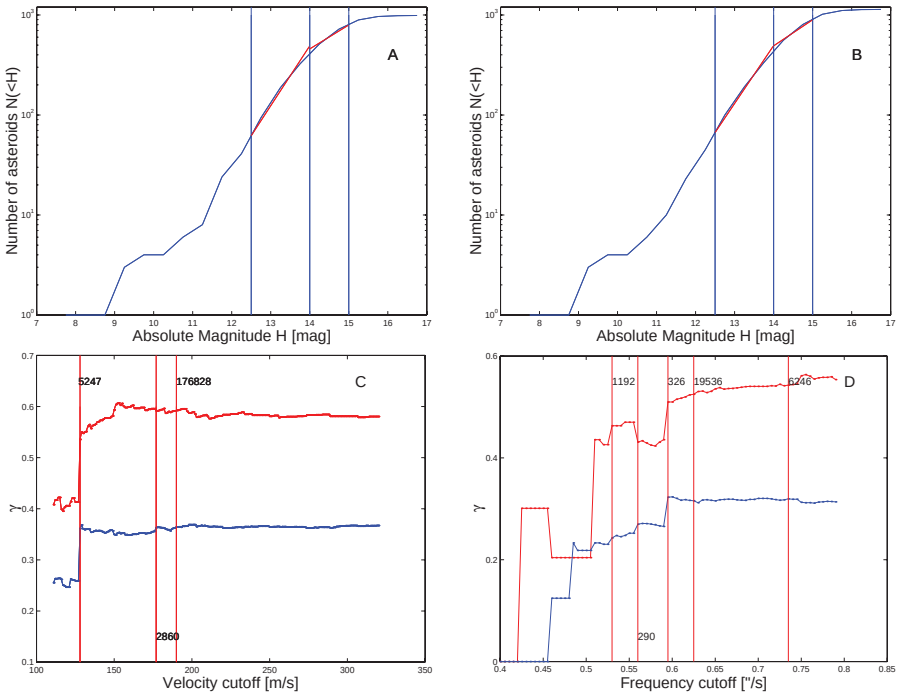

Figure 9. Panels A and B display the cumulative distribution $N(>H)$ of the classical and frequency members of the Phocaea family. Panels C and D display the dependence of the exponent of the cumulative H distribution $N(<H)$ as a function of the velocity and of the frequency cut-offs, found in the range of absolute magnitude H (12.5, 14.0) (red lines) and (14.0, 15.0) (blue lines).

7 LIGHT CURVE AND ROTATION RATE ANALYSIS

It has been recently proposed that binary asteroids can be formed because of the increase in the rotation rate of the parent body caused by the Yarkovsky-O'Keefe-Radzievskii-Paddack (YORP) effect (Pravec et al. 2008). Obtaining information on the asteroid periods is therefore of significant importance in understanding their dynamical evolution. Here I revised the current information available for members of the Phocaea classical and frequency families in the Asteroid Light-Curve Data Base (LCDB; Warner, Harris & Pravec 2008) as of 2009 March. There are a total of 1213 asteroids between the Phocaea classical and frequency family. Of these, 18 had a period estimate in the LCDB.

Fig. 10 displays a histogram of the distribution of rotation frequencies for the 18 asteroids for which such information is available.

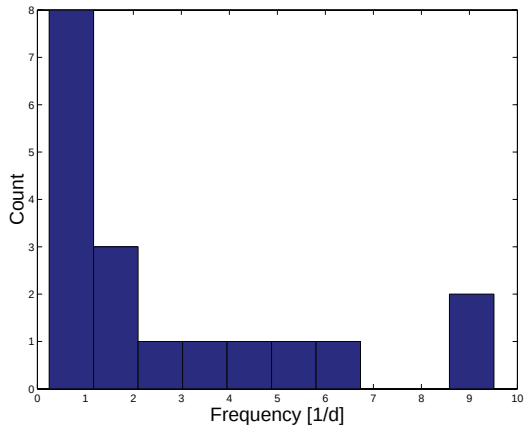

Figure 10. Histograms of rotation frequencies (in d^{-1} for the 18 Phocaea families members present in the Asteroid Light-Curve Data Base.

The sample is too limited to allow to obtain statistically significant information, but it can be noticed that there are two objects, (2000) Herschel and (4283) Stoffler, with periods longer than 50 h, and eight objects with periods longer than 1 d. As found by Warner et al. (2009) for asteroids in the Hungaria region, there seems to be an excess of slow rotators, while the distribution of spin rates in the range of $1\mathrm{d}^{-1} < f < 7\mathrm{d}^{-1}$ appears to be uniform. This can be possibly caused by the YORP effect, with the excess of slow rotators related to the longer time slowly rotating objects spend in that state (Pravec et al. 2008).

8 DYNAMICS IN THE REGION OF THE PHOCAEA FAMILY

As discussed in Knežević & Milani (2003), the Phocaea family is characterized by a region of shallow close encounters with Mars at $e > 0.3$, which displays significant chaotic behaviour. To further study and delimit this region it is useful to compute maximum Lyapunov exponents (MLE) for orbits in this area. A detailed explanation of the theory of Lyapunov exponents goes beyond the scope of this paper; instead, I refer the reader to Lyapunov (1907) and Benettin et al. (1980). The MLE is a measure of exponential stretching of nearby orbits. The Lyapunov exponents are equal to zero for regular orbits (they tend to zero in finite-time calculations), while they assume positive values for chaotic orbits. The inverse of a Lyapunov exponent is the Lyapunov time T_L. Smaller values of T_L indicate enhanced local stochasticity.

I start my analysis by looking at the values of MLEs currently available in the AstDyS data base in the Phocaea family region. Fig. 11 displays an $(a - e)$ (panel A), $(a - \sin(i))$ (panel B), (a, q) [panel C, where $q = a\,(1 - e)$ is the asteroid pericentre] projections of asteroid Lyapunov times in the region of the Phocaea family. Small black dots have Lyapunov times smaller than 20 000 yr, large

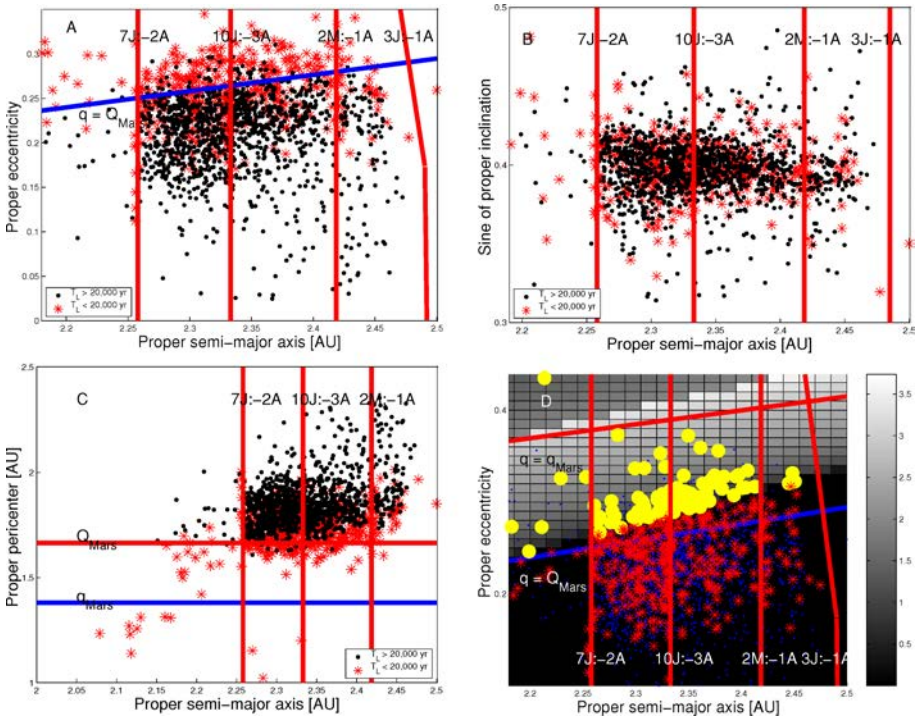

Figure 11. An (a, q) (panel A), $(a, \sin(i))$ (panel B), (a, q) (panel C) projection of asteroids Lyapunov times in the region of the Phocaea family. Small black dots have Lyapunov times smaller than 20 000 yr, large red asterisks have $T_L < 20\,000$ yr. Panel D displays an (a, e) projection of asteroids in the region of the Phocaea family (blue dots), superimposed with a colour plot of $[(\langle \Delta a^2 \rangle T)^{1/2}] \times 10^3$ caused by encounters with Mars. Full red dots are asteroids with Lyapunov times T_L smaller than 20 000 yr, and full yellow dots are asteroids with $T_L < 20\,000$ yr and $(\langle \Delta a^2 \rangle T)^1/2 > 0$.

red asterisks have $T_L < 20\,000$ yr. Panel C of Fig. 11 displays the MLE versus the asteroid pericentre. Vertical lines show the values of q equal to Mars pericentre (blue line) and apocentre (red line).

As can be seen in Fig. 11 (panel A), orbits with small Lyapunov times are generally (but not only) characterized by larger values of eccentricity, roughly speaking $e > 0.22$. The blue line in the figure displays the location of asteroids with the pericentre equal to the apocentre of Mars, which have the potential to be Mars crossers. With the exception of asteroids interacting with the 7J:-2A, the 2M:-1A or other mean-motion and secular resonances, most of the asteroids with low Lyapunov times are either Mars crossers or are objects that can be perturbed by encounters with Mars. This is more clearly shown in Fig. 11 (panel C), where I see that the lowest values of Lyapunov times are associated with Mars-crosser bodies. Note how there is no particular correlation between Lyapunov times and inclination (Fig. 11, panel B). This is also observed in the space of asteroid proper frequencies.

To further study the effect of close encounters with Mars on chaos in the Phocaea region, I turn my attention to the work of Greenberg (1982) on orbital interaction during close encounters. In his work, Greenberg assumed that the gravitational interaction between two closely approaching orbiting bodies can be modelled as a two-body hyperbolic encounter. As in Carruba et al. (2003), I used this approach to compute $(\langle \Delta a^2 \rangle\ T)^{1/2}$ (where Δa is the change in the semimajor axis and T is the orbital period of the perturbee, of the order of 3.72 yr) for a grid of particles in the (1.9–2.5) au range in a, (0–0.43) range in e and with the inclination equal to that of (25) Phocaea at J2000 (23.°414). I also computed the same quantity for all the 1736 objects in the local background of the Phocaea family. Fig. 11 (panel D) displays an (a, e) projection of asteroids in the region of the Phocaea family (blue dots), superimposed with a colour plot of $[(\langle \Delta a^2 \rangle\ T)^1/2] \times 10^3$ caused by encounters with Mars. Red asterisks are asteroids with Lyapunov times T_L smaller than 20 000 yr, and full yellow dots are asteroids with $T_L < 20\,000$ yr and $[(\langle \Delta a^2 \rangle\ T)^{1/2}\ ] > 0$.

As can be seen in the figure, we are now able to distinguish between the chaotic behaviour caused by close encounters with Mars (yellow full dots) and that caused by the overlapping of resonances or other criteria (red asterisks). A question that naturally arises is about the long-term stability of the chaotic objects that are Mars crossing. Are all these objects protected by deep close encounters with Mars by the Kozai mechanism proposed by Milani et al. (1989), or are some of these objects relatively young bodies only recently inserted in unstable regions? Answering this question involves long-term dynamical simulations, which are beyond the purpose of this paper. But this issue remains an interesting topic for future work.

The next logical step was obtaining estimates of Lyapunov times for regions where no current or few asteroids are found. This is especially important for example for the regions that were found to be stable in Section 8, but show a small density of asteroids. One may wonder if the small asteroid density may be caused by a long-term dynamical effect, or if it is primordial. One useful tool to obtain information on the long-term stability of orbits may be obtaining MLEs.

To estimate MLEs for orbits in the region, I used a modified version of SWIFT-LYAP2.F, a code that integrates the difference equation (Mikkola & Innanen 1999; Morbidelli 2002) in the SWIFT package (Levison & Duncan 1994). For each of the test particles, I integrated the difference equation with an initial difference vector of modulus $d(0) = \sqrt{6} \times 10^{-9}$, and determined the modulus $d(t)$ of the displacement vector between the two vectors at time t.

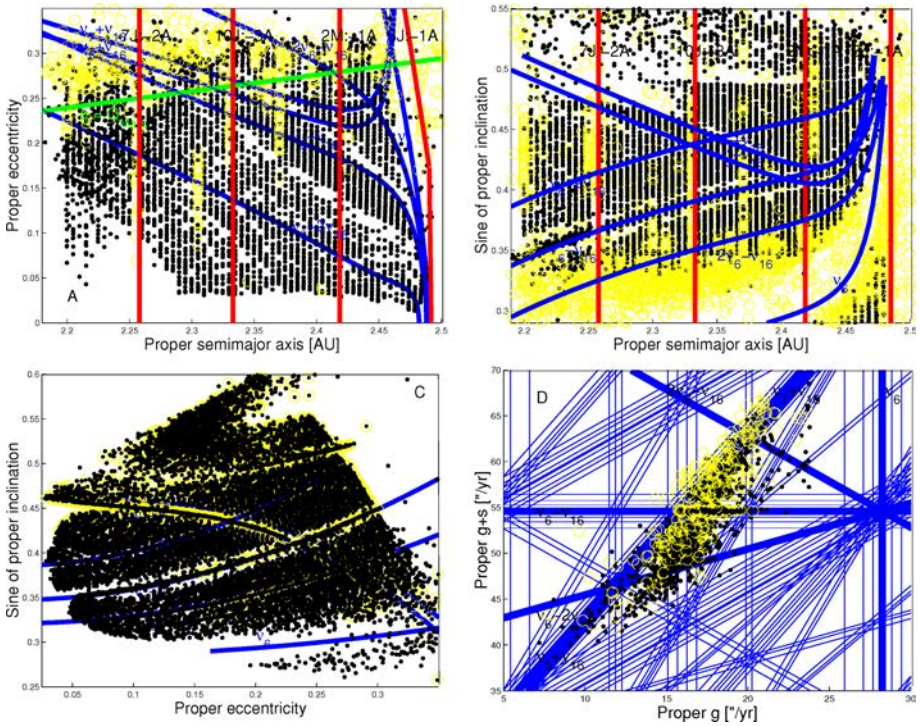

Figure 12. Lyapunov times projected in the space of averaged (a, e) (panel A), (a, sin(i)) (panel B) and (e, sin(i)) (panel C) elements. Panel D displays the Lyapunov times of real asteroids in the local background in the (g, $g - s$) space of proper frequencies. Yellow circles display Lyapunov times smaller than 20 000 yr, while black dots are associated with times larger than 20 000 yr.

I constructed a series (t, ln[$d(t)/d(0)$]), and performed a linear least-square fit on this series. Since $d(t) \simeq d(0)\exp(Lt)$, where L is the Lyapunov exponent, the slope of ln[$d(t)/d(0)$] versus time is equal to the maximum Lyapunov exponent. More information on the procedure used to obtain MLEs can be found in Carruba et al. (2004).

Fig. 12 displays a projection in the space of averaged elements of the Lyapunov times obtained for a 20 Myr numerical simulation. I used 5300 particles in the (a, e) plane, 9060 particles in the (a, sin(i)) plane, and 13 590 test particles in the (e, sin(i)) plane near the Phocaea family. I also used a step in a of 0.005 au, in e of 0.004 and in i of 0.°1, and took particles in an equally spaced grid of 60 by 90 particles in the (a, e) plane, of 60 by 151 particles in the (a, sin(i)) plane and of 90 by 151 particles in the (e, sin(i)) plane.[5] The initial values of sin(i), e, a (for the simulations in the (a, e)), (a, sin(i))- and (e, sin(i)) planes, respectively), and initial angular elements Ω, ω and λ of the test particles were fixed at those of (25) Phocaea at J2000.

In order to study the orbital evolution of asteroids in the region of the Phocaea families, I also performed an integration with the SWIFT-MVS integrator of Levison & Duncan (1994), modified by Mira Brož to include the second-order symplectic map from Laskar & Robutel (2001) (the code is publically available at http://sirrah.troja.mff.cuni.cz/mira/mp/) and the same test particles used for obtaining MLEs. All planets from Venus to Neptune were included in the simulation. Mercury was accounted for as a barycentric correction of the initial conditions. Non-singular orbital elements were Fourier filtered on line to eliminate all periods smaller than 600 yr, and averaged elements were obtained over the whole length of the integration.

[5] My test particles covered a range between 2.2 and 2.5 au in a, 0 and 0.36 in e and 15° and 30° in i, respectively.

Table 3. Argument and semimajor axis location of the main three-body resonances in the region of the Phocaea group.

Three-body resonance	Semimajor axis a (au)
9J:-5S:-2A	2.25838
3J:1S:-1A	2.30189
8J:-3S:-2A	2.30229
5J:-4S:-1A	2.30270
9J:-6S:-2A	2.34884
2J:3S:-1A	2.39647
4J:-2S:-1A	2.39736
6J:-7S:-1A	2.39825
7J:-2S:-2A	2.44847
9J:-7S:-2A	2.44893

The main two-body mean-motion resonances in the region (7J:-2A, 10J:-3A, 2M:-1A, 3J:-1A) are displayed in Fig. 12 (panels A and B). The limits of the 3J:-1A resonance in Fig. 12 (panel A) are defined according to equation (3) in Morbidelli & Vokrouhlický (2003). Table 3 reports the resonant argument and approximate location in the semimajor axis of the main three-body resonances, as identified by Michtchenko et al. (2009) (for simplicity, they are not shown in Fig. 12). The thick blue lines in Fig. 12 (panels A, B and C) display the location of the centre in the average element space of the main secular resonances in the region.

Yellow circles display Lyapunov times smaller than 20 000 yr, while black dots are associated with times larger than 20 000 yr. The green line in Fig. 12 (panel A) displays the location of orbits with $q = Q_{\rm Mars}$. As can be seen in Fig. 12 (panel A), most of the chaos is confined to the region of close encounters with Mars.

Vertical 'strips' of small Lyapunov times are associated with two-body mean-motion resonances or (not shown) three-body mean-motion resonances such as the 5J:-4S:-1A resonance. For what concerns the (a, sin(i)) projection (Fig. 12, panel B), I notice that there is a region of very low Lyapunov times in the proximity of the ν_6 secular resonance. In particular, almost no particle with inclination lower than that of the ($2\nu_6 - \nu_{16}$) resonance has Lyapunov times larger than 20 000. While the study of dynamical evolution of test particle on a time-scale longer than the 20 Myr used here for obtaining dynamical maps is beyond the purposes of this article, it is reasonable to expect that the chaotic region near the ν_6 resonance may reveal to be unstable on a time-scale of 100 Myr or more, in the same way as the analogous region near the 3J:-1A mean-motion resonance was found to be (Guillens, Vieira Martins & Gomes 2002). I believe that a more in-depth study of the chaotic layer found in this work, possibly caused by the overlapping of several non-linear secular resonances near the ν_6 resonance, may be an interesting topic for future research.

Fig. 12 (panel C) displays the results for the (e, sin(i)) plane. As can be seen in the figure, the zone of chaos associated with the Mars-crosser area for eccentricities larger than 0.22 is also found in this plane. The area of chaos near the ν_6 secular resonance is also encountered at low values of sin(i).

Finally, Fig. 12 (panel D) displays a projection of real asteroids in the Phocaea family local background in the (g, $g - s$) space. Chaotic bodies tend to be found beyond the ($2\nu_6 - \nu_{16}$) resonance, as also observed in the (a, sin(i)) survey. Other chaotic bodies are associated with Mars-crossing orbits (see Fig. 12, panel A).

9 CONCLUSIONS

In this work, I reviewed the current knowledge on the Phocaea dynamical family region. Among other things, I did the following.

(i) Obtained families and clumps in the domain of proper elements and frequencies (Carruba & Michtchenko 2007, 2009). With the exception of the family around (19536) (1999 JM4), formerly associated with the clump around (2860) Pasacentennium, the families and clumps found by Gil-Hutton (2006) are now substructures of the Phocaea family. Also, an interesting side result of this paper was the clump associated with (6246) Komurotoru. This, to my knowledge, is the first clump detected only in the frequency domain. It may be the first of a series of new 'frequencies' clumps and families that may be about to be discovered.

(ii) Revised the current knowledge on the taxonomy of objects in the Phocaea family region and found that most of the S-type objects in the region are members of the Phocaea families.

(iii) Obtained principal components based on the SDSS-MOC4 data, and used this information to obtain families in the space of colours and proper elements and colour and proper frequencies (Carruba & Michtchenko 2007, 2009).

(iv) Revised the current knowledge on absolute magnitudes and geometric albedos for objects in the region. Most of the objects with known albedo in the range between 0.10 and 0.25 (characteristic of S-type bodies) are members of the Phocaea families.

(v) Obtained Yarkovsky isolines and C-target function values (equation 6) for members of the Phocaea families. Using standard values for the Yarkovsky parameters for S-type objects, I obtained an upper limit for the age of the family of 2.2 Byr. Refining the family age estimate using the Monte Carlo approach of Vokrouhlický et al. (2006a,b,c) will be difficult, since the family age seems to be beyond the time-scales for which the YORP effect is correctly modelized. The family is also highly asymmetrical in the semimajor axis, and asteroids with a semimajor axis larger than that of the family barycentre seems to have been significantly depleted, possibly because of the effect of the local dynamics (see Section 8).

(vi) Computed the cumulative absolute magnitude H distribution ($N(<H)$) for the two Phocaea families. As in Parker et al. (2008), the Phocaea family distribution seems to be best approximated by a broken power law, for two intervals in H between 12 and 14 and between 14 and 15. While values of the γ exponents that fit the first interval are compatible with typical values found for inner main belt families, the values for the second interval are significantly lower, possibly suggesting a dynamical erosion for smaller sized objects.

(vii) Obtained the values of intrinsic collision probabilities for members of the Phocaea family with (25) Phocaea itself, (8) Flora and (15) Eunomia. The average collision probability of colliding with (8) Flora, a low-inclination inner main belt body, was even larger than that of impacting (25) Phocaea, suggesting that collision with inner main belt objects may have played an important role in the history of the Phocaea family.

(viii) Studied the available information on rotation rates for asteroids in the Phocaea family groups (Warner et al. 2008). 18 bodies have estimates for their rotation periods, and a histogram of the rotation frequencies shows that there is an excess of slow rotators, explainable in the framework of evolution of the spin axis via the YORP effect.

(ix) Obtained dynamical maps of averaged elements for grids in (a, e), (a, sin(i)) and (e, sin(i)) of osculating initial conditions and identified the mean-motion and secular resonances that seem to have a larger effect on the short-term (20 Myr) stability of asteroid averaged elements. The Phocaea family is bounded by a region delimited by the 7J:-2A mean-motion resonance at low a, the 3J:-1A mean-motion resonance at high a, the ν_6 secular resonance at low i and a region of close encounters with Mars at high e. It is characterized by its interaction with the ($\nu_6 - \nu_{16}$) secular resonance (Carruba & Michtchenko 2009). A stable region of a low asteroid density between the ($2\nu_6 - \nu_{16}$) and the ν_6 resonances in the (a, sin(i)) plane was identified, and further studied via the use of chaos indicators.

(x) Revised the values of MLE available in the literature for asteroids in the Phocaea family region and obtained MLEs for the same grids of initial conditions used to obtained averaged element maps. Areas of low Lyapunov time $T_L < 20\,000$ are associated with (i) two- and three-body mean-motion resonances, (ii) a zone of encounters with Mars and (iii) a region near the ν_6 separatrix, associated with the stable region of low-density asteroids identified with the averaged elements maps.

At the end of this preliminary analysis of the Phocaea family region there is a general vision of the origin and evolution of asteroids in the region that is starting taking shape. While it is certain that the Phocaea group is indeed in a stable island surrounded by very unstable dynamical regions (Knežević & Milani 2003), the fact that most of the S-type objects are associated with the dynamical Phocaea families seems to suggest that the Phocaea cluster should indeed be a real collisional family. No local background was identified in the cumulative H distribution, and it seems that the region, apart from a few large C-type objects, is dominated by the Phocaea family. This may suggest that very few bodies reached the highly inclined region studied here and, of those, one, the parent body of the Phocaea family, was targeted in the collision that created the family possibly up to 2.2 Byr ago. Values of collision probabilities suggest that the impactor may have come from the low i inner main

belt, but of course the exact orbital location of the impactor may never been proved.

The family subsequently lost several of its members, especially at values of a larger than that of the family barycentre, due to the interaction with the local web of mean-motion and secular resonances. Only the part of the family having low C-target function values may have survived in this scheme.

More important than the question that this work may have answered are, in my opinion, the new questions that arise from this paper. One of these questions regards the long-term stability of the smaller families and clump identified in this work in both proper element and frequency domains. How stable in time are the smaller families and clumps other than the Phocaea family, if we investigate the evolution of orbital elements caused by the Yarkovsky effect? Are these groups statistically significant and really associated with break-up of parent objects, or are they just a random association of objects that do not share a common origin? This in my opinion is particularly important for what concern the new frequency cluster around (6246) Komurotoru.

Another important question regards the objects that are present in the region and should not be there, i.e. the chaotic Mars crossers at $e > 0.3$. Knežević & Milani (2003) observed that these objects may be in the Kozai class of planetary close encounters, and that therefore could be protected by experiencing very close encounters with Mars. They therefore suggested that this population of objects might be primordial. Understanding the long-term evolution and stability of this kind of orbits, especially when the Yarkovsky effect is also considered, is a task that, however, to my knowledge, has not yet been performed.

Finally, on what time-scales, if any, are orbits in the chaotic region near the ν_6 separatrix unstable? What resonance overlapping is exactly causing the chaotic dynamic in the region? Many of these new questions may be answered only performing simulations on time-scales much longer than the 20 Myr used to obtain dynamical maps in this work. Answering these questions seems therefore to exceed the purpose of this paper, which was starting exploring the current state of the knowledge on the Phocaea family region. But they are certainly very interesting possible projects for further research, worth exploring in future works.

ACKNOWLEDGMENTS

I am grateful to the reviewer of this article, David Vokrouhlický, for helpful comments and remarks that helped us to improve this work. I would like to thank the São Paulo State Science Foundation (FAPESP) that supported this work via the grant 06/50005-5 and the Brazilian National Research Council (CNPq). I am also grateful to the Physics and Astronomy department of the IPD/UNIVAP for the use of their facilities.

REFERENCES

Beaugé C., Roig F., 2001, Icarus, 153, 391
Bendjoya P., Zappalà V., 2002. Asteroids III, Univ. of Arizona Press, Tucson, p. 613
Benettin G., Galgani L., Giorgilli A., Strelcyn J. M., 1980, Meccanica, 15, 9
Bottke W. F., Durda D. D., Nesvorný D., Jedicke R., Morbidelli A., Vokrouhlický D., Levison H., 2005, Icarus, 175, 111
Brož M., Vokrouhlický D., 2008, MNRAS, 390, 715
Bus J. S., Binzel R. P., 2002a, Icarus, 158, 106
Bus J. S., Binzel R. P., 2002b, Icarus, 158, 146
Carruba V., 2009, MNRAS, 395, 358
Carruba V., Michtchenko T., 2007, A&A, 475, 1145
Carruba V., Michtchenko T., 2009, A&A, 493, 267
Carruba V., Burns J., A., Bottke W., Nesvorny D., 2003, Icarus, 162, 308
Carruba V., Nesvorný D., Burns J. A., Ćuk M., Tsiganis K., 2004, AJ, 128, 1899
Carvano J. M., Lazzaro D., Mothé-Diniz T., Angeli C., 2001, Icarus, 149, 173
Farinella P., Vokrouhlický D., Hartmann W. K., 1998, Icarus, 132, 378
Foglia S., Masi G., 2004, Minor Planet Bull., 31, 100
Fukugita M., Ichikawa T., Gunn J. E., Doi M., Shimasaku K., Schneider D. P., 1996, AJ, 111, 1748
Greenberg R., 1982, AJ, 87, 184
Guillens S. A., Vieira Martins R., Gomes R. S., 2002, AJ, 124, 2322
Gil-Hutton R., 2006, Icarus, 183, 93
Knežević Z., Milani A., 2003, A&A, 403, 1165
Laskar J., Robutel P., 2001, Celest. Mech. Dyn. Astron., 80, 39
Lazzaro D., Angeli C. A., Carvano J. M., Mothé-Diniz T., Duffard R., Florczak M., 2004, Icarus, 172, 179
Levison H., Duncan M. J., 1994, Icarus, 108, 18
Lyapunov A. M., 1907, Ann. Fac. Sci. Univ. Toulose, 9, 203
Migliorini F., Zappalà V., Vio R., Cellino A., 1995, Icarus, 118, 271
Mikkola S., Innanen K. A., 1999, Celest. Mech. Dyn. Astron., 74, 59
Milani A., Knežević Z., 1994, Icarus, 107, 219
Milani A., Carpino M., Hahn G., Nobili A., 1989, Icarus, 78, 212
Morbidelli A., 2002, Modern Celestial Mechanics: Dynamics in the Solar System. Taylor & Francis, London
Morbidelli A., Vokrouhlický D., 2003, Icarus, 163, 120
Nesvorný D., Jedicke R., Whiteley R. J., Ivezić Ž. 2005, Icarus, 173, 132
Parker A., Ivezić, Ž., Jurić M., Lupton R., Sekora M. D., Kowalski A., 2008, Icarus, 198, 138
Pravec P. et al., 2008, Icarus, 197, 497
Roig F., Gil-Hutton R., 2006, Icarus, 183, 411
Tedesco E. F., Noah P. V., Noah M., Price S. D., 2002, AJ, 123, 1056
Tholen D. J., 1989, in Binzel R. P., Gehrels T., Matthews, M. S.. eds, Asteroid Taxonomic Classifications. University of Arizona Press, Tucson, p. 298
Vokrouhlický D., 1998, A&A, 375, 1093
Vokrouhlický D., Brož M., Morbidelli A., Bottke W. F., Nesvorný, Lazzaro D., Rivkin A. S., 2006a, Icarus, 182, 92
Vokrouhlický D., Brož M., Bottke W. F., Nesvorný D., Morbidelli A., 2006b, Icarus, 182, 118
Vokrouhlický D., Brož M., Bottke W. F., Nesvorný D., Morbidelli A., 2006c, Icarus, 183, 349
Warner B. D., Harris A. W., Pravec P., 2008, Asteroid Lightcurve Data Base (LCDB), http://www.MinorPlanetObserver.com
Warner B. D., Harris A. W., Vokrouhlický D., Nesvorný D., Bottke W. F., 2009, Icarus, submitted
Xu S., Binzel R. P., Burbine T. H., Bus S. J., 1995, Icarus, 115, 1
Zappalà V., Cellino A., Farinella P., Knežević Z., 1990, AJ, 100, 2030
Zappalà V., Bendjoya P., Cellino A., Farinella P., Froeschlé C., 1995, Icarus, 116, 291
Zellner B., Tholen D. J., Tedesco E. F., 1985, Icarus, 61, 355

This paper has been typeset from a TEX/LATEX file prepared by the author.

5

Erosão dinâmica de grupos de asteroides na região da família de Phocaea

Neste trabalho investigamos a evolução dinâmica dos grupos identificados em Carruba (2009b). Em particular, estudamos a evolução dinâmica de objetos em órbitas de cruzamento com Marte a alta excentricidade na região de Phocaea, e determinamos que os mecânismos mais eficazes para refornecer a população atual de objetos de alta excentricidade são as ressonâncias J3:-1A, J7:-2A, e M2:-1A. O tempo mínimo para que a população de objetos de alta excentricidade seja formada por estes mecânismos é de 370 Myr, o que implica que a idade da família de Phocaea tem que ser maior que 640 Myr.

Usando o modelo analítico da ressonância ν_6 de Yoshikawa (1987), introduzimos um críterio analítico para determinar a espessura da zona caótica na proximidade da separatriz da ressonância ν_6 com altos tempos de Lyapunov determinada em Carruba (2009b) e associada á asteroides em órbita de cruzamento com Marte.

Investigamos a evolução dinâmica dos famílias e clump encontrados no artigo anterior. Observamos que a família em volta de (19536) (1999 JM4) é observável por tempos de 200 Myr no espaço dos elementos próprios, e que o clump determinado no espaço das frequência em volta de (6246) Komurotoro, é observável por tempos de 50 Myr, e pode ser considerado o primeiro grupo somente observável no espaço das frequências que poderia ser associado a um evento colisional.

A seguir apresentamos o artigo, que foi publicado em Monthly Notices of the Royal Astronomical Society em 2010, volume 403, pp. 1834-1848.

Mon. Not. R. Astron. Soc. **403,** 1834–1848 (2010) doi:10.1111/j.1365-2966.2010.16288.x

Dynamical erosion of asteroid groups in the region of the Phocaea family

V. Carruba★

UNESP, Universidade Estadual Paulista, Grupo de Dinâmica Orbital e Planetologia, Guaratinguetá, SP 12516-410, Brazil

Accepted 2009 December 23. Received 2009 December 18; in original form 2009 November 10

ABSTRACT

In a previous paper, the current state of knowledge of the region containing the Phocaea dynamical family was revised. Here, the dynamical evolution and possible origin of the Phocaea dynamical family and asteroid groups in the region are investigated. First, I study the case of asteroids at high eccentricity ($e > 0.31$). I find that these objects are unstable because of encounters with Mars on time-scales of up to 270 Myr. The minimum time needed by members of the Phocaea classical family to reach the orbital locations of these objects, 370 Myr, can be used to set a lower limit on the age of the Phocaea family.

Next, attention is focused on the chaotic layer previously identified near the ν_6 secular resonance border. Using analytical and numerical tools, I find that the presence of the ν_6 secular resonance forces asteroids with $|g - g_6| < 2.55$ arcsec yr^{-1} to reach eccentricities high enough to allow them to experience deep, close encounters with Mars. Results of the analytical model of Yoshikawa and of my numerical simulations fully explain the low-inclination chaotic region found by Carruba.

Finally, I investigate the long-term stability of the minor families and clumps identified in the previous paper, with particular emphasis on a clump only identifiable in the domain of proper frequencies (n, g, $g - s$) around (6246) Komurotoru. I find that while the clumps identified in the space of proper elements quickly disperse when the Yarkovsky effect is considered, the family around (19536) is still observable for time-scales of more than 50 Myr. The (6246) clump, characterized by its interaction with the $\nu_5 + \nu_{16}$ and $2\nu_6 - \nu_{16}$ secular resonances, is robust on time-scales of 50 Myr. I confirm that this group may be the first clump ever detected in the frequency domain that can be associated with a real collisional event.

Key words: celestial mechanics – minor planets, asteroids.

1 INTRODUCTION

In Carruba (2009b), the current state of our knowledge regarding the Phocaea family region was revised. In that paper, among other things, families and clumps in the spaces of proper elements and proper frequencies were obtained and the current knowledge of asteroid taxonomy was revised, along with the albedo and absolute magnitude distribution of objects in the area. Furthermore, the dynamics of asteroids was studied using dynamical maps and chaos indicators. Several interesting results, like the identification of the first clump (around (6246) Komurotoru) that is only observable in the frequency domain, and an upper limit of 2.2 Gyr for the age of the family, were obtained in that paper.

Here I try to investigate the questions left unanswered by that work. Asteroids at high eccentricity, the orbits of which are characterized by very low values of Lyapunov time, may experience encounters with Mars that can quickly destabilize their orbits. In particular, I find that a population of asteroids at high e ($e > 0.31$) is unstable on time-scales of less than 270 Myr. The time needed by current members of the Phocaea classical family to reach the orbital location of these objects is of the order of 370 Myr, and can be taken as a lower limit on the otherwise not easily obtainable age of the Phocaea family.

Another question left unanswered by Carruba (2009b) concerns the cause and the stability of chaotic orbits near the ν_6 secular resonance border at the low-i boundary of the Phocaea family. Using analytical (Yoshikawa 1987) and numerical (Carruba et al. 2007) tools, in this work I study the effect of the proximity of the ν_6 secular resonance on asteroid eccentricity and find a simple analytical criterion to identify the asteroids most likely to present chaotic behaviour, as suggested in Carruba (2009b).

Finally, I investigate the long-term stability of the minor families and clumps identified in the previous paper, with particular emphasis on the clump only visible in the domain of proper frequencies (n, g, $g - s$) around (6246) Komurotoru. I find that while the clumps identified in the space of proper elements quickly disperse when the Yarkovsky effect is considered, the family around (19536)

★E-mail: vcarruba@feg.unesp.br

is still observable for time-scales of more than 50 Myr. The (6246) clump, characterized by its interaction with the $\nu_5 + \nu_{16}$ and $2\nu_6 - \nu_{16}$ secular resonances, is robust on time-scales of 50 Myr. I confirm that this group could be the first clump ever detected in the frequency domain alone that may be associated with a real collisional event.

The remainder of this paper is organized as follows. In Section 2 I review the preserving effect of the Lidov–Kozai resonance on highly inclined objects when planetary encounters are considered. In Sections 3 and 4 I investigate numerically the long-term stability of objects on highly eccentric orbits and the mechanisms that may replenish this asteroid population. In Section 5 I study the dynamics of chaotic orbits near the ν_6 resonance separatrix, while in Section 6 I investigate the long-term stability of minor families and clumps in the region. Finally, in Section 7 I present my conclusions.

2 THE LIDOV–KOZAI RESONANCE AND ITS CONSERVED QUANTITIES

It is well known that, under the effect of planetary perturbations, the argument of the pericentre ω of the orbit of a small body is forced to precess. In 1962, Lidov and Kozai pointed out that in the asteroid belt the precession of the argument of pericentre stops at large inclinations. The dynamics is then characterized by the libration of ω around $\pm 90^\circ$, locked into a resonance. This resonance is usually called the Lidov–Kozai resonance. Thomas & Morbidelli (1996) and Gronchi & Milani (1999) for the asteroid belt, and Carruba et al. (2002, 2004) for irregular satellites of Jovian planets, recently studied the secular behaviour of objects affected by this resonance. It can be shown (Thomas & Morbidelli 1996) that the Hamiltonian of a massless body perturbed by N planets on given orbits can be written as

$$H = H_0 + P = -\frac{1}{2L^2} - \sum_{j=1,N} m_j P_j(l, g, h, L, G, H), \qquad (1)$$

where m_j is the mass of the jth planet and P_J is a function of the Delaunay variables l, g, h, L, G and H ($l = M, g = \omega, h = \Omega, L = \sqrt{a}, G = \sqrt{a(1-e^2)}$ and $H = \sqrt{a(1-e^2)}\cos i$, where a denotes the semi-major axis, e the eccentricity, i the inclination (evaluated with respect to the invariable plane of the Solar system), Ω the longitude of the node, ω the argument of pericentre and M the mean anomaly of the massless body, respectively).

Since the Lidov–Kozai Hamiltonian after averaging over l and l_j does not depend on l and h, the Delaunay moments associated with these variables, L and H, are constants of the motion. As a consequence, the quantity $H = \sqrt{a(1-e^2)}\cos I$ is preserved ($\sqrt{a}$ is constant because of the conservation of L) in the averaged motion (Thomas & Morbidelli 1996; Gronchi & Milani 1999; Carruba et al. 2002). As discussed in Gronchi & Milani (1999), since the value of H is fixed from the initial conditions, both the averaged inclination and eccentricity have maximum allowed values:

$$I_{\max} = I(e = 0) = \arccos\frac{H}{\sqrt{a}}, \qquad (2)$$

$$e_{\max} = e(I = 0) = \sqrt{\frac{a - H^2}{a}}. \qquad (3)$$

When the eccentricity is large enough, the nodal distance at the ascending node,

$$d^+_{\rm nod} = \frac{a(1-e^2)}{1 + e\cos\omega} - a', \qquad (4)$$

and at the descending node,

$$d^-_{\rm nod} = \frac{a(1-e^2)}{1 - e\cos\omega} - a', \qquad (5)$$

between the ellipse of the asteroid orbit and the circular orbit (with radius a') of some perturbing planet can become zero. In this case a node-crossing is said to occur and a collision between the asteroid and the planet is possible. At $\omega = \pm 90^\circ$, $\cos\omega = 0$ and therefore the denominators in equations (4) and (5) become equal to 1. As a consequence, for values of ω for which the eccentricity is larger, the right-hand side of equations (4) and (5) reduces to its minimum value $a(1 - e^2) - a'$. The fact that for the maximal value of the eccentricity the nodal distance is not minimal is called the 'Lidov–Kozai protection mechanism'. For $\omega = 0^\circ$, equation (4) reduces to the first-order criterion $q = a'$, with q the asteroid pericentre distance $q = a(1 - e)$ (note that for $\omega = 0^\circ$ the value of the eccentricity is the minimum one).

In this section I consider what other information may be obtained by studying Lidov–Kozai conserved quantities in the region of the Phocaea dynamical family. For this purpose I start focusing my attention on the conserved values of the H integral.

Fig. 1(a) shows the current distribution of proper inclination and eccentricities for asteroids in the local background of the Phocaea family (black dots; see Carruba & Michtchenko 2009 for a definition of the Phocaea family local background), members of the Phocaea classical family (blue crosses) and members of the Phocaea

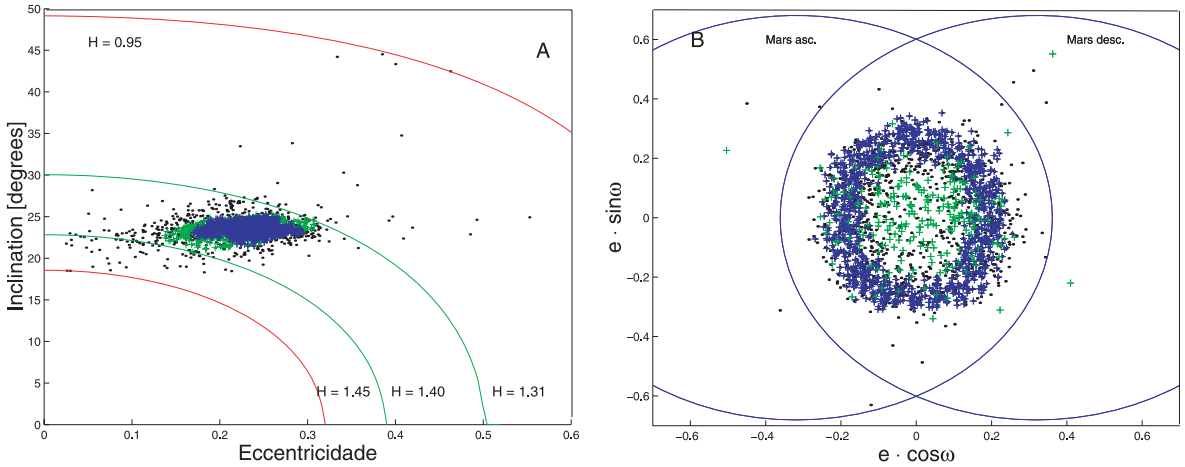

Figure 1. (a) (e, I) values of the H integrals for asteroids in the region of the Phocaea family. (b) Mars node-crossing lines for asteroids in the same region.

frequency family (green crosses). Superimposed are (e, I) values of the H integral in the range of H values for the Phocaea frequency family (green curves) and for the Phocaea local background (red curves).

Fig. 1(b) shows Mars node-crossing lines for asteroids with semi-major axis equal to that of the Phocaea classical family barycentre ($a = 2.3851$ au, Carruba 2009b), obtained with equations (4) and (5), assuming Mars is on a circular orbit of radius a'. As can be seen in the figure, all the members of the Phocaea classical family and the vast majority of the members of the Phocaea frequency family do not reach values of eccentricity large enough to experience a node-crossing with Mars. A few members of the Phocaea frequency family, however, reach eccentricities large enough to allow an interaction with Mars. I will investigate the long-term stability of these objects in the next section.

3 MARS-CROSSER ASTEROIDS IN THE REGION: NUMERICAL SIMULATIONS

As seen in the previous section and in Carruba (2009a), asteroids in the region of the Phocaea dynamical family at high eccentricities are characterized by interactions with Mars. In order to understand the long-term stability of asteroids in the region, I turn my attention to the results of numerical simulations. I start by performing short-term simulations on selected asteroids in the region.

3.1 Short-term numerical simulations

Since I am interested in studying Mars-interacting asteroids, I start by selecting objects with a non-zero possibility of interaction. In Carruba (2009a), I saw that a very simple criterion for identifying asteroids that possibly interact with Mars was to set $q = Q_{\rm Mars}$, with $q = a(1 - e)$ the pericentric distance of the asteroid and $Q_{\rm Mars} = a_{\rm Mars}(1 + e_{\rm Mars})$ the apocentric distance of Mars. In the previous section we saw that this is a simplistic criterion, and that a study of the nodal distance is more adequate to set limits on the Mars-interacting population. Nevertheless, the former criterion has the advantage of simplicity. Since I am interested in asteroids in the region of the Phocaea family, i.e. between the 7J:–2A resonance (approximately located at $a = 2.258$ au) and the 3J:–1A resonance (the left boundary of which is approximately located at $a \simeq 2.5$ au), I choose to work with asteroids with $e > 0.26$, which is the eccentricity of an asteroid with $q = Q_{\rm Mars}$ at the left boundary of the Phocaea dynamical family region, i.e. the 7J:–2A resonance. I remind the reader that all asteroids in this region are characterized by high inclinations, i.e. $\sin I > 0.3$. With these criteria, I identified 299 objects in the Phocaea local background.

Fig. 2(a) displays a proper (a, e) projection of these objects. Blue crosses are members of the Phocaea classical family and green crosses are members of the Phocaea frequency family. The green line displays the location for which $q = Q_{\rm Mars}$, the vertical red lines the locations of the main two- and three-body mean-motion resonances and the thick blue lines the location of the main secular resonances in the region.

As can be seen in the figure, the vast majority of the asteroids do not reach an eccentricity larger than 0.31. Only a few bodies, some possibly captured in the $2\nu_6 - \nu_{16}$ region, some captured by the 2M:–1A resonance and others that could possibly have interacted in the past with the 3J:–1A resonance, have eccentricity values larger than 0.31. To start investigating the orbital behaviour of these objects, I integrated the 299 asteroids with SWIFT-SKEEL, the symplectic integrator of Levison & Duncan (2000) that is able to model close encounters between a massive planet and a massless particle, over 20 Myr. Fig. 2(b) displays the values of maximal eccentricity attained by the integrated particles during the length of the simulation. Small blue dots display the initial orbital location in the proper (a, e) plane of the asteroids with $e_{\rm max} < 0.35$, medium-sized green dots show the orbital location of asteroids with $0.35 < e_{\rm max} < 0.40$, larger sized yellow dots display the orbits of asteroids with $0.40 < e_{\rm max} < 0.50$ and the largest red dots show the locations of asteroids with $e_{\rm max} > 0.5$ (during the length of the integration, three particles that reached values of $e_{\rm max} > 0.5$ were lost because of planetary close encounters). The other symbols are the same as in Fig. 2(a).

As can be seen in Fig. 2(b), the bodies with initial proper eccentricity > 0.31 are most of those characterized by $e_{\rm max} > 0.4$. To investigate the stability of orbits in the region further, I created a grid of test particles with initial osculating eccentricity between 0.20 and 0.40, for a range of semi-major axis between those of the 7J:–2A and 3J:–1A resonances, and with the values of inclination determined by the constancy of the H integral. In particular, I used a value of H equal to 1.3486, which is the median value of H for real asteroids in the region, once the high-e objects ($e > 0.4$) and high-I

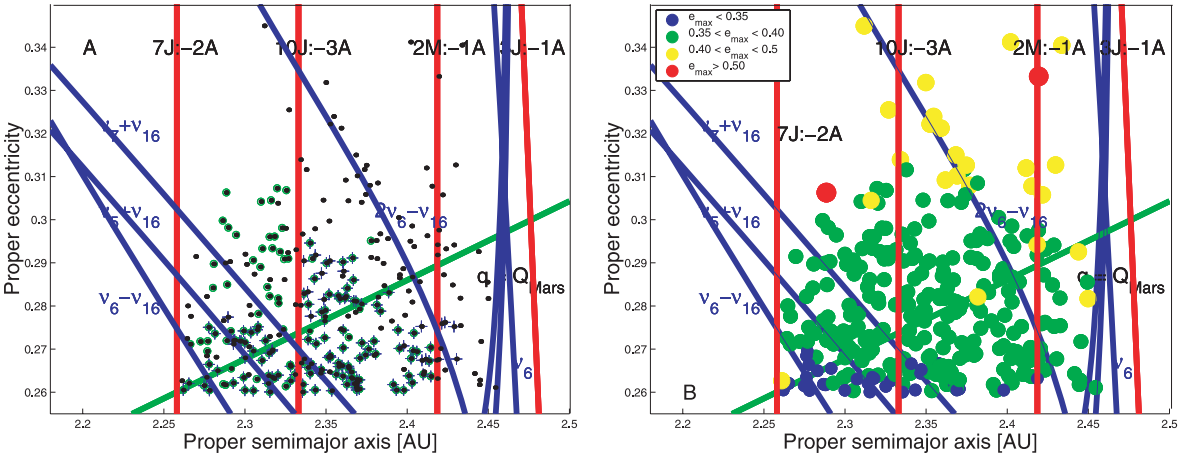

Figure 2. (a) An (a, e) projection of asteroids in the region of the Phocaea family, for $e > 0.26$. (b) The final status of the same asteroids at the end of the 20-Myr integration.

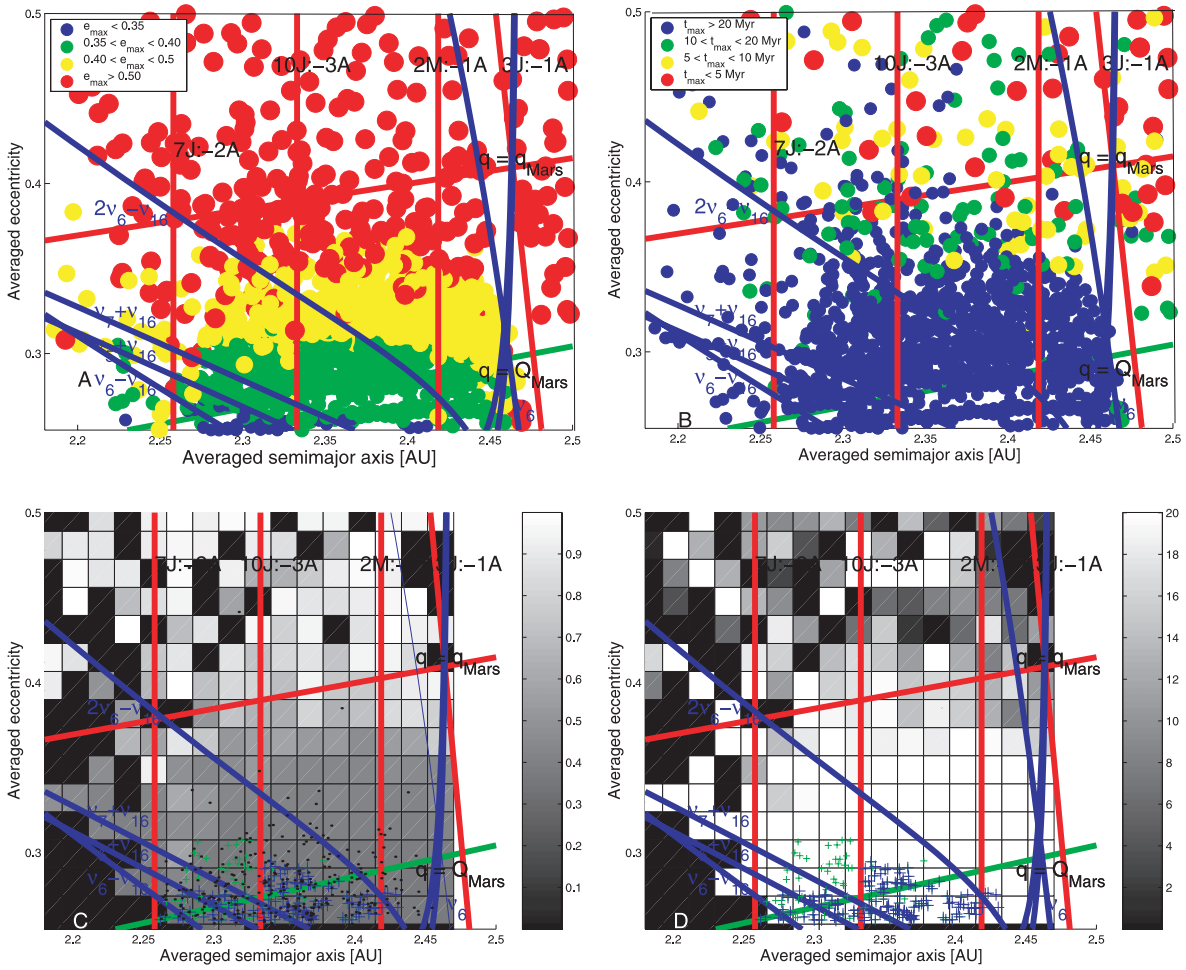

Figure 3. Projections in the space of averaged (a, e) of (a) maximum eccentricity values and (b) maximum survival time, for the simulated particles in the region. See text for a discussion of the colour code. Panels (c) and (d) display the position of real asteroids in the region, superimposed on density maps of maximum eccentricity and survival time.

objects ($\sin I > 0.45$) are excluded. The initial values of Ω, ω, and M were those of (77127) (2001 DJ93), an asteroid characterized by a value of $H = 1.3486$. There was a total of 2500 particles in this simulation, integrated over 20 Myr.

Fig. 3(a) shows a projection in the space of averaged (a, e) (the value of the mean of osculating elements during the integration length; I choose to work with mean elements rather than with proper elements because for many particles the survival time was too short to obtain a correct determination of proper elements) of the maximum osculating eccentricity achieved by the particle during the integration. The colour coding for the test particles and the other symbols is the same as in Fig. 2(b). Fig. 3(b) is similar, but shows the maximum survival times (see the figure legend for the description of the meaning of the particle colour codes).

As can be seen in the figures, particles with maximal value of eccentricity larger than 0.4 are confined to values of averaged eccentricity larger than 0.3. However, only particles with $e > 0.36$ were lost before the end of the integration (Fig. 3b). This is further confirmed by the density maps of $e_{\max}$ (Fig. 3c) and $t_{\max}$ (Fig. 3d). Following the approach of Carruba & Michtchenko (2009), in these figures I show the mean values of $e_{\max}$ and $t_{\max}$ on a grid covering the intervals (2.10–2.46) in a (I took 20 equally spaced intervals) and (0.225–0.5) in e (17 equally spaced intervals were used in this case). Superimposed on the density maps is the orbital location of asteroids in the background (black dots), in the Phocaea classical family (blue crosses) and in the Phocaea frequency family (green crosses), as obtained in Carruba (2009a).

During the length of the integration (20 Myr), particles in the region of real asteroids with $e > 0.31$ achieved larger values of maximal eccentricity, but they were not lost. To investigate further the long-term stability of asteroids in the region with $e > 0.31$, I performed simulations on longer time-scales for asteroids in this region. The set-up of the simulation and the results will be discussed in the next section.

3.2 Long-term stability of high-eccentricity objects

Fig. 2(a) displays an (a, e) projection of the 21 asteroids in the region of the Phocaea family. Of the objects with $e > 0.31$, (3343) Nezdel is the only one for which a spectral classification is available. Its S-type taxonomy is compatible with that of the Phocaea family. No information is available on the albedos of these objects.

As can be seen in Fig. 2(a), there are essentially six mechanisms that can increase an asteroid's eccentricity from the values observed in the region of the Phocaea family to $e > 0.31$: interaction with the 3J:–1A, 7J:–2A, 10J:–3A and 2M:–1A mean-motion resonances and interaction with the $\nu_5 - \nu_{16}$ and $2\nu_6 - \nu_{16}$ secular resonances. Of these mechanisms, the interaction of particles with the 3J:–1A

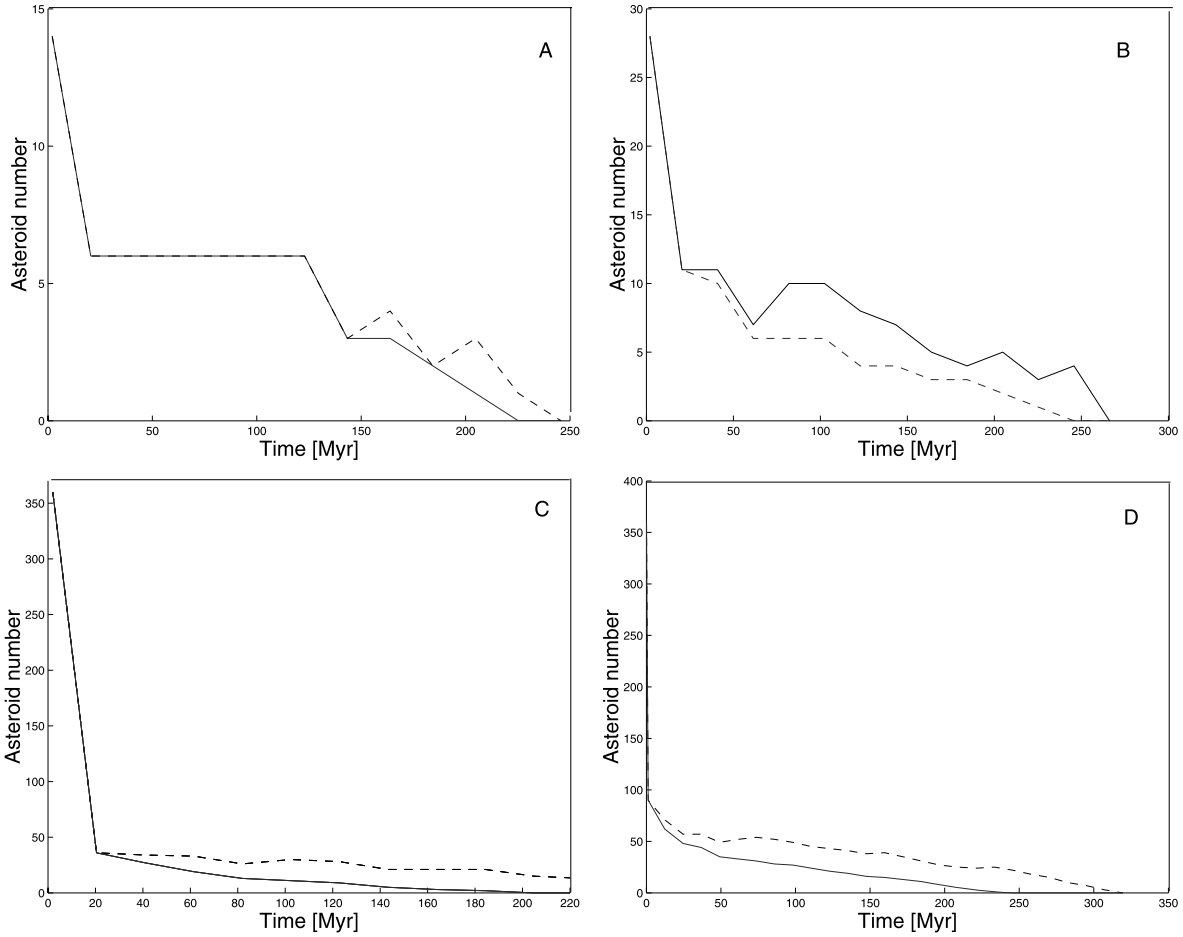

Figure 4. The number of objects (black line) and asteroids initially inside the high-*e* region defined in the text (blue dashed line), as a function of time. See text for a description of the different panels.

mean-motion resonance is a proven very effective mechanism in raising the eccentricity of test particles to Mars-crossing levels. In addition, the interplay of the Yarkovsky effect with the $\nu_5 + \nu_{16}$ and $2\nu_6 - \nu_{16}$ secular resonances and with the 2M:–1A mean-motion resonance may also increase the eccentricities of test particles to the level of the 21 observed objects with $e > 0.31$.

To investigate the long-term stability of these 21 asteroids further, I performed the following numerical experiments. First I integrated the 21 asteroids with SWIFT-SKEEL over 200 Myr under the gravitational influence of all planets from Venus to Neptune (Mercury was accounted for as a barycentric correction to the Sun's initial conditions). Following the approach of Nesvorný et al. (2008), I defined a region of interest which is between the 7J:–2A and and 3J:–1A mean-motion resonances and with $e > 0.31$, and checked how many objects remained in the area as a function of time during the numerical integration.

Fig. 4(a) shows this number as a function of time (black dashed line) and the number of objects initially in the area of interest that remained in the region as a function of time (blue line). I should emphasize that the parameter that gives information on the stability of objects is that related to the number of objects *initially* inside the area, i.e. the dashed line. The fact that other objects not originally in the area may be temporarily displaced inside the region of interest is, per se, not an indication of the stability of the initial asteroid population.

As can be seen in the figure, the number of high-*e* objects rapidly drops, tending to zero after 220 Myr if we consider the initial population and after 250 Myr if we consider the overall population of objects that passed through the region. As a second numerical experiment, I integrated the same particles with SWIFT_CE, an integrator developed in Carruba et al. (2007) that simultaneously models the effect of close encounters between a massive planet and a massless particle and the diurnal and seasonal versions of the Yarkovsky effect. I used typical values of Yarkovsky parameters for S-type asteroids (thermal conductivity $K = 0.001\,\mathrm{W\,m^{-1}\,K^{-1}}$, thermal capacity $C = 680\,\mathrm{J\,kg^{-1}\,K^{-1}}$, surface density $1500\,\mathrm{kg\,m^{-3}}$, density $2500\,\mathrm{kg\,m^{-3}}$, bond albedo 0.1 (Carruba et al. 2003), the asteroid radius computed using equation (1) in Carruba et al. (2003) and the average value of geometric albedo of Phocaea members, $p_V = (0.24 \pm 0.12)$ (Carruba 2009b)) and to one set of objects I gave an inclination of the spin axis of 90°, while to the second an obliquity of -90° was assigned. No re-orientations were considered, so that the drift caused by the Yarkovsky effect was the maximum possible.

Fig. 4(b) displays the number of objects in the area of interest, currently (black dashed line) and since the start of integration (blue line), during the length of the simulation. Similarly to the case without non-gravitational effects, the number of objects in the area drops quickly. Due to the interplay of the Yarkovsky effect with the $\nu_5 + \nu_{16}$ and $2\nu_6 - \nu_{16}$ secular resonances, which forced a few particles to stick to the resonances for longer, a few particles survived in the

high-eccentricity area for times up to 250 Myr. Eventually, all the initial population of resonant particles was lost after 270 Myr. I take this time as an upper limit on the stability of asteroids at high *e*.

One possible objection to these data is the low number of objects currently present at high *e*. To obtain a statistically more robust estimate of the stability time, I created a grid of 360 particles equally spaced in *a* by 0.005 au and in *e* by 0.004, in the range of *a* values 2.34–2.41 and of *e* values 0.26–0.352. The values of the other angles were obtained using the same procedure described in Section 3.1, and the test particles were integrated with both SWIFT_SKEEL and SWIFT_CE over 400 Myr. Again, I checked for the number of particles in the area around the $2\nu_6 - \nu_{16}$ resonance defined above. The results of my simulations are given in Figs 4(c) and (d). As can be seen in the figure, more than 90 per cent of the integrated test particles were lost in less than 20 Myr. For the integration with SWIFT_SKEEL, the last particle originally in the resonant area was lost after 200 Myr, while for the integration with SWIFT_CE the last particle was lost after 230 Myr. I believe that my integrations with a larger sample of test particles confirm that particles at high eccentricity are all lost by time-scales of at most of 270 Myr.

4 CREATING THE HIGH-ECCENTRICITY ASTEROID POPULATION

Now that I have investigated the stability of the high-eccentricity population, I want to understand on which time-scales the current population of 21 objects may be created starting from the orbital location of Phocaea family members. For this purpose, I selected 84 members of the classical Phocaea family with $a > 2.34$ au (these are particles that are able to interact with all of the major resonances that may increase their eccentricities, i.e. the 3J:–1A and 2M:–1A mean-motion resonances and the $\nu_5 + \nu_{16}$ and $2\nu_6 - \nu_{16}$ secular resonances; the other effective mechanism that can increase asteroid eccentricities, the ν_6 resonance, will be investigated in detail in Section 5) and created two clones for each of these particles. I integrated these clones with SWIFT_RMVSY.f, the symplectic code of Brož (1999), with the same set-up used for the SWIFT_CE integration over 400 Myr. I further divided the high-eccentricity area defined in Section 3.2 into two zones, Zone 1 with semi-major axis less than the value of the centre of the 2M:–1A resonance and Zone 2 between the 2M:–1A and 3J:–1A resonances, and I checked the number of objects that reached the resonant zones as a function of time.

Fig. 5 shows the number of objects that reached Zone 1, Zone 2 and the high-eccentricity region as a whole as a function of time. The first particle reached zone 1 only after 187 Myr of integration. It interacted with the 2M:–1A resonance, as did the only other particle that reached zone 1 during the integration. Four more particles reached the high-eccentricity zone 2. Of these, one interacted with the 3J:–1A resonance and was rapidly lost because of planetary close encounters, and three others interacted with the $\nu_5 - \nu_{16}$ secular resonance. On the whole, only six particles (7.14 per cent of the integrated bodies) achieved large values of eccentricity during the 370-Myr integration. While the sample that was integrated is somewhat limited to draw statistically significant conclusions from, I believe that the results obtained are sufficient to infer that, among the mechanisms that can produce a high-*e* population from the current Phocaea family members, the 3J:–1A, 2M:–1A and $\nu_5 - \nu_{16}$ resonances seems to be the most effective.

To test this hypothesis, I studied in detail the process of interaction of test particles evolving because of the Yarkovsky effect with each of the above-mentioned resonances. For each of the resonance

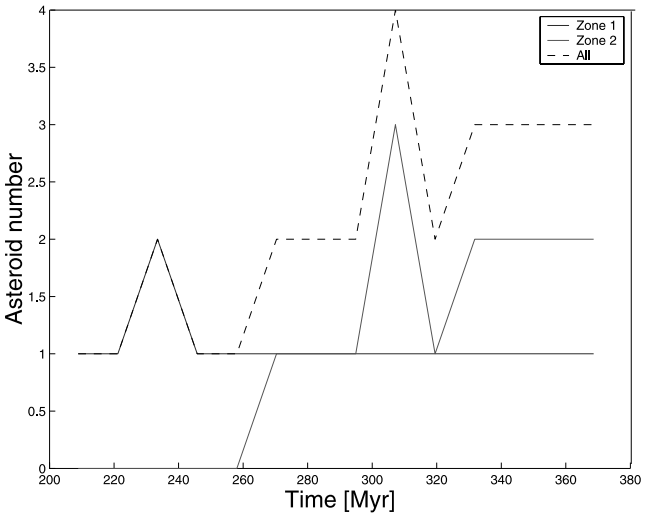

Figure 5. Number of asteroids that reached Zone 1 (blue line), Zone 2 (red line), and the high-eccentricity region as a whole (dashed black line) as a function of time. See text for the definition of Zones 1 and 2.

studies, I created test particles with spin inclinations of 90°, 60°, 30° and 15°, with positive values for particles with smaller semi-major axis than that of the resonance centre and negative ones for larger values of *a*. The other values of the Yarkovsky parameters are the same as used in the previous sections. I then let the test particles evolve and studied the changes in eccentricity caused by the interaction of the test particles with the resonances of interest. While the statistics of eccentricity changes provides far from a complete study of the resonance effect (which would involve a study of the resonance structure and the resonant angle at the time the particle was captured), I believe that this study may provide some first insights on the relative efficiency of the mechanisms studied in increasing the particle eccentricity.

The results of my simulations will be discussed in the next subsections.

4.1 3J:–1A resonance

The 3J:–1A mean-motion resonance is a well-known source of instability for asteroids in the inner main belt (see, among others, Morbidelli & Vokrouhlický 2003). It sets the lower limit in semi-major axis for the Phocaea dynamical family, and it is well known that a region of unstable chaotic orbits is found near the resonance separatrix (Guillens, Vieira Martins & Gomes 2002). Also, the non-linear dependence of the *g* frequency as a function of the semi-major axis in the proximity of the 3J:–1A resonance causes an increase in the density of secular resonances near the 3J:–1A resonance separatrix, as discussed in Carruba & Michtchenko (2009). Here I selected members of the Phocaea family with $a > 2.43$ au, which are the likeliest to interact with the 3J:–1A resonance. Fig. 6 displays their orbital location with respect to the 3J:–1A mean-motion resonance. The red line shows the location of the resonance separatrix, the magenta line the location of the chaotic layer near the resonance separatrix as defined in Morbidelli & Vokrouhlický (2003). Blue lines are associated with the main secular resonances in the region. Asteroids with Lyapunov times $T_{\rm L}$ larger than 50 000 yr are shown in red, asteroids with $20\,000 < T_{\rm L} < 50\,000$ yr are shown in green and asteroids with $T_{\rm L} < 20\,000$ are shown in black. One notices that the orbital behaviour of asteroids becomes more chaotic as they get closer to the layer of chaos near the resonance separatrix.

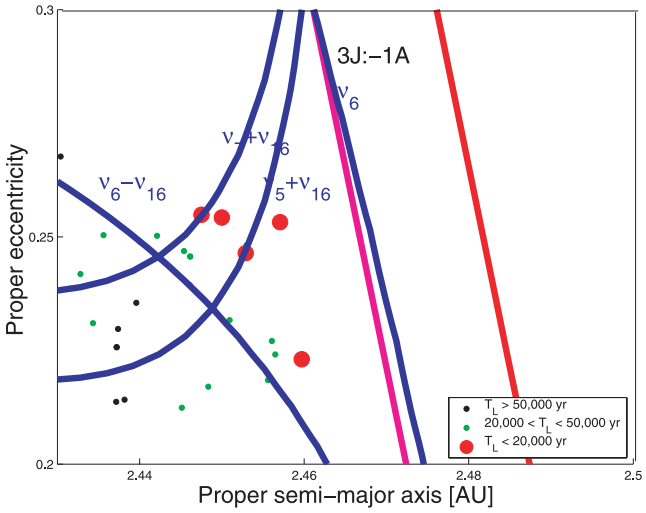

Figure 6. An (a, e) projection of Phocaea family members in the neighbourhood of the 3J:–1A resonance. See the text for an explanation of the other symbols.

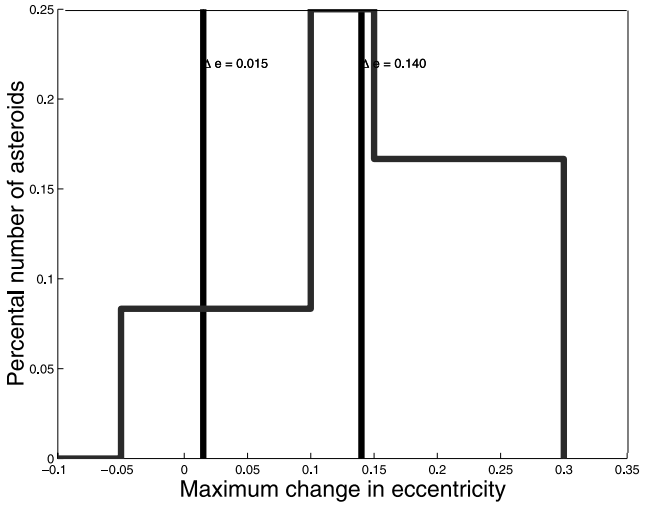

Figure 7. Histogram of maximal changes in eccentricity for particles in the simulation that interacted with the J7:–2A mean-motion resonance.

To study the interaction of family members with the 3J:–1A resonance, I selected 17 objects with $a > 2.43$ au and gave them the four positive values of orbital spins described in Section 4. As expected, none of the integrated particles survived the extent of the simulation. Before reaching the 3J:–1A mean-motion resonance, the test particles interacted with the ν_6 secular resonance, the proximity of which significantly increased the values of their eccentricity with a mechanism that will be described in detail in Section 5. This mechanism alone was sufficient to push the eccentricity of at least 56.4 per cent of the integrated test particles to Mars-crossing values, causing their loss. The remaining 44.6 per cent of particles, which survived the passage through the ν_6 secular resonance, did not survive the interaction with the 3J:–1A mean-motion resonance. Most of these particles had their eccentricity raised to Mars-crossing and Earth-crossing values with a mechanism well studied analytically (Ferraz-Mello et al. 1996) and numerically (Gladman et al. 1997), and were rapidly lost. Overall, I observed 35 particles that were pushed to the Zone 1 defined in Section 4 and then lost with timescales compatible with the results of Section 3.2. Based on these results, I believe that interaction with the J3:–1A mean-motion resonance (and the near ν_6 secular resonance) may be a valid mechanism to produce the currently observed $e > 0.31$ population.

4.2 7J:–2A resonance

The 7J:–2A mean-motion resonance sets the leftward limit in proper semi-major axis for the Phocaea dynamical family (only one family member, (57308) 2001 QL201, has a semi-major axis value less than the J7:–2A resonance centre). For that reason, I selected six asteroids within 0.01 au of the J7:–2A resonance centre, and I assigned to them only the four negative values of spin discussed in Section 4, so that their semi-major axis evolution will cause them to interact with the J7:–2A resonance.

Fig. 7 displays the changes in eccentricities caused by the passage through the J7:–2A resonance for my test particles. Vertical lines display the minimum and maximum change in eccentricity needed by a member of the Phocaea classical family to reach the $e > 0.31$ region. As can be seen in the histogram, there was only one case where there was a decrease in eccentricity. Most of the other particles experienced positive changes with Δe up to 0.25, more than enough to reach the 0.31 value from typical Phocaea family values of eccentricity. Most of the particles, due to their spin-axis orientation, evolved toward smaller values of semi-major axis and exited from the Phocaea local background. While it is possible that some of the particles with eccentricity increased beyond 0.31 may invert their spin-axis orientation and evolve towards the Phocaea local background, I also observed a few cases in which close encounters with Mars pushed back asteroids that passed through 7J:–2A in the Phocaea local background region. Based on these considerations, I believe that interaction with the 7J:–2A mean-motion resonance may be considered an effective mechanism for producing the currently observed high-eccentricity population.

4.3 2M:–1A resonance

As observed in Section 4, the 2M:–1A mean-motion resonance may be an effective mechanism for increasing the eccentricity of members of the Phocaea family to values larger than 0.31. To test the efficiency of this resonance in increasing particle eccentricities, I integrated 60 particles with a smaller than the resonance centre value (15 real asteroids with the four values of positive spin inclination described in Section 4) and 52 particles with a larger than the resonance centre value (13 particles, with four values of negative spin inclination).

Fig. 8 displays a histogram of maximal eccentricity changes for particles that interacted with the 2M:–1A resonance during the length of the 200-Myr numerical simulation with SWIFT_RMVSY.f. As can be seen in the figure, most of the particles experienced small variations in eccentricity when passing through the 2M:–1A resonance ($\Delta \simeq 0.001$), but about 15 per cent of the integrated test particles achieved values of $\Delta e > 0.05$. The largest negative values of Δe were found in test particles with positive spin values, but larger positive values of Δe were observed for this simulation as well. This seems to confirm that evolution in the 2M:–1A mean-motion resonance may be a viable mechanism to produce high-eccentricity objects.

4.4 $\nu_5 + \nu_{16}$ secular resonance

Another mechanism to increase particle eccentricity, the efficiency of which needs to be tested, is that of the interaction of the

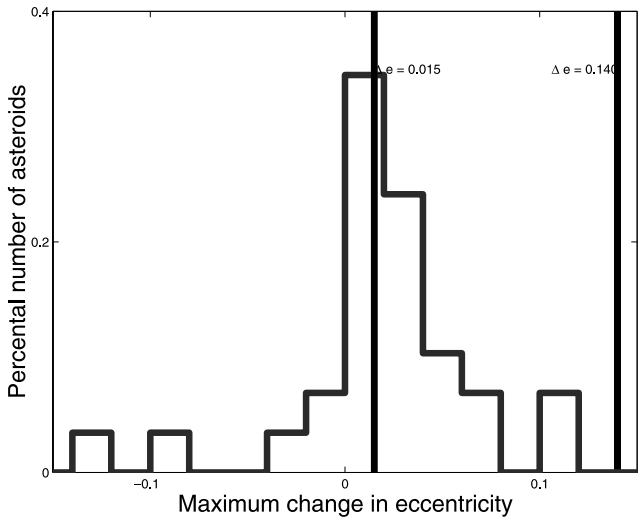

Figure 8. Histogram of maximal changes in eccentricity for particles in the simulation that interacted with the 2M:–1A mean-motion resonance.

$\nu_5 + \nu_{16}$ secular resonance with the Yarkovsky and YORP effects.[1] To test this mechanism, I selected 11 particles within ± 0.5 arcsec yr^{-1} of the resonance centre, for values of the semi-major axis larger than that of the 2M:–1A mean motion resonance and smaller than the 10J:–3A mean-motion resonance. Asteroids in the $\nu_5 + \nu_{16}$ secular resonance in between these two resonances have values of eccentricity too small to be a significant source of the high-eccentricity population (see Figs 2a and b). I assigned to these asteroids the eight values of spin obliquities discussed in Section 4 and integrated them over 200 Myr with SWIFT-RMVSY.

I analysed the resonant argument of the $\nu_5 + \nu_{16}$ secular resonance for the 88 particles that I integrated and found that 51 of them (58.0 per cent of the total) remained in librating states during the length of the integration, 32 (36.4 per cent) passed through the resonance or alternated phases of libration and circulation, and five of them (5.5 per cent) were not in resonant states. The orbital behaviour of librating particles showed characteristic oscillations in eccentricity of the order of the resonant argument librating period ($\simeq$5 Myr), which did not alter the particle eccentricity significantly during an oscillation period. Changes on longer time-scales were observed for a few particles, but were of minor importance (of the order of 0.02 at most, over 200 Myr) and, unfortunately, directed in the 'wrong' direction to explain the currently observed population of $e > 0.31$ asteroids. Particles with positive changes in e either evolved toward the J3:–1A resonance and had semi-major axis larger than that of the M2:–1A resonance (i.e. they could at best be objects created in Zone 2, as defined in Section 4) or evolved beyond the 10J:–3A resonance, outside the boundaries of Zone 1. Neither of these test cases could therefore have created the observed population of high-e objects.

For particles that crossed the $\nu_5 + \nu_{16}$ secular resonance, or its Uranian twin the $\nu_7 + \nu_{16}$ resonance, the highest change in eccentricity observed was 0.015, which is just barely enough to push the highest eccentricity members of the classical Phocaea family into the $e > 0.31$ region.

In view of these considerations, I believe that interaction with the $\nu_5 + \nu_{16}$ secular resonance may have had played at best an auxiliary role in the creation of the currently observed high-eccentricity population.

4.5 $2\nu_6 - \nu_{16}$ secular resonance

As was seen in Figs 2(a) and (b), most of the $e > 0.31$ population was found in proximity to the $2\nu_6 - \nu_{16}$ secular resonance. Can the interplay of this resonance with the Yarkovsky and YORP effects explain the current presence of some high-eccentricity objects? To test this hypothesis I selected 15 members of the Phocaea classical family, the $2g - s$ values of which were within ± 1.5 arcsec yr^{-1} from the resonance value. Five of these objects had semi-major axis larger than the resonance semi-major axis and were given the four negative values of spin obliquities discussed in Section 4, while the other 10 had smaller semi-major axis than the resonance centre and were given the four positive values of spin obliquities.

I integrated these objects over 200 Myr with SWIFT-RMVSY, and checked for each particle the resonant argument of the $2\nu_6 - \nu_{16}$ secular resonance. At the end of the integration only three particles (5 per cent of the total) were still inside the resonance. Passage through the resonance or the secular change caused by the resonant evolution in e was at most of order 0.010, insufficient to push even the more eccentric members of the Phocaea classical family inside the high-eccentricity region $e > 0.31$. Based on these considerations, I conclude that the $2\nu_6 - \nu_{16}$ secular resonance played at best a minor role in the creation of the currently observed high-e population. The alignment of asteroids at the centre of the $2\nu_6 - \nu_{16}$ secular resonance observed in Fig. 2 may therefore be just an artefact created by the procedure used to obtain synthetic proper elements, which causes asteroids in or near a secular resonance to appear at the resonance centre due to averaging over more than a libration period in the resonance (Knežević & Milani 2003).

5 CHAOTIC DYNAMICS NEAR THE ν_6 RESONANCE SEPARATRIX

One of the questions left unanswered by Carruba (2009b) was the cause of the chaotic dynamics near the ν_6 resonance separatrix. In this section I will investigate this problem with analytical and numerical tools.

5.1 Analytical model of the ν_6 secular resonance

Since the late 1980s, it has been known that asteroids in the proximity of the ν_6 secular resonance have their eccentricity raised to planetary-crossing values and are so destabilized on short time-scales (see, among others, Yoshikawa 1987). To estimate the effect of the proximity of the ν_6 secular resonance more quantitatively here, I briefly revise the non-linear model of Yoshikawa (1987) for the ν_6 resonance. In his model Yoshikawa kept terms up to third degree in eccentricity and inclination for the secular part of the disturbing function, and, under the hypothesis of proximity to the ν_6 resonance, assuming $l_6 = \varpi - \varpi_6^*$ moves much more slowly than $l_5 = \varpi - \varpi_5^*$, where $\varpi_i^* = \nu_i \cdot t + \beta_i$, and ν_i and β_i are known constants (Bretagnon 1974), obtained the following expression for the Hamiltonian of the problem:

$$F_{\nu_6} = \frac{1}{2}(b - \nu_6)e^2 + \frac{1}{4}ce^4 - d_6 e\cos(\varpi - \varpi_6^*), \quad (6)$$

[1] Due to the small difference in arcsec yr^{-1} between $g_5 = 4.257$ arcsec yr^{-1} and $g_7 = 3.093$ arcsec yr^{-1}, the $\nu_5 + \nu_{16}$ secular resonance is close in proper element space to the $\nu_7 + \nu_{16}$ resonance. Since resonances involving the g_5 frequency have a stronger effect on asteroid proper elements (Milani & Knežević 1994; Carruba & Michtchenko 2007, 2009), here I will focus my attention on the resonance involving the Jovian frequency.

where $\nu_6 = 26.217\,\mathrm{arcsec\,yr^{-1}}$ is the value of the precession frequency of the pericentre of Saturn and b, c and d_6 are coefficients with values given by

$$b = \frac{1}{na^2}\sum_{j=1}^{8} Gm_j[2A_j + 2D_j \sin^2(i) + C_j \sin(2i)\tan(i/2)], \tag{7}$$

$$c = \frac{1}{na^2}\sum_{j=1}^{8} Gm_j(4B_j - A_j), \tag{8}$$

$$d_i = -\frac{1}{na^2}\sum_{j=1}^{8} Gm_j E_j M_{ji}, \tag{9}$$

where m_j is the mass of the jth planet, M_{ji} are constants given in Bretagnon (1974) and expressions for the A_j, B_j, C_j, D_j, E_j coefficients are given by

$$A_j = \frac{1}{8a'}\alpha b^{(1)}_{3/2}, \tag{10}$$

$$B_j = \frac{1}{16a'}\left[\frac{1}{2}\alpha^3\frac{d^3 b^{(0)}_{1/2}}{d\alpha^3} + \frac{1}{8}\alpha^4\frac{d^4 b^{(0)}_{1/2}}{d\alpha^4}\right], \tag{11}$$

$$C_j = -\frac{1}{8a'}\alpha b^{(1)}_{3/2}, \tag{12}$$

$$D_j = \frac{1}{16a'}\left[-\alpha b^{(1)}_{(3/2)} - 2\alpha^2\frac{db^{(1)}_{3/2}}{d\alpha} - \frac{1}{2}\alpha^3\frac{d^2 b^{(1)}_{3/2}}{d\alpha^2}\right], \tag{13}$$

$$E_j = -\frac{1}{4a'}\alpha b^{(2)}_{3/2}, \tag{14}$$

where

$$\alpha = a/a_j, \quad a' = a_j \quad (a_j > a), \tag{15}$$

$$\alpha = a_j/a, \quad a' = a \quad (a_j < a). \tag{16}$$

The Laplace coefficients $b^{(m)}_s(\alpha)$ (with s a semi-integer number) are defined by

$$b^{(m)}_s(\alpha) = \frac{2}{\pi}\int_0^{\pi}\frac{\cos(m\theta)\,\mathrm{d}\theta}{(1 - 2\alpha\cos\theta + \alpha^2)}. \tag{17}$$

Useful expansions in series of α for the Laplace coefficients and relations between the Laplace coefficients and its derivatives are given in Murray & Dermott (1999), equations (6.68)–(6.72). To check if my numerical computation of the b, c and d_i coefficients agrees with that of Yoshikawa (1987), here I re-obtained b as a function of a and chosen values of i and c and d_5 and d_6 as functions of a (Figs 9a and b). The results are in excellent agreement with figs 3 and 4 of Yoshikawa (1987).

In this paper I am interested in investigating the dynamics of objects near the ν_6 resonance separatrix. Following Yoshikawa (1987), I introduce the k_6 parameter:

$$k_6 = b - \nu 6. \tag{18}$$

In the Phocaea family range of inclination values, only negative values of k_6 are observed. A limiting value of $k_6 = -2.55\,\mathrm{arcsec\,yr^{-1}}$ can be introduced to discriminate between two classes of orbital behaviour, based on the following considerations. Using equation (6) I can compute values of the ν_6 Hamiltonian in the $(\varpi - \varpi_6{}^*, e)$ plane, for $\varpi - \varpi_6{}^*$ in the range 0°–360° and e from 0–0.6 (the accuracy of the Yoshikawa model drops at higher eccentricities). Fig. 10 displays the resulting contour plots for (a) a body with $k_6 = -0.29\,\mathrm{arcsec\,yr^{-1}}$, (b) a body with $k_6 = -2.55\,\mathrm{arcsec\,yr^{-1}}$ and (c) an asteroid with $k_6 = -5.00\,\mathrm{arcsec\,yr^{-1}}$. The black line displays the level $F_{\nu_6} = 0$, red lines negative values of F_{ν_6} and blue lines positive values. The horizontal line shows the $e = 0.31$ level, which corresponds to eccentricity values that I found to be unstable on time-scales of up to 270 Myr in Section 3.2. Generally speaking, for any value of k_6 I observe an island of libration at negative energies centred at $\varpi - \varpi_6{}^* = 180°$ and another island of libration at positive energies centred at $\varpi - \varpi_6{}^* = 0°$.

Depending on the value of k_6, two different orbital behaviours for the libration island at $\varpi - \varpi_6{}^* = 180°$ are observed. For $k_6 > -2.55\,\mathrm{arcsec\,yr^{-1}}$, orbits in this libration island are forced to reach values of eccentricity higher than 0.31 for *any* value of initial eccentricity, because of the presence of the second libration island at $\varpi - \varpi_6{}^* = 0°$ (Figs 10a and b).

For $k_6 < -2.55\,\mathrm{arcsec\,yr^{-1}}$ (Fig. 10c), however, all orbits in the libration island at $\varpi - \varpi_6{}^* = 0°$ and some of the orbits in the libration island at $\varpi - \varpi_6{}^* = 180°$ reach values of maximal eccentricity well below 0.31, and are therefore protected from the effect of planetary close encounters.

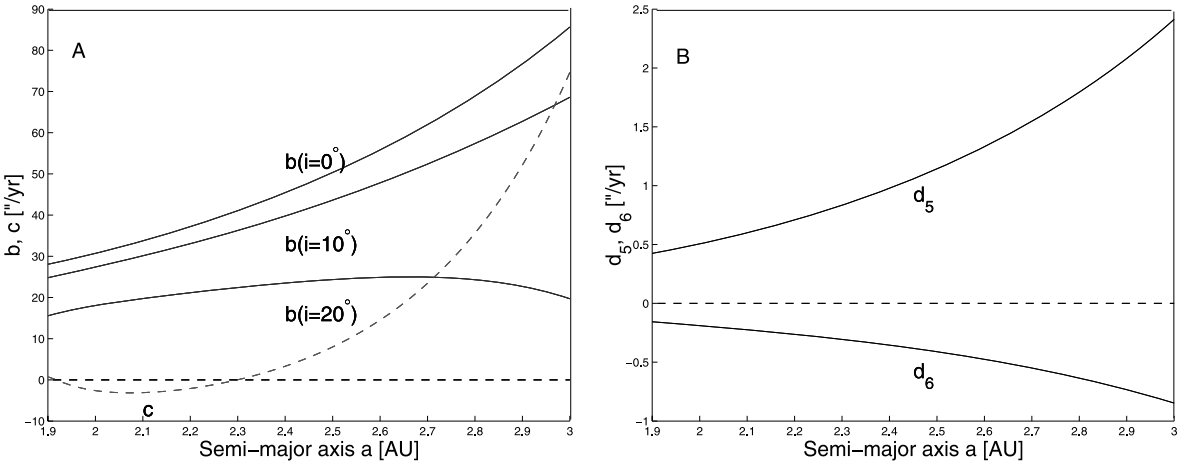

Figure 9. (a) Dependence of the b and c parameters of Yoshikawa (1987) on the semi-major axis and chosen values of inclination. (b) Dependence of d_5 and d_6 on the semi-major axis.

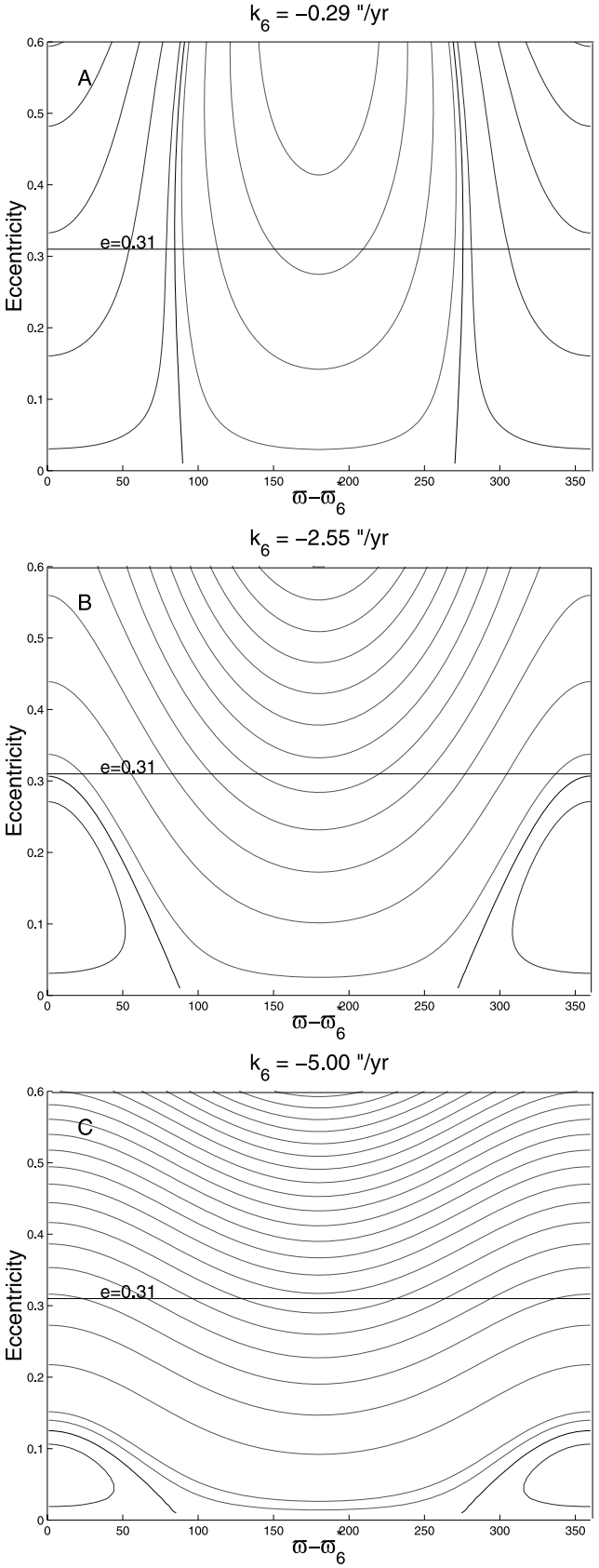

Figure 10. Contour plots of Hamiltonian values for asteroids with (a) $k_6 = -0.29\,\mathrm{arcsec\,yr^{-1}}$, (b) $k_6 = -2.55\,\mathrm{arcsec\,yr^{-1}}$ and (c) $k_6 = -5.00\,\mathrm{arcsec\,yr^{-1}}$. The horizontal lines display the limiting value of $e = 0.31$.

Can the effect of the proximity of the ν_6 secular resonance be responsible for the lower density of objects with $-2.55 < k_6 < 2.55\,\mathrm{arcsec\,yr^{-1}}$? To investigate this possibility further I turn my attention to the results of numerical simulations for real and fictitious objects in the region.

5.2 Numerical simulations

In Carruba (2009b), a zone of small Lyapunov times near the separatrix of the ν_6 secular resonance was identified. The causes of the chaotic behaviour were, however, left as an unanswered question. In the previous section we saw that near the separatrix of the ν_6 secular resonance and for values of k_6 in the range $-2.55 < k_6 < 2.55\,\mathrm{arcsec\,yr^{-1}}$ orbits are forced to reach values of eccentricities larger than 0.31, a value for which deep close encounters with Mars are possible. To confirm further that the chaotic behaviour of small-inclination asteroids is indeed caused by the ν_6 secular resonance, I computed values of k_6 for the test particles that I used for my estimates of Lyapunov times in the (a, sin (i)) plane in Carruba (2009b). Fig. 11(a) displays an enlarged view of the low-inclination region of small Lyapunov times found in Carruba (2009b), while Fig. 11(b) shows the orbital location of $-2.55 < k_6 < 2.55\,\mathrm{arcsec\,yr^{-1}}$ asteroids in the space of averaged (a, sin (i)) (red full dots). The agreement between the two figures is stunning: the core of chaotic behaviour is clearly associated with the $-2.55 < k_6 < 2.55\,\mathrm{arcsec\,yr^{-1}}$ region, with a few extra particles at slightly larger inclination that are associated with particles that do not reach $e = 0.31$ but are still able to experience shallow Martian close encounters, as observed during the simulation. I believe that this result fully explains the causes of the chaotic behaviour found in Carruba (2009b).

What about the long-term stability of the current low-inclination objects in the Phocaea family local background? As seen in Fig. 11(a) and in fig. 12(b) of Carruba (2009b), real objects are currently in regions of regular behaviour, characterized by $k_6 < -2.55\,\mathrm{arcsec\,yr^{-1}}$, so we would expect them to be relatively stable. To answer this question here I identified real asteroids in that region and numerically studied their long-term stability. I chose asteroids in the Phocaea local background as defined in Carruba & Michtchenko (2009), with a value of sin (i) smaller than the minimal value observed in the Phocaea frequency family (sin (i) = 0.3556) and with a range of semi-major axis between the 7J:–2A and 3J:–1A mean-motion resonances. Objects with inclination smaller than that of the centre of the ν_6 secular resonance were also excluded from the sample. There were 44 objects that satisfied this requirement, and I integrated them with SWIFT_CE and the same Yarkovsky parameters used in previous runs and a similar planetary set-up, over 200 Myr. I then checked how many particles remained in the low-inclination region that I defined above as a function of time.

Apart from two test particles that interacted with the 3J:–1A resonance and were lost, all the other particles remained in the low-inclination region during the length of the integration, thus confirming the stability of the current low-i population. While all of the test particles were considerably far away from the $-2.55 < k_6 < 2.55\,\mathrm{arcsec\,yr^{-1}}$ region, the three asteroids at lowest inclination, (87112) (2000 LB25), (111923) (2002 GW17) and (142401) (2002 SH23), displayed an orbital behaviour compatible with that observed in Fig. 10(b) (the actual orbital evolution in the ($\varpi - \varpi_6$, e) plane did not of course completely follow the Hamiltonian F_{ν_6} of equation (6), because of the fact that further away from the ν_6 separatrix the approximation that $l_5 = \varpi - \varpi_5^*$ no longer holds),

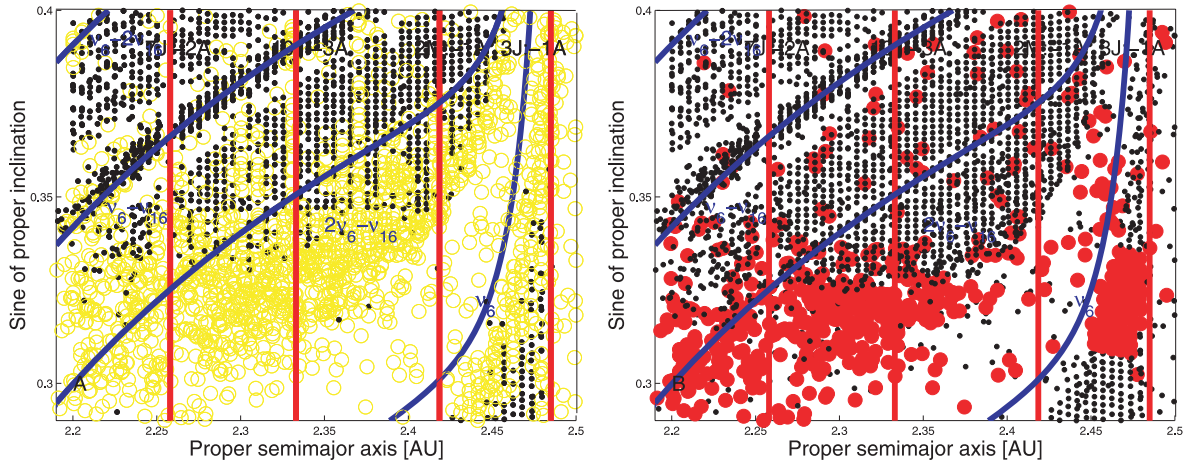

Figure 11. (a) Lyapunov times projected in the space of averaged (a, sin (i)) elements. Yellow circles display Lyapunov times smaller than 20 000 yr, while black dots are associated with times larger than 20 000 yr. (b) k_6 values in the same range of averaged (a, sin (i)) elements. Red full dots display values of k_6 in the range $-2.55 < k_6 < 2.55$ arcsec yr^{-1}.

and occasionally reached large values of osculating eccentricity (up to 0.35 for (111923) (2002 GW17)). While none of the three low-i asteroids was lost during the simulation, the fact that these three objects experienced episodes of high osculating eccentricity may explain why a region of low number density of asteroids at low i outside the $-2.55 < k_6 < 2.55$ arcsec yr^{-1} region was found in Carruba (2009b) (Figs 3c and d).

6 LONG-TERM STABILITY OF MINOR FAMILIES AND CLUMPS IN THE REGION

In Carruba (2009a), several small dynamical groups were identified in the region of the Phocaea dynamical family. Many of these groups had a limited number of members, sometimes just large enough for the group to be considered a clump. A question left unanswered by the previous work concerned the statistical significance of these groups. Were these clusters created by real collisions or were they just random association of bodies that happened to be in nearby orbits for a limited period of time? In order to estimate the statistical significance and the time-scales over which these clusters are still bound, I devised the following numerical experiment: I created two sets of clones of members of the clusters and integrated them with SWIFT-RMVSY.f, the symplectic integrator of Brož (1999) that simulates the diurnal and seasonal version of the Yarkovsky effect. Using typical values of the Yarkovsky parameters (Carruba et al. 2003) I gave to one set of objects an inclination of the spin axis of 90°, while to the second was assigned an obliquity of −90°. No re-orientations were considered, so that the drift caused by the Yarkovsky effect was the maximum possible.

I integrated the clones of members of the classical and frequency clusters over 200 Myr in the future and 200 Myr in the past[2] and obtained synthetic proper elements according to the definition of Knežević & Milani (2000) for the clones every 2.4576 Myr. I then re-obtained families and clumps for the set of synthetic proper elements of the clones at each time-step, using the barycentre of the clusters (Carruba 2009a, equation 7) as the first body for the family. As soon as the cluster (obtained for a value of velocity cut-off of 160 m s^{-1} and of frequency cut-off of 0.625 arcsec yr^{-1}, as in Carruba 2009a) failed to reach the minimum number of objects required to be considered a clump, the cluster was considered dispersed and a minimum limit for the dispersion time was found.

I will start by discussing the results for the classical families and clumps in the next subsection.

6.1 Classical groups

In Carruba (2009a), two minor clumps (one around (17628) (1996 FB5), the other one around (26142) (1994 PL1), both with 10 members) and a family (around (19536) (1999 JM4), with 27 members; this family merges with the asteroid associated with the Gil–Hutton clump (2860) Pasacentennium at a cut-off of 164 m s^{-1}) were identified in the space of proper elements. Here I start my analysis investigating the two clumps.

Fig. 12 displays the number of members of (a) the (17628) clump and (b) the (26142) clump as a function of time. As can be seen in the figure, except for isolated spikes for which the number of members occasionally rises above the clump level ($n = 9$ at a $v_{\rm cut-off} = 160$ m s^{-1}, horizontal line in the figure), both clumps are not recognizable as such for most of the integration length. Based on this consideration, I believe the two clumps may just be considered as statistical flukes. This is also confirmed by the fact that neither clump is recognizable in the space of proper frequencies (n, g, $g - s$) (Carruba 2009a).

Things are different for the case of the family around (19536). This family is recognizable in the space of proper frequencies (see next subsection for the discussion of this case) and it appears to be statistically robust: Fig. 13(a) displays the number of family members as a function of time, detected at a cut-off of 160 m s^{-1}. The horizontal green line displays the minimum number of members for the group to be identifiable as a family at this cut-off ($n = 22$). Notice that the family is still detectable for time-scales up to 190 Myr. Many of the family members are characterized by their interaction with the $\nu_6 - 2\nu_{16}$ secular resonance. At the beginning of the simulation, 26 particles were in the $\nu_6 - 2\,\nu_{16}$ librating state.

[2] Concerning the integration in the past, I should caution the reader that integrations with the Yarkovsky effect are not conservative, and therefore technically speaking not time-reversible. Backward integrations are however interesting from a statistical point of view, and while they are not accurate for a single asteroid, they still provide useful information for a statistically significant sample of objects.

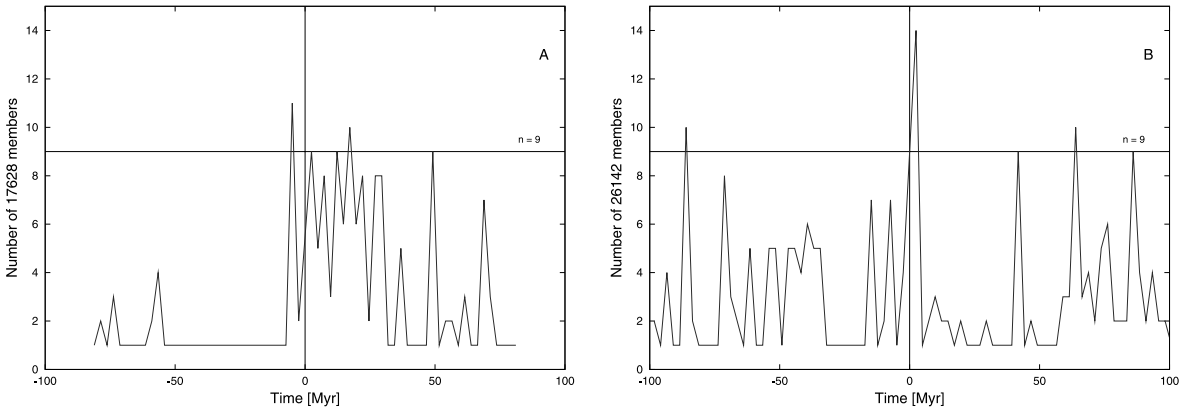

Figure 12. The number of members of (a) the (17628) clump and (b) the (26142) clump as a function of time.

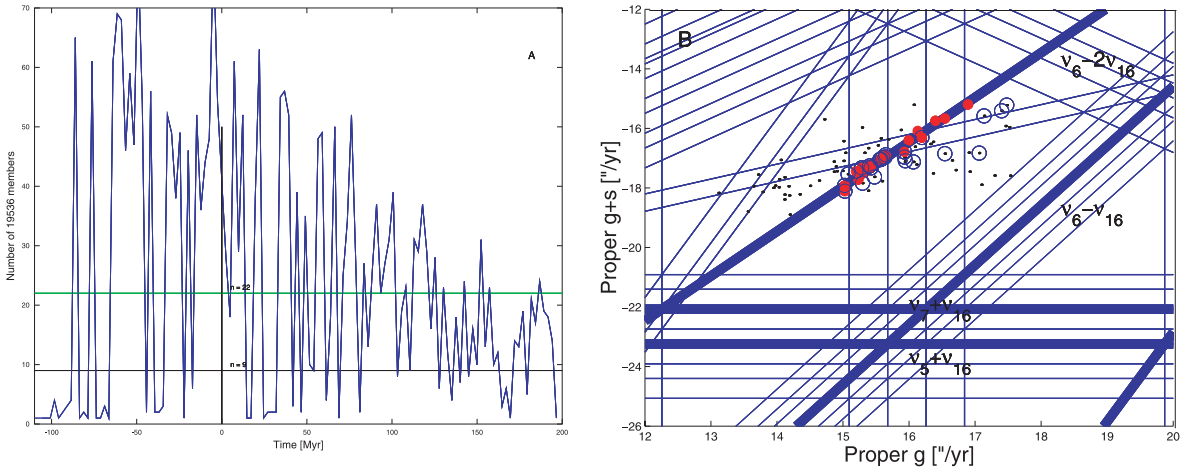

Figure 13. (a) The number of members of the 19536 classical family detected at a cut-off of 160 m s^{-1} as a function of time. (b) A (g, $g - s$) projection of the family clones at $t = 190$ Myr. The blue circles identify the clump members, the red full dots the asteroids in a librating $\nu_6 - 2\nu_{16}$ resonant state.

Fig. 13(b) displays a (g, $g + s$) projection of the family clone at $t =$ 190 Myr, the last time for which the family was still identifiable. Red full dots show asteroids in the $\nu_6 - 2\nu_{16}$ resonance, blue circles the members of the family and black dots the orbital location of all particles. Considering that the family was observable for more than 190 Myr into the future, and for more than 90 Myr in the past, I conclude that the group can be considered a good candidate for a collisional family.

6.2 Frequency groups

In the (n, g, $g - s$) frequency domain I identified two minor clumps in the region of the Phocaea family (Carruba 2009a): one around (19536) (1999 JM4) with 14 members at a cut-off of 0.625 arcsec yr^{-1} and another around (6246) Komurotoru, with nine members at the same cut-off. Of the two, the most interesting one was the clump around (6246), since this one was identifiable in the frequency domain only. Here I want to investigate how stable in time the clumps that I identified in Paper I (Carruba 2009b) are. I start my analysis with the clump around (6246) Komurotoru.

This clump is characterized by its interaction with two secular resonances: the $\nu_5 + \nu_{16}$ and the $2\nu_6 - \nu_{16}$ resonances. Of the 50 particles that I integrated (there were 25 members of the clump at the maximum cut-off of 0.745 arcsec yr^{-1}), six objects were in a $\nu_5 + \nu_{16}$ librating state during the whole simulation and four in a $2\nu_6 - \nu_{16}$ resonant state. 15 other particles had phases of libration in one of the two resonances during the integration. Fig. 14 displays the resonant angles of two particles trapped in the the $\nu_5 + \nu_{16}$ and $2\nu_6 - \nu_{16}$ resonances respectively. The thick red line displays the resonant argument passed through a digital filter so as to eliminate all frequencies with periods less than 1 Myr (see Carruba et al. 2005 for a discussion of the digital filtering procedure).

Fig. 15 displays the number of members of the 6246 frequency clumps in the Phocaea family region as a function of time. Panel (a) displays the data for a frequency cut-off of 0.625 arcsec yr^{-1}, while panel (b) shows the same for a cut-off of 0.745 arcsec yr^{-1}. While the numbers of members are obviously higher for the clumps found with the higher cut-off, the qualitative behaviour is roughly the same: after $\simeq$50 Myr the clump members disperse and they are no longer recognizable as a dynamical group, while for the integration backward in time the clump was identifiable up to -200 Myr. The fact that the clump is still identifiable before 200 Myr and after 50 Myr seems to indicate that it may be a robust dynamical group, and not just a statistical fluke.

It is interesting to view how the clump members disperse in time in the domain of proper frequencies and elements. Fig. 16 displays projections in the (a, sin(i)) and (g, $g + s$) planes of the orbital evolution of the (6246) clumps clones at $t = 0$ Myr (panels a and b), $t = 50$ Myr (panels c and d) and $t = 100$ Myr (panels e and f). As can be seen in the figure, the clump clones migrate towards smaller and

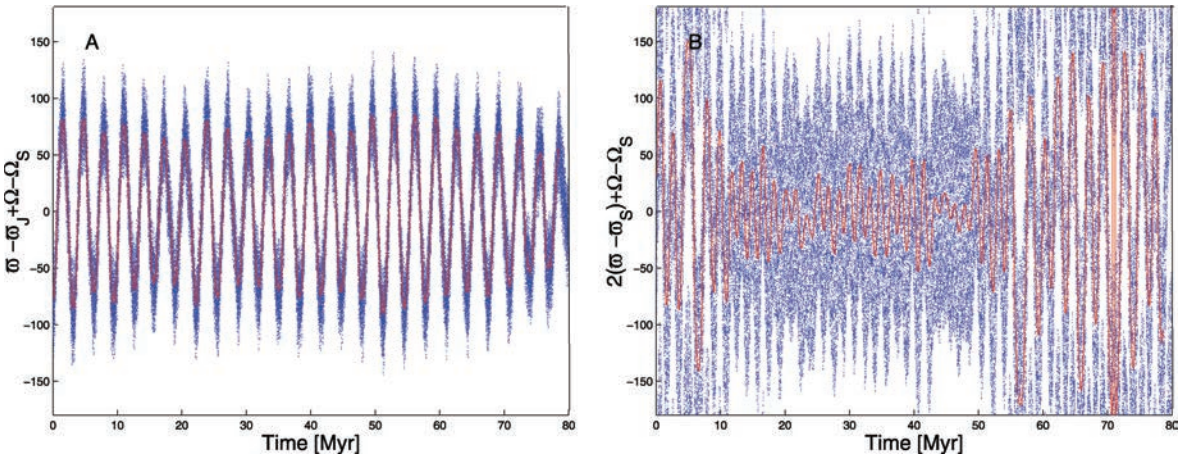

Figure 14. The resonant angles for particles trapped in (a) the $\nu_5 + \nu_{16}$ resonance and (b) the $2\nu_6 - \nu_{16}$ resonance.

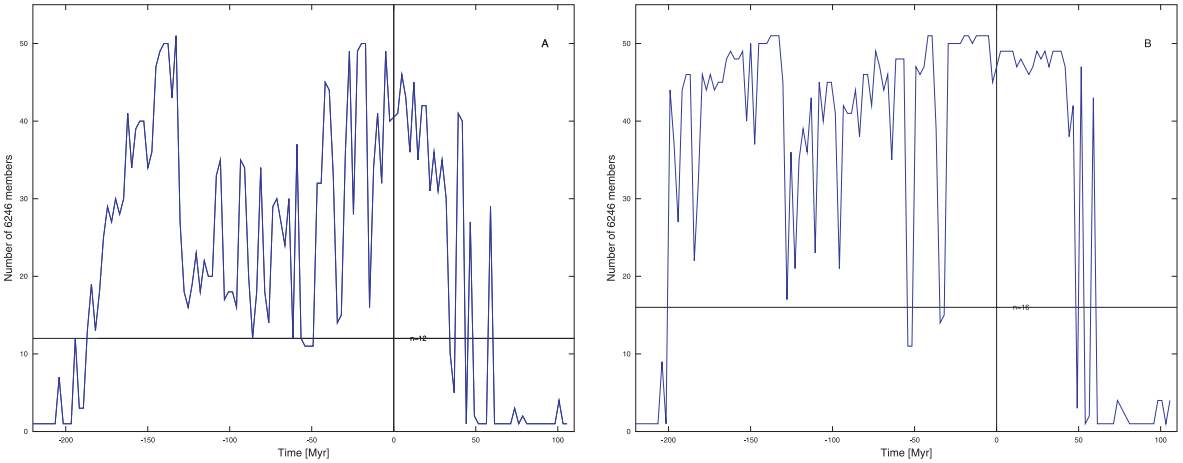

Figure 15. The number of members of the 6246 frequency clumps in the Phocaea family region as a function of time. (a) displays the data for a frequency cut-off of 0.625 arcsec yr^{-1}, while (b) shows the same for a cut-off of 0.745 arcsec yr^{-1}.

higher values of the semi-major axis, depending on their inclination. Several of the test particles are at least temporarily captured in the $\nu_5 + \nu_{16}$ secular resonance (yellow full dots), while fewer experience phases of libration in the $2\nu_6 - \nu_{16}$ resonance (red full dots). Blue circles display the member of the frequency clump, identified in the $(n, g, g + s)$ domain at a cut-off of 0.625 arcsec yr^{-1}. Notice how after 50 Myr the group essentially dispersed and was no longer identifiable as such. Since I am using maximal Yarkovsky drift, this time sets a lower limit on the dynamical stability of the (6246) clump.

I then proceeded with the analysis of the (19536) (1999 JM4) clump. As discussed in Section 6.1, this clump is characterized by its interaction with the $\nu_6 - 2\nu_{16}$ secular resonance. At the beginning of the integration there were 13 particles, the resonant argument of which was in a $\nu_6 - 2\nu_{16}$ librating state. The maximum frequency cut-off for which the clump was still distinguishable from the Phocaea family was 0.625 arcsec yr^{-1}, which was also the nominal cut-off used to determine all frequency groupings in Carruba (2009a).

Fig. 17(a) displays the number of members of the 19563 clump as a function of time, at a cut-off of 0.625 arcsec yr^{-1}. As for the case of the clump around (6246), this clump is detectable until a time of $\simeq$ 30 Myr, and has episodes of observability up to 95 Myr. This seems to suggest that the clump should be statistically significant.

Fig. 17(b) displays a $(g, g + s)$ projection of the clump clones at $t = 27$ Myr, the last time before the clump was no longer identifiable for the first time. Red full dots are asteroids in a librating $\nu_6 - 2\nu_{16}$ resonant state; the other symbols are the same as in Fig. 16. While eight objects were captured in the resonance at this time, the remaining 30 were already evolving far from the resonance separatrix. At $t = 30$ Myr the clump was no longer identifiable, and while there were episodes when the clump was still detectable at later times, after 100 Myr the clump was finally too dispersed to be identifiable. Based on these data, and considering that that the classical family around (19536) was observable for times up to 200 Myr, I believe that the frequency clump around (19536) should be considered statistically significant.

7 CONCLUSIONS

In this work I studied the dynamical evolution of asteroids in the region of the Phocaea dynamical family. This involved the following:

(i) I investigated the long-term stability of asteroids at high e ($e > 0.31$). I found that these objects are unstable on time-scales of at most 270 Myr. Among the mechanisms that can create this high-eccentricity population, the interaction of the Yarkovsky and

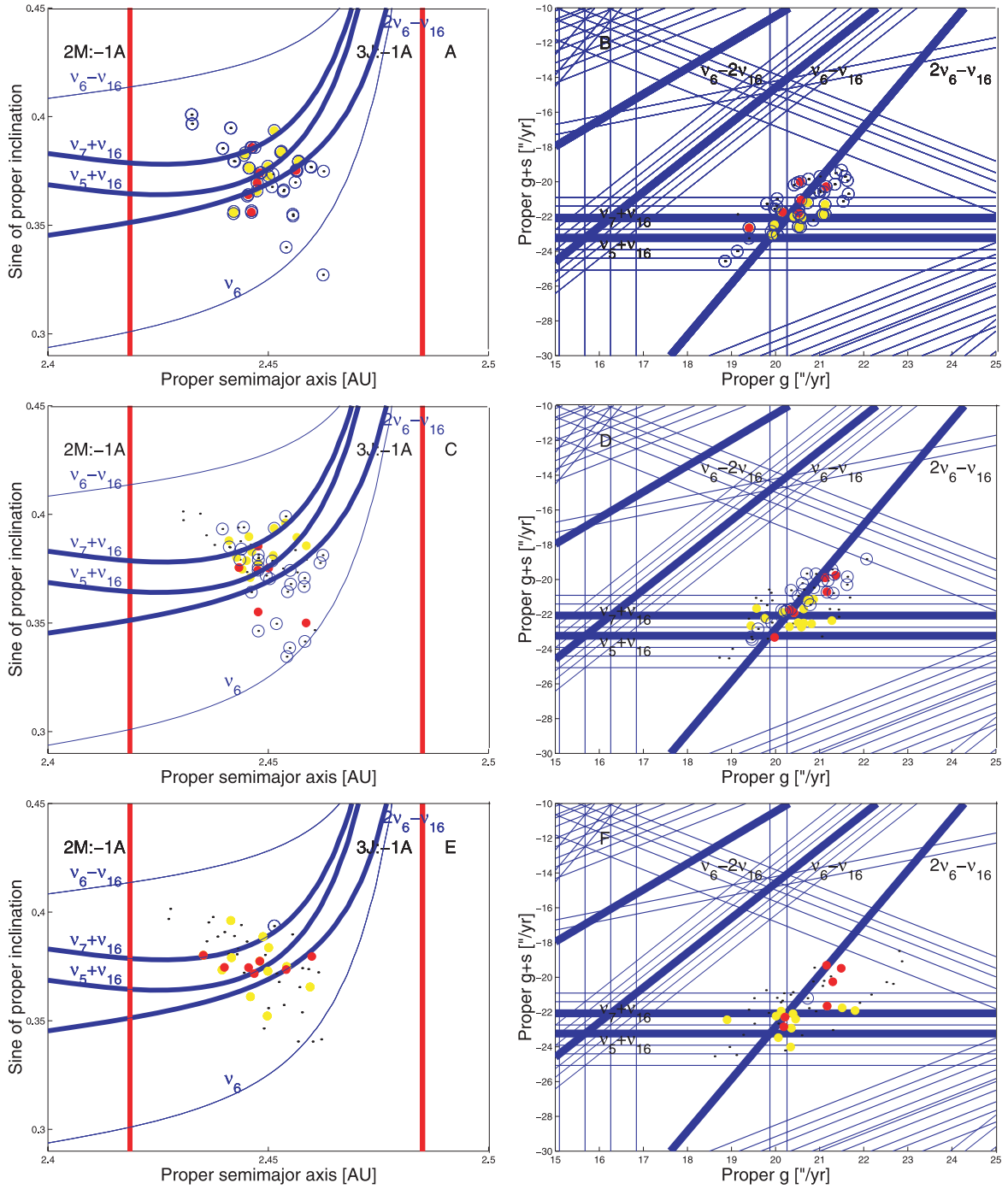

Figure 16. Projections in the $(a, \sin(i))$ and $(g, g+s)$ planes of the orbital evolution of the (6246) clumps clones at $t = 0$ Myr (panels a and b), $t = 50$ Myr (panels c and d) and $t = 100$ Myr (panels e and f).

YORP effects with the J3:–1A, J7:–2A and M2:–1A resonances are the most effective ones. The time needed for current members of the Phocaea family to replenish this population is of the order of 370 Myr. This set a lower limit on the Phocaea family age of $\simeq$640 Myr.

(ii) I studied the problem of asteroids in the proximity of the ν_6 secular resonance separatrix with analytical (Yoshikawa 1987) and numerical tools. Asteroids in a region with $-2.55 < k_6 < 2.55$ arcsec yr^{-1}, where $k_6 = b - \nu_6$ and b is given by equation (7) and roughly corresponds to the g frequency, are forced to reach values of eccentricity larger than 0.31, which is enough to allow them to experience deep close encounters with Mars. The region of $-2.55 < k_6 < 2.55$ arcsec yr^{-1} is associated with the chaotic low-inclination region found in Carruba (2009b) (see Figs 11a and b).

(iii) I investigated the dynamical evolution of the five minor clumps and families identified in Carruba (2009b) in the domain of proper elements and frequencies when the Yarkovsky effect was considered. While the two classical clumps around (17628) and (26142) quickly disperse and seem not to be statistically robust, the family around (19536) is observable for time-scales of 200 Myr for the proper element group, and 50 Myr for the proper frequency

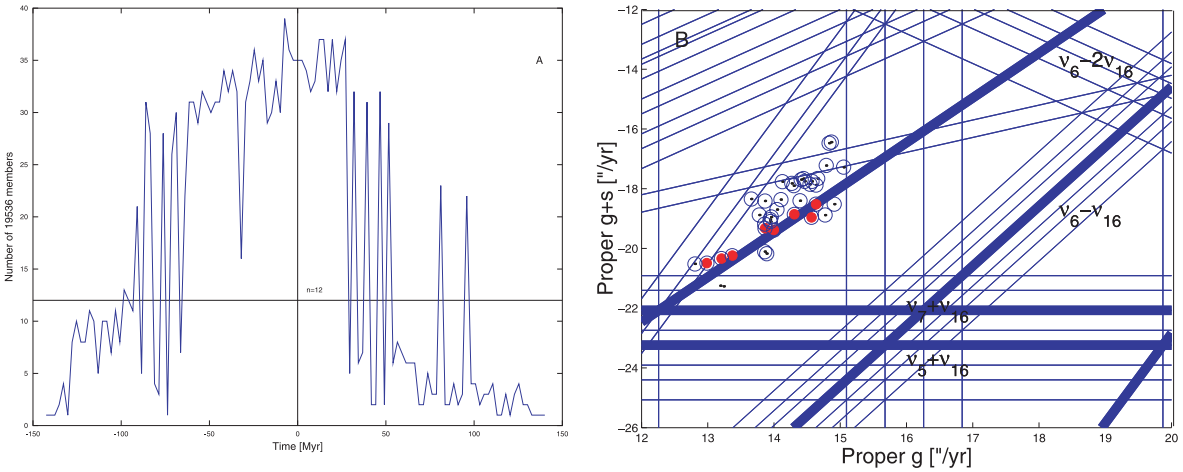

Figure 17. (a) The number of members of the 19536 frequency clump detected at a cut-off of 0.625 arcsec yr^{-1} as a function of time. (b) A $(g, g - s)$ projection of the clump clones at $t = 27$ Myr. The blue circles identify the clump members, the red full dots the asteroids in a librating $\nu_6 - 2\nu_{16}$ resonant state.

clump. I believe that this family should be considered a candidate for a collisional group. Finally, the clump around (6246) Komuro-toru, only identifiable in the frequency domain and characterized by its interaction with the $\nu_5 + \nu_{16}$ and $2\nu_6 - \nu_{16}$ secular resonances, is robust on time-scales of 50 Myr. I confirm that this group could be the first clump ever detected in the frequency domain alone that might be associated with a real collisional event.

I believe that this paper provides some answers to and further insights on the main questions raised by Carruba (2009b), i.e. the long-term stability of high-eccentricity objects, the causes of the layer of chaos near the ν_6 resonance separatrix and the statistical significance of the minor groups identified in the Phocaea family region. As often in science, other questions that were raised in these two works are still left unanswered, among them the following: Can I obtain better estimates of the Phocaea family age than those obtained in this and the previous work? How much mass was lost due to the dynamical erosion mechanisms described in this paper and how massive was the original parent body? Also, the fact that the two frequency groups around (19536) and (6246) are statistically significant does not yet prove that these two groups were created by collisions rather than by an aggregation of objects inside secular resonances.

A way to investigate this issue would be to obtain information on the taxonomy of the members of this groups. If they all share a common origin, it would be reasonable to expect that most of the members would have the same spectral type. Unfortunately, such information is not available for these objects. For SDSS-MOC4 data, as discussed in Carruba (2009b), three members of the (19536) group (all compatible with an S-type composition) are reported in the catalogue, while just one member of the (6246) group (yet another S-type compatible object) is currently listed.

In summary, at the moment we cannot rule out either hypothesis on the origin of these groups. Lists of members of the two groups are available to the observing community upon request. In any case, these and other questions on Phocaea asteroid groups remain, in my opinion, interesting subjects for future work.

ACKNOWLEDGMENTS

I am grateful to the reviewer of this article, David A. Minton, for suggestions and comments that helped improve the content of this paper. I thank the São Paulo State Science Foundation (FAPESP), which supported this work via the grant 06/50005-5, and the Brazilian National Research Council (CNPq, grants 302183/2008-6 and 473345/2009-9). I am also grateful to the Mathematics department of FEG-UNESP for the use of their facilities.

REFERENCES

Bretagnon P., 1974, A&A, 30, 141
Brož M., 1999, MSc thesis, Charles Univ., Prague
Carruba V., 2009a, MNRAS, 395, 358
Carruba V., 2009b, MNRAS, 398, 1512
Carruba V., Michtchenko T., 2007, A&A, 475, 1145
Carruba V., Michtchenko T., 2009, A&A, 493, 267
Carruba V., Burns J. A., Nicholson P. D., Gladman B., 2002, Icarus, 158, 434
Carruba V., Burns J. A., Bottke W., Nesvorný D., 2003, Icarus, 162, 308
Carruba V., Nesvorný D., Burns J. A., Cuk M., Tsiganis K., 2004, AJ, 128, 1899
Carruba V., Michtchenko T., Roig F., Ferraz-Mello S., Nesvorný D., 2005, A&A, 441, 819
Carruba V., Roig F., Michtchenko T., Ferraz-Mello S., Nesvorný D., 2007, A&A, 465, 315
Ferraz-Mello S., Klafke J. C., Michtchenko T., Nesvorný D., 1996, Celest. Mech. Dynamical Astron., 64, 93
Gladman B. J. et al., 1997, Sci, 277, 197
Gronchi G. F., Milani A., 1999, A&A, 341, 928
Guillens S. A., Vieira Martins R., Gomes R. S., 2002, AJ, 124, 2322
Knežević Z., Milani A., 2000, Celest. Mech. Dynamical Astron., 78, 17
Knežević Z., Milani A., 2003, A&A, 403, 1165
Levison H. F., Duncan M. J., 2000, AJ, 120, 2117
Milani A., Knežević Z., 1994, Icarus, 107, 219
Morbidelli A., Vokrouhlický D., 2003, Icarus, 163, 120
Murray C. D., Dermott S. F., 1999, Solar System Dynamics. Cambridge Univ. Press, Cambridge
Nesvorný D., Roig F., Gladman B., Lazzaro D., Carruba V., Mothé-Diniz T., 2008, Icarus, 183, 85
Thomas F., Morbidelli A., 1996, Celest. Mech., 64, 209
Yoshikawa M., 1987, Celest. Mech., 40, 233

This paper has been typeset from a TEX/LATEX file prepared by the author.

6

O arquipelago de ilhas de estabilidade no cinturão central de alta inclinação

Depois de termos investigado os asteroides de alta inclinação do cinturão interno, passamos a estudar a região do cinturão central. Knežević e Milani (2003) introduziram o conceito de ilha de estabilidade para descrever a região entre ressonâncias de movimento médio e seculares no cinturão interno. No cinturão central as ressonâncias seculares ν_6, ν_5, e ν_{16} e as ressonâncias de movimento médio 3J:-1A, 8J:-3A, e 5J:-2A dividem a região em oito ilhas de estabilidade, formando um verdadeiro arquipelago, onde cada ilha é populada com uma ou mais famílias de asteroides.

Em Carruba (2010) obtive um conjunto de elemento próprios sintéticos, de acordo com o método de Knežević e Milani (2003), para asteroides numerados e de múltipla oposição nesta região. Três novas famílias no espaço dos elementos próprios foram identificadas neste trabalho, incluindo a família de Tina, que, até hoje, é o único grupo de asteroides onde todos os membros estão em configuração anti-alinhada da ressonância ν_6, e que será o tópico de mais um trabalho apresentado nesta tese. Identifiquei também uma nova família no espaço das frequências próprias $(n, g, g + s)$ em volta do asteroide (4203) Brucato, que foi depois confirmada como família no espaço dos elementos próprios por Novakovic et al. (2011), usando um conjunto maior de asteroides com elementos próprios. Neste trabalho também estudei a taxonomia, as propriedades físicas e rotacionais dos grupos encontrados, e obtive uma estimativa preliminar das idades

destes grupos, usando o método das isolíneas de deslocamento em a causado pelo efeito Yarkovsky, também descrito em Nesvorný et al. (2005). Um estudo mais detalhado da evolução dinâmica destes grupos foi efetuado no trabalho seguinte.

A seguir apresentamos o artigo, que foi publicado em Monthly Notices of the Royal Astronomical Society em 2010, volume 408, pp. 580-600.

Monthly Notices
of the
ROYAL ASTRONOMICAL SOCIETY

Mon. Not. R. Astron. Soc. **408,** 580–600 (2010) doi:10.1111/j.1365-2966.2010.17146.x

The stable archipelago in the region of the Pallas and Hansa dynamical families

V. Carruba★

UNESP, Univ. Estadual Paulista, Grupo de Dinâmica Orbital e Planetologia, Guaratinguetá, SP 12516-410, Brazil

Accepted 2010 June 4. Received 2010 June 4; in original form 2010 April 6

ABSTRACT

Among highly inclined asteroids, the region of the central main belt between the 3J:–1A and 5J:–2A mean-motion resonances has long been known to host the Pallas and Hansa dynamical families. This region is characterized by the presence of the ν_6, ν_5 and ν_{16} secular resonances, which in conjunction with the 8J:–3A mean-motion resonance divide the area into eight regions, the stable islands of the archipelago. Using a set of proper elements available at the Asteroids Dynamic Site (AstDyS) at the time, Gil-Hutton identified a family around (686) Gersuind and two more minor clumps around (945) Barcelona and (148) Gallia in the space of synthetic proper elements. In this work I compute a new set of synthetic proper elements for 2310 numbered and 2142 multi-opposition objects in this region. The use of the frequency-modified Fourier transform method allowed me to obtain non-negative estimates of the proper frequency of argument of pericentre precession g for members of the Hansa families characterized by values of $e_{\rm forced}$ larger than $e_{\rm free}$, and to solve the problem of the non-linear dependence of g versus n observed by Carruba & Michtchenko.

My analysis shows that the two minor clumps of Gil-Hutton should now be considered dynamical families. Also, a new family in the domains of both proper elements (a, e, $\sin i$) and frequencies (n, g, $g + s$) around (1222) Tina is discovered in this work, as well as a new frequency family around (4203) Brucato. Nine minor clumps, one of which is visible in both domains, are also observed.

The taxonomical analysis of family members suggests that the Pallas family is compatible with a B-type composition (but two members are classified as C interlopers), while the Hansa family is possibly an S-type one. Sloan Digital Sky Survey Moving Object Catalog (SDSS-MOC3) data suggest that the Barcelona family might be an Sq group, and the Gersuind, Gallia and Tina ones should belong to the S complex. Geometric albedo data seem to confirm the possibility that the Barcelona and Gersuind families belong to the S complex. Data on cumulative size distributions, collisions time-scales, rotation rates and dynamics in this region are also revised in this work.

Key words: celestial mechanics – minor planets, asteroids: general.

1 INTRODUCTION

Among highly inclined asteroids (asteroids with $\sin i > 0.3$, for which the analytical theory used to obtain proper elements is not very accurate: Milani & Knežević 1994), the asteroids in the region of the Pallas and Hansa families are characterized by very interesting dynamics. This region is characterized by the presence of the ν_6, ν_5 and ν_{16} secular resonances, which in conjunction with the 8J:–3A mean-motion resonance divide the area into eight regions, the stable islands of the archipelago.

In these islands, the Pallas family was first suggested by Williams (1992) and Lemâitre & Morbidelli (1994), while the largest family in the region, Hansa, was originally proposed by Hergenrother, Larson & Spahr (1996). Gil-Hutton (2006) defines the region of the Pallas and Hansa families (zone B in his paper) as the region between the 3J:–1A and 5J:–2A mean-motion resonances (which roughly corresponds to the region between 2.501 and 2.825 au) and with $\sin i > 0.3$. As discussed in Knežević & Milani (2000), although it is not possible to obtain accurate analytical proper elements for this region, even some of the synthetic ones, as is the case for some low-eccentricity members of the Hansa family (Carruba & Michtchenko 2009), are affected by errors: objects with free eccentricity smaller than the forced one present difficulties in obtaining accurate values

★E-mail: vcarruba@feg.unesp.br

of the pericentre precession frequency g. The presence of linear resonances in the region, such as the ν_5, ν_6, ν_{16} and other non-linear resonances, also introduces difficulties in obtaining accurate values of proper elements and frequencies.

However, having an accurate data set of proper elements is essential to obtain dynamical families and clumps, and, in general, to investigate the local dynamics. In this paper I therefore first tried to obtain synthetic proper elements, not only for the numbered asteroids in the region, for which such elements are already listed within the Asteroids Dynamic Site (AstDyS)[1], but also for multi-opposition objects. Using the frequency-modified Fourier transform method of Šidlichovský & Nesvorný (1997) and the method described in Knežević & Milani (2000) for obtaining synthetic proper elements and frequencies, I also tried to obtain better estimates of proper g for those Hansa asteroids that appeared to have retrograde values in the AstDyS data set (Carruba & Michtchenko 2009). Overall, I obtained synthetic proper elements for 4452 asteroids in the region of the Hansa and Pallas families.

As a next step I identified families in the space of proper elements and proper frequencies using the Classical and Frequency Hierarchical Clustering Systems (CHCM and FHCM, respectively: Zappalà et al. 1995; Carruba & Michtchenko 2007, 2009). Family subgroups and asteroid-pair candidates (Pravec & Vokrouhlický 2009) were also detected in the region, and the data on taxonomy and Sloan Digital Sky Survey Moving Object Catalog (SDSS-MOC3) data for family members were reviewed. Analysis of the data on geometric albedo, absolute magnitude, cumulative distributions and collision time-scales, Yarkovsky isolines and C-target functions, light curves and dynamics in the region was also carried out, following the approach of Carruba (2009).

This work is set out as follows: the first section introduces the problems of dynamical families in the highly inclined central main belt. In the second section I discuss how the set of proper elements for asteroids in the region was obtained, and I compare my results with those available in the literature (namely at the AstDyS site). In the third section I obtain dynamical families and clumps in the domains of proper elements and proper frequencies, and candidates for possible broken asteroid pairs, while in the fourth section I discuss the taxonomy of asteroids in this area. In the fifth section I revise the current knowledge on asteroid albedos and absolute magnitudes, while the sixth section deals with cumulative distributions of family members. In the seventh section I obtain Yarkovsky isolines and C-target functions for the observed families. The eighth section analyses the data on rotation for the bodies for which such information is available, and the ninth section discusses the dynamics present in this region, with an emphasis on non-linear secular resonances and their effects. In the final section I present my conclusions.

2 SYNTHETIC PROPER ELEMENTS FOR ASTEROIDS IN THE PALLAS REGION

If we want to study the dynamical evolution of asteroid groups in the Pallas region, the first step is to determine their dynamical family in the space of proper elements (Bendjoya & Zappalà 2002) and proper frequencies (Carruba & Michtchenko 2007, 2009). For this purpose it is necessary to have a catalogue of asteroids for which proper elements were determined either analytically (Milani & Knežević 1994) or numerically (also called synthetic elements: Knežević & Milani 2003). For highly inclined asteroids ($\sin i > 0.3$) the analytical theory is not accurate enough to provide reliable proper elements, so one has to rely on the synthetic ones. The AstDyS site offers, as of 2009 November 25, a list of 214 414 asteroids for which proper elements and frequencies are available, as well as the standard deviation of the proper elements and frequencies.[2] Of these objects, 2336 have orbits in the region of the Pallas family as defined in Gil-Hutton (2006). Using the catalogue of proper elements available at the time, Gil-Hutton (2006) obtained families and clumps in the space of proper elements for asteroids in the region of the Pallas family, among others.

A problem with this approach is that several of the asteroids in the region reported by the AstDyS site have large errors in the proper frequencies, and many of them, especially in the Hansa family region, are characterized by negative values of the pericentre precession frequency g. This is caused, as discussed in Knežević & Milani (2003), by the fact that high-inclination and low-eccentricity objects may have their equinoctial elements ($e\cos\varpi$, $e\sin\varpi$) passing through zero, which makes a correct determination of the proper frequency g harder. This problem is of particular concern for asteroids with free eccentricity smaller than the forced one, since the motion of ϖ in (h, k) space, which describes a circle of radius $e_{\rm free}$ (which for synthetic proper elements coincides with $e_{\rm proper}$) centred at the point of a vector of magnitude $e_{\rm forced}$, may cover only a limited range of values rather than 2π, making it more difficult to obtain reliable values of the proper frequency g (Murray & Dermott 1999).

Fig. 1 displays plots of amplitude (in arbitrary units) versus frequency for the spectra of the Fourier transforms of equinoctial elements (h, k) of (a) (36) Atalante and (b) (480) Hansa. The first asteroid is characterized by a relatively large value of proper eccentricity (0.2747), but the second has a rather small proper eccentricity (0.0091). While the frequency spectra of the first asteroid are dominated by the proper frequency g, the values of planetary frequencies are larger than the asteroid proper one for the second body. This makes obtaining reliable values of synthetic proper frequencies g for such a class of bodies a difficult task, as discussed by Knežević & Milani (2000). More information on the values of proper frequencies in the region will be given in Section 2.1.

Also, strong secular resonances such as the $\nu_5 = g - g_5$, $\nu_6 = g - g_6$, $\nu_7 = g - g_7$ or resonance of arguments $2g - 2s$ for low-eccentricity objects may affect the current determination of proper values of g for asteroids in the region (but with relatively minor errors in the proper elements (a, e, $\sin i$). Knežević & Milani (2003) distinguish between 'stable' proper elements with relatively small errors (see Section 2.1 for a definition of 'small errors'), unstable proper elements and pathological cases, characterized by extremely large uncertainties in proper elements. Understanding the stability of proper elements in the complicated region of the Pallas family is of great importance if one wants to obtain reliable dynamical families.

To investigate this problem in this work, I decided to obtain my own set of proper elements for numbered objects, following the

[1] http://hamilton.dm.unipi.it/astdys

[2] Proper elements and frequencies were obtained with a 10-Myr numerical integration with a Burlisch–Stoer integrator. The elements were then computed over a 2-Myr period, and a running-box method was used to produce 10 data points. The values of proper elements and frequencies were the means of the data points, while as an approximation of the error the standard deviation was used. See Knežević & Milani (2003) for further details on the subject.

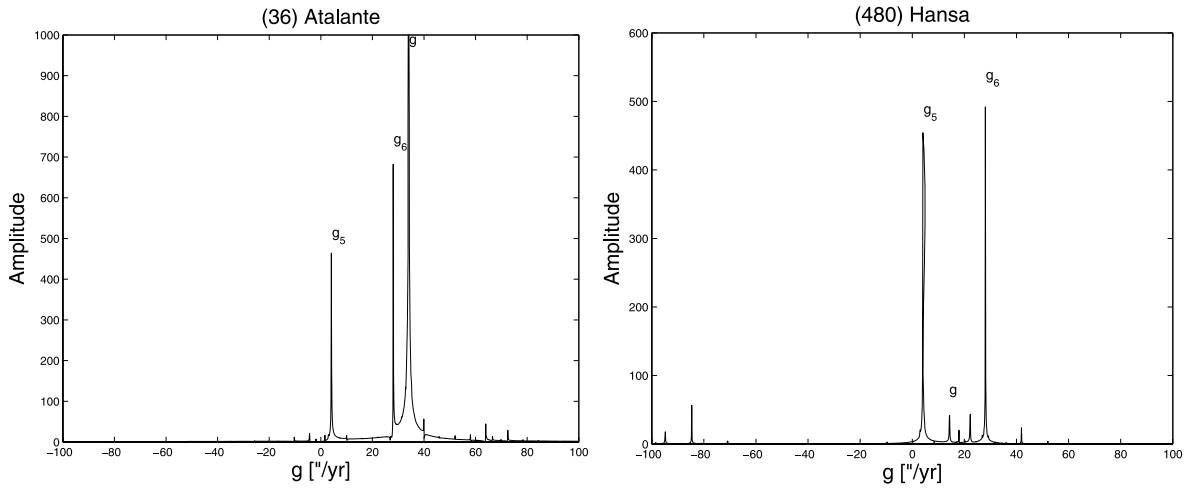

Figure 1. Amplitude (in arbitrary units) versus frequency for the spectra of the Fourier transform of equinoctial elements (h, k) of (a) (36) Atalante and (b) (480) Hansa.

approach of Knežević & Milani (2003) (proper frequencies were obtained using the frequency-modified Fourier transform (FMFT) of Šidlichovský & Nesvorný (1997) on the osculating equinoctial elements of the integrated asteroids), and to compare my results with those obtained by the two authors. I first downloaded the catalogue of osculating elements for numbered and multi-opposition asteroids and the catalogue of synthetic proper elements and frequencies from the AstDyS site,[3] accessed on 2009 November 25. At that time there were 140 235 asteroids in the catalogue of multi-opposition objects.

I integrated the 2336 numbered objects in the Pallas region and 4320 objects in the multi-opposition catalogue (asteroids with semi-major axis between the 3J:–1A and 5J:–2A mean-motion resonances and with an osculating inclination larger than 15°) with a Burlisch–Stoer integrator from the SWIFT package (Levison & Duncan 1994) modified by Brož (1999) so as to include on-line digital filtering to remove all frequencies with period less than 600 yr, and I integrated the objects over 10 Myr. Synthetic proper elements were obtained with the procedure described in Knežević & Milani (2003), except for the proper frequencies, which were derived with the FMFT using the following procedure: I eliminated from the spectra of the Fourier transform of the equinoctial elements all planetary frequencies and then assigned as proper frequency the largest value in the spectra that was still observable, rather than fitting the time series of $\varpi_{\rm f}$ and $\Omega_{\rm f}$ of the oscillations in the (k, h) and (p, q) plane.

As regards numbered objects, I first eliminated from my data set the 21 asteroids that did not survive the length of the integration. Five more objects that interacted with powerful mean-motion resonances and that had large errors (see next subsection) in proper elements as a result were also excluded from the data set. In order to calibrate the procedure for finding synthetic proper elements, we first need to compare the results of the numerical simulation for numbered objects with the proper elements in the AstDyS site. For this purpose, we need to revise the properties of the AstDyS proper elements in the region, which I will do in the next subsection.

2.1 Synthetic proper elements in the AstDyS catalogue

I start by analysing the behaviour of proper elements in the AstDyS catalogue. As discussed in Milani & Knežević (1994), asteroids with large standard deviation in the proper semi-major axis σ_a are usually associated with two- or three-body mean-motion resonances. The large standard deviation in a is caused by the averaging needed to produce the proper elements for asteroids involved in libration inside a resonance.

Fig. 2 displays (a) (a, e) and (b) (a, $\sin i$) projections of the AstDyS proper elements for the 2310 objects in the area (the 2336 objects minus the 21 that did not survive the 10-Myr integration and the five objects with large errors in their proper elements). Small full dots display asteroids with σ_a between 0.0003 au (the limit given by Knežević & Milani (2003) for 'stable' synthetic proper elements) and 0.01 au (the limit for pathological cases), while large full dots show asteroids with σ_a larger than 0.01 au. The magenta line displays the chaotic layer near 3J:–1A studied by Guillens, Vieira Martins & Gomes (2002), as defined in Morbidelli & Vokrouhlický (2003). Vertical red lines display the location of some of the most important two- and three-body mean-motion resonances in the region, while blue lines show the location of the main linear secular resonances, computed using the frek.f code of Milani & Knežević (1994) to compute the proper frequencies g and s for the grid of (a, e) and (a, $\sin i$) values shown in Fig. 2 and the values of angles and eccentricity for (480) Hansa. Non-linear secular resonances will be discussed in detail in Section 9 and later on in this section. The inclined blue and red lines shown in the (a, e) plane display the area where the pericentre of the asteroid is equal to the apocentre and pericentre of Mars, respectively.

As can be seen in the figure, one can easily identify the groups in the (a, $\sin i$) plane associated with the Hansa and Pallas families. Families in the (a, $\sin i$) plane appear to be confined in inclination because, as discussed in Michtchenko et al. (2010), to change the plane of its orbits an asteroid must gain several orders of kinetic energy more than the quantity necessary to produce a similar change in proper semi-major axis or eccentricity. Additionally, the Yarkovsky effect predominantly acts on the asteroid semi-major axis. Asteroids with large σ_a are associated with prominent mean-motion resonances such as the 8J:–3A, 1J:–3S–1A and 1J:2S:–2A. Object at high eccentricities with σ_a larger than 0.001 are likely to be associated with asteroids on planet-crossing orbits.

Due to the presence of the strong linear secular resonances ν_6, ν_5 and ν_{16}, in conjunction with the effect of the powerful 8J:–3A mean-motion resonance, eight regions, the stable islands of the archipelago, can be distinguished, each one identified by the lowest

[3] http://hamilton.dm.unipi.it/cgi-bin/astdys/astibo

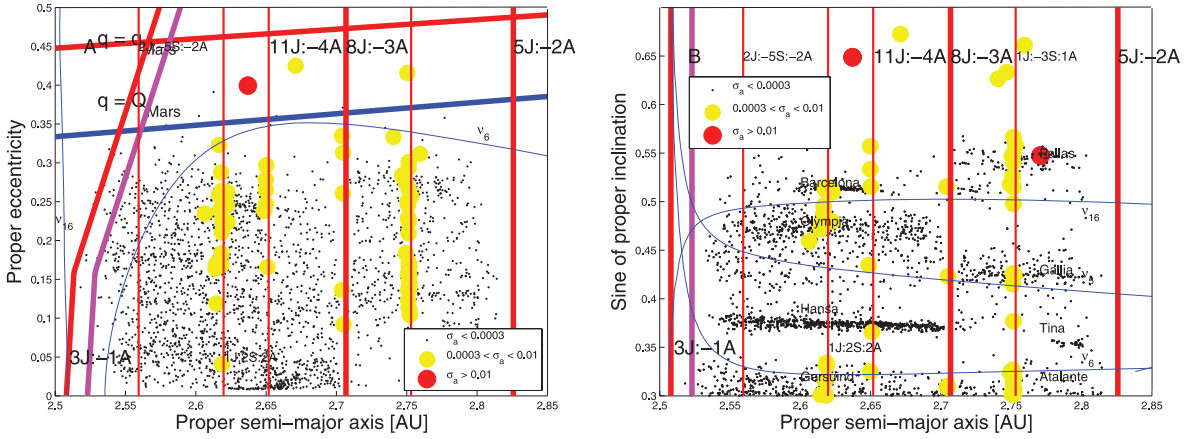

Figure 2. (a) An (a, e) projection of AstDyS asteroids in the region of the Pallas family. Small full dots display asteroids with standard deviation in σ_a between 0.0003 and 0.01, while large full dots show asteroids with σ_a larger than 0.01. (b) An (a, sin i) projection of the same asteroids.

numbered object in the area. From top to bottom in inclination they are the Barcelona region (above the ν_{16} secular resonance in inclination and between the 3J:–1A and 8J:–3A mean-motion resonances in semi-major axis), the Pallas region (above the ν_{16} resonance in inclination and on the right side of the 8J:–3A mean-motion resonance in semi-major axis), the Olympia region (between the ν_{16} and ν_5 resonances and on the left side of 8J:–3A), the Gallia region (in the same interval of inclination values as the Olympia region, but on the right side of the 8J:–3A resonance), the Hansa region (between the ν_5 and ν_6 resonances in inclination, and on the left side of the 8J:–3A mean-motion resonance in semi-major axis), the Tina region (the same as the Hansa region in inclination, but on the right side of the 8J:–3A mean-motion resonance in a) and the Gersuind and Atalante regions, below the ν_6 resonances and on the right and left sides of the 8J:–3A mean-motion resonance in a, respectively. All regions are marked in Fig. 2(b) and will be discussed in more detail in Section 3.

In Fig. 3 I display (e, sin i) projections of asteroids with values of the errors in (a) e and (b) i for 'stable' (black dots), 'unstable' (small full dots) and 'pathological' (large full dots) proper elements. As in Fig. 2, blue lines display the location of the main secular resonances in the region. As can be seen in the figure, errors in eccentricity and inclination are larger for asteroids at high inclination, with a few objects with large errors at low eccentricities that will be discussed in Section 2.2.

More important are the errors in proper frequencies. Fig. 4 displays (a) (a, g) and (b) (a, s) projections of AstDyS asteroids in the region of the Pallas family. Small full dots display asteroids with standard deviations of σ_g and σ_s between 1 and 10, while large full dots show asteroids with σ_g and σ_s larger than 10. Here I decided to plot g and s as functions of a rather than n to allow a more easy comparison of these figures with Fig. 2. As can be seen in the figure, while errors in s are uniformly spread among the observed asteroids, the errors in g are large and confined to negative or small values of g. For the Hansa family, as discussed in Carruba & Michtchenko (2009), negative values of g are related to objects with small eccentricities ($e < 0.0179$) and to the problem of determining correct proper elements for asteroids with equinoctial elements (k, h) passing through zero. The reliability of the negative g values from the AstDyS site for this region will be discussed in more detail in the next subsection.

Finally, I checked the total number of asteroids with completely 'stable' proper elements, i.e. with proper elements with small (as defined in this section) errors in a, e, sin i, n, g and s, and found a total

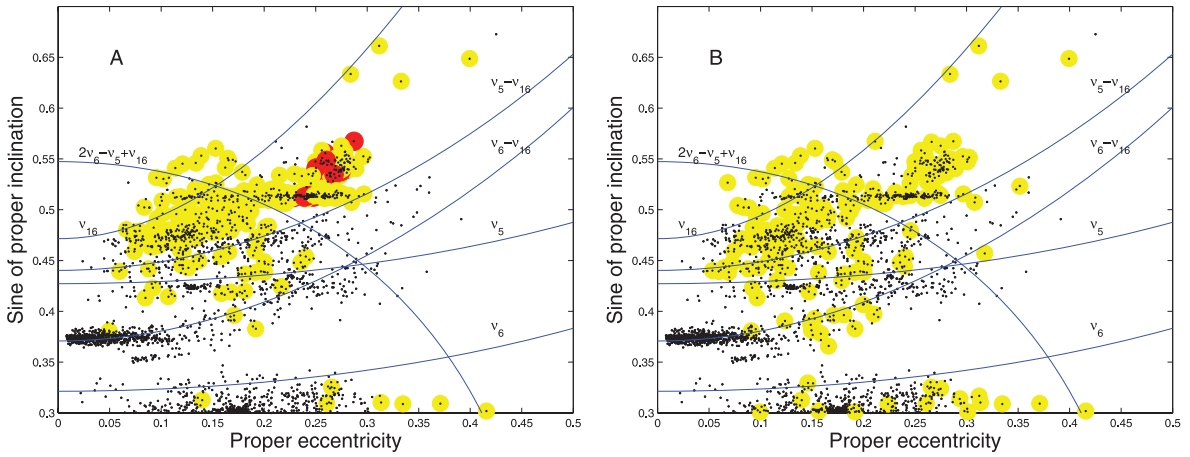

Figure 3. (a) An (e, sin i) projection of AstDyS asteroids in the region of the Pallas family. Small full dots display asteroids with standard deviation in σ_e between 0.003 and 0.1, while large full dots show asteroids with σ_e larger than 0.1. (b) An (e, sin i) projection of the same asteroids, but this time small full dots display asteroids with standard deviation in σ_i between 0.001 and 0.03, while large full dots show asteroids with σ_i larger than 0.03.

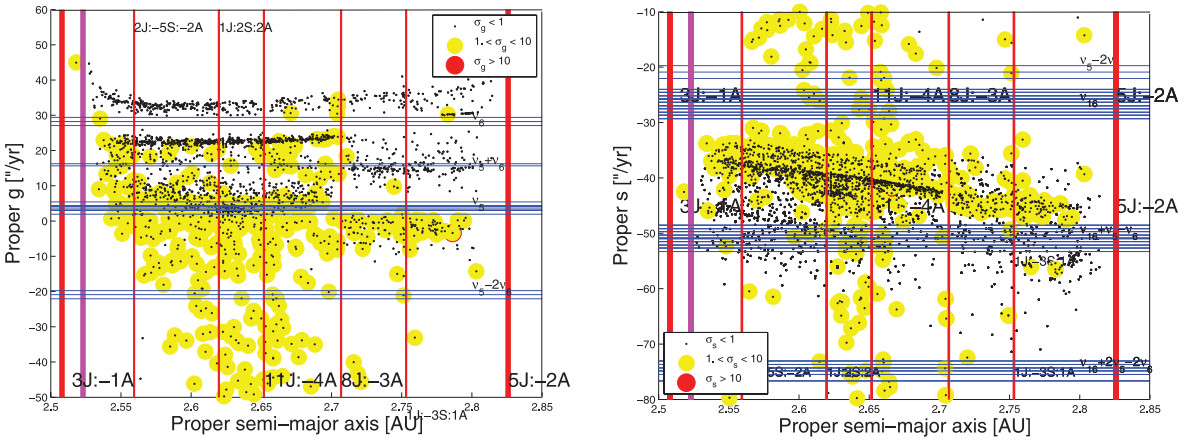

Figure 4. (a) An (a, g) projection of AstDyS asteroids in the region of the Pallas family. Small full dots display asteroids with standard deviation in σ_g between 1 and 10, while large full dots show asteroids with σ_g larger than 10. (b) An (a, s) projection of the same asteroids.

of 1475 objects. Further analysis of this number will be performed in the next subsection.

2.2 Numerically obtained synthetic proper elements

Once I had obtained my own set of proper elements for the 2310 numbered asteroids in the region, I then compared my results with those of the AstDyS site. I used the method described in Knežević & Milani (2000) applied to the results of my numerical simulation described in Section 2 for the 2310 objects that survived the simulation and have less than 'pathological' values of errors in proper elements. Planetary frequencies were discarded in the Fourier spectra of the equinoctial elements in order to obtain the values of proper g and s. Using the errors in proper $a, \sin i, n, g$ and s given at the AstDyS site, I verified for which objects the values of proper elements were outside the limits $\mathrm{el} - \sigma_{\mathrm{el}}$, $\mathrm{el} + \sigma_{\mathrm{el}}$, where 'el' is one of the five elements in the catalogue. According to this criterion, I found no discrepancy between the values of proper $a, e, \sin i, n$ and s from the AstDyS site and those obtained with my simulations. 26 objects (1.12 per cent of the total) have discrepancies in the values of proper eccentricities. All of these objects are objects either with very low values of proper eccentricity or strongly perturbed by secular resonances, and since, as discussed by Knežević & Milani (2000), these cases have large errors in proper eccentricities for reasons discussed in Section 2, I believe that the discrepancies are understandable.

More important are the discrepancies in the values of proper g, especially for the members of the Hansa family with $e_{\mathrm{proper}} < 0.0179$ (Carruba & Michtchenko 2009). For these objects, the ϖ angle in the (h, k) plane does not describe a full circle, and this yields negative values of the precession frequency g when the method of Knežević & Milani (2000) is applied, as described by the authors. 368 asteroids (15.93 per cent of the total, including the 26 asteroids with discrepancies in the values of proper eccentricities) have discrepancies between the AstDyS values of g and mine. Fig. 5 displays an (e, g) projection of (a) AstDyS asteroids and (b) my results in the region of the Pallas and Hansa families. As can be seen in the figure, the tail of objects with very retrograde values of proper g present in the Hansa family in the AstDyS catalogue is now removed in my own set of proper elements.

I have thus finally verified how many of the 1475 objects that had 'stable values' of proper elements in the AstDyS site were stable in my run and all of them were also found to be stable according to my simulations, stating a good agreement between the two methods.

Based on this result, I believe that it seems safe to use proper elements obtained with the results of numerical simulations, at least

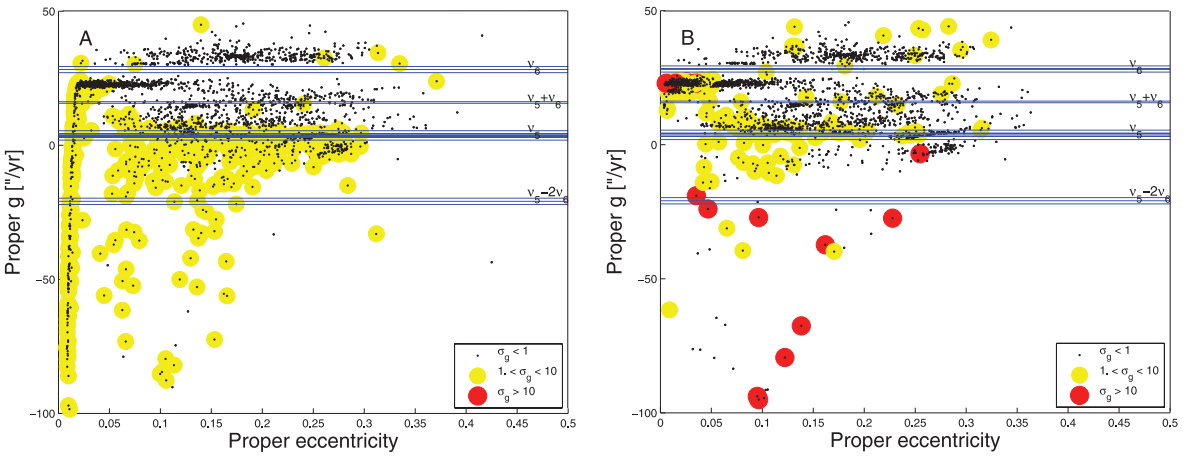

Figure 5. (a) An (e, g) projection of AstDyS asteroids in the region of the Pallas and Hansa families. Small full dots display asteroids with standard deviation in σ_g between 1 and 5, while large full dots show asteroids with σ_g larger than 5. (b) An (e, g) projection of the results of my simulation.

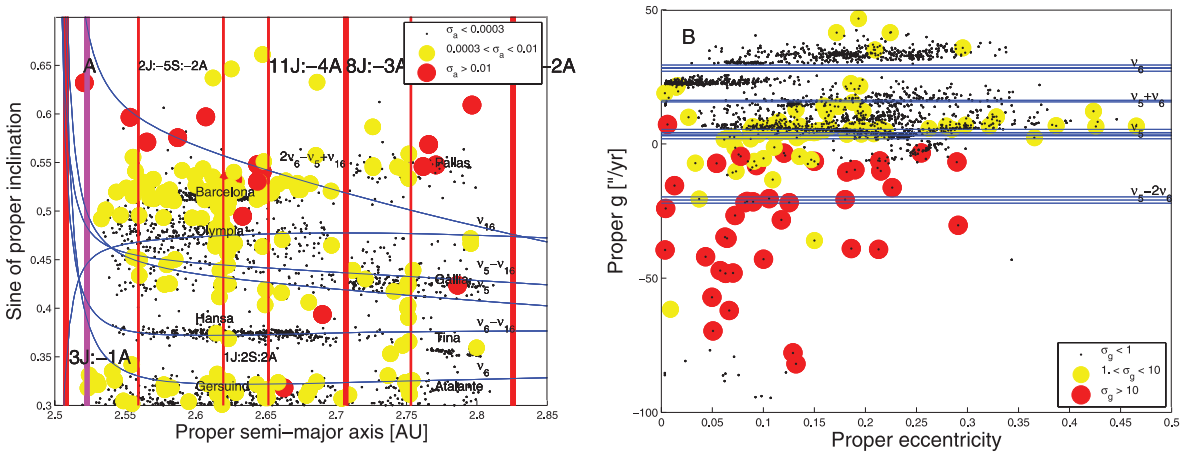

Figure 6. (a) (a, sin i) and (b) (e, g) projections of the synthetic proper elements and frequencies obtained for 2142 multi-opposition asteroids in the region of the Pallas and Hansa families.

with regard to proper semi-major axis, inclination and frequency of precession of the node. Caution should be used when dealing with proper eccentricity and, in greater part, the frequency of pericentre precession. This has a particular importance regarding families obtained in the space of proper frequencies. The problems associated with the inevitable uncertainties in the values of g when family determination is concerned will be discussed in Section 3.

Finally, now that the procedure for obtaining proper elements is calibrated, I have used this method to obtain proper elements for 4320 multi-opposition objects in the region. At the end of the 10-Myr simulation, 4173 objects survived the simulation and had less than 'pathological' values of errors in proper elements. Of these, 2142 objects had proper elements that are in the region of the Pallas and Hansa families, i.e. between the 3J:–1A and 5J:–2A mean-motion resonances and with $\sin i > 0.3$.

Fig. 6 shows (a) (a, sin i) and (b) (e, g) projections of the synthetic proper elements and frequencies obtained for 2142 multi-opposition asteroids in the region of the Pallas and Hansa families. As can be seen in the figure, the distribution of proper elements is quite similar to that of the numbered objects in the region (see Fig. 2b and Fig. 5b), thus confirming the validity of the approach used to obtain proper elements for multi-opposition objects.

3 DYNAMICAL FAMILIES AND CLUMPS IN THE PALLAS AND HANSA REGION

Now that I have obtained a reliable set of proper elements for both numbered and multi-opposition asteroids in the region of the Pallas and Hansa families, the next logical step is to identify dynamical families and clumps in the region.

In identifying asteroid families in the space of proper elements, two parameters are fundamental: the cut-off distance at which the family members are defined, d_0, and the minimum number of objects $N_{\rm min}$ for a cluster to be considered significant. Beaugé & Roig (2001) define a nominal distance cut-off as the average minimum distance between all neighbouring asteroids in the same region of the asteroid belt. The value of $N_{\rm min}$ is defined by Zappalà et al. (1995) as

$$N_{\rm min} = N_0 + 2\sqrt{N_0}, \quad (1)$$

where N_0 is the average number of orbits within a sphere of radius d_0 at every point of the proper-element space. A cluster with a number of objects larger than this critical value is called a clump, while a family is a cluster with a number of members larger than $2.5N_{\rm min}$. As I shall discuss in more detail in Section 9, the region of the Pallas and Hansa families is delimited by the 3J:–1A and 5J:–2A mean-motion resonances in proper a and by the ν_6 secular resonance at low inclination. The nominal distance velocity cut-off as defined in Beaugé & Roig (2001) is 139.33 m s^{-1} for all 2310 numbered objects in the region and 116.92 m s^{-1} for all 4452 numbered and multi-opposition asteroids in the area. Fig. 7 displays the average number N_0, $N_{\rm min}$ and the maximum number max (N_i) of asteroids as a function of the velocity cut-off, for (a) numbered and (b) all asteroids in the region. The value of $N_{\rm min}$ corresponding to $d_0 = 139.33$ m s^{-1} is 8, while the value of $N_{\rm min}$ corresponding to $d_0 = 116.92$ m s^{-1} is 11. As can be seen in Fig. 7, the fact that max (N_i) is much larger than $N_{\rm min}$ may be a hint that background objects are more numerous than family ones, in contrast to what happens in the Phocaea family region (Carruba 2009). Note that in the larger sample that includes multi-opposition objects, while the max (N_i) of asteroids as a function of the velocity cut-off is significantly larger than the case with just numbered asteroids, the values of N_0 and $N_{\rm min}$ only increase slightly. This is also observed in the domain of proper frequencies, as discussed later in this section.

Regarding the domain of proper frequencies, following the approach of Carruba & Michtchenko (2007) I determined the families with a metric of the form

$$f = \sqrt{h_1 \left(\frac{\Delta n}{h_0}\right)^2 + h_2(\Delta g)^2 + h_3[\Delta(g+s)]^2}, \quad (2)$$

where $h_1 = h_2 = h_3 = 1$. I determined the nominal frequency cut-off, defined as the average minimum distance between all neighbouring asteroids in the (n, g, $g + s$) domain, and found a value of $f_0 = 0.6273$ arcsec yr^{-1} for numbered objects and $f_0 = 0.5145$ arcsec yr^{-1} for all asteroids in the region. Fig. 7 also displays the average number N_0, $N_{\rm min}$ and the maximum number max(N_i) of asteroids as a function of the frequency cut-off defined by equation (2) for (c) numbered and (d) all objects in the region. The value of $N_{\rm min}$ corresponding to $f_0 = 0.6273$ arcsec yr^{-1} is 15, while the value corresponding to $f_0 = 0.5145$ arcsec yr^{-1} is 17. As observed for the values of $N_{\rm min}$ and max N_i obtained in the proper-element domain, in the domain of frequencies I still observe a much larger value of max N_i with respect to $N_{\rm min}$. Again, this may suggest that the local background of the Pallas and Hansa families is indeed

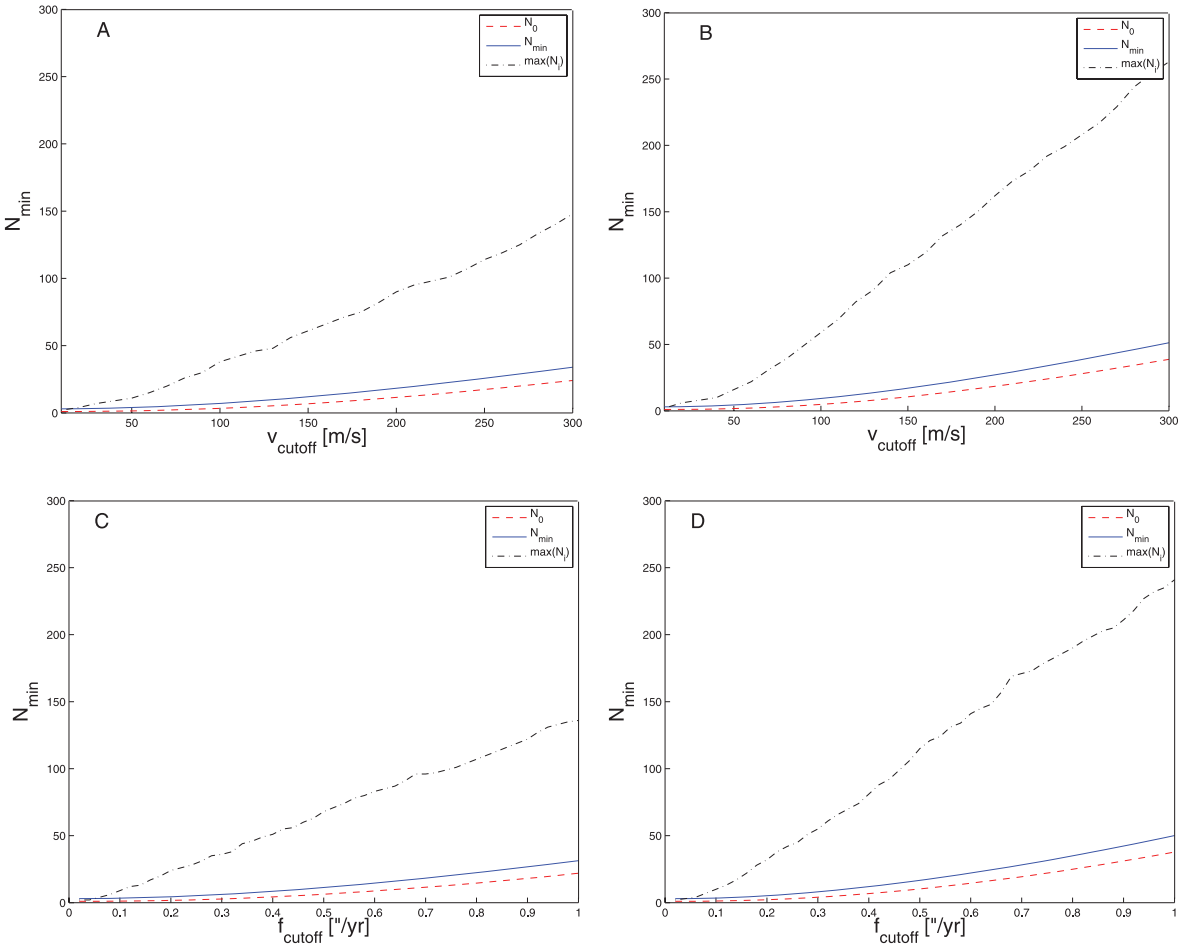

Figure 7. The average number $N_0, N_{\rm min}$ and the maximum number max(N_i) of asteroids as a function of the velocity cut-off for (a) numbered and (b) all asteroids in the region of the Pallas and Hansa families. (c) and (d) display the same numbers as a function of the frequency cut-off.

dominated by background objects, rather than by family ones, in contrast to the case of the Phocaea family (Carruba 2009).

The next logical step was to obtain dynamical families and clumps in the eight regions in the (a, sin i) plane defined in Section 2.1. Here I followed the same procedure used in Carruba (2009) to obtain families and clumps in spaces of both proper elements and proper frequencies for the region of the Phocaea family. Fig. 8 displays the procedure used for the Gallia family region; analogous results for the other seven regions will not be shown for the sake of brevity, but are available upon request to the author.

The Gallia clump of Gil-Hutton (2006) dominates the Gallia area, so I started by obtaining the dynamical family in the domain of proper elements (a, e, sin i) associated with this asteroid. Fig. 8(a) displays the number and differential number of the classical Gallia family as a function of the cut-off. For a cut-off of 224 m s^{-1} the family merges with the (40134) clump, while for a cut-off of 277 m s^{-1} the family joins the local background. The vertical line shows the nominal distance velocity cut-off d_0. Here I choose to work with a slightly larger value of d_0 (122 m s^{-1}) rather than the one found earlier of 116.92 m s^{-1}, in order to account for the behaviour of the highly inclined Pallas and Barcelona families, which merge with substructures (such as the (531) clump for the case of the Pallas family) for $d_0 = 121$ m s^{-1}. At this cut-off, a clump must have at least 12 members and a family 30 members.

To re-identify asteroid families I also constructed a stalactite diagram in the traditional way defined by Zappalà et al. (1990) and Brož & Vokrouhlický (2008): I started with (148) Gallia as the first central body and identified all the bodies associated with it at $d_{\rm cut-off} = 280$ m s^{-1}, a value for which no other independent cluster of asteroids was found. I then decreased the cut-off and identified the families and clumps among the asteroids not associated with (148) Gallia. Fig. 8(b) displays my results in the interval of cut-offs between 85 and 285 m s^{-1}. Full black squares are associated with families in the region, and empty black squares are associated with clumps, according to the limits displayed in Fig. 7. The (40134) clump is quite visible in the stalactite diagram and satisfies the criteria defined in Carruba (2009) for the identification of a clump: the clusters should be observable for a cut-off equal to d_0 and the 'length' of the 'stalactite' associated with the family should be at least 20 per cent of d_0, i.e. $\simeq$25 m s^{-1}.

I then repeated the same procedure using the frequency hierarchical clustering method (FHCM) in the (n, g, $g + s$) domain and Fig. 8(c) and (d) display the results in this domain. Again, the f_0 value that I used to work with was larger than the nominal one (0.605 arcsec yr^{-1} rather than 0.5145 arcsec yr^{-1}), to account for the behaviour of the Pallas and Barcelona families. At this cut-off a clump must have at least 22 members and a family 55 members. One may notice that the (40134) clump is no longer observable at a frequency cut-off equal to f_0 (but it is still detectable at larger cut-offs) and it is not therefore listed as a real dynamical group. Also, the frequency family at the 0.605 arcsec yr^{-1} cut-off connects to (71) Niobe, and should therefore called the Niobe family (for the

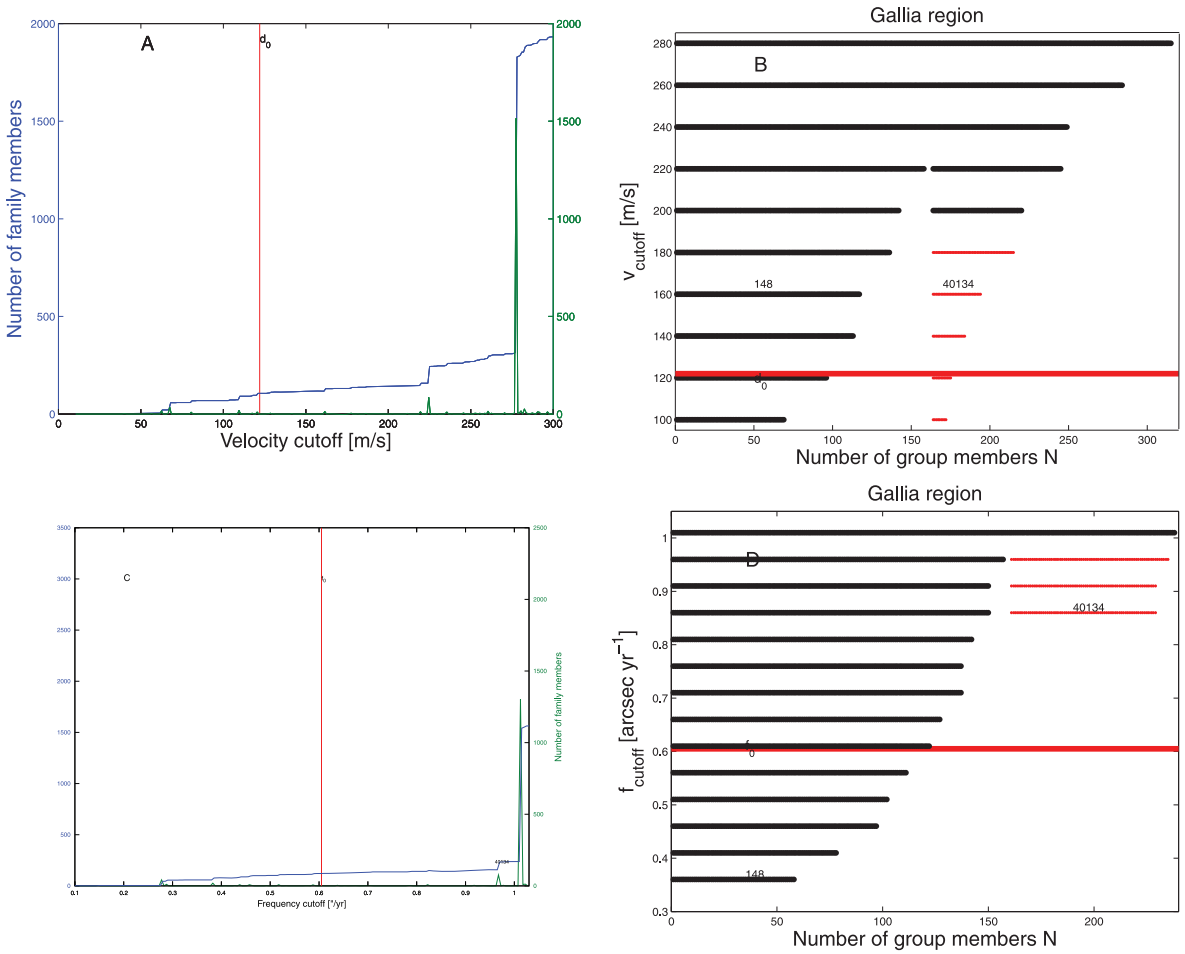

Figure 8. (a) The number and differential number of the classical Gallia family as a function of cut-off. The number at the peak of the differential number of family members is related to the (40134) clump that was englobed by the Gallia family at the higher velocity cut-off. (b) A stalactite diagram of the Gallia family region. (c) and (d) The same as (a) and (b), but for frequency groups in the (n, g, $g + s$) domain.

sake of simplicity, I will keep the Gallia name for the frequency family as well).

Table 1 summarizes the results of the search for families and clumps in the Pallas and Hansa regions. In the first column I report whether the group is a family or a clump; the letters 'c' or 'f' identify whether the family was found in the space of proper elements or proper frequencies. The second column reports the lowest numbered member of the group, while the third column shows the number of objects in the group. The fourth column displays how many objects in the group have 'stable' proper elements, i.e. with 'small errors' as defined in Section 2.1. Families with a larger proportion of objects with stable proper elements can be considered more reliable. Finally the fifth and sixth columns report the number of group members for which either spectral or SDSS-MOC3 information is available, respectively.

Here I will briefly discuss my findings in the eight regions in the (a, sin i) plane introduced in Section 2.1. In the region of Barcelona, the Barcelona clump of Gil-Hutton (2006) is now a family of 540 members in the proper-element domain, and of 550 members in the proper-frequency domain. Only five (0.9 per cent of the total) of the classical members have stable proper elements, while only three (0.5 per cent of the total) of the frequency ones have reliable proper elements, which seems to indicate that the family is in a region of highly unstable proper elements, possibly caused by its proximity to the ν_{16} secular resonance. A low-eccentricity clump around (208080) 1999 VV180 with 11 members, none which has stable proper elements, was identified in the proper-element domain but not in the proper-frequency one. The statistical significance of this clump should be further investigated with the method used for minor clumps in the Phocaea regions in Carruba (2010).

In the Olympia region I could not find any family in the space of proper elements, but five clumps were identifiable: (4203) Brucato, 12 members, none with stable proper elements; (18511) 1996 SH4, 12 members, none with stable proper elements; (36240) 1999 VN44, 11 members, one of which has stable proper elements; (70280) 1999 RA111, 14 members, all with unstable proper elements; (75938) 2000 CO80, 13 members, five of which have stable proper elements. The (4203) Brucato clump becomes a family with 249 members (14 of which have stable proper elements) and the (36240) 1999 VN44 clump is also visible in the proper-frequency domain, with 46 members. The other clumps observed in the proper-element domain are substructures of the (4203) Brucato family in the frequency domain.

The new proper elements obtained for the Hansa region permit a solution of the problem observed with the g frequency when the AstDyS data were used to obtain frequency families (Carruba & Michtchenko 2009). As discussed in Section 2, asteroids with values of forced eccentricities larger than the free one, such as is

Table 1. Families and clumps in the region of the Pallas and Hansa families.

ID	Name	N	$N_{\rm stable}$	$N_{\rm spec}$	$N_{\rm SDSS-MOC3}$
Family(c)	(945) Barcelona	540	5	1	10
Clump(c)	(208080) 1999 VV180	11	0	0	0
Family(f)	(945) Barcelona	550	3	1	12
Clump(c)	(4203) Brucato	12	0	0	0
Clump(c)	(18511) 1996 SH4	12	0	0	0
Clump(c)	(36240) 1999 VN44	11	1	0	1
Clump(c)	(70280) 1999 RA111	14	0	0	1
Clump(c)	(75938) 2000 CO80	13	5	0	1
Family(f)	(4203) Brucato	249	14	0	17
Clump(f)	(36240) 1999 VN44	46	10	0	5
Family(c)	(480) Hansa	859	201	3	0
Clump(c)	(33969) 2000 NM13	21	11	0	5
Family(f)	(480) Hansa	888	203	2	0
Clump(f)	(82426) 2001 NB20	24	1	0	1
Family(c)	(686) Gersuind	151	125	2	6
Family(f)	(686) Gersuind	174	143	2	10
Family(c)	(2) Pallas	35	33	5	3
Family(f)	(2) Pallas	79	71	6	5
Family(c)	(148) Gallia	106	100	1	5
Family(f)	(148) Gallia	121	106	2	6
Clump(c)	(40134) 1998 QO53	16	11	0	1
Family(c)	(1222) Tina	72	8	1	5
Family(f)	(1222) Tina	86	10	1	6

the case for (480) Hansa, may show retrograde values of proper frequency g when the Knežević & Milani (2000) approach to synthetic proper elements is used. The new synthetic proper elements used here allow identification of the Hansa family in the frequency domain (n, g, $g + s$) without the problems observed in Carruba & Michtchenko (2009).[4] The Hansa family in the proper-element domain had 859 members, 658 of which have stable proper elements. The new Hansa family in the frequency domain had 888 elements (685 with stable proper elements), without the need to perform any regularization such as the one described in Carruba & Michtchenko (2009). The fact that the number of frequency-family members is now comparable to the number of classical-family members without any regularization seems to confirm, in my opinion, the validity of the approach used to obtain synthetic proper elements in this paper. A clump around (33969) 2000 NM13 with 21 members found in the proper-element domain and one around (82426) 2001 NB20 with 24 members identified in the frequency domain were also encountered in the region.

In the region of Gersuind, the former Gil-Hutton (2006) family of (686) Gersuind with 28 members now has 151 members in the proper-element domain and 174 members in the frequency domain. Both families are characterized by a large proportion of members with stable elements (125 and 143, respectively).

No independent clump was observed in the region of the Pallas family but, as discussed earlier, the classical clump around (531) Zerlina merges with the Pallas family only for a cut-off of $d_0 = 121\,{\rm m\,s^{-1}}$, while the frequency clump around (3579) Rockholt merges with the Pallas frequency family for a cut-off of $f_0 = 0.600\,{\rm arcsec\,yr^{-1}}$, which motivated, along with similar considerations for the Barcelona family, my choice of cut-offs.

[4] To avoid the problem associated with the large errors in proper frequencies of (480) Hansa, as in Carruba & Michtchenko (2009) I used (40971) 1999 TY264 as the central body of the family.

The situation of groups in the Gallia region was already discussed earlier in this section, and no group was found in the Atalante region. More interesting is the situation of the Tina region, where a new family around (1222) Tina was found in both proper-element (72 members) and frequency (86 members) domains. The new family is characterized, as are families in the Barcelona and Olympia region, by the predominance of asteroids with unstable elements and by a large number of multi-opposition members (more than 60 per cent of the family members are objects with proper elements obtained for the first time in this work).

Fig. 9 displays contour plots of the number density of asteroids (see Carruba 2009 for a description of the procedure used to generate such plots; here I have used 33 steps of 0.02 au in a and 38 steps of 0.016 in $\sin i$) in the (a, $\sin i$) representative plane. Higher number densities of objects are shown in whiter tones. Following the example of Michtchenko et al. (2010), I divided my population of objects into small-eccentricity bodies ($e < 0.175$) and large-eccentricity ones ($e > 0.175$).

Fig. 9 displays density maps in the (a, $\sin i$) representative plane for (a) small-eccentricity bodies and classical groups, (b) small-eccentricity bodies and frequency groups, (c) large-eccentricity bodies and classical groups and (d) large-eccentricity bodies and frequency groups. Family members are shown as asterisks, while clump members are displayed as small circles. The effect of the linear secular resonances ν_5, ν_6, ν_{16} in removing the observed population of asteroids is quite clear in the density maps.

Among the differences between classical and frequency families, one may observe the presence of the Brucato family, observable in the (n, g, $g + s$) domain at low eccentricities but visible only as a clump in the (a, e, $\sin i$) space. At large eccentricities one may observe that the Pallas family is more extended in semi-major axis in the frequency domain than in the proper-element one. One may also notice the absence of the (40134) clump in the frequency domain; this is retrievable only for larger values of the cut-off than the one used.

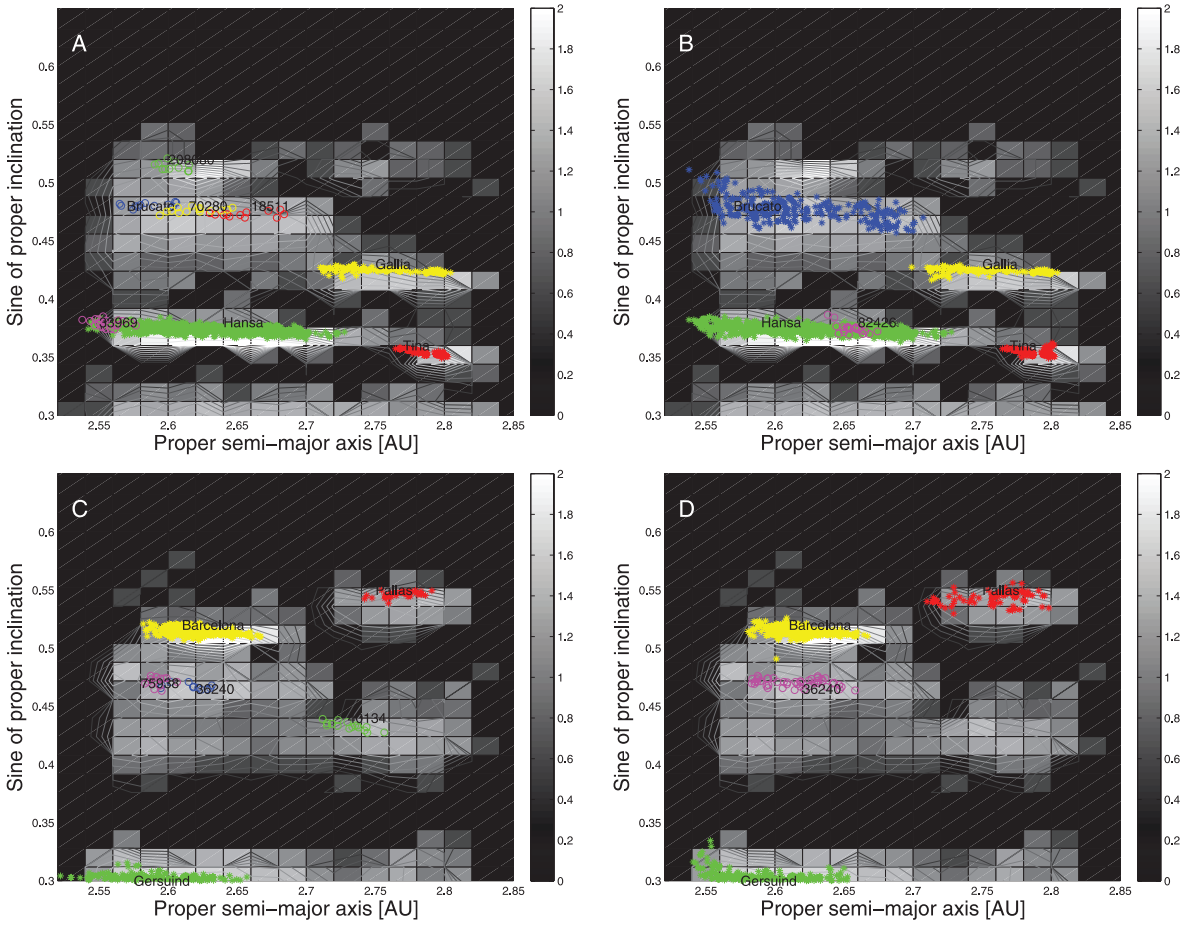

Figure 9. Density maps in the (a, sin i) representative plane for (a) small-eccentricity bodies and classical groups, (b) small-eccentricity bodies and frequency groups, (c) large-eccentricity bodies and classical groups and (d) large-eccentricity bodies and frequency groups.

To conclude, four new dynamical families (five if we include the Brucato frequency family) were discovered in this work: Gersuind, Barcelona, Gallia and Tina (the last was not known even as a clump in any previous work). Understanding whether these new families are the product of real collisional events will require an analysis of the taxonomy and properties of their members. I will concentrate my attention on these issues in the next sections. In the next subsection I will discuss family subgroups and asteroid pairs in the region.

3.1 Family subgroups and asteroid pairs

As a subproduct of the process of family determination, I obtained a few subgroups inside some of the families in the region. Table 2 displays the identification of the lowest numbered object in the subgroup, the name of the family to which it belongs ('c' identifies classical families, 'f' frequency ones) and the cut-off for which it merges with the family. Subgroups were identified for cut-offs larger than 100 m s^{-1} in proper-element space and greater than 0.400 arcsec yr^{-1} in frequency space. I refer the reader to Section 3 for a more in-depth discussion of the subgroups reported in Table 2.

Table 2. Subgroups in the region of the Pallas and Hansa families.

ID	Family	Cut-off
18511	Brucato(f)	0.500 arcsec yr^{-1}
70280	Brucato(f)	0.550 arcsec yr^{-1}
75938	Brucato(f)	0.575 arcsec yr^{-1}
6894	Hansa(c)	118 m s^{-1}
33167	Hansa(c)	119 m s^{-1}
531	Pallas(c)	119 m s^{-1}
3579	Pallas(f)	0.605 arcsec yr^{-1}

Also, recently Pravec & Vokrouhlický (2009) and Milani et al. (2010) looked for asteroid pairs in the main belt. These are objects that are extremely close in proper-element space and could be associated with double asteroids that recently split up. The first of the filters used by Milani et al. (2010) required asteroid pairs to be less distant in proper-element space by a distance of 4.2×10^{-4}, defined by the metric

$$d_{\rm p} = \sqrt{\frac{5}{4}\left(\frac{\delta a}{a_{\rm p}}\right)^2 + 2\delta e_{\rm p} + 2\delta I_{\rm p}}, \qquad (3)$$

where δ refers to the difference in proper elements between the parent body and the possible lost satellite. This distance corresponds to a distance of 9 m s^{-1} using the standard metric of Zappalà et al. (1995). Table 3 shows the 12 possible asteroid pairs identified in this work in increasing order of distance according to the metric given in equation (3) (for simplicity, distances are given using the standard metric of Zappalá et al. 1990). Here I only considered pairs with stable proper elements. Nine more pairs with one or both asteroids having unstable proper elements were also identified, but will not be given in this work.

Table 3. Candidates for past asteroid pairs in the region of the Pallas and Hansa families.

ID_1	ID_2	d (m s^{-1})
61728	216855	4.08
151802	2003 XO10	4.80
2001 XF16	2008 AD10	6.22
116053	146455	6.45
2006 UO5	2001 XG19	6.69
195451	2003 EB42	6.82
61226	95694	7.15
40853	114820	7.58
42800	110201	8.21
54896	70610	8.45
20949	2003 UA15	8.49
5438	208099	8.54

I should emphasize that further study is needed on the nature of these objects, since only the first filter of Milani et al. (2010) was applied here. The confirmation of these pair candidates as possible past broken couples should be considered as a possible line of research for future works.

4 THE COMPOSITIONAL ANALYSIS

As a preliminary step in the analysis of the local dynamical groups, I reviewed current knowledge about the taxonomical classification of members of the families and clumps in the region using the data present in three major photometric/spectroscopic surveys: the Eight-Color Asteroid Analysis Survey (ECAS: Zellner, Tholen & Tedesco 1985; Tholen 1989), the Small Main Belt Spectroscopic Survey (SMASS: Xu et al. 1995; Bus & Binzel 2002a,b) and the Small Solar System Objects Spectroscopic Survey (S3OS2: Lazzaro et al. 2004). I identified in the region of the Pallas and Hansa families two A-type, one L-type, 10 S-type, 10 X-type, 14 C-type, six B-type and one D-T-type object. Table 1 reports in the fifth column the number of group members with spectral identification.

Gil-Hutton (2006) reported that of the five members with spectral identification in the Pallas classical family four were B-type asteroids while one, (4969), was a C-type object and probably an interloper. The only two objects with spectral identification in the Hansa family were both S type, while in the Gersuind family one object, (686) Gersuind, was an S-type while (1609) was a D-type asteroid.

With respect to the work of Gil-Hutton (2006), I found that no taxonomical information is available on any of the clumps that I found in this work and very little is available for the families. The only object with spectral classification in the Barcelona family is (945) Barcelona, which is Sq type. No information is available for the groups in the Olympia region, while for the Hansa family three asteroid members of the classical family (480, 925 and 4880; 480 is not a member of the frequency family) are all S-type. I confirmed the two asteroids with spectral identification in the Gersuind family, and I found seven objects with spectral identification in the Pallas families (one of these, 5222, did not survive the length of my integration so that synthetic proper elements are not available for this object). Five of these objects, 2, 531, 2382, 3579 and 5234, are B-type, which seems to confirm the possibility of the Pallas family being a B-type group, but two family members, 1301 and 4969, are C-type, which undermines this possibility. The paucity of data on this family does not allow one to make a stringent conclusion on the family taxonomy. In the Gallia family one object, 148, is

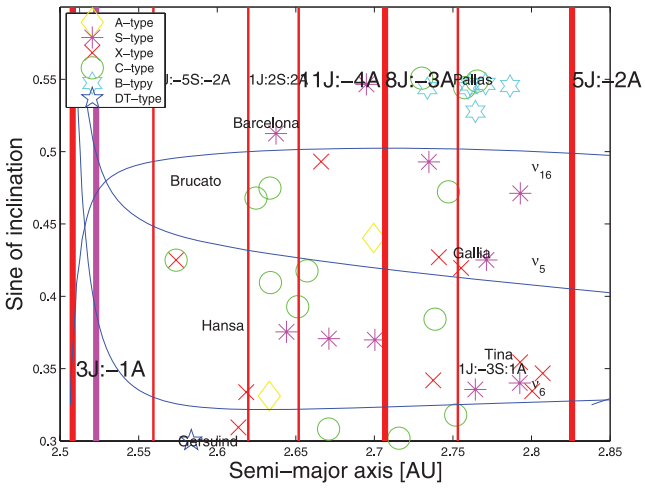

Figure 10. Taxonomic distribution of asteroids in the region of the Pallas and Hansa families.

S-type, while a member of the frequency family, 71 Niobe, is X-type. Finally, (1222) Tina is the only family member with a spectral classification (X-type).

Overall, with the possible exception of the Hansa and Pallas families, spectroscopic data are not enough to allow any stringent conclusions regarding any of the groups encountered in this work. Fig. 10, which shows an (a, sin i) projection of asteroids in the region with known spectral types, summarizes the results of my discussion. As can be seen in the figure, with the possible exception of the Hansa and Pallas family regions no area is taxonomically 'pure', with the predominance of a single spectral type. Further information is therefore needed before conclusions on the taxonomical validity of the groups found in this work can be confirmed.

For the purpose of extending the sample for which information on taxonomy is available, I turn my attention to SDSS-MOC3 data. The Sloan Digital Sky Survey Moving Object Catalog, denoted SDSS-MOC3 (3 stands for the third release, here I am using the third release rather than the fourth because of the better signal-to-noise ratio for the fluxes in that release), lists astrometric and photometric data for asteroids observed by the 2.5-m Sloan telescope located at Apache Point Observatory in Sunspot, New Mexico. To date (fourth release), the survey has determined positions, brightnesses and five-colour CCD photometry of 471 569 moving objects (Parker et al. 2008).

The flux reflected by the detected objects was measured almost simultaneously in five bands (measurements in two successive bands were separated in time by 72 s) with effective wavelengths 3557 Å (u band), 4825 Å (g band), 6261 Å (r band), 7672 Å (i band) and 9097 Å (z band), and with 0.1–0.3 μm bandwidths (Fukugita et al. 1996). Here I follow the approach of Roig and Gil-Hutton (2006) to obtain principal components in the space of albedos F_u, F_g, F_i, F_z. Using the criteria introduced by Roig & Gil-Hutton (2006) to reject data with large errors, I obtain a data set of 252 numbered objects with SDSS-MOC3 data in the Pallas and Hansa family regions.

Once the two first principal components are found, the data can be used to classify asteroids according to their taxonomic types and to determine asteroid families in the space of proper elements and colours simultaneously. The SDSS-MOC3 principal-component criteria are not of course a conclusive proof that an asteroid belongs to a given taxonomical class, but may furnish

precious hints on objects, such as V-type asteroids, for which no spectral information is available (Roig & Gil-Hutton 2006)).

Bus & Binzel (2002a,b) and Nesvorný et al. (2005) introduced the following extended metric in the space of proper elements and colours:

$$d_3 = \sqrt{d^2 + C_{PC}[(\delta PC_1)^2 + (\delta PC_2)^2]}, \quad (4)$$

where d is the distance given by the standard metric of Zappalá et al. (1990) and PC_1 and PC_2 are the two first principal components. Carruba & Michtchenko (2007, equation 3) also introduced a metric of colours and frequencies in the $(n, g, g + s, PC_1, PC_2)$ domain of the form

$$d_4 = \sqrt{f^2 + D_{PC}[(\Delta PC_1)^2 + (\Delta PC_2)^2]}, \quad (5)$$

where f is the standard distance metric in the $(n, g, g + s)$ frequency domain (Carruba & Michtchenko 2007) and D_{PC} is a numerical factor, empirically set equal to 200 to give comparable results for the typical differences in proper frequencies and those in principal components.

Following the approach of Carruba & Michtchenko (2007), I selected as first member of the colour groups one asteroid with principal-component data for each of the groups for which at least one member has SDSS-MOC3 data. I start my analysis by using the distance metric of principal components and proper elements. For a cut-off of 390 m s^{-1} the 33969 clump coalesces with asteroids in the local background of the Hansa family, so I decided to work with a cut-off of 385 m s^{-1}, which is in agreement with similar values found for the region of the Phocaea family (Carruba 2009). At this cut-off the Barcelona family has six members, five of them with principal components compatible with an Sq taxonomical class (see Fig. 11(a) and also Nesvorný et al. (2005) for the location of Sq asteroids in the principal-component plane), thus confirming the possible identification of Barcelona as an Sq-type family.

All the minor clumps found in the space of proper elements only have one or two members in the space of proper elements and colours, which is not enough to give information on their taxonomy. Most of them are compatible with an S-type class, but the 70280 and 33969 clumps also show the presence of SDSS-MOC3 objects compatible with X and C compositions. No member of the Hansa family was found in the SDSS-MOC3 catalogue, so it was not possible to obtain this family in the space of proper elements and colours, but most of the asteroids in the family local background are compatible with an S-type class, which seems to reinforce the information obtained from the spectral data of the family members. All seven members of the Gersuind family are in the region of the S-type complex, and no D–T asteroid was observed. This may suggest that the (1609) D–T asteroid in the Gersuind family may be an interloper. The Pallas family has two members that are compatible with either the B- or C-type class. Gallia has five S-type-compatible members, while Tina has two S-type objects. Overall, with the exception of the Pallas family and, possibly, the 70280 and 33969 clumps, the region seems to be dominated by S-type objects, but further study is needed to confirm this statement. Fig. 11(b) shows an $(a, \sin i)$ projection of the families with more than one object found in the space of proper elements and colours, which summarizes my results.

I then turned my attention to the domain of proper frequencies $(n, g, g + s)$ and colours. At a cut-off of 2.4 arcsec yr^{-1}, the 84646 frequency clump coalesces with asteroids in the local background of the Hansa family, so I decided to work with a cut-off of 2.3 arcsec yr^{-1} , which is in agreement with similar values found for the region of the Phocaea family (Carruba 2009). At this cut-off the Barcelona family has four members, all with principal components compatible with an Sq taxonomical class (see Fig. 12a), further confirming the possible identification of the Barcelona group as an Sq-type family.

The two frequency clumps around (36240) and (84646) all have one S-type member in the space of proper frequencies and colours. The Brucato frequency family has five members, almost equally divided between the C and X complexes. The Gersuind family has seven members, all in the S complex. The Pallas family has one member in the C complex and Gallia is characterized by four members in the S complex. Finally, the Tina family has one member in the S complex.

Overall, colour–frequency groups seems to confirm the findings for the colour–element groups. The Brucato frequency family, which englobes the 70280 classical clump, is characterized by the presence of both C- and X-type compatible objects, which seems to put in doubt the viability of the group as the product of a collisional event. Fig. 12(b) shows an $(a, \sin i)$ projection of the families with more than one object found in the space of proper frequencies and colours, which summarizes my results.

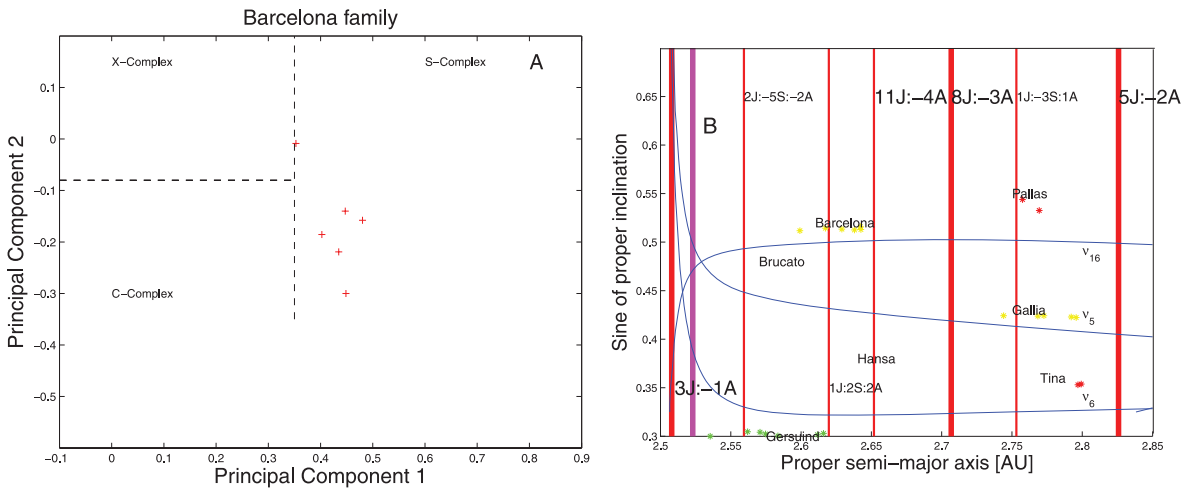

Figure 11. (a) The location in the principal-component (P_1, P_2) plane of the six members of the Barcelona colour–element family. (b) An $(a, \sin i)$ projection of families in the space of proper elements and colours.

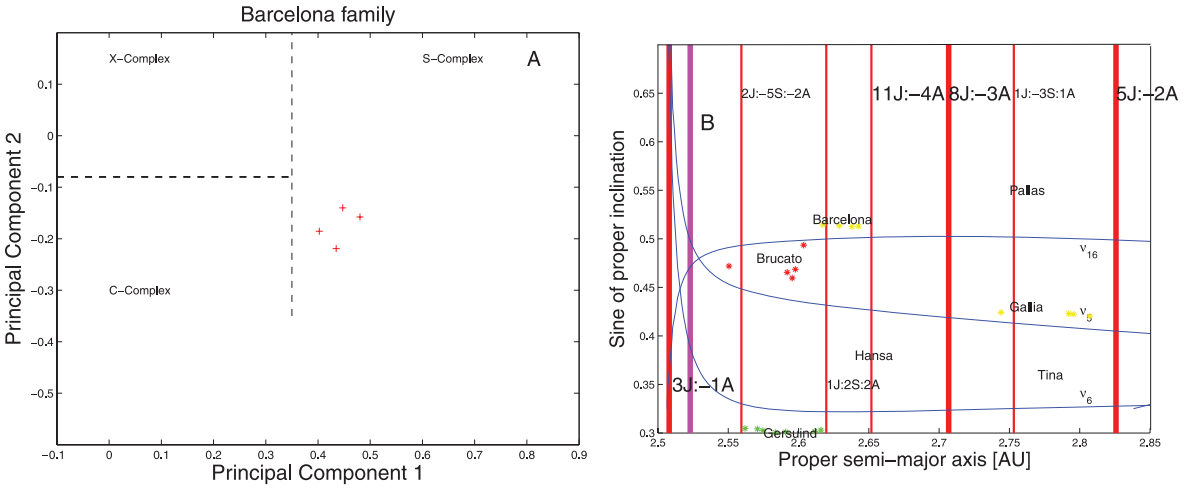

Figure 12. (a) The location in the principal-component (P_1, P_2) plane of the six members of the Barcelona colour–frequency family. (b) An (a, sin i) projection of groups in the space of proper frequencies and colours.

In the next section I will investigate the values of albedos and absolute magnitude for asteroids in the region that are available in the literature.

5 GEOMETRIC ALBEDOS AND ABSOLUTE MAGNITUDES

The cumulative size distribution of asteroid family members can be used to obtain important information about the collisional and orbital evolution of asteroid families (Vokrouhlický et al. 2006b). Estimates of the asteroid diameters can be obtained via the relationship

$$D = \frac{D_0}{\sqrt{p_V}} \times 10^{-0.2H}, \quad (6)$$

where $D_0 = 1329$ km, H is the asteroid absolute magnitude and p_V is the geometric albedo. To obtain reliable estimates of the diameters of asteroids, it is therefore important to first obtain good values of the geometric albedos and absolute magnitudes of the asteroids. Regarding asteroid albedos, I turn my attention to the work of Tedesco et al. (2002), which reported values of geometric albedo (with their uncertainties) for 2226 bodies. Of these, I found 43 objects in the region of the Pallas and Hansa families for which synthetic proper elements were also available. Eight of these objects belongs to either classical or frequency families and have a reported spectral classification.

Fig. 13(a) displays an (a, sin i) projection of the 43 objects with albedos in the region. Asteroids with albedos lower than 0.10 (usually associated with C-type bodies) are displayed with small black dots, those with albedos between 0.10 and 0.25 (associated with S-type objects, Bus & Binzel 2002a,b) are shown with medium full dots and asteroids with albedos larger than 0.25 are displayed with large full dots. As can be seen in the figure, low- and high-albedo objects are pretty much mixed, especially in the Olympia region, with the Brucato frequency family showing relatively low values of albedos, compatible with the C-complex membership of some of its members. The Barcelona and Gersuind families are characterized by values of albedos compatible with S-type composition, while the high value of albedo of the Gallia family is due to the fact that the only object with albedo data in the family, (71) Niobe, is probably an interloper. Overall, a slight majority of objects in the region have low-albedo values, 44 per cent of objects have albedos in the S-type range and only three objects have large albedo values. The

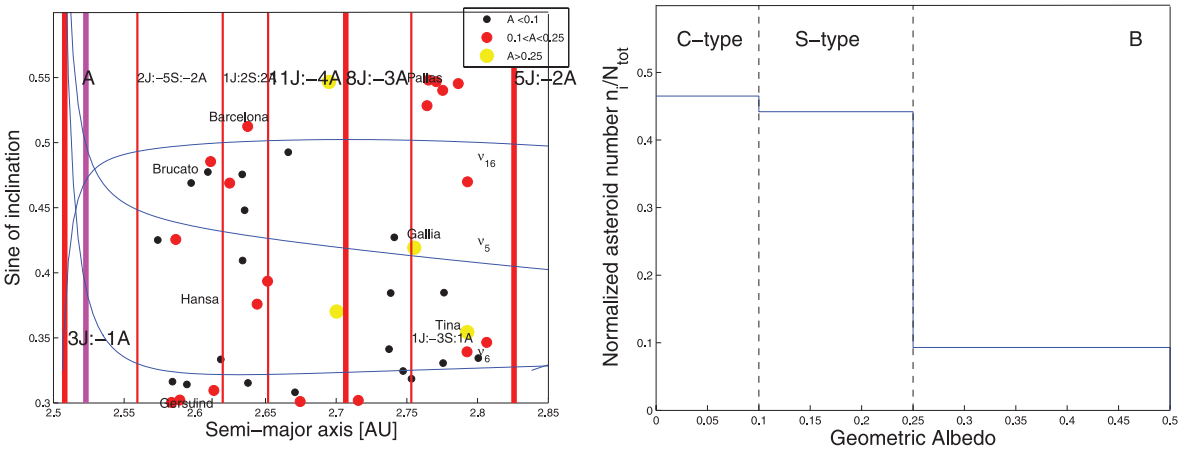

Figure 13. (a) An (a, sin i) projection of the orbital location of asteroids for which a value of the geometric albedo is available in the region of the Pallas and Hansa families. (b) Histogram of the normalized number of objects per unit bin in the albedo intervals 0.00–0.10 (C-type), 0.10–0.25 (S-type) and larger than 0.25, for all asteroids in the region (solid line).

Table 4. Mean value of the albedo for families in the region of the Pallas and Hansa families.

ID	Name	p_V	σp_V	$N_{\rm albedo}$
Family(c,f)	(945) Barcelona	0.2416	0.024	1
Family(f)	(4203) Brucato	0.0838	0.044	2
Family(c,f)	(686) Gersuind	0.1282	0.030	2
Family(c,f)	(2) Pallas	0.1560	0.009	3
Family(c,f)	(148) Gallia	0.3052	0.013	1
family(c,f)	(1222) Tina	0.3086	0.059	1

situation is summarized in Fig. 13(b), which shows a histogram of the normalized number of objects per unit bin in the albedo intervals 0.00–0.10 (C-type), 0.10–0.25 (S-type) and larger than 0.25, for all asteroids in the region (blue line).

Table 4 displays values of the mean albedo for the families for which such data are available in the region, with their errors (assumed as the standard deviation of albedo data for the families with more than one data point). With the exception of Barcelona and Tina, all families include asteroids that are likely interlopers, such as (1609) Brenda in the Gersuind family, which is a D–T asteroid in what most likely is an S-type family. Overall, the albedo data seem to confirm the possible identification of the Barcelona family as an Sq-type group, and possibly that of the Gersuind family as a S-type family, but very little else can be concluded from the available data.

Regarding the asteroid absolute magnitudes, Fig. 14(a) displays an (a, $\sin i$) projection of the asteroids with $e < 0.175$, while Fig. 14(b) shows the same for asteroids with $e > 0.175$. The location of the secular resonances is the one analytically obtained for the values of eccentricity and angles of (480) Hansa in Section 2. Small black dots display the locations of asteroids with absolute magnitude $H > 12$, medium full dots are associated with asteroids with $10 < H < 12$ and large full dots display the position of all objects with magnitude smaller than 10 for all 2310 numbered objects (no information on the absolute magnitude is available for multi-opposition asteroids).

As can be seen in the figure, the Pallas and Hansa family region is dominated by a population of small objects ($H > 12$). Overall, out of the 2310 numbered asteroids just 22 asteroids have absolute magnitude smaller than 10, and there are 20 with $10 < H < 12$ (one can safely assume that multi-opposition objects should all have $H > 12$ as well). Of the large $H < 10$ objects, only six are family members, and they are respectively (945) Barcelona, (480) Hansa, (686) Gersuind, (2) Pallas, (148) Gallia and (1222) Tina (71 Niobe, which is a member of the Gallia frequency family, is most likely an interloper). The situation is similar for medium-sized asteroids. The remaining 16 asteroids with $H < 10$ tend to concentrate in the Olympia and Atalante regions, and may be considered objects that have not been not broken up to form families (yet), which may also explain the lack of large asteroid groups in these two areas. Families in the region seem therefore to be either the result of cratering events, as seems most likely for the Pallas family, or formed by small-diameter objects, such as the Hansa and Tina families. More details on the size distribution of asteroid families will be given in the next section.

6 CUMULATIVE DISTRIBUTIONS OF FAMILY MEMBERS

The size distribution of asteroids is one of the most significant observational constraints on their history, and it is also one of the hardest quantities to determine because of strong selection effects (Parker et al. 2008). As a next step of my preliminary analysis of the Pallas and Hansa regions, I compute the cumulative H distribution $N(<H)$ (i.e. the number of objects in a group with an absolute magnitude less than a given value) for the classical and frequency families in the region. The size of a family member can be obtained using equation (6) and assuming that all members have the same albedo value, taken as the family mean value (see Table 4). Here I limit my analysis only to families in order to have statistically significant samples for the cumulative distribution. Even among families, not all groups have sufficient data. For instance, only 24 asteroids in the Pallas classical family and 21 in the Tina one have absolute magnitude data, which is not enough to provide statistically significant results. This analysis is also limited to numbered asteroids only, since multi-opposition ones do not have absolute magnitude data yet. Fig. 15 shows the cumulative H distribution $N(< H)$ for the two Hansa families, (a) classical and (b) frequency. Results are similar for the other families and will not be shown for the sake of brevity.

As is the case for several other families studied by Parker et al. (2008), family cumulative distributions for the groups in the region seem to be best approximated by a 'broken' power law, for the two intervals in H between 12 and 14 and between 14 and 15. According to Parker et al. (2008), data on absolute magnitude H were

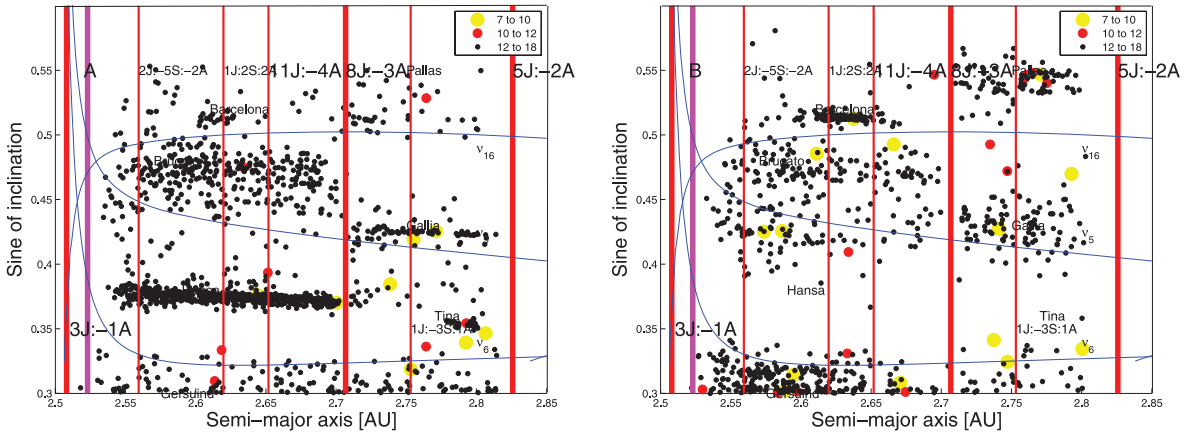

Figure 14. An (a, $\sin i$) projection of the asteroids in the region of the Pallas and Hansa families for asteroids with (a) $e < 0.175$ and (b) $e > 0.175$. Small black dots display the locations of asteroids with $H > 12$, medium full dots are associated with asteroids with $10 < H < 12$ and large full dots display the position of all objects with magnitude smaller than 10.

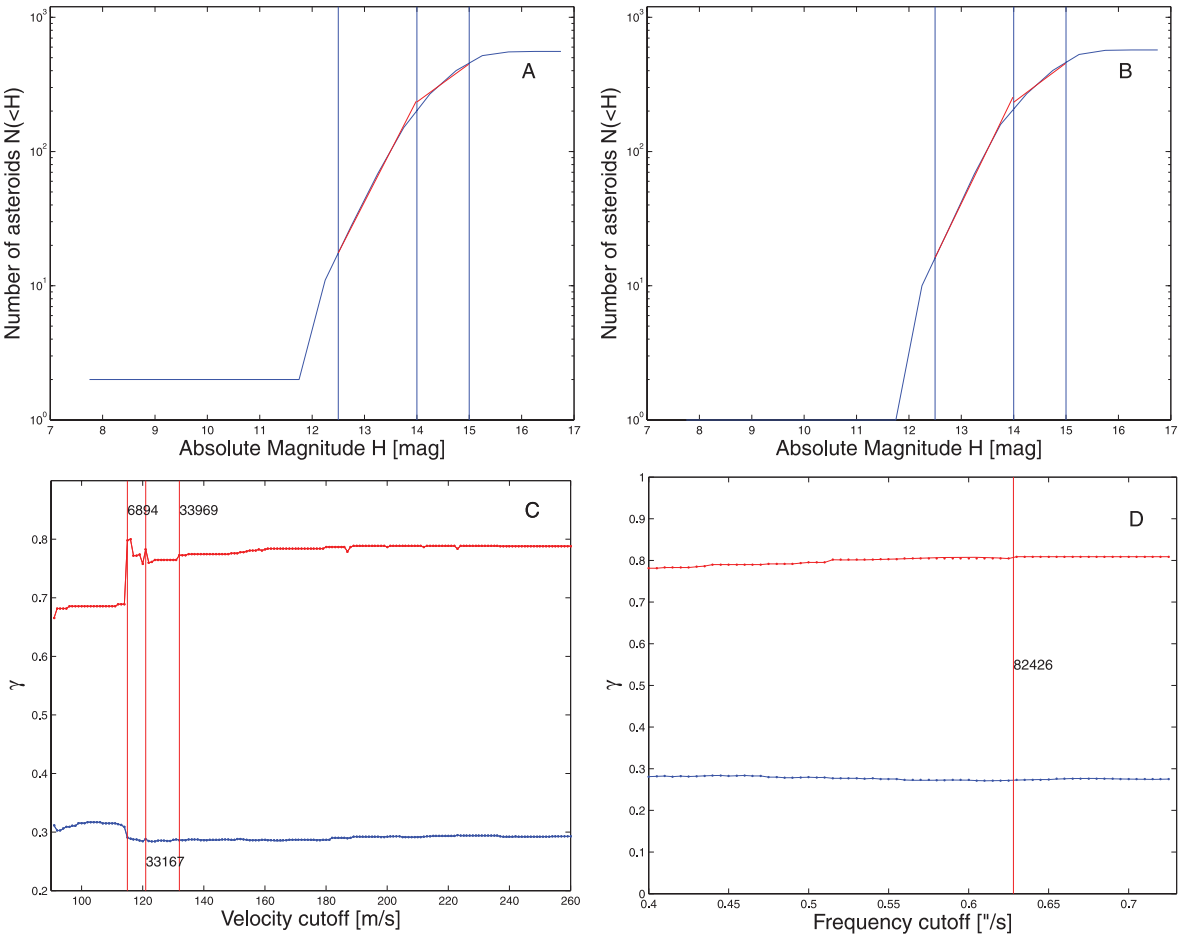

Figure 15. (a) and b display the cumulative distribution $N(>H)$ of the classical and frequency members of the Hansa family. (c) and (d) display the dependence of the exponent of the cumulative H distribution $N(<H)$ as a function of the velocity and frequency cut-offs, found in the range of absolute magnitude H (12.5, 14.0) (red lines) and (14.0, 15.0) (blue lines).

essentially complete up to magnitude 17 in the inner main belt and up to magnitude 15 in the outer one in January 2008. This, however, only applies to $\sin i < 0.3$ asteroids and absolute magnitude data may be lacking for highly inclined objects, especially at fainter magnitudes. To obtain information on the collisional evolution of the new families and to test the possible completion of highly inclined asteroid absolute-magnitude data, I computed the exponents γ_1 and γ_2 that best fit the cumulative distributions in the intervals in H between 12 and 14 and between 14 and 15, respectively.

I found that for the classical family the two exponents that best fit the two intervals are 0.760 and 0.285, respectively, while for the frequency family I obtained values of $\gamma_{1,2}$ of 0.804 and 0.274. The values of γ_1 are somewhat high (background asteroids usually have values of γ_1 of 0.61) and possibly suggest a relatively low age for the Hansa family. The values of γ_2 are instead quite low and may possibly be produced by incompleteness in the data for smaller asteroids. This situation could be improved once data on absolute magnitudes of multi-opposition asteroids become available.

In Fig. 15(c) and (d) I show the dependence of the exponent of the cumulative H distribution $N(<H)$ as a function of the velocity and frequency cut-offs[5] found in the range of absolute magnitude H (12.5, 14.0) ($\gamma > 0.5$) and (14.0, 15.0) ($\gamma < 0.5$). Vertical lines display the values of the cut-offs for which the Hansa family englobes other families and clumps in the region. As can be seen in the figure, the cumulative exponents fluctuate when the Hansa cluster englobes some of the minor groups in the region, then reaching an almost constant value for larger cut-offs. The Hansa family is limited by the powerful ν_5, ν_6 secular resonances and by the 3J:–1A and 8J:–3A mean-motion resonances, so the family merges with the local background only for very large values of the cut-off, not shown in the figure. This explains why there are no sudden drops in the γ exponents.

Values of the γ_1 and γ_2 exponents for the other families are summarized in Table 5 in the third and fourth columns (the second column reports the number of asteroids for which data on absolute magnitude are available, and the first column the name of the family (the suffix 'c' refers to classical families and suffix 'f' to frequency ones). Overall, the Barcelona, Brucato and Hansa families are characterized by relatively large values of the exponent γ_1, which could possibly suggest relatively low ages for these groups. In contrast, the Gersuind and Gallia families are characterized by lower values of γ_1, which may be compatible with a collisionally more evolved group.

In order to obtain more information on family ages I will now turn my attention to the time-scale isolines of the Yarkovsky effect.

[5] Due to its value of proper frequency g, (480) Hansa is not a member of the frequency family.

Table 5. Values of exponents of the cumulative size distributions γ_1 and γ_2 for families in the region of the Pallas and Hansa groups.

Name	$N(H)$	γ_1	γ_2
(945) Barcelona(c)	147	0.792	0.459
(945) Barcelona(f)	152	0.800	0.471
(4203) Brucato(f)	154	0.749	0.339
(480) Hansa(c)	557	0.760	0.285
(480) Hansa(f)	571	0.804	0.292
(686) Gersuind(c)	90	0.507	0.301
(686) Gersuind(f)	92	0.565	0.347
(148) Gallia(c)	49	0.637	0.371
(148) Gallia(f)	62	0.579	0.416

7 YARKOVSKY ISOLINES AND *C*-TARGET FUNCTIONS

Now that I have revised the information in the literature on geometric albedos and absolute magnitude, I am equipped to start setting constraints on an age estimate for families in the region. In Vokrouhlický et al. (2006), the authors used the (a, H) distribution of asteroid families to determine their ages. In particular, the authors introduced a target function C, defined as

$$0.2H = \log_{10}(\Delta a/C), \tag{7}$$

where $\Delta a = a - a_c$ and a_c is the 'central' value of semi-major axis of the family members. The most appropriate definition of the family centre relates to the concept of a barycentre. I took

$$a_c = \sum_{i=1}^{n_{ast}} \frac{a M_i}{M_{tot}}, \tag{8}$$

where n_{ast} is the number of family members and M_i is the mass of each asteroid, estimated assuming that all asteroids can be approximated as spheres using a density of 2500 kg m^{-3} for asteroids in the S complex and 1500 kg m^{-3} for asteroids in the C complex and a diameter obtained via equation (6). For asteroids for which the geometric albedo is not available, I used the mean value of the albedo reported in Table 4. Equations similar to equation (8) hold for e_c and i_c. With these approximations, I found that the total mass M_{tot} of the Barcelona families is of the order of 1.47×10^{17} kg, that its barycentre is at $a_c = 2.636$ au and that $\simeq$78 per cent of the current family mass is inside the largest body. Data for the other families are reported in Table 6. The mass of (2) Pallas [$(1.17 \pm 0.03) \times 10^{-10}$ M$_\odot$] is taken from Goffin (2001). In computing the family barycentres, I have excluded from the computation of the total mass obvious interlopers such as (925) Alphonsine (an S-type asteroid of low absolute magnitude $H = 7.78$ very far from the family barycentre) for the Hansa family and (71) Niobe (a X-type object in what appears to be an S-type family) for the Gallia frequency family.

Now that the values of family barycentres are computed, it is possible to obtain estimates on the upper limits of family ages by computing the time needed for an asteroid of a given size to cover the distance from the family centre to the extreme values in a of the family. Fig. 16(a) shows an (a, H) projection of Hansa classical-family members. This figure also shows the distance covered by asteroids to diffuse from the centre of the family via the Yarkovsky effect, computed using the Vokrouhlický (1999) model of the diurnal version of the Yarkovsky effect, for spherical bodies and in the linear approximation for heat conduction in a spherical, solid and rotating body illuminated by solar radiation. I used the following parameters to describe the Yarkovsky force: thermal conductivity $K = 0.0001$ W m^{-1} K^{-1}, specific heat capacity $C_p =$ 680 J kg^{-1} K^{-1}, density 2500 kg m^{-3} for S-complex asteroids and 1500 kg m^{-3}, surface density 1500 kg m^{-3}, bond albedo 0.11 and the mean geometric albedo appropriate for each family (Section 5). With these parameters, using the barycentric value of the family a-distribution a_c and assuming a rotation period inversely proportional to the radius (Farinella, Vokrouhlický & Hartmann 1998), I obtained lines of maximal Yarkovsky drift for the Hansa classical family for an age of 1600 Myr. Since I am not considering the effect of the primordial-ejection velocity field, this sets upper limits on the possible age of the family.

Fig. 16(b) shows the values of the C target function for the Hansa classical family.[6] As can be seen in the figure, the C distribution has two peaks and is not symmetrical. The excess of positive C values may possibly be associated with an excess of original prograde rotators, as observed in the Padua family among others (Carruba 2009). Further study is however needed to confirm this hypothesis.

Data on family upper-limit age estimates for the other families are available in the fifth column of Table 6. The Barcelona family seems to be a relatively young group, with an age of at most 350 Myr, which seems to confirm the results from the cumulative size exponents. It has an asymmetrical distribution in semi-major axis, with most of its members having values of a smaller than that of the family barycentre. This depletion may be possibly caused by the presence of the 11J:–4A mean-motion resonance in the area.

The Brucato family (if indeed is a real collisional family, which seems not to be confirmed by the taxonomical analysis) appears to have a greater age of at most 1300 Myr and a symmetrical distribution in the (a, H) plane. The Gersuind family also has a symmetrical distribution in the (a, H) plane and seems to be a relatively evolved family with 800 Myr as an upper limit on its age.

Regarding the Pallas families, there are very few members in the classical (35) and frequency (79) group, so any information on Yarkovsky isolines may suffer from the paucity of data. Both families have an upper-limit estimate of the age of 500 Myr, while an upper limit of 450 Myr applies for the Gallia families. Finally the Tina family seems to be a very young group, with an age of 150 Myr at most.

8 LIGHT CURVES AND ROTATION-RATE ANALYSIS

It has been recently proposed that binary asteroids can be formed because of the increase in the rotation rate of the parent body caused by the Yarkovsky–O'Keefe–Radzievskii–Paddack (YORP) effect (Pravec et al. 2008). Obtaining information on asteroid periods is therefore of significant importance in understanding their dynamical evolution. Here I have revised the current information available for members of families in the region in the Asteroid Light-Curve Data base (LCDB: Warner et al. 2008) as of March 2010. Of the 4310 asteroids in the Pallas and Hansa family regions, 39 have a period estimate in the LCDB.

Fig. 17 displays a histogram of the distribution of rotation frequencies for the 39 asteroids for which such information is available. Of these objects, 15 are family members (two belong to the Barcelona family, three to the Hansa one, four to the Gersuind group, four to the Pallas family and two to the Gallia group). The sample is too limited to allow statistically significant information to

[6] I computed the observed data $N_{obs}(C)$ for the classical and frequency families, obtained by (C, $C + \Delta C$) binning with $\Delta C = 5 \times 10^{-7}$.

Table 6. Barycentre, total mass and upper limits for families in the region.

Name	a_c (au)	M_{tot} (10^{17} kg)	M_L/M_{tot} (per cent)	Est. age (Myr)
(945) Barcelona(c)	2.636	1.48	77.2	350
(945) Barcelona(f)	2.636	1.46	78.4	350
(4203) Brucato(f)	2.628	2.02	7.8	1300
(480) Hansa(c)	2.644	38.7	90.6	1600
(480) Hansa(f)	2.641	36.8	95.1	1600
(686) Gersuind(c)	2.585	4.80	62.5	800
(686) Gersuind(f)	2.587	4.57	65.5	800
(2) Pallas(c)	2.771	2267.7	99.9	500
(2) Pallas(f)	2.771	2267.7	99.9	500
(148) Gallia(c)	2.771	26.6	99.7	450
(148) Gallia(f)	2.771	26.6	99.7	450
(1222) Tina(c)	2.792	0.2	82.1	150
(1222) Tina(f)	2.792	0.2	79.9	150

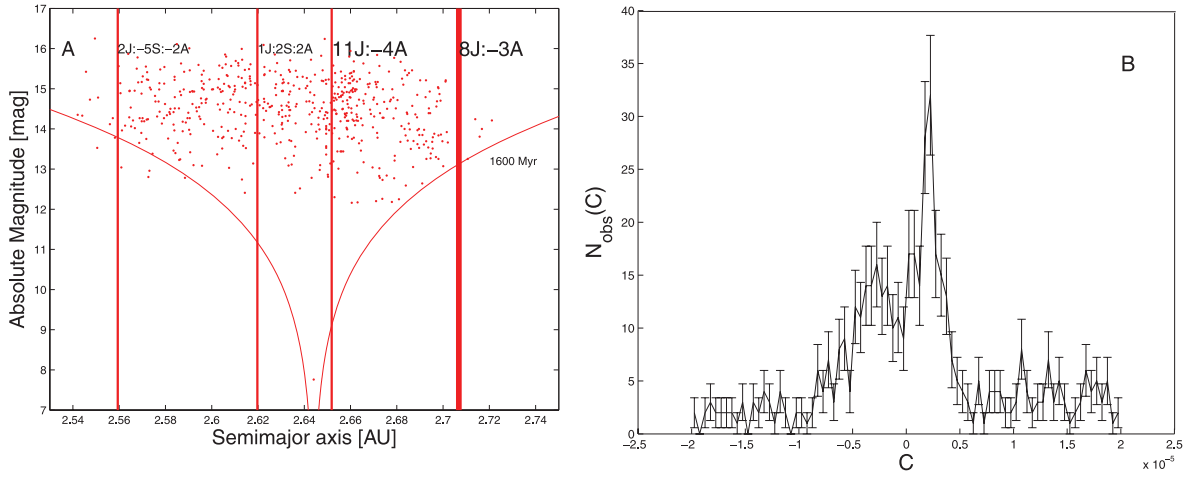

Figure 16. (a) An (a, H) projection of the members of the classical Hansa family. (b) Values of the C target function for the same family.

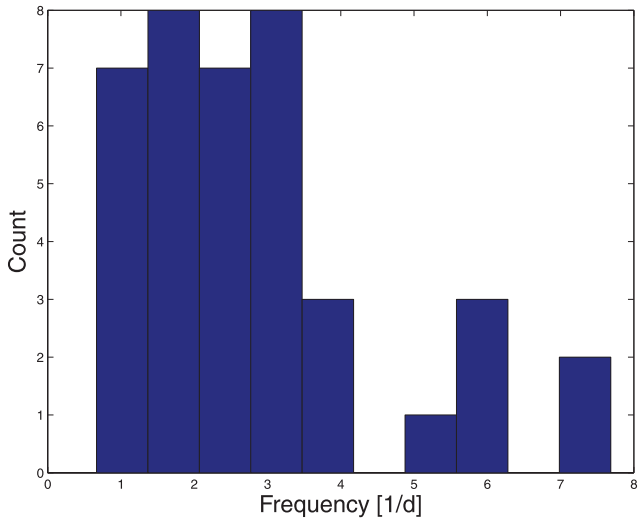

Figure 17. Histograms of rotation frequencies (in d^{-1}) for the 39 asteroids present in the Asteroid Light Curve Data Base.

be obtained, but it can be noted that there are 19 objects with periods longer than a day. As found by Warner et al. (2009) for asteroids in the Hungaria region, there seems to be an excess of slow rotators. This could possibly be caused by the YORP effect, with the excess of slow rotators related to the longer time slowly rotating objects spend in that state (Pravec et al. 2008).

9 DYNAMICS IN THE REGION OF THE PALLAS AND HANSA FAMILIES

A preliminary discussion on the dynamics in the region of the Pallas and Hansa families was carried out in Section 2.1. To gain further insights on the distribution of mean-motion and secular resonances in the region, I integrated 7000 particles in (a, e) space, 7000 particles in (a, $\sin i$) space and 10 000 particles in (e, $\sin i$) space. I used a step of 0.005 au in a, 0.005 in e and 0°.2 in i, and took particles in an equally spaced grid of 70 by 100 particles in the (a, e) plane, 70 by 100 particles in the (a, $\sin i$) plane and 100 by 100 particles in the (e, $\sin i$) plane.[7] The initial values of $\sin i$, e, a (for the simulations in the (a, e), (a, $\sin i$) and (e, $\sin i$) planes, respectively) and initial angular elements Ω, ω and λ of the test particles were fixed at those of (40971) 1999 TY264, a high-e asteroid in the Hansa family that was already used in Carruba & Michtchenko (2009) to obtain families in the domains of proper elements and colours and proper frequencies and colours. I choose this asteroid to avoid the problem of proper frequency determination associated

[7] My particles covered a range between 2.5 and 2.85 au in a, 0 and 0.5 in e and 15° and 35° in i, respectively.

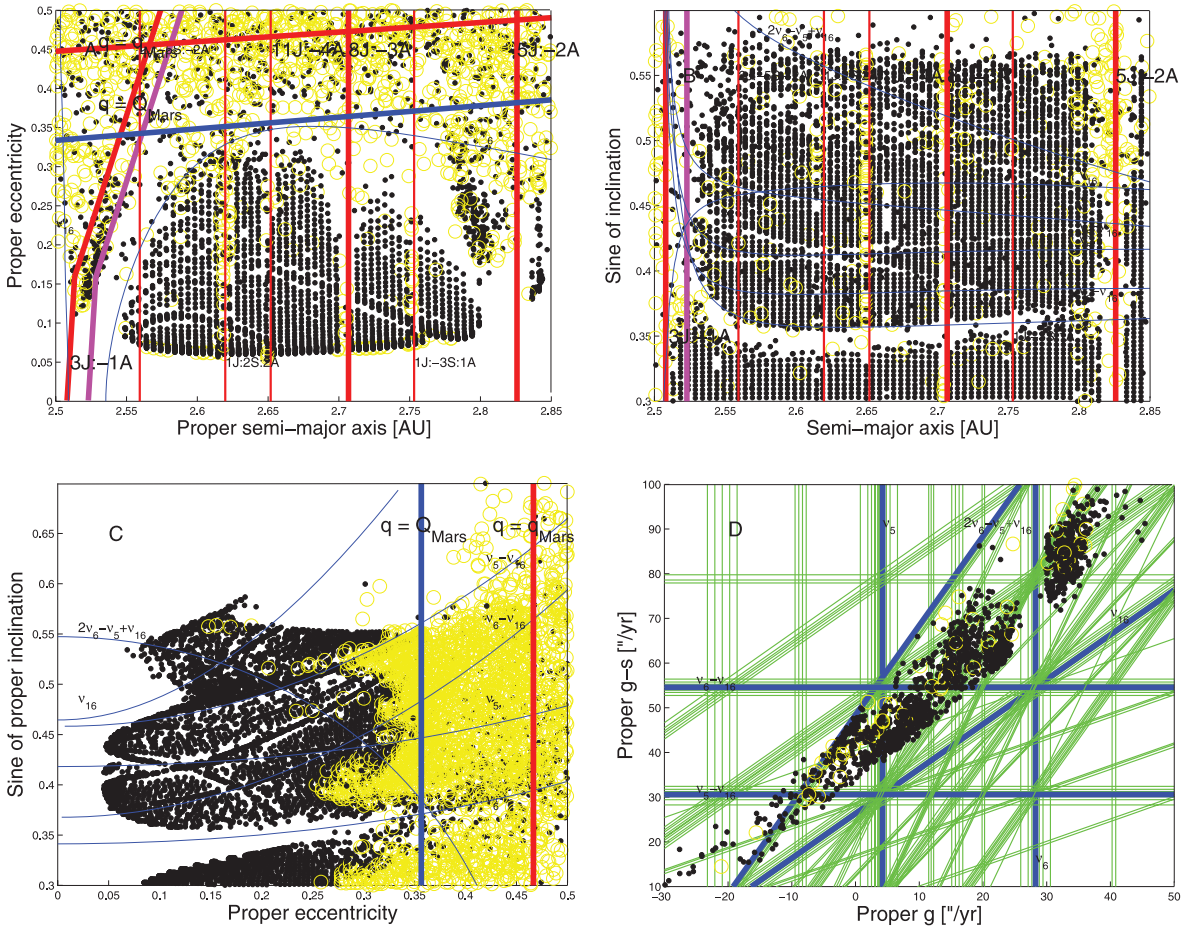

Figure 18. (a) (a, e), (b) $(a, \sin i)$ and (c) $(e, \sin i)$ projections of averaged elements for test particles in the region of the Pallas and Hansa families. (d) displays a $(g, g + s)$ projection of asteroid proper frequencies, with the location of the main secular resonances in the region.

with the low-eccentricity objects in the Hansa family, such as (480) Hansa itself.

Fig. 18 displays (a) (a, e), (b) $(a, \sin i)$ and (c) $(e, \sin i)$ projections of averaged elements for test particles in the region of the Pallas and Hansa families. Averaged elements are not constant in motion over millions of years as proper elements, but provide a qualitative insight on the local dynamics. Circles display Lyapunov times $T_{\rm L}$ smaller than 20 000 yr, while black dots are associated with times larger than 20 000 yr. The maximum Lyapunov exponent (MLE: Lyapunov 1907) is a measure of exponential stretching of nearby orbits. The Lyapunov exponents are equal to zero for regular orbits (they tend to zero in finite-time calculations), while they assume positive values for chaotic orbits. The inverse of a Lyapunov exponent is the Lyapunov time $T_{\rm L}$. Smaller values of $T_{\rm L}$ indicate enhanced local stochasticity. Lyapunov times were computed with the same procedures discussed in Carruba (2009).

Vertical lines display the location of mean-motion resonances, as discussed in Section 2, while blue lines show the location of the centres of the secular resonances that appeared in the map.[8]

As can be seen in Fig. 18(a), it is easy to spot the chaotic region with $q = Q_{\rm Mars}$ characterized by close encounters with Mars. This region is also clearly noticeable in the $(e, \sin i)$ plane (Fig. 18c). At lower eccentricities the presence of the ν_6 secular resonance destabilizes several of the test particles by increasing their eccentricity to Mars-crossing levels with a mechanism described in Carruba (2010). Other chaotic regions are associated with the separatrixes of mean-motion resonances such as the 3J:–1A, 5J:–2A, 8J:–3A and 1J:2S:2A.

The inclined alignment in the dynamical maps at $\simeq a$ =2.75 au and $e \simeq 0.1$ is caused by non-linear secular resonances such as $\nu_{16} + \nu_5 - \nu_6$. Since no real asteroid was found inside this resonance, I did not plot the resonance centre in this picture. Later on, the effect of other secular resonances will be discussed in more detail.

Finally, the fact that averaged eccentricities did not reach zero values arises from the fact that for asteroids in the Hansa region the forced eccentricity is larger than the free one, so that asteroids with small proper eccentricity are projected to their values of the forced one in the space of averaged elements.

More interesting and physically significant are the results shown in the space of $(a, \sin i)$ (Fig. 18b). The effect of the linear secular resonances ν_5, ν_6 and ν_{16} is clearly visible in this map. Three non-linear secular resonances have a significant population of objects to within the $\pm$ 0.3 arcsec yr^{-1} limit that Carruba (2009) show to be the location where 95 per cent of resonant objects are found: the $\nu_6 - \nu_{16}$, $\nu_5 - \nu_{16}$ and $2\nu_6 - \nu_5 + \nu_{16}$ secular resonances. These resonances are shown as blue lines in Fig. 18(b) and interact with members of the dynamical groups found in this work. More

[8] The location of secular resonances in the space of averaged proper elements is different from that in the space of proper elements.

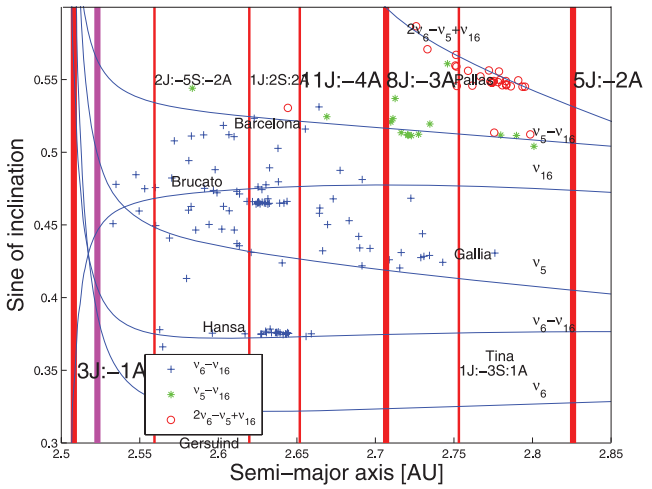

Figure 19. Orbital location in the (a, $\sin i$) plane of the asteroids in the $\nu_6 - \nu_{16}$ (blue crosses), $\nu_5 - \nu_{16}$ (green asterisks) and $2\nu_6 - \nu_5 + \nu_{16}$ (red circles) resonances.

information on this will be provided later on in this section. Two other secular resonances, the $2\nu_5 + \nu_{16}$ and the $\nu_5 + \nu_6 + \nu_{16}$, are responsible for some of the inclined alignments in the dynamical map but have just one asteroid to within the ± 0.3 arcsec yr^{-1} boundary (2000 YZ14 and 2004 DT39, respectively) and are therefore not shown in the figure.

Another very interesting feature is the limited amount of chaotic behaviour associated with the boundaries of the ν_5, ν_6 and ν_{16} secular resonances when compared with analogous results in the region of the Phocaea family (Carruba 2009, 2010). As discussed in Carruba (2010), the chaotic behaviour near the ν_6 secular resonance was caused by the fact that the resonance pushed asteroid eccentricities to a region of shallow Mars-crossing orbits ($e > 0.31$) when the difference in $|g - g_6|$ was less than 2.55 arcsec yr^{-1}. In this region asteroids had still pericentres lower than the aphelion of Mars, but were exposed to a series of shallow Martian close encounters that destabilized them over time-scales of 200 Myr or less. Eccentricities for reaching Mars-crossing orbits are, however, larger in the Pallas and Hansa region and it is possible that the semi-stable area at $e > 0.31$ found in the Phocaea region could be significantly smaller in the Pallas and Hansa region. This could explain why the chaotic layer near the ν_6 secular resonance is more limited in this area. Further study is, however, needed to test this hypothesis quantitatively.

Fig. 18(c) shows an (e, $\sin i$) projection of averaged elements of particles in the area. One may notice a chaotic region with eccentricity lower than that needed to reach the Martian apocentre, which is a region associated with shallow close encounters with Mars. The long-term stability of this region is an interesting topic for future research.

Finally, Fig. 18(d) displays the orbital location in the (g, $g - s$) plane of the numbered asteroids for which information on the Lyapunov time is available at the AstDyS site. Thin lines show the location of all secular resonances up to order 6, while thick lines are associated with resonances that have a resonant population larger than 1. One may clearly notice the alignment of asteroids in the $\nu_6 - \nu_{16}$, $\nu_5 - \nu_{16}$ and $2\nu_6 - \nu_5 + \nu_{16}$ secular resonances.

Fig. 19 displays the orbital location in the (a, $\sin i$) plane of the asteroids in the $\nu_6 - \nu_{16}$ (crosses, 105 objects), $\nu_5 - \nu_{16}$ (asterisks, 15 objects) and $2\nu_6 - \nu_5 + \nu_{16}$ (circles, 29 objects) resonances, to within 0.3 arcsec yr^{-1}. The $\nu_6 - \nu_{16}$ secular resonance interacts with the Hansa, Brucato, Barcelona and Gallia families. Understanding the long-term effect of this interaction, also using a distance metric in the (n, g, $g - s$) domain as in Carruba & Michtchenko (2009), may be an interesting challenge for future works. This may be particularly important for the Brucato family, which is observable only as a clump in proper-element space and may be significantly affected by secular dynamics.

The other two resonances, and in particular the $2\nu_6 - \nu_5 + \nu_{16}$ (a $g + s$ non-linear resonance), interact mostly with the Pallas family. It is worth noticing that Pallas is in a near 1:1 mean-motion orbital resonance with Ceres (Goffin 2001). Pallas also has a near 18:7 resonance (6500-yr period) and an approximate 5:2 resonance (83-yr period) with Jupiter (Taylor 1982). Further exploration of the dynamics of Pallas and its families is a very interesting subject for possible future research.

10 CONCLUSIONS

In this work I have investigated the current status of the knowledge of asteroids in the region of the Pallas dynamical family. Among other things I have done the following.

(i) Obtained values of synthetic proper elements for 2310 numbered and 2142 multi-opposition objects. With respect to published AstDyS values, 26 numbered objects had discrepancies in the values of proper e and 368 objects had discrepancies in the proper g values, which are connected mostly with the problem of obtaining values of g for objects with $e_{\rm free} < e_{\rm forced}$. These discrepancies are essentially intrinsic to the method used by Knežević & Milani (2000) to obtain synthetic proper elements. The larger sample of proper elements obtained by also considering multi-opposition objects was quite useful for asteroid family determination.

(ii) Identified asteroid families and clumps in this region using CHCM and FHCM. My analysis shows that the Gallia and Barcelona clumps of Gil-Hutton (2006) should now be considered proper dynamical families, in both proper-element and frequency domains. A new family around (1222) Tina was identified for the first time in this work in both proper-element and frequency domains. A frequency family around (4203) Brucato (the group appears as a clump in the proper-element domain) was also found, as well as nine other clumps, one of which (36240 1999 VN44) appears in both domains and is a good candidate for being the result of a real collisional event. Family subgroups and asteroid-pair candidates (Pravec & Vokrouhlický 2009; Milani et al. 2010) were also identified in the region.

(iii) Revised the current state of knowledge on the taxonomy of objects in the Pallas and Hansa family regions and found that the Hansa family could be taxonomically compatible with an S-type group, while the Pallas one is mainly composed of B-type objects (with two C-type asteroids as members as well). No sufficient information is available on the other groups found in this work to allow any other conclusions to be drawn.

(iv) Obtained principal components based on SDSS-MOC3 data, and used this information to obtain families in the space of colours and proper elements and colours and proper frequencies (Carruba & Michtchenko 2007; Carruba 2000). The Barcelona family seems to be consistent with an Sq-type composition, the Pallas family is compatible with a B-type composition and the Gersuind, Gallia and Tina families should belong to the S complex. Due to the presence of asteroids belonging to both the C- and X-type complexes, the

Brucato frequency family may not be the product of a collisional event.

(v) Revised the current knowledge of absolute magnitudes and geometric albedos for objects in the region. The albedo data seem to confirm that the Barcelona and (possibly) Gersuind families could belong to the S-type complex. The region is dominated by smaller bodies ($H > 12$), with the presence of very few (22) large ($H < 10$) asteroids (2 Pallas being one of the most notable exceptions). The 16 large asteroids that do not belong to the families tend to concentrate in the Olympia and Atalante regions, which are characterized by the lack of large asteroid groups.

(vi) Computed the cumulative absolute magnitude H distribution ($N(< H)$) for families in this region. As in Parker et al. (2008), the family distribution seems to be best approximated by a broken power law for two intervals in H between 12 and 14 and between 14 and 15. The exponents of the cumulative size distribution seem to suggest a relatively low age for the Barcelona and Brucato families, and higher ages for the Gersuind and Gallia ones.

(vii) Obtained Yarkovsky isolines and C-target function values (equation 7) for members of families in this region. I obtained an upper limit for the family ages of 350 Myr for the Barcelona families, 1300 Myr for the Brucato frequency family, 1600 Myr for the Hansa groups, 800 Myr for the Gersuind clusters, 500 Myr for the Pallas ones, 450 Myr for the Gallia families and 150 Myr for the Tina ones. Asymmetries in the semi-major axis distribution of family members, possibly caused by an excess of original prograde rotators or by local dynamics, are observed in the Barcelona and Hansa families.

(viii) Studied the available information on rotation rates for asteroids in the Pallas and Hansa family regions (Warner, Harris & Pravec 2008). 39 bodies have estimates for their rotation periods, and a histogram of the rotation frequencies shows that there is an excess of slow rotators, explainable in the framework of the evolution of the spin axis via the YORP effect.

(ix) Obtained dynamical maps of averaged elements for grids in (a, e), (a, $\sin i$) and (e, $\sin i$) of osculating initial conditions and identified the mean-motion and secular resonances that seem to have the largest effect on the short-term (20 Myr) stability of the asteroid averaged elements. The chaotic layer near the ν_6 secular resonance is of more limited dimensions than the one found in the Phocaea family region. Also, I found that the Brucato and Hansa families are characterized by their interaction with the $\nu_6 - \nu_{16}$ secular resonance, while the Pallas one is crossed by the $2\nu_6 - \nu_5 + \nu_{16}$ secular resonance. Several quasi-resonances with Jupiter and Ceres are present in the region of the Pallas families.

Among the issues not covered in this paper, the search for very close pairs of asteroids (Pravec & Vokrouhlický 2009) using the successive filtering approach of Milani et al. (2010) could be a very appealing topic of research, as well as the search for family subgroups. The candidates obtained in this work (see Table 1) passed just the first of the filters applied by Milani et al. (2010) and need further confirmation. I believe that this topic exceeds the purpose of this work, which was first and foremost to obtain synthetic proper elements for the region of the Hansa and Pallas families, obtain dynamical and spectroscopic families and review the current status of our knowledge regarding asteroids in the region. However, it remains an interesting topic of research for future work.

Another interesting line of research, in my opinion, could be studying the limited extent of chaotic dynamics near the boundaries of the ν_6, ν_5 and ν_{16} secular resonances, when compared with results around the ν_6 resonance in the Phocaea family region (Carruba 2009, 2010). The possibility that a region of semi-stable orbits at high eccentricities that experience shallow Martian close encounters could be of more limited extension in the region of the Pallas and Hansa families, because of the larger values of eccentricity needed to reach Mars-crossing orbits in the area and, possibly, of the resonance topologies, is in my opinion interesting and worth exploring in a future paper.

The long-term stability of some of the groups found in this work is also a very appealing possible topic of research. Exploring the statistical significance of the clumps identified in the space of proper elements and frequencies when the Yarkovsky effect is considered is important, especially considering the limited amount of information available on the taxonomy for some of these groups.

The effect of non-linear secular resonances, such as the $\nu_6 - \nu_{16}$ one, on the Hansa and Brucato families may possibly explain some of the discrepancies found in this work, such as the fact that the Brucato family is just a clump in the proper-element domain. The use of the (n, g, $g - s$) distance metric may provide useful information for such families.

A very different region seems to be the one associated with the Pallas families, which is characterized by the presence of the $2\nu_6 - \nu_5 + \nu_{16}$ secular resonance and by several quasi-resonances with Jupiter and Ceres. Understanding the complex dynamics of the region is a challenge for future papers.

More important than the effect of non-linear resonances is, however, the effect of linear resonances such as the ν_6. It has long been known that (1222) Tina was in an apocentric librating state of the ν_6 (Morbidelli & Henrard 1991). In such a state the resonant argument σ of the ν_6 resonance, $\varpi - \varpi_6$, oscillates around the stable point at 180°, rather than around 0° as is the case for librating orbits. Preliminary results (Carruba & Winter 2010) suggest that all members of the Tina families (classical and frequency) are currently in such a state, making the Tina family the first group in the Solar system to be completely inside a secular resonant configuration. The very interesting dynamics of the Tina family will be further investigated in future works.

Finally, the use of a Monte Carlo model that includes Yarkovsky and YORP effects, as has been done for the Padua family (Carruba 2009) and other cases, could help in obtaining better estimates for the ages of the younger groups found in this work.

As often in science, this work has answered some questions but produced several new ones, in many cases completely unanticipated when this work started. The large number of unanswered questions is once again proof of the vitality of asteroid dynamics as a field of research.

ACKNOWLEDGMENTS

I am grateful to an unknown reviewer for revision of my paper. I thank the São Paulo State Science Foundation (FAPESP), which supported this work via grant 06/50005-5, and the Brazilian National Research Council (CNPq, grants 302183/2008-6 and 473345/2009-9). I am also grateful to Dr Tatiana A. Michtchenko for several discussions on the peculiar nature of the proper frequencies of Hansa family members and to Professor Dr Kleomenis Tsiganis for a helpful conversation on asteroid synthetic proper elements. I thank Professor Dr Silvia G. Winter for reading and correcting the last version of this paper. Finally, I am also grateful to the department of Mathematics of FEG-UNESP for the use of their facilities.

REFERENCES

Beaugé C., Roig F., 2001, Icarus, 153, 391
Bendjoya P., Zappalà V., 2002. Asteroids III. Univ. Arizona Press, Tucson, p. 613
Brož M., 1999, Thesis, Charles Univ., Prague
Brož M., Vokrouhlický D., 2008, MNRAS, 390, 715
Bus J. S., Binzel R. P., 2002a, Icarus, 158, 106
Bus J. S., Binzel R. P., 2002b, Icarus, 158, 146
Carruba V., 2009, MNRAS, 398, 1512
Carruba V., 2010, MNRAS, 403, 1834
Carruba V., Michtchenko T., 2007, A&A, 475, 1145
Carruba V., Michtchenko T., 2009, A&A, 493, 267
Carruba V., Winter O. C. 2010, Nat. Commun., submitted
Farinella P., Vokrouhlický D., Hartmann W. K., 1998, Icarus, 132, 378
Fukugita M., Ichikawa T., Gunn J. E., Doi M., Shimasaku K., Schneider D. P., 1996, AJ, 111, 1748
Gil-Hutton R., 2006, Icarus, 183, 93
Goffin E., 2001, A&A, 365, 627
Guillens S. A., Vieira Martins R., Gomes R. S., 2002, AJ, 124, 2322
Hergenrother C. W., Larson S. M., Spahr T. B., 1996, Bull. Am. Astron. Soc., 28, 1097
Knežević Z., Milani A., 2000, Cel. Mech. Dyn. Astron., 78, 17
Knežević Z., Milani A., 2003, A&A, 403, 1165
Lazzaro D., Angeli C. A., Carvano J. M., Mothé-Diniz T., Duffard R., Florczak M., 2004, Icarus, 172, 179
Lemâitre A., Morbidelli A., 1994, Cel. Mech., 60, 29
Levison H. F., Duncan M. J., 1994, Icarus, 108, 18
Lyapunov A. M., 1907, Ann. Fac. Sci. Univ. Toulouse, 9, 203
Milani A., Knežević Z., 1994, Icarus, 107, 219
Milani A., Knežević Z., Novaković B., Cellino A., 2010, Icarus, 207, 769
Michtchenko T. A., Lazzaro D., Carvano J. M., Ferraz-Mello S., 2010, MNRAS, 401, 2499
Morbidelli A., Henrard J., 1991, Cel. Mech. Dyn. Astron., 51, 169
Morbidelli A., Vokrouhlický D., 2003, Icarus, 163, 120
Murray C. D., Dermott S. F., eds, 1999, Solar System Dynamics. Cambridge Univ. Press, Cambridge
Nesvorný D., Jedicke R., Whiteley R. J., Ivezić Ž., 2005, Icarus, 173, 132
Parker A., Ivezić Ž., Jurić M., Lupton R., Sekora M. D., Kowalski A., 2008, Icarus, 198, 138
Pravec P., Vokrouhlický D., 2009, Icarus, 204, 580
Pravec P. et al., 2008, Icarus, 197, 497
Roig F., Gil-Hutton R., 2006, Icarus, 183, 411
Šidlichovský M., Nesvorný D., 1997, Cel. Mech. Dyn. Astron., 65 137
Taylor D. B., 1982, MNRAS, 199, 255
Tedesco E. F., Noah P. V., Noah M., Price S. D., 2002, AJ, 123, 1056
Tholen D. J., 1989, in Binzel R. P., Gehrels T., Matthews M. S., eds, Asteroid Taxonomic Classifications. University of Arizona Press, Tucson, p. 298
Vokrouhlický D., 1999, A&A, 344, 362
Vokrouhlický D., Brož M., Bottke W. F., Nesvorný D., Morbidelli A., 2006, Icarus, 182, 118
Warner B. D., Harris A. W., Pravec P., 2008, Asteroid Light Curve Data Base (LCDB) (http://www.MinorPlanetObserver.com)
Warner B. D., Harris A. W., Vokrouhlický D., Nesvorný D., Bottke W. F., 2009, Icarus, 398, 1512
Williams J. G., 1992, Icarus, 96, 251
Xu S., Binzel R. P., Burbine T. H., Bus S. J., 1995, Icarus, 115, 1
Zappalà V., Cellino A., Farinella P., Knežević Z., 1990, AJ, 100, 2030
Zappalà V., Bendjoya P., Cellino A., Farinella P., Froeschlé C., 1995, Icarus, 116, 291
Zellner B., Tholen D. J., Tedesco E. F., 1985, Icarus, 61, 355

This paper has been typeset from a TEX/LATEX file prepared by the author.

7

Erosão dinâmica de grupos de asteroides na região da família de Pallas

Neste trabalho investigamos a evolução dinâmica dos grupos encontrados em Carruba (2010b). Estudamos a origem da população de objetos de alta excentricidade ($e > 0.31$) em órbitas de cruzamento com Marte, que são instáveis com tempo escala de 340 Myr, e verificamos que asteroides do "background" local são hoje a fonte principal destes objetos, mas que os asteroides da família de Barcelona fornecerão a maior parte desta população em 250 Myr. Encontramos um críterio analítico, baseado no trabalho de Yoshikawa (1987), para obter a largura da zona caótica em volta da ressonância ν_6. A limitada largura desta zona no cinturão principal central é devida ao maior valor de excentricidades necessárias às órbitas de asteroides na região para que suas òrbitas possam cruzar aquela de Marte. Investigamos também a evolução dinâmica dos grupos identificados em Carruba (2010b), confirmando a viabilidade da família de Brucato e dos grupos em volta dos asteroides (40134) 1998 QO53, (75938) 2000 CO80, (33969) 2000 NM13, (208080) 1999 VV180 e (70280) 1999 RA111.

A seguir apresentamos o artigo, que foi publicado em Monthly Notices of the Royal Astronomical Society em 2011, volume 412, pp. 2052-2062.

Monthly Notices
of the
ROYAL ASTRONOMICAL SOCIETY

Mon. Not. R. Astron. Soc. **412,** 2052–2062 (2011) doi:10.1111/j.1365-2966.2010.18040.x

Dynamical erosion of asteroid groups in the region of the Pallas family

V. Carruba,⋆ J. F. Machuca and H. P. Gasparino

UNESP, Univ. Estadual Paulista, Grupo de dinâmica Orbital e Planetologia, Guaratinguetá, SP 12516-410, Brazil

Accepted 2010 November 16. Received 2010 October 27; in original form 2010 September 15

ABSTRACT

In a previous paper, the current state of knowledge on the region of the Pallas dynamical family was revised. Here the dynamical evolution and possible origin of dynamical groups in the region are investigated. First, we study the case of asteroids at high eccentricity ($e > 0.31$). These objects are unstable because of encounters with Mars on time-scales of up to 340 Myr. Local background asteroids are currently the major source of high-eccentricity objects, but Barcelona family members will become the dominant source in about 250 Myr.

Next, attention is focused on the lack of chaotic dynamics near the ν_6 secular resonance border in the region. Contrary to the case of the Phocaea family region, very limited chaotic behaviour was observed for real and fictitious particles in the central main belt near the ν_6 resonance. Using analytical and numerical tools, we find that the limited amplitude of the inclination region near the ν_6 resonance in the Pallas family region for which close encounters with Mars are possible explains the lack of chaotic behaviour found in a previous paper by Carruba.

Finally, we investigate the long-term stability of the minor families and clumps identified in the previous paper, when non-gravitational effects are considered. We find that none of the minor clumps obtained by Carruba is currently interacting with non-linear secular resonances in the region. The classical clumps around (40134) 1998 QO53, (75938) 2000 CO80, (33969) 2000 NM13, (208080) 1999 VV180 and (70280) 1999 RA111 have large detectability times and could be considered reasonable candidates for groups originating from collisional events. We confirm the presence of the (4203) Brucato family observable in the space of proper frequencies (n, g, $g + s$) that has the largest detectability time of all groups in the region.

Key words: celestial mechanics – minor planets, asteroids: general.

1 INTRODUCTION

In Carruba (2010b), the current status of our knowledge regarding the Pallas family region was revised. In that paper, amongst other things, families and clumps in the space of proper elements and frequencies (Carruba & Michtchenko 2007) were obtained and the current knowledge of asteroid taxonomy was revised, along with the albedo and absolute magnitude distribution of objects in the area. Furthermore, the dynamics of asteroids were studied using dynamical maps and chaos indicators. Several interesting results, such as the identification of the frequency family around (4203) Brucato, of the new family of (1222) Tina and of several clumps were obtained in that paper.

Here we try to investigate the questions left unanswered by that work. Asteroids at high eccentricity, the orbits of which are characterized by very low values of Lyapunov time, may experience encounters with Mars that can quickly destabilize their orbits. Here we study the long-term stability of these high-eccentricity objects and identify the orbital regions that may replenish this population.

Another question left unanswered by Carruba (2010b) concerns the lack of chaotic behaviour near the ν_6 secular resonance border, especially when the Pallas family region is compared with the much more chaotic Phocaea area (Carruba 2009b). Using analytical (Yoshikawa 1987) and numerical (Carruba et al. 2007) tools, here, we study the effect of the proximity of the ν_6 secular resonance on asteroid eccentricity and find a simple analytical criterion to identify the asteroids most likely to show chaotic behaviour.

Finally, we investigated the long-term stability of the minor families and clumps identified in the previous paper, when non-gravitational effects are considered, and studied the influence (or lack of) that non-linear secular resonances may have on asteroids in the region.

The layout of this paper is as follows. In Section 2, we review the preserving effect of the Lidov–Kozai resonance on highly inclined objects when planetary effects are considered. In Section 3, we investigate the mechanisms that could create the currently observed high-eccentricity population. In Section 4, we study the dynamics of orbits near the ν_6 resonance centre and why so little chaotic

⋆E-mail: vcarruba@feg.unesp.br

behaviour was observed in the region in Carruba (2010b). In Section 5, we investigate the long-term stability of minor families and clumps in the region. Finally, in Section 6, we present our conclusions.

2 MARS-CROSSER ASTEROIDS IN THE REGION: NUMERICAL SIMULATIONS

As seen in Carruba (2010b), asteroids in the region of the Pallas dynamical family at high eccentricities are characterized by interactions with Mars. In order to understand the long-term stability of asteroids in the region, we turn our attention to the results of numerical simulations. We start by performing short-term simulations on selected asteroids in the region.

2.1 Short-term numerical simulations

In Carruba (2010a), we investigated the long-term stability of high-eccentricity asteroids in the region of the Phocaea family and saw that objects with $e > 0.31$ were unstable because of encounters with Mars on time-scales of up to 270 Myr. Here we start by repeating the same analysis. There are 105 asteroids in the region of the Pallas family (25 numbered ones) that have eccentricities larger than 0.31. Two of these objects belong to the Barcelona frequency family (Carruba 2010b) and a member of the Pallas frequency family with an eccentricity of 0.3077 is in the proximity of this region, but, overall, the great majority of high-eccentricity asteroids in the region do not belong to families.

For asteroids at high inclination, it is possible to use the Lidov–Kozai Hamiltonian approximation (Carruba 2010a). The conserved integral of the Lidov–Kozai Hamiltonian is (Thomas & Morbidelli 1996; Gronchi & Milani 1999; Carruba 2010a):

$$H = \sqrt{a(1-e^2)}\cos i, \tag{1}$$

where a, e and i are the semimajor axis, eccentricity and inclination (evaluated with respect to the invariable plane of the Solar system), respectively. At a given semimajor axis, the conservation of H implies that there are maximum allowed values of eccentricity and inclination (see Carruba 2010a). When the eccentricity is large enough, the nodal distance at ascending node

$$d^{+}_{\rm nod} = \frac{a(1-e^2)}{1+e\cos\omega} - a' \tag{2}$$

and that at descending node

$$d^{-}_{\rm nod} = \frac{a(1-e^2)}{1-e\cos\omega} - a' \tag{3}$$

between the ellipse of the asteroid orbit and the circular orbit (with radius a') of some perturbing planets can become zero. In this case, a node crossing is said to occur and a collision between the asteroid and the planet is possible. At $\omega = \pm 90^{\circ}$, $\cos\omega = 0$ and therefore the denominators in equations (2) and (3) become equal to 1. As a consequence, for the values of ω for which the eccentricity reaches its maximum value, the right-hand side in equations (2) and (3) reduces to its minimum value $a(1-e^2) - a'$. The fact that for the maximal value of the eccentricity the nodal distance is not minimal is called the 'Lidov–Kozai protection mechanism'. For $\omega = 0^{\circ}$, equation (2) reduces to the first-order criterion $q = a'$, with q the asteroid pericentre distance, $q = a(1-e)$ (note that for $\omega = 0^{\circ}$ the value of the eccentricity is the minimum one).

In this section, we want to know what other information can be obtained by studying Lidov–Kozai conserved quantities in the region of the Pallas dynamical family. For this purpose, we focus our attention on the conserved values of the H integral.

Fig. 1 (panel A) shows the current distribution of proper inclination and eccentricities for asteroids in the region with $e > 0.31$. Superimposed, we plotted (e, I) values of the H integral in the range of H values for asteroids in the region. The minimum value of H is 0.8679, the maximum value is 1.4955 and the median value is 1.3152.

Fig. 1 (panel B) shows Mars node crossing lines for asteroids with semimajor axes equal to the median value of semimajor axes for $e > 0.31$ asteroids in the region ($a = 2.635$ au), obtained with equations (2) and (3), assuming Mars on a circular orbit of radius a'. As can be seen in the figure, with the exception of three asteroids, all objects in the region have nodal distances smaller than the value needed to collide with Mars. However, the long-term stability of these objects and the ability of the Lidov–Kozai mechanism to protect them from close encounters with Mars needs further research.

To start investigating the orbital behaviour of these objects, we integrated the 105 asteroids with SWIFT-SKEEL, the symplectic integrator of Levison & Duncan (2000) that is able to model close encounters between a massive planet and a massless particle, over 20 Myr and under the gravitational influence of all planets from

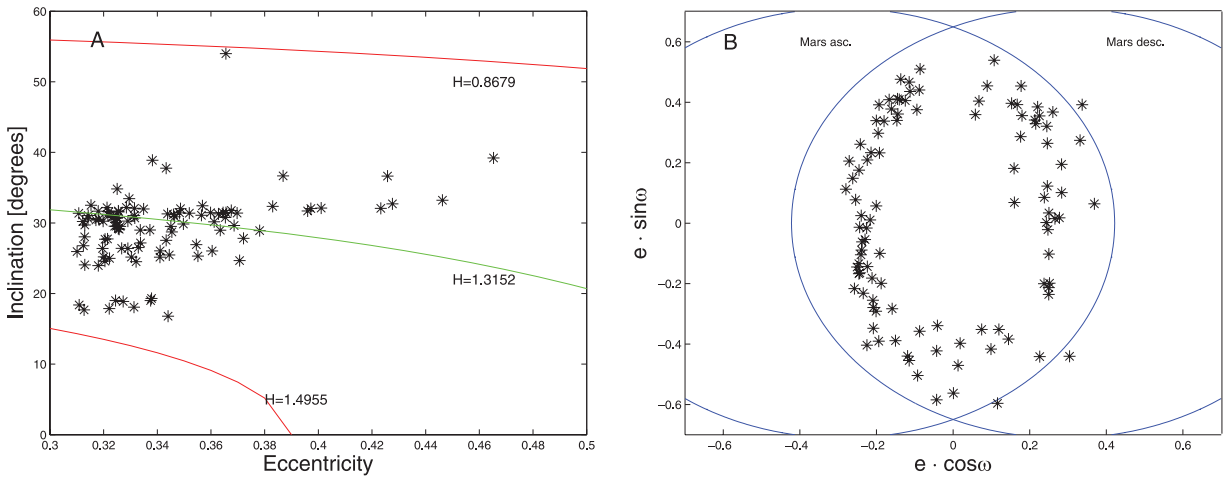

Figure 1. Panel A: (e, I) values of the H integrals for asteroids in the region of the Pallas family. Panel B: Mars node crossing lines for asteroids in the same region.

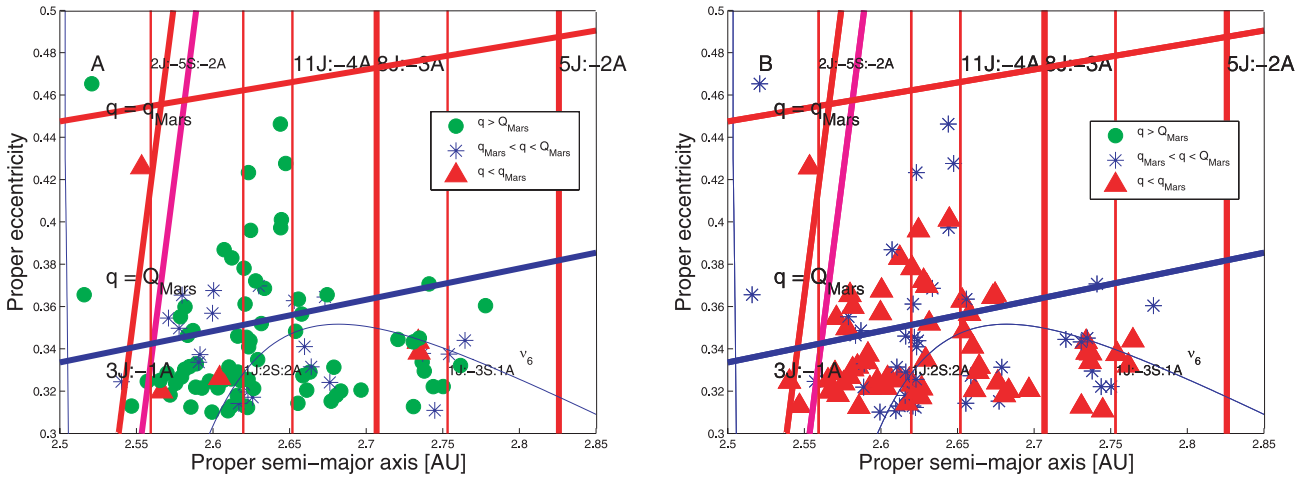

Figure 2. Panel A: an (a, e) projection of asteroids in the region of the Pallas family, for $e > 0.30$, with average values of pericentres. Panel B: the minimal values of pericentres of the same asteroids at the end of the 20-Myr integration.

Venus to Neptune (Mercury was accounted for as a barycentric correction in the initial condition of the system).

Fig. 2 (panel A) displays a proper (a, e) projection of the final fate of asteroids in the region. The red triangles are associated with asteroids whose mean pericentre was less than the pericentre of Mars, the blue asterisks are associated with asteroids whose mean pericentre was between the values of the pericentre and apocentre of Mars, and the green circles are associated with asteroids that had mean pericentres above the apocentre of Mars. The vertical red lines display the location of mean-motion resonances, the magenta lines display the location of the chaotic layer near the $3J:-1A$ mean-motion resonance as defined in Guillens, Vieira Martins & Gomes (2002) and the blue lines are associated with the secular resonances in the area. Inclined lines show the location of orbits with $q = Q_{\rm Mars}$ (in blue) and $q = q_{\rm Mars}$ (in red). Fig. 2 (panel B) shows the same, but for the minimum values of the pericentre that was reached by the particles during the simulation.

As can be seen in the figure, several asteroids near the ν_6 separatrix attain values of the mean pericentre low enough to allow them to interact with Mars. All asteroids in the region with $e > 0.31$ had values of minimum pericentres during the integration, low enough to plunge into the orbit of Mars. To further investigate the stability of orbits in the region, we created a grid of test particles with initial osculating eccentricity between 0.20 and 0.40, in the range of the semimajor axis between those of the $3J:-1A$ and the $5J:-2A$ mean-motion resonances, and with the values of inclination determined by the constancy of the H integral. In particular, we used the median value of H for asteroids in the region ($H = 1.3152$). The initial values of Ω, ω and M were those at J2000 of 1999 VF87, an asteroid with the median H value. There was a total of 2601 particles in this simulation, integrated with SWIFT-SKEEL over 20 Myr.

Fig. 3 (panel A) shows an averaged (a, e) projection for test particles in the region of the Pallas family, for $e > 0.30$, with minimum values of pericentres. Here we used averaged elements rather than the proper ones, because many particles were lost before a time-span long enough to obtain reliable proper elements. The colour code for the test particles and the other symbols is the same as in Fig. 2 (panel B). Fig. 3 (panel B) does the same, but for the maximum survival times (see the figure legend for the description of the meaning of the particle colour codes).

As can be seen in the figures, essentially, all asteroids above the ν_6 resonance had values of pericentres lower than Mars' apocentre and could therefore experience martian close encounters. Yet, only particles with $q < q_{\rm Mars}$ were lost before the end of the integration (Fig. 3, panel B). This is further confirmed by the density maps of $q_{\rm min}$ (panel C) and $t_{\rm max}$ (panel D) values. Following the approach of Carruba & Michtchenko (2009), in these figures, we show the mean values of $q_{\rm max}$ and $t_{\rm max}$ in a grid covering the intervals (2.50–2.85) in a (we took 20 equally spaced intervals) and (0.3–0.5) in e (also 20 equally spaced intervals). Superimposed to the density maps, there is the orbital location of real asteroids in the region (black asterisks). The density map scale of the $q_{\rm min}$ values was scaled up to the value of Mars' apocentre.

During the length of the integration (20 Myr), some particles in the region with $q < Q_{\rm Mars}$ achieved larger values of maximal eccentricity, but they were not lost. To further investigate the long-term stability of asteroids in the region, we performed simulations on longer time-scales for asteroids in these regions. The setup of the simulation and the results will be discussed in the next section.

2.2 Long-term numerical simulations

Fig. 2 (panel A) displays an (a, e), projection of the 105 asteroids in the region of the Pallas family. Of the objects with $e > 0.31$, (3712) Kraft is the only one for which a spectral classification is available (it is an S-type object in the Pallas family area). SDSS-MOC3 data are available for (123237) (2000 UH58) and suggest that this object, also in the Pallas family region, belongs to the C-complex. No information is available on the albedos of these 105 objects.

As can be seen in Fig. 2 (panel A), there are essentially seven mechanisms that can increase the asteroid eccentricity from the values observed in the region of the Pallas family to Mars-crossing values: interaction with the $3J:-1A$, $11J:-4A$, $8J:-3A$ and $5J:-2A$ two-body mean-motion resonances, and interaction with the $2J:-5S:2A$, $1J:-2S:-2A$ and $1J:-3S:1A$ three-body resonances. Of these mechanisms, the interaction of particles with the $3J:-1A$ mean-motion resonance is a proven very effective mechanism in raising the eccentricity of test particles to Mars-crossing levels. Secondary, the interplay of the Yarkovsky effect with higher order two- and three-body mean-motion resonances as a mechanism to

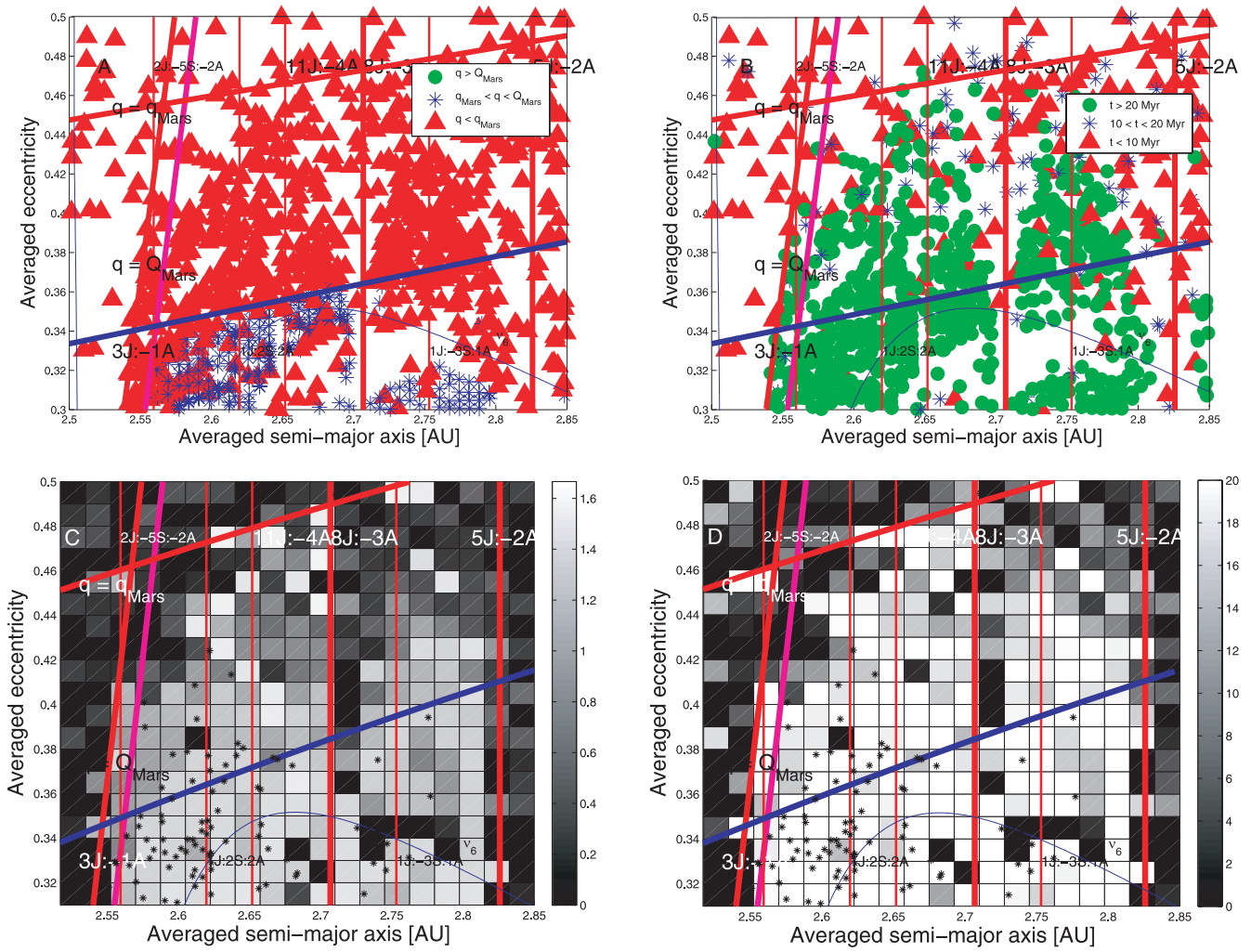

Figure 3. Panel A: an (a, e) projection of test particles in the region of the Pallas family, for $e > 0.30$, with minimum values of pericentres. Panel B: the maximum survival time of the same test particles at the end of the 20-Myr integration. Panels C and D display the position of real asteroids in the region, superimposed with density maps of minimum pericentre (in au) and survival time (in Myr).

increase asteroid eccentricities should also be investigated. More information on these mechanisms will be given in Section 3.

To further investigate the long-term stability of these 105 asteroids, we performed the following numerical experiments. First, we integrated the 105 asteroids with SWIFT-SKEEL over 300 Myr under the gravitational influence of all planets from Venus to Neptune (Mercury was accounted for as a barycentric correction to the Sun initial conditions). Following the approach of Nesvorný et al. (2008), we define a region of interest, which is between the $3J: -1A$ and the $5J: -2A$ mean-motion resonances, with $e > 0.31$ and $q < Q_{\rm Mars}$. The last condition was set so as to investigate the asteroids with large eccentricity that could potentially be destabilized by close encounters with Mars. We then checked how many objects remained in the area as a function of time during the numerical integration.

Fig. 4 (panel A) shows this number as a function of time (blue-dashed line) and the number of objects initially in the area of interest that remained in the region as a function of time (black line). We should emphasize that the parameter that gives information on the stability of objects is the one related to the number of objects *initially* inside the area, that is, the black line. The fact that other objects originally not in the area may be temporarily displaced inside the region of interest is per se not an indication of the stability of the initial asteroid population.

As can be seen in the figure, the number of objects with $q < Q_{\rm Mars}$ rapidly drops and goes to zero after 140 Myr, if we consider the initial population. As a second numerical experiment, we integrated the same particles with SWIFT_CE, an integrator developed in Carruba et al. (2007) that simultaneously models the effect of close encounters between a massive planet and a massless particle, and the diurnal and seasonal versions of the Yarkovsky effect. We used typical values of Yarkovsky parameters for S-type asteroids (thermal conductivity $K = 0.001\,{\rm W\,m^{-1}\,K^{-1}}$, thermal capacity $C = 680\,{\rm J\,kg^{-1}\,K^{-1}}$, surface density of 1500 ${\rm kg\,m^{-3}}$, density of 2500 ${\rm kg\,m^{-3}}$, bond albedo of 0.1, Carruba et al. 2003). The asteroid radius was computed using equation (1) in Carruba et al. (2003) and the average value of the geometric albedo of Phocaea members, $p_V = (0.24 \pm 0.12)$ (Carruba 2009b), and we gave to one set of objects an inclination of the spin axis of 90°, while to the second was assigned an obliquity of −90°. No re-orientations were considered, so that the drift caused by the Yarkovsky effect was the maximum possible. We integrated our test particles over 400 Myr.

Fig. 4 (panel B) displays the number of objects currently (blue-dashed line) and since the integration begun (black line) in the

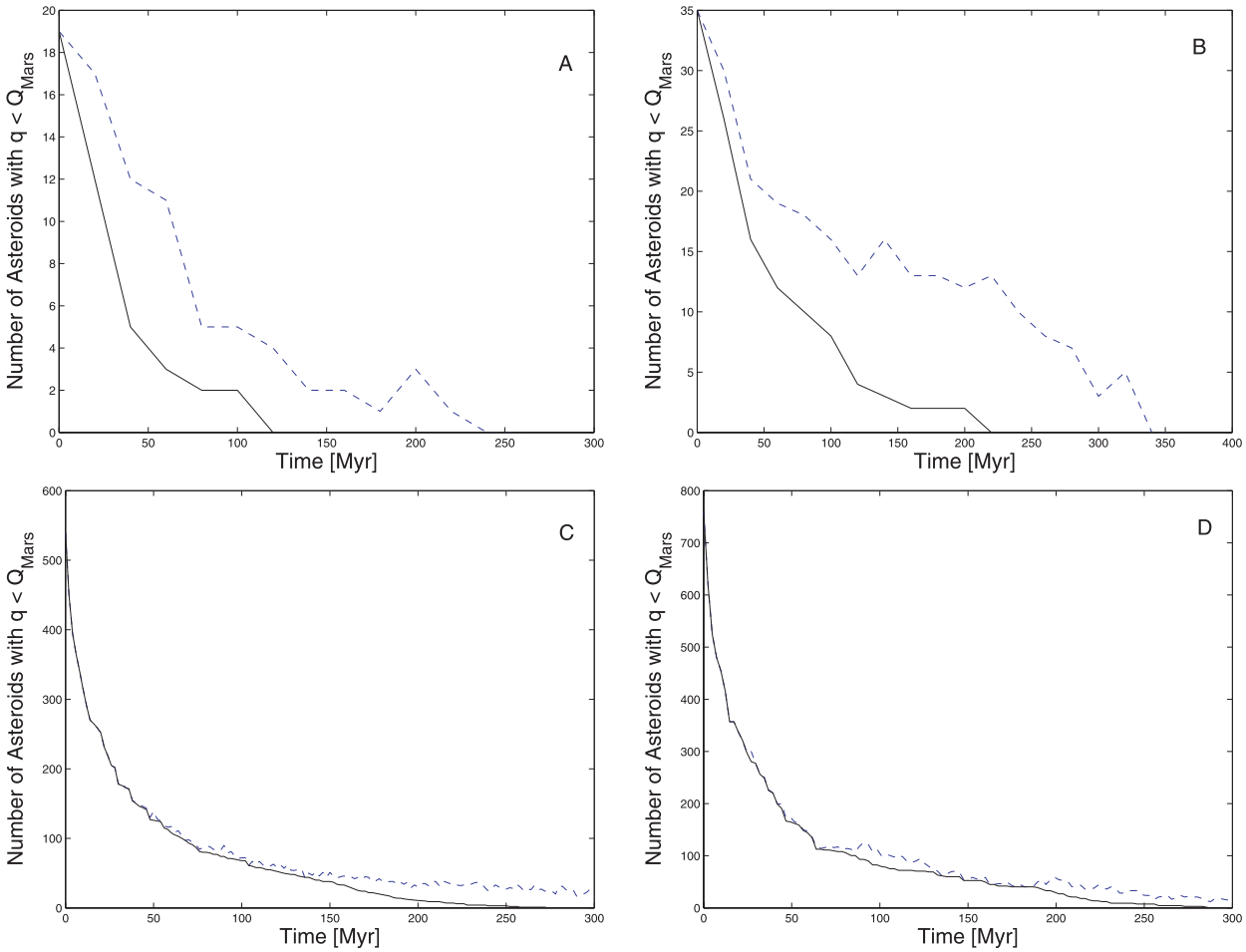

Figure 4. The number of objects (blue-dashed line) and of asteroids initially inside the $q < Q_{\rm Mars}$ region defined in the text (black line), as a function of time. See text for a description of the different panels.

area of interest during the length of the simulation. As for the case without non-gravitational effects, the number of objects in the area still drops, but on a somewhat longer time-scale. The last particle originally in the area of interest was removed after 220 Myr and all particles left the region after 340 Myr. As observed for the high-eccentricity, Mars-crossing region in the Phocaea family area (Carruba 2010a), test particles in the simulation with non-gravitational effects tend to stick longer than the same particles in the conservative integration. This is due to the interplay of the Yarkovsky effect with some of the local non-linear secular resonances, such as the $2\nu_6 - \nu_5 + \nu_{16}$ resonance in the Pallas region, that forced a few particles to stick to the resonances (and to the high-eccentricity area for longer times). Overall, this phenomenon only delays the inevitable loss of the original high-eccentricity, $q < Q_{\rm Mars}$ population, which is lost on time-scales of at most 220 Myr.

One possible objection to these data is the low number of objects currently present at high eccentricity. To obtain a statistically more robust estimate on the stability time, we integrated the same grid of 2600 high-eccentricity particles defined in Section 2.1 with SWIFT-SKEEL and SWIFT_CE over 300 Myr. Fig. 4 (panels C and D) shows the number of objects (blue-dashed line) and of asteroids originally inside the $q < Q_{\rm Mars}$ region (black line) as a function of time.

As can be seen in the figure, the times-scales for survival of the high-eccentricity, $q < Q_{\rm Mars}$ population are of 260 Myr for the particles in the SWIFT-SKEEL simulation and of 280 Myr for the particles in the SWIFT_CE simulation, in agreement with what found in the previous run with real asteroids. In the next section, we will investigate the mechanisms that can create the observed high-eccentricity population.

3 CREATING THE HIGH-ECCENTRICITY ASTEROID POPULATION

Now that we have estimated the lifetime of high-eccentricity objects, one natural question that may arise is how to create and sustain such an unstable population of asteroids. Three natural possible sources of high-eccentricity objects are the local background asteroids and the two families in the region with largest eccentricities: the Barcelona and Pallas families.[1] In principle, the source of these asteroids could be distinguished based on the taxonomy: C-type asteroids would be more likely to come from the Pallas family and S-type asteroids should be associated with the Barcelona one. Unfortunately, taxonomical information is available for only

[1] The 208080 clump in the region of the Barcelona family is composed of low-eccentricity objects and could not possibly furnish members to the high-eccentricity region in short time-scales.

one high-eccentricity object, (3712) Kraft, which is an S-type asteroid. SDSS-MOC3 data are also only available for just one object, (123237) (2000 UH58), also belonging to the S-complex. At this stage of our knowledge, it seems therefore that only dynamics can provide some clues about the possible origin of these high-eccentricity objects.

To investigate the possible mechanisms to replenish the high-eccentricity region, as defined in Section 2.2, we simulated the evolution under the Yarkovsky effect of two sets of clones of local background asteroids [asteroids with $\sin i > 0.5$ that do not belong to the Barcelona, Pallas or 208080 dynamical groups], the Barcelona and Pallas families, one with a spin axis obliquity of 90° and the other with a spin axis obliquity of −90°, so as to maximize the speed of migration towards larger and smaller semimajor axes. The periods were obtained assuming that the rotation frequency was inversely proportional to the radius and that a 1-km asteroid had a rotation period of 5 h (Farinella, Vokrouhlický & Hartmann 1998). We used the set of Yarkosvky parameters typical of S-type objects for the Barcelona family members (thermal conductivity of $0.001\,\mathrm{W\,m^{-1}\,K^{-1}}$, thermal capacity of $680\,\mathrm{J\,kg^{-1}\,K^{-1}}$, density of $2500\,\mathrm{kg\,m^{-3}}$, surface density of $1500\,\mathrm{kg\,m^{-3}}$, bond albedo of 0.1 and thermal emissivity of 0.95, Carruba et al. 2003) and typical of C-type objects for the Pallas family members (same as for S-type objects, but with a density of $1500\,\mathrm{kg\,m^{-3}}$), and integrated the members of both classical and frequency families over 300 Myr. The radius of each test particle was estimated using the median value of the geometric albedo for the family as found in Carruba (2010a) ($p_V = 0.2416$ for the Barcelona family, $p_V = 0.1569$ for the Pallas one and $p_V = 0.2000$ for local background objects) and the absolute magnitude of each object, using the formula

$$D = \frac{D_0}{\sqrt{p_V}} 10^{-0.2H}. \quad (4)$$

Multi-opposition objects for which no absolute magnitude data were available were given a radius of 1000 m. At each time-step, we checked the number of objects that reached the high-eccentricity region, as defined in Section 2.2.

Fig. 5 shows the number of high-eccentricity objects that originated as a member of the Barcelona family (blue line), as a member of the Pallas family (black dashed line) or as a background object (red dashed line), as a function of time, over the length of the integration (300 Myr). Among the mechanisms that can increase the eccentricity of asteroids, we found that powerful mean-motion resonances with Jupiter, such as the $3J:-1A$, $5J:-2A$ and $8J:-3A$ resonances, and the ν_6 secular resonance effectively increased the eccentricity of test particles on short time-scales, but also tended to create a population of objects on short time-scales (2 Myr or less). Three-body mean-motion resonances, such as the $1J:2S:2A$ and $1J:-3S:1A$ resonances, increased the asteroid eccentricities on longer time-scales, but also produced a longer lived high-eccentricity population.

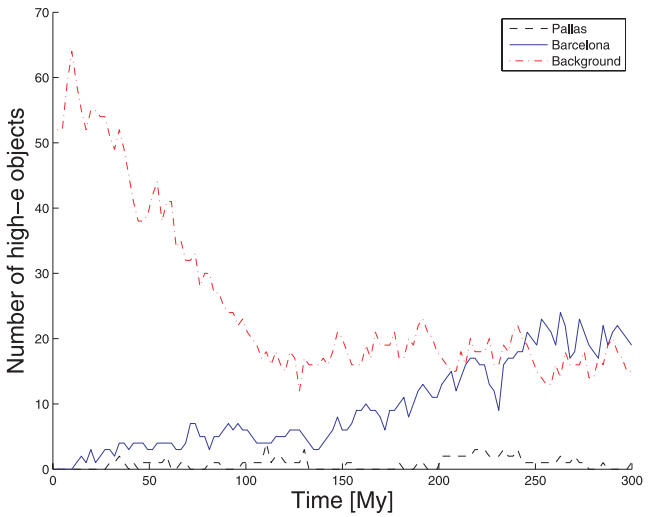

Figure 5. The number of high-eccentricity objects that originated as a member of the Barcelona family (blue line), as a member of the Pallas family (black dashed line) or as bakground object (red dashed line), as a function of time.

As can be seen in the figure, the current high-eccentricity population is dominated by background objects, with a secondary contribution from the Barcelona family and a very minor influx of Pallas objects. According to our simulations, Barcelona family members will become the dominant source of high-eccentricity asteroids 250 Myr into the future. The fact that background objects dominate the current high-eccentricity population in the region implies that, contrary to the case of the Phocaea family region (Carruba 2010a), it is not possible to set lower limits on the age of either the Barcelona or the Pallas family based on the time-scales needed to family members to reach the high-eccentricity region.

4 THE (ABSENCE OF) CHAOTIC DYNAMICS NEAR THE ν_6 SECULAR RESONANCE SEPARATRIX

One of the questions left unanswered in Carruba (2010b) was the absence of significant chaotic behaviour near the ν_6 secular resonance separatrix. In this section, we will investigate this problem with analytical and numerical tools.

4.1 Analytical model of the ν_6 resonance

Since the late 1980s, it is known that asteroids in the proximity of the ν_6 secular resonance have their eccentricity raised to planetary crossing values and are so destabilized on short time-scales (see, amongst others, Yoshikawa 1987). To more quantitatively estimate the effect of the proximity of the ν_6 secular resonance, here, we briefly revise the non-linear model for the ν_6 resonance of Yoshikawa (1987). In his model, Yoshikawa kept terms up to third degree in eccentricity and inclination for the secular part of the disturbing function and, under the hypothesis of proximity to the ν_6 resonance that $l_6 = \varpi - \varpi_6^*$ moves much slower than $l_5 = \varpi - \varpi_5^*$, where $\varpi_i^* = \nu_i t + \beta_i$, ν_i and β_i being known constants (Bretagnon 1974), obtained the following expression for the Hamiltonian of the problem:

$$F_{\nu_6} = \frac{1}{2}(b - \nu_6)e^2 + \frac{1}{4}ce^4 - d_6 e\cos(\varpi - \varpi_6^*), \quad (5)$$

where $\nu_6 = 26.217\,\mathrm{arcsec\,yr^{-1}}$ is the value of the precession frequency of the pericentre of Saturn and b, c and d_6 are coefficients whose values can be found in Yoshikawa (1987) and Carruba (2010a) (b roughly corresponds to the g pericentre precession frequency).

In this paper, we are interested in investigating the dynamics of objects near the ν_6 resonance separatrix. Following Yoshikawa (1987), we introduce the k_6 parameter:

$$k_6 = b - \nu_6. \quad (6)$$

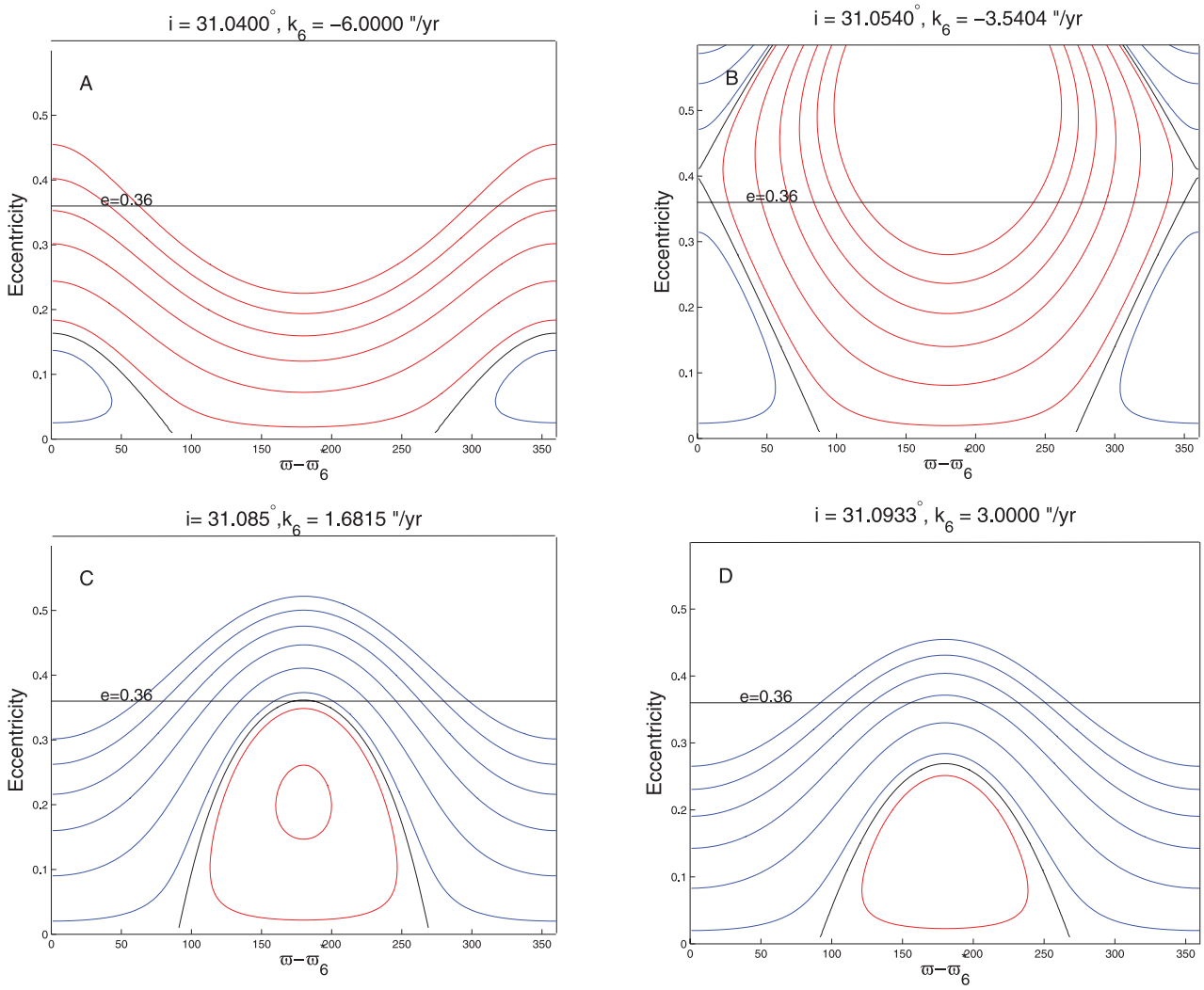

Figure 6. Diagrams of equi-Hamiltonian curves for $a = 2.6$ au and four values of inclinations and of the corresponding k_6 parameters.

For the $e > 0.31$ asteroids in the region of the Pallas family, values of k_6 in the range -120.5 to 10.3 arcsec yr^{-1} are observed. Only five asteroids have values of $|k_6| < 6$ arcsec yr^{-1} and are therefore close enough to the ν_6 resonance separatrix so that the approximations of the Yoshikawa model (i.e. we are in the proximity of the ν_6 resonance, so that the $l_6 = \varpi - \varpi_6$ variable moves much slower than the $l_5 = \varpi - \varpi_5$ one, Yoshikawa 1987) hold.

Following the approach of Yoshikawa (1987), we computed equi-Hamiltonian curves for two values of the semimajor axis [$a = 2.6$ au in the Barcelona area (Fig. 6) and $a = 2.8$ au in the Pallas region (Fig. 7)] and four different values of the inclination and of the corresponding value of k_6.

Fig. 6 (panel A) displays equi-Hamiltonian curves for $k_6 = -6.000$ arcsec yr^{-1} in the $(e, \varpi - \varpi_6^*)$ plane.[2] Since the Yoshikawa model is not accurate for eccentricities larger than 0.6, the plots display values of e in the range (0,0.6) only. The black line displays the level $F_{\nu_6} = 0$, red lines represent negative values of F_{ν_6} and blue lines represent positive values. The horizontal line shows the $e = 0.360$ level that corresponds to the eccentricity that an asteroid at $a = 2.6$ au should have in order to have its pericentre equal to the apocentre of Mars. For $k_6 = -6.000$ arcsec yr^{-1}, there is a libration island at $\varpi - \varpi_6^* = 0°$, but overall this does not perturb significantly the circulating red orbits. Objects with eccentricities at $\varpi - \varpi_6^* = 0°$ less than 0.360 are not pushed into a region of Martian close encounters and should present high values of Lyapunov times. For $k_6 = -3.5404$ arcsec yr^{-1} (Fig. 6, panel B), circulating orbits of negative energies are now trapped in a libration island, while the former librating orbits of positive energies now become circulating ones. All asteroids in the libration island and several of the asteroids on circulation orbits are eventually forced to reach Mars-crossing eccentricities, and should be expected to present low Lyapunov times.

For $k_6 = 1.6815$ arcsec yr^{-1} (Fig. 6, panel C), the curve of zero Hamiltonian has a maximum at $\varpi - \varpi_6^* = 90°$ for $e = 0.360$. As a consequence, all circulating curves are forced to reach Mars-crossing values of eccentricities and should be rather chaotic. Finally, for $k_6 = 3.0000$ arcsec yr^{-1} (Fig. 6, panel D), most of the low-eccentricity circulating orbits are unperturbed even at $\varpi - \varpi_6^* = 90°$ and should have rather high Lyapunov times.

Overall, circulating orbits at $a = 2.6$ au in the k_6 range -3.5404 to 1.6815 arcsec yr^{-1} are forced to reach Mars-crossing values of eccentricity and should be strongly perturbed by that planet. One

[2] See Yoshikawa (1987) for the definition of ϖ_6^*.

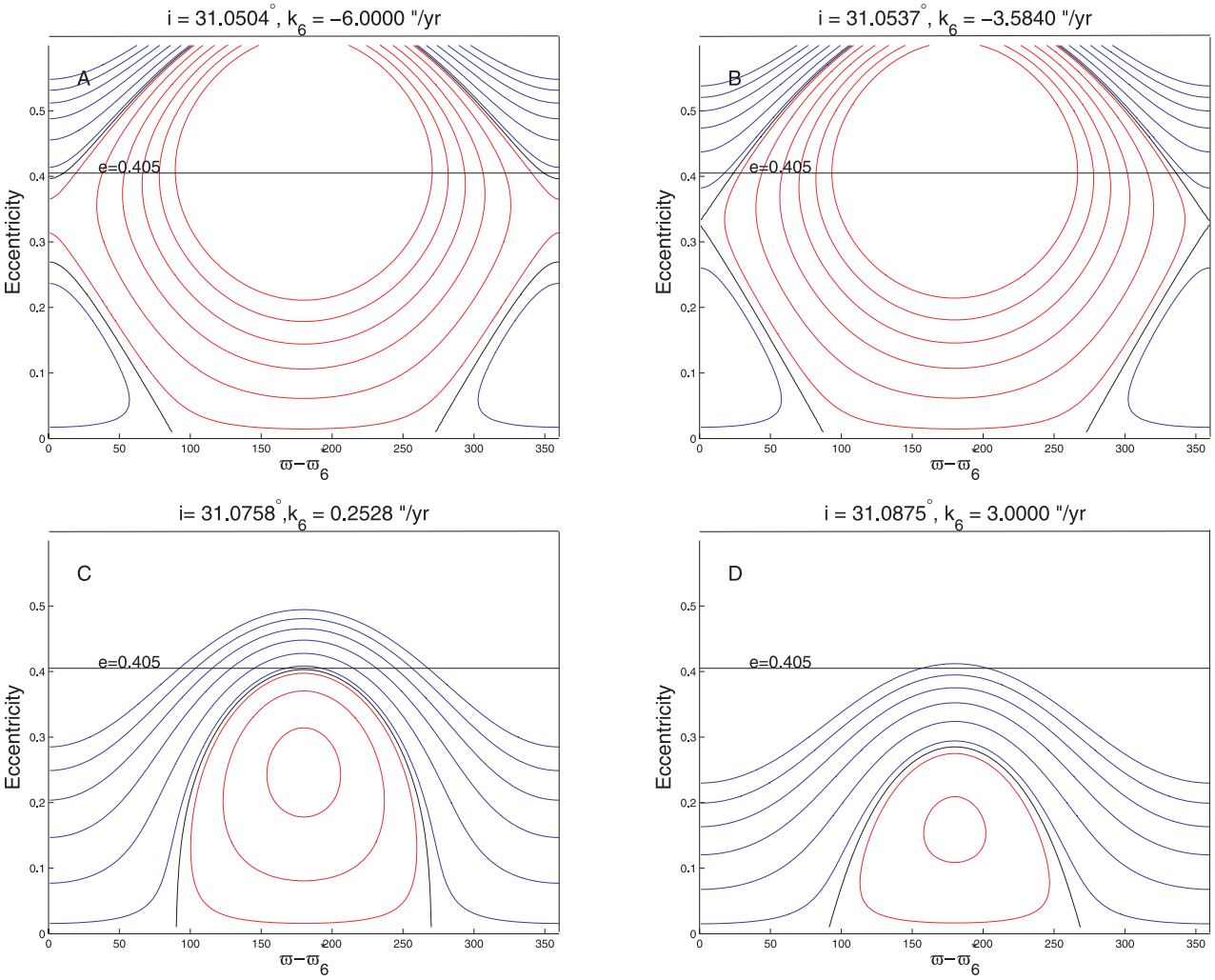

Figure 7. Diagrams of equi-Hamiltonian curves for $a = 2.8$ au and four values of inclinations and of the corresponding k_6 parameters.

may be expecting that chaotic orbits of low Lyapunov times could be found in this range of k_6 values. One may notice that the amplitude in inclination of this chaotic layer is quite limited: only $0.^{\circ}0313$. This, in principle, may be explaining the lack of significant chaotic dynamics found in Carruba (2010b). We will further investigate this hypothesis in Section 4.2.

The topology of the ν_6 resonance is different at larger semimajor axes, as is the minimum value of the eccentricity needed so that $q = Q_{\rm Mars}$ (0.405 at $a = 2.8$ au, in the Pallas region). Fig. 7 (panel A) displays equi-Hamiltonian curves at $a = 2.8$ au, for $k_6 = -6.0000$ arcsec yr^{-1}. For this value of k_6, there are two islands of libration for positive energy orbits at $\varpi - \varpi_6^* = 0^{\circ}$ and some of the circulating negative energy orbits are not pushed into the Mars-crossing region. Libration, positive energy orbits become circulating for $k_6 = -3.5840$ arcsec yr^{-1} (Fig. 7, panel B) and the libration island of negative energy orbits has a maximum at $e = 0.405$ for $k_6 = 0.2528$ arcsec yr^{-1} (Fig. 7, panel C). Fig. 7 (panel D) shows relatively unperturbed orbits at $k_6 = 3.0000$ arcsec yr^{-1}. In this case, the chaotic layer in the k_6 range -3.5840 to 0.2528 arcsec yr^{-1} is even more limited in inclination than for $a = 2.6$ au, with a width of just $0.^{\circ}0221$. We will further investigate the implication of this fact for chaotic orbits in the next section.

4.2 Numerical results

In Carruba (2010b), very little chaotic behaviour was found for orbits near the ν_6 resonance separatrix in the region of the Pallas family, contrary to what observed for orbits near the ν_6 resonance in the Phocaea region. The causes of the absence of significant chaotic behaviour were left as an unanswered question. In the previous section, we saw that chaotic behaviour should be expected, according to the Yoshikawa (1987) model of the ν_6 resonance, for values of k_6 in the range -3.5404 to 1.6815 arcsec yr^{-1} at 2.6 au and in the range -3.5840 to 0.2528 arcsec yr^{-1} at 2.8 au. In both cases, the amplitude in inclination of the chaotic layer was of only $0.^{\circ}0313$ at 2.6 au and less at 2.8 au.

To further confirm that the chaotic behaviour of small-inclination asteroids is indeed caused by the ν_6 secular resonance, we computed values of k_6 for the test particles that we used for estimates of Lyapunov times in the (a, $\sin i$) plane in Carruba (2010b). Fig. 8 (panel A) displays a blow-up of the low-inclination region of small Lyapunov times found in Carruba (2009b). Orbits with Lyapunov times of less than 20 000 yr are displayed as yellow dots. Fig. 8 (panel B) shows the orbital location of $-3.5404 < k_6 < 1.6815$ arcsec yr^{-1} asteroids in the space of averaged (a, $\sin i$) (red

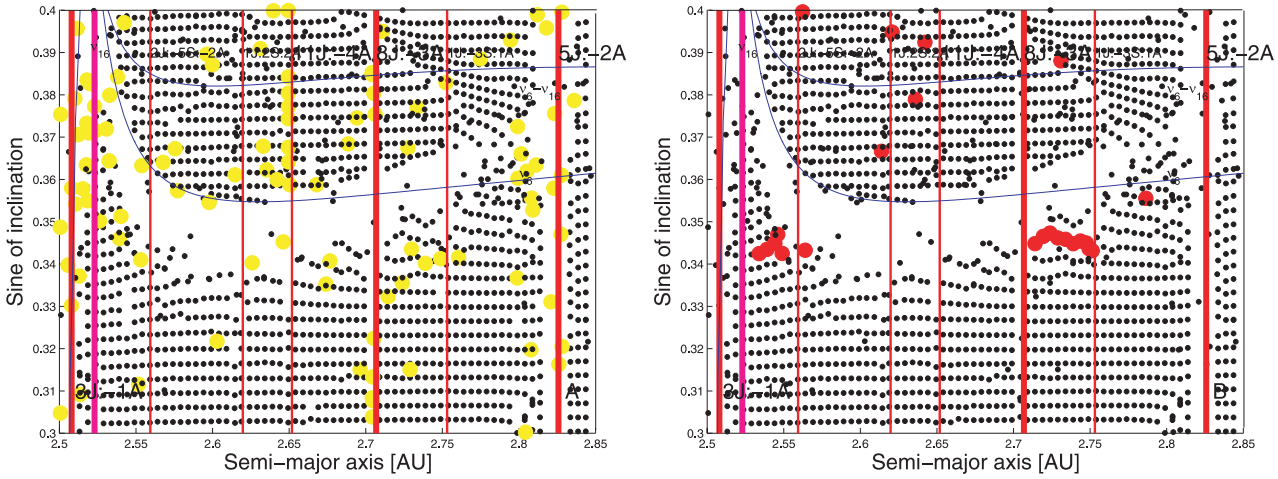

Figure 8. Panel A: Lyapunov times projected in the space of averaged (a, $\sin i$) elements. Yellow circles display Lyapunov times smaller than 20 000 yr, while black dots are associated with times larger than 20 000 yr. Panel B: k_6 values in the same range of averaged (a, $\sin i$) elements. Red full dots display values of k_6 in the range $-3.5404 < k_6 < 1.6815$ arcsec yr^{-1}.

full dots). Here, we are using the wider 2.6-au criterion in order to maximize the amplitude of the chaotic layer in inclination.

As can be seen in the figure, there is a very good agreement between Lyapunov times near the ν_6 separatrix and results of the Yoshikawa model: only very few particles have values of k_6 in the right range and several of these were so much destabilized by Martian close encounters that they were lost during the length of the integration. The result is that only a few chaotic particles were visible and those match well the predictions of the Yoshikawa model. This result, in our opinion, should explain the absence of the chaotic behaviour near the ν_6 secular resonance separatrix found in Carruba (2010b).

5 LONG-TERM STABILITY OF MINOR FAMILIES AND CLUMPS IN THE REGION

In Carruba (2010b), several small dynamical groups were identified in the region of the Pallas dynamical family. Many of these groups had a limited number of members, sometimes just large enough for the group to be considered a clump. A question left unanswered by the previous work was about the statistical significance of these groups. Were these clusters created by real collisions or were they just random association of bodies that happened to be in nearby orbits for a limited period of time? In order to estimate the statistical significance and the time-scales over which these clusters are still bound, we devised the following numerical experiment: we created two sets of clones of members of the clusters and integrated them with SWIFT-RMVSY.f, the symplectic integrator of Brož (1999), which simulates the diurnal and seasonal versions of the Yarkovsky effect. Using typical values of the Yarkovsky parameters (Carruba et al. 2003), we gave to one set of objects an inclination of the spin axis of 90°, while to the second was assigned an obliquity of −90°. No re-orientations were considered, so that the drift caused by the Yarkovsky effect was the maximum possible.

We integrated the clones of members of the classical and frequency clusters over 200 Myr in the future and 200 Myr in the past,[3] and obtained synthetic proper elements according to the definition of Knežević & Milani (2000) for the clones every 2.4576 Myr. We then re-obtained families and clumps for the set of synthetic proper elements of the clones at each time-step, using the barycentre of the clusters (Carruba 2009b, equation 7) as the first body for the family. As soon as the cluster (obtained for the values of the velocity cut-off of 160 m s^{-1} and of the frequency cut-off of 0.605 arcsec yr^{-1}, Carruba 2009b) reached the minimum number of objects for being considered a clump, the cluster was considered dispersed and a minimum limit for the dispersion time was found .

We will start by discussing the results for the classical families and clumps in the next section.

5.1 Classical groups

In Carruba (2010b), eight minor clumps were identified in the space of proper elements at a velocity cut-off of 122 m s^{-1}: a clump around (208080) 1999 VV180 in the Barcelona area, five clumps around (4203) Brucato, (18511) 1996 SH4, (36240) 1999 VN44, (70280) 1999 RA111 and (75938) 2000 CO80 in the Olympia region, a clump around (33969) 2000 NM13 in the Hansa area and a clump around (40134) 1998 QO53 in the region of the Gallia family. For simplicity, in this section and in the next section, we will refer to the dynamical groups by their first body number only, omitting the name.

Fig. 9 displays the number of members of the integrated (4203) clump (panel A) and of the (40134) clump (panel B), as a function of time. The horizontal black line shows the limit ($N_{\rm min} = 12$) for a group to be recognized as a clump, while the horizontal red line in panel B shows the limit for a group to be classified as a family ($N_{\rm fam} = 30$), at a velocity cut-off of 122 m s^{-1}. The vertical line separates the backward and forward integrations. The higher the time

[3] Concerning the integration in the past, we should caution the reader that integrations with the Yarkovsky effect are not conservative and therefore technically speaking not time-reversible. Backward integrations are, however, interesting from a statistical point of view, since they allow to increase our sample of integrated objects.

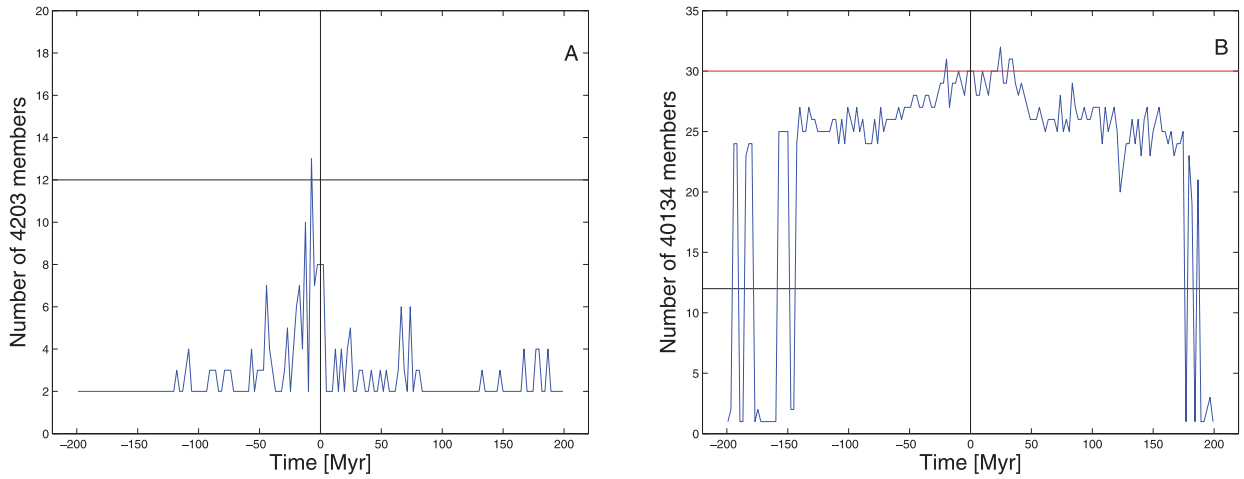

Figure 9. The number of members of the integrated (4203) clump (panel A) and of the (40134) clump (panel B), as a function of time.

Table 1. Detectability times over 400 Myr for classical groups in the Pallas region.

Name	T ($N > 12$) (Myr)
(208080)	14.75
(4203)	1.25
(18511)	7.38
(36240)	2.46
(70280)	12.30
(75938)	51.61
(33969)	15.98
(40134)	173.26

the integrated clumps have more than $N_{\rm min}$ members (hereinafter detectability time), the more likely that they are real collisional groups rather than statistical flukes. The (4203) and (40134) groups have the lowest and highest detectability times with $N > N_{\rm min}$, respectively, taken as the average of the detectability times over the length of the forward and backward integrations. Detectability times for all the classical clumps in the region are given in Table 1.

None of the members of the clumps in the area seems to be currently interacting with non-linear secular resonances (the Hansa families interact with the $\nu_6 - \nu_{16}$ resonance and the Pallas ones with the $2\nu_6 - \nu_5 + \nu_{16}$ resonance). Of all the clumps, those around (40134), (75938), (33969), (208080) and (70280) have the largest detectability time and should be considered reasonable candidates for groups originating from collisional events. The three other clumps have very short detectability times and may be considered statistical flukes. The fact the they are englobed by larger groups in the $(n, g, g + s)$ frequency domain [(4203), (18511) and (70280) are all part of the frequency (4203) family (Brucato family), while (75938) and (36240) form the larger frequency clump around (36240)] seems to confirm this analysis. More details on this subject will be given in Section 5.2.

5.2 Frequency groups

In the $(n, g, g + s)$ domain, two frequency clumps were identified in Carruba (2010b): one around (36240) 1999 VN44 in the Olympia area and the other around (82426) 2001 NB20 in the Hansa area. The group around (4203) Brucato in the Olympia area was a family in the frequency domain. These groups were identified with a cut-off of 0.605 arcsec yr^{-1}. At this cut-off, a group should have at least 22 members to be identified as a clump and 55 members to be recognized as a family.

The clump in the Hansa area around (82426) quickly dispersed after 1.25 Myr and should not be considered statistically significant. More interesting was the case of the Olympia groups. The (36240) frequency clump that englobes the (75938) and (36240) classical groups was observable as a family for a large interval of time [but not at $T = 0$ Myr, see Fig. 10 (panel A)] and only dispersed for $T = 150$ Myr. It is observable in the past for times up to -180 Myr and it has a detectability time, $N > N_{\rm min}$ (see Section 5.1), of 149.92 Myr. It should therefore be considered as a statistically robust group.

The (4203) frequency family that englobes the (4203), (18511) and (70280) classical clumps, finally disperses for $T = \pm 330$ Myr (Fig. 10, panel B), and it has a detectability time, over 200 Myr, of 129.03 Myr. It is the largest dynamical group observed in the Olympia region and it should be considered a reliable dynamical family. Results are summarized in Table 2.

6 CONCLUSIONS

In this work, we studied the dynamical evolution of asteroids in the region of the Pallas dynamical family. Amongst other things:

(i) We investigated the long-term stability of asteroids at high eccentricity ($e > 0.31$). These objects are unstable because of encounters with Mars on time-scales of up to 340 Myr. Local background asteroids are currently the major source of high-eccentricity objects, but Barcelona family members will become the dominant source in about 250 Myr;

(ii) We studied the problem of asteroids in the proximity of the ν_6 secular resonance separatrix with analytical (Yoshikawa 1987) and numerical tools. Asteroids with $-3.5404 < k_6 < 1.6815$ arcsec yr^{-1}, where $k_6 = b - \nu_6$, b being a coefficient that roughly corresponds to the pericentre precession frequency g,[4] are forced to reach values of pericentres low enough to allow them to experience deep close encounters with Mars. The fact that this chaotic layer has a very limited amplitude in inclination (only $0\overset{\circ}{.}0313$) explains why very

[4] See Yoshikawa (1987) and Carruba (2010) for the exact definition of b.

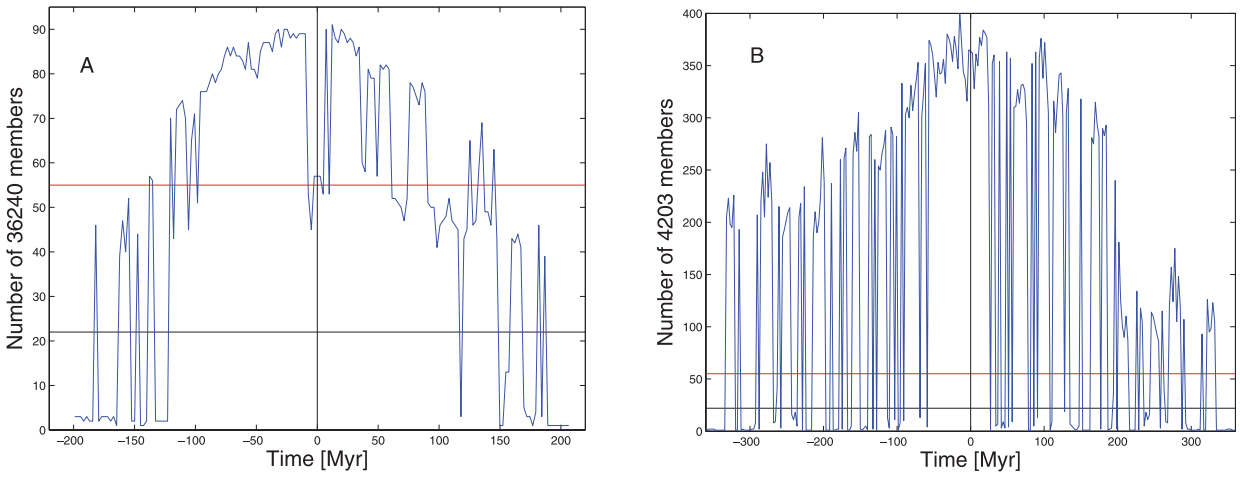

Figure 10. The number of members of the integrated (36240) clump (panel A) and of the (4203) frequency family (panel B), as a function of time.

Table 2. Detectability times over 400 Myr for frequency groups in the Pallas region.

Name	T ($N > 22$) (Myr)
(4203)	129.03
(36240)	149.92
(82426)	1.25

limited chaotic behaviour was observed near the ν_6 separatrix in Carruba (2010b);

(iii) We investigated the dynamical evolution when the Yarkovsky effect is considered of minor clumps and families identified in Carruba (2010b) in the domains of proper elements and frequencies. We find that none of the minor clumps obtained in Carruba (2010b) is currently interacting with non-linear secular resonances in the region. The classical clumps around (40134) 1998 QO53, (75938) 2000 CO80, (33969) 2000 NM13, (208080) 1999 VV180 and (70280) 1999 RA111 have large detectability times and could be considered reasonable candidates for groups originating from collisional events. We confirm the presence of the (4203) Brucato family observable in the space of proper frequencies (n, g, $g + s$) that has the largest detectability time of all groups in the region.

We believe that this work should have answered some of the questions raised by Carruba (2010b), but as often in science, many other questions are left unanswered. For instance, what is the long-term effect that the $2\nu_6 - \nu_5 + \nu_{16}$ secular resonance and several quasi-resonances with Jupiter and Ceres have on the Pallas family members? Also, is the Brucato frequency family a real collisional group or, as suggested by the presence of asteroids belonging to both the C- and X-type complexes, just an agglomeration of nearby objects? Our current analysis suggests that the family is dynamically stable, so are some of the members of the Brucato family that belong to the C- or X- complexes interlopers? No information is currently available to draw a final conclusion on these issues that remain, in our opinion, interesting subjects for future work.

ACKNOWLEDGMENTS

We are grateful to the reviewer of this paper, Ricardo Gil-Hutton, for his careful revision and comments that significantly improved the quality of this paper. We would like to thank the São Paulo State Science Foundation (FAPESP) that supported this work via the grant 06/50005-5 and the Brazilian National Research Council (CNPq, grants 302183/2008-6 and 473345/2009-9).

REFERENCES

Bretagnon P., 1974, A&A, 30, 141
Brož M., 1999, Thesis, Charles Univ., Prague, Czech Republic
Carruba V., 2009b, MNRAS, 398, 1512
Carruba V., 2010a, MNRAS, 403, 1834
Carruba V., 2010b, MNRAS, 408, 580
Carruba V., Michtchenko T., 2007, A&A, 475, 1145
Carruba V., Michtchenko T., 2009, A&A, 493, 267
Carruba V., Burns J. A., Bottke W., Nesvorný D., 2003, Icarus, 162, 308
Carruba V., Roig F., Michtchenko T., Ferraz-Mello S., Nesvorný D., 2007, A&A, 465, 315
Farinella P., Vokrouhlický D., Hartmann W. K., 1998, Icarus, 132, 378
Gronchi G. F., Milani A., 1999, A&A, 341, 928
Guillens S. A., Vieira Martins R., Gomes R. S., 2002, AJ, 124, 2322
Knežević Z., Milani A., 2000, Celest. Mech. Dyn. Astron., 78, 17
Levison H. F., Duncan M. J., 2000, AJ, 120, 2117
Nesvorný D., Roig F., Gladman B., Lazzaro D., Carruba V., Moth-Diniz T., 2008, Icarus, 183, 85
Thomas F., Morbidelli A., 1996, Celest. Mech., 64, 209
Yoshikawa M., 1987, Celest. Mech., 40, 233

This paper has been typeset from a TEX/LATEX file prepared by the author.

8

A família de Tina

Entre as famílias identificadas em Carruba (2010b), aquela de Tina foi a de maior interesse. A família de Tina é caracterizada pelo fato de todos seus atuais membros estarem em configurações anti-alinhadas da ressonância ν_6. Isto significa que a diferença entre o argumento do pericentro do asteroide e de Saturno oscila em volta de 180°. Asteroides nesta configuração não podem chegar a valores de excentricidade suficientes para cruzar a órbita de Marte e estão, portanto, em uma ilha de estabilidade dinâmica de novo tipo. Quantidades preservadas da ressonância ν_6 permitem estimar com maior precisão a entidade do campo de ejeção de velocidades desta família, que, de acordo com simulações Monte Carlo da evolução do semi-eixo maior devido aos efeitos Yarkovsky e YORP, deveria ter uma idade de 170^{+20}_{-30} Myr. Estima-se que a família deveria se dispersar em tempo-escala de 150-200 Myr.

A seguir apresentamos o artigo, que foi publicado em Monthly Notices of the Royal Astronomical Society em 2011, volume 412, pp. 2040-2051.

Monthly Notices
of the
ROYAL ASTRONOMICAL SOCIETY

Mon. Not. R. Astron. Soc. **412,** 2040–2051 (2011) doi:10.1111/j.1365-2966.2010.18083.x

On the first ν_6 anti-aligned librating asteroid family of Tina

V. Carruba[1⋆] and A. Morbidelli[2]

[1]*UNESP, Univ. Estadual Paulista, Grupo de dinâmica Orbital e Planetologia, Guaratinguetá, SP 12516-410, Brazil*
[2]*Université de Nice Sophia Antipolis, CNRS, Observatoire de la Côte d'Azur, Laboratoire Cassiopée, BP 4229, 06304, Nice Cedex 4, France*

Accepted 2010 November 23. Received 2010 November 18; in original form 2010 August 27

ABSTRACT

Asteroid families are groups of bodies identified in the space of proper elements or of frequencies that share a common origin in the collisional break-up of their progenitors. Their dynamical evolution is shaped by the interaction with the local web of mean-motion and secular resonances, and by non-gravitational effects, such as the 'Yarkovsky' and 'Yarkovsky–O'Keefe–Radzievskii–Paddack' (YORP) effects. Thus, obtaining information on their age and original ejection velocity field is generally a difficult task. Recently, two families were found to have a large fraction of members in the non-linear secular resonance z_1: the Agnia and Padua families. Conserved quantities of the $z_1$resonance allowed for a more precise determination of their ages and ejection velocity fields. So far, however, no family was known to be in a linear secular resonance, such as the ν_6 resonance, although individual asteroids were known to be in ν_6 anti-aligned librating states. The ν_6 resonance occurs when there is a commensurability between the frequency of precession of the pericentre of an asteroid and that of Saturn. As a consequence, in librating states, the resonant argument oscillates around a stable point. In anti-aligned librating states, the resonant argument oscillates around the stable point at 180°. Here we show that the newly identified Tina family is characterized by having all its members in such a state, making it the only family in the asteroid belt known to be completely embedded in a secular resonance configuration. This rare dynamical configuration limits the maximum eccentricity of Tina members, preventing them from experiencing Martian close encounters and forming a stable island of a new dynamical type. The current dispersion of asteroid resonant elements suggests that the family should be at least 2.5 Myr old, while Monte Carlo simulations including the Yarkovsky and YORP effects suggest that the Tina family should be 170^{+20}_{-30} Myr old.

Key words: celestial mechanics – minor planets, asteroids: general.

1 INTRODUCTION

Asteroid families are groups of small bodies that share a common collisional origin. They form clusters in the space of proper elements (a, e, $\sin(i)$) (semimajor axis, eccentricity and sine of the inclination, Zappalà et al. 1995; Bendjoya & Zappalà 2002) or proper frequencies ($n, g, g + s$) [mean motion (n) and frequency of precession of the argument of the pericentre (g) and of the longitude of the node (s), Carruba & Michtchenko 2007, 2009]. Sometimes resonant proper elements are also used, as for the Schubart and Hilda families in the 3:2 mean-motion resonance with Jupiter (denoted by $3J{:}-2A$ hereinafter, Brož & Vokrouhlický 2008), and for the youngest asteroid families, one may also use the osculating elements (for instance, the cases of the Datura and Emilkowalski families, Nesvorný & Vokrouhlický 2006). The current orbital locations of family members are, however, different from the one observed at the family formation. Family members interacted with the local web of mean-motion and secular resonances, migrated due to the effect of non-gravitational forces, such as the Yarkovsky and Yarkovsky–O'Keefe–Radzievskii–Paddack (YORP) effects, and, in some cases, experienced close encounters with massive asteroids. Since the current orbital position depends on both the original location of family members and the time when the asteroid evolved since the family formation, obtaining reliable estimates for the family ages is quite difficult and subject to a degree of uncertainty.

Secular resonances occur when there is a commensurability between the precession frequency of the asteroid longitude of the pericenter g or node s and the precession frequencies of the planets g_2, g_3, g_4, g_5, g_6, g_7, g_8 and s_2, s_3, s_4, s_6, s_7, s_8, where the suffixes 2, 3, 4, 5, 6, 7 and 8 stand for Venus, Earth, Mars, Jupiter, Saturn, Uranus and Neptune, respectively. They are distinguished between linear resonances, such as the ν_6 resonance, which occurs when $g - g_6 = 0$, the ν_5 resonance ($g - g_5 = 0$) and the ν_{16} resonance

⋆E-mail: vcarruba@feg.unesp.br

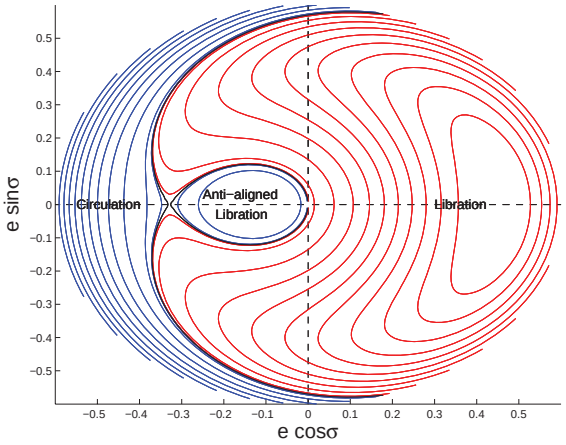

Figure 1. A diagram of equi-Hamiltonian curves for $a = 2.6$ au in the $(e\cos\sigma, e\sin\sigma)$ plane, computed for $i = 18.^{\circ}8$ (at $e = 0$) using the analytical model of Morbidelli & Henrard (1991). Circulating orbits are shown in blue, while librating orbits are shown in red. The black line displays the separatrix.

$(s - s_6 = 0)$, and non-linear ones, such as the $z_1 = \nu_6 + \nu_{16}$ resonance $(g - g_6 + s - s_6 = 0)$, that are in many cases combinations of the linear resonances (Williams 1969; Milani & Knežević 1994). Among linear secular resonances, the ν_6 resonance is among the most prominent ones in the asteroid belt, being very effective in increasing asteroid eccentricities to Mars-crossing and Earth-crossing levels.

Several asteroid families interact with secular resonances, but so far only few groups were found to have a large fraction of their members in resonant configurations. For example, two families – Agnia (Vokrouhlický et al. 2006b) and Padua (Carruba 2009a) – have been found to have the majority of their members librating in the z_1 resonance. Constraints provided by conserved quantities of this resonance allowed to obtain accurate estimates of the family ages and original ejection velocity fields. Another clump of objects around (6246) Koromotoru was found (Carruba 2009b, 2010a) to reside inside the $\nu_5 + \nu_{16}$ secular resonance. Apart from these families, only isolated objects (Froeschlé & Scholl 1987; Morbidelli & Henrard 1991) were known to be in anti-aligned librating states inside linear secular resonances, such as the ν_6 resonance. In the dynamics of the ν_6 resonance, two classes of orbits are possible in phase space: circulators and librators. For librators, the resonant argument $\sigma = \varpi - \varpi_S$ (where ϖ is the longitude of the pericentre of the asteroid and ϖ_S that of Saturn) oscillates around a fixed value. For circulating orbits, the resonant argument varies over 360°. The regions of libration and circulation are separated by a critical curve, the separatrix, originating from the unstable point at $\sigma = 180^{\circ}$ (see Fig. 1). The critical curve makes a loop around a stable point at $\sigma = 180^{\circ}$ and, inside this loop, for orbits that do not cross the origin, a different class of libration is possible: the anti-aligned libration.

Anti-aligned librators, while characterized by a libration of the resonant argument around the stable point at $\sigma = 180^{\circ}$, are actually circulating orbits that rotate in the opposite direction of external circulators. Such orbital behaviour is predicted by analytical models of the ν_6 resonance (Morbidelli & Henrard 1991) for orbits at 2.6 au, near the location of the Tina family. The reader may note from Fig. 1 that the fact that anti-aligned librating orbits do not cross the separatrix sets an upper bound on the maximum value of eccentricity achievable by bodies on these orbits, so protecting them from close encounters with terrestrial planets.

In this paper, we show that the newly discovered Tina family (Carruba 2010b) is characterized by the fact that all its known members are currently in anti-aligned librating states around $\sigma = 180^{\circ}$. It is therefore the first case of the ν_6 anti-aligned librating family and its peculiar nature can be used to set constraints on the family age (see Section 6.1).

This paper is structured as follows. In Section 2, we discuss the peculiar resonant nature of the Tina family. In Section 3, we obtain synthetic proper elements for the ν_6 resonance and in Section 4, we show numerical results that map the region of anti-aligned librating orbits in the vicinity of the Tina family. Section 5 discusses the conserved quantities of the ν_6 resonance and how these can be used to set constraints on the original ejection velocities of Tina members. The evolution of family members under the Yarkovsky force is also discussed in this section. Section 6 deals with constraints on the family age that can be obtained by virtue of the resonant dynamics or by using Monte Carlo simulations. Section 7 discusses the case of (759) Vinifera and addresses why we do not observe any family around this ν_6 anti-aligned librator. Finally, in Section 8, we present our conclusions.

2 THE RESONANT NATURE OF THE TINA FAMILY

Recently, Carruba (2010b) computed synthetic proper elements (Knežević & Milani 2000, 2003) for highly inclined [$\sin(i) > 0.3$] numbered and multiopposition objects in the region of the Pallas and Hansa families. Based on these results, a new family in the space of proper elements (a, e, $\sin(i)$) and in the space of proper frequencies (n, g, $g + s$) was identified around (1222) Tina for the first time.

Fig. 2 shows an (a, $\sin(i)$) projection of the members of the family, as identified from the clustering of proper elements (hereinafter the 'classical family', shown as full blue dots) or from the clustering of frequencies (hereinafter the 'frequency family'; we show in green the members of the Tina frequency family that do not belong to the classical one). The black dots refer to other asteroids in the region. The vertical red lines display the location of mean-motion resonances, while the blue line shows the centre of the ν_6 resonance, computed for the eccentricity value of (1222) Tina by using the second-order and fourth-degree secular perturbation theory of Milani & Knežević (1992). We warn the reader that this secular

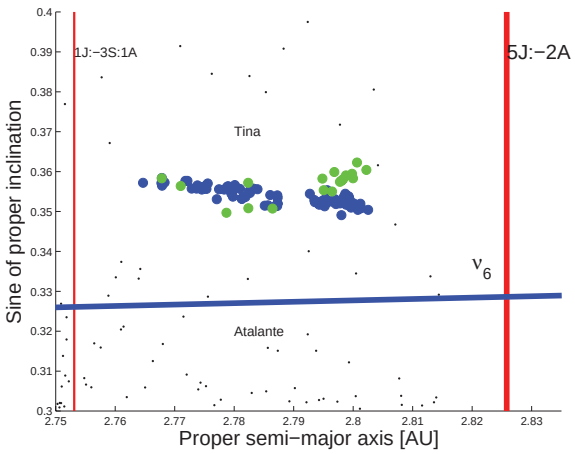

Figure 2. An (a, $\sin(i)$) projection of classical (full blue dots) and frequency (full green dots) members of the Tina families.

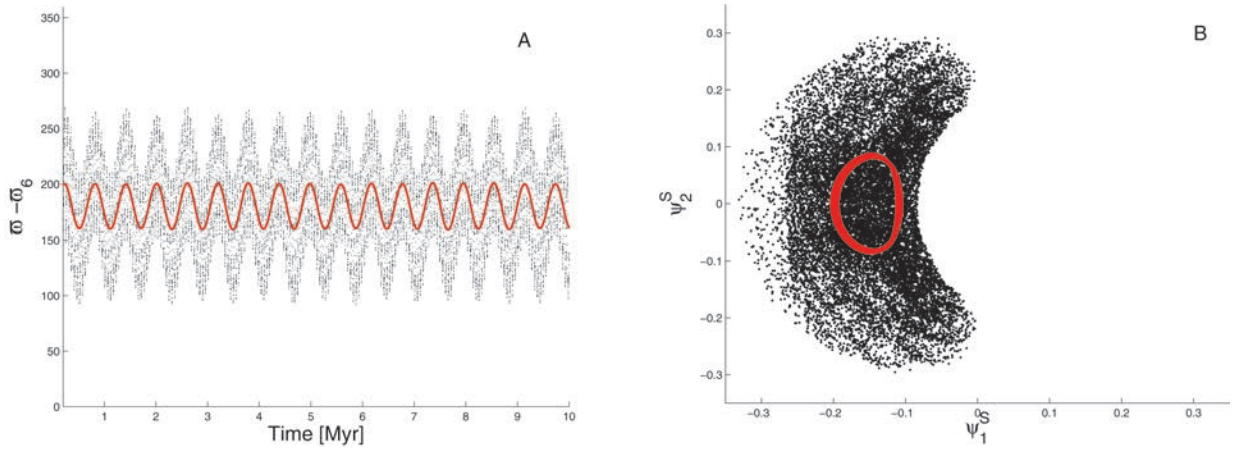

Figure 3. Panel A: the time-evolution of the resonance argument $\sigma = \varpi - \varpi_6$. The line shows the argument after being digitally filtered so as to remove all frequencies corresponding to periods less than 300 000 yr. Panel B: orbital evolution in the polar plane (ψ_1^S, ψ_2^S). The resonant elements (ψ_1^S, ψ_2^S) were also digitally filtered with the same procedure (red points).

perturbation theory loses accuracy at high inclination and close to mean-motion resonances. Thus, in Fig. 2, and in the subsequent plots, we report the location of the ν_6 resonance given by this theory just as a qualitative indication, but we do not expect it to match the distribution of the Tina family members.

It has been known since the late 1980s (Froeschlé & Scholl 1987) that (1222) Tina and the nearby asteroid, (759) Vinifera, are in an anti-aligned librating state of the ν_6 resonance. Only recently, however, fainter members of the Tina family were discovered (Carruba 2010b), while no family has yet been identified near (759) Vinifera (see Section 7). To confirm the anti-aligned librating nature of the family members, we integrated all its known 90 members of the classical and frequency families with a Burlisch–Stoer integrator modified to filter orbital elements so to eliminate all frequencies corresponding to period less than 700 yr (Brož 1999). The initial conditions of the test particles, such as inclination, longitudes of the node and pericentre, in this and all other simulations in this paper are referred to the invariable plane of the Solar system. Fig. 3 (panel A) shows the time-behaviour of the resonant argument σ for (1222) Tina. To emphasize the long-time behaviour of the angle and eliminate all short-period perturbations such as the g_5 frequency in the precession of Saturn's pericentre, the argument σ was digitally filtered so to eliminate all frequencies corresponding to periods less than 300 000 yr (see red curve, Carruba et al. 2005).

The reader may note how the resonant argument oscillates in a sinusoidal way around 180°, which is the typical behaviour for an anti-aligned oscillator. Fig. 3 (panel B) shows the orbital evolution in a polar diagram, with axes (ψ_1^S, ψ_2^S) defined as

$$\psi_1^S = \sqrt{2(1-\sqrt{1-e^2})}\cos(\varpi - \varpi_6) \quad (1)$$

and

$$\psi_2^S = \sqrt{2(1-\sqrt{1-e^2})}\sin(\varpi - \varpi_6), \quad (2)$$

respectively, where e is the asteroid eccentricity. Charlier (1902) introduced these variables (which are asymptotically equal to $e\cos\sigma$ and $e\sin\sigma$ for small e) in his theory for secular resonances. Again, black dots show the evolution with orbital elements filtered up to a period of 700 yr, while the curve shows the evolution with elements filtered up to a period of 300 000 yr. The red curve describes an oval, consistent with an anti-aligned libration (compare with Fig. 1), with period of about 50 000 yr, and the same behaviour is shared by all the 90 Tina family members. Just two other asteroids in the region, (215209) 2000 SL39 and (2002) PM7, but not connected to the family, are on anti-aligned librating orbits. While the amplitude of libration of the oscillation of the resonant argument varies among members with a maximum of 230° for 2009 NG (a member of the frequency family but not of the classical family), we found that none of the Tina asteroids was on a ν_6 circulating orbit for all the length of the integration (20 Myr).

The resonant nature of the Tina family prompts us to compute appropriate proper elements for its members with the procedure discussed in the next section.

3 SYNTHETIC PROPER ELEMENTS OF THE ν_6 RESONANCE

Synthetic proper elements are usually obtained numerically by performing a 10-Myr numerical integration (Knežević & Milani 2000). The proper semimajor axis a is then computed by averaging the osculating elements over a 2 Myr period with a running box, so as to produce 10 data points. The mean result is the proper semimajor axis and the standard deviation yields an estimate of the uncertainty of the proper semimajor axis with this procedure.

The procedure is different for the proper eccentricity e and precession frequency of the pericentre g, and for the proper inclination i and precession frequency of the longitude of the node s. The equinoctial elements $(e\cos(\varpi), e\sin(\varpi))$ and $(\sin i/2\cos(\Omega), \sin i/2\sin(\Omega))$ are Fourier analysed so as to determine the frequencies g and s associated to the largest amplitudes in the spectrum. The amplitudes associated with such frequencies are identified, respectively, with the proper eccentricity and with the sine of half the proper inclination. For a vast majority of asteroids, the frequencies of largest amplitude are the proper frequencies. However, some asteroids such as (480) Hansa are characterized by forced eccentricities larger than the free (proper) eccentricities. For these asteroids, the frequency associated with the largest amplitude in the spectrum may be one of the planetary frequencies, such as g_5 or g_6. To deal with such cases, Knežević & Milani (2000) exclude from the Fourier spectra of the equinoctial elements the terms associated with the planetary frequencies.

This procedure is not appropriate for the Tina family members, since they are currently in the ν_6 resonance and therefore their proper frequency g is very close to g_6. To deal with the special

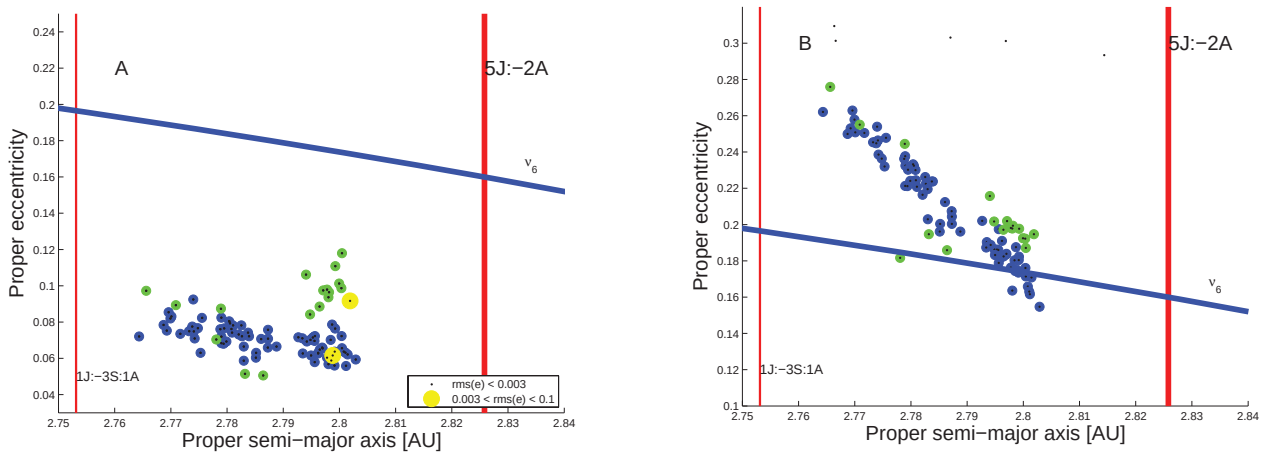

Figure 4. Panel A: a proper (a, e) projection of AstDyS asteroids in the region of the Tina family. Proper elements were obtained with the first method described in the text. Yellow circles display asteroids with standard deviation on e between 0.003 and 0.1. Panel B: a proper (a, e) projection of the same asteroids, but for proper elements obtained with the second method.

nature of the Tina asteroids, we can introduce two kinds of resonant proper elements. In the first case, we compute the resonant equinoctial elements ($e\cos(\varpi - \varpi_6)$, $e\sin(\varpi - \varpi_6)$ filtered so as to eliminate all frequencies corresponding to periods of 300 000 yr and analyse the Fourier spectra of these new quantities. The second frequency of largest amplitude (the first is associated with the forced eccentricity of Tina asteroids) is identified with the new proper frequency (g_σ) and the amplitude associated with this frequency is identified with the new proper (or free) 'eccentricity'. For orbits in anti-aligned libration, as Tina's, g_σ is the frequency of libration and the proper eccentricity is the amplitude of libration. But, in principle, the proper eccentricity and g_σ can be defined for any orbit, even if their geometrical meaning is different. Errors on the proper e and g_σ frequencies are computed with the same method used for the traditional synthetic proper elements, while the other proper elements are still computed with the Knežević & Milani (2000) approach.

Fig. 4 (panel A) shows an (a, e) projection of asteroids in the region of the Tina family, with errors on the resonant proper e. Following the approach of Carruba (2010b), we consider 'stable' asteroids whose proper eccentricities have errors (hereinafter standard deviation-rms) smaller than 0.003. Only two asteroids in the region have unstable elements according to this definition and none of them has pathological values of rms(e) > 0.1. The blue line displays the location of the centre of the ν_6 resonance analytically computed for the inclination of (1222) Tina using the second-order and fourth-degree secular perturbation theory of Milani & Knežević (1992), which does not fit the distribution of the family very well. The other symbols have the same meaning as in Fig. 2. Maximum osculating eccentricities for anti-aligned asteroids are quite smaller than the minimum value necessary to experience close encounters with Mars ($e = 0.4$, obtained by equating the pericentre of an asteroid with Tina's semimajor axis with Mars' apocentre and by solving for the asteroid eccentricity).

A second approach for obtaining resonant proper elements is similar to the one used for asteroids in mean-motion resonances with Jupiter, such as the Hilda population (Brož & Vokrouhlický 2008). At the simplest level of perturbation theory, the ν_6 resonance is characterized by the conservation of the quantities $K_1 = \sqrt{a}$ and $K_2 = \sqrt{a(1-e^2)}(1-\cos i)$ (Morbidelli 2002). Obviously, K_1 and K_2 are conserved only when the sole resonant perturbations are taken into account. Non-resonant effects introduce oscillations with small amplitudes and short periods, which are removed by digital filtering of the numerical output. Here, we introduce a modified quantity $K_2' = K_2/K_1 = \sqrt{1-e^2}(1-\cos i)$ that is conserved by virtue of the conservation of K_1 and K_2. The conservation of the K_1 integral implies that the mean value of the time-series of the semimajor axis may be taken as a first proper element. The conservation of K_2' implies that oscillations of eccentricities are correlated with oscillations of inclination. One can therefore define as proper eccentricity the value of e when $\sigma = \varpi - \varpi_6 = 180^\circ$ and $\frac{\mathrm{d}\sigma}{\mathrm{d}t} > 0$, that is, the maximum value of e during the resonant cycle (Brož & Vokrouhlický 2008). Values of the proper inclination would then be obtained using the conservation of K_2'. Since this method does not allow to estimate proper frequencies, for the purpose of obtaining frequency families, we will use the elements obtained with the first method in this paper.

We applied this procedure after filtering the elements ($e\cos\sigma$, $e\sin\sigma$) so as to eliminate all frequencies corresponding to periods less than 300 000 yr, which is enough to remove short-period terms, but not the terms corresponding to periods of $\simeq$700 000 yr associated with the changes in the ν_6 libration amplitudes, and results are shown in Fig. 4 (panel B). Values of eccentricities obtained with the second method are in general shifted by 0.14 relative to those computed with the first method. This is caused by the fact that in the second method, the proper eccentricity is taken as the maximum eccentricity during the libration cycle that corresponds to the sum of the eccentricity of the centre of libration (forced eccentricity) plus the radius of the libration cycle (free eccentricity). Since the first method gives as proper eccentricity the free eccentricity only, the difference between the two values of proper eccentricities is associated with the forced eccentricity of each object.

Using the two new sets of resonant proper elements and proper frequencies, we performed a new search for the members of the Tina family, using the same cut-off distance as used in Carruba (2010b). We found no difference in membership between the families found with resonant and non-resonant proper elements.

4 NUMERICAL EXPLORATION

In this section, we study the dynamics of the family and in its vicinity, using numerical tools, also including the effects of non-gravitational forces. We start by computing dynamical maps in the vicinity of the Tina family.

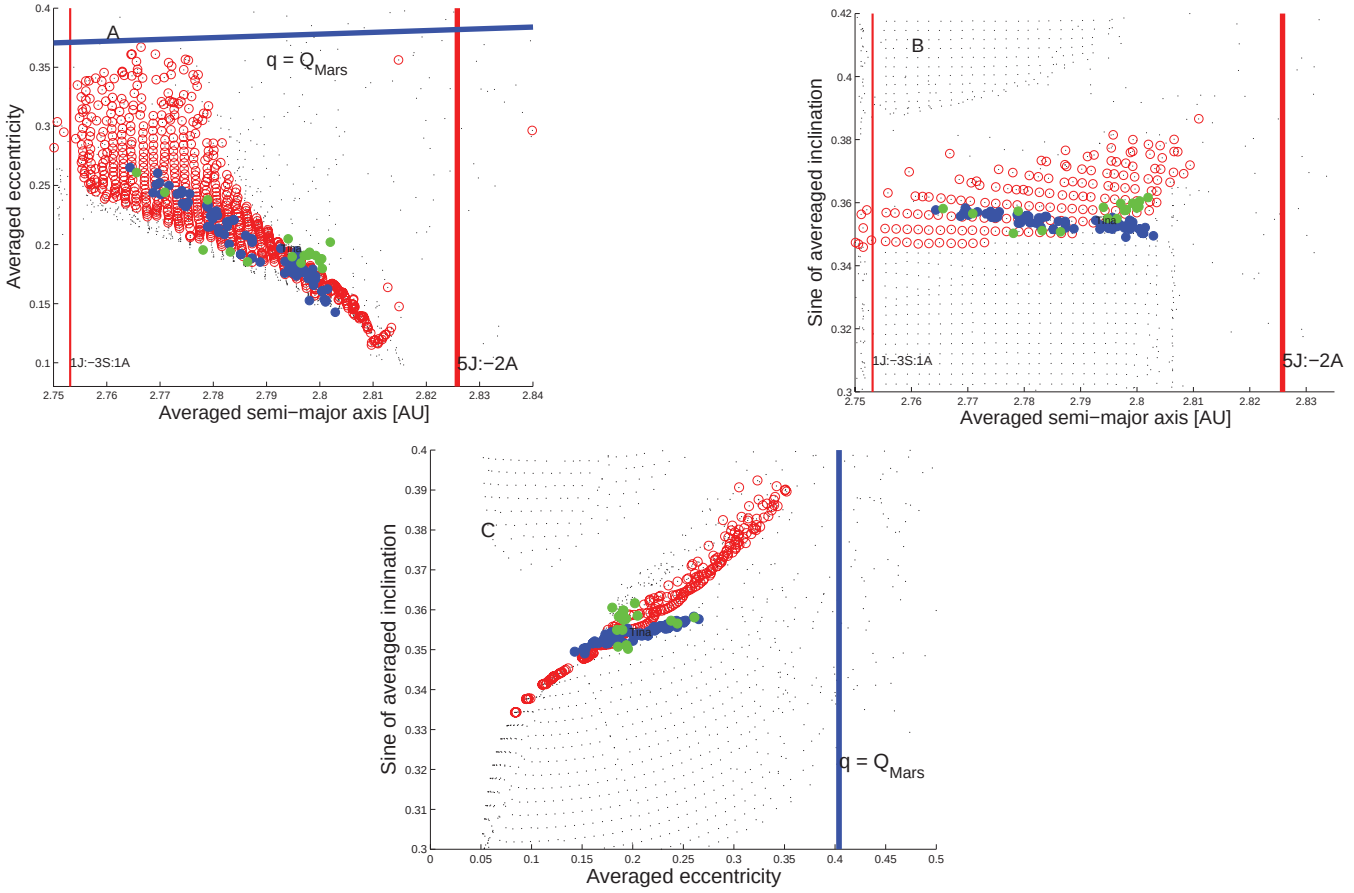

Figure 5. An (a, e) (panel A), (a, sin(i)) (panel B) and (e, sin(i)) (panel C) projection of averaged elements for test particles in the region of the Tina family.

4.1 Dynamical maps

To gain further insight into the distribution of mean-motion and secular resonances in the region, and on the orbital location of the ν_6 anti-aligned librators, we integrated with SWIFT_MVSF [the symplectic integrator of the original SWIFT package (Levison & Duncan 1994), modified by Mira Brož (1999) to account for online filtering of the osculating elements] 2400 particles in the (a, e) plane, 1600 particles in the (a, sin(i)) plane and 2400 particles in the (e, sin(i)) plane, over 20 Myr. We used a grid of 40 by 60 particles in the (a, e) plane, 40 by 40 particles in the (a, sin(i)) plane and 60 by 40 particles in the (e, sin(i)) plane, with a resolution of 0.002 au in a, 0.01 in e and 0.°2 in i. Our particles covered a range 2.75–2.83 au in a, 0–0.59 in e and 16.°0–23.°8 in i. The initial values of sin(i), e and a [for the simulations in the (a, e), (a, sin(i)) and (e, sin(i)) planes, respectively], and the initial angular elements Ω, ω and λ of the test particles were set equal to those of (1222) Tina at J2000.

Fig. 5 (panel A) displays the semimajor axis and eccentricity of the test particles averaged over the numerical simulation. Averaged elements are not constants of the motion, unlike the proper elements, but are also much simpler to compute for chaotic orbits, and can still provide qualitative insight into the local dynamics (Carruba 2009b). Red circles in the figure denote particles in anti-aligned libration and black dots denote the other particles. We do not plot any symbol for particles that did not survive for the full integration time-scale. Thus, strongly unstable regions appear empty in such a dynamical map. The red vertical lines show the location of mean-motion resonances in the region and the blue line shows the location of orbits with $q = Q_{\rm Mars}$. The full blue and green dots show the location of members of the Tina classical and frequency families, respectively. Real family members other than (1222) Tina are reported in this figure just for a qualitative comparison with the dynamical map, since their initial angles Ω, ω, M and i are not the same as those used for the map.

As can be seen in the figure, the vast majority of orbits in the region that survived the integration are anti-aligned librating particles (the red circles dominate in number over the black dots). This is due to the fact that, for anti-aligned librators, the maximum value that the eccentricity can reach over a libration cycle is small. Instead, circulating and librating orbits can easily reach Mars-crossing eccentricity values and be removed. We believe that the mechanism provided by the anti-aligned librating nature of the orbits of the Tina family members may protect these asteroids for long periods from close encounters with the terrestrial planets; we will further investigate this subject in Section 4.2, where we will be dealing with non-conservative dynamics. Note that in Fig. 5 (panel A), the region covered by red circles extends almost up to the Mars-crossing boundary ($q = Q_{\rm Mars}$ in the first approximation).

Fig. 5 (panel B) displays the averaged elements of the test particles in the (a, sin(i)) plane. The gap in the distribution of dots and circles slightly above the family illustrates the region destabilized by the ν_6 resonance (see Carruba 2010a for a discussion of the destabilizing mechanism).

Finally, Fig. 5 (panel C) displays the averaged elements of the test particles in the (e, sin(i)) plane. The vertical blue line displays the value of eccentricity (0.4) needed for a particle with Tina's semi-major axis to have a pericentre equal to Mars' apocentre. Particles with $e > 0.4$ are rapidly lost because of close encounters with Mars. As can be seen in the figure, the layer of anti-aligned librators is very thin in inclination in this projection, but it still encompasses Tina and other family members.

4.2 Yarkovsky integrations

To investigate the orbital evolution over a long time-span of the members of the Tina classical and frequency families, we numerically integrated the family members with SWIFT-RMVSY, the symplectic integrator of Brož (1999) that simulates the diurnal and seasonal versions of the Yarkovsky effect. Since the Tina family seems to be made mostly of S-type asteroids (Carruba 2010b), we used values of the Yarkovsky parameters appropriate for such bodies (Carruba et al. 2003): a thermal conductivity $K = 0.001\,\mathrm{W\,m^{-1}\,K^{-1}}$, a thermal capacity $C = 680\,\mathrm{J\,kg^{-1}\,K^{-1}}$, surface density $1500\,\mathrm{kg\,m^{-3}}$, a Bond albedo of 0.1, a thermal emissivity of 0.95 and a bulk density of $2500\,\mathrm{kg\,m^{-3}}$. We used two sets of spin-axis orientations, one with an obliquity of $+90^\circ$ and the other with an obliquity of -90° with respect to the orbital plane, and periods obtained assuming that the rotation frequency is inversely proportional to the object's radius and that a 1-km asteroid had a rotation period of 5 h (Farinella, Vokrouhlický & Hartmann 1998). The radius of each body was estimated from its absolute magnitude, assuming an albedo of 0.3086, the mean value of the geometric albedo for Tina family members (Carruba 2010b).

No re-orientations were considered, so that the drift caused by the Yarkovsky effect was the maximum possible. We integrated the 182 clones of members of the classical and frequency families over 300 Myr in the future and 300 Myr in the past,[1] and computed synthetic resonant proper elements (see Section 3) for each particle every $\simeq$2.5 Myr.

Fig. 6 shows an (a, sin(i)) projection of the forward time-evolution of resonant proper elements, computed with the first approach of Section 3, of the 182 clones of members of the Tina families evolving under the action of the Yarkovsky effect. Results are similar for the backward integrations. The blue and green full dots show the orbital location of the members of the classical and frequency Tina families, respectively. The vertical lines display the location of mean-motion resonances and inclined lines display the location of secular resonances. Test particles in ν_6 anti-aligned librating states are identified by red dots and test particles in ν_6 circulating or aligned librating states are shown as black dots. Each dot corresponds to the ν_6 resonant proper elements of a particle obtained over $\simeq$2.5 Myr. As can be seen in the figure, test particles evolve towards larger or smaller values of the semimajor axis under the influence of the Yarkovsky effect, until interacting with the two main mean-motion resonances in the region: the $5J{:}-2A$ two-body and the $1J{:}-3S{:}1A$ three-body resonances with Jupiter and Saturn (two particles interacted with the $\nu_6 - \nu_{16}$ secular resonance). As an effect of their interaction with mean-motion and secular resonances, test particles exited the ν_6 anti-aligned librating region and consequently increased the orbital eccentricity above Mars-crossing

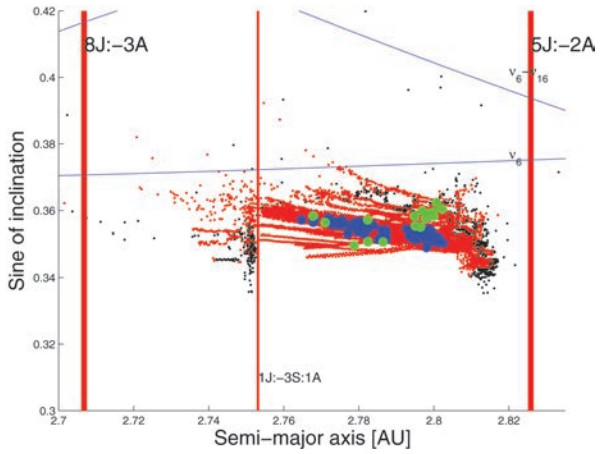

Figure 6. An (a, sin(i)) projection of the forward time-evolution of resonant proper elements of the 182 clones of members of the Tina families evolving under the action of the Yarkovsky effect.

values. All these particles were lost on time-scale of 10 Myr or less (a particle was lost in our simulation if it collided with the Sun or if it had a semimajor axis larger than 100 au), which explains why there are so few black dots, corresponding to particles alive but not in an anti-aligned librating state (see Fig. 6).

Fig. 7 shows the last stages of the time-evolution of the ν_6 resonance argument σ (panel A) and osculating eccentricity (panel B) for a clone of the asteroid (211412) (2002 VL103), a typical case of an object that left the ν_6 anti-aligned state and was lost shortly afterwards. While the asteroid was in a ν_6 anti-aligned state, the maximum eccentricity reached by the asteroid never exceeded the critical value of 0.4 to encounter Mars. As soon as the test particle escaped from this state and σ started to circulate, the eccentricity quickly increased above the Mars-crossing threshold and the particle was lost in less than 4 Myr.

To quantitatively study the longevity of the Tina family, we computed the number of family members in the space of proper elements (a, e, sin(i)) and proper frequencies (n, g, $g + s$) at each time-step. We used a distance cut-off of $122\,\mathrm{m\,s^{-1}}$ in the space of proper elements and of 0.605 arcsec $\mathrm{yr^{-1}}$ in the domain of proper frequencies, as in Carruba (2010b).

Fig. 8 displays the number of the integrated Tina classical family members as a function of time. The horizontal black line shows the limit ($N_{\mathrm{min}} = 12$) for a group to be recognized as a clump, while the horizontal red line in panel B shows the limit for a group to be classified as a family ($N_{\mathrm{fam}} = 30$), at a velocity cut-off of $122\,\mathrm{m\,s^{-1}}$. The dashed vertical line separates the results of the integration forward in time from those of the integration backward in time. The higher the time during which the integrated clump has more than N_{min} members (hereinafter detectability time), the more likely is that the clump is a real collisional family rather than a statistical fluke. The Tina family is detectable as a group for 150–200 Myr in both the forward and the backward integrations. We repeated the same analysis for the Tina frequency family and, again, the Tina family is detectable for about 200 Myr. We conclude that the Tina family seems to be a statistically robust group, with an estimated minimum dispersion time of about 150–200 Myr. The actual dispersion time may be a factor of 2 longer, since here we used extreme obliquity values (0°, 180°) that maximize the Yarkovsky effect. Constraints on the original ejection velocities and family age will be obtained in the following sections.

[1] Yarkovsky integrations are not time-reversible. Backward integrations are equivalent to forward integrations and thus double our statistics on the family spreading as a function of time.

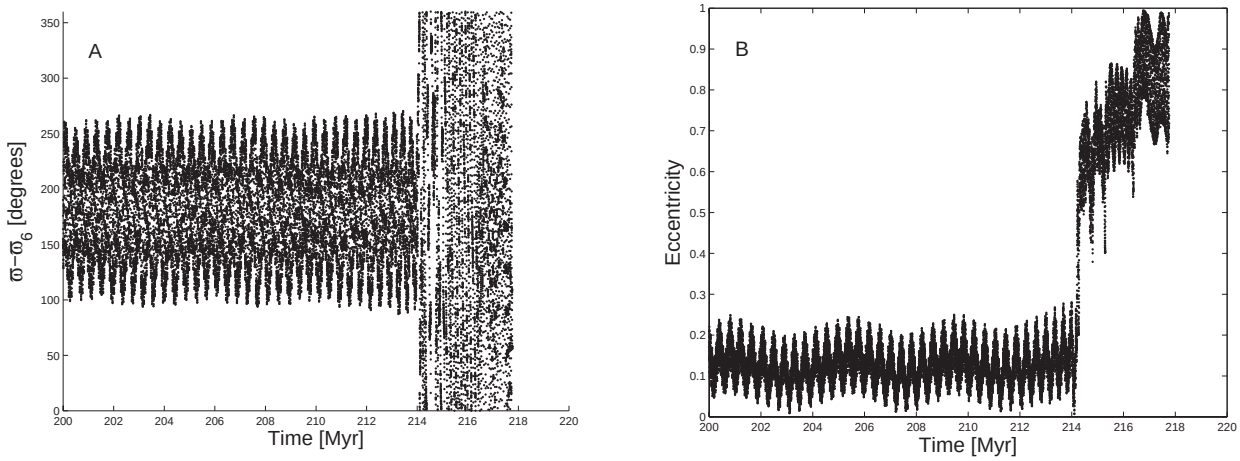

Figure 7. Panel A: the time-evolution of the osculating resonance argument $\varpi - \varpi_6$ for a clone of the asteroid (211412) (2002 VL103). Panel B: the time-evolution of the osculating eccentricity of the same test particle.

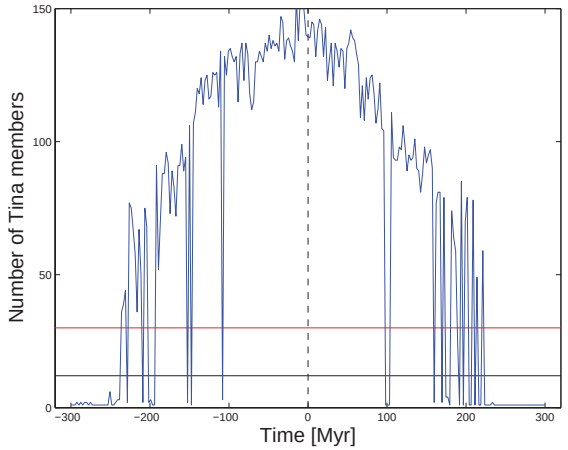

Figure 8. The number of integrated Tina family classical members as a function of time.

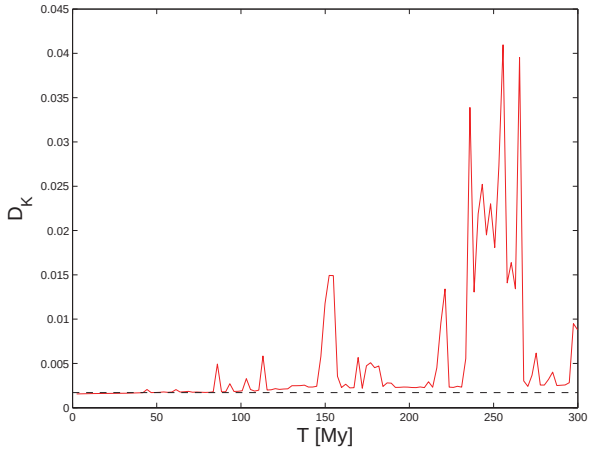

Figure 9. Value of D_K over time for the simulations that include the Yarkovsky effect. The dotted line displays the value of D_K computed on the subset of anti-aligned librating particles.

5 CONSERVED QUANTITIES OF THE ν_6 RESONANCE AND CONSTRAINTS ON THE ORIGINAL EJECTION VELOCITIES

Each resonance is characterized by one or more 'conserved quantities', which are combinations of the orbital elements that do not show any variation associated with the motion of the resonant argument. Because these quantities do not change over time, their values reflect the original values that the family had at the time of collisional break-up. This can give a valuable indication of the magnitude of the initial ejection velocity field, as shown in the cases of the families of Agnia and Padua by Vokrouhlický et al. (2006) and Carruba (2009a). Here we repeat this approach to estimate the initial ejection velocity field of the Tina family. Here, we used the conservation of the K_2' quantity (see Section 3) for the same purpose. We computed K_2' values for the Tina family members integrated under the action of the Yarkovsky effect. Because K_2' does not depend on a, we expect that this quantity is almost invariant with time under the Yarkovsky effect. To quantify the time-invariance of the values of K_2', we define a 'dispersion' D_K of the values of K_2' as

$$D_K = \frac{1}{N(N-1)} \sum_{i \neq j} [K_2'(i) - K_2'(j)]^2, \quad (3)$$

where $N = 91$ is the number of integrated bodies and $K_2'(i)$ is the conserved quantity of the ith body ($i = 1, \ldots, N$).

Fig. 9 displays the time-evolution of D_K. As expected, D_K is nearly constant for the first 40 Myr of the simulation; fluctuations from its initial value then start to occur, because of particles escaping from the ν_6 anti-aligned region. After 150 Myr, several of the integrated family members escaped from the anti-aligned configuration and therefore the values of D_K oscillate wildly. However, if we restrict the calculation of D_K on the subset of the particles that remain in the ν_6 anti-aligned configuration, then its value remains remarkably constant (see Fig. 9, dotted line). From this experiment, we conclude that the distribution of the values of K_2' is invariant, as long as family members do not escape from the resonance, even if the Yarkovsky effect is acting. This distribution therefore reflects the original distribution and can be used to estimate the initial dispersion velocity of the family. We do this estimation as follows.

First, we compute the distribution of the values of K_2' for the Tina classical members with available absolute magnitude data (Fig. 10). It is a near-Gaussian distribution with a standard deviation of $\simeq 4.3 \times 10^{-4}$. Then, we construct synthetic asteroid families, where we impose that the family members are ejected relative to the family barycentre with a velocity field that is isotropic and Gaussian,

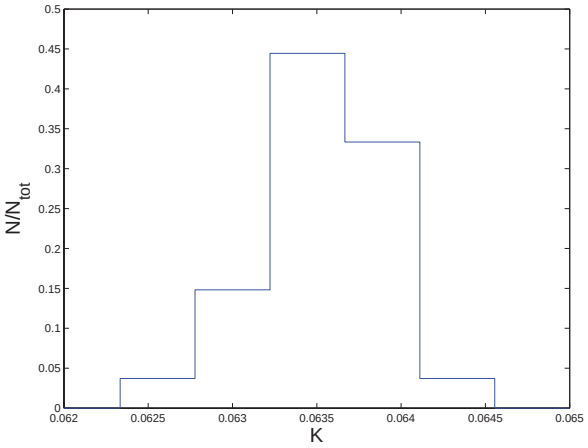

Figure 10. Normalized histogram of the distribution of the values of K'_2 for the Tina family members.

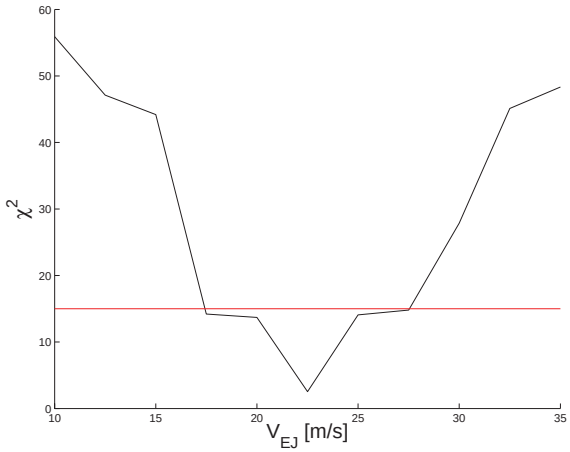

Figure 11. The values of χ^2 of the synthetic families as a function of the values of $V_{\rm EJ}$ adopted in the construction of the observed classical family.

centred around zero and with a size-dependent standard deviation that follows the relationship

$$V_{\rm SD} = V_{\rm EJ}\left(\frac{5\,{\rm km}}{D}\right), \tag{4}$$

where $V_{\rm EJ}$ is a free parameter characterizing the size of the family in velocity space and D is the asteroid diameter. We use for each synthetic family the same number of asteroids known for the Tina family and the same values of their diameters, estimated from their absolute magnitudes assuming a geometric albedo $p_V = 0.3086$ (the mean value of the geometric albedo for Tina family members, Carruba 2010b). The velocity distribution relative to the barycentre of the family is then translated into an (a, e, i) distribution by using Gauss equations (Carruba et al. 2003) and adopting for the values of Ω, ω and M the current values of (1222) Tina in the frame J2000.

Finally, for each synthetic family, we compute the distribution of the values of K'_2. We aim at determining the value of the parameter $V_{\rm EJ}$ for which the K'_2-distribution of the synthetic family best fits that of the observed family. For this purpose, for each family, we introduce a χ^2-like variable defined as

$$\chi^2 = \sum_{i=1}^{N_{\rm int}} \frac{(q_i - p_i)^2}{q_i}, \tag{5}$$

where $N_{\rm int}$ is the number of interval used for the values of K'_2 (10 equally spaced intervals, starting from $K'_2 = 0.061$ up to 0.065), q_i is the number of real objects in the ith interval in K'_2 and p_i is the number of synthetic family members in the same ith interval. We found that the distribution of K'_2 values for the synthetic family with the smallest value of χ^2 (the best-fitting family) is almost identical to the K'_2 distribution of real objects.

Fig. 11 shows how the value of χ^2 changes with the value of $V_{\rm EJ}$ adopted to generate the synthetic family. The minimal value of χ^2 (best fit) is obtained for $V_{\rm EJ} \simeq 22\,{\rm m\,s^{-1}}$. To have an estimate of the uncertainty on $V_{\rm EJ}$, we consider that, given the number of intervals (10) used for binning the distribution of K'_2, a value of $\chi^2 < 15$ corresponds to the two distributions having a probability larger than 95 per cent to be derived from the same parent distribution (Press et al. 2001). Then, we consider 'acceptable' all values of $V_{\rm EJ}$ giving $\chi^2 < 15$. This yields $V_{\rm EJ}$ of $22.5 \pm 5.0\,{\rm m\,s^{-1}}$, which is consistent with the escape velocity $V_{\rm esc} = 11.3\,{\rm m\,s^{-1}}$ from the Tina parent body, estimated using

$$V_{\rm esc} = \sqrt{\frac{2GM_{\rm Tot}}{R_{\rm PB}}}, \tag{6}$$

where G is the gravitational constant, and $M_{\rm Tot} = 0.2 \times 10^{17}$ kg and $R_{\rm PB} = 20.8$ km are the estimated mass of the family and the radius of the parent body (the values of these two parameters are taken from Carruba 2010b), respectively. An alternative way to estimate $V_{\rm EJ}$ (but providing a consistent result) will be discussed in Section 6.2.

6 CONSTRAINTS ON THE FAMILY AGE

In this section, we will set constraints on the family age by using the unique resonant configuration of the family members (Section 6.1) and by performing Monte Carlo simulations of diffusion in the semimajor axis caused by the Yarkovsky and YORP effects (Section 6.2). We will start by studying the current orbital dispersion of family members in the ($\psi_1^{\rm S}$, $\psi_2^{\rm S}$) plane.

6.1 Orbital dispersion in the ($\psi_1^{\rm S}$, $\psi_2^{\rm S}$) plane

The unique dynamical nature of the Tina family can be used to set constraints on its age. Fig. 12 shows a ($\psi_1^{\rm S}$, $\psi_2^{\rm S}$) projection of the current orbital distribution of the members of the classical (blue full dots) and frequency (green full dots) families. The fact that the asteroids are not clustered around a specific location in this plane but are dispersed all around the stable equilibrium point at $\sigma = 180^\circ$ suggests that the family did not form recently. In fact, reasonable ejection velocity field produced by collisional break-up events produces longitude of the pericentre and node dispersed by less than 10° (Vokrouhlický et al. 2006; Carruba 2009a). Thus, at the family formation time, the family members should be clustered in σ within a comparable dispersion. Then, the distribution in σ spreads with time, because each asteroid has a slightly different frequency of libration, g_σ, and eventually the σ distribution has to be uniform. The time it takes to achieve such a uniform distribution sets a lower limit on the age of the Tina family that we evaluate below.

To quantitatively estimate the rate at which the Tina family disperses along the σ-libration cycles, we performed the following numerical experiment: we started with a synthetic Tina family generated as a compact cluster in a, e, sin(i), $\psi_1^{\rm S}$ and $\psi_2^{\rm S}$. To better define

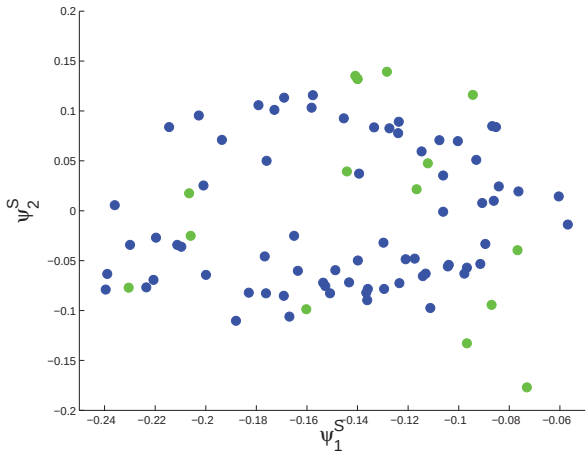

Figure 12. Projection in the (ψ_1^S, ψ_2^S) plane of the Tina family members at $t = 0$ Myr. Members of the classical family are shown as blue full dots, while members of the frequency family that do not belong to the classical family are displayed as green full dots.

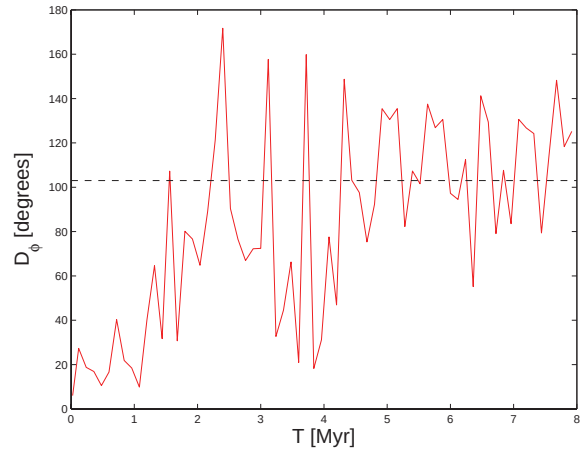

Figure 13. Time-evolution of the polar angle dispersion for the synthetic Tina family.

the spreading time along the libration cycles, the fake family is composed of a subgroup of eight observed Tina family members with values of σ to within 10°, and four sets of clones produced by adding and subtracting small values of the eccentricities and inclination of the real objects. The stable point of libration depends on the proper values of (a, i) of each object and is slightly different for different asteroids. We chose eight Tina members characterized by similar values of the location of the libration point and averaged the values of ψ_1^S and ψ_2^S of these objects. The stable point for these eight objects has coordinates $(-0.16, 0)$ in the (ψ_1^S, ψ_2^S) plane. Overall, we integrated 40 clones of Tina members. To quantitatively describe the distribution of bodies around the stable $\sigma = 180°$ point, we obtained at each time-step of the integration a polar angle ϕ in a (ψ_1^S, ψ_2^S) plane rescaled so that the stable $\sigma = 180°$ point is at the origin. We then computed at each step of the numerical integration the dispersion D_ϕ, in the polar angle ϕ, defined as

$$D_\phi{}^2 = \frac{1}{N(N-1)} \sum_{i \neq j} (\phi_i - \phi_j)^2, \tag{7}$$

where $N = 40$ is the number of integrated bodies and ϕ_i is the polar angle of the ith body $(i = 1, \ldots, N)$. Fig. 13 shows the time-behaviour of D_ϕ: since we started with a compact cluster, D_ϕ is initially small ($\simeq 5°$), but grows with time because of the differential libration of the bodies in the resonance. After 2.5 Myr, it reaches the saturation level at 103.°0, which corresponds to a uniform distribution of bodies along a circle (Vokrouhlický et al. 2006, Carruba 2009b).[2] This result suggests that the Tina family is at least 2.5 Myr old, that is, about three times the anti-aligned libration oscillation period of (1222) Tina. The dispersion of D_ϕ on a time-scale of three libration oscillation periods is quite a typical result (Vokrouhlický et al. 2006; Carruba 2009b).

In the next section, we will investigate a better constraint on the family age that comes from the diffusion in the semimajor axis caused by the Yarkovsky and YORP effects.

6.2 Monte Carlo simulations

In this section, we will analyse the semimajor axis evolution of the Tina family members for the classical and frequency cases. The methods used here follow the work of Vokrouhlický et al. (2006a,b) that showed that the peculiar a-distribution of some asteroid families can be explained as a consequence of the combination of the Yarkovsky and YORP effects. In essence, the YORP effect forces the spin axes of asteroids to evolve towards the direction perpendicular to the orbital plane. In this configuration, the semimajor axis drift caused by the Yarkovsky effect is maximized. Asteroids either drift towards smaller a (if their rotation is retrograde) or larger a (if their rotation is prograde). This depletes the centre of the family in the semimajor axis distribution.

The family's final semimajor axis distribution resulting from this evolution depends on its initial velocity dispersion (parametrized by V_{EJ}; see equation 4), its age (Age), as well as on the YORP strength (C_{YORP}), which are all unknown a priori. To determine the values of these parameters, we proceed as follows: we fix a set of values of the parameters and we compute the expected final distribution of semimajor axes. The latter is then transformed into a one-dimensional distribution by computing for each body the parameter C using the following equation:

$$0.2H = \log_{10}\left(\frac{\Delta a}{C}\right), \tag{8}$$

where H is the absolute magnitude of the body and $\Delta a = a - a_c$ is the difference between its semimajor axis and the value a_c characterizing the centre of the family (i.e. its barycentre). The distribution of the values of C for the simulated family, $N(C)$, is then compared to that for the real family, $N_{obs}(C)$. We computed the number of objects for C-interval, using 20 intervals in C, starting from $C = -2 \times 10^{-5}$ with a step $\Delta C = 2 \times 10^{-6}$. The quality of the match between the two distributions is quantified by computing the χ^2-like value:

$$\psi_{\Delta C} = \sum_{\Delta C} \frac{[N(C) - N_{obs}(C)]^2}{N_{obs}(C)}. \tag{9}$$

We finally search for the values of the parameters that minimize $\psi_{\Delta C}$, that is, fit best the observed semimajor C-distribution of the family. More detail on the procedure outlined here can be found in Vokrouhlický et al. (2006a,b) and Carruba (2009a). We do not consider the effects of low-energy collisions (Dell'Oro & Cellino 2007), because Carruba (2009a) showed that they play at best a minor role with respect to the semimajor-axis evolution caused by the Yarkovsky and YORP effects.

[2] The current value of D_ϕ for the Tina family members is 96.°1.

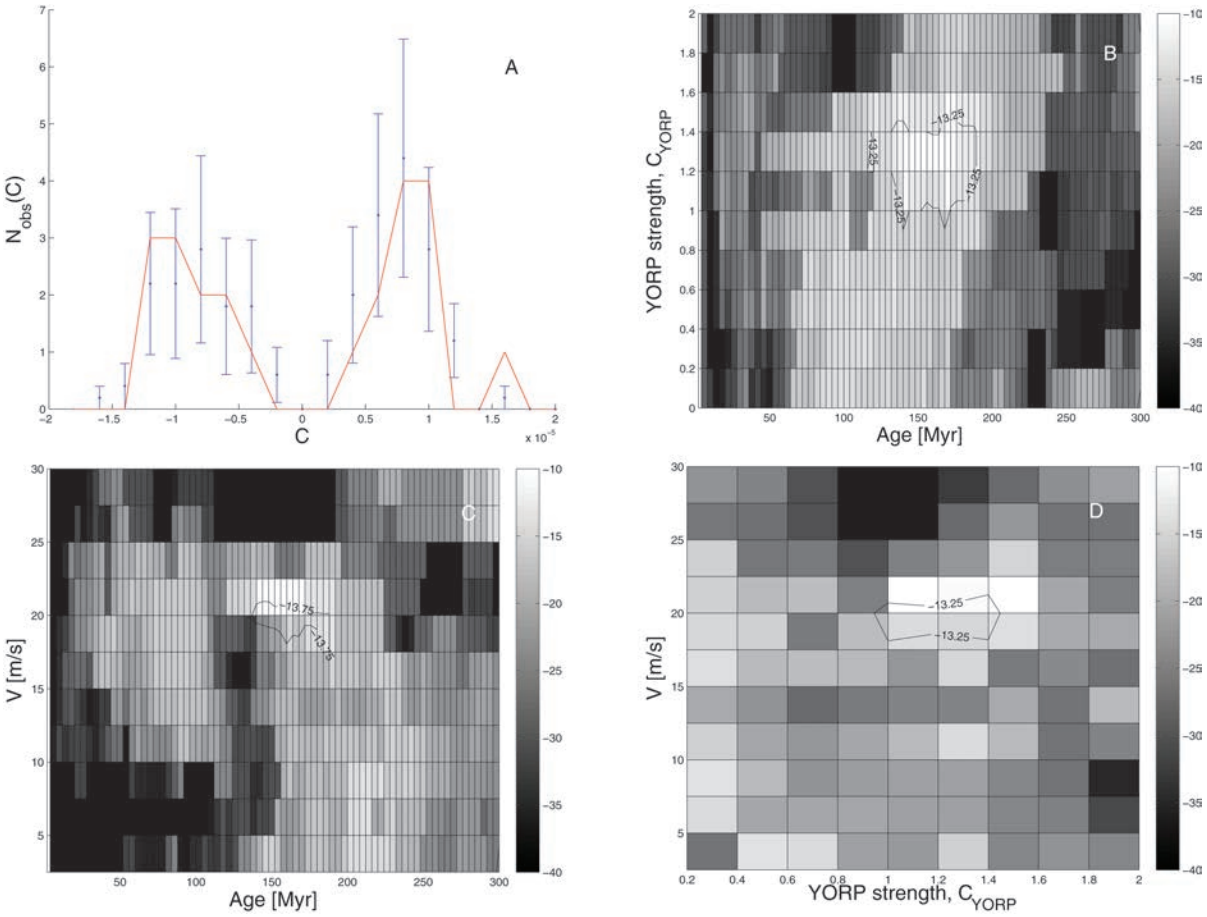

Figure 14. Panel A displays the best-fitting distribution $N(C)$ (red line) and the observed distribution $N_{\rm obs}(C)$ (in blue) for the classical family. The other panels show the values of the target function, $\psi_{\Delta C}$, in the (Age, $C_{\rm YORP}$) plane (panel B), in the (Age, V) plane (panel C) and in the ($C_{\rm YORP}$, V) plane (panel D). For these maps, in each cell, we report the minimal value of $\psi_{\Delta C}$ over the hidden dimension.

6.2.1 *Fitting the semimajor-axis distribution: the classical family*

We start by computing $N_{\rm obs}(C)$ for the classical family of Tina. This function depends on the adopted value for the family barycentre, $a_{\rm c}$, which is not very precisely determined. So, following Vokrouhlický et al. (2006a,b), we computed $N_{\rm obs}(C)$ as the average of the C-distribution for $a_{\rm c}$ in the interval (2.790, 2.794). The result is shown in Fig. 14 (panel A).

The other panels of Fig. 14 show the values of the target function $\psi_{\Delta C}$ in the (Age, $C_{\rm YORP}$) plane (panel B), in the (Age, V) plane (panel C) and in the ($C_{\rm YORP}$, V) plane (panel D).[3] Since there were 20 intervals in C, we used a value of $\psi_{\Delta C}$ of 13.25 as a limit for an acceptable fit, as this would correspond to a probability of 95 per cent that the simulated distribution is equivalent to the observed (Press et al. 2001).

From this analysis, we obtain the following best-fitting solution for the age, T, the characteristic ejection velocity field, $V_{\rm EJ}$, and the YORP strength ($C_{\rm YORP}$): $T = 170^{+20}_{-30}$ Myr, $V_{\rm EJ} = 20.0^{+1.0}_{-2.5}$ m s^{-1} and $C_{\rm YORP} = 1.00^{+0.45}_{-0.10}$. Note that the estimate of the initial velocity dispersion of the family is in perfect agreement with that obtained in Section 5. This is remarkable, because the two methods used in Section 5 and here are truly independent.

[3] To associate lower levels of $\psi_{\Delta C}$ with whiter tones, we plotted colour plots of $-\psi_{\Delta C}$.

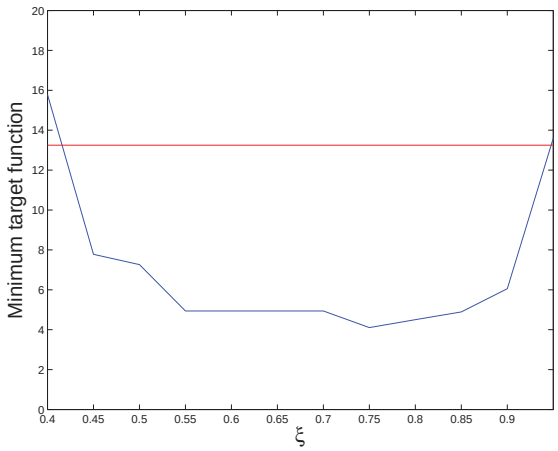

Figure 15. Minimum values of the target function $\psi_{\Delta C}$ as a function of the asymmetry parameter ξ for the classical family.

Following the Vokrouhlický et al. (2006b) approach, we introduced the fourth parameter, ξ, which yields the fraction of initially prograde rotating asteroids. Fig. 15 displays minimum values of the target function, $\psi_{\Delta C}$, for different values of the asymmetry parameter, ξ, characterizing the initial proportion of the prograde versus the retrograde rotating fragments. As also found in Vokrouhlický et al. (2006b) for the Agnia family and by Carruba (2009a) for the Padua

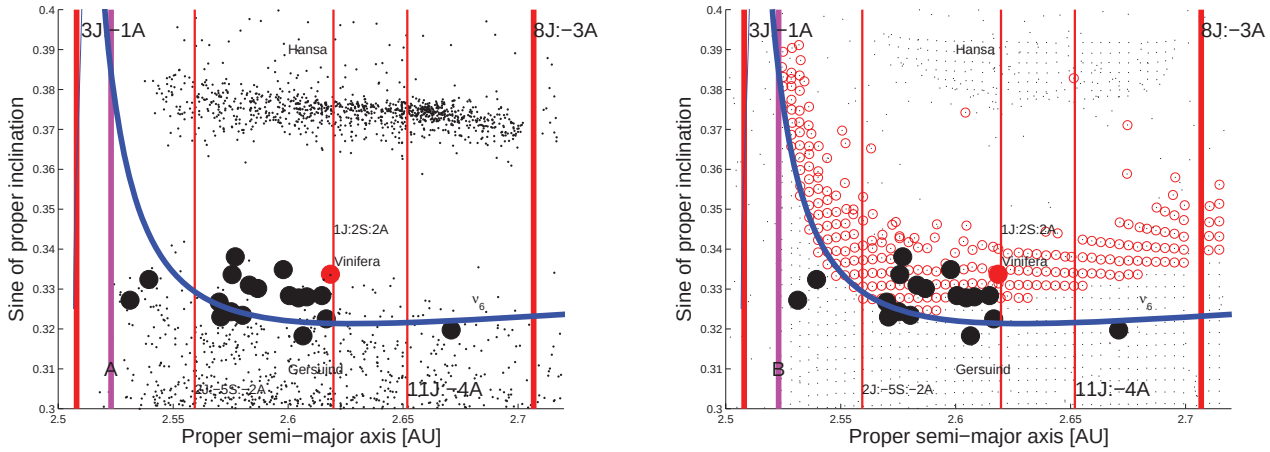

Figure 16. Panel A: an (a, sin(i)) projection of the asteroids in the region around (759) Vinifera. Panel B: an (a, sin(i)) projection of averaged elements of test particles in the region of (759) Vinifera.

family, the Tina family also seems to be characterized by an asymmetry between the prograde and retrograde rotators. The fraction of initially prograde rotating asteroids, ξ, is, however, poorly constrained: we found a value of $\xi = 0.75^{+0.20}_{-0.33}$, which seems to indicate a prevalence of prograde rotating asteroids, but it is also compatible with a balanced distribution or even with a slight prevalence of initially retrograde rotating asteroids.

Concerning the frequency family, we repeated the Monte Carlo analysis and the results are in very good agreement with those of the classical family. We found an Age $= 160^{+20}_{-30}$ Myr, $V_{\rm EJ} = 20.0^{+1.0}_{-2.5}$ m s^{-1}, $C_{\rm YORP} = 1.0^{+0.1}_{-0.1}$ and $\xi = 0.55^{+0.17}_{-0.08}$.

7 (759) VINIFERA

Until recently, the only other asteroid that was known to be in an anti-aligned librating state of the ν_6 resonance was (759) Vinifera (Froeschlé & Scholl 1987). Fig. 16 (panel A) displays an (a, sin(i)) projection of the asteroids in the region of (759) Vinifera. The latter is identified by a red full dot, whereas the other 18 anti-aligned librating asteroids in the region are shown as full black dots in Fig. 16. At the moment, no dynamical family was found around (759) Vinifera (Carruba 2010b), nor around any of the other librating asteroids. A small clump with 10 members around (59494) 1999 JN5 is identifiable in the domain of proper frequencies (n, g, $g + s$), but this number is below the minimum one required for statistical significance (22 members, Carruba 2010b).

One may wonder why there is no family in the region of (759) Vinifera. Is this due to dynamical causes, such as the dimension of the region of anti-aligned libration in the vicinity of the asteroid, or simply is it just a consequence of the fact that (759) Vinifera was never broken up by a collision? To investigate the dimension of the anti-aligned librating island, we integrated with SWIFT_MVSF 2200 particles for 20 Myr, with initial conditions chosen on a regular 55 by 40 grid in the (a, sin(i)) plane. We used a resolution in a of 0.004 au and in i of 0.°2. Our particles covered a range 2.500–2.716 au in a and 16.°0–23.°8 in i. The initial values of e and of the angular elements Ω, ω, and λ of the test particles were set equal to those of (759) Vinifera.

Fig. 16 (panel B) shows the averaged elements of test particles in the (a, sin(i)) plane. The blue line shows the location of the secular resonance centre in the region, as computed by the analytical theory of Milani & Knežević (1994). Red circles identify the location of anti-aligned librators. The reader may note that the anti-aligned librating region covers a smaller range of inclination values with respect to the same region near Tina (see Fig. 5, panel B). To investigate the dynamical stability of asteroids in the (759) Vinifera region, we studied the dynamical evolution of the (59494) frequency clump when the Yarkovsky effect is considered, as well as of all the 18 ν_6 anti-aligned librating asteroids in the region. We used typical Yarkovsky parameters of S-type objects, which is consistent with the taxonomy of asteroids in the region (Carruba 2010b), and the same set-up as used for the Yarkovsky integrations of Tina members (see Section 4.2). We observed that the group around (59494) dispersed in less than 2 Myr and should therefore not be considered statistically significant. Concerning the anti-aligned asteroids in the (759) Vinifera region, with the exception of two objects, (109429) (2001 QQ195) and (2000) QV14, which switched to circulating states before the end of the integration, all the other 16 initially anti-aligned asteroids remained in librating states for the whole length of the integration (300 Myr). Thus, we conclude that putative (759) Vinifera families in anti-aligned libration orbits could remain identifiable for a time-scale of at least 300 Myr. In conclusion, the fact that we do not observe them can be due to either of the following two reasons: (i) there has been no collisional break-up in the last 300 Myr; or (ii) there is a family of small objects but the latter has not yet been detected. A more complete asteroid catalogue in the region is therefore needed before drawing a conclusion on this subject.

8 CONCLUSIONS

In this work:

(i) We investigated the dynamics of the Tina family, which is, so far, the only asteroid family completely embedded in a secular resonance (i.e. all family members are in resonant libration). Contrary to the case of the Agnia and Padua families in the z_1 resonances, members of the Tina families that escape from the ν_6 anti-aligned libration island are unstable on time-scales of up to 10 Myr because of close encounters with Mars and other terrestrial planets, which explains why no Tina members are currently found outside the stable island.

(ii) We defined and computed ν_6 resonant proper elements in two different ways for the family members.

(iii) We obtained dynamical maps for the Tina region and investigated the long-term orbital evolution of Tina members when the Yarkovsky effect is considered. Anti-aligned librators cannot reach Mars-crossing eccentricities and are not destabilized unlike ν_6 circulators and aligned librators in the region. As a consequence, the Tina family resides in a stable island of motion.

(iv) We used the $K_2' = \sqrt{1-e^2}(1-\cos i)$ conserved quantity of the ν_6 resonance to set constraints on the original ejection velocities of Tina family members. Current values of K_2' are compatible with an original value of $V_{\rm EJ}$ (see equation 4) of $22.5 \pm 5.0\,{\rm m\,s^{-1}}$.

(v) We put constraints on the family age (170^{+20}_{-30} Myr) and on the initial velocity dispersion ($20^{+1}_{-2.5}\,{\rm m\,s^{-1}}$).

(vi) We studied the case of the other large anti-aligned librating asteroid in the region, (759) Vinifera, and briefly discussed why it is not associated to any known family.

A natural question that now arises is on the nature of the Tina family. Since all its members seem to lie in a stable island, they could be, in principle, just asteroids that happened to survive in this stable dynamical niche. Information on the taxonomy of family members could help solve this problem, but, unfortunately, this information is only available for (1222) Tina itself (Carruba 2010b). Six objects in the region have SDSS-MOC3 flux data that are compatible with an S-complex composition, but this is clearly not enough to reach a definitive conclusion on the genetic link between the family members and more data need to be collected.

An interesting issue for future research is the response of anti-aligned librators to giant planet migration. Giant planet migration causes the ν_6 resonance to sweep through the asteroid belt from larger to smaller semimajor axes. It will be interesting to investigate whether objects in anti-aligned libration configuration could have been captured in this dynamical state during the phase of secular resonance sweeping and under which conditions. Coupled with other existing constraints on giant planet migration, this study could therefore lead to a better characterization of the real dynamical evolution that the planets had at the time they cleared the planetesimal disc from their vicinity.

More important than the real status of the Tina family as an actual collisional group and the possible lines of research that may arise from it is, however, the discovery of a new kind of resonant dynamical family. The identification of the first ν_6 anti-aligned librating family is, in our opinion, an interesting result in orbital dynamics, which further emphasizes the vitality of asteroid dynamics as a field of research.

ACKNOWLEDGMENTS

We thank the reviewer of this paper, David Vokrouhlický, for careful revision of this paper and his fruitful comments that significantly improved its quality. We would like to thank the São Paulo State Science Foundation (FAPESP) that supported this work via the grant 06/50005-5 and the Brazilian National Research Council (CNPq, grants 302183/2008-6 and 473345/2009-9). VC is also grateful to the Department of Mathematics of FEG-UNESP for the use of their facilities.

REFERENCES

Bendjoya Ph., Zappalà V., 2002, in Bottke W. F., Jr, Cellino A., Paolicchi P., Binzel R. P., eds, Asteroids III. Univ. Arizona Press, Tucson, p. 613
Brož M., 1999, Thesis, Charles Univ., Prague, Czech Republic
Brož M., Vokrouhlický D., 2008, MNRAS, 390, 715
Carruba V., 2009a, MNRAS, 395, 358
Carruba V., 2009b, MNRAS, 398, 1512
Carruba V., 2010a, MNRAS, 403, 1834
Carruba V., 2010b, MNRAS, 408, 580
Carruba V., Michtchenko T., 2007, A&A, 475, 1145
Carruba V., Michtchenko T., 2009, A&A, 493, 267
Carruba V., Burns J. A., Bottke W., Nesvorný D., 2003, Icarus, 162, 308
Carruba V., Michtchenko T., Roig F., Ferraz-Mello S., Nesvorný D., 2005, A&A, 441, 819
Charlier C. V. L., 1902, Die Mechanik des Himmels, 410-413. Verlag von Veit & Co., Leipzig
Dell'Oro A., Cellino A., 2007, MNRAS, 380, 399
Farinella P., Vokrouhlický D., Hartmann W. K., 1998, Icarus, 132, 378
Froeschlé Ch., Scholl H., 1987, A&A, 179, 294
Knežević Z., Milani A., 2000, Celest. Mech. Dyn. Astron., 78, 17
Knežević Z., Milani A., 2003, A&A, 403, 1165
Levison H. F., Duncan M. J., 1994, Icarus, 108, 18
Milani A., Knežević Z., 1992, Icarus, 98, 211
Milani A., Knežević Z., 1994, Icarus, 107, 219
Morbidelli A., 2002, Modern Celestial Mechanics: Aspects of Solar System Dynamics. Taylor & Francis, London
Morbidelli A., Henrard J., 1991, Celest. Mech. Dyn. Astron., 51, 169
Nesvorný D., Vokrouhlický D., 2006, AJ, 132, 1950
Press V. H., Teukolsky S. A., Vetterlink W. T., Flannery B. P., 2001, Numerical Recipes in Fortran 77. Cambridge Univ. Press, Cambridge
Vokrouhlický D., Brož M., Bottke W. F., Nesvorný D., Morbidelli A., 2006a, Icarus, 182, 118
Vokrouhlický D., Brož M., Bottke W. F., Nesvorný D., Morbidelli A., 2006b, Icarus, 183, 349
Williams J. G., 1969, PhD thesis, Univ. of California, Los Angeles
Zappalà V., Bendjoya Ph., Cellino A., Farinella P., Froeschlé C., 1995, Icarus, 116, 291

This paper has been typeset from a TEX/LATEX file prepared by the author.

9

Famílias dinâmicas no cinturão externo

O enfoque deste artigo foi a identificação de famílias dinâmicas no cinturão externo de alta inclinação e sua evolução dinâmica em ressonâncias seculares. Para esta finalidade, obtivemos elementos próprios para 6841 asteroides numerados e 4034 asteróides de oposição múltipla. Detectamos todas as ressonâncias seculares lineares e não-lineares, até a ordem seis, e identificamos todos os objetos em estado de libração em ressonâncias seculares lineares. Identificamos dois "clumps" entre os objetos em estados anti-alinhado da ressonância ν_6, sendo estes grupos o segundo e o terceiro grupo atualmente conhecidos nesta configuração no Sistema Solar, depois da família de Tina. Para uma melhor determinação destes grupos, também computamos elementos próprios ressonante com métodos descritos em Carruba e Morbidelli (2011). Obtivemos também famílias dinâmicas nos espaços dos elementos próprios e das frequências próprias, mais adequadas para descrever as ressonâncias seculares presentes na região.

Identificamos 18 nova famílias e 38 "clumps", doze desta famílias visíveis em espaços das frequências próprias. De particular interesse foi o clump em volta do asteroide (69559) (1997 UG5), que se encontra no cruzamento de cinco ressonâncias seculares, configuração esta até agora única no Sistema Solar. Finalmente, introduzimos novas técnicas para a identificação de famílias em proximidade de ressonâncias seculares, que poderiam ser, a princípio, aplicadas para outras regiões do cinturão principal.

A seguir apresentamos o artigo, que foi publicado em Monthly Notices of

the Royal Astronomical Society em 2012, volume 420, pp. 1779-1798.

Monthly Notices
of the
ROYAL ASTRONOMICAL SOCIETY

Mon. Not. R. Astron. Soc. **420,** 1779–1798 (2012) doi:10.1111/j.1365-2966.2011.20178.x

Secular dynamics and family identification among highly inclined asteroids in the Euphrosyne region

J. F. Machuca and V. Carruba★

UNESP, Univ. Estadual Paulista, Grupo de dinâmica Orbital e Planetologia, Guaratinguetá, SP 12516-410, Brazil

Accepted 2011 November 9. Received 2011 October 28; in original form 2011 September 21

ABSTRACT

Among highly inclined asteroids the external region of the main belt beyond the 5J:2A mean-motion resonance with Jupiter has long been known to host the Euphrosyne and Alauda families. The region is confined in semimajor axis between the 5J:-2A and 2J:-1A mean-motion resonances with Jupiter, and is characterized by the presence of the ν_6, ν_5 and ν_{16} linear secular resonances, as well as by the z_1, z_2, z_3 and other non-linear secular resonances.

In this work we employed the frequency modified Fourier transform method to obtain synthetic proper elements for 6841 numbered and 4034 multi-opposition objects in the region of the Euphrosyne family, and used this data to obtain families and clumps in the domain of proper elements and frequencies. With respect to other works on family identification in the area, here we focused our investigation on the effect that the complicated local web of secular resonances has had on the dynamical evolutions of families and clumps. We detected all main linear and non-linear secular resonances, up to order six, in the region and identified for the first time new populations of objects in ν_6 anti-aligned librating and ν_5 anti-aligned and aligned librating resonant states. We identified two new clumps among ν_6 anti-aligned librating objects, making them the second and the third groups in this resonant configuration ever found after the discovery of the Tina family. Once the local dynamics was fully understood, we then obtained dynamical groups in the domain of proper elements and in the domain of proper frequencies most apt to study the secular resonance present in each region, and computed ν_6 resonant proper elements to study groups in regions affected by the ν_6 secular resonance.

We identified 18 families and 39 clumps in the Euphrosyne region, of which 12 families and five clumps were in frequency domains. Of particular interest was the group around (69559) (1997 UG5), found in both proper element and frequency domains, characterized by its interaction with five secular resonances. It is the first time that a group of asteroids is found in such an interesting resonant configuration. More importantly, we introduced new techniques for asteroid family identification in presence of secular resonances, which could in principle be used for other areas of the asteroid belt.

Key words: celestial mechanics – minor planets, asteroids: general – minor planets, asteroids: individual: Euphrosyne.

1 INTRODUCTION

Highly inclined asteroids, asteroids with $\sin(i) > 0.3$, are objects for which the analytical theory used to obtain proper elements, being based on series expansions of the perturbing functions based on the assumption of small values of eccentricities and inclinations, is not very accurate (Milani & Knežević 1994). Dynamically, one can define an asteroid as 'highly inclined' if its inclination is higher than that of the centre of the $\nu_6 = g - g_6$ secular resonance at the same semimajor axis, where g is the precession frequency of the asteroid pericentre and g_6 is the precession frequency of Saturn pericentre.[1] Since current mechanism of dynamical mobility cannot easily increase a main belt asteroid inclination to values higher than those of the ν_6 centre, highly inclined asteroids are thought to be remnants of early phases of Solar system formation.

★E-mail: vcarruba@feg.unesp.br

[1] Secular resonances occur when there is a commensurability between the precession frequency of an asteroid pericentre g or node s and that of a planet g_i or s_i where $i = 1, \ldots, 8$, refers to one of the planets, 1 for Mercury, 8 for Neptune.

The region of the Euphrosyne family, contained in semimajor axis between the 5J:-2A and 2J:-1A mean-motion resonances (the letter J stands for Jupiter, while A for asteroid, so 2J:-1A is the 2:1 mean-motion resonance with Jupiter in the notation used by other researchers), and with $\sin(i) > 0.3$ asteroids is considered highly inclined if we use the $\sin(i) > 0.3$ criterion, but it is not for the dynamical criterion, since the great majority of the asteroids in the region have inclinations smaller than the ν_6 centre. The region is however very interesting because of the secular dynamics. All three main linear secular resonances of our Solar system, the $\nu_6 = g - g_6$, the $\nu_5 = g - g_5$ and the $\nu_{16} = s - s_6$ are crossing the region. Because of the presence mainly of the 2J:-1A and of other mean-motion resonance with Jupiter, the behaviour of the g frequency as a function of semimajor axis near the 2J:-1A separatrix is highly non-linear. As a consequence, many non-linear secular resonances[2] such as the one in the $z_k = k\nu_6 - \nu_{16}$ series, where $k = 1, 2, 3$, and others are all observed in the region. This has a profound effect on the dynamical evolution of asteroid groups in the region, whose distributions in the proper element domain are shaped by the intricated local web of resonances. Asteroids may be trapped in resonant configurations such as the anti-aligned states of the ν_6 secular resonance, as observed for Tina family members in the central main belt (Carruba & Morbidelli 2011). For such asteroids, special proper resonant elements must be used and this affects family identification. Family members that were captured into linear or non-linear secular resonances because of the effect of non-gravitational forces such as the Yarkovsky and YORP effect may drift away from the family core, and no longer be recognizable as member of the groups by standard methods of family identification such as the hierarchical clustering method (HCM) in the proper element domain of Zappalá et al. (1995).

Using a set of proper elements for numbered asteroids available at the AstDyS[3] at the time, Gil-Hutton (2006) identified seven families and 13 clumps in the region in the proper (a, e, $\sin(i)$) element domain. Using a set of 9538 numbered and multi-opposition asteroids, Novaković, Cellino & Knežević (2011) recently identified 17 families, 21 clumps and four clusters in the region. Neither of these authors, however, studied in detail the effects of secular dynamics on family identification and evolution.

In this work we used an extended sample of 10 875 numbered and multi-opposition objects in the area to identify dynamical groups using the standard HCM in the proper element domain, and the frequency hierarchical clustering method (FHCM; Carruba & Michtchenko 2007, 2009) in various domains of the proper frequencies n (mean motion), g and s. More than re-obtaining family groups in the area, however, our focus is to understand the effect that the local web of secular and mean-motion resonances has had on the local asteroidal population. With respect to similar work by our and other groups on asteroid family identification, in this paper we will use a different approach: rather than first obtaining proper elements and families and then studying the effect of the local dynamics on the groups, we will first obtain dynamical maps of the area and study the effect that linear and non-linear secular resonances had on the local population, by identifying objects in circulating, aligned and anti-aligned librating states in the main linear and non-linear secular resonances. Once a good understanding of the local dynamics is obtained, appropriate proper elements for each object will be computed and only then we will work on the problem of family identification. New methods for studying the problem of identifying family members in secular resonance states will also be introduced in this work.

This paper is divided in the following manner: in the first section we introduced the problem of secular dynamics and family identification in the Euphrosyne region. In the second section we numerically study the local dynamics using synthetic proper elements maps and Lyapunov times for fictitious asteroids in the region. In the third section we obtain synthetic proper elements for numbered and multi-opposition asteroids in the area. In the fourth section we identify the asteroids in linear secular resonant configurations. In the fifth section we identify families and clumps in the region in both proper elements and frequencies domains. In the sixth section we used resonant proper elements of the ν_6 resonance to study dynamical groups in or near ν_6 orbital configurations. Finally, in the seventh section we present our conclusions.

2 DYNAMICS IN THE REGION OF THE EUPHROSYNE FAMILY

While much information can be gained by studying real objects, sometimes it is useful to turn one attention to fictitious body in the regions. This is especially important for the highly inclined asteroids, since it has been shown (Carruba & Machuca 2011) that there exist dynamically stable regions characterized by lower asteroid number densities and vice versa. To gain further insights on the distribution of mean motion and secular resonances in the region we integrated 6100 particles in the (a, e) space, 11 600 particles in the (a, $\sin(i)$) space and 6960 particles in the (e, $\sin(i)$) space under the influence of the eight planets and (1) Ceres using the SWIFT_MVES symplectic integrator from the SWIFT package (Levison & Duncan, 1994) modified by Brož (1999) so as to include on-line digital filtering to remove all frequencies with period less than 600 yr. We used a step in a of 0.005 au, 0.01 in e and in i of 0.°2, and took particles in an equally spaced grid of 100 by 61 particles in the (a, e) plane, of 100 by 116 particles in the (a, $\sin(i)$) plane and of 60 by 116 particles in the (e, $\sin(i)$) plane.[4] The initial values of $\sin(i)$, e, a (for the simulations in the (a, e), (a, $\sin(i)$) and (e, $\sin(i)$) planes, respectively) and initial angular elements Ω, ω and λ of the test particles were fixed at those of (31) Euphrosyne, the lowest numbered object in the region. We computed synthetic proper elements of these test particles with the same procedure used for real objects. We also obtained maximum Lyapunov exponents (MLE) for all the test particles in our simulations. The MLE (Lyapunov 1907) is a measure of exponential stretching of nearby orbits. The Lyapunov exponents are equal to zero for regular orbits (they tend to zero in finite-time calculations), while they assume positive values for chaotic orbits. The inverse of a Lyapunov exponent is the Lyapunov time $T_{\rm L}$. Smaller values of $T_{\rm L}$ indicate enhanced local stochasticity. Lyapunov times were computed with the same procedures discussed in Carruba (2009b).

We start our analysis by looking at the particles in the (a, e) plane. Fig. 1 shows the synthetic proper elements map in such plane. The inclined line in Fig. 1 describes the orbital location of the region for which the asteroid pericentre is equal to Mars apocentre. The lack of objects at very small eccentricities is an artefact of the method used for computing synthetic proper elements for asteroids with

[2] Non-linear secular resonances are secular resonances of order higher than 2, often obtained as combinations of linear resonances.

[3] http://hamilton.dm.unipi.it/astdys/

[4] Our particles covered a range between 2.83 and 3.325 au in a, 0 and 0.6 in e and 16° and 38° in i, respectively.

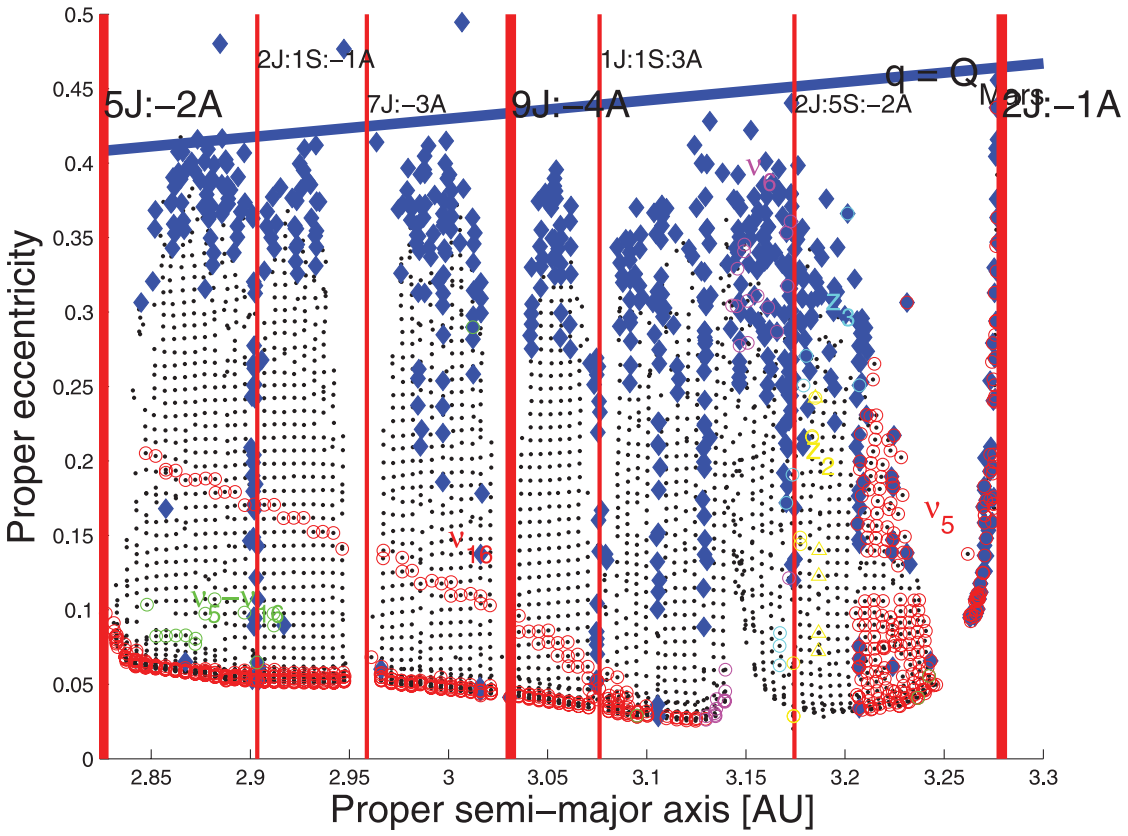

Figure 1. Synthetic proper element map in the (a, e) plane. Vertical red lines show the location of the main mean-motion resonances, blue diamonds are associated with test particles with Lyapunov times of less than 10 000 yr. Red circles are particles with frequencies in the range of the ν_5 and ν_{16} secular resonances. Magenta circles are associated with particles near the ν_6 secular resonance. Green circles, yellow circles and cyan circles are associated with asteroids inside the $\nu_5 - \nu_{16}$, $z_2 = 2\nu_6 + \nu_{16}$ and $z_3 = 3\nu_6 + \nu_{16}$ secular resonances, respectively. The inclined line in figure describes the orbital location of the region for which the asteroid pericentre is equal to Mars apocentre.

$e_{\rm free} < e_{\rm forced}$ (see Carruba 2010a), and the large apparent number of objects with frequencies near g_5 in the vicinity of the 2J:-1A mean-motion resonance is caused by the presence of the near resonance that forces the perihelion of asteroid to precess with a frequency near to that of Jupiter. One can also notice the role of the ν_6 resonance that crosses vertically the region of the Euphrosyne family, near the 2J:5S:-2A. With respect to the case of real objects, we found a more limited number of four-body resonances in the Euphrosyne region (they appear as vertical strip of low Lyapunov times), fact this that may be caused by a binning effect of our test particles grid. Among the numerous four- and five-bodies resonances that may be causing the appearance of chaos in the region, we identified the 5J:-2S:-2U:1A four-body resonance of order 1 at $a \simeq 3.140847$ au and the -5J:-6S:6U:-1M:6A resonance of order zero at $a \simeq 3.1292997$ au. But may other combinations are possible in the region, driving a non-destabilizing chaotic dynamics.

We then turned our attention to the (a, $\sin(i)$) representative plane. Since current mechanisms of dynamical mobility can only slightly modify the inclination of asteroid orbits, asteroid families tend to appear in this plane as horizontal strips. As also found in Carruba & Machuca (2011), we identified a region of relative stable orbits between the 5J:-2A and the 9J:-4A mean-motion resonances that presents a relatively low asteroidal population. As found in the Pallas region, there are orbits in stable ν_6 anti-aligned states (identified by magenta dots in Fig. 2) that are in orbital configurations equivalent to those of the Tina family asteroids (Carruba & Morbidelli 2011). One may also notice how the unstable area associated with the ν_6 resonance is somewhat more limited in the Euphrosyne region. The role of the ν_6 secular resonance will be further investigated later on in this section. As for the dynamical map in the (a, e) plane, we also notice the influence of several four- and five-body mean-motion resonances in the Euphrosyne region, which appear as blue lines of low Lyapunov time in the figure. Finally, as a consequence of the non-linear behaviour of the g frequency as a function of a near the 2J:-1A mean-motion resonance (see Fig. 6, panel A), several secular resonances involving pericentre frequencies are squeezed together in a limited area in the Euphrosyne region: we identified the z_1 (magenta circles), the z_2 (yellow circles), the z_3 (cyan circles), the $\nu_5 - \nu_{16}$ (green circles), the $2\nu_6 - \nu_5$ (blue circles) among others. We will discuss more in detail the effect of these resonances on the local population of asteroids when analysing the projection of asteroids orbital elements in the (g, $g + s$) plane, the plane more suitable for analysing secular dynamics (Carruba & Michtchenko 2007, 2009).

We also obtained synthetic proper elements map in the (e, $\sin(i)$) plane. Fig. 3 displays the synthetic proper elements of test particles in this plane, mean-motion resonances are not visible in this plane, so the effect of secular dynamics is more evident. One can easily notice the destabilizing effect of the ν_5 resonance and the limited destabilizing effect of the ν_6 resonance. As observed in the (a, e) plane, the ν_{16} resonance tends to align asteroids near its centre. Also, we do more easily observe in this plane the effect of pericentre resonances such as the $2\nu_6 - \nu_5$ (blue circles), $3\nu_6 - \nu_5$ and $2\nu_5 + \nu_6$, as well as that of other non-linear resonances already discussed

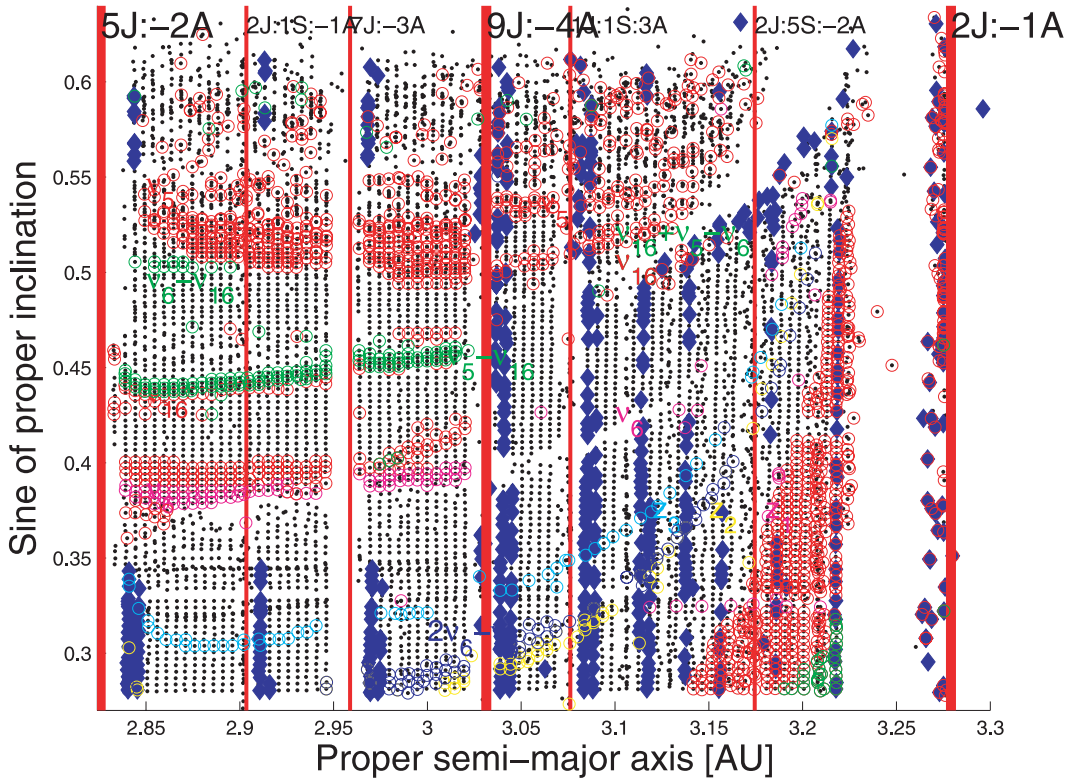

Figure 2. Synthetic proper element map in the (a, $\sin(i)$) plane. Symbols have the same meaning as in Fig. 1.

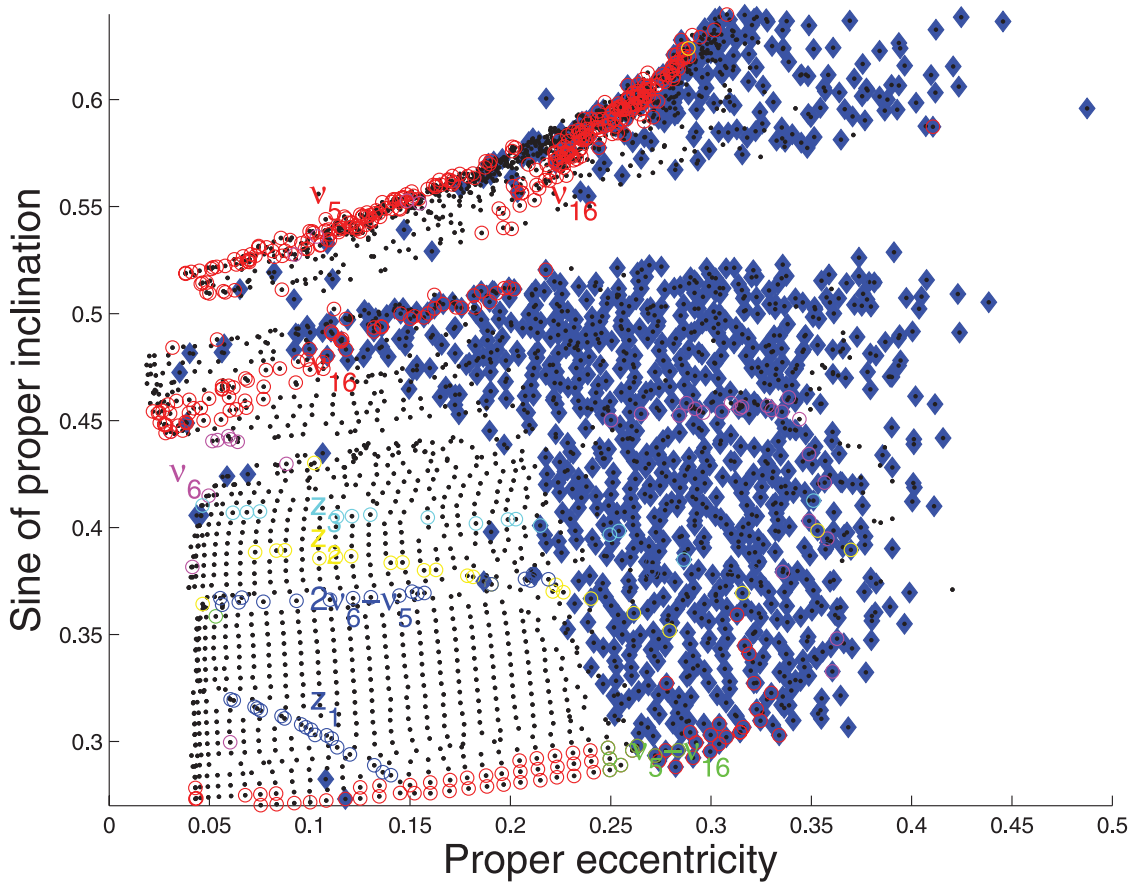

Figure 3. Synthetic proper element map in the (e, $\sin(i)$) plane. Symbols have the same meaning as in Fig. 1.

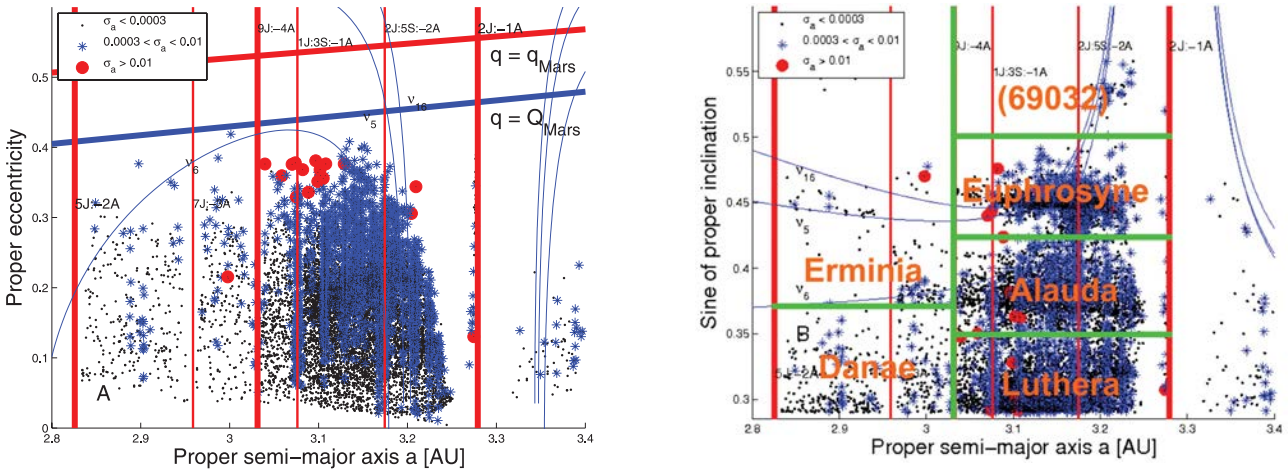

Figure 4. Panel A: an (a, e) projection of highly inclined asteroids in the region of Euphrosyne. Blue asterisks display asteroids with standard deviation on a σ_a between 0.0003 and 0.01, while red circles show asteroids with σ_a larger than 0.01. Panel B: an (a, $\sin(i)$) projection of the same asteroids.

for previous dynamical maps. Once again, the absence of particles at small eccentricity values is an artefact of the method used to compute synthetic proper elements.

In the maps in all planes, (a, e), (a, $\sin i$) and (e, $\sin i$), we observed gaps produced by the main linear secular resonances ν_5, ν_6 and ν_{16}. How efficient are these resonances in depleting the local asteroidal population in the Euphrosyne region? And how effective as a barrier they are when non-gravitational forces are considered? We will try to investigate these issues in the next section.

3 SYNTHETIC PROPER ELEMENTS FOR ASTEROIDS IN THE EUPHROSYNE REGION

If we want to study the dynamical evolution of asteroids groups in the Euphrosyne region a preliminary step is to have a catalogue of asteroids for which proper elements were determined either analytically (Milani & Knežević 1994) or numerically (also called synthetic proper elements; Knežević & Milani 2003). For highly inclined asteroids ($\sin i > 0.30$, here we use a value of $\sin i > 0.29$ so as not to introduce artificial barriers in our families), the analytical theory is not accurate enough to provide reliable proper elements, so one has to rely on the synthetic ones. Here we obtained synthetic proper elements according to the method described in Knežević & Milani (2003) for the numbered and multi-opposition asteroids in the region of Euphrosyne, defined as the region between the 5J:-2A and 2J:-1A mean-motion resonances with Jupiter and values of $\sin i > 0.29$. At this stage of our investigation, we do not yet worry about the possibility of having asteroids in secular resonant configuration, so we do not yet compute resonant proper elements for objects in such configurations. We pre-selected a set of 9608 numbered objects and 6172 multi-opposition asteroids downloaded from the AstDyS site (http://hamilton.dm.unipi.it/astdys) on 2011 May 25 that satisfied the criteria of having osculating semimajor axis between the two resonances centres ($2.8258 < a < 3.4$ au) and osculating inclination larger than 16° or $\sin i = 0.2756$, so as to include objects with small osculating inclination that may have values of proper $\sin i$ in the Euphrosyne region. We then integrated these objects for 20 Myr under the influence of all planets from Venus to Neptune (Mercury was accounted for as a barycentric correction of the initial conditions), with a Burlisch–Stoer integrator from the SWIFT package (Levison & Duncan 1994) modified by Brož (1999) so as to include on-line digital filtering to remove all frequencies with period less than 600 yr. Synthetic proper element were obtained with the same procedure discussed in Carruba (2010b). Of the surviving bodies, 6841 numbered and 4034 multi-opposition asteroids were found to have proper elements in the region of Euphrosyne. This is a significantly larger data set than that used by Gil-Hutton (2006) and somewhat larger (9835 objects against the 9538 objects with $\sin(i) > 0.295$) than that most recently used by Novaković et al. (2011) in the Euphrosyne region.

Fig. 4 displays an (a, e) (panel A) and an (a, $\sin(i)$) (panel B) projections of the obtained proper elements for the numbered and multi-opposition asteroids in the area. Blue asterisks display asteroids with σ_a between 0.0003 au (the limit given by Knežević & Milani 2003 for 'stable' synthetic proper elements) and 0.01 au (the limit for pathological cases), while red circles show asteroids with σ_a larger than 0.01 au. As discussed in Milani & Knežević (1994), asteroids with large standard deviation in proper semimajor axis σ_a are usually associated with two-, three- or four-body mean-motion resonances. The large standard deviation in a is caused by the averaging needed to produce the proper elements for asteroids involved in libration inside a resonance. Vertical red lines display the location of some of the most important two- and three-body mean-motion resonances in the region, while blue lines show the location of the main linear secular resonances, using the second-order and fourth-degree secular perturbation theory of Milani & Knežević (1994) to compute the proper frequencies g and s for the grid of (a, e) and (a, $\sin(i)$) values shown in Fig. 4 and the values of angles and eccentricity of (31) Euphrosyne. Non-linear secular resonances and four-body resonances will be discussed in Section 2. The inclined lines in Fig. 4, panel A, describe the orbital location of the region for which the asteroid pericentre is equal to Mars apocentre and to Mars pericentre, respectively.

As can be seen in the figure one can easily notice that (i) most of the asteroidal population is concentrated in the region between the 9J:-4A and the 2J:-1A mean-motion resonances, (ii) the asteroidal population at inclinations higher than that of the centre of the ν_6 secular resonance is sparse, contrary to what observed in the central main belt (Carruba 2010b; Carruba & Machuca 2011) and (iii) there exists a population of objects inside the 2J:-1A mean-motion resonance (the stable Zhongguos and the unstable Griquas populations; Roig, Nesvorný & Ferraz-Mello 2002). Many asteroids with 'unstable' values of proper a are characterized by the interaction with a local web of four- and possibly even five-body resonances that

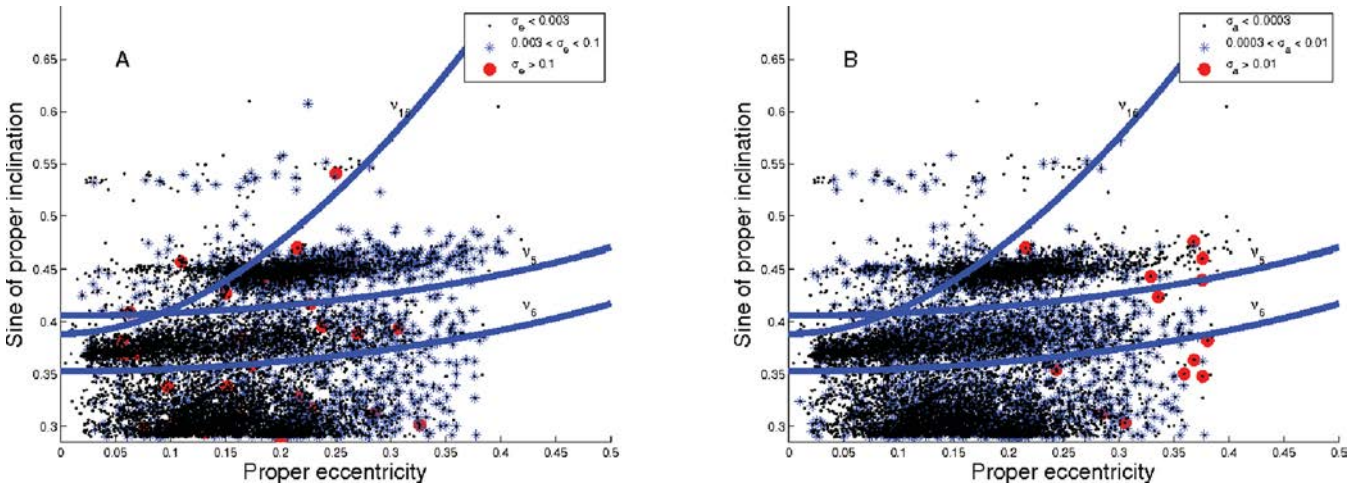

Figure 5. Panel A: an $(e, \sin(i))$ projection of asteroids in the region of the Euphrosyne family. Blue asterisks display asteroids with standard deviation on a σ_e between 0.003 and 0.1, while red circles show asteroids with σ_e larger than 0.1. Panel B: an $(e, \sin(i))$ projection of the same asteroids, but this time blue asterisks display asteroids with standard deviation on a σ_i between 0.001 and 0.03, while red circles show asteroids with σ_i larger than 0.03.

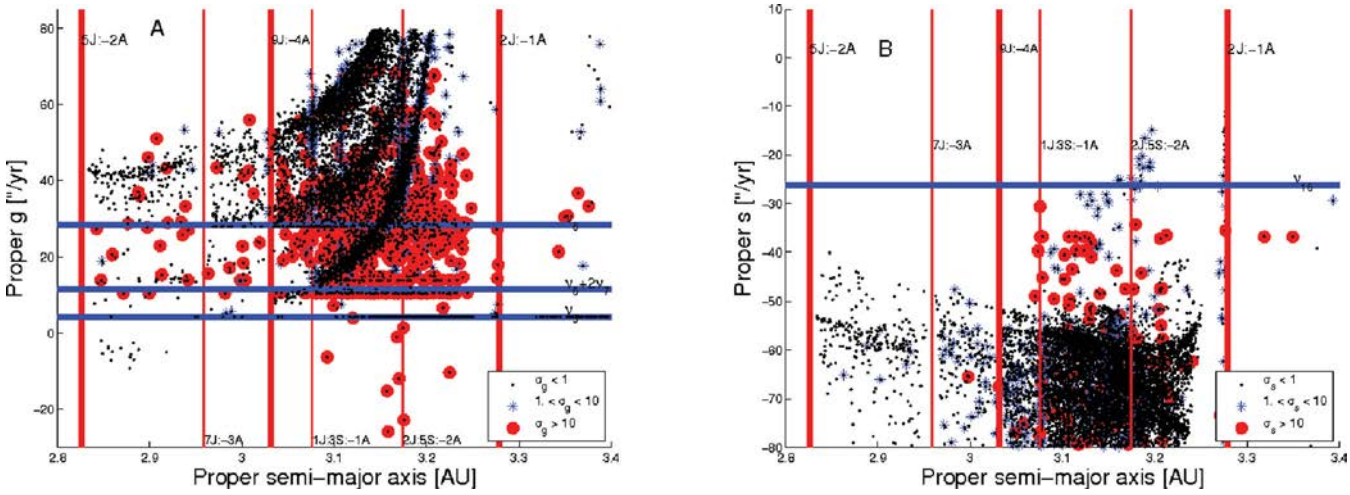

Figure 6. Panel A: an (a, g) projection of asteroids in the region of the Euphrosyne family. Blue asterisks display asteroids with standard deviation on σ_g between 1 and 10, while red circles show asteroids with σ_g larger than 10. Panel B: an (a, s) projection of the same asteroids.

will be discussed in Section 5. We also observe that many asteroid families in the area seem to be crossed by the ν_6 secular resonance. The role of this resonance will also be investigated in more detail in Section 5.

An analysis of the $(a, \sin(i))$ projection shows that the Euphrosyne region can be divided in two areas by the 9J:-4A mean-motion resonances. The region between the 5J:-2A and the 9J:-4A has a much lower asteroidal density than the region between the 9J:-4A and the 2J:-1A. The ν_6 secular resonance divide this region in two areas, one associated with (61) Danae, the lowest numbered object in the region, at inclinations lower than the ν_6 centre, and one associated with (705) Erminia, at higher inclination. For semi-major axis in between the 9J:-4A and the 2J:-1A we can distinguish four major groups at increasing inclinations: from bottom to top, the clusters associated with (1303) Luthera, (702) Alauda, (31) Euphrosyne) and (69032) (2002 WG17). The ν_6 secular resonance marks the boundary of the Alauda region at small semimajor axis, while the ν_{16} resonance delimitate the boundary of the Euphrosyne area. Overall, we introduce six regions names to describe the areas that we identified in this preliminary analysis: the Erminia, the Danae, the Luthera, the Alauda, the Euphrosyne and the (2002 WG17) regions. The boundaries of each region are marked in Fig. 4, panel B.

In Fig. 5 we display an $(e, \sin(i))$ projections of asteroids with values of the errors in e (panel A) and i (panel B) for 'stable' (black dots), 'unstable' (blue asterisks) and 'pathological' (red circles) proper elements. As in Fig. 4, blue lines display the location of the main secular resonances in the region. One can notice the regions of lower asteroid number density associated with the linear pericentre secular resonances ν_5 and ν_6, and how the number density is lower, but not null, in regions near the ν_6 resonance. Also, as can be seen in the figure, errors in eccentricity and inclination are larger for asteroids at high inclination, but not negligible for asteroids at lower inclinations, contrary to what observed for highly inclined objects in the region of the Pallas family (Carruba 2010b).

Finally, we displayed in Fig. 6 an (a, g) (panel A) and an (a, s) (panel B) projections of asteroids in the region of the Euphrosyne family. Blue asterisks display asteroids with standard deviation on σ_g and σ_s between 1 and 10, while red circles show asteroids with σ_g and σ_s larger than 10. Here we decided to plot g and s as functions

of a rather than n to allow a more easy comparison of these figures with Fig. 4. Note the perturbing effect on g values as a function of a near the 2J:-1A mean-motion resonances (panel A) also discussed in Carruba & Michtchenko (2009). Objects with semimajor axis near the values of the 2J:-1A separatrix have values of errors on the g and s frequencies classified as pathological. Many objects that seem to reside inside the ν_6, ν_5 and ν_{16} secular resonances have their value of proper frequencies so perturbed by the presence of the 2J:-1A that their resonant status is quite probably not real (with the possible exception of a small population of object at low a whose frequencies put it inside the ν_6 resonance whose status will be investigated in Section 5). This concern also applies for objects inside the $\nu_6 + 2\nu_7$ resonance. This and other non-linear secular resonances will be investigated in more detail in Section 5.

To have a preliminary idea of the relative importance of the effect of each secular resonance here we started to check how many real objects are inside each of the secular resonance involving the Jupiter and Saturn frequencies g_5, g_6 and s_6 in the region, up to order six.[5] We do not included at this stage resonances involving other planets. One can however notice that because of the close values of g_5 and g_7 the location of Uranian resonances are close in proper element space to that of pericentre resonance involving Jupiter. We divided resonances according to what asteroidal frequencies are involved in the resonance argument. So, resonances as the $\nu_6 = g - g_6$ are g-type resonance, resonances like the $z_1 = g - g_6 + s - s_6$ are $g + s$ resonances and so forth. As a preliminary criterion justified from past experiences with secular resonances (Carruba 2009a), we considered asteroids as more likely to be inside a secular resonance if the resonant combination of their proper frequencies is to within 0.3 arcsec yr^{-1} from the resonance centre. For instance, in the case of the z_1 resonance we considered resonant candidates asteroids with values of $g + s$ to within $\pm$ 0.3 arcsec yr^{-1} from the planetary frequency combination $g_6 + s_6$. We warn the reader that this is a preliminary method and that the effective orbital behaviour of such asteroids needs to be checked by performing numerical simulations and by verifying the time dependence of the resonant argument. The results of our analysis are listed in Table 1. The large apparent number of asteroids in the ν_5 resonance is an artefact caused by the proximity effect of the 2J:-1A mean-motion resonance. We can notice the relative large number of objects in some pericentre resonances such as the $3\nu_6 - \nu_5$, and surprisingly in a $2g + s$ resonance such as the $2\nu_5 + \nu_{16}$. We will further investigate these and other secular resonances in the next sections.

Table 1. Main secular resonances in the Euphrosyne region, frequency value and number of resonant asteroids.

Resonance argument	Frequency value (arcsec yr^{-1})	Number of resonant asteroids
	g resonances	
ν_5	4.257	2445
ν_6	28.243	210
$2\nu_5 + \nu_6$	12.2523	7
$2\nu_6 + \nu_5$	20.2476	58
$2\nu_5 - \nu_6$	−19.729	0
$2\nu_6 - \nu_5$	52.229	66
$3\nu_5 - \nu_6$	−7.736	0
$3\nu_6 - \nu_5$	40.236	106
$3\nu_5 - 2\nu_6$	−43.715	0
$3\nu_6 - 2\nu_5$	76.215	39
	s resonances	
ν_{16}	−26.345	82
	$g + s$ resonances	
$\nu_5 + \nu_{16}$	−22.088	0
$\nu_6 + \nu_{16}$	1.898	21
$2\nu_5 - \nu_6 + \nu_{16}$	-46.074	0
$2\nu_6 - \nu_5 + \nu_{16}$	25.884	1
	$g + 2s$ resonances	
$\nu_5 + 2\nu_{16}$	−48.433	73
$\nu_6 + 2\nu_{16}$	−24.447	1
	$g - s$ resonances	
$\nu_5 - \nu_{16}$	30.602	47
$\nu_6 - \nu_{16}$	54.588	1
$2\nu_5 - \nu_6 - \nu_{16}$	6.616	0
$2\nu_6 - \nu_5 - \nu_{16}$	78.574	78
	$g - 2s$ resonances	
$\nu_5 - 2\nu_{16}$	56.947	70
$\nu_6 - 2\nu_{16}$	80.933	1
	$2g + s$ resonances	
$2\nu_5 + \nu_{16}$	−17.831	138
$2\nu_6 + \nu_{16}$	30.141	45
$\nu_5 + \nu_6 + \nu_{16}$	6.155	56
	$2g - s$ resonances	
$2\nu_5 - \nu_{16}$	34.859	72
$2\nu_6 - \nu_{16}$	82.831	86
$\nu_5 + \nu_6 - \nu_{16}$	58.845	3

4 LINEAR SECULAR RESONANCES IN THE EUPHROSYNE REGION

To improve our understanding of the local dynamics in this section we study the behaviour of the resonant argument of asteroids that we found to satisfy the 0.3 arcsec yr^{-1} criterion for the ν_5 and ν_{16} secular resonances and the 0.8 arcsec yr^{-1} criterion for the ν_6 secular resonance. How many of these objects are actually in a resonant configuration, and what kind of resonant configurations are possible?

Asteroids in or near secular resonances can show essentially five types of behaviour of the resonant argument as a function of time: circulating orbits (the resonant argument circulates from 0° to 360°), aligned librating states (the resonant argument oscillates around 0°), anti-aligned librating states (the resonant argument oscillates around 180°) and orbits switching from aligned librating to circulating states and from anti-aligned librating to circulating states.

Each of the objects to within the resonant frequency criterion was integrated with SWIFT_MVSF over 20 Myr under the gravitational influence of all planets and (1) Ceres and its resonant argument was analysed. Objects in circulating orbits will be indicated by black dots in the next figures, asteroids in aligned librating states will be shown by blue full dots, while objects in orbits that switch between circulation and libration (either aligned or anti-aligned) will be displayed by green asterisks. Identifying asteroids in resonant configurations will allow us to better deal with the problem of family identification. We will start our analysis with the case of the ν_6 secular resonance.

[5] In view of its importance (Carruba & Michtchenko 2009), we also considered the eight-order resonance $z_3 = 3\nu_6 + \nu_{16}$; there are 33 objects to within 0.3 arcsec yr^{-1} from the resonance centre.

4.1 The role of the ν_6 secular resonance

The ν_6 secular resonance is the main linear secular resonance in the asteroid belt (Morbidelli & Henrard 1991) and it is a well-known dynamical mechanism to produce Earth's meteorites (Bottke et al. 2006). We analysed the behaviour of the resonant argument of the 210 asteroids that satisfied the ± 0.8 arcsec yr^{-1} criterion described in Section 3. We found 63 objects in circulating orbit, identified by black dots in Fig. 7, and 30 asteroids alternating phases of circulation and librations (green asterisks in Fig. 7), seven of them having phases of aligned libration and 23 of them showing phases of anti-aligned libration. Not surprisingly, we did not identify asteroids on aligned librating orbits, since these objects are highly unstable (Carruba & Morbidelli 2011). What was surprising was the high number of anti-aligned asteroids (red full dots in Fig. 7): we identified 92 asteroids (see Tables A1 and A2) in anti-aligned configurations of the ν_6 resonance, which is a higher number than that of asteroids in the region of the newly identified Tina family in the same orbital configuration (91; Carruba & Morbidelli 2011). The large presence of anti-aligned librating asteroids in the region of the Alauda family, apart from being a very interesting dynamical result in itself, has consequence for what concerns family identification: since there is a large population of ν_6 anti-aligned librating asteroids in the region, appropriate resonant proper elements should be computed for the such bodies, following one of the approaches described in Carruba & Morbidelli (2011). Furthermore, it can be clearly seen that anti-aligned ν_6 asteroids form the boundary of the Alauda region. How effective is the ν_6 secular resonance in forming a dynamical boundary for the local asteroidal population, when non-gravitational forces are present? We will investigate this subject in a later section.

4.2 The role of the ν_5 secular resonance

The other main linear secular resonance involving pericentre frequencies is the ν_5 resonance. A large number of objects (2445) satisfied the ± 0.3 arcsec yr^{-1} criterion of Section 3. Fig. 8 displays an (a, $\sin(i)$) projection of objects in circulating (2284 objects, black dots), anti-aligned librating (seven asteroids, red full dots), aligned librating (20 objects, blue full dots) and objects on switching orbits (133 bodies, green asterisks). Remarkably, we identified for the first time objects in aligned and anti-aligned librating orbits in the region. Objects in ν_5 anti-aligned states are mostly found at high inclinations, in the (69032) 2002 WG17 and Euphrosyne regions, while objects in aligned librating are found in all the regions, with the exception of the (61) Danae area. The list of objects in ν_5 librating states is given in Table A3.

With respect to the ν_6 resonance, we found that the number of objects in librating states is somewhat limited: there is a total of 27 resonant asteroids against the 94 asteroids in ν_6 anti-aligned librating states. This is understandable if we consider the larger width in the (a, e, $\sin(i)$) domain of the ν_6 resonance with respect to the ν_5, predicted by analytical models such as those described in

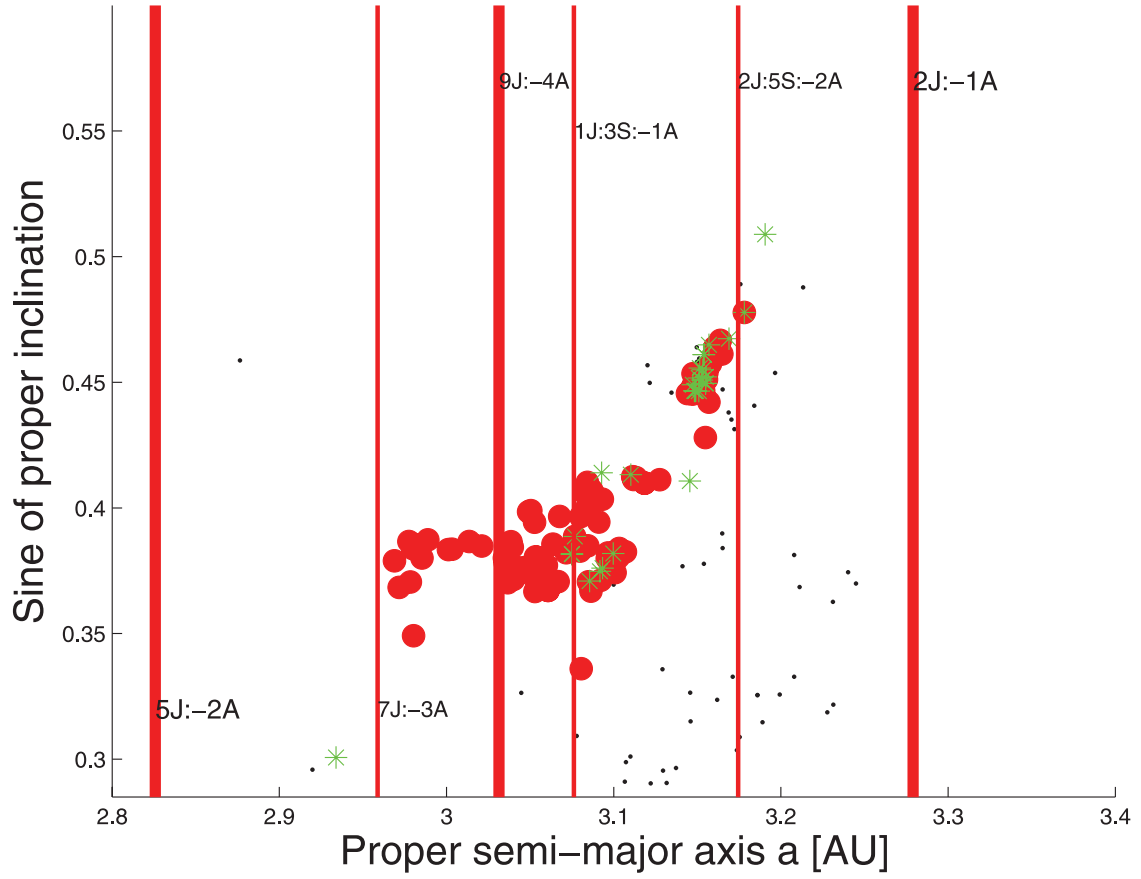

Figure 7. A (a, $\sin(i)$) projection of asteroids to within 0.8 arcsec yr^{-1} from the centre of the ν_6 secular resonance. Black dots show the orbital locations of asteroids on circulating orbits, red full dots display asteroids in anti-aligned librating orbits and green asterisks identify asteroids on orbits alternating circulation with libration.

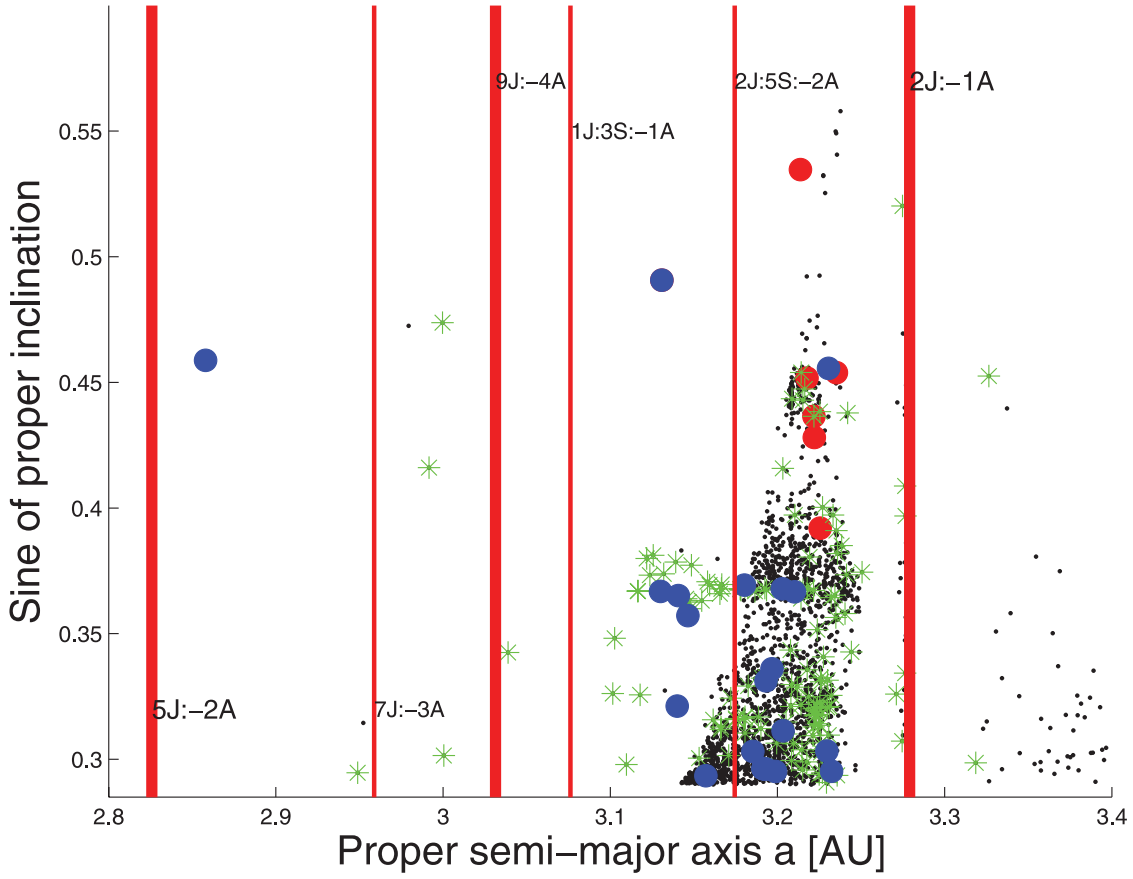

Figure 8. A (a, $\sin(i)$) projection of asteroids to within 0.3 arcsec yr^{-1} from the centre of the ν_5 secular resonance. Blue dots identify objects in aligned librating states, the other symbols have the same meaning as in Fig. 7.

Yoshikawa (1987) and Morbidelli & Henrard (1991). We could not find a more stringent criterion for identifying resonant objects on the base of their g frequency. Objects in aligned and anti-aligned states have frequency values in the same range of objects in circulating states. Only an analysis of their resonant angle time behaviour is therefore able to correctly identify these objects, at this stage of our knowledge.

4.3 The role of the ν_{16} secular resonance

We identified a total of 74 asteroids (47 numbered and 27 multi-opposition) that satisfied our 0.3 arcsec yr^{-1} pre-selection criterion for the ν_{16} secular resonance. None of these asteroids was found to be in a pure ν_{16} librating state. We however observed one object that alternated phase of aligned libration with circulation [(145555) 2006 MQ12] and two asteroids that alternated phases of anti-aligned libration and circulation [(165809) 2001 RK78 and (176579) 2004 BF73]. All three asteroids did not survive the length of the integration, which may suggest a destabilizing effect of this resonance in the region. We will further investigate the role of the ν_{16} resonance in the next subsection, where the Yarkovsky effect is considered as a mechanism of dynamical mobility.

4.4 Yarkovsky integrations

It has been observed (Carruba & Machuca 2011) that the region between the 5J:-2A and 9J:-4A mean-motion resonances and above the ν_6 resonance is dynamically stable, even when the Yarkovsky force is considered, over time-scales of 100 Myr, but yet characterized by a low number of asteroids, that seems to had been caused by the mechanisms that populated the highly inclined asteroid belt in the early phase of the Solar system history. How effective as dynamical barriers are the main secular and mean-motion resonances in the region, i.e. the ν_6, the ν_{16} and the 9J:-4A? Can the low density of asteroids between the 5J:-2A and 9J:-4A mean-motion resonances be explained by the effect of these resonances on the population of objects migrating to smaller semimajor axis because of the Yarkovsky effect from the Alauda, Euphrosyne and (69032) regions?

To answer this question we numerically integrated the real asteroids near the ν_6 and ν_{16} that satisfied the frequency criterion of proximity to the secular resonances with SWIFT-RMVSY, the symplectic integrator of Brož (1999) that simulates the diurnal and seasonal versions of the Yarkovsky effect, over 200 Myr and the gravitational influence of all planets from Venus to Neptune (Mercury was accounted for as a barycentric correction in the initial conditions). We choose asteroids near these two secular resonance because the ν_6 resonance marks the boundary of the Alauda region and the ν_{16} that of the Euphrosyne one. Since asteroids in the region are mostly C-type, we used values of the Yarkovsky parameters appropriate for such bodies (Carruba et al. 2003): a thermal conductivity $K = 0.001\,\mathrm{W\,m^{-1}\,K^{-1}}$, a thermal capacity $C = 680\,\mathrm{J\,kg^{-1}\,K^{-1}}$, surface density $1500\,\mathrm{kg\,m^{-3}}$, a Bond albedo of 0.1, a thermal emissivity of 0.95 and a bulk density of $1500\,\mathrm{kg\,m^{-3}}$. We used one set of spin axis orientations with -90° with respect to the orbital plane, since our goal is to investigate the diffusion of asteroids from the

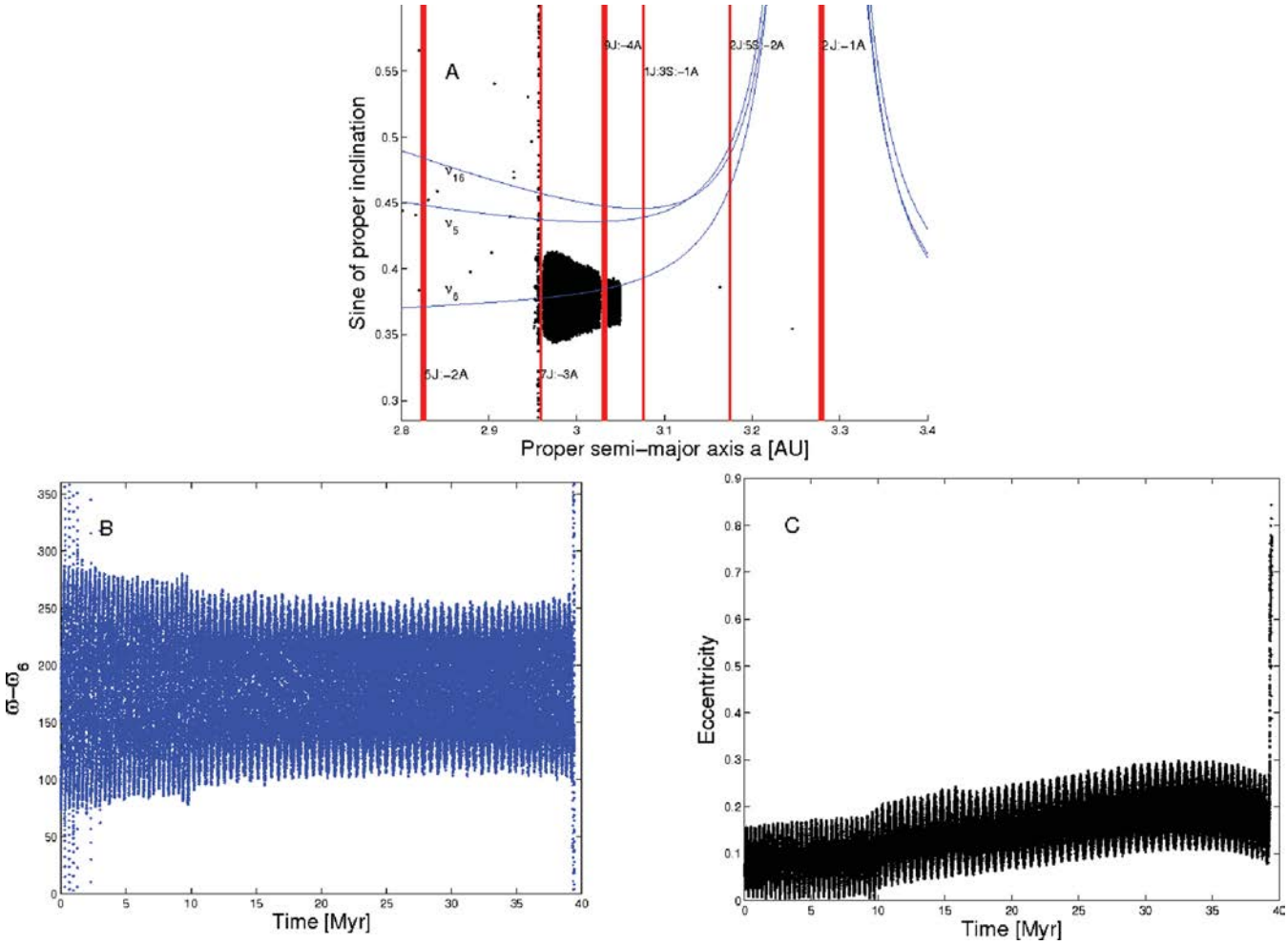

Figure 9. Panel A: an osculating (a, $\sin(i)$) projection of the orbital evolution of a clone of 1998 SD16, each dot shows the orbital position every 600 yr. The other symbols are the same as in Fig. 4. Panel B: the time evolution of the ν_6 resonant argument ($\varpi - \varpi_6$) for the same particle (blue dots). Panel C: the time evolution of the particle eccentricity (black dots); note the increase in the eccentricity when the particle leave the anti-aligned librating ν_6 configuration.

Alauda, Euphrosyne and (69032) regions to lower semimajor axis, and for negative spin-axis orientations the Yarkovsky drift reduces the asteroid a. We assumed periods obtained under the approximation that the rotation frequency is inversely proportional to the object's radius, and that a 1-km asteroid had a rotation period of 5 h (Farinella, Vokrouhlický & Hartmann 1998). No re-orientations were considered, so that the drift caused by the Yarkovsky effect was the maximum possible. We integrated on set of bodies with radii of 100 m so as to obtain information on resonance crossing at a somewhat enhanced drift rate that that for km-size objects. Since our goal was to obtain information on the possibility of asteroids to reach the Danae and Erminia regions from larger initial semimajor axis, we believe that our approach was justified.

Of the 122 clones of asteroids that had an initial frequency near the centre of the ν_6 resonance, only seven particles (5.7 per cent of the total) survived the passage of the three main-motion resonances in the region, the 1J:-3S:-1A, the 9J:-4A and the 7J:-3A, which may explain the low number density of objects in the Danae and Erminia regions. The other particles, in anti-aligned librating or in circulating ν_6 configurations, had their eccentricity increased to planet crossing level because of the passage through one of these resonances and were lost on time-scales of at most Myr. 15 particles were lost at the passage of the 1J:-3S:-1A, 41 were lost at the passage of the 9J:-4A and 57 at the passage of the 7J:-3A (two particles were lost because of the interaction with other minor resonances such as the 2J:-2S:-2A). Fig. 9, panel A, shows an (a, $\sin(i)$) projection of the orbital evolution of a clone of 1998 SD16, an asteroid in a ν_6 anti-aligned configuration, that had the typical behaviour shown by many objects in such orbital configuration. The clone of the asteroid survived the passage through the 1J:-3S:-1A and the 9J:-4A resonances, while remaining in a ν_6 anti-aligned librating configuration (see the resonant argument in Fig. 9, panel B). This configuration prevented the asteroid from reaching planet-crossing values of the eccentricity (see Carruba & Morbidelli 2011, for a description of this protection mechanism) until the asteroid reached the 7J:-3A mean-motion resonance, escaped from the anti-aligned configuration, had its eccentricity increased to planet crossing levels, and was then lost in time-scales of a few thousand years.

The mechanism of crossing of the three resonances, consequent increase in the particle eccentricity and loss because of planets encounters applied to particles in ν_6 circulating states and also to the 71 test particles near the ν_{16} secular resonance that we integrated, of which only four (again, about 5.7 per cent of the total) reached the Danae and Erminia regions (none of these particles remained in a ν_{16} librating configuration during the length of the simulation). Overall, the passage through the multiple barriers (the three

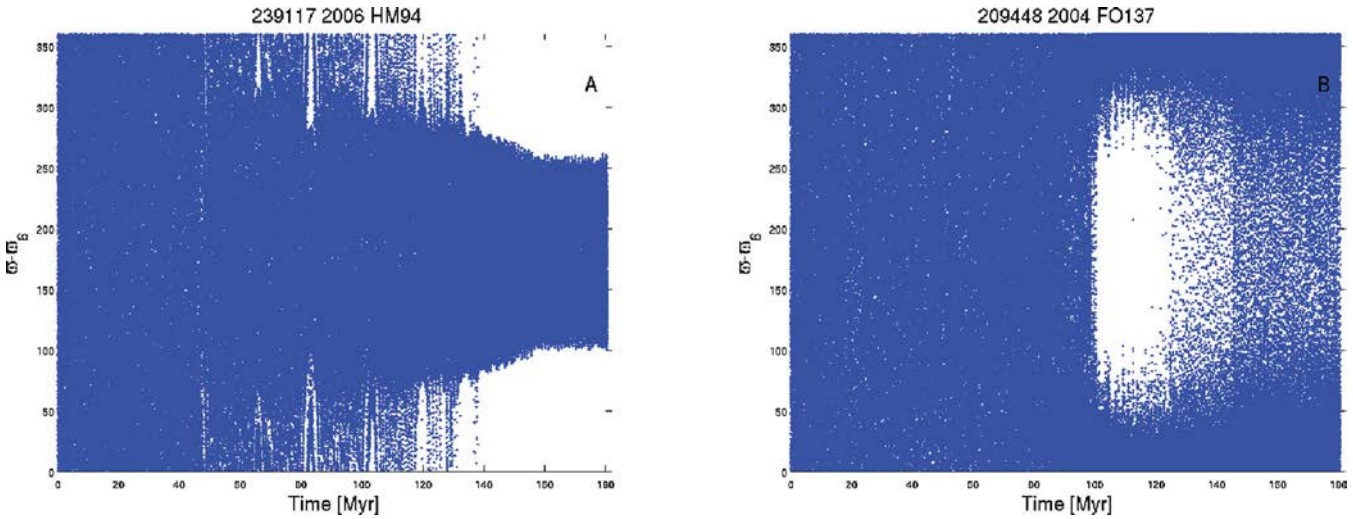

Figure 10. Time evolution of the ν_6 resonant argument of a clone of (239117) 2006 HM94 (Panel A, capture into an anti-aligned ν_6 resonant state), and of (209448) 2004 FO137 (Panel B, capture into an aligned ν_6 resonant state).

mean-motion resonances in the region) may explain why the number density of objects in the Danae and Erminia regions is relatively low. If only about 6 per cent of the asteroids at higher semimajor axis can reach these regions, we would expect that the density of objects should be an increasing function of the semimajor axis, i.e. maximum for larger semimajor axis and minimum on the left-hand side of the 7J:-3A mean-motion resonance, that is what we observe. This if no object was originally present in the Danae and Erminia regions. The fact that these regions are dynamically stable (Carruba & Machuca 2011) and yet underpopulated may therefore be related to the mechanisms that created the primordial population of highly inclined asteroids.

Among the objects originally in circulating ν_6 states, we found two interesting orbital evolutions. Fig. 10, panel A, displays the time evolution of the ν_6 resonant argument of a clone of (239117) 2006 HM94, an object that was captured into an anti-aligned ν_6 resonant state. The fact that such capture is possible may have interesting consequences for the origin of the Tina family, an asteroid family in the central main belt whose members are all in such resonant configuration (Carruba & Morbidelli 2011). This simulation may indicate that ν_6 anti-aligned asteroids may be currently be captured inside such configuration, and that (1222) Tina, the larger asteroid in the family, may not need to have been captured in the primordial phases of our Solar system. Further work is however needed to conclude if capture into a ν_6 anti-aligned state by Yarkovsky mobility may apply to the Tina family.

Finally, Fig. 10, panel B, shows the resonant angle of (209448) 2004 FO137, an object temporarily captured into an aligned ν_6 resonant state. It was the only object that we found in our integration to have been captured into such state that survived for a quite long time (about 40 Myr), without experiencing planetary encounters.

5 DYNAMICAL FAMILIES AND CLUMPS IN THE EUPHROSYNE REGION

Now that we obtained a reliable set of proper elements for both numbered and multi-opposition asteroids in the region of the Euphrosyne family, the next logical step is to obtain dynamical families and clumps in the region.

Dynamical asteroid families are groups of objects that are close in the domain of proper elements (a, e, $\sin(i)$) or in the domain of proper frequencies (n, g, $g+s$) being one of the most commonly used frequency domain. We will start our analysis by considering dynamical groups in the space of proper elements. In order for two objects in such space to be considered related, their distance should be less than a critical value, called cut-off. The 'standard metrics' of Zappalá et al. (1995) in the (a, e, $\sin(i)$) space computes the distance between two asteroids using the metric:

$$d = na\sqrt{k_1(\Delta a/a)^2 + k_2(\Delta e)^2 + k_3(\Delta \sin(i))^2}, \quad (1)$$

where n is the asteroid mean motion, Δx the difference in proper a, e and $\sin(i)$ and k_1, k_2, k_3 are weighting factors, equal to 5/4, 2 and 2, respectively, in the standard metric of Zappalà et al. (1995).[6] Such distances are related to the ejection velocity field that allegedly originated the family and are measured in $\mathrm{m\,s^{-1}}$. If the second asteroid is less distant than the cut-off, it is added to the dynamical group originating with the first asteroid. The procedure is then repeated for the second objects until no other member of the group is found. In identifying asteroid families in the space of proper elements two parameters are fundamental: the cut-off distance at which the family members are defined, d_0, and the minimum number of objects $N_{\min}$ for a cluster to be considered significant. Beaugé & Roig (2001) define a nominal distance cut-off as the average minimum distance between all the neighbouring asteroids in the same region of the asteroid belt. The value of $N_{\min}$ is defined by Zappalà et al. (1995) as

$$N_{\min} = N_0 + 2\sqrt{N_0}, \quad (2)$$

where N_0 is the average number of orbits within a sphere of radius d_0 at every point of the proper element space. A cluster with a number of objects larger than this critical value is called a clump, while a family is a cluster with a number of members larger than $2.5\,N_{\min}$. The region of the Euphrosyne family is delimited by the 5J:-2A and 2J:-1A mean-motion resonances in proper a. For the purpose

[6] This choice of weighting factor was made to give a greater weight to the proper semimajor axes. Other choices of weighting factors, giving for instance a greater weight to the proper inclinations, are possible and were used in the past (Zappalá et al. 1995).

of family identification, we can distinguish six regions, defined in Section 3, named after the asteroid with the lowest number in the region: Erminia, Danae, Luthera, Alauda, Euphrosyne and (69032 2002 WG17). The 9J:-4A mean-motion resonance separates Danae and Erminia from the more populated areas of Luthera, Alauda and Euphrosyne. The small region at high inclination around (69032) is finally separated from the Euphrosyne area by a gap in inclination and is connected to this region only for very high values of the cut-off d_0. In view of the dynamical boundaries in the area, we can compute the nominal distance cut-off d_0 and $N_{\rm min}$ for three areas: the Danae and Erminia region, the Luthera, Alauda and Euphrosyne area and the small (69032) region.

The nominal distance velocity cut-off as defined in Beaugé & Roig (2001) is of 164.05 m s^{-1} for asteroids in the first areas,[7] and of 64.4 m s^{-1} for asteroids in the second, more populated region. At these cut-offs, the corresponding values of $N_{\rm min}$ are 6 and 9, respectively. Concerning the Luthera, Alauda and Euphrosyne region, the fact that max (N_i) is much larger (more than twice) than $N_{\rm min}$ may be a hint that background objects are more numerous than family ones, contrary to what happens in the Phocaea family region (Carruba 2009b).[8] Finally, the nominal distance velocity cut-off d_0 for the (69032) region is 269 m s^{-1}, and at this cut-off eight objects are needed to form a clump and 20 for a family.

To identify families and clumps in a region a stalactite diagram is usually used. Stalactite diagrams display groups identified at various cut-offs by colour code. If an asteroid at a given cut-off is a member of a dynamical family is identified by a black square, if it is a member of a clump by a red square and is not shown if it is not a group member. The procedure to create a stalactite diagram is the following: first we identified the cut-off for which all asteroids within the dynamical barriers of the region are found, for instance, in the case of the (69032) region, at 550 m s^{-1} the family found in the region merges with the Euphrosyne family, so 550 m s^{-1} is the maximum limit for which the region is defined. The cut-off is then lowered and among the asteroids that are no longer members of the group one looks for possible other clusters. The cut-off is then lowered again and the procedure repeated until no clusters are found in the region.[9] Now that we have introduced the tools for family determination, we are ready to look for families and clumps in the region. We will first look for groups in the space of proper elements and then consider possible agglomerations in the domain of proper frequencies (Carruba & Michtchenko 2007, 2009). Asteroids close in the frequency domain may either be members of a collisional group that drifted inside a secular resonance, or objects trapped by the local dynamics in a limited region. Since in this work our goal is to investigate the effect that secular dynamics had on the local asteroidal population, we will focus our efforts on studying groups in the frequency domains inside or near non-linear secular resonances, by using distance metrics appropriate for the case of each secular resonance of interest (Carruba & Michtchenko 2007, 2009). In particular, for groups in $g + s$, $g + 2s$, $g - s$, $g - 2s$, $2g + s$ and $2g - s$ type of resonance, the following distance metrics can be used:

$$f = \sqrt{h_1 \left(\frac{\Delta n}{h_0}\right)^2 + h_2(\Delta g)^2 + h_3(\Delta(g+s))^2}, \quad (3)$$

$$f = \sqrt{h_1 \left(\frac{\Delta n}{h_0}\right)^2 + h_2(\Delta g)^2 + h_3(\Delta(g+2s))^2}, \quad (4)$$

$$f = \sqrt{h_1 \left(\frac{\Delta n}{h_0}\right)^2 + h_2(\Delta g)^2 + h_3(\Delta(g-s))^2}, \quad (5)$$

$$f = \sqrt{h_1 \left(\frac{\Delta n}{h_0}\right)^2 + h_2(\Delta g)^2 + h_3(\Delta(g-2s))^2}, \quad (6)$$

$$f = \sqrt{h_1 \left(\frac{\Delta n}{h_0}\right)^2 + h_2(\Delta g)^2 + h_3(\Delta(2g+s))^2}, \quad (7)$$

$$f = \sqrt{h_1 \left(\frac{\Delta n}{h_0}\right)^2 + h_2(\Delta g)^2 + h_3(\Delta(2g-s))^2} \quad (8)$$

(where $h_1 = h_2 = h_3 = 1$). We should emphasize that the objective of looking for cluster in the frequency space is not to try to reconstruct the original ejection velocity field, but to look for objects that were either members of a family that drifted into a non-linear secular resonance or for groups of asteroids that are inside such resonances. Traditional HCM method in proper element domain may not recognize these bodies as members of a family. For instance, in the regions of the Eos and the Vesta families former family members of the typical *K* and *V* taxonomical types drifted into such resonances and are no longer recognized as part of the group by the traditional HCM. It is to address such cases that we will look for groups in the appropriate proper frequency domain. We start our analysis by considering the Euphrosyne region.

5.1 Euphrosyne region

The Euphrosyne region is limited in semimajor axis by the 9J:-4A and 2J:-1A mean-motion resonances. Is separated by the (69032) region by a low-density area of asteroids at 0.5 in sin (i) and by the Alauda region by a low-density region at sin $(i) \simeq 0.41$. Communications between the Euphrosyne region is possible via Yarkovsky-driven mobility through the secular resonance ν_5, that connects it to the (69032) region and the Erminia area, the ν_6 resonance (connection to the Erminia region) and through the 2J:-5S:-2A mean-motion three-body resonance (and other resonances in the area) that connect the region to the Alauda zone. The nominal distance velocity cut-off as defined in Beaugé & Roig (2001) is of 64.4 m s^{-1} for asteroids in this area, and $N_{\rm min}$ was nine asteroids, and 21 for a family.

We identified four families and three clumps in the area. Fig. 11, panel A, displays a stalactite diagram for the region. At 65 m s^{-1} the Euphrosyne family splits into four families and three clumps, but since all these splinter groups are not visible at lower cut-offs and they do not satisfy the criteria introduced in Carruba (2010b) for a robust dynamical group (a family should be visible over at least 20 per cent of the cut-off used, i.e. about 20 m s^{-1}) we do not consider them as possible dynamical groups. The (7605) group, identified as a family in Novaković et al. (2011), is not observable as a group at 64.4 m s^{-1}, but we identified a separated new clump around (140072) not reported in other works. Fig. 11, panel B, shows an (a, sin (i)) projection of the family and clump identified

[7] We excluded from these areas the few asteroids at inclination higher than 0.5 that are clearly not connected to any family and that would significantly increase the nominal distance velocity cut-off if included.

[8] Regions where background asteroids are more numerous than family ones are characterized by larger values of max (N_i) with respect to $N_{\rm min}$ because in this case a single object may be associated at a given cut-off value with a large number of asteroids that are not members of a family.

[9] Using the Beaugé and Roig method to determine N_0, the minimal number of objects needed to form a clump or a family is a function of the cut-off.

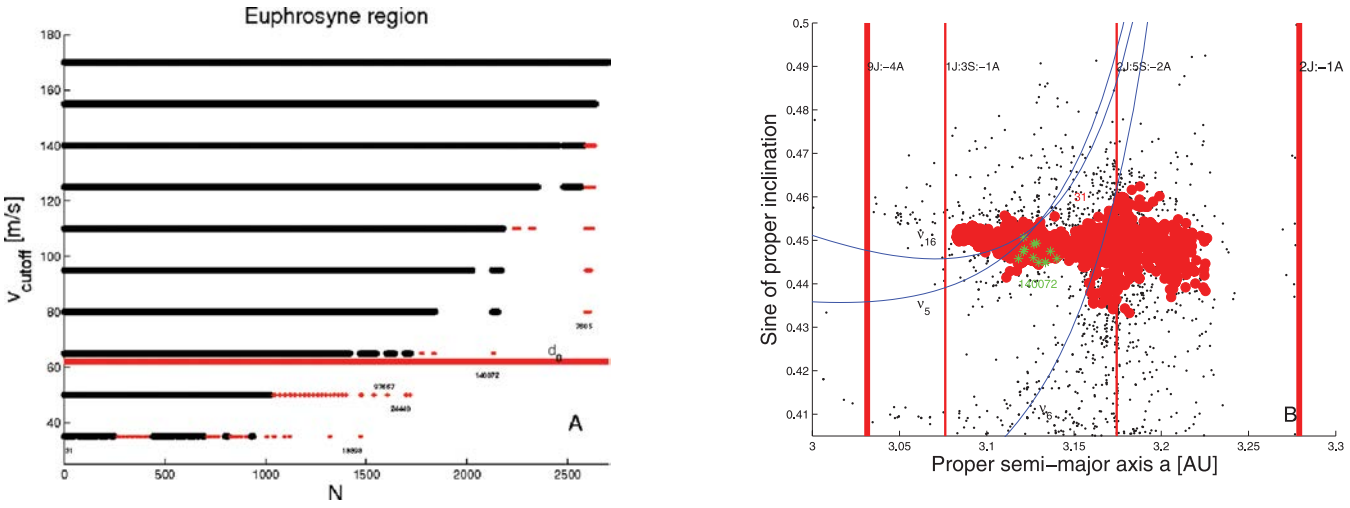

Figure 11. A stalactite diagram for objects in the Euphrosyne region (panel A), the horizontal red line shows the nominal distance cut-off level, and an (a, $\sin(i)$) projection of the families (full circles), clumps (asterisks) and background asteroids in the region (black dots) (panel B).

in this work. Quite interestingly, we identified in the Euphrosyne family 13 asteroids in ν_6 anti-aligned librating states, one in a ν_5 anti-aligned librating state (242435) and one in a ν_5 aligned librating state (2009 UL136). Since for objects in linear secular resonance configurations the standard approach to compute asteroid families is not applicable, one has to conclude that the Euphrosyne family should be looked for in the space of more appropriate ν_6 resonant proper elements, as defined in Carruba & Morbidelli (2011). A discussion on this subject will be given in Section 6.

We then analysed, using our preliminary 0.3 arcsec yr^{-1} criterion, how many asteroids in non-linear secular resonances were present in the Euphrosyne region. The region is crossed by a very rich web of non-linear secular resonances: concerning g-type resonances, we identified six asteroids near the $2\nu_5 + \nu_6$ resonance, seven near the $2\nu_6 + \nu_5$ resonance, 50 near the $2\nu_6 - \nu_5$ resonance, three near the $3\nu_6 - 2\nu_5$ and 27 near the $3\nu_6 - \nu_5$ resonance. Six objects were near the $g + s$-type $\nu_6 + \nu_{16}$, 47 asteroids were near the $g - s$ type $2\nu_6 - \nu_5 - \nu_{16}$ resonance, 17, nine and 57 asteroids were near the $2g + s$-type $\nu_5 + \nu_6 + \nu_{16}$, $2\nu_6 + \nu_{16}$ and $2\nu_5 + \nu_{16}$ resonances and 11 near the $2g - s$-type $2\nu_6 - \nu_{16}$ resonance. Overall, we find asteroids near $g, g + s, g - s, 2g + s, 2g - s$ type non-linear secular resonances, so that four distance metrics given by equations (3), (5), (7) and (8) should be used to find dynamical groups in frequency domains in the region. The nominal frequency cut-off in these domains was of 0.47 arcsec yr^{-1}, and at this cut-off a clump needed to have at least eight members, a family 20 asteroids. We did not find any clump in the investigated frequency domains, but we identified six families, two associated with g-s resonances, three associated with $2g + s$ resonances, and one associated with a $2g - s$ resonance. The families around (18318) and (16708) are chunks of the (31) Euphrosyne family (not containing (31) Euphrosyne itself) elongated along the $2\nu_6 - \nu_5 - \nu_{16}$ and $2\nu_5 + \nu_{16}$ secular resonances. We found four new families along the $2\nu_6 - \nu_5 - \nu_{16}$ (73524, six near-resonant objects), the $\nu_5 + \nu_6 + \nu_{16}$ (34846, two near-resonant objects), the $2\nu_5 + \nu_{16}$ (105597, 12 near-resonant objects) and the $2\nu_6 - \nu_{16}$ (101810, seven near-resonant objects) resonances. The very interesting clump near (105597), characterized by its interaction with the $2\nu_5 + \nu_{16}$ resonance, is the equivalent of the clump found in the proper element domain near (140072). A complete list of the identified families and clumps in the region is given in Table A4.

5.2 Alauda region

The Alauda region is in the same semimajor axis range of the Euphrosyne region, from which it is separated by a low-density region at $\sin(i) \simeq 0.41$. It is separated by the Luthera region by a low-density area at $\sin(i) \simeq 0.34$. Communication to the Danae region is possible via migration through the ν_6 resonance, and the region is connected to the Euphrosyne and Luthera region via the 2J:-5S:-2A mean-motion three-body resonance and other, weaker mean-motion resonances. The nominal distance velocity cut-off and the value of $N_{\rm min}$ are the same as for the Euphrosyne region (64.4 m s^{-1} and 9 asteroids, respectively). It may be worth noticing that (702) Alauda itself is a binary system, according to Margot & Rojo (2007).

We identified two families around (1101) and (18996), and nine clumps around (702), (3025), (10654), (10813), (21224), (26324), (30995), (84404) and (182817) (Fig. 12). As also found by Novaković et al. (2011), the (702) Alauda family of Gil-Hutton (2006) is now spitted into minor group, the (702) clump and the (1101) and (18996) families. We retrieved the (702) and (3025) clumps of Novaković et al. (2011), other minor clumps found in this work are either new or identified by other asteroids in Novaković et al. (2011). The clump around (26324) interacts with the $3\nu_6 - \nu_5$ secular resonance (three members are to within 0.3 arcsec yr^{-1} from the resonance centre), but we did not find any other clump interacting with non-linear secular resonances. Of particular interest is a group around (182817) of six members. While the group has a number of members not large enough for being classified as a clump, four of its members are in ν_6 anti-aligned librating configurations, making it the third group in the main belt to be found in such kind of orbit (Carruba & Morbidelli 2011). We will further investigate this group in Section 6.

We then analysed, using our preliminary 0.3 arcsec yr^{-1} criterion, how many asteroids in non-linear secular resonances were present in the Alauda region. We found three asteroids near the $3\nu_6 - 2\nu_5$ resonance, 24 near the $3\nu_6 - \nu_5$ and 15 near the $2\nu_6 - \nu_5$ resonance, all g-type resonances. We also identified 11 asteroids near the $\nu_6 + \nu_{16}$ $g + s$ resonance, and seven asteroids each near the $2g + s$ resonances $2\nu_6 + \nu_{16}$ and $\nu_5 + \nu_6 + \nu_{16}$. Other secular resonances had populations of 2 asteroids or less. Overall, we found

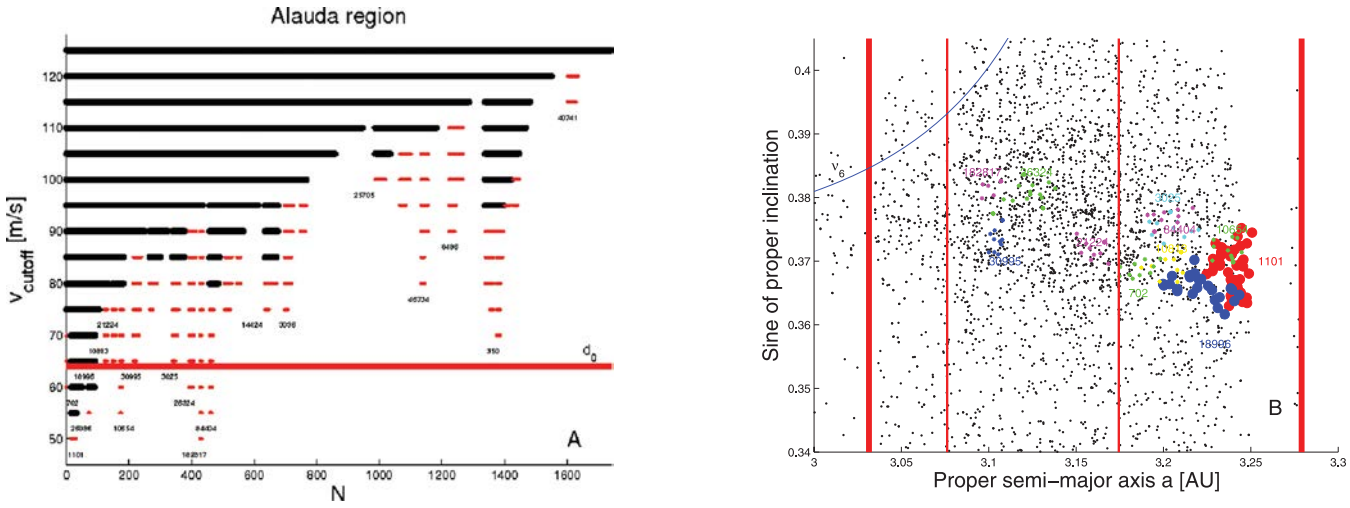

Figure 12. A stalactite diagram for objects in the Alauda region (panel A) and an (a, $\sin(i)$) projection of the families (full circles), clumps (asterisks) and background asteroids in the region (black dots) (panel B).

asteroids near $g, g + s$ and $2g + s$ type non-linear secular resonances, so that two distance metrics given by equation (3), and (7) should be used to retrieve dynamical groups in frequency domains in the region. The nominal frequency cut-off in these domains was of 0.44 arcsec yr^{-1}, and at this cut-off a clump needed to have at least 11 members, a family 28 asteroids. We did not find any group associated with $g + s$ resonances, but in the $(n, g, g + s)$ domain we found one clump of 16 members near (276), associated with the $3\nu_6 - \nu_5$ secular resonance (three resonant members), and a group of 10 objects (not enough just by a member to form a clump) near (30575) again associated with the $3\nu_6 - \nu_5$ secular resonance (six resonant members, is the equivalent of the (26324) clump in the proper element domain). We could not find any new clumps in the $(n, g, 2g + s)$ domain. A complete list of the identified families and clumps in the region is given in Table A5.

5.3 Luthera region

The Luthera region is in the same semimajor axis range of the Euphrosyne region, and in a range of sine of inclinations between 0.29 and 0.34. Nominal distance cut-off and the value of $N_{\min}$ are the same as for the Euphrosyne region.

We identified five families around (780), (781), (1040), (21799) and (103668) in the region (see stalactite diagram in Fig. 13). We retrieved the (780) and (781) families and the (5931) clump found by Novaković et al. 2011, and found three new family in the region, two of which at the limit of detection (21799 and 103668), with 21 members each. 18 minor clumps, mostly at low inclinations, were also identified in this work around (285), (4152), (5931), (5959), (10606), (13684), (19078), (19696), (20409), (26558), (28904), (31762), (40218), (42386), (62633), (69559), (71335) and (87944). In view of the large numbers of clumps in the area, we are not showing their orbital projection in the (a, $\sin(i)$) domain in Fig. 13, panel B.

We then analysed, using our preliminary 0.3 arcsec yr^{-1} criterion, how many asteroids in non-linear secular resonances were present in the Luthera region. The Luthera region is crossed by a very rich web of non-linear secular resonances, concerning g-type resonances we found three objects near the $2\nu_6 + \nu_5$ resonance, five asteroids near the $2\nu_6 - \nu_5$ resonance, one in the $3\nu_6 - \nu_5$ resonance and 20

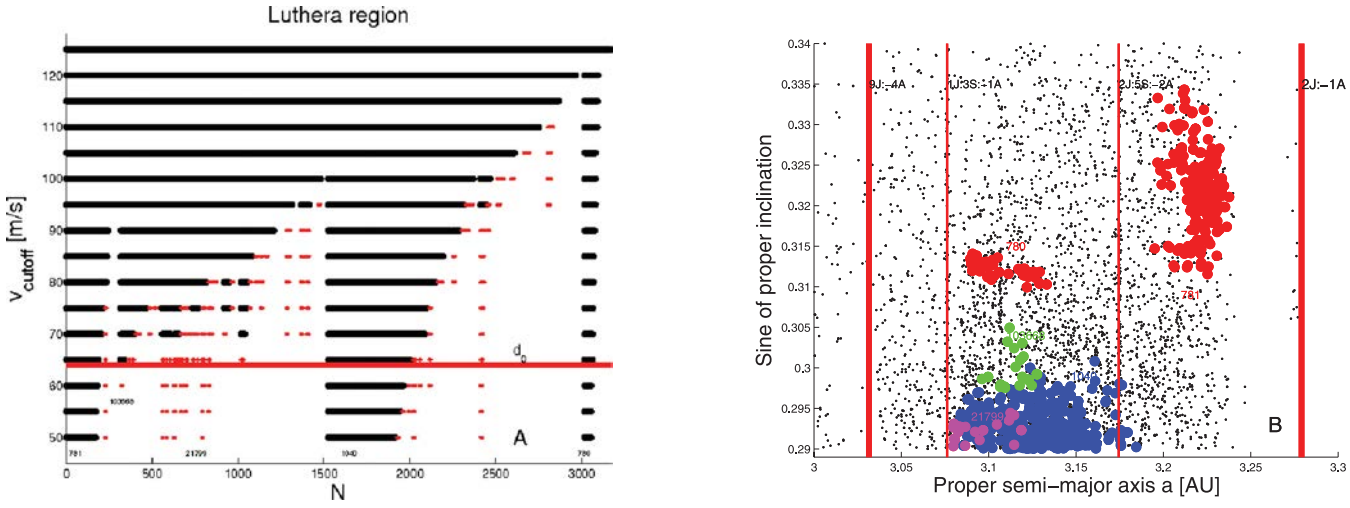

Figure 13. A stalactite diagram for objects in the Luthera region (panel A) and an (a, $\sin(i)$) projection of the families, clumps and background asteroids in the region (panel B). All the symbols have the same meaning as in Fig. 12.

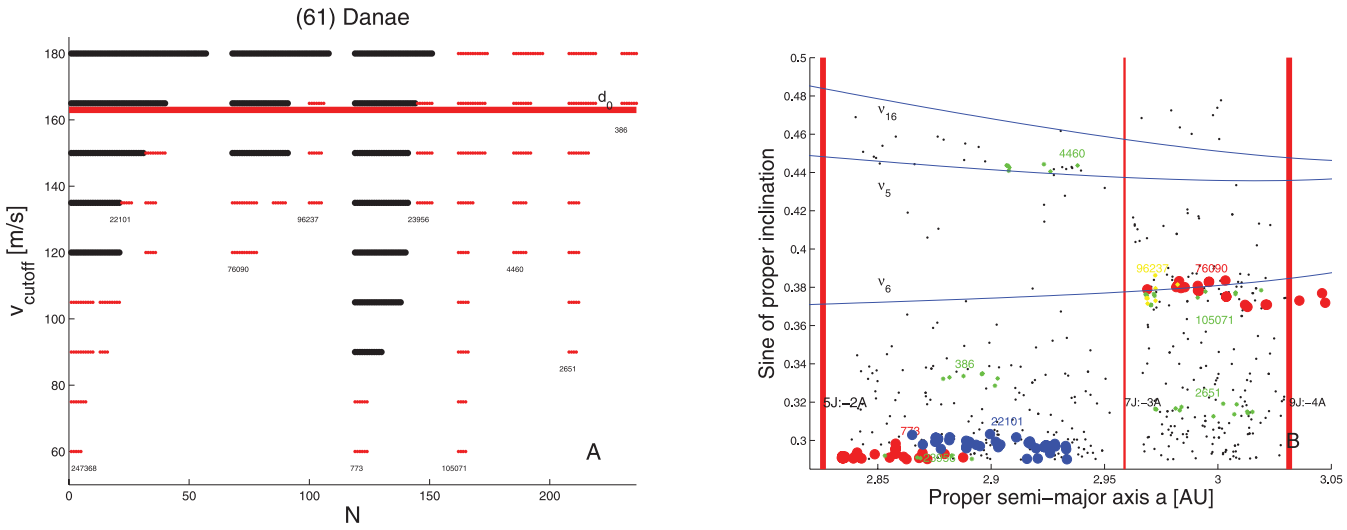

Figure 14. A stalactite diagram for objects in the Danae and Erminia region (panel A) and an (a, $\sin(i)$) projection of the families (full circles), clumps (asterisks) and background asteroids in the region (black dots) (panel B).

in the $3\nu_6 - 2\nu_5$ resonance. We identified 10 objects near the $\nu_5 + 2\nu_{16}$ $g + 2s$ resonance, 10 and 52 asteroids near the $g - s$ $\nu_5 - \nu_{16}$ and $2\nu_6 - \nu_5 - \nu_{16}$ resonances each, 10 objects in the proximity of the $g - 2s$ $\nu_5 - 2\nu_{16}$ resonance, three and 11 asteroids near the $2\nu_6 + \nu_{16}$ and $2\nu_5 + \nu_{16}$ $2g + s$ resonances and 10 and 52 objects near the $2g - s$ $2\nu_5 - \nu 16$ and $2\nu_6 - \nu 16$ resonances each. Overall, we found asteroids near $g, g + 2s, g - s, g - 2s, 2g + s$ and $2g - s$ type non-linear secular resonances, so that the distance metrics given by equations (4)–(8) should be used to retrieve dynamical groups in frequency domains in the region. The nominal frequency cut-off in these domains was of 0.47 arcsec yr^{-1}, and at this cut-off a clump needed to have at least 12 members, a family 30 asteroids.

A group of 10 asteroids near (54571) was of exceptional interest because of the interaction of eight of its members with the $\nu_5 + 2\nu_{16}$, $\nu_5 - \nu_{16}$,$\nu_5 - 2\nu_{16}$, $2\nu_5 + \nu_{16}$ and the $2\nu_5 - \nu_{16}$ secular resonances. The clump at the crossroad of these five resonances was also observable in the proper element domain near (69559) and present similarities with the (6246) clump near the Phocaea family (Carruba 2010a) that was also at the crossroad of two secular resonances (the $\nu_5 + \nu_{16}$ and the $2\nu_6 - \nu_{16}$, in that case). Such groups may possibly be formed by asteroids that drifted in the area because of the local dynamics rather than real collisional groups. It should be noticed that it is the first time that a group of asteroids is found at the crossroad of five non-linear secular resonances. In the $(n, g, g - s)$ and $(n, g, 2g - s)$ domains we also found a family near (781) with 572 members, with 52 members near the $2\nu_6 - \nu_5 - \nu_{16}$ and with 52 members near the $2\nu_6 - \nu_{16}$ secular resonance. This large frequency family corresponds to the proper element based (781) family and it also includes the (4152), (5959), (13684), (26558), (28904) and (87944) clumps. A complete list of the identified families and clumps in the region is given in Table A6.

5.4 Danae and Erminia regions

The Danae and Erminia regions are delimited in semimajor axis by the 5J:-2A and the 9J:-4A mean-motion resonances. The Danae region is separated by the Erminia region by the ν_6 secular resonance, and the Erminia region is crossed by the ν_5 and ν_{16} secular resonances. The nominal distance velocity cut-off is of 164.05 m s^{-1} for asteroids in these areas, and $N_{\min}$ was six asteroids.

We identified three families and six clumps in the region, none of which was reported in previous works, that used smaller velocity cut-offs appropriate for the Euphrosyne region as a whole. Fig. 14, panel A, displays the stalactite diagram for the area, while panel B of the same figure shows the (a, $\sin(i)$) orbital location of families (full circles), clumps (asterisks) and background asteroids in the region (black dots). Two of our families, the one around (773) and (22101), are located at relatively low values of inclinations and should actually be considered 'low-inclination' families. More interesting is the family around (76090): we found that three of its members are actually in ν_6 anti-aligned librating states: (140410, 224545 and 2006PR19). The fact that this family is also made of ν_6 anti-aligned librators implies that the use of standard proper elements is not appropriate in this region, ν_6 secular elements defined with one of the procedures described in Carruba & Morbidelli (2011) should rather be used for this area. We will further investigate this subject in a next section. Finally of the six clumps identified in this work, only one is in the Erminia region, the one around (4460). Three clumps were found at semimajor axes larger than the 7J:-3A centre and two at lower semimajor axis in the Danae region. The lowest number of clumps found at smaller semimajor axes is compatible with our scenario in which Danae asteroids are objects that migrated from higher semimajor axes, as investigated in Section 4.4.

We then analysed, using our preliminary 0.3 arcsec yr^{-1} criterion, how many asteroids in non-linear secular resonances were present in the Danae region. We found one asteroid each in these three non-linear secular resonances: (2006 YQ7) inside the $2\nu_6 - \nu_5 - \nu_{16}$, (199575) inside the $2\nu_5 + \nu_{16}$ resonance, and (2003 SM193) inside the $\nu_5 + \nu_6 + \nu_{16}$. Eight asteroids were found in the $2\nu + \nu_{16}$ resonance and five inside the $\nu_5 + \nu_6 + \nu_{16}$, a 2g+s secular resonances. Since most of the possible resonant objects in the area are in g and 2g+s type resonances, we used the distance metric in the space $(n, g, g - s)$ defined by the equation (7) to obtain groups in the proper frequency domain. The nominal frequency cut-off in this domain was of 1.1 arcsec yr^{-1}, and at this cut-off a clump needed to have at least 17 members, a family 43 asteroids. We found two groups near the two 2g+s secular resonances: a clump of 23 objects

near (43522), three members of which satisfied the 0.3 arcsec yr^{-1} criterion for the $\nu_5 + \nu_6 + \nu_{16}$ secular resonance, and a family around (1191) of 105 members with six members possible $2\nu_6 + \nu_{16}$ librators. The (1191) frequency family englobes the two families found in the proper element domain around (773) and 22101), but oddly enough not the two lowest numbered asteroids in these two families. The (43522) clump does not include any ν_6 anti-aligned librators. A complete list of the identified families and clumps in the region is given in Table A7.

5.5 (69032) region

The 69032 region is delimited in semimajor axis by the 2J:5S-2A and 2J:-1A mean-motion resonances and in inclination for values of $\sin(i) > 0.5$. The region is crossed by all three main linear secular resonances, and it has a population of 54 objects. We first obtained families and clumps in the $(a, e, \sin i)$ domain. The nominal distance velocity cut-off d_0 for the region is 269 m s^{-1}. At this cut-off eight objects are needed to form a clump and 20 for a family. The lowest numbered group of objects we can identify at this cut-off is the clump around (77899) (2001 TS117) with 10 members. Two other clumps are visible in the region, one around (101950) (1999 RB29) with nine members and one around (101674) (1999 CU106) with 10 members. A clump around (138756) (2000 SC273) that is visible at higher cut-offs is not distinguishable at $d_0 = 270$ m s^{-1}. It has however some importance in view of the resonant nature of some of its members that will be discussed in more detail later on. Results are summarized in Fig. 15, panel A, where we show a stalactite diagram for the region. Again, none of these groups could be found in previous works, due to the smaller cut-off in the area by other researchers. In panel B we show an $(a, \sin(i))$ projection of the same clumps. The fact that these groups are quite dispersed in inclination may suggest that they are either not originating from collisional events or that they are groups dispersed by the local web of resonances. Further study would be needed to clarify this point.

We then checked how many asteroids in secular resonances are present in the region, according to the 0.3 arcsec yr^{-1} criterion defined in Section 3. We found that 11 asteroids are near the ν_5 resonance and three objects are inside the $2\nu_6 - \nu_5 - \nu_{16}$ resonance. One object each was in one of the following resonances: ν_6, $2\nu_5 + \nu_6$, $2\nu_6 + \nu_5$, $3\nu_6 - \nu_5$, z_1 and $2\nu_5 - \nu_6$. Since most of the resonant objects are in g- and $g - s$-type resonances, we used the distance metric in the space $(n, g, g - s)$ defined by the equation (5) to obtain groups in the proper frequency domain. The nominal frequency cut-off in this domain was of 3.3 arcsec yr^{-1}, and at this cut-off a clump needed to have at least six members. We only found a clump around (90551) (2004 FR121) that correspond to the proper element-based clump around (138756) and whose members are close to the centre of the ν_5 resonance. Another clump around (111676) (2002 BJ21) was not distinguishable at the nominal frequency cut-off. We also checked the behaviour of the ν_5 resonant angle of all 11 asteroids that satisfied our 0.3 arcsec yr^{-1} criterion. While the majority of members was in circulating states, we found that (90551) was alternating states of anti-aligned libration with circulation, and (116808) was alternating among states of aligned libration and circulation. The role of the ν_5 secular resonance as a possible source of asteroids in the region needs, in our opinion, further investigating. A complete list of the groups identified in this region is given in Table A8.

6 FAMILIES IN THE SPACE OF ν_6 RESONANT PROPER ELEMENTS

The Euphrosyne region is characterized by the presence of several asteroids in ν_6 (and ν_5) anti-aligned librating states. For these objects the standard approach of Knežević & Milani (2003) to compute synthetic proper elements does not hold, and more appropriate resonant elements should be computed. Two approaches for this problem are possible (Carruba & Morbidelli 2011). In the first approach the resonant proper eccentricity is taken as the maximum eccentricity in the anti-aligned libration cycle when $\sigma = \varpi - \varpi_6 = 180^\circ$ and $\mathrm{d}\sigma/\mathrm{d}t > 0$. Since at the simplest level of perturbation theory the ν_6 resonance is characterized by the conservation of the quantity:

$$K_2' = \sqrt{1 - e^2}(1 - \cos i), \tag{9}$$

the resonant proper inclination can be computed from the resonant proper eccentricity via equation (9). The proper semimajor axis is computed with the standard approach for synthetic proper elements of Knežević & Milani (2003). In the second approach proper semimajor axis and inclination are computed with the standard Knežević & Milani (2003) method. The proper eccentricity is calculated

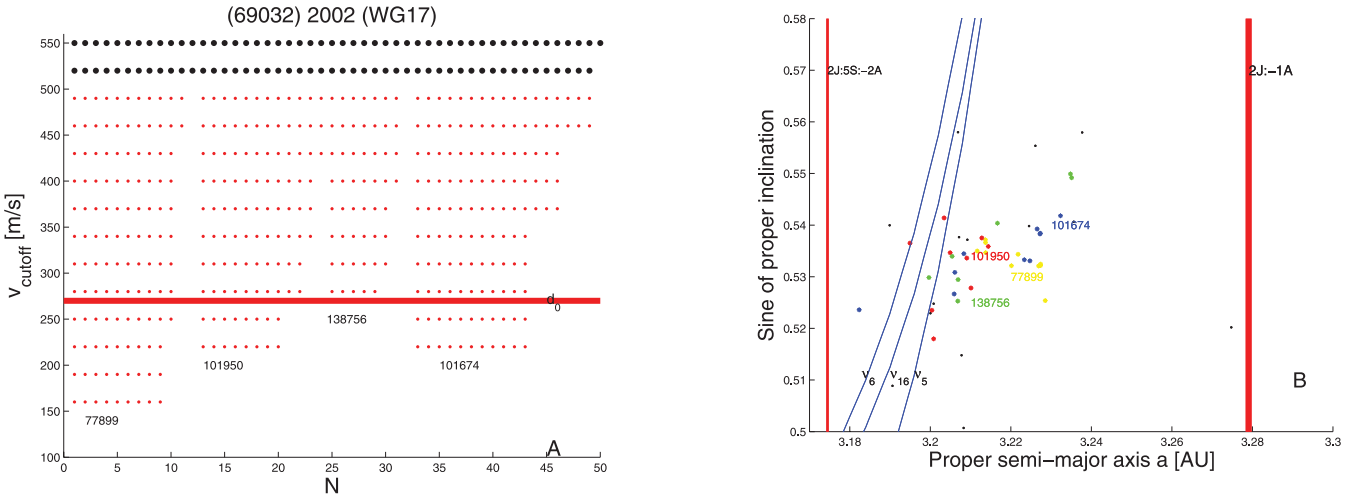

Figure 15. Panel A: stalactite diagrams for the 69032 region in the $(a, e, \sin(i))$ proper element domain. The horizontal line displays the value of the nominal distance cut-off. Panel B: an $(a, \sin(i))$ projection of the proper elements clumps (asterisks) in the region.

with the following procedure: we compute the resonant equinoctial elements ($e\cos(\varpi - \varpi_6)$, $e\sin(\varpi - \varpi_6)$ filtered so as to eliminate all frequencies corresponding to periods of 300 000 yr, and analyse the Fourier spectra of these new quantities. The second frequency of largest amplitude (the first is associated with the forced eccentricity of Tina asteroids) is identified with the new proper frequency (g_σ), and the amplitude associated with this frequency is identified with the new proper (or free) 'eccentricity'. For orbits in anti-aligned libration g_σ is the frequency of libration and the proper eccentricity is the amplitude of libration. But in principle the proper eccentricity and g_σ can be defined for any orbit, even if their geometrical meaning is different. Errors on the proper e and g_σ frequencies are computed with the same method used for the traditional synthetic proper elements.

Since the second approach can be extended to orbits not in linear secular resonances anti-aligned librating states, and since our goal is to see how linear secular resonances affect the process of family determination in this unique region of the asteroid belt, we decided to use the second method and computed resonant proper elements for all asteroids in the region. We found that for the Euphrosyne region the nominal distance velocity cut-off is higher in the resonant proper element domain, being 71.3 m s^{-1} versus the 64.4 m s^{-1} for the standard proper elements. At this cut-off we found that the (31) Euphrosyne family, that had 1419 members in the synthetic proper elements space, 12 of which were ν_6 anti-aligned librators and one of which a ν_5 anti-aligned librator, had 1422 members and only six of these objects was a ν_6 anti-aligned librator (no ν_5 anti-aligned librator was found in the family).

The use of resonant proper elements allowed us to reduce the number of anti-aligned librators in the Euphrosyne family by a factor of 50 per cent, and since these objects are in clearly distinct dynamical states that the rest of the family members, using resonant proper element lead to a more robust family identification, in our opinion. A similar behaviour was observed for the family in the Danae region near (76090), that contained three ν_6 anti-aligned librating asteroids, none of which retrieved in the space of resonant proper elements.

On the contrary, the clump in the Alauda region of six objects near (182817), four of which were ν_6 anti-aligned librators, appeared as a clump of nine members in the space of resonant proper elements, five of which in the anti-aligned librating configuration. Overall, we found that the use of resonant proper elements reduced the number of anti-aligned librating asteroids found in families made up mostly of circulators, and increased the number of members in groups made mostly of anti-aligned librators. No significant difference was observed concerning families made only of circulators.

7 CONCLUSIONS

In this work we investigated the current status of the knowledge of asteroids in the region of the Euphrosyne dynamical family. Among other things we did the following.

(i) Identified new populations of asteroids in ν_6 anti-aligned and ν_5 aligned and anti-aligned librating configurations (Tables A1–A3). A new population of 92 ν_6 anti-aligned resonant objects adds to the previously known population in the area of the Tina family and near asteroid Vinifera. Also, we identified seven asteroids in ν_5 anti-aligned librating configurations, and 22 asteroids in ν_5 aligned librating configurations, previously unknown in the literature.

(ii) Studied the possible migration of objects into the Danae and Erminia regions from larger semimajor axes when the Yarkovsky effect is considered. Only 5 per cent of the simulated objects reached the Danae and Erminia regions, while the rest of the population was lost because of interaction with either the 1J:3S:-1A, 9J:-4A or the 7J:-3A mean-motion resonances, that increased the eccentricities of the test particles to planet-crossing levels. Particles in ν_6 anti-aligned librating states, whose eccentricity is protected by the resonant configuration from reaching Mars-crossing levels, where ejected from the stable island because of the interaction with one of the mentioned resonances (Fig. 9). Very interestingly, we found that capture into ν_6 anti-aligned or aligned librating states via Yarkovsky evolution is possible (Fig. 10), which yields some insights on the possible origin of other groups in ν_6 anti-aligned librating states, such as the Tina family (Carruba & Morbidelli 2011).

(iii) Identified families and clumps in the domain of proper elements and in the domains of proper frequencies most appropriate for the non-linear secular resonances in the region. We introduced a new approach to studying groups interacting with non-linear secular resonance, where we first map the local web of resonances, identified possible resonant asteroids, and then looked for groups in the domain most appropriate to study the particular resonance.

(iv) Identified two new groups in ν_6 anti-aligned librating states around (76090) and (182817), which are respectively the second and third group in the Solar system ever to be found in such configuration after the Tina family (Carruba & Morbidelli 2011), and a clump near (54571), visible in the $(a, e, \sin(i))$ and various frequency domains, which is the first group ever found to be at the crossroad of five non-linear secular resonances, the $\nu_5 + 2\nu_{16}$, $\nu_5 - \nu_{16}$, $\nu_5 - 2\nu_{16}$, $2\nu_5 + \nu_{16}$, and the $2\nu_5 - \nu_{16}$ secular resonances.

(v) Studied groups in the domain of linear secular resonances proper elements. Since the is a family around (31) Euphrosyne and two clumps that have some members in ν_6 anti-aligned librating states, we checked what difference in family determination would be found if proper element appropriate for the resonant configurations of these objects were used. We found that the use of resonant proper elements reduced the number of anti-aligned librating asteroids found in families made up mostly of circulators, and increased the number of members in groups made mostly of anti-aligned librators. No significant difference was observed concerning families made only of circulators.

While in this work we answered many question on family identification, many issues still remain to be addressed. A taxonomical analysis of asteroids in the region, including Sloan Digital Sky Survey (SDSS)-Moving Objects Catalog 4 (MOC4) data would be helpful to detect possible interlopers in the families that we identified here (see for instance the work of Novaković et al. 2011 for a most recent review of this data in the area). Study of dispersion via Yarkovsky effect, Yarkovsky iso-lines, Monte Carlo methods to detect the family age could provide information on possible interlopers, family age, and original ejection velocity field of the studied groups. Review of collisional and rotational properties could also be of help to gain a better understanding of the processes that shaped the Euphrosyne region. While these are certainly worthy field of research, we believe that they exceed the purposes of this paper, whose goal was to study the effect that the local web of secular resonances had and has on the process of family identification. More than the retrieval of resonant groups, some of particular dynamical effect such as the new ν_6 anti-aligned librating groups and other, we believe that the new approach based on a good understanding of the local dynamics is one of the main results of this work.

ACKNOWLEDGMENTS

We thank the reviewer of this paper, Ricardo Gil-Hutton, for hints and suggestions that increased the quality of this work. We would like to thank the São Paulo State Science Foundation (FAPESP) that supported this work via the grant 06/50005-5, and the Brazilian National Research Council (CNPq, grants 302183/2008-6 and 473345/2009-9).

REFERENCES

Beaugé C., Roig F., 2001, Icarus, 153, 391
Bottke W. F., Nesvorný D., Grimm R. E., Morbidelli A., O'Brien D. P., 2006, Nat, 439, 821
Brož M., 1999, Thesis, Charles University, Prague, Czech Republic
Carruba V., 2009a, MNRAS, 395, 358
Carruba V., 2009b, MNRAS, 398, 1512
Carruba V., 2010a, MNRAS, 403, 1834
Carruba V., 2010b, MNRAS, 408, 580
Carruba V., Machuca J. F., 2011, MNRAS, 418, 1102
Carruba V., Michtchenko T., 2007, A&A, 475, 1145
Carruba V., Michtchenko T., 2009, A&A, 493, 267
Carruba V., Morbidelli A., 2011, MNRAS, 412, 2040
Carruba V., Burns J. A., Bottke W., Nesvorný D., 2003, Icarus, 162, 308
Farinella P., Vokrouhlický D., Hartmann W. K., 1998, Icarus, 132, 378
Gil-Hutton R., 2006, Icarus, 183, 93
Knežević Z., Milani A., 2003, A&A, 403, 1165
Levison H. F., Duncan M. J., 1994, Icarus, 108, 18
Lyapunov A. M., 1907, Ann. Fac. Sci. Univ. Toulose, 9, 203
Margot J.-L., Rojo P., 2007, BAAS, 38, 440
Milani A., Knežević Z., 1994, Icarus, 107, 219
Morbidelli A., Henrard J., 1991, Celest. Mech. Dynamical Astron., 51, 169
Novaković B., Cellino A., Knežević Z., 2011, Icarus, 216, 69
Roig F., Nesvorný D., Ferraz-Mello S., 2002, MNRAS, 335, 417
Yoshikawa M., 1987, Celest. Mech., 40, 233
Zappalà V., Bendjoya Ph., Cellino A., Farinella P., Froeschlé C., 1995, Icarus, 116, 291

APPENDIX A

Table A1. Identification and resonant configuration of numbered asteroids in ν_6 linear secular resonances in the Euphrosyne region.

Asteroid id.	Resonant configuration	Asteroid group, if any
3939	ν_6 anti-aligned	
6613	ν_6 anti-aligned	31
8563	ν_6 anti-aligned	
19565	ν_6 anti-aligned	
30995	ν_6 anti-aligned	
48193	ν_6 anti-aligned	
66772	ν_6 anti-aligned	
77426	ν_6 anti-aligned	
78385	ν_6 anti-aligned	
81888	ν_6 anti-aligned	
92174	ν_6 anti-aligned	
94213	ν_6 anti-aligned	
94225	ν_6 anti-aligned	
99010	ν_6 anti-aligned	
106114	ν_6 anti-aligned	
106676	ν_6 anti-aligned	31
117433	ν_6 anti-aligned	
127414	ν_6 anti-aligned	
138605	ν_6 anti-aligned	
140410	ν_6 anti-aligned	76090
144673	ν_6 anti-aligned	
157706	ν_6 anti-aligned	
158591	ν_6 anti-aligned	
160254	ν_6 anti-aligned	
163632	ν_6 anti-aligned	
165085	ν_6 anti-aligned	
170037	ν_6 anti-aligned	
172410	ν_6 anti-aligned	31
185714	ν_6 anti-aligned	
188172	ν_6 anti-aligned	31
189017	ν_6 anti-aligned	
192580	ν_6 anti-aligned	
199536	ν_6 anti-aligned	182817
202346	ν_6 anti-aligned	
202625	ν_6 anti-aligned	
217311	ν_6 anti-aligned	31
224545	ν_6 anti-aligned	76090
232079	ν_6 anti-aligned	31
242600	ν_6 anti-aligned	
242681	ν_6 anti-aligned	
243427	ν_6 anti-aligned	
243446	ν_6 anti-aligned	31
246676	ν_6 anti-aligned	

Table A1 – *continued*

Table A2. Identification and resonant configuration of multi-opposition asteroids in ν_6 linear secular resonances in the Euphrosyne region.

Asteroid id.	Resonant configuration	Asteroid group, if any
1998UZ5	ν_6 anti-aligned	
2001LR1	ν_6 anti-aligned	
2001SW87	ν_6 anti-aligned	
2002RM225	ν_6 anti-aligned	31
2002TL263	ν_6 anti-aligned	182817
2002VO10	ν_6 anti-aligned	
2003GL2	ν_6 anti-aligned	
2004RE207	ν_6 anti-aligned	31
2005JD49	ν_6 anti-aligned	
2005WQ20	ν_6 anti-aligned	
2006DZ190	ν_6 anti-aligned	31
2006QT22	ν_6 anti-aligned	
2007RQ24	ν_6 anti-aligned	182817
2008UN32	ν_6 anti-aligned	
2000TD33	ν_6 anti-aligned	
2001QP135	ν_6 anti-aligned	
2002CG139	ν_6 anti-aligned	
2008DU81	ν_6 anti-aligned	
2008HN66	ν_6 anti-aligned	
2001KV63	ν_6 anti-aligned	
2003AR62	ν_6 anti-aligned	
2003BP9	ν_6 anti-aligned	
2005SE178	ν_6 anti-aligned	
2006SD371	ν_6 anti-aligned	31
2002PL33	ν_6 anti-aligned	
2002RK175	ν_6 anti-aligned	
2002SD25	ν_6 anti-aligned	
2003QX76	ν_6 anti-aligned	
2004BY54	ν_6 anti-aligned	182817
2004CL20	ν_6 anti-aligned	
2004RE333	ν_6 anti-aligned	31
2004TD11	ν_6 anti-aligned	
2004TD279	ν_6 anti-aligned	
2005EJ25	ν_6 anti-aligned	
2005SR22	ν_6 anti-aligned	

Table A2 – *continued*

Asteroid id.	Resonant configuration	Asteroid group, if any
2005WN37	ν_6 anti-aligned	
2006KH20	ν_6 anti-aligned	
2006PR19	ν_6 anti-aligned	76090
2006QH113	ν_6 anti-aligned	
2007RV38	ν_6 anti-aligned	
2007TK170	ν_6 anti-aligned	
2008CR50	ν_6 anti-aligned	
2008DZ52	ν_6 anti-aligned	
2008YT137	ν_6 anti-aligned	
2009CS56	ν_6 anti-aligned	

Table A3. Identification and resonant configuration of asteroids in ν_5 linear secular resonances in the Euphrosyne region.

Asteroid id.	Resonant configuration	Asteroid group, if any
49606	ν_5 anti-aligned	
90551	ν_5 anti-aligned	
138890	ν_5 anti-aligned	
150652	ν_5 anti-aligned	
157401	ν_5 anti-aligned	
242435	ν_5 anti-aligned	31
2004HT56	ν_5 anti-aligned	
7215	ν_5 aligned	
13936	ν_5 aligned	
38550	ν_5 aligned	
40500	ν_5 aligned	
48218	ν_5 aligned	
51263	ν_5 aligned	
68014	ν_5 aligned	
97399	ν_5 aligned	
102492	ν_5 aligned	
106792	ν_5 aligned	
115750	ν_5 aligned	
139759	ν_5 aligned	
160242	ν_5 aligned	
212547	ν_5 aligned	
2009SZ96	ν_5 aligned	
2005GA10	ν_5 aligned	
2006TF68	ν_5 aligned	
2007TR398	ν_5 aligned	
2009UM88	ν_5 aligned	
2009UL136	ν_5 aligned	31

Table A4. Dynamical groups identified in the Euphrosyne region.

Group id.	Number of members	Resonances	Number of resonant objects
Proper element families			
31	1419	$\nu_6(12)$, $\nu_5(2)$	14
Proper element clumps			
140072	8	$2\nu_5 + \nu_{16}$	3
Frequency families			
18318	453	$2\nu_6 - \nu_5 - \nu_{16}$	26
73524	47	$2\nu_6 - \nu_5 - \nu_{16}$	6
34846	36	$\nu_5 + \nu_6 + \nu_{16}$	2
16708	484	$2\nu_5 + \nu_{16}$	34
105597 (140072)	15	$2\nu_5 + \nu_{16}$	12
101810	47	$2\nu_6 - \nu_{16}$	7

Table A5. Dynamical groups identified in the Alauda region.

Group id.	Number of members	Resonances	Number of resonant objects
Proper element families			
1101	42		
18996	24		
Proper element clumps			
702	10		
3025	11		
10654	11		
10813	10		
21224	10		
26324	18	$3\nu_6 - \nu_5$	3
30995	11		
84404	10		
182817	6	ν_6	4
Frequency clumps			
276	16	$3\nu_6 - \nu_5$	3
30575	10	$3\nu_6 - \nu_5$	6

Table A6. Dynamical groups identified in the Luthera region.

Group id.	Number of members	Resonances	Number of resonant objects
Proper element families			
780	47		
781	189	$2\nu_6 - \nu_{16}$	15
1040	475		
21799	21		
103668	21		
Proper element clumps			
285	19		
4152	9		
5931	19		
5959	16		
10606	12		
13684	12		
19078	13		
19696	15		
20409	15		
26558	10		
28904	13		
31762	14		
40218	17		
42386	10		
62633	10		
69559	16	$\nu_5 + \nu_{16}$, $\nu_5 \pm 2\nu_{16}$, $2\nu_5 \pm \nu_{16}$	10
71335	9		
87944	9		
Frequency families			
781	572	$2\nu_6 - \nu_5 - \nu_{16}(52)$, $2\nu_6 - \nu_{16}(52)$	104
Frequency clumps			
54571(69559)	10	$\nu_5 + \nu_{16}$, $\nu_5 \pm 2\nu_{16}$, $2\nu_5 \pm \nu_{16}$	10

Table A7. Dynamical groups identified in the Danae and Erminia region.

Group id.	Number of members	Resonances	Number of resonant objects
Proper element families			
773	26	$2\nu_6 + \nu_{16}$	2
22101	40		
76090	24	ν_6	3
Proper element clumps			
386	7		
2651	12		
4460	8		
23956	7		
96237	7		
Frequency families			
1191	105	$2\nu_6 + \nu_{16}$	6
Frequency clumps			
43522	23	$\nu_5 + \nu_6 + \nu_{16}$	3

Table A8. Dynamical groups identified in the (69032) region.

Group id.	Number of members	Resonances	Number of resonant objects
Proper element clumps			
77899	10		
101674	10		
101950	9		
138756	7	ν_5	2
Frequency clumps			
90551	6	ν_5	2

This paper has been typeset from a TEX/LATEX file prepared by the author.

10

A distribuição "Emmenthal" dos asteroides de alta inclinação

Como encontrado nos artigos anteriores, a distribuição dos asteroides de alta inclinação não é uniforme, mas tem regiões de baixa densidade de objetos não associadas a regiões de instabilidade dinâmica. Em uma analogia com um queijo "emmenthal", estas regiões seriam os "buracos". Neste trabalho identificamos duas regiões no cinturão central e externo caracterizadas por uma densidade numérica de objetos muito baixa, e tempo de permanencia de objetos fictícios de 100 Myr ou mais, até em presença da força Yarkovsky. Mostramos que esta baixa densidade de objetos não pode ser produzida por flutuações de simples distribuição estatísticas unidimensionais, como as distribuição uniforme, de Poisson, e Gaussiana, e que também flutuações em distribuições tridimensionais, como a distribuição trivariata normal, não justificam estas regiões. A presença de regiões estáveis não ocupadas indica que a população primordial de asteroides não chegou a popular estas regiões, e isso coloca importantes limitações nos cenários de formação do nosso Sistema Solar.

A seguir apresentamos o artigo, que foi publicado em Monthly Notices of the Royal Astronomical Society em 2011, volume 418, pp. 1102-1114.

Monthly Notices
of the
ROYAL ASTRONOMICAL SOCIETY

Mon. Not. R. Astron. Soc. **418,** 1102–1114 (2011) doi:10.1111/j.1365-2966.2011.19576.x

On the Emmenthal distribution of highly inclined asteroids

V. Carruba★ and J. F. Machuca

UNESP, Univ. Estadual Paulista, Grupo de dinâmica Orbital e Planetologia, Guaratinguetá, SP, 12516-410, Brazil

Accepted 2011 August 1. Received 2011 July 11; in original form 2011 March 25

ABSTRACT

Highly inclined asteroids are objects with $\sin(i) > 0.3$. Among highly inclined asteroids, we can distinguish between objects with inclinations smaller than that of the centre of the $\nu_6 = g - g_6$ secular resonance and objects at higher inclinations. Using the current mechanisms of dynamical mobility, it is not easy to increase the values of an asteroid with an initial small inclination to values higher than that of the centre of the ν_6 resonance. The presence of highly inclined objects might therefore be related to the early phases of the Solar system.

It has been observed that several dynamically stable regions are characterized by a very low number density of objects, unlike low-inclined bodies that tend to occupy all the dynamically viable regions. The distribution of asteroids at a high inclination in the domain of proper elements in dynamically stable regions resembles an Emmenthal cheese, with regions of low number density close to highly populated areas. While this phenomenon has been observed qualitatively in the past, no quantitative study has yet been carried out on the extent and long-term stability of these regions.

In this paper, we identify two dynamically stable regions characterized by very low values of number density and permanence times of 100 Myr or more when the Yarkovsky force is considered. We show that the low number density of objects in these areas cannot be produced as a statistical fluctuation of any simple one-dimensional statistical distribution, such as the Poissonian, uniform and Gaussian distributions, or of a tri-dimensional distribution, such as the tri-variate normal distribution. The presence of unoccupied dynamically stable regions could indicate that the primordial asteroidal population might not have reached all available zones at high-i. This sets constraints on the scenarios for the early phases of the history of our Solar system.

Key words: celestial mechanics – minor planets, asteroids: general.

1 INTRODUCTION

Highly inclined asteroids are objects with $\sin(i) > 0.3$. For these bodies, the analytical theory used to obtain the proper elements is not very accurate. Highly inclined asteroids are also characterized by a non-uniform distribution. It has been observed that several dynamically stable regions are characterized by a very low number density of objects, unlike low-inclined bodies that tend to occupy all the dynamically viable regions. While this phenomenon has been observed qualitatively in the past (Carruba 2009b, 2010b; Michtchenko et al. 2010), no quantitative study has yet been carried out on the extent and long-term stability of these regions. This is important because it might provide information on the origin of the highly inclined population. If dynamically stable regions are not occupied, this could indicate that the primordial population might not have reached all available zones at high-i. This sets constraints on the scenarios for the early phases of the history of our Solar system. The void zones in the asteroid distribution (in our analogy, the holes in the Emmenthal cheese), as well as the regions of higher asteroid number density, might therefore still carry the memory of events associated with the primordial phase of planetary migration.

In this paper, we investigate the long-term stability of underpopulated areas of highly inclined asteroids by using synthetic proper-element maps and simulations of highly inclined real and fictitious objects, which include the Yarkovsky force. We then determine the probability that an originally uniform distribution of asteroids, a population following Poissonian or uni- and tri-variate Gaussian statistical distributions, describes the currently observed asteroid distribution.

This paper is arranged as follows. Having introduced the problem of stable underpopulated and overpopulated areas among highly inclined objects in the introduction, we revise the current knowledge on asteroid synthetic proper elements for highly inclined asteroids in Section 2. In Section 3, we discuss the orbital distribution of large asteroids and in Section 4 we consider statistically the probability

★E-mail: vcarruba@feg.unesp.br

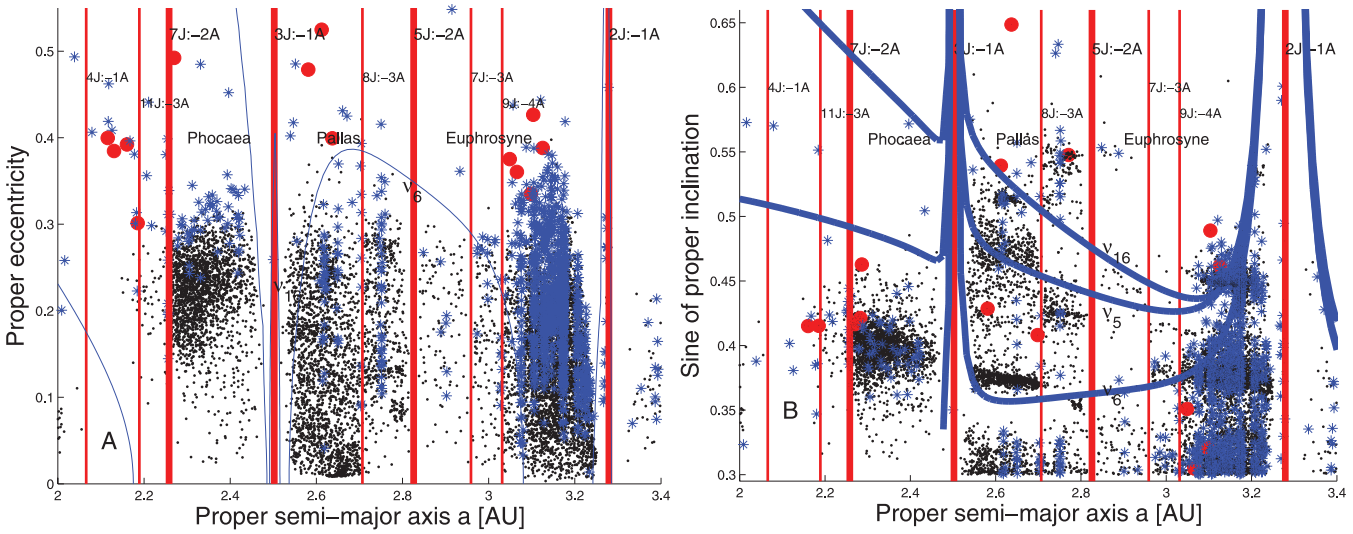

Figure 1. Panel A shows the (a, e) projection of highly inclined AstDyS asteroids. The blue asterisks display asteroids with a standard deviation on σ_a between 0.0003 and 0.01, while red circles show asteroids with σ_a larger than 0.01. The vertical red lines display the locations of mean-motion resonances, while the blue lines show the positions of linear secular resonances. Panel B shows the [a, sin (i)] projection of the same asteroids.

that various asteroid distributions might replicate the observed distribution. In Section 5, we obtain the number density distributions (density maps) of such objects for large ($H < 12$) and small objects, and we identify potential dynamically stable regions with a low number density of objects. In Section 6, we obtain synthetic proper-element maps for the underpopulated areas identified in Section 3. In Section 7, we study the long-term stability of these regions when the Yarkovsky force is considered. Finally, in Section 8, we present our conclusions.

2 SYNTHETIC PROPER ELEMENTS FOR HIGHLY INCLINED OBJECTS

The first step to identifying underpopulated dynamically stable regions is to have a reliable and updated set of asteroid proper elements. We start by revising the data available in the literature.

On 2010 December 8, the AstDyS site[1] listed a set of 240 831 asteroids for which the synthetic proper elements (and their errors) – obtained using the approach of Knežević & Milani (2003) – are available. We selected 10 073 objects of high inclination characterized by a semimajor axis in the range of 2.0–3.4 au and by sin (i) > 0.3. We start by looking at projections in the (a, e) and [a, sin (i)] planes.

Fig. 1 displays (a, e) (panel A) and [a, sin (i)] (panel B) projections of the AstDyS proper elements for the highly inclined objects. Following Gil-Hutton (2006), we can divide the highly inclined population of asteroids into three regions: the Phocaea region (zone A in Gil-Hutton 2006) between the 7J:-2A and 3J:-1A mean-motion resonances, the Hansa and Pallas region (zone B) between the 3J:-1A and the 5J:-2A mean-motion resonances and the Euphrosyne region (zone C) between the 5J:-2A and the 2J:-1A mean-motion resonances. The thick vertical lines are associated with the main mean-motion resonances with Jupiter, while the thin lines show the location of higher-order mean-motion resonances. The blue lines show the location of the centre of the three main linear secular resonances ($\nu_6 = g - g_6$, $\nu_5 = g - g_5$ and $\nu_{16} = s - s_6$), computed using the second-order and fourth-degree secular perturbation theory of Milani & Knežević (1992, 1994). Secular resonances occur when there is a commensurability between the precession frequency of an asteroid's pericentre g or node s and that of a planet g_i, s_i, where the suffix $i = 1, \ldots, 8$ indicates the planet number as a function of the distance from the Sun (1 for Mercury, 2 for Venus, etc.). We warn the reader that the secular perturbation theory of Milani & Knežević (1992, 1994), which is based on an expansion in series of eccentricities and inclination of the perturbing function, loses accuracy at high inclination and close to mean-motion resonances. Thus, in Fig. 1 and in the subsequent figures, we report the location of the secular resonances given by this theory just as a qualitative indication, but we do not expect it to match the distribution of actual asteroids. The blue asterisks display asteroids with σ_a (the standard deviation of the values of the semimajor axis as computed with the approach of Knežević & Milani 2003) between 0.0003 au (the limit given by Knežević & Milani 2003 for 'stable' synthetic proper elements) and 0.01 au (the limit for pathological cases). The red circles show asteroids with σ_a larger than 0.01 au.[2] We remind the reader that objects at very high eccentricities (larger than about 0.4) are subject to close encounters with Mars and other planets, and are unstable on time-scales of a few Myr.

As can be seen in the figure, we can observe a region of low asteroid density near the ν_6 resonance border, which is caused by an increase in the eccentricity that asteroids on circulating and librating orbits experience because of the resonance topology (for a more in-depth discussion of the mechanism of asteroid depletion, see also Carruba 2010a; Carruba, Machuca & Gasparino 2011b). An exception to this mechanism is observed for asteroids in antialigned librating states of the ν_6 resonance, such as those of the Tina family (Carruba & Morbidelli 2011a), whose resonant states shield them from experiencing planetary close encounters. Besides the regions influenced by the ν_6 resonance, we can see a region of low asteroid

[1] Knežević & Milani (2003) http://hamilton.dm.unipi.it/astdys

[2] Knežević & Milani define stable, unstable and pathological proper elements as elements having 'small', 'medium' and 'large' relative errors. The thresholds for the three cases with respect to each element are discussed in the text.

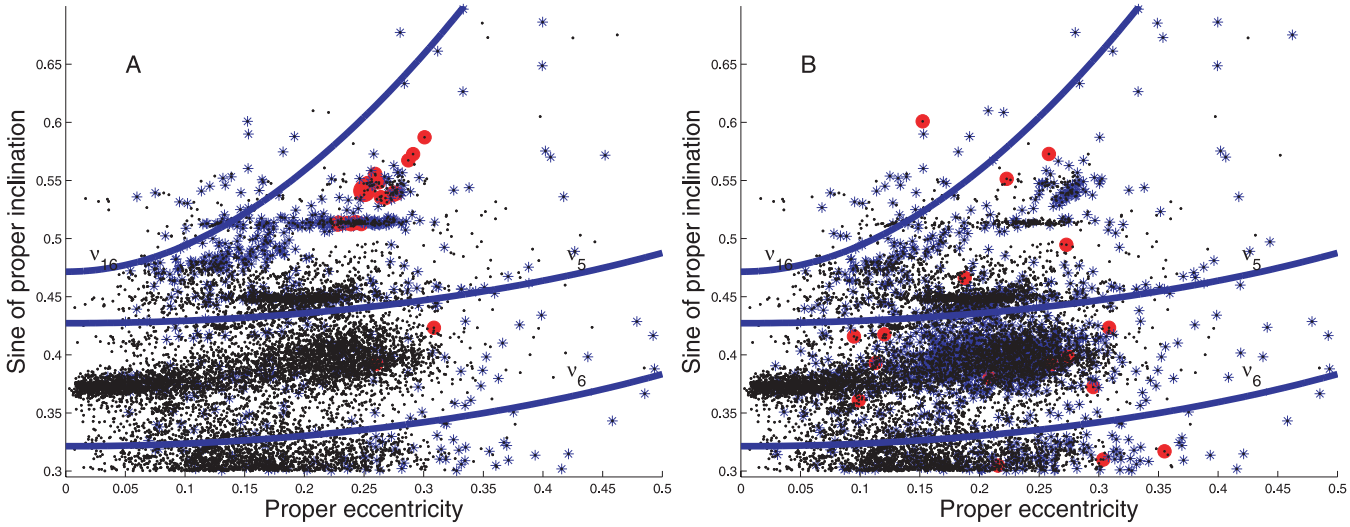

Figure 2. Panel A shows the [e, sin (i)] projection of highly inclined AstDyS asteroids. The blue asterisks display asteroids with a standard deviation on σ_e between 0.003 and 0.1, while red circle show asteroids with σ_e larger than 0.1. The blue lines show the positions of linear secular resonances. Panel B shows the [e, sin (i)] projection of the same asteroids, but this time the blue asterisks display asteroids with a standard deviation on σ_i between 0.001 and 0.03, while the red circles show asteroids with σ_i larger than 0.03.

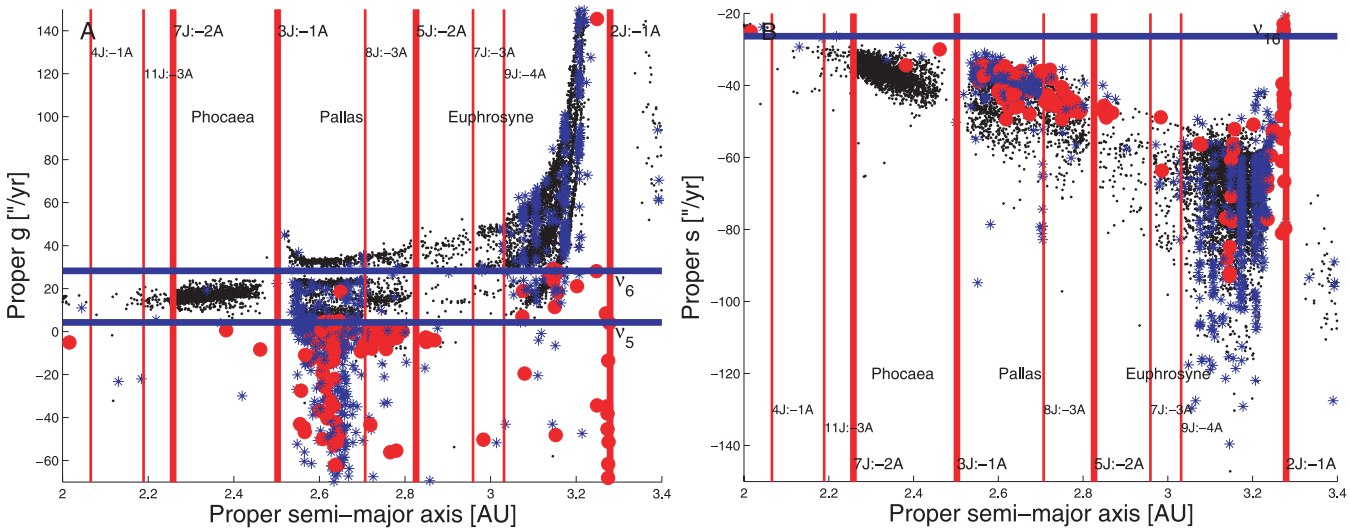

Figure 3. Panel A shows the (a, g) projection of highly inclined AstDyS asteroids. The blue asterisks display asteroids with a standard deviation on σ_g between 1 and 10, while the red circles show asteroids with σ_g larger than 10. Panel B shows the (a, s) projection of the same asteroids, but this time the symbols refer to σ_s (the range of values for the errors is the same).

density between the ν_5 and ν_{16} resonances in the [a, sin (i)] plane in the region of the Pallas family (see Fig. 1, panel B, and Carruba 2010b). More strikingly, there is a low-density region of asteroids between the 5J:-2A and 7J:-3A mean-motion resonances, which seems otherwise to be relatively stable. We investigate these subjects further in Sections 3 and 6.

In Fig. 2, we display [e, sin (i)] projections of asteroids with values of the errors in e (panel A) and i (panel B) for 'stable' (black dots), 'unstable' (blue circles) and 'pathological' (red circles) proper elements, according to Knežević & Milani (2003). As in Fig. 1, the blue lines display the locations of the main secular resonances in the region. As can be seen, the errors in eccentricity and inclination are larger for asteroids at high inclination, with very few objects having large errors at low eccentricities.

Finally, Fig. 3 displays (a, g) (panel A) and (a, s) (panel B) projections of highly inclined AstDyS asteroids. We can see the departure from a linear dependence for g values as a function of a near the 2J:-1A and 3J:-1A mean-motion resonances, as discussed by Carruba & Michtchenko (2009). The negative values of g near the Hansa family are related to objects with small proper eccentricities ($e < 0.0179$), and to the problem of determining the correct proper frequency g for asteroids whose elements (k, h) pass through zero (Carruba 2010b). The 'inclined' dependence of s values as a function of a is discussed by Carruba & Michtchenko (2007).

3 ASTEROID ORBITAL DISTRIBUTION

When studying the current orbital distribution of objects, it is necessary to distinguish between 'large' and 'small' asteroids. Large objects have experienced very little orbital mobility, which is caused by the Yarkovsky effect, and it can be assumed that their current position is not far from the position they reached during the last stages

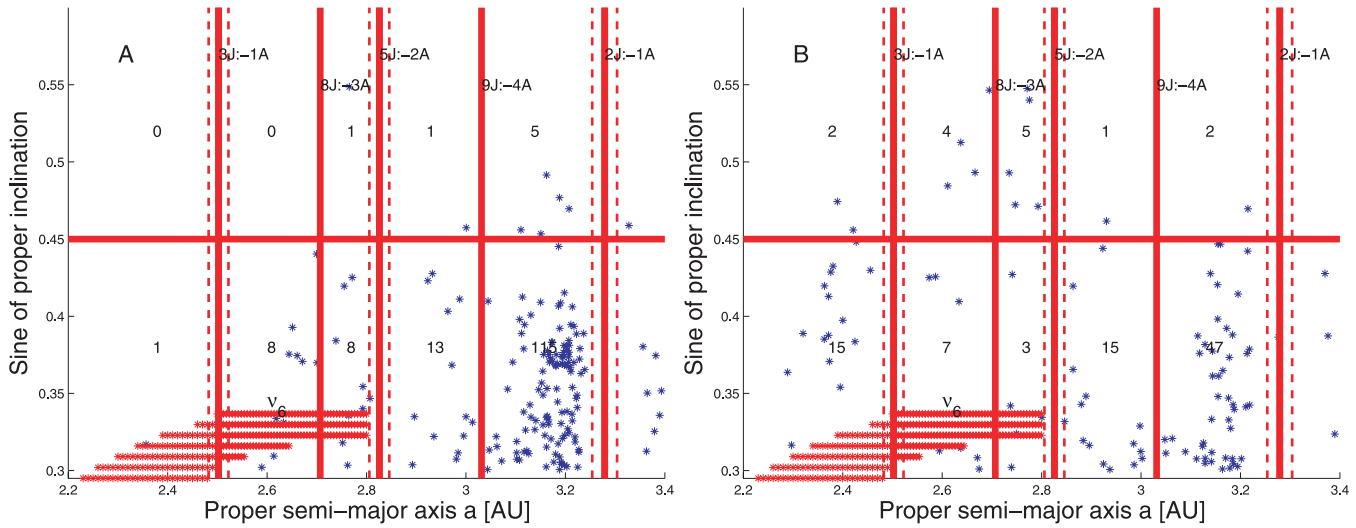

Figure 4. An [a, sin $i(i)$] plot of low-eccentricity ($e < 0.175$) $H < 12$ asteroids (panel A) and high-eccentricity ($e > 0.175$) $H < 12$ asteroids (panel B). The red asterisks identify regions affected by the ν_6 resonance, according to the model of Yoshikawa (1987). The dashed vertical lines display regions partially depopulated of asteroids near the mean-motion resonances.

of planetary migration. However, small objects tend to be displaced by the Yarkovsky force and, as a result, by mean-motion and secular resonances. Their current distribution can provide hints about the dynamical stability of the regions: underpopulated areas might be associated with dynamical unstable regions (but not necessarily, as we see later in this paper).

We define a 'large' object as an asteroid with an absolute magnitude $H > 12$. We choose this criterion because asteroids with this absolute magnitude are not significantly affected by non-gravitational effects. If we estimate the asteroid diameter using the relationship (Carruba et al. 2003)

$$D = \frac{D_0}{\sqrt{p_V}} \times 10^{-0.2H}, \quad (1)$$

where $D_0 = 1329$ km, p_V is the geometric albedo and H is the asteroid's absolute magnitude. Even for very large values of $p_V = 0.5$, an asteroid with $H = 12$ will have a diameter of 7.5 km. At this size, the YORP effect is negligible. Using an obliquity of the spin axis of $\pm 90^\circ$ and parameters typical of C-type asteroids (Carruba et al. 2003), the mobility caused by the Yarkovsky force is at most 0.1635 au over 4.5 Gyr. Therefore, we should not expect the current orbital locations of such bodies to have changed much since the formation of the Solar system.[3]

To investigate the locations of stable areas characterized by a low population of objects, we have obtained the distribution of the number density of asteroids in the [a, sin (i)] representative plane. We concentrate on the [a, sin (i)] plane because we are interested in areas that were originally depleted in asteroids, and eccentricities are more easily changed by mechanisms of dynamical mobility than by proper inclinations (semimajor axes are affected by the Yarkovsky force). Regions in the [a, sin (i)] plane with inclinations different from those of the bodies originally injected in highly inclined orbits can therefore still be characterized by a relatively low number density of objects.

To identify regions that were originally underpopulated, we need to eliminate areas whose low number density is caused by the destabilizing effects of the local dynamics. Based on several previous studies of the dynamics of highly inclined objects (see, for instance, Carruba 2009a,b, 2010a,b; Carruba et al. 2011b), we can distinguish between destabilizing resonances (resonances that cause a change in the asteroid eccentricity that is large enough to bring its pericentre to regions of terrestrial planet encounters, causing the loss of at least 50 per cent of the bodies initially inside the resonance because of a collision with the Sun or other planets during time-scales of 10 Myr or less, in conservative simulations of the orbital evolution of an asteroid subjected to the influence of the Sun and all the planets) and diffusive resonances (resonances whose passage through causes a significant change in the asteroid proper elements, but not large enough to cause the loss of the body). We can safely assume that bodies in regions affected by or near destabilizing resonances will be lost on time-scales of up to 10 Myr, so that local low densities do not reflect a non-uniform primordial distribution. The destabilizing effect of the resonances discussed are also investigated in some detail later in this paper.

Among destabilizing mean-motion resonances, we can identify from previous works the 7J:-2A, 3J:-1A, 5J:-2A and 2J:-1A mean-motion resonances with Jupiter. Fig. 4 shows [a, sin (i)] projections of asteroids with absolute magnitude $H < 12$ in the highly inclined area. Following the example of Michtchenko et al. (2010), we divided the population of objects into low-eccentricity ($e < 0.175$; Fig. 4, panel A) and high-eccentricity ($e > 0.175$; Fig. 4, panel B) asteroids. Both panels show vertical band (red dashed lines) that are related to the boundaries of the unstable regions associated with the destabilizing mean-motion resonances. To estimate the sizes of these boundaries, we used the following procedure. First, we computed the size of the resonance in the (a, e) plane using the approach described in Morbidelli (2002). Then, we added 0.015 au, the size of the depopulated region near the borders of the 3J:-1A mean-motion resonance, as observed by Guillens, Vieira Martins & Gomes (2002), to the value of the size in the semimajor axis

[3] Of course, the orbital mobility of an object depends on several other parameters than the absolute magnitude, such as the spin axis obliquity, the thermal inertia, the thermal conductivity, the surface density, the bond albedo, etc. Thus, this criterion is approximated at best. However, because many of these parameters are not known for large numbers of asteroids, it is helpful to have a simple criterion that can be used for statistical considerations.

Table 1. Cell identification, the limits in a, e and $\sin(i)$, and the number of real $H < 12$ objects.

Cell identification	Intervals in a	Intervals in e	Intervals in $\sin(i)$	No. of real $H < 12$ objects
1	$a < a_{31}$	$e < 0.175$	$0.3 < \sin i < 0.45$	1
2	$a < a_{31}$	$e < 0.175$	$\sin i > 0.45$	0
3	$a < a_{31}$	$0.175 < e < 0.6$	$0.3 < \sin i < 0.45$	15
4	$a < a_{31}$	$0.175 < e < 0.6$	$\sin i > 0.45$	2
5	$a_{31} < a < a_{83}$	$e < 0.175$	$0.3 < \sin i < 0.45$	8
6	$a_{31} < a < a_{83}$	$e < 0.175$	$\sin i > 0.45$	0
7	$a_{31} < a < a_{83}$	$0.175 < e < 0.6$	$0.3 < \sin i < 0.45$	7
8	$a_{31} < a < a_{83}$	$0.175 < e < 0.6$	$\sin i > 0.45$	4
9	$a_{83} < a < a_{52}$	$e < 0.175$	$0.3 < \sin i < 0.45$	8
10	$a_{83} < a < a_{52}$	$e < 0.175$	$\sin i > 0.45$	1
11	$a_{83} < a < a_{52}$	$0.175 < e < 0.6$	$0.3 < \sin i < 0.45$	3
12	$a_{83} < a < a_{52}$	$0.175 < e < 0.6$	$\sin i > 0.45$	5
13	$a_{52} < a < a_{94}$	$e < 0.175$	$0.3 < \sin i < 0.45$	13
14	$a_{52} < a < a_{94}$	$e < 0.175$	$\sin i > 0.45$	1
15	$a_{52} < a < a_{94}$	$0.175 < e < 0.6$	$0.3 < \sin i < 0.45$	15
16	$a_{52} < a < a_{94}$	$0.175 < e < 0.6$	$\sin i > 0.45$	1
17	$a_{94} < a < a_{21}$	$e < 0.175$	$0.3 < \sin i < 0.45$	115
18	$a_{94} < a < a_{21}$	$e < 0.175$	$\sin i > 0.45$	5
19	$a_{94} < a < a_{21}$	$0.175 < e < 0.6$	$0.3 < \sin i < 0.45$	47
20	$a_{94} < a < a_{21}$	$0.175 < e < 0.6$	$\sin i > 0.45$	2

calculated at $e = 0.25$, the mean value of the eccentricity of asteroids in the region. Asteroids in these areas can be destabilized by mean-motion resonances either directly or indirectly via migration caused by the Yarkovsky force.

Concerning secular resonances, we considered the effect of the ν_6 resonance, and we computed the unstable regions using the criterion described in Carruba (2010a) and Carruba et al. (2011b). We first computed the k_6 parameter, defined as

$$k_6 = b - \nu_6, \tag{2}$$

where $\nu_6 = 28.243$ arcsec yr^{-1} is the precession frequency of Saturn's pericentre and b is a frequency-like parameter computed using the Yoshikawa (1987) model of the ν_6 resonance. Asteroids with k_6 values in the interval to $-2.55 < k_6 < 2.55$ arcsec yr^{-1} in the internal main belt (values of a smaller than the centre of the 3J:-1A mean-motion resonance; Carruba 2010a) and in the interval $-3.5400 < k_6 < 1.6815$ arcsec yr^{-1} in the central main belt (between the 3J:-1A and 5J:-2A mean-motion resonances; Carruba et al. 2011b) are considered likely to have their eccentricity pushed to terrestrial planet-crossing levels and to be destabilized on timescales of 10 Myr.[4] In the external main belt, it is not possible to use the Yoshikawa approach because of the perturbing effect of the 2J:-1A mean-motion resonance, not accounted for in the model. However, the effect of the ν_6 resonance is more limited in this region of the asteroid belt than in the internal part (see Section 6).

In order to have a sample of objects as close as possible to the primordial population, we have eliminated from the list of 313 highly inclined $H < 12$ asteroids those objects that are members of the following families: Phocaea, Barcelona, Hansa, Gersuind, Pallas, Gallia, Tina, Euphrosyne, Alauda, Luthera and (16708) (1995 SP1); see Carruba (2009b, 2010b) for the determination of the family membership of highly inclined objects. This left us with a list of 253 asteroids whose current orbits should not have been greatly modified since the formation of the asteroid belt.

Then, we divided the highly inclined asteroid regions into 20 areas according to these criteria. We have used the main mean-motion resonances with Jupiter as 'natural dynamical boundaries' and we have created five regions: $a < a_{31}$, $a_{31} < a < a_{83}$, $a_{83} < a < a_{52}$, $a_{52} < a < a_{94}$ and $a_{94} < a < a_{21}$.[5] This division creates slightly unequal cells in the semimajor axis, but we believe that this inconvenience is more than compensated by the fact that such a division respects the local dynamics and does not tend to incorporate in the same cell objects belonging to different dynamical groups. We then divided the asteroids into two large eccentricity cells, one for objects with $e < 0.175$ and the other for objects with larger eccentricity. We assume that, as observed, no asteroid has an eccentricity larger than 0.6, so that the limits of the cells at high eccentricity are $0.175 < e < 0.6$. Finally, we also created two cells in inclination separated by the value $\sin(i) = 0.45$, which roughly corresponds to the inclination of the centre of the ν_5 resonance in the central main belt. Overall, we created 20 cells in the [a, e, $\sin(i)$] domain. Fig. 4 shows [a, $\sin(i)$] projections of low-eccentricity ($e < 0.175$; panel A) and high eccentricity ($e > 0.175$; panel B) objects. Real asteroids in the region, selected according to the criterion described earlier in this section, are identified as blue asterisks, and the numbers in each cell are related to the number of objects per cell. Table 1 displays the cell numbers (from 1 to 20), the intervals in a, e and $\sin i$ of each cell and the number of real objects in each cell.

From this preliminary analysis, we can see that the number of $H < 12$ objects above the ν_6 resonance is indeed limited, especially at low eccentricities. We have identified 23 objects at low eccentricities ($e < 0.175$) and 59 objects at high eccentricities [$e > 0.175$; (2) Pallas is one of these objects]. These are characterized as having values of proper g, the frequency of precession of the pericentre, lower than 28.243 arcsec yr^{-1}, a value that corresponds to the ν_6 resonance. The limited number of large objects above the ν_6 resonance

[4] The exception is the Tina family members in the central main belt whose orbits have k_6 values in the range discussed in Carruba et al. (2011b), but whose eccentricities do not reach planet-crossing levels because of the protecting effect of the antialigned ν_6 resonant configuration, as discussed in Carruba & Morbidelli (2011a).

[5] For the cell boundaries, we have used the centre of the resonance, and the suffixes (e.g. 21) refer to the mean-motion resonances.

when compared with the analogous population at lower inclinations could suggest that the original population of highly inclined objects was limited to begin with.

4 STATISTICAL CONSIDERATIONS

In the previous sections, we have seen that there are large variations in the orbital distribution of asteroids in highly inclined regions. In this section, we try to understand whether this phenomenon is compatible with normal statistical fluctuations of a uniformly spaced or Gaussian-spaced population or whether we need some further hypothesis on the mechanisms that formed the original highly inclined populations. In our statistical analysis, we use two approaches. First, we consider the one-dimensional probability distributions for the $H < 12$ asteroid population using the cells defined in Section 3, checking for possible correlations among cells. Secondly, we try to see if the [a, e, $\sin(i)$] tri-dimensional distribution follows a trivariate Gaussian distribution by performing a normality test. We start by looking at the one-dimensional probability distributions.

4.1 One-dimensional probability distributions

When looking at one-dimensional probability distributions, there are two possible approaches. We can look at the $H < 12$ asteroid population and verify whether it follows simple one-dimensional probability distributions, such as the Poissonian, uniform or Gaussian distributions, in each cell. We can also check if there are correlations among cells at same inclinations or in the same range of semimajor axes. We start our analysis by looking at the Poissonian statistical distribution.

Table 2 displays the cell identification, as given in Table 1, the number of real objects in each cell, the weighted mean number of objects per cell, the probability that this number is generated by Poissonian statistics, the number of objects that would be produced in each cell if we assume a uniform distribution of objects in [a, e, $\sin(i)$], which best fit the data, and the number of objects that would be produced if we assume a Gaussian distribution in [a, e, $\sin(i)$], which best fit the data. We have found that the $H < 12$ asteroid population has mean values of a, e and $\sin(i)$ of 3.0270 au, 0.1516 and 0.3656, respectively. The variances in a, e and $\sin(i)$ are 0.0653 au, 0.0057 and 0.0030, respectively. We have estimated the probability that a number of objects are produced by the Poissonian distribution, assuming that the expected number of k occurrences in a given interval is given by

$$f(k, \lambda) = \frac{\lambda^k e^{-\lambda}}{k!}. \quad (3)$$

Here, λ is a positive real number, equal to the expected number of occurrences in the given interval. For our purposes, we used for λ the mean values of objects per cell of real asteroids, weighted to account for the different volume occupied by each cell. This is given by

$$\lambda = N_{\rm ast} \frac{V_{\rm cell}}{V_{\rm Tot}}, \quad (4)$$

where $N_{\rm ast}$ is the total number of objects with $H < 12$ in stable regions (253), $V_{\rm cell}$ is the volume in (a, e, i) space occupied by each cell – see Section 3 for the limits of the cell in the (a, e, i) domain – and $V_{\rm Tot}$ is the total volume in the region. Using standard statistical terminology, we define the null hypothesis as the possibility that the data are drawn from a given distribution. We can reject the null hypothesis if it is associated with a probability lower than a threshold that is usually of the order of 1 per cent or 0.01. Our results show that 13 cells have negligible probability that their numbers can be reproduced by a Poissonian distribution. The cells compatible with a Poissonian distribution (cells 5, 7, 8, 9, 11, 12 and 13) are those associated with the Hansa, Gallia and Brucato, Gersuind, Pallas and Danae regions. Other cells have an orbital distribution of highly inclined objects incompatible with a Poissonian distribution, either because they are underpopulated (cells 1, 2, 4, 6, 10, 14, 16, 18 and 20) or overpopulated (cells 3, 15, 17 and 19). Because 14 out of

Table 2. Number of real objects, the weighted mean number of objects per cell, the probability of real objects being a product of a Poissonian statistical distribution, the number of simulated objects with uniform and Gaussian distributions as a function of the cell in the [a, e, $\sin(i)$] domain.

Cell identification	No. of real objects	Weighted mean number of objects per cell	Poissonian probability	Uniform distribution	Gaussian distribution
1	1	11.598	1.1×10^{-4}	15	2
2	0	18.761	7.1×10^{-9}	15	8
3	15	7.543	0.0058	41	51
4	2	18.320	1.8×10^{-6}	23	39
5	8	6.810	0.1264	4	1
6	0	16.548	6.5×10^{-8}	4	2
7	7	4.431	0.0792	18	31
8	4	10.760	0.0119	4	27
9	8	3.274	0.0123	7	2
10	1	7.950	0.0028	6	2
11	3	2.128	0.1913	8	11
12	5	5.170	0.1750	7	3
13	13	8.520	0.0400	6	5
14	1	20.692	2.1×10^{-8}	3	3
15	15	5.540	0.0004	19	10
16	1	13.457	1.9×10^{-5}	14	13
17	115	8.394	$<10 \times 10^{-11}$	12	4
18	5	20.385	4.1×10^{-5}	6	3
19	47	5.459	$<10 \times 10^{-11}$	20	14
20	2	13.257	1.5×10^{-4}	21	22

20 of the considered cells do not satisfy the null hypothesis for the Poissonian distribution, it seems unlikely that the observed changes in orbital distribution can be explained as simple fluctuations of a Poissonian distribution for the whole region.

We have checked whether the asteroid number distribution in areas in the same ranges of semimajor axes, eccentricities and inclinations can be approximated by a Poissonian distribution. We started by looking at asteroids in the same range of semimajor axes, with $a < a_{31}$ (Phocaea region), $a_{31} < a < a_{83}$ (Hansa region), $a_{83} < a < a_{52}$ (Pallas region), $a_{52} < a < a_{94}$ and $a_{94} < a < a_{21}$ (Euphrosyne region). Using equation (3), we computed the probability that the asteroid proper inclination followed the Poissonian distribution. Because the Poissonian distribution is only computed for integer values of k, we multiply values of $\sin(i)$ by a factor of 100 and take only the first two digits. We best-fitted the value of λ in equation (3) for the observed asteroids using the MATLAB routine poissfit. We generated a random population of asteroids following the Poissonian distribution using the MATLAB routine poissrnd. To check if the simulated distribution was compatible with the observed distribution, we performed a Pearson χ^2 test by computing a χ^2-like variable, defined as

$$\chi^2 = \sum_{i=1}^{n_{\rm int}} \frac{(q_i - p_i)^2}{q_i}. \quad (5)$$

Here, $n_{\rm int}$ is the number of intervals of our variables, corresponding to the number of asteroids in each region, q_i is the number of real objects in the ith interval and p_i is the number of simulated objects in the same interval. Values of χ^2 of the order of the number of intervals are consistent with a good fit. For each region of interest, we obtained 1000 random populations, and we computed the value of χ^2 for each simulated population. Then, using the standard χ^2 probability distribution (Press et al. 2001), we calculated the probability that the real population might be following a Poissonian distribution. The minimum value of χ^2 among the 1000 simulated populations gave the best likelihood estimation that such hypotheses were true.

The lowest χ_2 value (52.98) was observed for a set of 18 simulated bodies in the Phocaea region. This corresponds to a probability that the real distribution is Poissonian of just 8.2×10^{-9}. All the other regions have higher values of χ_2 and negligible probabilities that the observed orbital distributions are Poissonian. We also checked the distributions in the semimajor axes for low-inclined [$\sin(i) < 0.45$] and high-inclined [$\sin(i) > 0.45$] asteroids, and for low-eccentricity ($e < 0.175$) and high-eccentricity ($0.175 < e < 0.600$) objects. Once again, we did not find values of χ_2 compatible with a Poissonian distribution. With the possible exception of the Phocaea region, large asteroids in the area are not distributed according to Poissonian statistics.

We then tried a different approach by hypothesizing that fluctuations in a uniform distribution could explain the observed asteroid distribution. Using a random number generator (Press et al. 2001), we created a set of 253 fictitious bodies with a uniform distribution in the [a, e, $\sin(i)$] domain. (If a body was in one of the unstable regions discussed in Section 3, we eliminated it from our database and created a new one. The procedure was repeated until we obtained a set of 253 bodies.) Using different seeds[6] (from a value of -1 up to -1000, the seed must be a negative number) for the random number generator, we produced 1000 sets of 253 fictitious asteroids with a uniform distribution in the given range of [a, e, $\sin(i)$] values. The fifth column of Table 2 displays the number of objects per cell produced with a uniform distribution in the [a, e, $\sin(i)$] domain that best fitted the results. To check if the observed distribution is compatible with the uniform distribution, we performed a one-dimensional Kolmogorov–Smirnov (KS) test. This is a test used to verify the validity of the hypothesis that a random deviate follows a continuous probability distribution. Given two cumulative distributions, $S_{N_1}(x)$ and $S_{N_2}(x)$, the KS statistics D is given by the maximum value of their absolute difference. For given values of D, we can obtain the probability of the null hypothesis that the two data sets are drawn from the same distribution (Press et al. 2001). For the uniform distribution, not even considering the cells with $a_{94} < a < a_{21}$, whose large asteroidal population could be caused by the larger inclination values of the ν_6 resonance in the region (more asteroids could come to these areas from low-inclinations regions compared to other cells), the KS test yields for the best-fitting case the low probability of 4.3×10^{-4} that the two data sets are drawn from the same distribution. This is enough to reject the null hypothesis.

We have also checked if the uniform distribution can approximate the number distribution of asteroids in the same range of a, e, i, as done for the Poissonian distribution. We generated 1000 sets of uniform deviates in inclination for the observed range of values of real asteroids in each of the regions in a used for the Poissonian analysis, and for low- and high-eccentricity and inclined objects, and we performed a KS test for each of the samples compared with the observed population. The highest probability results of the KS test were once again obtained for the Phocaea region, with a probability that the distribution follows a uniform deviate of 4.26×10^{-3}. The low value of this probability seems to infer that it is unlikely that asteroids in the Phocaea region follow a uniform deviate. Surprisingly, we obtained a probability of 1.5×10^{-3} that highly inclined asteroids are distributed according to uniform deviates. All other KS tests yielded lower probability results.

Finally, we also created 1000 sets of 253 synthetic objects that have a Gaussian distribution in (a, e, i), using the same criteria used for the bodies created with the uniform distribution. Mean values and variances were computed from the observed sample of large asteroids. We did not account for possible correlations among the variables in this preliminary test. We discuss this point in more detail in Section 4.2. The sixth column in Table 2 displays the number of objects per cell produced with such a distribution. We then implemented our KS test for cells up to $a = a_{94}$ and for all cells, and we obtained best probability values of the two data set drawn from the same distribution of 4.3×10^{-4} and 4.1×10^{-4}, low enough to be able to safely reject the null hypothesis. In either case, it is unlikely that the current asteroid distribution is compatible with the simulated distribution.

Once again, we checked if the Gaussian distribution can approximate the number distribution of asteroids in the same range of a, e and i. We repeated the analysis as for the uniform distribution and we also used the MATLAB built-in routine kstest.m to check for normality. The results are in agreement with those found previously for the uniform distribution – there is a low probability (4.5×10^{-3}) that asteroids in the Phocaea region might follow a Gaussian distribution and a relatively high (when compared with other results) likelihood (1.7×10^{-3}) that highly inclined asteroids might be distributed normally. All other KS tests gave lower probabilities that the two distributions, real and fictitious, could both be Gaussian.

[6] Random number generators are algorithms that can automatically create long runs of numbers with good random properties. The string of values generated by such algorithms is generally determined by a fixed number, called a seed.

Overall, it seems that current non-uniformities in the number distributions of asteroids cannot be explained as fluctuations of one-dimensional statistical distributions, such as the Poissonian, uniform and Gaussian distributions, except possibly for the Phocaea region, which is marginally compatible with a Poissonian distribution of the inclinations. In the following subsection, we investigate if a multivariate Gaussian distribution could better approximate our sample of large asteroids.

4.2 Tri-variate Gaussian probability distributions

In Section 4.1, we checked if one-dimensional probability distributions can account for the observed fluctuations in the number of large ($H < 12$) asteroids. Here, we investigate if a multidimensional distribution in the [a, e, $\sin(i)$] domain, which accounts for possible correlations among the different dimensions, could better explain the observed distribution.[7]

We assume that the distribution in the [a, e, $\sin(i)$] domain has a tri-variate Gaussian probability density function, given by

$$f(\boldsymbol{x}) = \frac{1}{(2\pi)^{3/2}\sqrt{|\Sigma|}} \exp\left[-\frac{1}{2}(\boldsymbol{x}-\mu)'\Sigma^{-1}(\boldsymbol{x}-\mu)\right]. \quad (6)$$

Here, $\boldsymbol{x}$ is the vector [a, e, $\sin(i)$] and μ is the vector with components equal to the mean values of a, e and $\sin i$ of the observed population (see Section 4.1). Σ is the covariance matrix, which can be estimated numerically having n $\boldsymbol{x}_j$ vectors using

$$\Sigma = \frac{1}{n}\sum_{j=1}^{n}(\boldsymbol{x}_j - \mu)\cdot(\boldsymbol{x}_j - \mu)^{\mathrm{T}}. \quad (7)$$

The numerical elements of Σ for the 253 highly inclined asteroids in the region are equal to

$$\Sigma = \begin{vmatrix} 0.0653 & -0.0066 & -0.0031 \\ -0.0066 & 0.0057 & 0.0007 \\ -0.0031 & 0.0007 & 0.0030 \end{vmatrix}. \quad (8)$$

$|\Sigma| = 9.2913 \times 10^{-7}$ au is the determinant of the covariance matrix. We first draw 253 random vectors from this tri-variate Gaussian distribution using the following procedure. Because Σ is positive defined, we use the Choleski decomposition to obtain a matrix $\mathbf{A}$ such that $\mathbf{A}\cdot\mathbf{A}^{\mathrm{T}} = \Sigma$. The $\mathbf{A}$ matrix is a triangular matrix whose elements in the triangle below the main diagonal are all zero. We then generated 253 tri-dimensional vectors $\boldsymbol{Z}$, whose components are N independent standard normal variates, using standard MATLAB routines, such as randn.m, based on the Box–Muller transform. Finally, we obtained 1000 sets of 253 vectors in the [a, e, $\sin(i)$] domain, following the given tri-variate Gaussian distribution, using

$$X = \mu + \mathbf{A}\boldsymbol{Z}. \quad (9)$$

These vectors have the desired distribution because of the affine transformation property; see Press et al. (2001) for information on the Choleski decomposition and see the MATLAB support website for information on randn.m. To check if the current observed asteroidal population follows a tri-variate normal distribution, we performed two tests. First, we computed the number of generated fictitious asteroids per cell, using the cells defined in Section 3. Secondly, we performed a Pearson χ^2 test by computing a χ^2-like variable defined by equation (5), where n_{int} is the number of intervals of our variables (20 in our case), q_i is the number of real objects in the ith interval and p_i is the number of simulated objects in the same interval. Once again, we remind the reader that values of χ^2 of the order of the number of intervals are consistent with a good fit. Even without considering the cells with $a_{94} < a < a_{21}$, whose large asteroidal population might be caused by the larger inclination values of the ν_6 resonance in the region (more asteroids could come to these areas from low-inclinations regions compared to other cells), we find that the lowest value of χ^2 for regions with $a < a_{94}$ is 73.22 for 16 intervals for a given set of the simulated 253 asteroids. Using the standard χ^2 probability distribution (Press et al. 2001), we find that the null hypothesis has a probability of just 5.3×10^{-10}, which is low enough for us to be able to reject it safely.

In order not to incur possible binning problems associated with our choice of cells, we also performed the Mardia test (Mardia 1970) on the multivariate normality for the whole 253 asteroid population.[8] The Mardia test is based on multivariate extensions of skewness and kurtosis measures. For a sample ($x1, \ldots, xn$) of p-dimensional vectors, we can compute the A and B parameters given by

$$A = \frac{1}{6n}\sum_{i=1}^{n}\sum_{j=1}^{n}\left[(\boldsymbol{x}_i - \mu)^{\mathrm{T}}\Sigma^{-1}(\boldsymbol{x}_j - \mu)\right]^3 \quad (10)$$

and

$$B = \frac{\sqrt{n}}{\sqrt{8p(p+2)}} \times \left\{\frac{1}{n}\sum_{i=1}^{n}\left[(\boldsymbol{x}_i - \mu)^{\mathrm{T}}\Sigma^{-1}(\boldsymbol{x}_i - \mu)\right]^2 - p(p+2)\right\}. \quad (11)$$

Here, Σ^{-1} is the inverse of the covariance matrix given by equation (7). Under the null hypothesis of multivariate normality, the statistic A will have approximately a χ^2 distribution with $(1/6)p(p+1)(p+2)$ degrees of freedom (10 for $p = 3$) and B will be approximately standard normal with a zero mean and a standard deviation equal to 1. We computed A and B for our sample of 253 asteroids and we obtained $A = 166.98$ and $B = 7156.20$, which have probabilities lower than 10^{-6} of being associated with χ^2 and normal distributions. Once again, we can safely assume that, on the whole, large highly inclined asteroids do not follow a tri-variate Gaussian distribution.

What about smaller samples of asteroids? To check this hypothesis, we again looked at asteroids in the same range of a, e and $\sin(i)$ as used in Section 4.1. We found that all asteroid samples have values of the Mardia test B parameter that are too high to satisfy the null hypothesis. However, the value of the A parameter for asteroids in the regions of Phocaea, Hansa and Pallas was below 10. This yielded a non-negligible probability (33 per cent for the lowest values of A of 7.7 in the Hansa region) that asteroids in the regions can be fitted by a tri-variate normal distribution. We also found a relatively small value of A for asteroids at very large inclinations ($A = 12.8$). While the large values of the B parameters should favour

[7] We limit our analysis to the [a, e, $\sin(i)$] proper-element domain because the g and, to a lesser extent, s frequencies are strongly perturbed in the proximity of mean-motion resonances, such as 2J:-1A and 3J:-1A (see Fig. 3). While there are techniques to normalize the dependence of the g frequency as a function of the mean-motion resonance or of the semimajor axis (Carruba & Michtchenko 2009), such a normalization requires an in-depth study of local family membership, which we feel is beyond the purposes of this study.

[8] Other tests on multivariate normality, such as the tri-dimensional KS test (Fasano & Franceschini 1987), the Cox–Small test (Cox & Small 1978) and others, are also adequate choices for testing multivariate normality.

the exclusion of the null hypothesis, the fact that large asteroids in the same range of the semimajor axis are more likely to belong to tri-variate normal distributions could indicate that the mechanism that populated the highly inclined regions might have acted 'vertically' from lower values of inclinations to higher values, rather than 'horizontally', moving asteroids originally at the same inclinations to a different semimajor axis – with the possible exception of very highly inclined objects with $\sin(i) > 0.45$. Further studies on such a mechanism are needed before this hypothesis can be confirmed.

5 DENSITY MAPS

In Section 4, we analysed the statistical likelihood that fluctuations of the orbital distributions of asteroids at high inclination might be caused by fluctuations in the one- and three-dimensional statistical distributions. Here, we would like to address the dynamical causes of underpopulated and overpopulated areas by asking whether the observed underpopulated regions are caused by any dynamical mechanism.

Information on the dynamics of asteroids can be obtained by an analysis of the number densities of asteroids. Fig. 5 displays contour plots of such densities. See Carruba (2009b) for a description of the procedure used to generate such plots; here, we have used 70 steps of 0.02 au in a and 30 steps of 0.04 in $\sin(i)$. Higher number densities of objects are shown in whiter tones. Once again, we divided the population of objects into small-eccentricity bodies ($e < 0.175$; Fig. 5, panel A) and large-eccentricity bodies ($e > 0.175$; Fig. 5, panel B).

As can be seen in Fig. 5 (panels A and B), underpopulated areas (in black) in the Phocaea region are clearly associated with the border of the ν_6 secular resonance. Therefore, they can be understood within the framework of the interaction of the ν_6 resonance topology, which causes the asteroid eccentricity to increase, and of planetary close encounters, which remove such particles in short time-scales (see Carruba 2010a for an in-depth description of these mechanisms). In the Pallas area, we can identify an underpopulated area, especially visible at high eccentricities, between the 8J:-3A and 5J:-2A mean-motion resonances and the ν_5 and ν_{16} secular resonances (roughly, this corresponds to values of $\sin i$ between 0.45 and 0.50). This area is shown by white boxes in Fig. 5, and corresponds to cell 10 in Section 4, which has a low probability that the large asteroidal population follows a Poissonian distribution. The underpopulated area in the region between 2.5 and 2.82 au in a and 0.36 and 0.42 in $\sin(i)$ is caused by the presence of the ν_6 resonance. The destabilizing effect of this resonance on local asteroids has been studied in Carruba et al. (2011b) and in Carruba & Morbidelli (2011a). Finally, in the Euphrosyne area, the whole region above the ν_6 resonance and between the 5J:-2A and 9J:-4A mean-motion resonances is characterized by a remarkable low number density of objects. We have identified the underpopulated stable areas in Fig. 5 (panels A and B), corresponding to cells 14, 15 and 16 in Section 4, with white boxes. For comparison purposes, we also selected a region in a high asteroid population area in the Euphrosyne region. This region is identified by a green box in Fig. 5, and corresponds to the last four cells (17, 18, 19 and 20) in Section 4.

To investigate if these regions are dynamically stable or not, we performed a numerical analysis, the results of which are discussed in Section 6.

6 DYNAMICAL MAPS

We start by investigating the region between the 8J:-3A and 5J:-2A mean-motion resonances, previously identified in Section 3 as a stable region with a low asteroid population. For this purpose, we obtained the synthetic proper elements of 2160 test particles integrated with swift_mvsf, the integrator from the SWIFT package (Levison & Duncan 1994) modified by Brož (1999), so as to include on-line digital filtering in order to remove all frequencies with periods less than 600 yr. We integrated the objects over 10 Myr. The synthetic proper elements were obtained with the procedure described in Knežević & Milani (2003), except for the proper frequencies, which were derived with the frequency modified Fourier transform (FMFT) of Šidlichovský & Nesvorný (1997) using the following procedure. We eliminated from the spectra of the Fourier transform of the equinoctial elements all planetary frequencies and we then assigned as the proper frequency the largest value in the spectra that was still observable, rather than fitting the time series of ϖ_f and Ω_f of the oscillations in the (k, h) and (p, q) planes. The test particles were integrated under the influence of all planets from

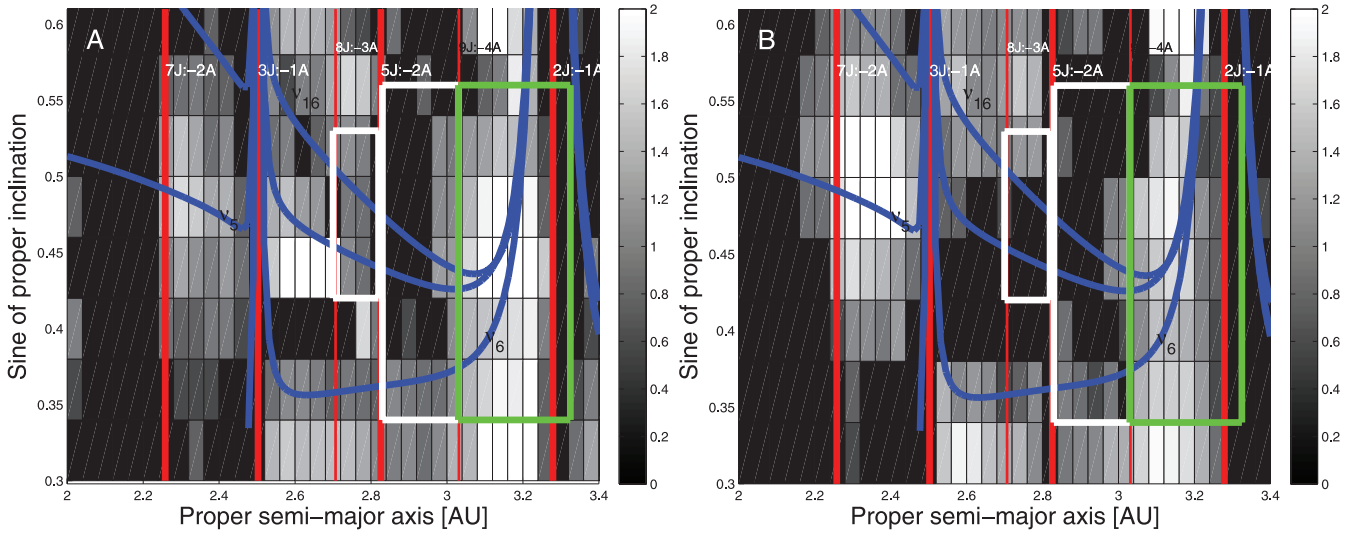

Figure 5. An [a, $\sin i(i)$] density map of low-eccentricity ($e < 0.175$, panel A) and high-eccentricity ($e > 0.175$, panel B) asteroids. The white boxes identify the underpopulated stable areas and the green box displays the stable sample area. The other lines have the same meanings as in Fig. 1.

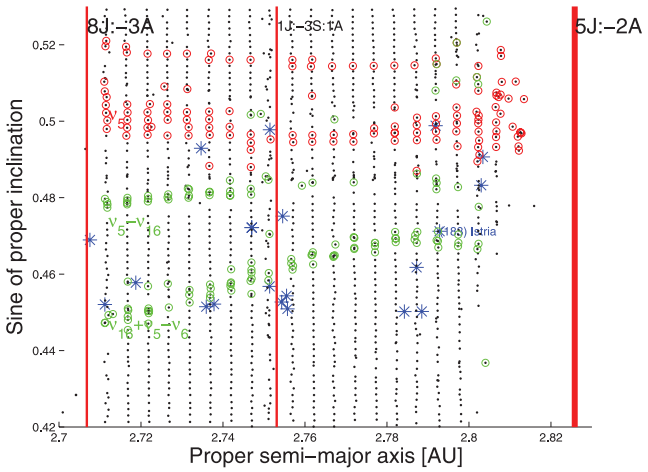

Figure 6. Synthetic proper-element map of the region of (183) Istria. The vertical lines display the mean-motion resonances, the blue asterisks identify real objects in the region, the red circles are associated with asteroids in linear secular resonances and the green circles display bodies in non-linear secular resonances.

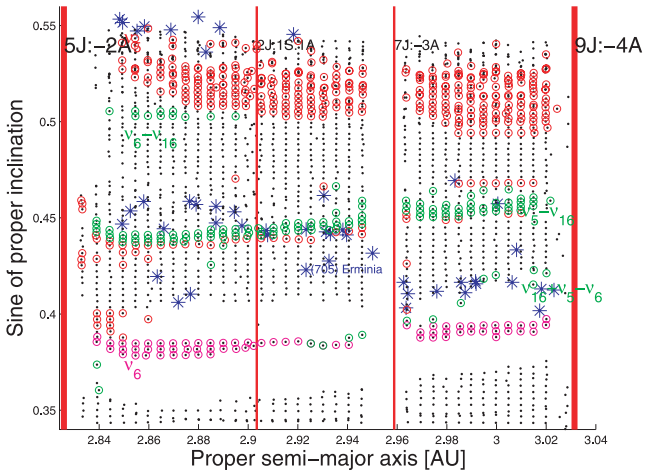

Figure 7. Synthetic proper-element map of the region of (705) Erminia. The magenta circles are associated with bodies in the ν_6 secular resonance. The other symbols are the same as in Fig. 6.

Venus to Neptune (Mercury was accounted for as a barycentric correction of the initial conditions) and we referred the inclination and the arguments of pericentre and node to the invariable plane of the Solar system. The initial conditions of planets and particles were computed on 2000 January 1. Our test particles covered the interval between 2.7 and 2.83 au, and between 23° and 31°, and we set the values of initial eccentricity and other angles equal to those of (183) Istria, the real object in the area with the lowest identification. Finally, we used 27 intervals in a and 80 in i.

Fig. 6 shows the [a, sin (i)] projection of the synthetic proper elements of our test particles (black dots). Regions unaffected by resonances appear as regular vertical alignments of objects in this map, while areas affected by mean-motion resonances appear as void of asteroids (see the area near the 5J:-2A resonance). Objects in secular resonances appear to form inclined alignments. Vertical red lines show the locations of the main mean-motion resonances in the region, as identified in Carruba (2010b). Red circles show the objects to within 0.3 arcsec yr^{-1} from the centre of the linear secular resonance in the region, $\nu_5 = g - g_5$. Green circles show the locations of the non-linear secular resonances in the area, $\nu_5 - \nu_{16} = g - g_5 - (s - s6)$ and $\nu_{16} + \nu_5 - \nu_6 = s - s_6 + (g - g_5) - (g - g_6)$. For simplicity, we do not show secular resonances involving the Uranus frequency g_7, such as the ν_7 resonance, because these are close in proper-element space to the resonances involving the g_5 frequency. Finally, real asteroids are identified by blue asterisks.

As can be seen, the region below the ν_5 resonance appears to be stable over the length of the integration (the role of non-linear secular resonances is investigated in Section 7, yet the number of real objects observed is very limited. Between sin (i) equal to 0.45 and 0.50, we only observe 21 objects, three of them with an absolute magnitude lower than 12.

To check if our results are independent of the choice of initial conditions and of the length of the integration, we also performed two numerical experiments. We integrated 1530 particles in the region with different initial conditions (the orbital elements of the planets and test particles were computed on 2010 January 1) and with the same initial conditions previously used, but for a longer time-scale. We find no significant difference concerning lost and unstable objects between the three simulations; however, there are small differences concerning ≃30 particles in secular resonances, which have slightly different values of proper frequencies g and, in some cases, of proper $sin(i)$. Because our goal is to study the long-term stability of test particles and not to focus on the details of secular dynamics, we believe that our choice of initial conditions and integration length should be reasonable.

We now turn our attention to the underpopulated area in the Euphrosyne region. To investigate the dynamical stability of this region, we integrated 3000 particles between 2.83 and 3.03 au (roughly speaking, between the 5J:-2A and 9J:-4A mean-motion resonances) and between 20° and 35° in inclination (corresponding to values of sin (i) between 0.20 and 0.55), under the same conditions as the previous simulation. The initial eccentricities and the other angles of the test particles were those of (705) Erminia, the lowest numbered object in the region.

Fig. 7 shows the synthetic proper-element map for this region. We can see the line of asteroids in ν_6 antialigned librating states (in magenta) that are stable near the centre of the unstable region as a result of the ν_6 resonance (see Carruba & Morbidelli 2011a for a description of the dynamics of asteroids in ν_6 antialigned librating states). As observed for the region around (183) Istria, the region between the ν_5 resonance (asteroids in this resonance are shown as red circles) and the ν_6 resonance appears to be stable, yet underpopulated. For this region, we observe the possible role that the $\nu_5 - \nu_{16}$, $\nu_6 - \nu_{16}$ and $\nu_{16} + \nu_5 - \nu_6$ non-linear secular resonances might play in the dynamical evolution of asteroids in the region. The long-term effect of these resonances when non-gravitational forces are present is discussed in Section 7.

Finally, we turn our attention to the highly populated area (the 'test area') in the Euphrosyne region discussed in Section 3. Using the same set-up as for the previous runs, we integrated 4500 particles between 3.03 and 3.325 au, and between 20° and 35°. The initial eccentricities and the other angles of the test particles were those of (31) Euphrosyne. Fig. 8 shows the synthetic proper-element map for this region. Particles in the ν_6 resonance are shown as magenta circles, those in ν_5 are identified by red circles[9] and particles in the

[9] The large number of red circles near the 2J:-1A mean-motion resonance is an effect of the perturbation caused by the resonance on the asteroid frequency g. This does not necessarily indicate that the particles are in a secular resonance.

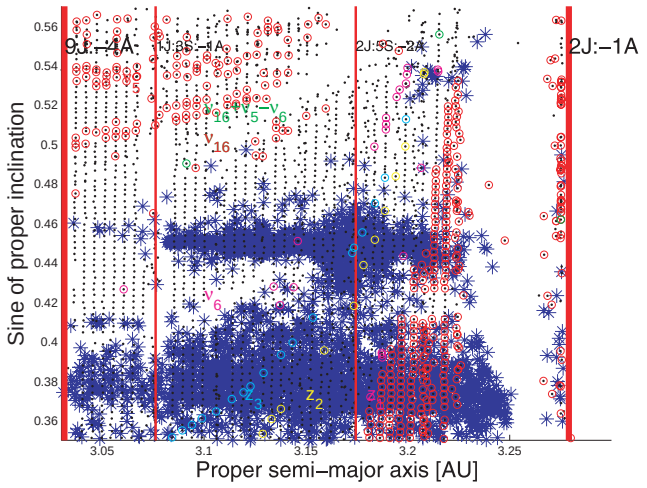

Figure 8. Synthetic proper-element map of the region of (31) Euphrosyne. The magenta circles show bodies inside the z_1 resonance, the yellow circles show asteroids inside the z_2 resonance and the cyan circles are associated with objects inside the z_3 resonance. The other symbols are the same as in Fig. 6.

ν_{16} resonance are indicated as green circles. The two main unstable areas in the Euphrosyne regions caused by secular resonances are associated with the ν_6 and ν_{16} resonances. We also show particles to within 0.3 arcsec yr^{-1} of the $z_1 = \nu_6 + \nu_{16}$ resonance (magenta circles), of the $z_2 = 2\nu_6 + \nu_{16}$ resonance (yellow circles), of the $z_3 = 3\nu_6 + \nu_{16}$ resonance (cyan circles) and of the $\nu_{16} + \nu_5 - \nu_6$ resonance (green circles). Other secular resonances that are known to affect the orbits of real asteroids are the $\nu_5 + \nu_6$ and $2\nu_5 + \nu_6$ resonances (not shown for simplicity). We also observe the effects of the 1J:3S:-1A and 2J:5S:-2A three-body mean-motion resonances. Finally, real asteroids are identified by blue asterisks.

Two things can be noticed about the test area. First, the region is significantly affected by the presence of the 2J:-1A mean-motion resonance, which, with the exception of the population of asteroids near the resonance centre (the stable Zhongguos and the unstable Griquas populations; Roig, Nesvorný & Ferraz-Mello 2002), significantly destabilized objects near the resonance separatrix. Overall, the region is less 'stable' than the two regions previously studied, yet it hosts a much larger asteroid population than that found in previous areas. Secondly, many of the objects found in the region are at an inclination lower than that of the ν_6 resonance centre. This leads us to wonder if the vast majority of the $\sin(i) > 0.3$ population in the Euphrosyne region might actually be considered as 'highly' inclined. In Section 7, we investigate further the long-term effect of the local web of resonances when non-gravitational forces are considered.

7 LONG-TERM STABILITY

To investigate the orbital evolution over a long time-span of particles in the areas discussed in the previous sections, we numerically integrated test particles with SWIFT-RMVSY, the symplectic integrator of Brož (1999), which simulates the diurnal and seasonal versions of the Yarkovsky effect. Because objects in the hole in the Pallas region are mostly of S-type (Carruba 2010b), we used values of the Yarkovsky parameters appropriate for such bodies (Carruba et al. 2003): a thermal conductivity $K = 0.001$ W m^{-1} K^{-1}, a thermal capacity $C = 680$ J kg^{-1} K^{-1}, a surface density 1500 kg m^{-2}, a Bond albedo of 0.1, a thermal emissivity of 0.95 and a bulk density of 2500 kg m^{-3}. We used two sets of spin-axis orientations, one with an obliquity of $+90^\circ$ and one with -90° with respect to the orbital plane, and periods obtained by assuming that the rotation frequency is inversely proportional to the object's radius, and that a 1-km asteroid had a rotation period of 5 h (Farinella, Vokrouhlický & Hartmann 1998). We used particles with a radius of 2 km, and no reorientations were considered, so that the drift caused by the Yarkovsky effect was the maximum possible. We integrated the 2160 test particles of the first simulation over 100 Myr, the time-scale used to study the effect of proximity to the 3J:-1A mean-motion resonance by Guillens et al. (2002), under the gravitational influence of seven planets (Mercury was accounted for as a barycentric correction of the initial conditions).

Fig. 9 shows the maximum permanence times for our particles that remained in the hole 1 region as a function of the synthetic proper elements computed in Section 6. The black dots show objects with permanence times of less than 10 Myr while the red full circles are associated with particles with permanence times longer than 100 Myr. Blue asterisks show the orbital location of real asteroids

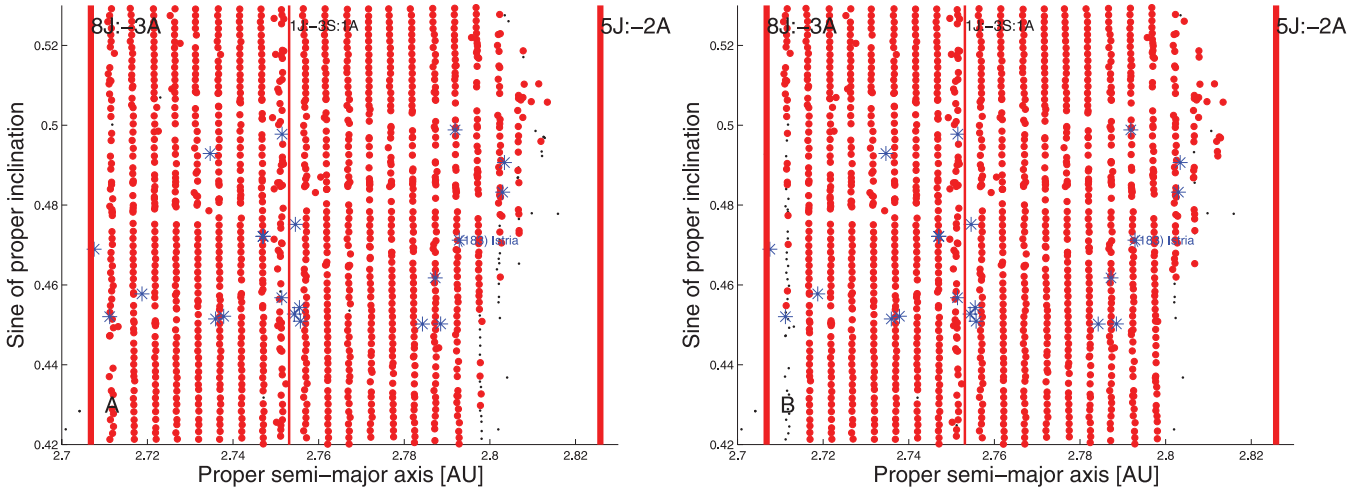

Figure 9. Maximum permanence times for particles in the hole 1 region for asteroids with an initial obliquity of $+90^\circ$ (panel A) and -90° (panel B). The black dots show objects with permanence times less than 10 Myr, while the red full circles are associated with particles with permanence times longer than 100 Myr. The other symbols are the same as in Fig. 1.

in the region. Panel A is associated with asteroids with an initial obliquity of $+90^\circ$ and panel B shows the fate of objects with initial obliquities of -90°. We note that most of the km-sized asteroid were not lost during the integration. Objects lost at times between 10 and 100 Myr were mostly particles close to the boundaries of the 5J:-2A and 8J:-3A mean-motion resonances. Overall, the region between the 5J:-2A and 8J:-3A mean-motion resonances seems to be quite stable for km-sized objects on a 100-Myr time-scale.

We then integrated the same 3000 test particles used for the dynamical map of the hole in the Euphrosyne region (see Section 6) over 100 Myr with SWIFT-RMVSY. The set-up of the simulation was the same used for the particles in the Pallas hole, but here we used parameters for the Yarkovsky force typical of C-type asteroids, which are predominant in the Euphrosyne region (the same parameters as for an S-type asteroid, but with a bulk density of 1500 kg m^{-3}; Carruba et al. 2003). See Gil-Hutton (2006) for a discussion of the spectral types of asteroids in the Euphrosyne region.

Fig. 10 shows the maximum permanence times for our particles that remained in the hole 2 region as a function of the synthetic proper elements computed in Section 6. The symbols used are the same as for Fig. 9. Just as for the simulation for the Pallas hole, we observe that the layer of particles with permanence times of less than 10 Myr is limited to the boundaries of the main resonances in the region (5J:-2A, 7J:-3A, 9J:-4A and ν_6), but we observe that the rest of the region is stable for km-sized objects on a 100-Myr time-scale.

Finally, we turn our attention to the test area defined in Section 3. Fig. 11 shows maximum permanence times for the same 4500 particles in the area as a function of the synthetic proper elements computed in Section 6, assuming Yarkovsky parameters typical of C-type asteroids. The symbols used are the same as for Fig. 9. We observe that the region is overall stable over a 100-Myr time-scale, with the exceptions of asteroids in the 2J:-1A central island of stability and a few objects near the borders of the ν_6, ν_{16} and 1J:3S:-1A resonances.

Because our dynamical analysis has shown that the studied underpopulated areas are dynamically stable, even when non-gravitational effects are considered, we have to conclude that the low population of objects in these regions is real, and is not caused by fluctuations in statistical distributions, as seen in Section 4. The

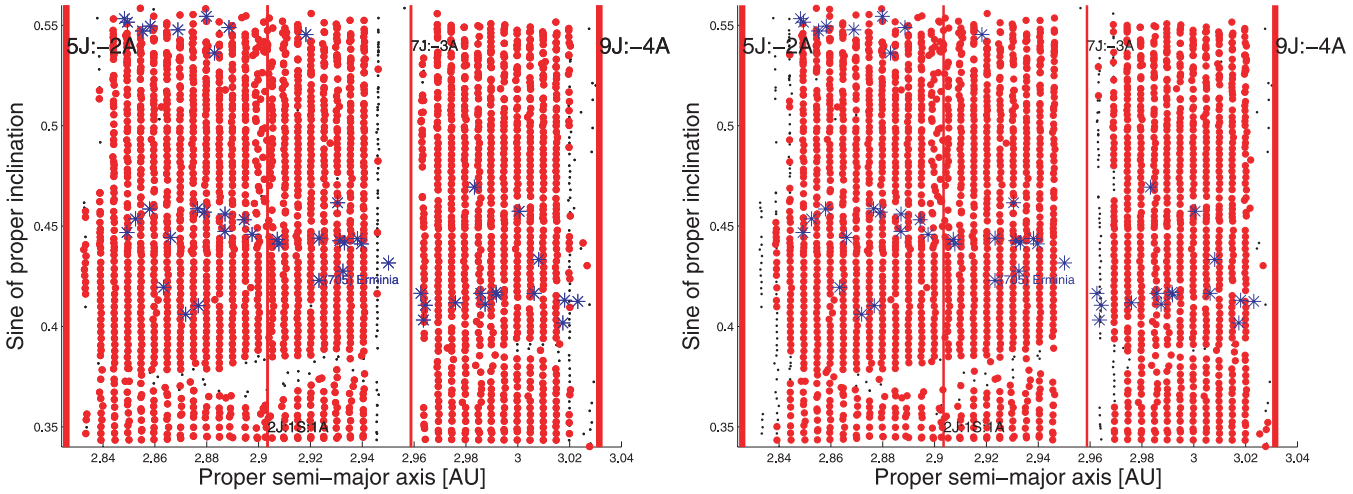

Figure 10. Maximum permanence times for particles in the hole 2 region for asteroids with an initial obliquity of $+90^\circ$ (panel A) and -90° (panel B). All symbols are the same as in Fig. 9.

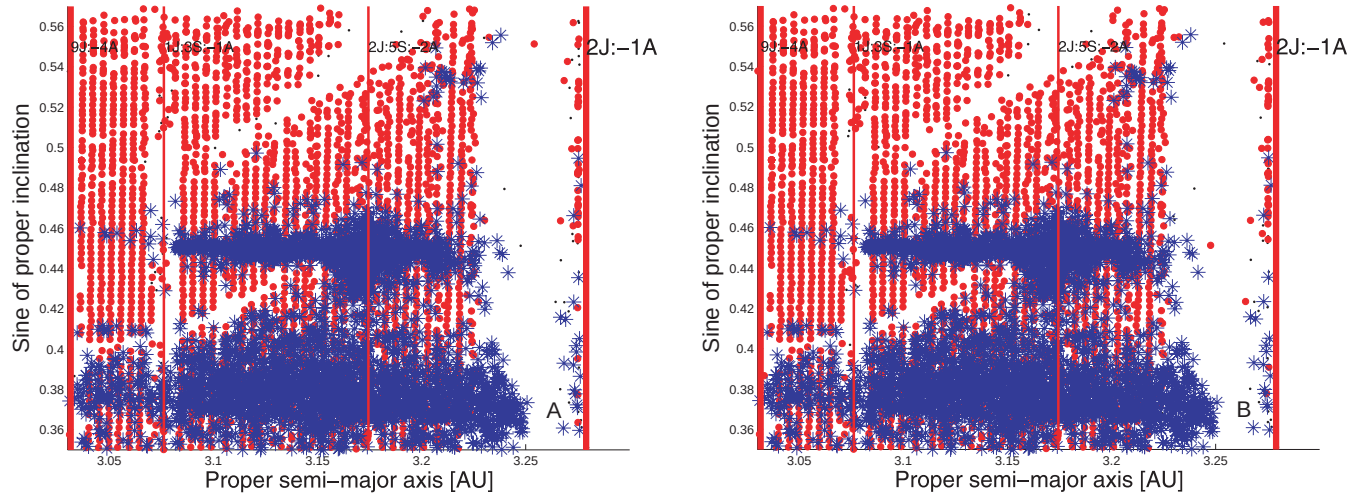

Figure 11. Maximum permanence times for particles in the test region for asteroids with an initial obliquity of $+90^\circ$ (panel A) and -90° (panel B). All symbols are the same as in Fig. 9.

low number of objects observed in these areas might therefore be a fossil indication of phenomena that occurred in the early phase of the formation of the Solar system.

8 CONCLUSIONS

(i) We have revised the knowledge of the synthetic proper elements of asteroids in the highly inclined region $\sin(i) > 0.3$. We have found 10 073 numbered objects from the AstDyS site between 2.0 and 3.4 au.

(ii) We have obtained synthetic proper-element maps for the two candidate regions and a test region with a high number density of asteroids. We have identified all the main two-, three- and four-body mean-motion and non-linear secular resonances in these areas.

(iii) We have verified the possibilities that dynamically stable regions can be explained as fluctuations of simple statistical one-dimensional distributions, such as Poissonian, uniform and Gaussian distributions. Our results show that, while asteroids in the Phocaea region might possibly follow a Poissonian distribution in inclinations, dynamically stable underpopulated regions cannot be explained as simple fluctuations of these statistical distributions. These must be caused either by disuniformities in the mechanism that populated the highly inclined regions or by some mechanism that depopulated the currently stable areas.

(iv) We verified the possibility that highly inclined asteroids might follow a tri-variate Gaussian probability distribution. Once again, we found that this is not likely. Multidimensional normality tests show that it is highly unlikely that highly inclined asteroids, as a whole, might follow a tri-variate normal distribution. Asteroids in the same range of semimajor axis in the Phocaea, Hansa and Pallas regions show a small but non-negligible probability of belonging to a tri-variate normal distribution. This could indicate that the mechanisms that populated the highly inclined regions might have acted 'vertically' from lower values of inclinations to higher, rather than 'horizontally' (i.e. moving asteroids originally at the same inclinations to different semimajor axes). The possible exception is very highly inclined objects with $\sin(i) > 0.45$. Further studies on such mechanisms are needed before this hypothesis can be confirmed.

(v) We have obtained density maps of the region and identified two areas that are characterized by low probabilities that the observed distributions of large asteroids might follow a Poissonian statistics. The first candidate area is in the central main belt (the Pallas region), while the second is in the outer main belt (the Euphrosyne region).

(vi) We have simulated the long-term dynamical evolution of test particles in these regions when the Yarkovsky force is considered. Despite the low number density of objects observed, the two areas with low number density were both mostly characterized by large permanence times, of the order of 100 Myr or more. These showed no significant qualitative differences from the highly populated test area.

Overall, our results show that the low number densities of asteroids in dynamically stable areas cannot be explained by simple fluctuations of Poissonian, uniform or Gaussian distributions. Some other mechanism has to be responsible for the observed non-uniformities. There are two hypotheses: (i) the current high-inclination population was created by a non-uniform mechanism; (ii) some as yet unknown dynamical effect depopulated the currently dynamically stable regions.

The first hypothesis could be coherent with what was observed by Ribeiro & Roig (2010) for the external main belt, where most of background objects seem to be associated with a family, suggesting that primordial bodies in the main belt are limited and scattered. The second hypothesis could justify the paucity of objects observed between the 5J:-2A and 9J:-4A mean-motion resonances, also noticeable in the main belt with a low inclination ($\sin(i) < 0.3$). However, there could be some difficulty explaining why the region of low asteroid density in the Pallas area is adjacent to a region of relatively high asteroidal populations at higher and lower inclinations. In any case, much more work is needed in order to understand the causes of the current 'Emmenthal structure' of the highly inclined asteroids.

ACKNOWLEDGMENTS

We thank the referee, Hagai Perets, for hints and suggestions that significantly improved the quality of this work. We are grateful to A. Morbidelli for discussions in which this work was conceived. We would like to thank the São Paulo State Science Foundation (FAPESP), which supported this work via the grant 06/50005-5, and the Brazilian National Research Council (CNPq, grants 302183/2008-6 and 473345/2009-9). We are also grateful to the Department of Mathematics of FEG-UNESP for allowing us to use their facilities.

REFERENCES

Brož M., 1999, Thesis, Charles Univ., Prague, Czech Republic
Carruba V., 2009a, MNRAS, 395, 358
Carruba V., 2009b, MNRAS, 398, 1512
Carruba V., 2010a, MNRAS, 403, 1834
Carruba V., 2010b, MNRAS, 408, 580
Carruba V., Michtchenko T., 2007, A&A, 475, 1145
Carruba V., Michtchenko T., 2009, A&A, 493, 267
Carruba V., Morbidelli A., 2011, MNRAS, 412, 2040
Carruba V., Burns J. A., Bottke W., Nesvorný D., 2003, Icarus, 162, 308
Carruba V., Machuca F., Gasparino H., 2011, MNRAS, 412, 2052
Cox D. R., Small N. J. H., 1978, Biometrika, 65, 263
Farinella P., Vokrouhlický D., Hartmann W. K., 1998, Icarus, 132, 378
Fasano G., Franceschini A., 1987, MNRAS, 225, 155
Gil-Hutton R., 2006, Icarus, 183, 93
Guillens S. A., Vieira Martins R., Gomes R. S., 2002, AJ, 124, 2322
Knežević Z., Milani A., 2003, A&A, 403, 1165
Levison H. F., Duncan M. J., 1994, Icarus, 108, 18
Mardia K. V., 1970, Biometrika, 57, 519
Michtchenko T. A., Lazzaro D., Carvano J. M., Ferraz-Mello S., 2010, MNRAS, 401, 2499
Milani A., Knežević Z., 1992, Icarus, 98, 211
Milani A., Knežević Z., 1994, Icarus, 107, 219
Morbidelli A., 2002, Modern Celestial Mechanics. Taylor and Francis, London
Press V. H., Teukolsky S. A., Vetterlink W. T., Flannery B. P., 2001, Numerical Recipes in Fortran 77. Cambridge Univ. Press, Cambridge
Ribeiro A. O., Roig F., 2010, in Fernandez J. A., Lazzaro D., Prialnik D., Schulz R., eds, Proc. IAU Symp. 263, Icy Bodies of the Solar System. Kluwer, Dordrecht, p. 237
Roig F., Nesvorný D., Ferraz-Mello S., 2002, MNRAS, 335, 417
Šidlichovský M., Nesvorný D., 1997, Celest. Mech. Dyn. Astron., 65, 137
Yoshikawa M., 1987, Celest. Mech., 40, 233

This paper has been typeset from a TEX/LATEX file prepared by the author.

11

Difusão caótica nas regiões das famílias de Pallas e Euphrosyne

Um dos mecânismos de mobilidade orbital no cinturão principal é devido aos encontros próximos de um corpo menor com alguns dos asteroides mais massivos. A mobilidade orbital causada por encontros próximos com (1) Ceres e (4) Vesta já foi objeto de estudo em trabalhos anteriores. Poucos trabalhos estudaram a difusão causada por encontros próximos com (2) Pallas, e nenhum estudo tinha sido efetuado, até 2013, para encontros próximos com (31) Euphrosyne. A variação em elementos próprios causada por encontros próximos depende da distância e velocidade mínima do encontro. Asteroides de alta inclinação tendem a ter encontros próximos de alta velocidade mútua. Acreditava-se portanto que o efeito a longo prazo de encontros com (2) Pallas sobre a variação de elementos próprios de membros da família de Pallas fosse pequeno. Em Carruba et al. (2013a) estudamos tais efeitos para asteroides nas regiões orbitais de (2) Pallas, (10) Hygiea, e (31) Euphrosyne. Encontrando baixos valores de coeficiente de espalhamento em a próprio por (2) Pallas, definido como o desvio padrão da distribuição de valores de mudanças em a, eliminando ruídos não causado pelos encontros próximo, confirmamos o cenário geralmente acreditado sobre o espalhamento causado por este asteroide. Surprendentemente, encontramos valores elevados de coeficientes de scattering causados por (10) Hygiea e (31) Euphrosyne, este último um asteroide de alta inclinação. Estimamos analiticamente que o número mínimo de encontros próximos necessário para obter uma distribuição de frequência de mudança em a compatível à um nível 3σ (ou 99.7%) com a verdadeira distribuição de

probabilidade seja da ordem de 6000 encontros. Trabalhos recentes sobre a evolução orbital da família de Hygiea confirmaram esta predição.

A seguir apresentamos o artigo, que foi publicado em Astronomy and Astrophysics em 2013, volume 550, article 85.

A&A 550, A85 (2013)
DOI: 10.1051/0004-6361/201220448

Astronomy & Astrophysics

Chaotic diffusion caused by close encounters with several massive asteroids

II. The regions of (10) Hygiea, (2) Pallas, and (31) Euphrosyne⋆

V. Carruba[1], M. Huaman[1], R. C. Domingos[2], and F. Roig[3]

[1] UNESP, Univ. Estadual Paulista, Grupo de dinâmica Orbital e Planetologia, Guaratinguetá, SP, 12516-410, Brazil
e-mail: vcarruba@feg.unesp.br
[2] INPE, Instituto Nacional de Pesquisas Espaciais, São José dos Campos, SP, 12227-010, Brazil
[3] ON, Observatório Nacional, Rio de Janeiro, RJ, 20921-400, Brazil

Received 26 September 2012 / Accepted 12 December 2012

ABSTRACT

Context. Close encounters with (1) Ceres and (4) Vesta, the two most massive bodies in the main belt, are known to be a mechanism of dynamical mobility able to significantly alter proper elements of minor bodies, and they are the main source of dynamical mobility for medium-sized and large asteroids ($D > 20$ km, approximately). Recently, it has been shown that drift rates caused by close encounters with massive asteroids may change significantly on timescales of 30 Myr when different models (i.e., different numbers of massive asteroids) are considered.

Aims. So far, not much attention has been given to the case of diffusion caused by the other most massive bodies in the main belt: (2) Pallas, (10) Hygiea, and (31) Euphrosyne, the third, fourth, and one of the most massive highly inclined asteroids in the main belt, respectively. Since (2) Pallas is a highly inclined object, relative velocities at encounter with other asteroids tend to be high and changes in proper elements are therefore relatively small. It was thus believed that the scattering effect caused by highly inclined objects in general should be small. Can diffusion by close encounters with these asteroids be a significant mechanism of long-term dynamical mobility?

Methods. By performing simulations with symplectic integrators, we studied the problem of scattering caused by close encounters with (2) Pallas, (10) Hygiea, and (31) Euphrosyne when only the massive asteroids (and the eight planets) are considered, and the other massive main belt asteroids and non-gravitational forces are also accounted for.

Results. By finding relatively small values of drift rates for (2) Pallas, we confirm that orbital scattering by this highly inclined object is indeed a minor effect. Unexpectedly, however, we obtained values of drift rates for changes in proper semi-major axis a caused by (10) Hygiea and (31) Euphrosyne larger than what was previously found for scattering by (4) Vesta. These high rates may have repercussions on the orbital evolution and age estimate of their respective families.

Key words. minor planets, asteroids: general – minor planets, asteroids: individual: (10) Hygiea – celestial mechanics – minor planets, asteroids: individual: (31) Euphrosyne – minor planets, asteroids: individual: (2) Pallas

1. Introduction

Orbital mobility caused by close encounters with massive asteroids has been studied in the past and could be a viable mechanism to produce the current orbital location of some of the V-type asteroids presently outside the Vesta family. It is well known, however, that the proper frequencies of precession of pericenter g and longitude of the node s of terrestrial planets change when one or more of the other planets is not considered in the integration scheme. For instance, the g_4 and s_4 frequencies of Mars are different when the full solar system is considered or when only Mars and the Jovian planets are accounted for. Carruba et al. (2012) showed that (4) Vesta proper frequencies are dependent on the number of other massive asteroids included in the integration scheme and that, as a result, the whole statistics of encounters with (4) Vesta is also affected.

Delisle & Laskar (2012) showed that dynamical mobility caused by close encounters with massive asteroids is dominated by encounters with (4) Vesta and (1) Ceres, with the other massive asteroid playing a lesser role. Previous studies on this subject (Carruba et al. 2003, 2007) also focused on the dynamical mobility caused by the two largest bodies. Can the third, fourth, or other most massive bodies have also played a role in the dynamical mobility of minor bodies, at least in their orbital proximities? And if that is possible, how much is the drift rate in semi-major axis affected by the choice of the model used to simulate the long-term effect of close encounters with massive asteroids, as observed in the region of (4) Vesta (Carruba et al. 2012)?

In this work we will focus on the dynamical mobility caused by close encounters with the third ((2) Pallas) and the fourth ((10) Hygiea) asteroid in the main belt, with attention on the scattering effect on members of their respective families. Since one of the goals of this investigation is to study the long-term effect of close encounters with highly inclined massive asteroids, we also considered the case of (31) Euphrosyne. Previous studies (Baer et al. 2011) have indicated that this body was the fifth-largest in the main belt. New estimates (Carry 2012) have considerably reduced its mass, but it remains one of

⋆ Appendix A is available in electronic form at
http://www.aanda.org

the most massive bodies that are part of a significantly large asteroid family (Machuca & Carruba 2011). Since the population of large asteroids is somewhat limited in the orbital proximity of (2) Pallas, we studied the long-term orbital diffusion caused by close encounters with this body also to better assess how relevant this effect is for highly inclined asteroids. In particular, if we consider the frequency distribution function of relative velocities at close encounters for highly inclined asteroids, does there exist a significant statistical tail for which relative velocities are small enough that large changes in proper semi-major axis a can be observed?

This work is structured as follows: in Sect. 2 we study the orbital neighborhood of (2) Pallas, (10) Hygiea, and (31) Euphrosyne by obtaining dynamical maps. Section 3 is dedicated to estimating the changes in the proper frequencies of these massive asteroids observed when different integration schemes are considered. In Sect. 4 we obtain the statistics of changes in proper semi-major axis caused by close encounters only when different models of the main belt are considered. In Sect. 5 we discuss the statistical completeness of the frequency distribution functions that we obtained in Sect. 4. In Sect. 6 we also include in our models non-gravitational forces such as the Yarkovsky and YORP effects. Finally, in Sect. 7 we present our conclusions.

2. Dynamical maps

We start our analysis by studying the orbital regions where the massive asteroids of interest are currently located in the main belt. With a mass of 8.63×10^{19} kg, (10) Hygiea is the fourth most massive body in the main belt. According to Milani & Knežević (1994), (10) Hygiea and its family reside in a fairly stable area of the outer main belt, between the 9J:-4A and the 2J:-1A mean-motion resonances in semi-major axis. The most notable secular resonance in the area is the $z_1 = g - g_6 + s - s_6$, that, computed for the values of proper a, e, and i of (10) Hygiea, crosses a region just above the typical inclination values of Hygiea family members.

To confirm this scenario, we obtained a dynamical map of synthetic proper elements, computed with the approach of Knežević & Milani (2003), Carruba (2010), for the region of (10) Hygiea. We took 6464 particles between 2.950 and 3.265 AU in semi-major axis, 0° and 10° and in i, with a step-size of 0.005 AU in a and 0.1° in i. All the other elements of the test particles were those of (10) Hygiea at the osculating date of J2000. Our results are shown in Fig. 1, where the test particles appear as black dots. Mean-motion resonances will appear in this map as vertical strips with lower densities of test particles, while secular resonances appear as elongated diagonal alignments of bodies (the names of secular resonances in the region are shown in red). Regular regions show a uniform population of test particles. The position of (10) Hygiea itself is shown as a magenta full dot. We also show in the figure the orbital position of all real asteroids with absolute magnitudes $H < 13.5$ in the same $a - i$ range of our test particles as blue asterisks[1]. As in Carruba et al. (2012), we choose only the largest bodies because asteroids with diameters larger than ≃20 km are the ones for which close encounters are the dominant mechanism of dynamical mobility on

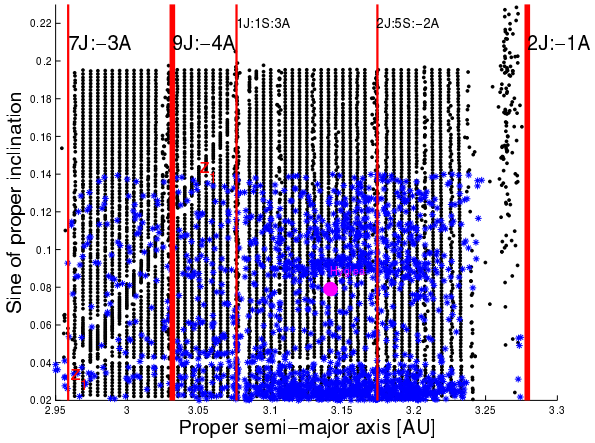

Fig. 1. Dynamical map of 6464 test particles in the region of the Hygiea family (black dots). We note the presence of the z_1 secular resonance, which appears as an elongated diagonal strip of aligned test particles, near the Koronis family. Real asteroids in the region with $H < 13.5$ are shown as blue asterisks, the orbital position of (10) Hygiea itself appears as a magenta full dot.

timescales of 250 Myr, according to Delisle & Laskar (2011; see also a discussion in Carruba et al. 2003). Using the relationship

$$D(\mathrm{km}) = 1329 \frac{10^{(-H/5)}}{\sqrt{p_V}}, \quad (1)$$

where p_V is the geometric albedo, equal approximately to 0.05 for typical C-type objects and 0.1 for typical S-type objects (Bowell et al. 1989), we find that $H = 13.5$ corresponds to diameters of approximately 11.86 km for C-type objects and 8.39 km for S-type objects, respectively. These diameters are still in the regime where orbital mobility caused by close encounters is not negligible when compared with the mobility caused by the Yarkovsky effect.

To avoid including Koronis family members we only selected $\sin(i) < 0.14$ asteroids for the Hygiea region. The Hygiea family lies in a fairly regular region, at about 0.1 in $\sin(i)$. We then considered the region of (2) Pallas. We took 5000 particles between 2.7 and 2.85 AU in semi-major axis, 25° and 48° in i, with a step-size of 0.0025 AU in a and 0.2° in i. All the other elements of the test particles were those of (2) Pallas at J2000. Our results are shown in Fig. 2, where the test particles appear as black dots. The position of (2) Pallas itself is shown as a magenta full dot. We also show in the figure the orbital position of all real asteroids with absolute magnitudes $H < 13.5$ in the same $a - i$ range of our test particles.

Finally, we investigate the case of (31) Euphrosyne. We took 4500 particles between 3.02 and 3.32 AU in semi-major axis, 20° and 35° in i, with a step-size of 0.005 AU in a and 0.2° in i. All the other elements of the test particles were those of (31) Euphrosyne at J2000. Our results are shown in Fig. 3, where the test particles appear as black dots. The position of (31) Euphrosyne itself is shown as a magenta full dot. All real asteroids with absolute magnitudes $H < 13.5$ in the same $a - i$ range of our test particles are also shown in the figure.

Euphrosyne lies above the more highly populated region of the Alauda family and is crossed by a rich web of linear and non-linear secular resonances (see Machuca & Carruba 2011, for a more in-depth discussion of the local dynamics and family determination). Now that we have studied the problem of local dynamics, we may start quantifying the indirect effect that the presence of other asteroids may have on the drift

[1] The dynamical map was computed using the orbital elements of (10) Hygiea at J2000. The location of secular resonances may vary when computed for the orbits of other asteroids. See also Carruba & Morbidelli (2011).

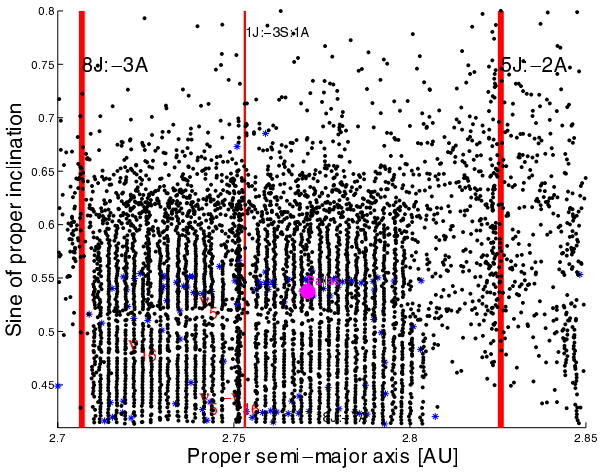

Fig. 2. Dynamical map of 5000 test particles in the region of the Pallas family (black dots). The orbital location of (2) Pallas is shown as a magenta dot, the other symbols are the same as in Fig. 1.

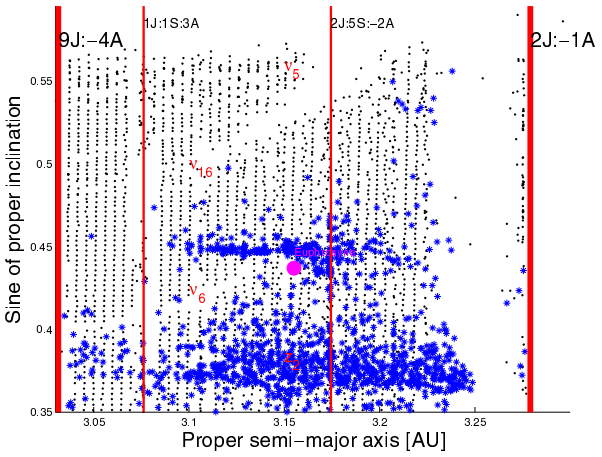

Fig. 3. Dynamical map of 4500 test particles in the region of the Euphrosyne family (black dots).

rates caused by close encounters with (2) Pallas, (10) Hygiea, and (31) Euphrosyne. This is the subject of the next section.

3. The indirect effect of other massive asteroids: choosing the right model

To investigate for possible indirect effects caused by the presence of other massive asteroids in the model, we obtained the values of the proper frequencies of pericenter and longitude of the node precession g and s for (2) Pallas, (10) Hygiea, and (31) Euphrosyne for simulations involving progressively all 39 main belt asteroids more massive than 8.5×10^{18} kg in the Carry (2012) paper[2]. The proper frequencies were computed with the frequency modified Fourier transform method of Laskar (1988, 1990, 1993), using an algorithm also described in Šidlichovský & Nesvorný (1997). A list of the first 39 most massive asteroids is given in Table A.1. For the mass of (4) Vesta, we used the value obtained from the DAWN mission (Russel et al. 2012). Following the approach of Carruba et al. (2012), we integrated our asteroids as massive bodies over 30 Myr with SWIFT-SKEEL, the symplectic integrator using the Wisdom and Holman mapping (Wisdom & Holman 1991; Levison & Duncan 2000). Results for the g frequency (for simplicity we do not show the s data) are shown in Fig. 4, panels A, C, and E. For each of the 39 simulations with massive asteroids, we computed the values of the g and s frequencies over four time intervals of 8.192 Myr using the approach of Knežević & Milani (2003). We took the mean of the four values as an estimate of the proper frequencies and the standard deviation as an estimate of the error. Vertical black lines display the error associated with each frequency value, the blue horizontal line shows the mean value of g for all the 39 simulations, and the horizontal red lines display the values of frequencies between the mean value minus and plus the standard deviation of the data (we refer to this interval as the "confidence level"). Panels B, D, and F of Fig. 4 display the number of close encounters among massive asteroids as a function of the number of massive asteroids included in the model.

For the case of (10) Hygiea, the number of close encounters experienced by this asteroid during the simulation was somewhat limited when compared with results observed for (4) Vesta (Carruba et al. 2012). The models for which this number was the highest correspond to values of g frequencies beyond a 3σ level, but not to the highest (or lowest) peaks (models with 12 and 14 asteroids, for instance). Mechanisms other than close encounters with massive asteroids, possibly such as secular perturbation of the precession frequency of (10) Hygiea by other massive asteroids, should be at play to explain the different values of secular frequencies in these cases. The first model for which the frequency was close to the mean value occurred for six asteroids, while the first peak in the g frequency for models with more than four asteroids was observed for nine asteroids.

In the (2) Pallas case, while the number of close encounters was higher than in the (10) Hygiea one, we still do not see a clear correspondence between the models with the largest number of close encounters and the peaks in the g distribution. The largest peaks (models S16 and S28) are not associated with close-encounter events. The first model with more than four asteroids for which the frequency was close to the mean value was the S6, while the first peak in the g frequency was observed in the S9.

Finally, (31) Euphrosyne, more than (10) Hygiea and (2) Pallas, experienced only a very limited number of close encounters with massive asteroids. The first model for which the frequency was close to the mean value occurred for seven asteroids, while the first peak in the g frequency for models with more than five asteroids (the four most massive plus (31) Euphrosyne) were observed for six asteroids.

Table 1 summarizes our results for the three massive asteroids that we investigated. The second column shows the model for which the asteroid g frequency was closer to the mean value, and the third column the model for which the first peak beyond a 3σ level was observed. We will use these models in Sect. 4 to investigate the long-term behavior of chaotic diffusion caused by close encounters with these massive asteroids.

4. Chaotic diffusion caused by close encounters

To obtain the statistics of changes in proper a caused by close encounters with the three considered massive asteroids, we used

[2] The first simulation for obtaining Pallas frequencies had the eight planets plus (2) Pallas (S1 model), the second also included (1) Ceres (S2 model), the third included all of the above plus (4) Vesta (S3 model), and so on.

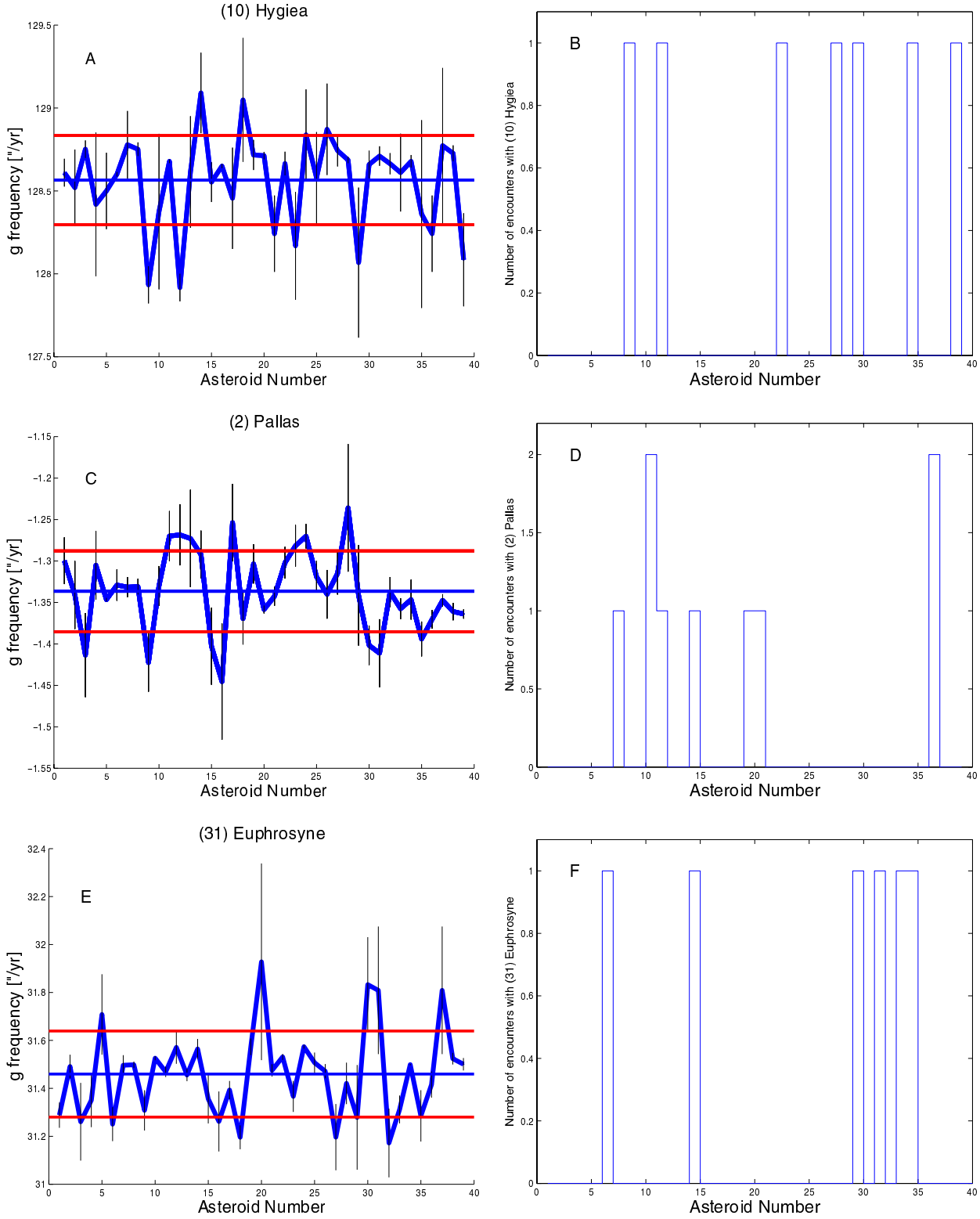

Fig. 4. Panels **A)**, **C)**, **E)** dependence of the precession frequency of the Hygiea, Pallas, and Euphrosyne pericenter g on the number of other massive asteroids included in the simulation. Asteroids are given in the order of Table A.1. Panels **B)**, **D)**, **F)** number of close encounters among massive asteroids as a function of the number of asteroids in the model.

the SWIFT-SKEEL code of the SyMBA package of Levison & Duncan (2000). We integrated our asteroids over 30 Myr and used the S0 simulation to estimate the noise in the change in proper a caused by secular effects with the method described in Delisle & Laskar (2012). Since the Bienaymé formula states that the variance of the sum (or the difference) of uncorrelated random variables is the sum of their variances, the variance in jump sizes obtained from a numerical simulation with massive

Table 1. Integration schemes for which the asteroid g frequency was closer to the mean value (second column) and for which the first peak beyond a 3σ level was observed.

Asteroid	First mean value	First peak in g
(10) Hygiea	S6	S9
(2) Pallas	S6	S9
(31) Euphrosyne	S7	S6

asteroids will be the sum of the variance of the real diffusion and the variance of the noise. Therefore, the real diffusion resulting from close encounters will be given by

$$\overline{\sigma}^2_a[1] = \sigma^2_a[1] - \sigma^2_{\rm noise}[1]. \quad (2)$$

We used the results of the S0 simulation to estimate the value of the variance caused by the noise. As in Carruba et al. (2012), we found a value of the standard deviation, the square root of the variance, equal to $\sigma_{\rm noise} \simeq 2 \times 10^{-4}$ AU. Since the stronger changes in proper a (identified as Δa hereafter) are those that i) are more significant for the dynamical mobility caused by close encounters with massive asteroids (Carruba et al. 2003); and ii) are those that are less likely to be caused by secular effects, we concentrated our attention on the values of $\Delta a > 3\sigma_{\rm noise} = 6 \times 10^{-4}$ AU.

We also computed the skewness, kurtosis higher moments of the distributions of changes in proper a, and the The Hurst exponent T of the changes in $\overline{\sigma}_a[1]$. The skewness gives a measure of the asymmetry of the probability distribution of a real-value random variable, while the kurtosis is any measure of the "peakedness" of the probability distribution of a real-value random variable (see Carruba et al. 2012, for a more in-depth description of these parameters). We assumed that the Hurst exponent could be fitted by a power law of the time of the form

$$\overline{\sigma}_a[1](t) = Ct^{\rm T}, \quad (3)$$

where C is a constant. The Hurst exponent gives a measure of how much the diffusion process differs from a random walk. It is equal to 0.5 for random walk-like processes, and is between 0.5 and 1.0 for correlated and persistent processes. Previous values of T for diffusion caused by close encounters with (1) Ceres for members of the Adeona and Gefion families were of the order of 0.58–0.72 (Carruba et al. 2003). Here we compute this exponent using Eq. (3) to best fit T using three values of $\overline{\sigma}_a[1](t)$ computed at each 10 Myr. For each of our simulations, we therefore computed the following parameters: the total number of encounters, the number of encounters for which Δa was larger than $3\sigma_{\rm noise}$, the reduced standard deviation $\overline{\sigma}_a[1]$ without the "noise" of the simulation, obtained from Eq. (2), the skewness, kurtosis, and Hurst exponent. We start our analysis by investigating the Hygiea region.

4.1. (10) Hygiea

For the region of (10) Hygiea, we simulated the 2914 real $H < 13.5$ asteroids under the influence of all planets plus (10) Hygiea with a time-step of two days (see Carruba et al. 2012, for a discussion on the choice of this parameter), and we monitored during the simulation if the distance from this asteroid was less than 0.001 AU (see discussion in Carruba et al. 2012, for the choice of this parameter). We used five integration schemes: S0, S1, S4, and the ones whose proper frequencies g and s differed most from the mean value (S6 and S9, respectively). As in Carruba et al. (2012), we found that the same asteroids did not experience close encounters in different integration schemes (for instance, asteroids that experienced large changes in a in one integration scheme may not have experienced close encounters at all in another) and that there were fluctuations in the statistics of Δa as well.

Table 2 summarizes our results. Histograms of frequencies of changes of proper a ($N_i/N_{\rm tot}$, where N_i is the number of encounters in the ith bin and $N_{\rm tot}$ is the total number of encounters) for the four integration schemes used are also shown in Fig. 5, panel A. Unexpectedly, we found large values of $\overline{\sigma}_a[1]$ caused by encounters with (10) Hygiea: the mean value of 90.8×10^{-5} AU is even larger than the corresponding mean value of $\overline{\sigma}_a[1] = (78.6 \pm 15.6) \times 10^{-5}$ AU caused by encounters with (1) Ceres, the main perturber in the main belt, in the (4) Vesta region as found in Carruba et al. (2012). We also found that 12.4% of the encounters satisfied our criterion for relevance of causing a change in Δa larger than $3\sigma = 6 \times 10^{-4}$ AU. This is by far the largest percent fraction found in our simulations so far. The unexpected high rate of drift in proper a caused by encounters with (10) Hygiea, unknown in previous works in the literature, may have played a yet to be investigated significant role in the evolution of the Hygiea family.

4.2. (2) Pallas

For the region of (2) Pallas, we simulated the 300 real $H < 13.5$ asteroids under the influence of all planets plus (2) Pallas, using the same integration schemes as discussed in Sect. 4.1. The limited number of known objects in the Pallas region is caused by the fact that this is a highly inclined region well above the ν_6 and ν_5 secular resonances (see Carruba & Machuca 2011, for a more in-depth discussion on the highly inclined asteroid population in stable and unstable areas). We used the standard S1 and S4 integration schemes, plus the S6 and S9 schemes associated with the first mean value and the first peak in the g frequency of (2) Pallas discussed in Sect. 3. Results for the Δa statistics caused by close encounters with (2) Pallas are summarized in Table 2. A histogram of frequency of Δa values is shown in Fig. 5, panel B.

Contrary to what was found for (10) Hygiea, we found the rather low value of mean $\overline{\sigma}_a[1]$ (20.8×10^{-5} AU), just a factor two higher than what was found for encounters with (2) Pallas in the Vesta region in Carruba et al. (2012). Only a very limited number of close encounters satisfied our criterion for relevance of causing a change in Δa larger than 3σ (at most, just three for the S9 simulation). The very low value of drift in proper a caused by encounters with (2) Pallas seems to confirm the hypothesis of Bottke et al. (1994) that encounters with this highly inclined asteroid occur mostly at high relative speed and distances and therefore cause limited changes in proper elements. To further investigate this hypothesis, we consider the case of (31) Euphrosyne in the next sub-section.

4.3. (31) Euphrosyne

For the region of (31) Euphrosyne, we simulated the 2138 $H < 13.5$ asteroid under the influence of all planets plus (31) Euphrosyne, using the integration schemes listed in Table 2. Results are also given in Table 2, with a histogram of frequency of Δa values shown in Fig. 5, panel C.

Table 2. Numbers of encounters, numbers of encounters with $|\mathrm{d}a| > 3\sigma_{\mathrm{noise}}$, and moments (in AU) of the distribution of changes in proper a caused by (10) Hygiea, (2) Pallas, and (31) Euphrosyne in the S1, S4, first mean value, and first peak integrations.

Asteroid	Simulation	Number of encounters	$N(\|\mathrm{d}a\| > 3\sigma_{\mathrm{noise}})$	$\overline{\sigma}_a[1] \times 10^5$	γ_1	γ_2	T
(10) Hygiea	S1	4484	558	71.2	2.4	36.1	0.48
(10) Hygiea	S4	4348	551	109.8	10.2	246.1	0.94
(10) Hygiea	S6	4410	543	107.3	–9.3	463.1	0.52
(10) Hygiea	S9	4422	543	74.8	–1.6	108.8	0.71
(10) Hygiea	All	(4416 ± 56)	(548 ± 7)	(90.8 ± 20.6)	(0.4 ± 8.1)	(213.5 ± 187.8)	(0.66 ± 0.21)
(2) Pallas	S1	65	1	14.6	–2.3	11.0	0.50
(2) Pallas	S4	57	1	21.9	–2.4	10.3	0.61
(2) Pallas	S6	69	2	24.2	–4.8	30.5	0.56
(2) Pallas	S9	60	3	22.5	–3.4	12.3	0.63
(2) Pallas	All	(62 ± 5)	(2 ± 1)	(20.8 ± 4.2)	(−3.2 ± 1.1)	(16.0 ± 9.7)	(0.57 ± 0.05)
(31) Euphrosyne	S1	459	92	61.7	3.7	36.3	0.50
(31) Euphrosyne	S5	606	138	92.5	2.9	20.4	0.54
(31) Euphrosyne	S6	474	113	71.8	–1.2	12.7	0.86
(31) Euphrosyne	S7	434	82	65.5	–10.0	12.8	0.60
(31) Euphrosyne	All	(493 ± 77)	(106 ± 24)	(72.9 ± 13.7)	(−1.2 ± 6.3)	(20.6 ± 11.1)	(0.63 ± 0.16)

Quite surprisingly, considering the results for (2) Pallas, we found a rather high value of mean $\overline{\sigma}_a[1]$ (72.9×10^{-5} AU), which is higher than the mean value for (4) Vesta in Carruba et al. (2012), but lower than the mean value for (1) Ceres in the same article. This unexpected result shows that there is no simple correlation between high inclination and drift rates by close encounters in proper a and that values of drift rates need to be investigated with a case-by-case approach.

5. Completeness of the frequency distribution functions

In the previous section, we obtained several distributions of changes in proper a (frequency distribution functions hereafter) for different massive asteroids and integration schemes. As discussed in Sect. 4, we do observe fluctuations in the numbers of encounters and in the moments of the distributions. A question that may now arise is how far from obtaining a statistically complete sample our results are. Are our frequency distribution functions (or *fdf*) of Δa values a good approximation of the real probability distribution function (*pdf* hereafter), or is a larger sample of close encounters needed to obtain a more complete statistics? And if a larger sample is needed, what could be the minimum number of close encounters needed to obtain a good approximation of the *pdf* at, for example, a 3σ level[3].

To test how complete our frequency distribution functions are in the interval of Δa changes that we are more interested in ($0.0006 < |\Delta a| < 0.006$ AU, i.e., between $3\sigma_{\mathrm{noise}}$ values in proper a and ten times this value), we performed Kolmogorod-Smirnoff probability tests (KS tests hereafter) for each of the observed distributions at confidence levels of 1σ, 2σ, and 3σ, with probabilities for the distributions to be compatible of 68.27%, 95.34%, and 99.73%, respectively. Figure 5 shows histograms of frequency of changes in proper a caused by (10) Hygiea (panel A), (2) Pallas (panel B), and (31) Euphrosyne (panel C) in the various integration schemes that we used in this work. None of the obtained distributions was compatible at a 3σ level. However, we found that all Hygiea distributions were compatible at a 2σ level in this $|\Delta a|$ interval, all Euphrosyne distributions were compatible at 1σ level (but only the S1 and S5, and the S6 and the S7 were compatible at a 2σ level), and only the S1 and S6 Pallas distributions were compatible at a 1σ level. We believe that our results show that we are obtaining a good approximation of the probability distribution function for (10) Hygiea, a decent one for (31) Euphrosyne, and a poor one for (2) Pallas. In our opinion, improving the completeness of our *fdf*s, possibly to a 3σ level, remain a challenge for future works[4]. But, before doing so, we could question what the minimum number of close encounters needed to obtain a more complete statistics could be.

To try answering this question, we turn our attention to the work of Greenberg (1982). In that work, the author computed the change of heliocentric velocity, ΔU_0, caused by a close encounter with a massive body as a function of distance at closest approach r_{min} and relative velocity with respect to the massive asteroid V. In Greenberg's model[5] the sine of the angle χ at which the asteroid orbit will be deflected due to the close encounter is given by

$$\sin\chi = \left[1 + \left(\frac{r_{\mathrm{min}} \cdot V^2}{G(M+m)}\right)^2\right]^{-\frac{1}{2}}, \tag{4}$$

where G is the gravitational constant, M the mass of the massive body, and m the (assumed negligible) mass of the incoming asteroid. The change in heliocentric velocity ΔU_0 is then given by

$$\Delta U_0 = \left(\frac{M}{M+m}\right) V \left[\sin 2\chi \boldsymbol{d} + (\cos 2\chi - 1)\boldsymbol{V}\right], \tag{5}$$

where $\boldsymbol{d}$ is the unit vector pointing in the direction of r_{min} and $\boldsymbol{V}$ is the unit vector pointing in the direction of V. Figure 6 shows a contour plot of changes in heliocentric velocities as a function of r_{min} and V for (10) Hygiea (for brevity we do not show analogous plots for (2) Pallas and (31) Euphrosyne). The encounters

[3] By σ we mean here the standard deviation of the normal or Gaussian distribution. A 3σ level means that there is a 99.73% probability that the two distributions were compatible.

[4] In the case of (2) Pallas, one may question the merit of improving our knowledge of the details of an effect that is quite certainly fairly small.

[5] This model is based on a "patching conics" approach, where the encounter is treated as a hyperbolic flyby of the massive body. Such a model would not be able to account for other massive body perturbations, resonant encounters, etc. Since our goal here is to obtain a first-order approximation of the number of encounters needed to obtain a decent fit of the *pdf*, we believe that our approach is justified.

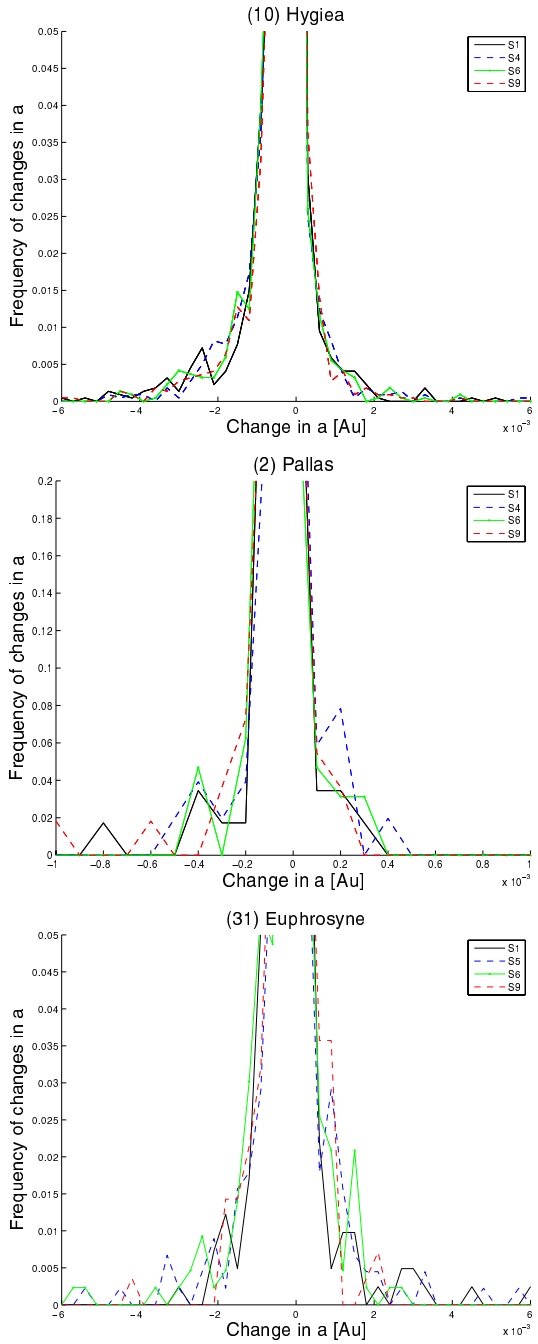

Fig. 5. Histograms of frequency of changes in proper a caused by (10) Hygiea (panel A), (2) Pallas (panel B) and (31) Euphrosyne (panel C) in the integration schemes listed in Table 1.

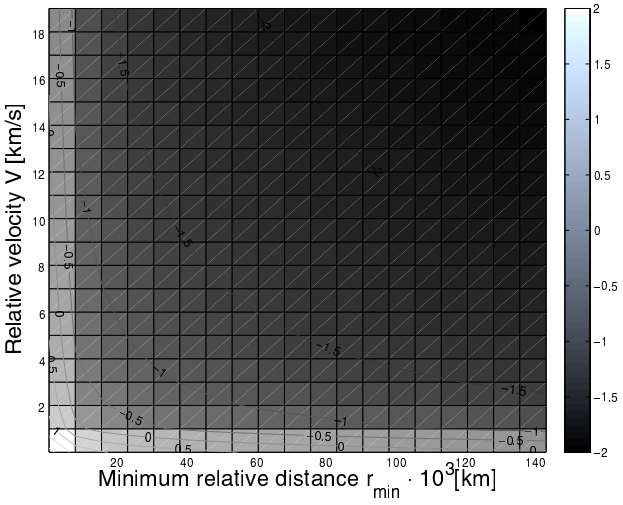

Fig. 6. Contour plot of the $\log_{10}$ of changes in heliocentric velocities ΔU_0 as a function of $r_{\rm min}$ and V for (10) Hygiea according to Eq. (5).

at low relative velocities and low minimum distances cause the maximum change in heliocentric velocities, and, as discussed in Carruba et al. (2007), the maximum change in heliocentric velocity is of the order of the escape velocity from the massive body (of the order of 200 m/s for bodies of the masses and sizes of (2) Pallas, (4) Vesta, and (10) Hygiea).

Since here we are interested in determining the minimum number of close encounters needed to obtain a fairly complete *fdf* in proper a, we used the Gauss equation

$$\frac{\Delta a}{a} = \frac{2}{na(1-e^2)^{1/2}}\left[(1+e\cos f)\Delta V_T + (e\sin f)\Delta V_R\right], \quad (6)$$

where ΔV_T, ΔV_R, (and ΔV_W) are the tangential, radial, and perpendicular to the orbital plane components of the change in heliocentric velocity ΔU_0, n is the minor body mean-motion, a and e its semi-major axis and eccentricity, and f is the true anomaly at the instant of close encounter. With the simplistic assumptions that the eccentricity of the minor body is zero and that all the change in velocity goes into the tangential component (this last hypothesis may introduce an error of a factor $\sqrt{3}$), Eq. (6) reduces to

$$\Delta a = \frac{2}{n}\Delta U_0. \quad (7)$$

We can then use Greenberg's model to compute maximum changes in proper a for different values of $r_{\rm min}$ and V. Figure 7 shows frequency of Δa values computed with Eqs. (7) and (5) for different, equally spaced, numbers of close encounters with (10) Hygiea at different and equally spaced values of $r_{\rm min}$ and V (results are similar for (2) Pallas and (31) Euphrosyne). The values of $r_{\rm min}$ and V used in Eq. (5) are in the same range of those shown in Fig. 6. Standard KS tests show that the distributions start to be compatible for ≃3000 equally spaced encounters (we tested distributions for up to 6 million encounters with similar results), which sets a lower limit on the minimum number of close encounters that needs to be tested to obtain a fairly complete *fdf* and that seems to be in agreement with what we found numerically for the simulations with (10) Hygiea. As a further numerical test, we also computed the standard deviation of changes in a obtained with Greenberg's model for 600, 1500, 3000, and 60 000 close encounters. Since this approach only gives absolute values of changes in a, the standard deviation of Δa does not correspond to drift rates, so we computed the variance of the distributions, rescaled to a mean equal to zero, using this formula

$$\sigma_a^2 = \frac{1}{N}\sum_{i=1}^{N}\left((\Delta a - 0)^2\right) = \frac{1}{N}\sum_{i=1}^{N}\left(|\Delta a|^2\right), \quad (8)$$

where N is the number of close encounters. Here we assumed that the mean value of the distributions of changes in a was 0, which seems to be confirmed by our results of Sect. 4, where the mean values were all less than 10^{-6} AU, i.e., less than the numerical error on Δa. Drift rate values will be equal to the square root

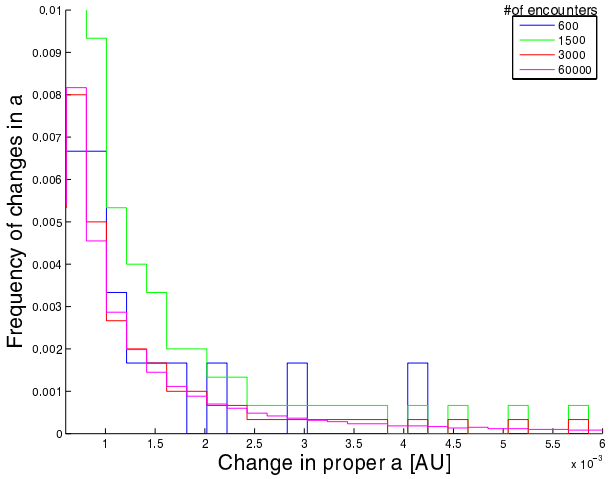

Fig. 7. Histogram of Δa changes computed using Greenberg (1982) model for different numbers of close encounters with (10) Hygiea.

of the rescaled variance given by Eq. (8). To more easily compare these results with those of Sect. 4, we also multiplied them by 10^5. We obtained values of drift rates of 230.7, 180.1, 127.4, and 102.6×10^5 AU for the four distributions, with the last two values in the range of what was found in Sect. 4 for the actual simulations with symplectic integrators. KS tests for values of $\Delta a > 3\sigma_{\rm noise}$ show that the distributions for 3000 and 60 000 encounters are compatible between them, but not with those with 600 and 1500 encounters. Increasing the number of observed close encounters may, of course, improve the completeness of the *fdf*. Obtaining better fits for the *pdf* of (10) Hygiea and (31) Euphrosyne remains a challenge for future works.

6. Close encounters with massive asteroids when the Yarkovsky and YORP effects are considered

In the previous sections, we analyzed the orbital diffusion caused by close encounters with massive asteroids when non-gravitational forces such as the Yarkovsky and YORP effects are not considered. Here we further investigate the subject when these effects are taken into account. For this purpose, we use the São Paulo (SP) integrator, which is able to simulate both close encounters with massive asteroids and the Yarkovsky effect. See Carruba et al. (2007) for a treatment of the integrator and of the Yarkovsky effect. Here we just point out that we used the Vokrouhlický model (Vokrouhlický 1999) for the diurnal and seasonal versions of the Yarkovsky effect, so that the drift rate in semi-major axis is given by

$$\frac{da}{dt} = k_1 \cos\epsilon + k_2 \sin^2\epsilon, \quad (9)$$

where k_1 and k_2 are functions depending on the surface thermal parameters and size, and ϵ is the spin axis obliquity (see Vokrouhlický 1999, for the exact expressions of the k_1 and k_2 functions). In this work, we integrated the same real asteroids with $H < 13.5$ in the regions of the Hygiea, Pallas, and Euphrosyne families considered in the previous sections over 30 Myr with two spin obliquities, $\epsilon = 0°$ and $\epsilon = 180°$, which maximizes the drift caused by the diurnal version of the Yarkovsky effect. Using Eq. (1), we computed the radius of each object using its absolute magnitude and a geometric albedo equal to 0.1, a value typical for B- and C-type objects, the most commonly found asteroids in the regions of (2) Pallas, (10) Hygiea, and (31) Euphrosyne. We used Yarkovsky parameters that are also typical for B- and C-type objects: a thermal conductivity $K = 0.001$ W/m/K (Delbo et al. 2007), a thermal capacity of 680 J/kg/K, a surface density of 1500 kg/m^3, a bulk density of 1500 kg/m^3, a Bond albedo of 0.1, and a thermal emissivity of 0.95 (see also Carruba et al. 2003, for a more in-depth discussion of these parameters).

Table 3. Number of encounters, $\overline{\sigma}_a[1] \times 10^5$, and Hurts exponents T for clones of real $H < 13.5$ asteroids.

Asteroid id.	Spin orientation	$N_{\rm enc}$	$\overline{\sigma}_a[1] \times 10^5$ [AU]	T
(10)	$\epsilon = 0°$	4880	(70.8 ± 16.3)	$(0.83^{+1.16}_{-0.83})$
(10)	$\epsilon = 180°$	4719	(81.8 ± 18.8)	$(0.81^{+0.84}_{-0.81})$
(10)	All	9599	(76.3 ± 17.5)	(0.82 ± 0.64)
(2)	$\epsilon = 0°$	71	(7.9 ± 1.6)	$(0.63^{+1.02}_{-0.63})$
(2)	$\epsilon = 180°$	66	(7.5 ± 1.5)	$(0.56^{+0.74}_{-0.56})$
(2)	All	137	(7.7 ± 1.5)	(0.60 ± 0.57)
(31)	$\epsilon = 0°$	508	(39.1 ± 7.3)	$(0.65^{+0.95}_{-0.65})$
(31)	$\epsilon = 180°$	507	(51.5 ± 9.7)	$(0.55^{+0.69}_{-0.55})$
(31)	All	1015	(45.3 ± 8.5)	(0.60 ± 0.53)

Following the approach of Delisle & Laskar (2012), we assumed that the obliquity remains constant during a YORP cycle, with maximal values of $\epsilon = 0°$ or $\epsilon = 180°$, which yields a maximum strength for the diurnal version of the Yarkovsky effect and a minimal strength for the seasonal one. We also assumed that re-orientations act almost instantaneously at the end of each YORP cycle, with an assumed timescale of 30 Myr for km-sized objects (Delisle & Laskar 2012). We integrated our real asteroids using our S1 and S0 integration schemes (the latter was used to estimate the values of $\sigma_{\rm noise}$, as discussed in the previous section), and we used the values of the standard deviations on the moments obtained in the previous section to estimate the possible errors associated with the particular integration scheme used in this work.

As in Sect. 4, we used the three values of $\overline{\sigma}_a[1](t)$ computed at each 10 Myr to determine the T value of the Hurst exponent. However, with respect to previous works, we also account for the uncertainty associated with changes in $\overline{\sigma}_a[1](t)$ between integrations with different schemes in the following manner: assuming that errors in $\overline{\sigma}_a[1](t)$ are of the order of the standard deviations found in Sect. 4 for (10) Hygiea, (2) Pallas, (31) Euphrosyne, i.e. 22.7%, 20.0%, and 18.8% of the mean value, respectively, we can estimate the value of T and its error using standard techniques of linear regression (see Press et al. 2001, Eqs. (15.2.4), (15.2.6), and (15.2.9)).

Table 3 shows values of number of encounters $N_{\rm enc}$, of $\overline{\sigma}_a[1] \times 10^5$ AU, and Hurts exponents T for (10) Hygiea, (2) Pallas, and (31) Euphrosyne for (i) the simulation with clones of real asteroids with initial zero obliquity; (ii) the simulation with clones of real asteroids with $\epsilon = 180°$; and iii) for all asteroid clones. For the sake of brevity, we do not report the other moments γ_1 and γ_2 listed in Table 2. Errors on $\overline{\sigma}_a[1] \times 10^5$ are assumed of the order of what was found in Sect. 4. Values of $\overline{\sigma}_a[1] \times 10^5$ for the simulations with the São Paulo integrator are in the same range (to within the errors) of what was found for the conservative case in Sect. 4 for (10) Hygiea, but somewhat smaller for (2) Pallas and (31) Euphrosyne. This fact may be caused by the limited number of close encounters that occurred during the simulations for these asteroids, which was

considerably lower than the completeness level of ≃3000 encounters found in Sect. 5 for the *fdf* to converge. Also, while the T values that best fitted our data are still compatible with scattering with massive asteroids being a persistent and correlated process, we unfortunately confirm that, as found in Carruba et al. (2012), the uncertainties are so large that no final conclusions can be positively achieved.

7. Conclusions

We studied the problem of orbital diffusion in semi-major axis of minor bodies for the case of encounters with (10) Hygiea, (2) Pallas, and (31) Euphrosyne. Our main results can be summarized as follows:

- We obtained the proper frequencies of precession of the argument of pericenter g and of longitude of the node s for the three massive asteroids when other massive asteroids (up to 38) are considered along with the eight planets. The values fluctuated beyond a 3σ confidence level for various integration schemes, such as the S9 and S6. Lower fluctuations were also observed when different numbers of massive asteroids were considered.
- We investigated the dynamical mobility caused by close encounters with massive asteroids for real asteroids in the orbital regions of (10) Hygiea, (2) Pallas, and (31) Euphrosyne with absolute magnitude $H < 13.5$. As in Carruba et al. (2012), we found that not only different asteroids experienced close encounters with the three massive bodies when different integration schemes were considered, but also that the whole statistics of close encounters fluctuated. Variances of the change in proper a massive asteroids varied up to 23% in the four integration schemes that we used. We confirm the hypothesis of Bottke et al. (1994) that encounters with highly inclined objects as (2) Pallas are indeed a minor effect because of rather high relative speed and distances at encounters between perturber and perturbee. Unexpectedly, we found a very large mean value of drift rate in proper a caused by close encounters with (10) Hygiea, $\overline{\sigma}_a[1] \times 10^5 = (90.8 \pm 20.6)$ AU, and (31) Euphrosyne, $\overline{\sigma}_a[1] \times 10^5 = (72.9 \pm 13.7)$ AU. These values are higher than the drift rate caused by (4) Vesta for its orbital region ($\overline{\sigma}_a[1] \times 10^5 = (29.5 \pm 10.7)$ AU), as found in Carruba et al. (2012), and may have repercussion on the orbital evolution of members of their respective families.
- We performed KS tests on the completeness of the *fdf* obtained for the three massive asteroids. The frequency distributions obtained with the different integration schemes are compatible among themselves to a 2σ level for (10) Hygiea, to a 1σ level for (31) Euphrosyne, and to lower levels for (2) Pallas. Considerations based on the model of Greenberg (1982) suggest that the minimum number of close encounters needed to obtain a good fit of the *pdf* are of the order of 3000, with expected uncertainties on the measured drift rates of the order of 10% for this number of encounters. Obtaining better fits of the *pdf* for (10) Hygiea and (31) Euphrosyne, possibly to a 3σ level, remains a challenge for future works.
- We studied the effect of close encounters with massive asteroids when the Yarkovsky and YORP effects were also considered and computed the value of the Hurst exponent T of the diffusion as a function of time, including the effect of the uncertainty caused by differences in the integration schemes as found in this work. Drift rate values and Hurst exponents for the Hygiea region are in the same range, to within the errors, as those found in the conservative integrations (for the Pallas and Euphrosyne areas, they are somewhat smaller, but this may be due to the limited number of close encounters that occurred during the simulations for asteroids in these regions), and Hurst exponents indicate scattering with massive asteroids being a persistent and correlated process ($0.5 < T < 1.0$, but values are affected by large uncertainties). This suggests that in order to obtain estimates of these parameters on the timescales used in this work (30 Myr), including the Yarkovsky and YORP effects may not be necessary.

In this work we investigated for the first time the long-term effect that close encounters with massive asteroids such (10) Hygiea, (2) Pallas, and (31) Euphrosyne may have had on the orbital evolution of asteroids in their orbital proximity. In particular, the unexpected high rate of drift in proper a caused by encounters with (10) Hygiea and (31) Euphrosyne, unknown in previous works in the literature, suggests that this diffusion mechanism may have played a significant role in the evolution of their respective families that is yet to be investigated. Also, the relative large value of drift rate found for (31) Euphrosyne shows that there is no simple correlation between the high inclination of the perturber and the drift rates caused by close encounters. According to our results, values of drift rates need therefore to be investigated with a case-by-case approach.

Acknowledgements. We are grateful to the anonymous referee of this paper for comments and suggestions that significantly improved the quality of our work. We also thank G. Valsecchi for discussions and hints that opened interesting new lines of research. This work was supported by the Brazilian National Research Council (CNPq), project 305453/2011-4, by the Foundation for Supporting Scientific Research in the São Paulo state (FAPESP), grant 11/19863-3, and by the Coordenation for Improvement of Higher Education Personnel (CAPES), grant 23038.007093/2012-13.

References

Baer, J., Chesley, S. R., & Matson, R. D. 2011, AJ, 141, 143
Bottke, W. F., Nolan, M. C., Greenberg, R., & Kolvoord, R. A. 1994, Icarus, 107, 255
Bowell, E., Hapke, B., Domingue, D., et al. 1989, in Asteroids II (Tucson: Univ. of Arizona), 524
Carruba, V. 2010, MNRAS, 408, 580
Carruba, V., & Machuca, J. F. 2011, MNRAS, 420, 1779
Carruba, V., & Michtchenko, T. A. 2007, A&A, 475, 1145
Carruba, V., & Morbidelli, A. 2011, MNRAS, 412, 2040
Carruba, V., Burns, J. A., Bottke, W., & Nesvorný, D. 2003, Icarus, 162, 308
Carruba, V., Roig, F., Michtchenko, T. A., Ferraz-Mello, S., & Nesvorný, D. 2007, A&A, 465, 315
Carruba, V., Huaman, M., Douwens, S., & Domingos, R. C. 2012, A&A, 543, A105
Carry, B. 2012, Planet. Space Sci., accepted [arXiv:1203.4336]
Delisle, J.-B., & Laskar, J. 2011, A&A, 540, A18
Knežević, Z., & Milani, A. 2003, A&A, 403, 1165
Greenberg, R. 1982. AJ, 87, 184
Laskar, J. 1988, A&A, 198, 341
Laskar, J. 1990, Icarus, 88, 266
Laskar, J. 1993, Phys. Rev. Lett. 70, 2975
Levison, H. F., & Duncan, M. J. 2000, AJ, 120, 2117
Milani, A., & Knežević, Z. 1994, Icarus, 107, 219
Machuca, J. F., & Carruba, V. 2011, MNRAS, 420, 1779
Press, V. H., Teukolsky, S. A., Vetterlink, W. T., & Flannery, B. P. 2001, Numerical Recipes in Fortran 77 (Cambridge: Cambridge Univ. Press)
Russell, C. T., Raymond, C. A., Coradini, A., et al. 2012, Science, 336, 684
Šidlichovský, M., & Nesvorný, D. 1997, Celest. Mech. Dyn. Astron., 65, 137

Appendix A: Asteroid astrometric masses

We report in Table A.1 the identification of each asteroid used in this work, its mass and mass uncertainty as in Carry (2012), and the percentile errors associated with each asteroid mass (see Carry 2012, for a discussion of the methods used to determine the asteroid masses, and their uncertainties).

Table A.1. Asteroid astrometric masses with their uncertainties.

Asteroid	Mass (in 10^{15} kg)	Mass uncertainty (in 10^{15} kg)	Percentile error
1 Ceres	944 000.	6000.	0.006
4 Vesta	259 000.	0.	0.000
2 Pallas	204 000.	4000.	0.020
10 Hygiea	86 300.	5200.	0.060
511 Davida	33 800.	10 200.	0.302
704 Interamnia	32 800.	4500.	0.137
15 Eunomia	31 400.	1800.	0.057
3 Juno	27 300.	2900.	0.106
16 Psyche	27 200.	7500.	0.276
536 Merapi	26 100.	4700.	0.180
52 Europa	23 800.	5800.	0.244
165 Loreley	19 100.	1900.	0.099
88 Thisbe	15 300.	3100.	0.203
87 Sylvia	14 800.	0.	0.000
420 Bertholda	14 800.	900.	0.061
6 Hebe	13 900.	1000.	0.072
65 Cybele	13 600.	3100.	0.228
212 Medea	13 200.	1000.	0.076
7 Iris	12 900.	2100.	0.163
29 Amphitrite	12 900.	2000.	0.155
690 Wratislavia	12 800.	300.	0.023
31 Euphrosyne	12 700.	6500.	0.512
57 Mnemosyne	12 600.	2400.	0.190
147 Protogeneia	12 300.	500.	0.041
675 Ludmilla	12 000.	2400.	0.200
409 Aspasia	11 800.	2300.	0.195
532 Herculina	11 500.	2800.	0.243
107 Camilla	11 200.	300.	0.027
451 Patientia	10 900.	5300.	0.486
200 Dynamene	10 700.	1600.	0.150
444 Gyptis	10 600.	2800.	0.264
324 Bamberga	10 300.	1000.	0.097
602 Marianna	10 200.	500.	0.049
895 Helio	9870.	6050.	0.613
154 Bertha	9190.	5200.	0.566
381 Myrrha	9180.	800.	0.087
8 Flora	9170.	1750.	0.191
13 Egeria	8820.	4250.	0.482
19 Fortuna	8600.	1460.	0.170

12

Um método multi-variado para a determinaçaõ de famílias de asteroides

Como último trabalho desta dissertação consideramos um artigo sobre um novo método para identificar famílias de asteroides em um espaço composto de elementos próprios, cores do Sloan Digital Sky Survey Moving Objects Catalog, version 4 (ou SDSS-MOC4), e albedo geométrica da missão WISE (Wide-field Infrared Space Explorer), que também foi aplicado à região de asteróides de alta inclinação, incluindo os asteróides do tipo Hungaria. Neste trabalho sugerimos procurar famílias neste espaço multi-variado, para limitar o número de possíveis "interlopers", ou seja, objetos membros da família dinâmica obtida no espaço dos elementos próprios, mas que por características taxonômica não são compatíveis com a composição dos demais membros. Mostramos que este novo método reduz o número de "interlopers" de até um fator dois com respeito à métodos anteriores, como a identificação de famílias nos espaços dos elementos próprios, dos elementos próprios e as cores do SDSS-MOC4, ou os elementos próprios e a albedo geométrica. Identificamos sessenta e duas famílias no cinturão principal e nas regiões dos asteroides Hungarias e Cybele. Nosso resultados foram publicados em MNRAS e estão disponíveis em VizieR, o repositório de dados astronômicos da Universidade de Estrasburgo, neste endereço:

http://vizier.cfa.harvard.edu/viz-bin/VizieR?-source=J/MNRAS/433/2075

A seguir apresentamos o artigo, que foi publicado em Monthly Notices of the Royal Astronomical Society em 2011, volume 433, pp. 2075-2096.

Monthly Notices
of the
ROYAL ASTRONOMICAL SOCIETY

MNRAS **433,** 2075–2096 (2013) doi:10.1093/mnras/stt884
Advance Access publication 2013 June 24

A multidomain approach to asteroid families' identification

V. Carruba,[1⋆] R. C. Domingos,[2] D. Nesvorný,[3] F. Roig,[4] M. E. Huaman[1] and D. Souami[5,6]

[1]*UNESP, Univ. Estadual Paulista, Grupo de dinâmica Orbital e Planetologia, Guaratinguetá, SP 12516-410, Brazil*
[2]*INPE, Instituto Nacional de Pesquisas Espaciais, São José dos Campos, SP 12227-010, Brazil*
[3]*SWRI, SouthWest Research Institute, 1050 Walnut Street, Suite 300, Boulder, CO 80302, USA*
[4]*Observatório Nacional (ON), Rua General José Cristino 77, Rio de Janeiro, RJ 20921-400, Brazil*
[5]*UPMC, Université Pierre et Marie Curie, 4 Place Jussieu, F-75005 Paris, France*
[6]*SYRTE, Observatoire de Paris, Systèmes de Référence Temps Espace, CNRS/UMR 8630, UPMC, F-75014 Paris, France*

Accepted 2013 May 15. Received 2013 May 14; in original form 2013 April 16

ABSTRACT

It has been shown that large families are not limited to what found by hierarchical clustering methods in the domain of proper elements (a, e, $\sin(i)$), which seems to be biased to find compact, relatively young clusters, but that there exists an extended population of objects with similar taxonomy and geometric albedo, which can extend to much larger regions in proper elements and frequencies domains: the family 'halo'. Numerical simulations can be used to provide estimates of the age of the family halo, which can then be compared with ages of the family obtained with other methods. Determining a good estimate of the possible orbital extension of a family halo is therefore quite important, if one is interested in determining its age and, possibly, the original ejection velocity field. Previous works have identified families' haloes by an analysis in proper elements domains, or by using Sloan Digital Sky Survey-Moving Object Catalog data, fourth release (SDSS-MOC4) multiband photometry to infer the asteroid taxonomy, or by a combination of the two methods. The limited number of asteroids for which geometric albedo was known until recently discouraged in the past the extensive use of this additional parameter, which is however of great importance in identifying an asteroid taxonomy. The new availability of geometric albedo data from the *Wide-field Infrared Survey Explorer* (*WISE*) mission for about 100 000 asteroids significantly increased the sample of objects for which such information, with some errors, is now known.

In this work, we proposed a new method to identify families' haloes in a multidomain space composed by proper elements, SDSS-MOC4 (a^*, $i - z$) colours, and *WISE* geometric albedo for the whole main belt (and the Hungaria and Cybele orbital regions). Assuming that most families were created by the breakup of an undifferentiated parent body, they are expected to be homogeneous in colours and albedo. The new method is quite effective in determining objects belonging to a family halo, with low percentages of likely interlopers, and results that are quite consistent in term of taxonomy and geometric albedo of the halo members.

Key words: Celestial mechanics – minor planets, asteroids: general.

1 INTRODUCTION

Asteroid families are groups of asteroids that are supposed to have a common origin in the collisional event that shattered the parent body. They are usually determined by identifying clusters of objects close in proper elements domain (a, e, $\sin(i)$). The hierarchical clustering method (HCM hereafter) as described by Bendjoya & Zappalà (2002) operates by identifying all objects that are closer than a given distance (cutoff) with respect to at least one other member of a family. If an object is closer than this distance, it is associated with the dynamical family, and the procedure is repeated until no new family members are found. The choice of this cutoff distance is then of paramount importance in determining the family. For small values of the cutoff, only the objects closest in proper element domain are identified as family members: the family 'core'. At

⋆ E-mail: vcarruba@feg.unesp.br

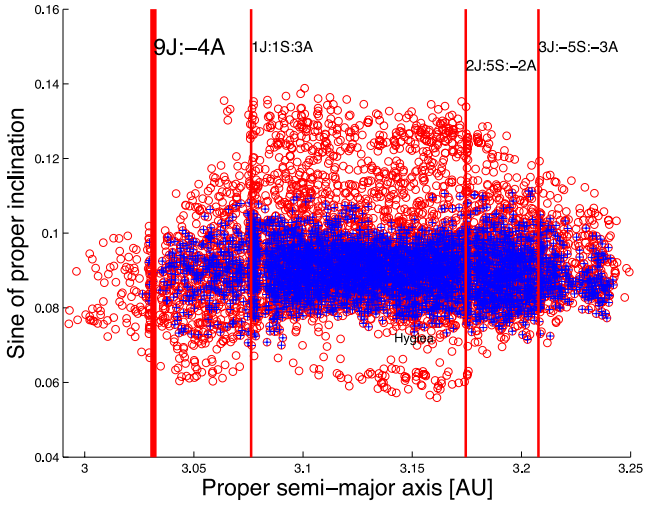

Figure 1. An (a, $\sin(i)$) projection of the Hygiea family core (blue crosses) and halo (red circles), as obtained in Carruba (2013). Vertical red lines display the location of the main mean-motion resonances in the region.

larger cutoff one is able to identify objects that, while still belonging to the collisional group, may have dynamically evolved since the family formation and drifted apart from the core: the family 'halo'.[1]

To illustrate this issue, Fig. 1 displays the family core (blue crosses) and halo (red circles), as obtained in Carruba (2013) for the Hygiea family, at cutoff of 66 and 76 m s^{-1}, respectively. At cutoffs larger than 76 m s^{-1} the family merged with other dynamical groups in the region (such as the Veritas and Themis family) and with the local background, thus it was no longer identifiable as a separate entity. Numerical simulations can be used to provide estimates of the age of the family halo, as done, for instance, by Brož & Morbidelli (2013) for the Eos halo, that can then be compared with ages of the family obtained with other methods. Determining a good estimate of the possible orbital extension of a family halo is therefore quite important, if one is interested in determining its age and, possibly, the original ejection velocity field.

One problem in obtaining a good determination of a family halo is however the presence of objects in the orbital region of the halo that might not be connected with the local family. Assuming that most families were created by a breakup of an undifferentiated parent body, we would expect that most of its members should be homogeneous in colours and albedo. Objects that belong to the dynamical families but that differ in colours or albedo may possibly be asteroids of the local background that just happened to lie in the orbital region of a given family: the interlopers. An analysis of spectral properties of local asteroids may provide insights on the possible presence of such interlopers in groups found in proper elements domains, but such information is usually available only for 2 per cent or less of the main belt asteroids. Yet including too many interlopers into the family may change the perceived orbital structure of the group and cause to obtain distorted estimates of its properties. Recently, the Sloan Digital Sky Survey-Moving Object Catalog data, fourth release (SDSS-MOC4 hereafter; Ivezić et al. 2002), provided multiband photometry on a sample two order of magnitude larger than any available in any current spectroscopic catalogues (about 60 000 numbered objects). While for the purpose of deriving very reliable inferences about asteroid surface compositions, multiband photometry is not as precise as spectroscopy. Nesvorný et al. (2005) showed that the SDSS-MOC is a useful data set to study general statistical variations of colours of main belt asteroids. These authors used an automatic algorithm of principal component analysis (PCA) to analyse SDSS photometric data and to sort the objects into different taxonomical classes. In particular, PCA can be used to derive linear combinations of the five SDSS colours (u, g, r, i, z), in order to maximize the separation between a number of different taxonomic classes in SDSS data. Two large separated complexes were found in the PCA first two components: the C/X complex and the S complex, with various subgroups identified inside the main complexes. A problem with this approach was however the large errors that affected colours in the ultraviolet band u, and that propagated into the computation of the principal components. To avoid including the u-data, other authors (Ivezić et al. 2002; Parker et al. 2008) constructed a colour-code diagram in a (a^*, $i-z$) plane, where

$$a^* = C_1 * (g-r) + C_2 * (r-i) + C_3, \quad (1)$$

and C_1, C_2 and C_3 are numerical coefficients that depend on the colour values and on the number of observations in the given data base (Roig & Gil-Hutton 2006), and g, r, i and z, the other SDSS colours, had an accuracy of about 0.03 mag, higher than the average errors in the u-band. As in the plane of (PC_1, PC_2), asteroids divided in the (a^*, $i-z$) plane into three fairly distinct groups, the C-complex ($a^* < 0$), the S-complex ($a^* > 0$, $i-z > -0.13$) and the V-type asteroids ($a^* > 0$, $i-z < -0.13$; Parker et al. 2008).[2]

Asteroid taxonomy is however also defined by the geometric albedo p_V (roughly, the ratio of reflected radiation from the surface to incident radiation upon it, at zero phase angle (i.e. as seen from the light source), and from an idealized flat, fully reflecting, diffusive scattering (Lambertian) disc with the same cross-section). C-type asteroids tend to have lower values of geometric albedo than S-type ones, and Tholen asteroid taxonomy (Tholen 1989) used values of p_V to distinguish classes of asteroids inside the X-complex, such as the M-, E- and P-types. Until recently, however, only about two thousand asteroids had reliable values of geometric albedos (see Tedesco et al. 2002). Initial results from the *Wide-field Infrared Survey Explorer* (*WISE*) (Wright et al. 2010), and the NEOWISE (Mainzer et al. 2011) enhancement to the *WISE* mission recently allowed us to obtain diameters and geometric albedo values for more than 100 000 main belt asteroids (Masiero et al. 2011), increasing the sample of objects for which albedo values were known by a factor of 50. Masiero et al. (2011) showed that, with some exceptions, such as the Nysa–Polana group, asteroid families typically show a characteristic albedo for all members, and that a strongly bimodal albedo distribution was observed in the inner, middle and outer portions of the main belt.

Previous works, such as Bus & Binzel (2002a,b), Nesvorný et al. (2005), found asteroid families in extended domains of proper elements and SDSS-MOC4 principal components data in order to minimize the number of possible interlopers, but such an analysis was not extended to asteroids' geometrical albedo. Here, we take full advantage of the newly available *WISE* data and we introduce a new HCM [see Bendjoya & Zappalà (2002) for details of the method in proper elements space] in a multidomain space

[1] The term halo was first introduced to describe this population of objects by Nesvorný et al. (2006), and then adopted by other authors such as Parker et al. (2008).

[2] The a^* colour is nothing but the first principal component PC_1 of the data distribution in the ($g-r$) versus ($r-i$) colour–colour diagram.

composed by asteroids proper elements (a, e, $\sin(i)$), SDSS-MOC4 colours (a^*, $i-z$) and *WISE* geometric albedo (p_V), to identify haloes associated with main belt asteroid families. The great advantage of this approach is that any group identified in these domains will most likely to belong to the same taxonomical group, since its members have to share not only similar values of proper elements, but also of taxonomically related information, such as (a^*, $i-z$) and p_V. A shortcoming of this approach is related to the more limited number of asteroids that have data in the three domains at the same time, when compared with the larger number of objects that have only proper elements and frequencies, only SDSS-MOC4 principal components data, only *WISE* albedo data or a dual combination of these three quantities. However, groups determined with this new approach may serve as a first step in determining the real orbital extension of the families' cores and haloes, with a precision that other methods already in use in the literature may lack.

This work is so divided: in Section 2, we discuss the basics of our approach for finding haloes in the multidomain space. In Section 3, we compare the efficiency of this approach in finding low numbers of interlopers with the results of other methods used for identifying asteroid families. In Sections 4, 5 and 6, we apply our method to all the currently known major families in the inner, central and outer main belt. In Sections 7 and 8, we discuss the case of the asteroids in the Cybele group and in the Hungaria region. Finally, in Section 9, we present our conclusions.

2 METHODS

In this work, we are trying to make best use of all the new data on surface colours (SDSS-MOC4) and geometric albedo (*WISE* and NEOWISE) that is currently available to try to find the most possibly accurate determination of all major main belt family haloes. For this purpose, we determined the main belt asteroids with synthetic proper elements available at the AstDyS website http://hamilton.dm.unipi.it/cgi-bin/astdys/astibo, accessed on 2013 January 15 (Knežević & Milani 2003) that also have SDSS-MOC4 and *WISE* albedo data, and errors in proper elements (a, e, $\sin(i)$) less than what described as 'pathological' in Knežević & Milani (2003), i.e. $\Delta a > 0.01$ au, $\Delta e > 0.1$ and $\Delta \sin(i) > 0.03$. We computed the SDSS-MOC4 colours (a^*, $i-z$) and their errors, computed with standard propagation of uncertainty formulas under the assumption that the SDSS-MOC4-calibrated magnitude behave as uncorrelated variables. For our sample of 58 955 asteroids with SDSS colours, we found values of the coefficients C_1, C_2, and C_3 in equation (1) of 0.939 67, 0.342 08 and −0.6324, respectively. To avoid including data affected by too large uncertainties, we eliminated from our sample asteroids with errors in a^* or $(i-z)$ larger than 0.1 mag. As a test of the validity of our approach we also computed PC_1, PC_2 principal components according to the approach of Novaković, Cellino & Knežević (2011), with their errors, and also rejected objects with errors larger than 0.1. While 68.1 per cent of the asteroids in the SDSS-MOC4 sample passed the conversion into (a^*, $i-z$) colours and the rejection of noisy data, only 42.08 per cent of the same asteroids had errors in PC_1, PC_2 less than 0.1.[3] Based on these results, we decided to work with (a^*, $i-z$) colours rather than principal components. We also eliminated from our sample asteroids with errors in p_V larger than 0.05 if $p_V < 0.2$, and asteroids with errors in p_V larger than 0.1 if $p_V > 0.2$. The stringent constraint on errors in geometric albedo p_V for low-albedo asteroids was required to better distinguish between CX-complex asteroids ($p_V < 0.1$) and S-complex asteroids ($p_V > 0.1$). Since some objects in the inner main belt and Hungaria region have values of albedo in the *WISE* survey that are too high (up to 0.8–0.9) and are possibly an artefact of the method used to calculate absolute magnitude (Masiero et al. 2011), we also eliminated all objects in these two regions (essentially those with semimajor axis smaller than that of the centre of the 3J:-1A mean-motion resonance, i.e. about 2.5 au) with $p_V > 0.5$ from our data base.

We then defined a distance metrics between two asteroids in a multidomain space as

$$d_{\rm md} = \sqrt{d^2 + C_{\rm SPV}[(\Delta a^*)^2 + (\Delta(i-z))^2 + (\Delta p_V)^2]}, \quad (2)$$

where $\Delta a^* = a_2^* - a_1^*$ and similar relations hold for $\Delta(i-z)$ and Δp_V. Following the approach of Bus & Binzel (2002a,b) for a similar distance metric of proper elements and SDSS-MOC principal components (see also Nesvorný et al. 2005; Carruba & Michtchenko 2007), $C_{\rm SPV}$ is a weighting factor equal to 10^6 (other choices in a range between 10^4 and 10^8 have been tested without significantly changing the robustness of the results), and d is the standard distance metrics in proper element domain defined in Zappalà et al. (1995) as

$$d = na\sqrt{k_1\left(\frac{\Delta a}{a}\right)^2 + k_2(\Delta e)^2 + k_3(\Delta \sin(i))^2}, \quad (3)$$

where n is the asteroid mean motion; Δx the difference in proper a, e and $\sin(i)$; and k_1, k_2, k_3 are weighting factors, defined as $k_1 = 5/4$, $k_2 = 2$, $k_3 = 2$ in Zappalà et al. (1990, 1995). As first halo members, we selected asteroids that belong to the asteroids family, whose spectral type is compatible with that of the other members according to Mothé-Diniz et al. (2005), Nesvorný et al. (2006), Carruba (2009a,b, 2010b) and other authors, and that, of course, also have acceptable SDSS-MOC4 and *WISE*/NEOWISE data. For families not treated by these authors, we consulted the list of asteroid families available at the AstDyS website, and the Nesvorný (2012) HCM Asteroid Families V2.0, on the Planetary Data System, available at http://sbn.psi.edu/pds/resource/nesvornyfam.html, accessed on 2013 March 13. We then obtained dynamical groups using equation (2), for a value of cutoff $d_{\rm md}$ a bit less than the value for which the family halo merges with the local background (and other families in the region). As an example of this procedure, we choose the case of the Themis family. Fig. 2 displays the total number of members of this group (blue line) and the number of new members of the group (green line, as new members we mean the number of objects that became part of the group at that given velocity cutoff), as a function of the velocity cutoff $d_{\rm md}$. For $d_{\rm md} = 315\,{\rm m\,s^{-1}}$, the Themis halo merged with other Local Groups, such as the Hygiea family, so we choose in this case to work with a halo defined at $d_{\rm md} = 310\,{\rm m\,s^{-1}}$.

An advantage of the method proposed here is that it should automatically select asteroids close in proper elements, SDSS-MOC4 and *WISE* albedos, so reducing the number of interlopers usually

[3] The large rejection of noisy data in this later approach is due to the inclusion of the magnitudes in the u filter, which are affected by larger errors that the magnitudes in the other filters. An alternative approach based on principal components PC_1, PC_2 only in g, r, i and z colours domain was also tried. 67.7 per cent of our data passed the conversion into this space with errors less than 0.1. Since the (a^*, $i-z$) approach was slightly more efficient and it provided results that are easier to analyse in terms of taxonomies than the principal component approach, in this work we have decided to opt for the (a^*, $i-z$) method.

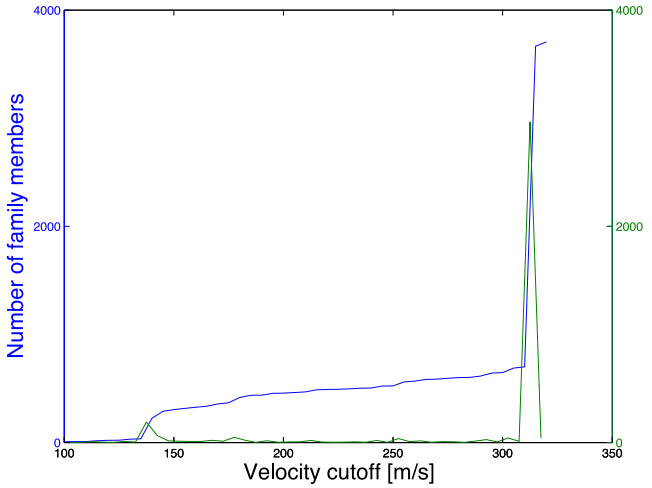

Figure 2. The number of members (blue line) and new members (green line) of the Themis group as a function of the velocity cutoff $d_{\rm md}$.

found in dynamical group encountered in proper elements (or frequencies) domains only. This can be verified by an analysis of the SDSS-MOC4 and *WISE* albedo data of the group so obtained. Again, for the case of the Themis family, Fig. 3 shows a projection in the (a^*, $i-z$) plane (panel A) and a histogram of the relative distribution of p_V values (panel B) of members of the Themis halo obtained with this method. The Themis family is made mostly by asteroids with CX-complex taxonomy, which in the (a^*, $i-z$) plane appear on the left of the vertical dotted line, but nine asteroids have colours incompatible with such classification and should be considered as interlopers. This is confirmed by an analysis of p_V values, where most of the albedos are below 0.1, the threshold for CX-complex asteroids, but there is a tail of objects with higher albedos. The percentage of possible interlopers found with this method, 1.30 per cent, is indeed quite inferior to the $\simeq$10 per cent statistically expected in dynamical families obtained only in proper elements domains (Migliorini et al. 1995). We will discuss how this new approach fares when compared with other methods already known in the literature in the next section.

3 COMPARISON WITH HCM IN OTHER DOMAINS

A natural question that may arise is why study families' haloes in a domain of proper elements, SDSS-MOC4 colours, and *WISE* albedos. How do the results obtained with this approach compare to those obtained with more traditional methods, such as the HCM in proper elements domain, or in a domain of proper elements and SDSS-MOC a^* and $i-z$ colours? To answer this question, we obtained asteroid families' haloes for several groups with the standard distance metric in proper element domain d of Zappalà et al. (1995), with a metric in proper elements and SDSS-MOC4 colours domains, given by

$$d_{\rm md} = \sqrt{d^2 + C_{\rm SPV}[(\Delta a^*)^2 + (\Delta(i-z))^2]}, \quad (4)$$

where $C_{\rm SPV}$, as discussed in Section 2, is a weighting factor equal to 10^6, and with a newly defined distance metric in proper elements and *WISE* geometric albedo p_V domain, given by

$$d_{\rm md} = \sqrt{d^2 + C_{\rm SPV}(\Delta p_V)^2}. \quad (5)$$

We determined families' haloes with the standard metrics of Zappalà et al. (1995), and equations (4), (5) and (2) for several large families in the main belt. Table 1 summarizes our results for the Hygiea, Koronis, and Eos family haloes, where we report the value of the cutoff at which the family was found, the number of halo members, the percentage of SDSS-MOC4 and geometric albedo likely interlopers (see Section 2 for a definition of the concept of SDSS-MOC4 and geometric albedo likely interlopers), for the four methods that we used (we will refer to these methods as metrics *D*, *DS*, *DPV* and *DSPV*). The last column, which reports the sum of the percentage of SDSS-MOC4 and geometric albedo likely interlopers, gives a measure of the efficiency of the method in finding likely interlopers: the lower this index, the better the method is working in avoiding taxonomically uncorrelated asteroids to the family halo. Among the several large families' haloes that we analysed, we choose to display the results for the Hygiea, Koronis and Eos groups because these are families for which the new multidomain method showed one of the best, medium and worse results in term of not finding interlopers when compared with the other methods, respectively.

The Hygiea family case was the one for which the new method had the best results among the families analysed, with an overall efficiency of only 9.86 per cent. In the case of the Koronis family,

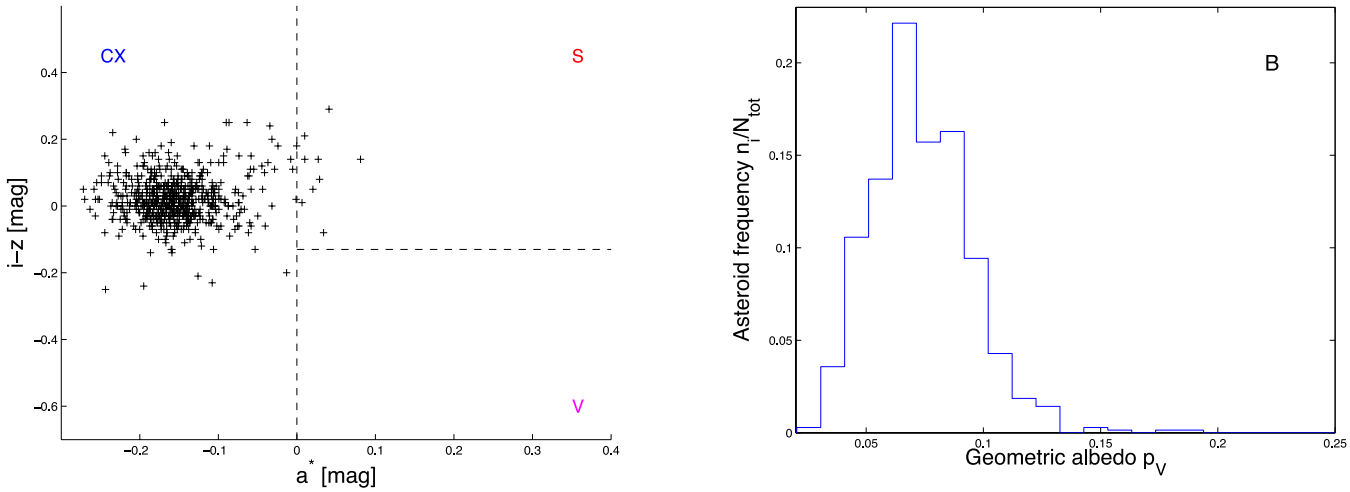

Figure 3. An (a^*, $i-z$) projection (panel A), and a histogram of the relative distribution of p_V values (panel B) of members of the Themis halo.

Table 1. Efficiency of distance metrics in several domains in finding asteroid families' halo members.

Family name	d_{md} cutoff value (m s^{-1})	Number of members	Percentage of SDSS-MOC4 likely interlopers	Percentage of p_V likely interlopers	Metric efficiency
Hygiea halo					
Metric *D*	80	6152	7.58	15.59	23.17
Metric *DS*	225	728	5.63	14.02	19.65
Metric *DPV*	140	2977	8.63	6.45	15.08
Metric *DSPV*	290	426	1.41	8.45	9.86
Koronis halo					
Metric *D*	65	6958	15.71	14.36	30.07
Metric *DS*	230	1054	13.54	13.11	26.65
Metric *DPV*	80	1366	14.32	21.74	36.06
Metric *DSPV*	215	200	16.00	7.00	23.00
Eos halo					
Metric *D*	40	5322	52.70	17.35	70.05
Metric *DS*	135	1886	55.99	11.08	67.07
Metric *DPV*	80	846	57.01	18.94	75.95
Metric *DSPV*	165	738	51.36	17.89	69.25

the efficiency was lower (23.00 per cent), but the new method still provided the best results when compared with other approaches. The Eos family was a very peculiar case: most of the family members are K-type, an S-complex type whose a^* values are very close to zero, the limiting value separating CX-complex asteroids and S-complex ones. The family is surrounded by CX-complex asteroids, and an analysis only based on distance metric inevitably recognizes as family members many background objects not necessarily connected to the family. Only in the case of this family, we found an efficiency of the new method slightly inferior to the results of the *DS* metric (69.25 per cent with respect to 67.07 per cent). Overall, the new approach was at its best a factor of 2 more efficient in eliminating interlopers than other methods, and at its worse provided comparable results to what obtained in the domain of proper elements and *Sloan* colours.

Having concluded that the method described by equation (2) is the most efficient in term of low numbers of interlopers, we are now ready to start our analysis of the main belt. We will do this by investigating asteroids family haloes in the inner main belt.

4 INNER MAIN BELT

The inner main belt is dynamically limited in semimajor axis by the 3J:-1A mean-motion resonance at high *a* (Zappalà et al. 1995). The 7J:-2A mean-motion resonance is sometimes used by some authors as the boundary between the inner main belt at high inclination and the region of the Hungaria asteroids. In this work, we will just use the upper limit in *a* given by the 3J:-1A mean-motion resonance. The linear secular resonance ν_6 separates the low-inclined asteroid region from the highly inclined area, dominated by the Phocaea family (see Carruba 2009b, 2010a for a discussion of the local families' groups and dynamics). The Phocaea family is located in a stable island limited by the 7J:-2A and 3J:-1A in semimajor axis, and by the ν_6 and ν_5 secular resonances in inclination (Knežević & Milani 2003). We found 2366 objects that have proper elements and frequencies, SDSS-MOC (a^*, $i - z$) colours, *WISE* geometric albedo data in the inner main belt, and reasonable errors, according to the criteria defined in Section 2. We will start our analysis by studying the case of the Belgica family.

4.1 The Belgica family

The Belgica group was a clump associated with the former Flora family and identified by Mothé-Diniz et al. (2005) as a small and sparse group of only 41 members at a cutoff in proper element domain of 57.5 m s^{-1}. Here, we found that the halo of the Belgica family merges with that of the Baptistina group already at a cutoff of 100 m s^{-1}. We will therefore treat the Belgica family together with the Baptistina cluster.

4.2 The Baptistina family

The Baptistina family, as the Belgica group, was studied by Mothé-Diniz et al. (2005) and was part of the former Flora family. It is located in a very complex dynamical region (Michtchenko et al. 2010), being crossed by powerful mean-motion resonances such as the 7J:-2A and interacting with secular resonances such as the $z_2 = 2(g - g_6) + (s - s_6)$. It has been obtained in the (n, g, s) frequency domain by Carruba & Michtchenko (2009) to study possible diffusion of its members in $s-$type resonances such as the $\nu_{17} + \nu_4 + \nu_5 - 2\nu_6$. Here, we identified a 56-member CX halo at a cutoff of 250 m s^{-1}. The taxonomical structure of the halo is indeed very complex and puzzling. The majority of the Baptistina halo members have SDSS-MOC4 data compatible with a CX-complex taxonomy, with only two members (3.6 per cent of the total) that are possible interlopers. The albedo data are however very puzzling, since 47 members (83.9 per cent of the total) have values of $p_V > 0.1$, not usually associated with dark CX-complex asteroids. Baptistina family members seem to behave as the members of the Hungaria group, a CX-complex family, characterized by large values of albedos (see Section 8.1). Understanding the properties of the Baptistina halo will require a much more in depth analysis than what we performed in this work.

4.3 The Vesta family

The Vesta family is unique in the main belt, since it is made mostly by V-type asteroids that are associated with a basaltic composition, typical of differentiated objects with a crust. Of the many possible differentiated or partially differentiated asteroids that may have

existed in the primordial main belt, (4) Vesta is the largest remnant for which a basaltic crust is still present and was observed by a space mission (Russel et al. 2012). Many V-type objects are observed outside the limits of the traditional HCM family (Carruba et al. 2005, Nesvorný et al. 2008), making this family a test-bed for the application of methods on halo determinations.

We determined a 161-member halo at a cutoff of $d_{\rm md} = 275\,{\rm m\,s^{-1}}$. 46 halo members (28.6 per cent of the total, a considerable fraction of the halo) are possible SDSS-MOC4 interlopers, and 26 asteroids (16.2 per cent of the total) are possible albedo interlopers. Among the asteroids with $a^* > 0$, 58.6 per cent are in a region of the (a^*, $i - z$) plane associated with V-type objects, according to the criteria defined in Section 1, and can be considered as possible V-type candidates.

How efficient is the new method in identifying V-type asteroids outside the Vesta family as members of the halo? Among the V-type asteroids not connected to the traditional HCM Vesta family listed in Carruba et al. (2005), only four objects are present in our multidomain catalogue: (3849), (3869), (4188) and (4434). Of these, two (50 per cent of the total), (3869) and (4188), were part of the Vesta halo as found by our method. Having such a limited sample of objects in our catalogue and in the halo, we are not able to achieve any conclusions on the validity of the method for the Vesta halo. The Sidwell, Somekawa, Henninghaack and Ausonia AstDyS family merge with the Vesta halo at a cutoff of less than $320\,{\rm m\,s^{-1}}$.

4.4 The Erigone family

The Erigone family was identified by Nesvorný et al. (2006) as a CX-complex group at a cutoff of $80\,{\rm m\,s^{-1}}$. Their analysis appears to be confirmed by this work: we found a 57 member CX-complex group at a cutoff $d_{\rm md}$ of $400\,{\rm m\,s^{-1}}$. No SDSS-MOC4 interlopers were found in the halo, and only one object (1.8 per cent of the total) was (barely) a possible albedo interloper. The Maartes AstDyS family merges with the Erigone halo at a cutoff of $d_{\rm md} = 165\,{\rm m\,s^{-1}}$.

4.5 The Massalia family

The Massalia family was identified by Nesvorný et al. (2006) as an S-complex family at a cutoff of $50\,{\rm m\,s^{-1}}$. In this work, we identified 19 S-complex members at a cutoff $d_{\rm md}$ of $250\,{\rm m\,s^{-1}}$. Seven SDSS-MOC4 interlopers (36.8 per cent of the total) were found in the halo, and 10 objects (52.6 per cent of the total) were possible albedo interlopers. Incidentally, (20) Massalia itself is a C-type asteroid, and quite likely an interloper in its own family.

4.6 The Nysa/Mildred/Polana family

The Nysa/Polana family was studied by Mothé-Diniz et al. (2005) that confirmed previous results about the dual structure of the family, made by an S-type member group around (878) Mildred, and an F-type group around (142) Polana. In this work, we find a CX-complex halo of 147 members at a cutoff $d_{\rm md}$ of $280\,{\rm m\,s^{-1}}$. The halo is dominated by the CX-complex Polana group, which is also made by the largest bodies in the area (Mothé-Diniz et al. 2005): we found no possible SDSS-MOC4 interlopers, and one (0.7 per cent of the total) albedo interloper. A smaller halo associated with the Mildred family merges with the larger Polana halo at about $150\,{\rm m\,s^{-1}}$, and the Clarissa Planetary Data System is englobed at a cutoff of $345\,{\rm m\,s^{-1}}$.

4.7 The Euterpe family

The Euterpe family is a low-inclination group listed by the Planetary Data System. In this work, we identified an S-complex halo at a cutoff $d_{\rm md}$ of $335\,{\rm m\,s^{-1}}$. Two objects (22.2 per cent of the total) were possible SDSS-MOC4 interlopers, and one asteroid (11.1 per cent of the total) is a possible albedo interloper.

4.8 The Lucienne family

The Lucienne family is a relatively high-inclination group listed by the Planetary Data System. Unfortunately, we could not find any member of this group in our multidomain sample of asteroids for the inner main belt, so no conclusions are possible to achieve on this cluster.

4.9 The Phocaea family

The Phocaea family has been studied by Knežević & Milani (2003) and by Carruba (2009b). It is located in a stable island bounded by the ν_6 and ν_5 secular resonances in inclination and the 7J:-2A and 3J:-1A mean-motion resonances in semimajor axis. Despite the peculiar dynamical configuration, Carruba (2009b) concluded that it was likely that the Phocaea family was a real S-complex collisional family, with an estimated age of about 2.2 billion years. In this work, we found an 80-member S-complex halo at a cutoff $d_{\rm md} > 800\,{\rm m\,s^{-1}}$, which is the value for which all asteroids in the stable island in our data base were found connected to the Phocaea family. 27 objects (33.8 per cent of the total) were possible SDSS-MOC4 interlopers, and 16 asteroids (20.0 per cent of the total) had values of $p_V < 0.1$. Overall, we confirm the analysis of Carruba (2009b) on the possible reality of the Phocaea family as an S-complex collisional group.

4.10 The inner main belt: an overview

Our results for the inner main belt are summarized in Table 2, where we give information on the first halo member used to determine the family halo, the cutoff value used to identify the halo, the number of bodies in the halo, the spectral complex to which the majority of halo members belongs and the number of possible interlopers, according to SDSS-MOC4 and geometric albedo considerations.

Fig. 4, panel A, displays an (a, $\sin(i)$) projection of asteroids in our multivariate sample in the central main belt. Vertical red lines identify the orbital position of the main mean-motion resonances in the area. Blue lines show the location of the main linear secular resonances, using the second order and fourth-degree secular perturbation theory of Milani & Knežević (1994) to compute the proper frequencies g and s for the grid of (a, e) and (a, $\sin(i)$) values shown in Fig. 4, panel A, and the values of angles Ω, ω, M and eccentricity of (25) Phocaea, the highly inclined asteroid associated with the largest family in the region (Carruba 2009b). The orbital position in the (a, $\sin(i)$) plane of the first numbered asteroid in all the inner main belt groups is also identified in Fig. 4, panel A. In panel B of the same figure, we display a density map of the inner main belt, according to the approach described in Carruba & Michtchenko (2009). Density maps display regions characterized by strong mean-motion or secular resonances by a relatively low number of asteroids per unit bin. To quantitatively determine the local density of asteroids, we computed the $\log_{10}$ of the number of all asteroids with proper elements per unit square in a 22 by 67 grid in a (starting at $a = 2.18$ au, with a step of 0.015 au) and $\sin(i)$

Table 2. Asteroid families' haloes in the inner main belt.

First halo member	d_{md} cutoff value (m s^{-1})	Number of members	Spectral complex	Number of SDSS-MOC4 likely interlopers	Number of p_V likely interlopers
(298) Baptistina: (4691)	250	56	CX	2	47
(4) Vesta: (2011)	275	161	S(V)	46	26
(163) Erigone: (9566)	400	57	CX	0	1
(20) Massalia: (10102)	250	19	S	7	10
(44) Nysa/Mildred/Polana: (1768)	280	147	CX	0	1
(27) Euterpe: (5444)	335	9	S	2	1
(25) Phocaea: (3322)	>800	80	S	27	16

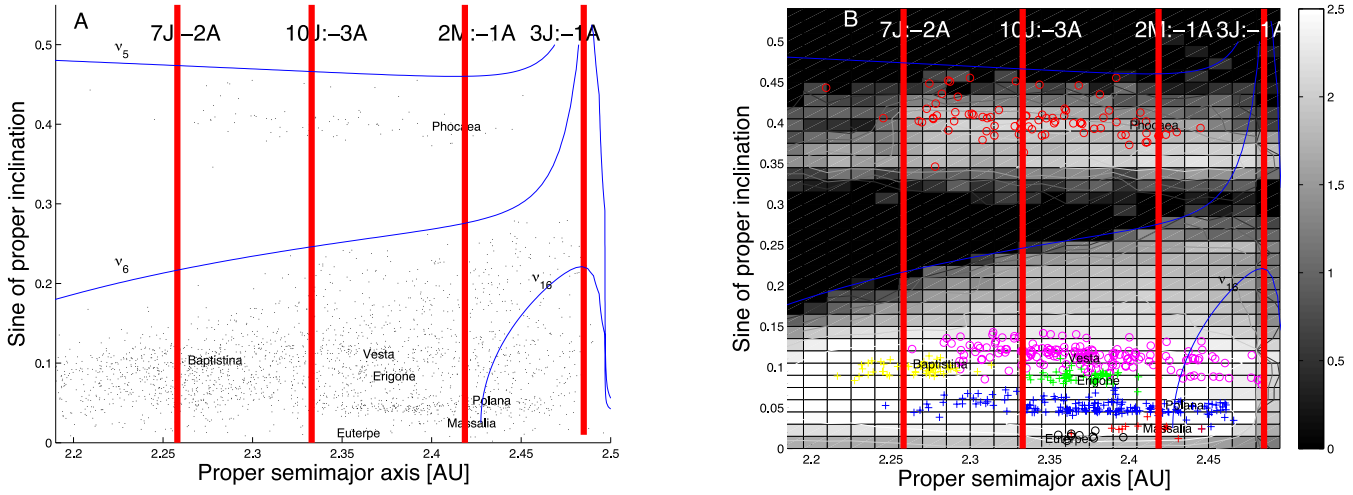

Figure 4. Panel A: an (a, sin (i)) projection of inner main belt asteroids in our multivariate sample. Panel B: contour plot of the number density of asteroids in the proper element sample. Superimposed, we display the orbital location of asteroid families in the CX-complex (plus signs), and in the S-complex (circles).

(starting at 0, with a step of 0.015). Superimposed to the density map, we also show the orbital projection of the haloes found in this work shown as plus signs for CX-complex families, and circles for S-complex families. The other symbols are the same as in Fig. 4, panel A.

Fig. 5 displays a projection in the (a^*, $i - z$) plane of all asteroids in our multidomain sample (panel A), and an (a, sin (i)) projection of the same asteroids, (panel B), where objects in the CX-complex are shown as blue circles, and asteroids in the S-complex are identified as red plus signs. The inner main belt is slightly dominated by S-complex asteroids, but with a significant minority of CX-complex bodies. V-type asteroids are mostly concentrated in the Vesta family, but with a significant population outside the dynamical group (see also Carruba et al. 2005).

This is confirmed by an analysis of *WISE* p_V geometrical albedo data, a histogram of which is presented in Fig. 6, panel A. Fig. 6, panel B, displays an (a, sin (i)) projection of the same asteroids, where blue full dots are associated with asteroids with $p_V < 0.1$, red full dots display asteroids with $0.1 < p_V < 0.3$ and magenta full dots show asteroids with $p_V > 0.3$. The majority of asteroids in the inner main belt is made by high-albedo objects, associated with S-complex taxonomies, but with a significant minority of CX-complex bodies.

5 CENTRAL MAIN BELT

The central main belt is dynamically limited in semimajor axis by the 3J:-1A and 5J;-2A mean-motion resonances (Zappalà et al. 1995). The linear secular resonance ν_6 separates the low-inclined asteroid region from the highly inclined area, dominated by the Hansa and Pallas families (Carruba 2010b). As discussed in Carruba (2010b), in the highly inclined region the local web of linear secular resonances and mean-motion resonances divided the region into six separated stable islands, each hosting one or more major families, and that can be considered as a stable archipelago. Of particular interest in this region is the Tina family, whose members are all in anti-aligned states of the ν_6 linear secular resonance (Carruba & Morbidelli 2011). We found 3693 objects that have proper elements and frequencies, SDSS-MOC4 a^* and $i - z$ colours, *WISE* geometric albedo data, and satisfy our error analysis criteria, in the central main belt, and we will start our analysis by studying the case of the Hestia family.

5.1 The Hestia family

The Hestia family was identified in Nesvorný et al. (2005) as a 154-member group with S-taxonomy at a cutoff in proper element domain of 80 m s^{-1}. Here, we obtained a CX-halo of 26 members at a cutoff $d_{md} = 360$ m s^{-1}. 11 objects (42.3 per cent of the total) were SDSS-MOC4 interlopers, and 12 (46.2 per cent of the total) had $p_V < 0.1$.

5.2 The Astraea family

The Astraea family is listed at the AstDyS. We identified a small CX-complex halo of four members at a cutoff of 320 m s^{-1}, with no interlopers.

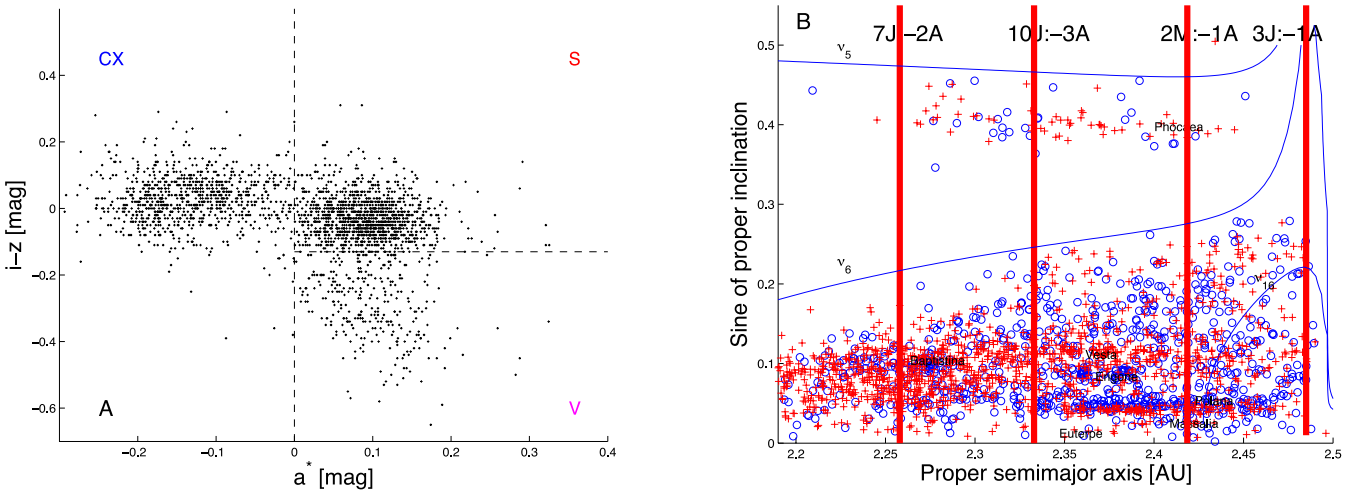

Figure 5. Panel A: an $(a^*, i - z)$ projection of inner main belt asteroids in our multidomain sample. Panel B: an $(a, \sin(i))$ projection of the same asteroids, where objects in the CX-complex are shown as blue circles, and asteroids in the S-complex are identified as red plus signs.

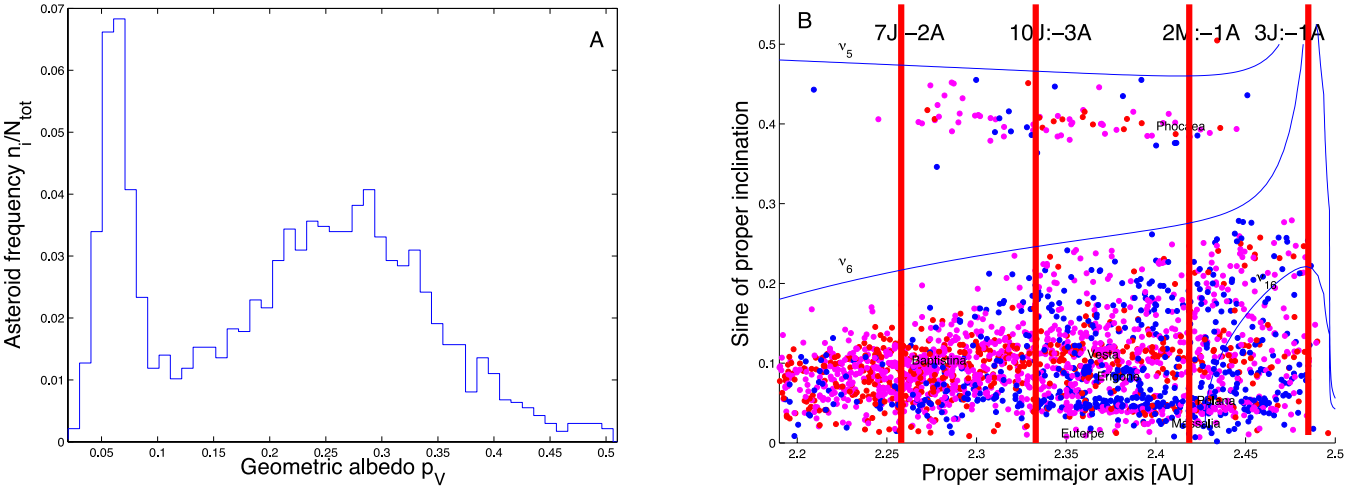

Figure 6. Panel A: a histogram of number frequency values $n_i / N_{\rm Tot}$ as a function of geometric albedo p_V for inner main belt asteroids in our multidomain sample. Panel B: an $(a, \sin(i))$ projection of the same asteroids, where blue full dots are associated with asteroids with $p_V < 0.1$, red full dots display asteroids with $0.1 < p_V < 0.3$ and magenta full dots show asteroids with $p_V > 0.3$.

5.3 The Aeolia family

The Aeolia family was identified in Nesvorný et al. (2005) as a group of 28 members at a cutoff of 20 m s^{-1} with no identifiable dominant taxonomy. Here, we obtained a halo of 14 members at a cutoff $d_{\rm md} = 320$ m s^{-1}, all with CX-complex taxonomies. Two objects (14.3 per cent of the total) have values of $p_V > 0.1$.

5.4 The Chloris family

The Chloris family was a group of 135 members identified in Nesvorný et al. (2005) at a cutoff in proper element domain of 120 m s^{-1}. Most of the members of this group belonged to the C-class. In this work, we found a halo of 35 members at a cutoff of 340 m s^{-1}. One object (2.9 per cent of the total) was a possible SDSS-MOC4 interloper, and eight objects (22.9 per cent of the total) had values of $p_V > 0.1$.

5.5 The Misa family

The Misa family was a large C-class group of 119 asteroids identified at a cutoff of 80 m s^{-1} in proper element domain by Nesvorný et al. (2005). Here, we found a halo of 33 members at a cutoff $d_{\rm md} = 355$ m s^{-1} all belonging to the CX-complex. One object (3.0 per cent of the total) was a possible SDSS-MOC4 and albedo interloper. The Leonidas AstDyS group merges with this family at a cutoff of less than 150 m s^{-1}.

5.6 The Brangane family

The Brangane group was a 30-member S-type cluster identified in proper element domain by Nesvorný et al. (2005) at a cutoff of 30 m s^{-1}. In this work, we identified an S-complex halo of just three members at a cutoff $d_{\rm md} = 355$ m s^{-1}. One member (33.3 per cent of the total) was a possible SDSS-MOC4 interloper, and, as observed for some other S-complex families, all objects had $p_V < 0.1$.

5.7 The Bower family

The Bower family was a 82-member cluster identified by Nesvorný et al. (2005) at a cutoff of 100 m s^{-1} with no dominant taxonomical information. In this work, we identified a 27-member halo at a cutoff $d_{\rm md} = 260$ m s^{-1}. Most of the members belonged to the CX-complex, but six (22.2 per cent of the total) were possible SDSS-MOC4 interlopers, and seven objects (25.9 per cent of the total) had $p_V > 0.1$.

5.8 The Cameron family

The Cameron group was identified at a cutoff of 60 m s^{-1} by Nesvorný et al. (2005). It was a 162 group made mostly by S-type asteroids. The halo that we identified in this work had three members at $d_{\rm md} = 310$ m s^{-1}. Contrary to what was found by Nesvorný et al. (2005), all members have SDSS-MOC4 colours compatible with a CX-complex taxonomy, but two objects (66.7 per cent of the total) had $p_V > 0.1$. The Innes AstDyS group merges with this family at cutoff lower than 150 m s^{-1}.

5.9 The Rafita family

The Rafita family was an S-complex group identified by Nesvorný et al. (2005) in the (a, e, sin (i)) proper elements domain at a cutoff of 100 m s^{-1}. Unfortunately, we could not identify any member of this family in our multidomain sample of proper elements, SDSS-MOC4 colours and geometric albedos. Therefore, we could not analyse this family halo.

5.10 The Eunomia family

The Eunomia family is the largest family in the central main belt. Mothé-Diniz et al. (2005) analysed the spectra of 43 members of this family, most of which belonging to the S-complex, but with a large taxonomical diversity that suggested surface inhomogeneities or the action of space weathering. The presence of T- and X-class asteroids, classes these compatible with iron meteorites, suggested the possibility that the formation of the Eunomia family may have been the result of the catastrophic breakup of a differentiated (or partially differentiated) parent body. The identification of three V-type asteroids in the orbital proximity of the Eunomia family provided further hints for this possibility. Carruba, Michtchenko & Lazzaro (2007) showed that it is possible to migrate from the Eunomia dynamical family to the current orbital location of (21238) 1995 WV7, the largest of the V-type asteroids in the Eunomia region, via the interplay of the Yarkovsky effect and the $\nu_5 - \nu_6 + \nu_{16}$ non-linear secular resonance, on time-scales of at least 2.6 Gyr.

In this work, we identified a halo with 52 members, at a cutoff $d_{\rm md}$ of 90 m s^{-1}. As found in Mothé-Diniz et al. (2005), the Eunomia family halo is quite diverse, with a predominance of objects belonging to the S-complex, but with a fairly large minority of C- and X-complex asteroids. We found seven SDSS-MOC4 interlopers and seven asteroids with $p_V < 0.1$, which yields a percentage of 13.5 per cent likely interlopers. The Planetary Data System group of Schulhof merges with the Eunomia family at a cutoff of 195 m s^{-1}.

5.11 The Iannini family

The Iannini family was studied in Nesvorný et al. (2005), where it was identified in proper element domain at a cutoff of 30 m s^{-1}. The group was listed as an S-type, but here we found a 93-member halo dominated by CX-complex asteroids, at a cutoff $d_{\rm md}$ of 305 m s^{-1}. The discrepancy with Nesvorný et al. (2005) spectral classification may possibly be caused by the low number (18) of objects found in this family at the time. There were no SDSS-MOC4 interloper, and six asteroids (6.5 per cent of the total) had $p_V > 0.1$.

5.12 The Gefion family

The Gefion family, previously identified as the Ceres family (Zappalà et al. 1995) and also as the Minerva/Gefion family (Mothé-Diniz et al. 2005), was identified in Mothé-Diniz et al. (2005) as a fairly homogeneous family, with members mostly belonging to the S-complex. Because of its orbital proximity to (1) Ceres, it was studied in Carruba et al. (2003) as a test case for chaotic diffusion caused by close encounters with massive asteroids. The Gefion family halo was identified at a cutoff $d_{\rm md}$ of 210 m s^{-1}, with 146 members. Mothé-Diniz et al. (2005) found that the local background of this family is mostly dominated by distinguished C-type asteroids. Indeed, our halo is contaminated by a minority of bodies belonging to the C-complex: we found 43 SDSS-MOC4 interlopers and 33 asteroids with $p_V < 0.1$, which yields a percentage of 29.5 and 22.6 per cent likely interlopers, respectively. The Minerva AstDys group merges with this family halo at cutoff lower than 150 m s^{-1}.

5.13 The Adeona family

The Adeona family was analysed by Mothé-Diniz et al. (2005) that found it to be a very homogeneous family, made mostly in its entirety by asteroids belonging to the CX-complex. Because of its orbital proximity to (1) Ceres, it was also studied in Carruba et al. (2003) to understand the long-term effects of diffusion caused by close encounters with massive asteroids. The Adeona family halo has been identified in this work at a cutoff $d_{\rm md}$ of 295 m s^{-1}, with 149 members. We found one SDSS-MOC4 interloper (0.7 per cent of the total), and four objects with geometric albedo (barely) larger than 0.1, which corresponds to a percentual of possible interlopers of 2.7 per cent. This high uniformity of the Adeona albedo confirms the results found in Mothé-Diniz et al. (2005).

5.14 The Maria and Renate families

The Maria family was analysed together with the Renate family in Mothé-Diniz et al. (2005), and both families had a majority of members with known taxonomies belonging to the S-complex, indistinguishable from the local background. Zappalà et al. (1997) analysed this family and found that the spectra of 10 family members were compatible with those of near-Earth asteroids (433) Eros and (1036) Ganymede, conclusion not supported by the work of Mothé-Diniz et al. (2005). The Maria family halo has been identified in this work at a cutoff of 240 m s^{-1} with 135 members. We found 21 objects that can be classified as SDSS-MOC4 interlopers, five of which barely in the area of the CX-complex, and 10 asteroids with $p_V < 0.1$, which yields a percentual of possible interlopers of 15.6 and 7.4 per cent, respectively. The Renate family, considered together with the Maria family in Mothé-Diniz et al. (2005), and also classified as an S-complex group in that work, merges with the Maria family at a cutoff of 225 m s^{-1}. For the purpose of halo analysis, the two families can be considered as an unique group.

5.15 The Padua family

This family, previously associated with the asteroid (110) Lydia, is made mostly by X-type asteroids indistinguishable from the local background, according to Mothé-Diniz et al. (2005). The family is very important from a dynamical point of view, since it is the second family, after the Agnia, to have most of its members in a non-linear secular resonance configuration. More than 75 per cent of its members, according to Carruba (2009a), are currently in a z_1 librating state. Conservation of the $K_2^{'} = \sqrt{2 - e^2}(2 \cos i)$ quantity associated with this secular allowed us to set limits on the original ejection velocity field, which was in agreement with result obtained with an alternative Monte Carlo model that included Yarkovsky and Yarkovsky-O'Keefe-Radzievsky-Paddack (YORP) semimajor axis mobility. The current spread of values in the $(\sigma, g - g_6 + s - s_6)$ plane, where σ is the resonant argument of the z_1 resonance allowed to set a lower limit on the age of the family of 25 Myr, which was then used to set an upper limit on the effect of low-energy collisions. The Padua halo was identified at a cutoff of 130 m s^{-1}, with 31 members, and no interlopers. The Zdenekhorsky AstDyS group merges with the Padua halo at cutoff lower than 100 m s^{-1}.

5.16 The Juno family

The Juno family was identified in Nesvorný et al. (2005) as a 74-member S-type group. Here, we identified a halo of 61 members at a cutoff of 275 m s^{-1}, which, contrary to what published in Nesvorný et al. (2005), is made mostly by CX-complex bodies, with (3) Juno itself, an Sk object and a possible interloper. There were no SDSS-MOC4 interlopers, and four asteroids (6.6 per cent of the total) had values of $p_V > 0.1$.

5.17 The Dora family

The Dora family was classified by Mothé-Diniz et al. (2005) as a very homogeneous C-complex family, with the majority of members belonging to the Ch class, and five objects in the C and B classes. The family was very differentiated from the local background, made mostly by asteroids belonging to the S-complex. The Dora halo was identified at a cutoff of 265 m s^{-1}, with 108 members. Only two members were possible SDSS-MOC4 interlopers and had $p_V > 0.1$ (1.9 per cent), confirming the very homogeneous nature of this family, as found in Mothé-Diniz et al. (2005).

5.18 The Merxia and Nemesis family

The Merxia family was found to be made mostly by S-complex asteroids in Mothé-Diniz et al. (2005), and was dominated by the two largest bodies, (808) Merxia, and (1327) Namaqua, the second of which was most likely an interloper because of its low albedo. The family is crossed by the 3J:-1S:-1A three-body mean-motion resonance, which divides it into two lobes and cause a depletion in the number of members at the centre of the family, and it was well differentiated from the local background, dominated by CX-complex objects, according to Mothé-Diniz et al. (2005). Nesvorný et al. (2005) also identified in the region the Nemesis family, but its halo merges with that of the Merxia family at a cutoff of $\simeq$200 m s^{-1}, and we therefore decided to treat the two families as a single case. We found a CX-halo at a cutoff of 250 m s^{-1}, with 19 members, 5 of which could be SDSS-MOC4 interlopers and 9 of which have $p_V < 0.1$. The large percentual of possible interlopers (26.3 and 42.1 per cent) may be caused by the fact that, possibly, there is no Merxia halo, and the family is small and limited to the S-complex core found in Mothé-Diniz et al. (2005).

5.19 The Agnia family

The Agnia family, previously identified as the Liberatrix family, was the first group to be found having the majority of its members in z_1 librating states (Vokrouhlický et al. 2006b). Conserved quantities of the z_1 resonance and spread in the $(\sigma, g - g_6 + s - s_6)$ plane, as discussed for the case of the Padua family, were introduced in that work to obtain constraints on the family original ejection velocity field and age. The family, first analysed by Bus (1999), appears compatible with an S-complex taxonomy in Mothé-Diniz et al. (2005), while the local background is dominated by CX-complex bodies. Here, we determined a halo at a cutoff of 190 m s^{-1}, with 12 members. As for the Merxia family halo, we found a large number of possible interlopers: four SDSS-MOC4 CX-complex members and four $p_V < 0.1$ asteroids (33.3 per cent of the total), which may suggest that the actual Agnia family is small and with a limited halo.

5.20 The Astrid family

The Astrid family was identified in Bus (1999) and Mothé-Diniz et al. (2005) as a very tight clump, with most members belonging to the C-complex. No asteroid in the local background had taxonomical information at the time of Mothé-Diniz et al. (2005) analysis. Here, we found a very robust and isolated group, with a halo that was separated from the local background for cutoffs as large as 435 m s^{-1}, with six members, and no interlopers, confirming that this is a very homogeneous and robust group.

5.21 The Hoffmeister family

The Hoffmeister family was found to be a very compact and spectrally homogeneous CX-group in Mothé-Diniz et al. (2005). Here, we determined a halo with 62 members at a cutoff of 210 m s^{-1}. No interlopers were detected, so confirming previous analysis of this group.

5.22 The Lavrov family

The Lavrov group, previously known as the Henan clump, is a small group formed mostly by L-type asteroids, that are also typical of the local background (Mothé-Diniz et al. 2005). We identified a halo of eight members at a cutoff of 200 m s^{-1}. We identified only one possible SDSS-MOC interloper and two asteroids with $p_V < 0.1$ (12.5 and 25.0 per cent of the total, respectively), which confirms that this should be a fairly compact and robust L-class group.

5.23 The 1995 SU37 family

The 1995 SU37 group is listed at the Planetary Data System. We identified a small S-complex halo of four members, at a cutoff of 105 m s^{-1}, with no interlopers.

5.24 The Watsonia family

The Watsonia family is listed at the AstDyS. We identified a CX-complex halo of 10 members at a cutoff of 425 m s^{-1}. Three objects (30.0 per cent of the total) were possible SDSS-MOC4 interlopers, and five objects (50 per cent of the total) had $p_V > 0.1$.

5.25 The Ino, Atalante and Anacostia families

The Ino, Atalante and Anacostia families are listed at the AstDyS. Unfortunately, we could not find any of their members in our multidomain data base. No information is therefore available for this family in this work.

5.26 The Gersuind family

With the Gersuind family we start the analysis of the highly inclined $\sin i > 0.3$ asteroid groups in the central main belt, that were the subject of the study of Carruba (2010b). The Gersuind family was studied in Gil-Hutton (2006). While having most of its members at $\sin i > 0.3$, it lies at lower inclinations than the centre of the ν_6 resonance, and it is not therefore considered a proper high-inclination family by other authors, such as Machuca & Carruba (2011). The few objects with SDSS-MOC3 data in the family obtained by Carruba (2010b) were compatible with an S-complex taxonomy. Here, we found a halo at 310 m s^{-1} with seven members, the majority of which were compatible with an S-complex taxonomy. Three objects (42.9 per cent of the total) were SDSS-MOC4 interlopers, and two objects (28.6 per cent of the total) had albedos smaller than 0.1, confirming the analysis of Carruba (2010b). The Planetary Data System Emilkowalski group merges with this family at cutoff lower than 100 m s^{-1}.

5.27 The Myriostos family

The Myriostos family is listed at the AstDyS. We identified a 7-member CX-complex halo at a cutoff of 580 m s^{-1}, with two SDSS-MOC4 interlopers (28.6 per cent of the total). Six objects (85.7 per cent of the total) have $p_V > 0.1$.

5.28 The Kunitaka family

The Kunitaka family is listed at the AstDyS. We could not find any of its members in our multidomain data base, so no information is available on this group in this work.

5.29 The Hansa family

The Hansa family is the largest dynamical group among high-inclination families in the central main belt. The Hansa family was originally proposed by Hergenrother, Larson & Spahr (1996), studied in Gil-Hutton (2006) and re-analysed in Carruba (2010b) that found a large group compatible with an S-type taxonomy. The family is located in a stable island limited in inclination by the ν_6 and ν_5 linear secular resonances. This is confirmed by our analysis: we found a 20-member halo at a cutoff of $>$535 m s^{-1} (at cutoff as large as 1000 m s^{-1} the family does not yet connect with the local background), with all but one member (95 per cent of the total) with an S-complex taxonomy. We did not detected asteroids with $p_V <$ 0.1. The 2001 YB113 AstDyS group merges with this family halo for cutoff less than 150 m s^{-1}.

5.30 The Brucato family

The Brucato family was first identified as a clump in proper elements domain and as a family in the $(n, g, g + s)$ proper frequencies domain in Carruba (2010b).[4] Novaković et al. (2011) then re-obtained this group in proper element domains as a family, using a larger sample of asteroid proper elements. The family is located in a stable island limited in inclination by the ν_5 and ν_{16} linear secular resonances. The group was made mostly by CX-complex asteroids, and this is confirmed by the current analysis: we identify a family halo at a cutoff of 950 m s^{-1} with 32 members, all belonging to the CX-complex. Two albedo interlopers (6.3 per cent of the total) were identified in this family halo. The 1998 DN2, 1999 PM1, 1998 LF3 and 2004 EW7 AstDyS groups merge with this family at cutoffs lower than 150 m s^{-1}.

5.31 The Dennispalm family

The Dennispalm family is listed at the AstDys. We could not find any of its members in the multidomain data base, so no information is available on this group in this work.

5.32 The Barcelona family

The Barcelona family was first identified as a clump in Gil-Hutton (2006). Carruba (2010b) identified the group as a dynamical family, and this was confirmed by the later work of Novaković et al. (2011). The Barcelona family was made mostly by Sq asteroids. Very few objects were present in our multidomain sample of asteroids at this inclinations: we identified an S-complex halo of only one member at a cutoff of 730 m s^{-1}.

5.33 The Tina family

The Tina family, first identified in Carruba (2010b), is unique in the Solar system because all of its members are in ν_6 anti-aligned librating states, making it the only family currently known to lie in a stable island of a linear secular resonance. Carruba & Morbidelli (2011) studied its dynamics and obtained estimates of the family age and possible survival time before the family members escape from the stable island (both events happened and will happen on timescales of 150 Myr). (1222) Tina itself belongs to the X-complex. The one halo object that we identified at a cutoff of 890 m s^{-1} is compatible with such taxonomy. The very limited number of objects with known taxonomy does not, however, allow us to determine if the Tina's group is a real family or a conglomerate of asteroids happening to be lying in the local stable island, yet.

5.34 The Gallia family

The Gallia family was first identified as a clump in Gil-Hutton (2006), and was re-obtained as a family in Carruba (2010b), and Novaković et al. (2011). It is located in a stable island limited in inclination by the ν_5 and ν_{16} linear secular resonances. Its taxonomy was compatible with an S-complex composition, according to the analysis of Carruba (2010b). Here, we identified a halo of just three members at a cutoff of $>$410 m s^{-1}. All members were compatible with an S-complex taxonomy.

[4] See Carruba & Michtchenko (2007) for a more in depth discussion of frequency families.

5.35 The Pallas family

Williams (1992) first proposed the Pallas family, that was later re-analysed by Gil-Hutton (2006), Carruba (2010b) and Novaković et al. (2011). Most of the Pallas family members have B-type taxonomies, but C-type objects are also observed in the orbital region. In this work, we identified a halo of eight members at a cutoff of $>920\,\mathrm{m\,s^{-1}}$. No SDSS-MOC4 interloper was found, but, as observed for Hungaria family members, all eight asteroids have large values of p_V, in principle incompatible with a B- or C-type taxonomy.

5.36 The central main belt: an overview

Our results for the central main belt are summarized in Table 3, that has the same format as Table 2.

Fig. 7, panel A, displays an (a, $\sin(i)$) projection of asteroids in our multivariate sample in the central main belt. Blue lines show the location of the main linear secular resonances, using the second-order and fourth-degree secular perturbation theory of Milani & Knežević (1994) to compute the proper frequencies g and s for the grid of (a, e) and (a, $\sin(i)$) values shown in Fig. 10, panel A, and the values of angles and eccentricity of (480) Hansa, the highly inclined asteroid associated with the largest family in the region (Carruba 2010b). Other symbols have the same meaning as in Fig. 4, panel A. In panel B of the same figure, we display a density map of the central main belt. We computed the $\log_{10}$ of the number of all asteroids with proper elements per unit square in a 22 by 67 grid in a (starting at $a = 2.500$ au, with a step of 0.015 au) and $\sin(i)$ (starting at 0, with a step of 0.015). Superimposed on to the density map, we also show the orbital projection of the haloes found in this work shown as red plus signs for CX-complex families and as blue circles for S-complex families. The other symbols are the same as in Fig. 10, panel B. The reader may notice that regions with higher number density of asteroids are associated with the families' haloes found in this work. The haloes that we determined do not have multiple membership, i.e. an asteroid in a given family halo is not present in another family halo.

Fig. 8 displays a projection in the (a^*, $i - z$) plane of all asteroids in our multidomain sample (panel A), and an (a, $\sin(i)$) projection of the same asteroids, (panel B). We refer the reader to the caption of Fig. 6 for a more detailed description of this figure symbols. The central main belt is a transitional region, where CX-complex and S-complex asteroids are rather mixed. A greater proportion of S-type asteroids can be found at lower semimajor axis (and vice versa), but overall, no group dominates the local taxonomy.

This is confirmed by an analysis of *WISE* p_V geometrical albedo data, a histogram of which is presented in Fig. 9, panel A. Fig. 9, panel B, displays an (a, $\sin(i)$) projection of the same asteroids, where we used the same colour code as in Fig. 6, panel B.

One can notice the clearly bi-modal distribution of asteroid albedos, and the mixture of objects with low albedo and high albedo that dominates the central main belt. Having analysed the families of the central main belt, we are now ready to move on to the outer main belt.

6 OUTER MAIN BELT

The outer main belt is dynamically limited in semimajor axis by the 5J:-2A and 2J:-1A mean-motion resonances (Zappalà et al. 1995). The linear secular resonance ν_6 separates the low-inclined asteroid region from the highly inclined area, dominated by the Euphrosyne family (Machuca & Carruba 2011). We found 5385 objects that have proper elements and frequencies, SDSS-MOC4 colours, *WISE* geometric albedo data and satisfy our error analysis criteria in the outer main belt. We start our analysis of families' haloes by investigating the Koronis family.

6.1 The Koronis family

The Koronis family is one of the most interesting families in the main belt. Bottke et al. (2002) explained its shape in eccentricity as originating by the interaction of asteroids evolving via Yarkovsky effect into secular resonances such as the $2\nu_5 - 3\nu_6$. Carruba & Michtchenko (2007) showed that its upper boundary in eccentricity is limited by the $\nu_6 + 2\nu_5 - 2\nu_7 + \nu_{16}$ non-linear secular resonance. The interesting subgroup of the Karin cluster, identified by Nesvorný et al. (2002a) opened new perspectives in the understanding of recent breakups among asteroids. Mothé-Diniz et al. (2005) identified this family as predominantly belonging to the S-complex, with a few interlopers belonging to the C and D types, which predominate in the background. The presence of a few K-type asteroids in the family was somehow puzzling, and justified by Mothé-Diniz et al. (2005) as a possible remnant of a pre-existing family.

In this work, we identified a halo with 200 members, at a cutoff d_{md} of $215\,\mathrm{m\,s^{-1}}$. 32 of the halo members have SDSS-MOC4 colours not compatible with an S-complex taxonomy, which yields to a 16.0 per cent fraction of possible interlopers in the halo, somewhat in agreement with the finding of Mothé-Diniz et al. (2005). About 14 asteroids (7.0 per cent of the total) have values of p_V smaller than 0.1, which is the limit for S-complex asteroid albedos, and that may be related with the presence of the interloper population found in Mothé-Diniz et al. (2005).

6.2 The Lau family

The Lau cluster is listed at the Planetary Data System. In this work, we identified a 10-object CX halo at a cutoff of $490\,\mathrm{m\,s^{-1}}$. No interloper was found in this group.

6.3 The (1993) FY12 family

The cluster around (18405) (1994 FY12) was identified for the first time in Nesvorný et al. (2005) at a cutoff of $50\,\mathrm{m\,s^{-1}}$ as an 11-asteroid X group. Here, we find a halo at a cutoff d_{md} of $355\,\mathrm{m\,s^{-1}}$ of just two members, one of which (50.0 per cent of the total) have $p_V > 0.1$. The possible X-type composition of this small group appears to be confirmed by our analysis.

6.4 The Fingella family

The Fingella family is listed at the Planetary Data System. In this work, we identified a 16-object CX halo at a cutoff of $480\,\mathrm{m\,s^{-1}}$. No interloper was found in this group.

6.5 The Naema family

The Naema group is another family discussed in Nesvorný et al. (2005), where it was visible at a cutoff of $40\,\mathrm{m\,s^{-1}}$ as a 64 C-type group. Here, we found a halo of 43 members at a cutoff of $390\,\mathrm{m\,s^{-1}}$, with all members belonging to the CX-complex. No interlopers were found in this group.

Table 3. Asteroid families' haloes in the central main belt.

First halo member	d_{md} cutoff value (m s^{-1})	Number of members	Spectral complex	Number of SDSS-MOC4 likely interlopers	Number of p_V likely interlopers
(46) Hestia: (7321)	360	26	CX	11	12
(5) Astraea: (4018)	320	4	CX	0	0
(396) Aeolia: (76144)	320	14	CX	0	2
(410) Chloris: (9545)	340	35	CX	1	8
(569) Misa: (2289)	355	33	CX	1	1
(606) Brangane: (56748)	355	3	S	1	3
(1639) Bower: (26703)	260	27	CX	6	7
(2980) Cameron: (4067)	310	3	CX	0	2
(15) Eunomia: (630)	90	52	S	7	7
(4652) Iannini: (143366)	305	93	CX	0	6
(1272) Gefion: (2373)	210	146	S	43	33
(145) Adeona: (1783)	295	149	CX	1	4
(170) Maria/Renate: (4104)	240	135	S	21	10
(363) Padua: (2560)	130	31	CX	0	0
(3) Juno: (22216)	275	61	CX	0	4
(668) Dora: (1734)	265	108	CX	2	2
(808) Merxia/Nemesis: (3439)	250	19	CX	5	8
(847) Agnia: (1020)	190	12	S	4	4
(1128) Astrid: (2169)	435	6	CX	0	0
(1726) Hoffmeister: (1726)	210	62	CX	0	0
(2354) Lavrov: (2354)	200	8	S	1	2
(18466) 1995 SU37: (95534)	105	4	S	0	0
(729) Watsonia: (5492)	425	10	CX	3	5
(686) Gersuind: (14627)	310	7	S	3	2
(10000) Myriotos: (101897)	580	7	CX	2	6
(480) Hansa: (13617)	>535	20	S	1	0
(4203) Brucato: (4203)	950	32	CX	0	2
(945) Barcelona: (11028)	730	1	S	0	0
(1222) Tina: (16257)	890	1	CX	0	0
(148) Gallia: (40853)	>410	3	S	0	0
(2) Pallas: (24793)	>920	8	CX	0	8

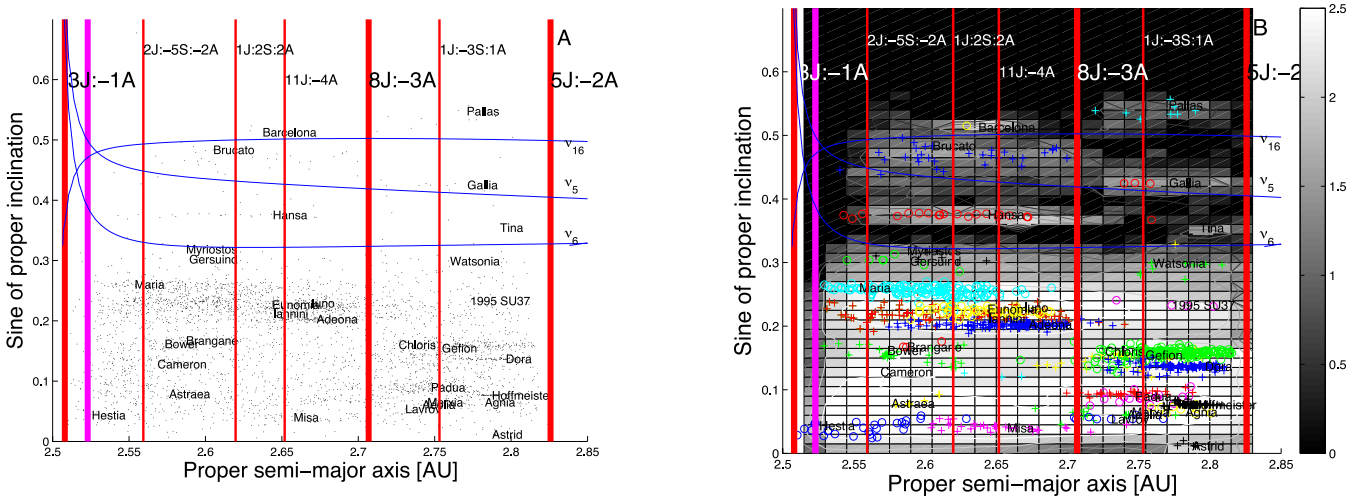

Figure 7. Panel A: an $(a, \sin(i))$ projection of central main belt asteroids in our multivariate sample. Panel B: contour plot of the number density of asteroids in the proper element sample. Superimposed, we display the orbital location of asteroids of families in the CX-complex (plus signs) or in the S-complex (circles).

6.6 The Brasilia family

The Brasilia family was identified as a small clump of 96 members in Mothé-Diniz et al. (2005), of which only 4 had known spectral type, all belonging to the CX-complex. We identified a small halo of 24 objects, most belonging to the CX-complex, that merges with the local background at a cutoff of 440 m s^{-1}. While all but three halo members (12.5 per cent of the total) have SDSS-MOC4 colours compatible with a taxonomy in the CX-complex, the vast majority of these asteroids (17, 70.8 per cent of the total) has large albedos ($p_V >$ 0.1), not usually associated with a CX-composition. The reason for the large-albedo values of these objects remains unexplained.

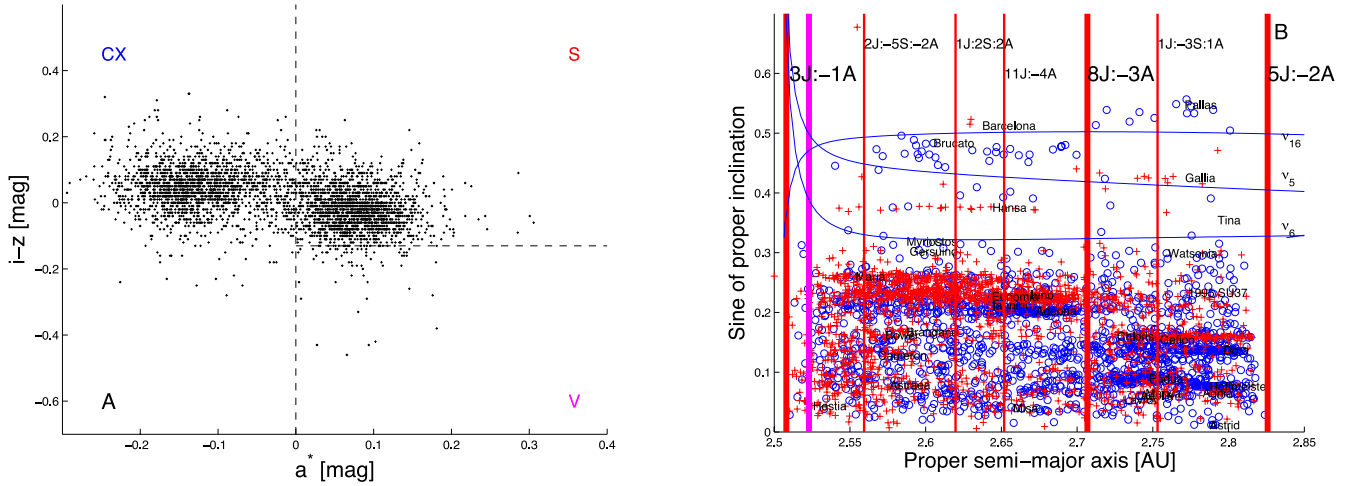

Figure 8. Panel A: an $(a^*, i - z)$ projection of central main belt asteroids in our multidomain sample. Panel B: an $(a, \sin(i))$ projection of the same asteroids, where objects in the CX-complex are shown as blue circles, and asteroids in the S-complex are identified as red plus signs.

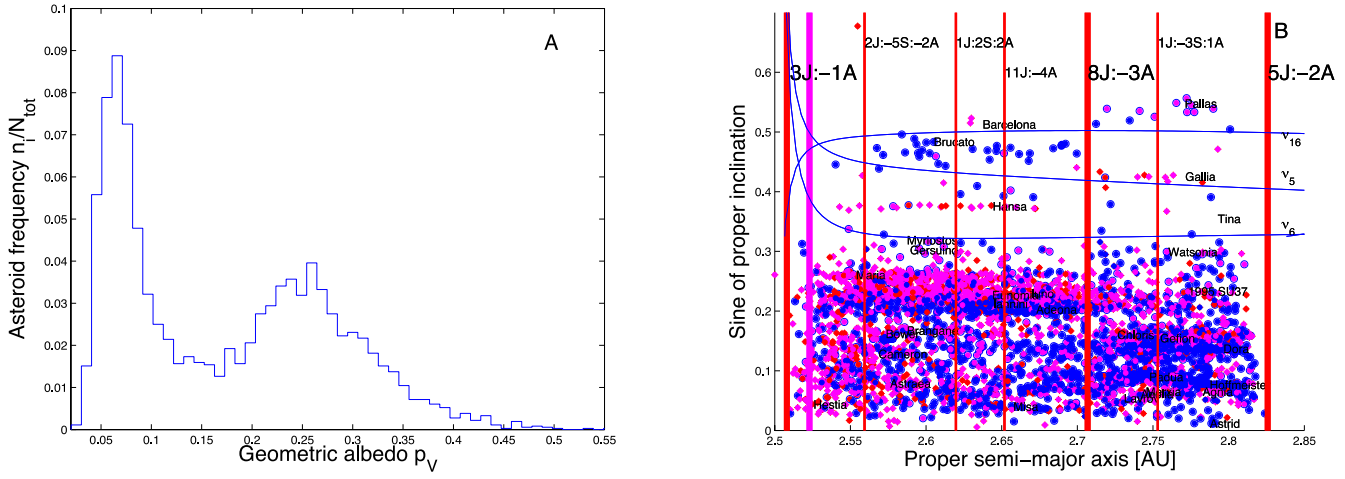

Figure 9. Panel A: a histogram of number frequency values $n_i / N_{\rm Tot}$ as a function of geometric albedo p_V for central main belt asteroids in our multidomain sample. Panel B: an $(a, \sin(i))$ projection of the same asteroids, where blue full dots are associated with asteroids with $p_V < 0.1$, red full dots display asteroids with $0.1 < p_V < 0.3$, and magenta full dots show asteroids with $p_V > 0.3$.

6.7 The Themis family

The Themis family is a rather large, homogeneous group, made mostly by asteroids of types belonging to the C/X-complex. Mothé-Diniz et al. (2005) discuss that the spectral type of the family members is not distinguishable from that of asteroids in the background, which is dominated by C and X-type objects. Tanga et al. (1999) suggest that this family originated from the breakup of a large (≃370 km in diameter) C-type parent body. In this work, we identified a halo with 700 members, at a cutoff $d_{\rm md}$ of 310 m s^{-1}. Nine of the halo members have SDSS-MOC4 colours not compatible with a C/X-complex taxonomy, which yields a 1.3 per cent fraction of possible interlopers in the halo. 50 asteroids have values of p_V larger than 0.1, which is the limit for CX-complex asteroid albedos, which yields a percentage of possible albedo interlopers of 7.1 per cent. The AstDys Ashkova group merges with the Themis halo at a cutoff of 205 m s^{-1}.

6.8 The Eos family

Vokrouhlický et al. (2006b) studied in detail the dynamical evolution of this asteroid family, also pioneering the use of Monte Carlo methods for asteroid families' chronology. The Eos family is crossed by the powerful 9J:-4A mean-motion resonance, and interacts with the z_1, $2\nu_5 - 3\nu_6$ and $2\nu_5 - 2\nu_6 + \nu_{16}$ secular resonances (see also Carruba & Michtchenko 2007). More recently, Brož & Morbidelli (2013) identified Eos halo members based on SDSS-MOC4 data, and obtained an estimate of the halo age, that is in agreement with what found by Vokrouhlický et al. (2006b). In this work, we identified a halo at a cutoff of 165 m s^{-1}, with 738 members. In agreement with what was found by Mothé-Diniz et al. (2005), the taxonomy of the family is quite inhomogeneous, but well distinguished from the local background that is dominated by C and X asteroids. Most members of the Eos family have a characteristic K-type taxonomy, and we found that many members of the halo members have $(a^*, i - z)$ colours compatible with an S-complex taxonomy. But, as discussed in Section 3, the Eos family lies at the separation between CX-complex and S-complex asteroids in the $(a^*, i - z)$. Our simple criterion for identifying S-complex asteroids, $a^* > 0$, does not apply well to the case of the Eos family. 379 asteroids (51.4 per cent of the total) have values of $a^* < 0$ and may be considered interlopers. 132 Eos halo asteroids have values of $p_V < 0.1$, which yields that 17.9 per cent of the halo asteroids

may actually be albedo interlopers. The quite diverse mineralogy of bodies in the Eos family area provides challenges that should be confronted with more advanced tools than the one used in this paper, in our opinion. The Telramund cluster, which was identified as an S-type 70-member group at a cutoff of 60 m s^{-1} by Nesvorný et al. (2005), merges at very low cutoff with the Eos family, so we consider this group as a substructure of the larger family.

6.9 The Hygiea family

(10) Hygiea is the fourth most massive asteroid of the main belt, and the family associated with this body has been studied in Zappalà et al. (1995), Mothé-Diniz et al. (2005), and, more recently by Carruba (2013). It is made mostly by bodies belonging to the CX-complex, and, as the Themis family, is not easily distinguishable from the local background of objects. We identified a halo with 426 objects at a cutoff of 290 m s^{-1}. The slightly higher number of objects that we found in the Hygiea halo with respect to Carruba (2013) might be due to the larger sample of bodies in our data set. Of the 426 possible halo members, 6 (1.4 per cent) may be interlopers based on SDSS-MOC4 colours analysis and 36 have $p_V > 0.1$, which is incompatible with CX-complex asteroids. Overall, we found a maximum of 8.5 per cent of objects that are possibly not correlated with the Hygiea halo. The AstDys Filipenko group merges with this family halo at a cutoff of 125 m s^{-1}.

6.10 The Emma family

The Emma family was identified by Nesvorný et al. (2005) as a 76-member group at a cutoff of 40 m s^{-1} in proper elements domain. No information on its taxonomy was given in that paper. In this work, we found a family halo of 43 members at a cutoff $d_{\rm md}$ of 270 m s^{-1}. No interlopers were identified in this family halo.

6.11 The Veritas family

The Veritas family is a relatively small group, made mostly by CX-complex asteroids. Milani & Farinella (1994) used for the first time chaotic chronology on this family to determine its relatively young age, later confirmed by other works. We identified a halo of 148 members at a cutoff of 240 m s^{-1}. Two objects have colours not compatible with a CX-complex taxonomy, and nine have values of $p_V > 0.1$. Overall, up to 6.1 per cent of the halo members encountered may be interlopers of the Veritas halo.

6.12 The Lixiaohua family

The Lixiaohua family was identified by Nesvorný et al. (2005) as a 97 CX-complex group at a cutoff of 50 m s^{-1}. It was the subject of a dynamical study by Novaković, Tsiganis & Knežević (2010) that extensively studied the local dynamics and the diffusion in the (e_p, i_P) plane using Monte Carlo modelling. In this work, we identified a 69-member CX halo at a cutoff of $d_{\rm md} = 255$ m s^{-1}. Only one object (1.4 per cent of the total) was a possible SDSS-MOC4 interloper, and all asteroids in the halo had $p_V < 0.1$. The AstDyS Gantrisch group merges with this family at cutoffs lower than 50 m s^{-1}.

6.13 The Aegle family

The Aegle family is an AstDyS group. We identified a 21 CX-complex group at a cutoff of 290 m s^{-1}. Two objects (9.5 per cent of the total) were possible SDSS-MOC4 interlopers, and all members had low albedos.

6.14 The Meliboea family

The Meliboea family was discussed by Zappalà et al. (1995) and Mothé-Diniz et al. (2005). It is a small group, mainly composed of asteroids belonging to the CX-complex. It is a rather inclined family ($i_p \simeq 15^\circ$), characterized by the presence of several weak mean-motion and secular resonances. We identified a halo with 73 members at a cutoff of 270 m s^{-1}. As found by Mothé-Diniz et al. (2005), the Meliboea family is fairly homogeneous, with only three members of the halo with colours not compatible with a CX-complex taxonomy. Only one halo member has $p_V > 0.1$, which yields a percentage of up to 4.1 per cent possible interlopers. The AstDyS group of Inarradas merges with this family halo at a cutoff of 140 m s^{-1}, while the Traversa cluster is englobed at a cutoff of 205 m s^{-1}.

6.15 The Klumpkea/Tirela family

The Klumpkea family was identified in Machuca & Carruba (2011) and corresponds to the old Tirela family of Nesvorný et al. (2005). Nesvorný et al. (2005) listed the Tirela family as a D-group. Here, we found a halo at a cutoff of 290 m s^{-1} with 21 members, 2 of which (9.5 per cent of the total) have colours (barely) in the S-complex area. All members of the halo have $p_V < 0.1$, which makes this family compatible with a C-complex taxonomy. The AstDyS Zhvanetskij cluster is annexed by this halo at a cutoff of 165 m s^{-1}, the Ursula family is englobed at 200 m s^{-1}, and the Pannonia group merges at a cutoff of 245 m s^{-1}.

6.16 The Theobalda family

The Theobalda family is also an AstDyS group. We identified a 34-member CX-complex halo, with two (5.9 per cent of the total) possible albedo interlopers.

6.17 The Kartvelia family

The Kartvelia family is listed at the AstDyS. We found a 26-member CX-complex halo at a cutoff of 280 m s^{-1}, with just one (3.8 per cent of the total) possible SDSS-MOC4 interloper.

6.18 The Alauda family region

The orbital region of the Alauda family has been most recently analysed by Machuca & Carruba (2011) that found several small groups, among which the Alauda and Luthera families, in the area. In this work, we identified a 158 CX-complex group at a cutoff of 420 m s^{-1}. Two members, 1.3 per cent of the total, have colours in the S-complex region, and 19 objects, 12.0 per cent of the total, have $p_V > 0.1$. The AstDys Higson cluster merges with this halo at a cutoff of 235 m s^{-1}, the AstDyS Moravia and Snelling groups merge at a cutoff of 240 m s^{-1}, while the AstDyS Vassar cluster is annexed at 255 m s^{-1}.

6.19 The Euphrosyne family

Machuca & Carruba (2011) most recently analysed the orbital region of this highly inclined asteroid family. This familyis characterized by its interaction with linear secular resonances. In particular,

13 of its members are in ν_6 anti-aligned librating states, one in a ν_5 anti-aligned librating state (242435), and one in a ν_5 aligned librating state (2009 UL136), according to Machuca & Carruba (2011). The long-term effect of close encounters of asteroids with absolute magnitude $H < 13.5$ with (31) Euphrosyne was recently studied in Carruba et al. (2013). As discussed in Machuca & Carruba (2011), the Euphrosyne family is separated by the near regions of (69032) and Alauda in inclination by areas with very low asteroid densities. It is a region with a relatively small population of objects, separated among them by large distances, which explains why the 75-member halo that we identified in this work is encountered at the high cutoff value of 575 m s^{-1}. All halo members have colours in the S-complex area, and three members have $p_V > 0.1$. As for the case of the Klumpkea family, this is a group highly compatible with a C-complex taxonomy, with a 4.0 per cent of possible interlopers.

6.20 The outer main belt: an overview

Having obtained estimates for the haloes of the main families in the outer main belt, we are now ready to outline our results. As done for previous asteroid regions, our results are summarized in Table 4.

Fig. 10, panel A, displays an (a, sin (i)) projection of asteroids in our multivariate sample in the outer main belt, using the same symbols for analogous figure in the inner and central main belt. Here, however, blue lines show the location of the main linear secular resonances, using the second-order and fourth-degree secular perturbation theory of Milani & Knežević (1994) to compute the proper frequencies g and s for the grid of (a, e) and (a, sin (i)) values shown in Fig. 10, panel A, and the values of angles and eccentricity of (31) Euphrosyne, the highly inclined asteroid associated with the largest family in the region (Machuca & Carruba 2011). In panel B of the same figure, we display a density map of the outer main belt. To quantitatively determine the local density of asteroids, we computed the $\log_{10}$ of the number of all asteroids with proper elements per unit square in a 67 by 67 grid in a (starting at $a = 2.805$ au, with a step of 0.015 au) and sin(i) (starting at 0, with a step of 0.015). The other symbols are the same as in Fig. 4, panel A. The reader may notice that regions with higher number density of asteroids are associated with the families' halo found in this work. Families' haloes are indeed more extended in proper elements domain than the core families found with the standard HCM.

To study how the family haloes found in this work are related to the local taxonomy, we also plotted in Fig. 11 a projection in the (a^*, $i - z$) plane of all asteroids in our multidomain sample (panel A), and an (a, sin (i)) projection of the same asteroids, (panel B). The great majority of asteroids in the region belong to the CX-complex, but there is a sizeable minority of bodies belonging to the S-complex, that, as shown in Fig. 11, panel B, are mostly associated with the Eos and Koronis families.

This is confirmed by *WISE* p_V geometrical albedo data, a histogram of which is presented in Fig. 12, panel A. Fig. 12, panel B, displays an (a, sin (i)) projection of the same asteroids, with the colour code used in Fig. 6, panel B. The great majority of objects have low albedos, characteristics of the dark C-type objects that predominates in the outer main belt, but there is a fraction of asteroids that are associated with the Eos and Koronis families, with medium and high values of geometric albedo.

Overall, we confirmed the results of the taxonomical analysis of Mothé-Diniz et al. (2005): the outer main belt is dominated by CX-complex dark asteroids, with the two notable exceptions of the Eos and Koronis families. S-complex asteroids in the local background may be escapers from these two large families. Dynamical studies on the orbital evolution of members of these families are however needed to confirm this conclusion.

7 CYBELE GROUP

The Cybele group, usually not considered part of the main belt, is located beyond the 2J:-1A mean motion resonance in semimajor axis and its orbital region is usually defined to lie between 3.27 and 3.70 au in proper a and to $i < 30^\circ$. Currently, there are 1111 asteroid in the Cybele orbital region. The largest collisional family in the region is associated with (87) Sylvia, a triple asteroid (Vokrouhlický et al. 2010). The same authors investigated the orbital region of two other large binary asteroids in the region, (107) Camila and (121) Hermione, that are currently not part of any recognizable

Table 4. Asteroid families' haloes in the outer main belt.

First halo member	$d_{\rm md}$ cutoff value (m s^{-1})	Number of members	Spectral likely interlopers	Number of SDSS-MOC4 complex	Number of p_V likely interlopers
(158) Koronis: (761)	215	200	S	32	14
(18405) 1993 FY12: (29959)	355	2	CX	0	1
(10811) Lau: (51707)	490	10	CX	0	0
(709) Fingella: (1337)	480	16	CX	0	0
(845) Naema: (21257)	390	43	CX	0	0
(293) Brasilia: (3985)	440	24	CX	3	17
(24) Themis: (981)	310	700	CX	9	50
(221) Eos: (320)	165	738	S	379	132
(10) Hygiea: (867)	290	426	CX	6	36
(283) Emma: (3369)	270	43	CX	0	0
(490) Veritas: (5592)	240	148	CX	2	9
(3556) Lixiaohua: (18477)	255	69	CX	1	0
(96) Aegle: (29579)	290	21	CX	2	0
(137) Meliboea: (1165)	270	73	CX	3	1
(1040) Klumpkea/Tirela: (18399)	290	21	CX	2	0
(778) Theobalda: (3432)	310	34	CX	0	2
(781) Kartivelia: (781)	280	26	CX	1	0
(702) Alauda/Luthera: (11911)	420	158	CX	2	19
(31) Euphrosyne: (16712)	575	75	CX	0	3

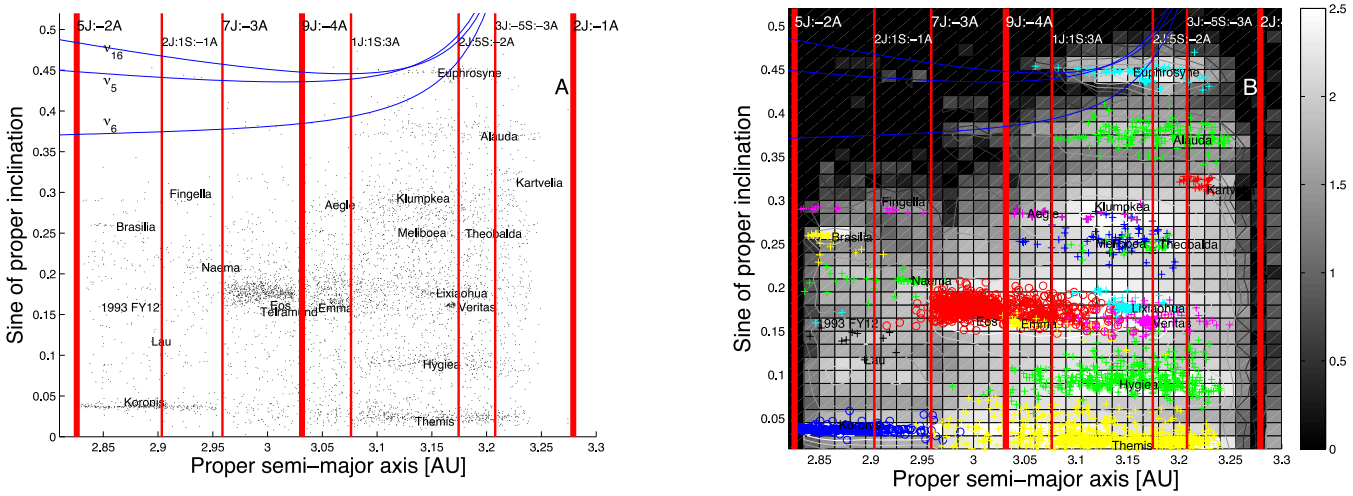

Figure 10. Panel A: An $(a, \sin(i))$ projection of outer main belt asteroids in our multivariate sample. Panel B: contour plot of the number density of asteroids in the proper element sample. Superimposed, we display the orbital location of asteroids of families in the CX-complex (plus signs) or in the S-complex (circles).

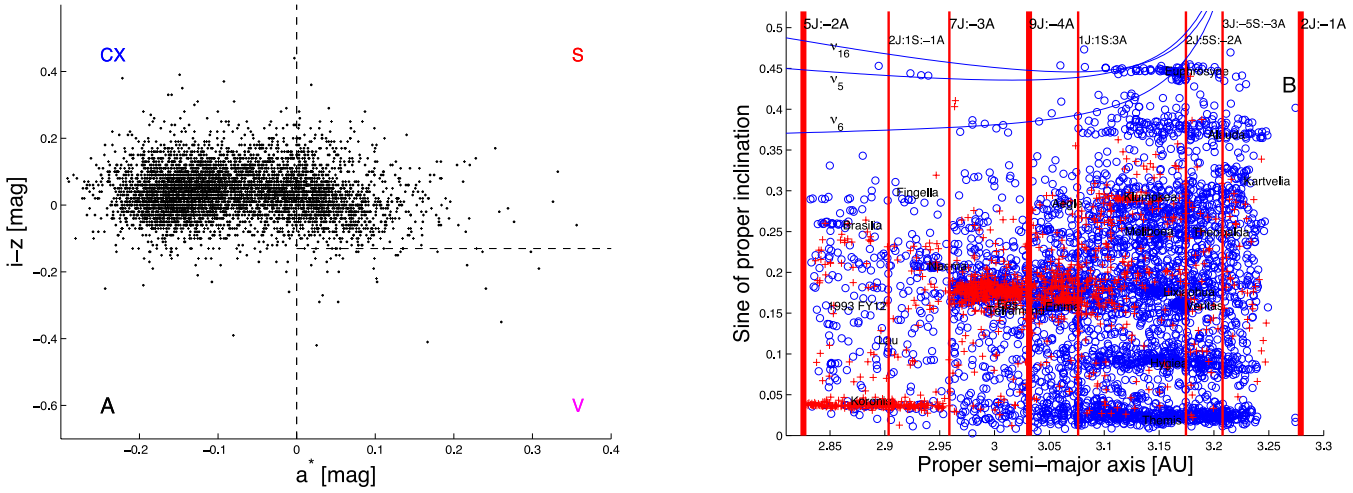

Figure 11. Panel A: an $(a^*, i - z)$ projection of outer main belt asteroids in our multidomain sample. Panel B: a $(a, \sin(i))$ projection of the same asteroids, where objects in the CX-complex are shown as blue circles, and asteroids in the S-complex are identified as red plus signs.

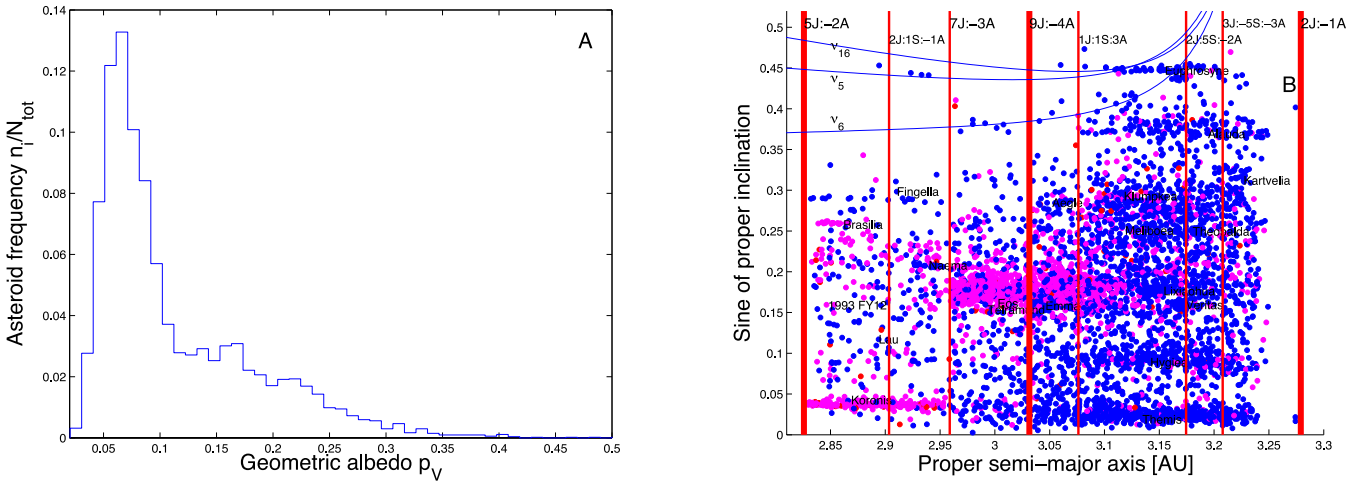

Figure 12. Panel A: a histogram of number frequency values $n_i / N_{\rm Tot}$ as a function of geometric albedo p_V for outer main belt asteroids in our multidomain sample. Panel B: an $(a, \sin(i))$ projection of the same asteroids, where blue full dots are associated with asteroids with $p_V < 0.1$, red full dots display asteroids with $0.1 < p_V < 0.3$ and magenta full dots show asteroids with $p_V > 0.3$.

family. They concluded that, while it is possible that Yarkovsky/YORP driven mobility in the orbital region of these asteroids may have depleted possible local collisional families in time-scales of 4 billion years, other mechanisms, such as resonance sweeping or other perturbing effects associated with the late Jupiter's inward migration may have been at play in the region in order to justify the current lack of dynamical groups. The AstDyS report three more families in the region of the Cybele group: Huberta, Ulla and (2000) EK76. No halo group was found for the (2000) EK76 AstDyS cluster, which will not therefore be treated in this section. There were 128 asteroids in our multidomain sample in this region, and we will start our analysis by investigating the Sylvia family halo.

7.1 The Sylvia family

The Sylvia family was first identified in Nesvorný et al. (2006) and was the first dynamical group found in the Cybele region. Its dynamical evolution was studied in detail in Vokrouhlický et al. (2010). In this work, we identified a CX-complex halo of 13 members at a cutoff $d_{\rm md}$ of 395 m s^{-1}. There were no SDSS-MOC4 interlopers, and just one object (7.7 per cent of the total) was identified as a possible albedo interloper.

7.2 The Huberta family

The Huberta family is a group reported at the AstDyS website. We identified a CX-complex halo of four members at a cutoff of 495 m s^{-1}. One object (25.0 per cent of the total) was a possible SDSS-MOC4 and albedo interloper.

7.3 The Ulla family

The Ulla family is a very isolated group at relatively high inclination of $\sin(i) \simeq 0.3$ and slightly lower than the centre of the ν_6 secular resonance. It is listed as a dynamical family at the AstDys website, and we identified a small CX-complex halo of four members for cutoffs larger than 220 m s^{-1}. No interlopers were identified in this halo.

7.4 Cybele group: an overview

We summarize our results for the Cybele group in Table 5 that has the same format as similar tables used for the inner, central and outer main belt.

Fig. 13, panel A, displays an (a, $\sin(i)$) projection of asteroids in our multivariate sample in the outer main belt, with the same symbols used for analogous figure for the inner, central and outer main belt. Here, however, blue lines show the location of the main linear secular resonances, using the second-order and fourth-degree secular perturbation theory of Milani & Knežević (1994) to compute the proper frequencies g and s for the grid of (a, e) and (a, $\sin(i)$) values shown in Fig. 13, panel A, and the values of angles and eccentricity of (87) Sylvia, the asteroid associated with the largest family in the region (Vokrouhlický et al. 2010). We also display the location of the z_1 secular resonance as a red line, since this resonance is important in the dynamical evolution of the Sylvia group. In panel B of the same figure, we display a density map of the outer main belt, according to the approach described in Carruba & Michtchenko (2009). To quantitatively determine the local density of asteroids, we computed the $\log_{10}$ of the number of all asteroids with proper elements per unit square in a 67 by 67 grid in a (starting at $a = 3.27$ au, with a step of 0.015 au) and $\sin(i)$ (starting at 0, with a step of 0.015). The other symbols are the same as in Fig. 4, panel B.

To study how the family haloes found in this work are related to the local taxonomy, we also plotted in Fig. 14 a projection in the (a^*, $i - z$) plane of all asteroids in our multidomain sample (panel A), and an (a, $\sin(i)$) projection of the same asteroids, (panel B). The majority of asteroids in the Cybele region belong to the CX-complex, but there is a sizeable minority of S-complex bodies. This is confirmed by *WISE* p_V geometrical albedo data, a histogram of which is presented in Fig. 15, panel A. Fig. 15, panel B, displays an (a, $\sin(i)$) projection of the same asteroids, with the same colour code used in similar figures for the inner, central and outer main belt. The vast majority of asteroids in the Cybele region are dark objects, typical of CX-complex taxonomy. Overall, the predominance of dark, CX-complex asteroids in the Cybele group, confirms the taxonomical analysis performed by Vokrouhlický et al. (2010). The last region to be analysed in this work will be that of the Hungaria asteroid family.

8 THE HUNGARIA REGION

The Hungaria region is located at the inner edge of the asteroid main belt (at semimajor axis $a < 2$ au), and it is located at high inclinations and low to moderate eccentricities. The limitations in eccentricity allow for a perihelion large enough to avoid strong interactions with Mars, even considering secular changes in the Mars eccentricity. (Milani et al. 2010). The ν_3 and ν_5 secular resonances fix the dynamical limits of the Hungaria region in inclination. Only one family has been so far positively identified in the Hungaria orbital region, the namesake (434) Hungaria group by Milani et al. (2010). Other authors (Cañada-Assandri et al. 2013, private communication) pointed out that the highly inclined Hungaria population is dominated by S-type objects, and fairly distinguished from the C-complex population observed in the Hungaria dynamical family. But no family in proper elements domain has yet been observed in this highly inclined region. We identified only 37 objects in our multidomain sample, with reasonable errors, and we will start our analysis of the Hungaria region by studying the Hungaria family halo.

8.1 The Hungaria family

The most recent identification of the Hungaria family was obtained by Milani et al. (2010), who also found no evidence for other

Table 5. Asteroid families' haloes in the Cybele group.

First halo member	$d_{\rm md}$ cutoff value (m s^{-1})	Number of members	Spectral likely interlopers	Number of SDSS-MOC4 complex	Number of p_V likely interlopers
(87) Sylvia: (18959)	395	13	CX	0	1
(260) Huberta: (260)	495	4	CX	0	1
(909) Ulla: (85036)	>220	4	CX	0	0

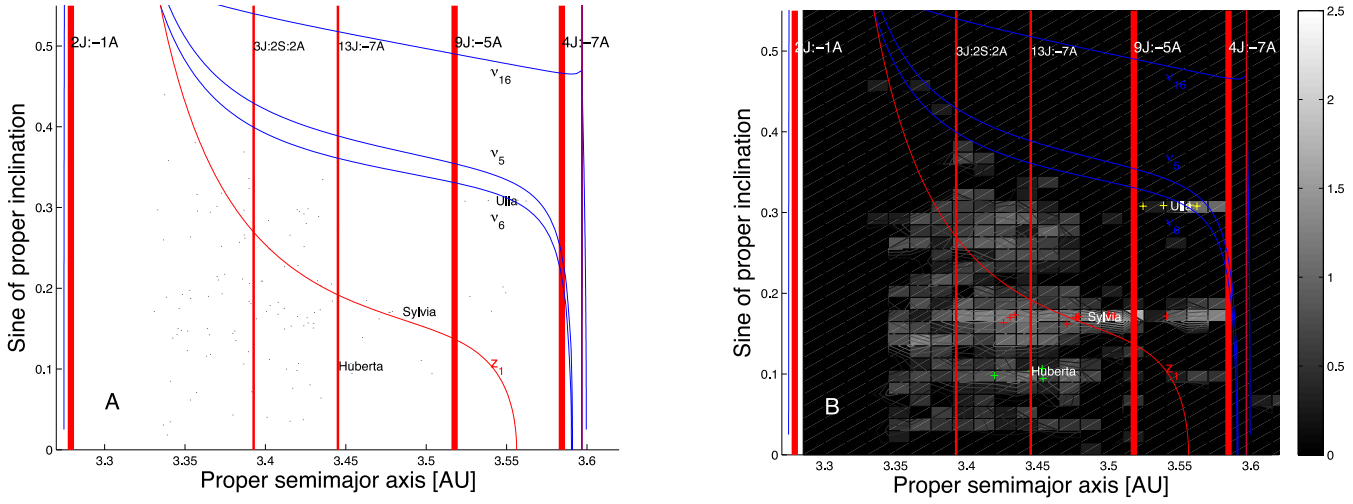

Figure 13. Panel A: an $(a, \sin(i))$ projection of Cybele-group asteroids in our multivariate sample. Panel B: contour plot of the number density of asteroids in the proper element sample. Superimposed, we display the orbital location of asteroids of families in the CX-complex (plus signs).

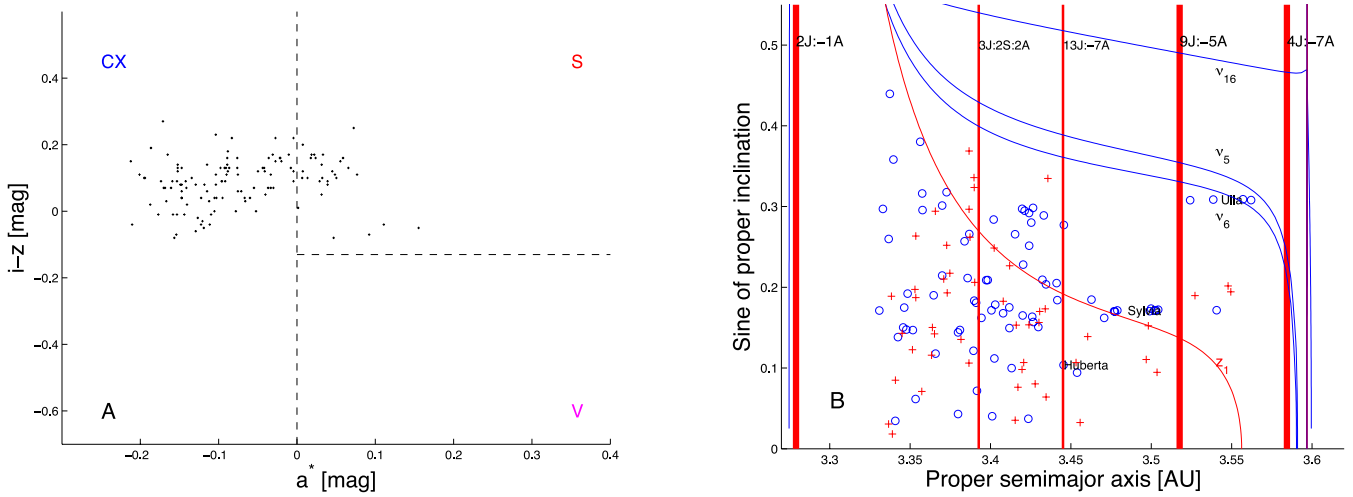

Figure 14. Panel A: an $(a^*, i - z)$ projection of Cybele-group asteroids in our multidomain sample. Panel B: an $(a, \sin(i))$ projection of the same asteroids, where objects in the CX-complex are shown as blue circles, and asteroids in the S-complex are identified as red plus signs.

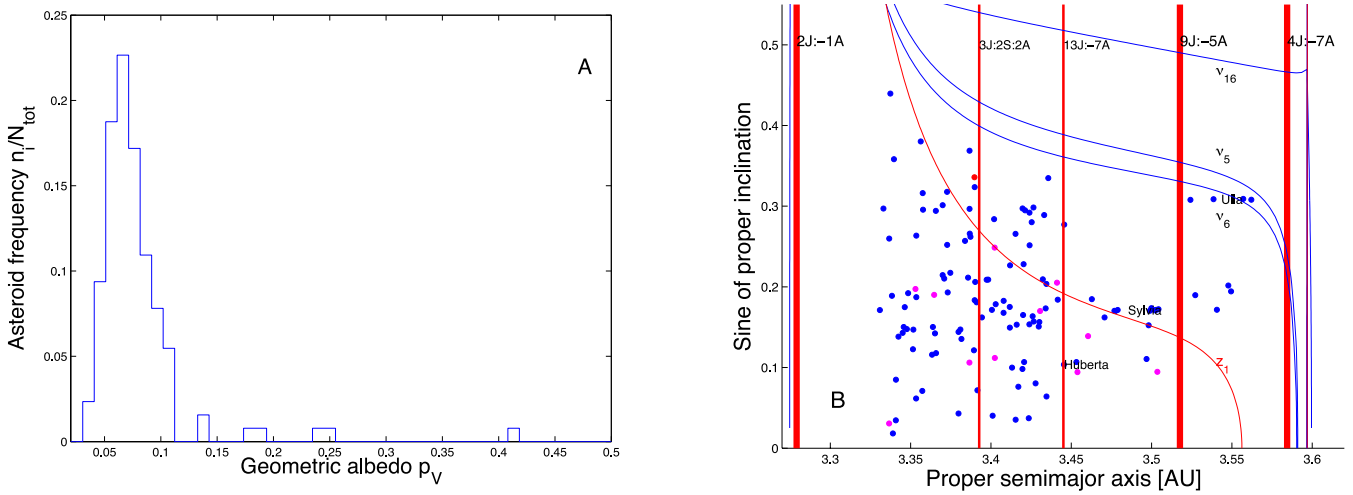

Figure 15. Panel A: a histogram of number frequency values $n_i / N_{\rm Tot}$ as a function of geometric albedo p_V for Cybele-group asteroids in our multidomain sample. Panel B: an $(a, \sin(i))$ projection of the same asteroids, where blue full dots are associated with asteroids with $p_V < 0.1$, red full dots display asteroids with $0.1 < p_V < 0.3$ and magenta full dots show asteroids with $p_V > 0.3$.

possible dynamical groups in the region (but identified possible sub-structures inside the Hungaria family). Here, we identified a 2-CX-complex halo at a cutoff of 590 m s^{-1}. One object, 50 per cent of the total, was however more compatible with S-complex taxonomy and could therefore be a possible interlopers. All asteroids in the halo had $p_V > 0.1$, which is usually incompatible with a CX-complex taxonomy, but that seems typical of Hungaria objects, as discussed by Warner et al. (2009).

8.2 The highly inclined Hungaria population

No family has been currently identified in the highly inclined ($\sin(i) > 0.4$) Hungaria region in the domain of proper elements. Cañada-Assandri et al. (2013) pointed out that the highly inclined Hungaria region is dominated by S-complex objects, and taxonomically fairly different than the members of the CX-complex Hungaria group. While no family is yet identifiable in the proper element domain in this region, we checked for the presence of a halo, possibly associated with hypothetical local frequency families. We identified a S-complex halo of seven members at a cutoff $d_{\rm md} = 655$ m s^{-1}, around (2049) Grietje. One object, 14.3 per cent of the total, is a possible SDSS-MOC4 interlopers, and there were no albedo interlopers.

8.3 The Hungaria region: an overview

We summarize our results for the Hungaria region in Table 6, which has the same format as similar tables used for the inner, central, outer main belt and Cybele group.

Fig. 16, panel A, displays an (a, $\sin(i)$) projection of asteroids in our multivariate sample in the outer main belt, with the same symbols used for analogous figures in the inner, central and outer main belt, and the Cybele region. Here, however, blue lines show the location of the ν_5 linear secular resonances, using the second-order and fourth-degree secular perturbation theory of Milani & Knežević (1994) to compute the proper frequencies g and s for the grid of (a, e) and (a, $\sin(i)$) values shown in Fig. 13, panel A, and the values of angles and eccentricity of (434) Hungaria, the asteroid associated with the largest family in the region. We also display the location of the ν_4, ν_3 (blue lines), and ν_{14} (red line) secular resonances, since this resonance are important in setting dynamical boundaries in the region. The orbital position in the (a, $\sin(i)$) plane of the first numbered asteroid in all the Hungaria groups is also identified in Fig. 13, panel A. In panel B of the same figure, we display a density map of the outer main belt, according to the approach described in Carruba & Michtchenko (2009). To quantitatively determine the local density of asteroids, we computed the $\log_{10}$ of the number of all asteroids with proper elements per unit square in a 15 by 24 grid in a (starting at $a = 1.8$ au, with a step of 0.015 au) and $\sin(i)$ (starting at 0.25, with a step of 0.015). The other symbols are the same as in Fig. 4, panel B.

To study how the family haloes found in this work are related to the local taxonomy, we also plotted in Fig. 17 a projection in the (a^*, $i - z$) plane of all asteroids in our multidomain sample (panel A), and an (a, $\sin(i)$) projection of the same asteroids (panel B). The majority of asteroids in the Hungaria region in our sample belong to the S-complex, but there is a sizeable minority of CX-complex bodies.

The analysis of *WISE* p_V geometrical albedo data, a histogram of which is presented in Fig. 18, panel A, show some peculiarities. Fig. 18, panel B, displays an (a, $\sin(i)$) projection of the same asteroids, with the same colour code used in similar figures for the inner, central and outer main belt. The vast majority of asteroids in the Hungaria region and the Hungaria family are very bright objects, typical of S-complex taxonomy. The fact that many asteroids in the Hungaria family show high albedo and CX-taxonomy remains yet to be explained.

Table 6. Asteroid families' haloes in the Hungaria region.

First halo member	$d_{\rm md}$ cutoff value (m s^{-1})	Number of members	Spectral likely interlopers	Number of SDSS-MOC4 complex	Number of p_V likely interlopers
(434) Hungaria: (5968)	590	2	CX	1	2
(2049) Grietje: (3043)	655	7	S	1	0

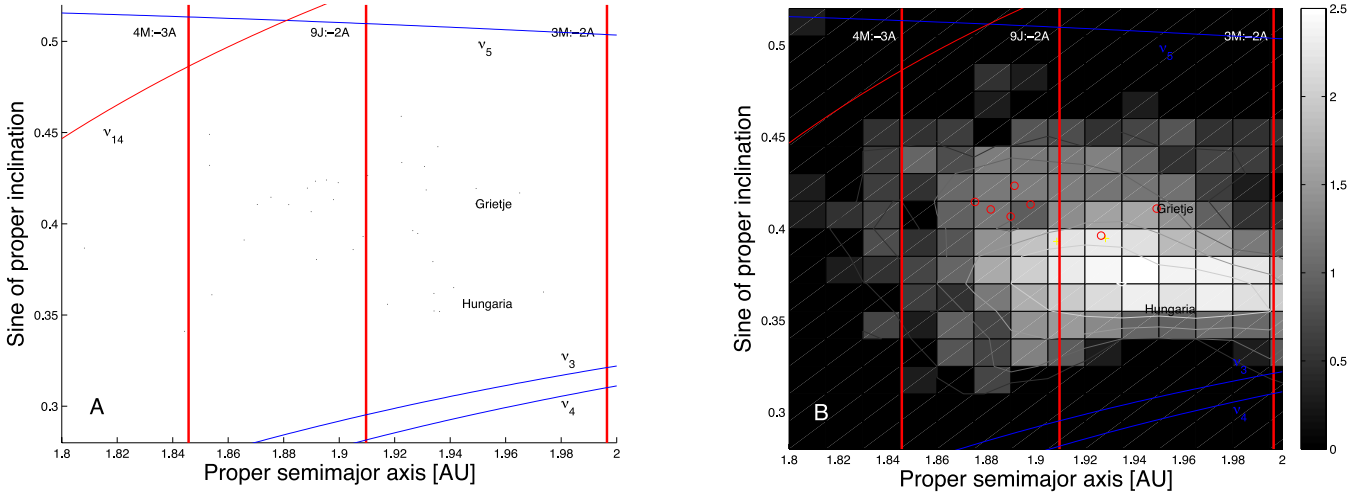

Figure 16. Panel A: an (a, $\sin(i)$) projection of Hungaria-region asteroids in our multivariate sample. Panel B: contour plot of the number density of asteroids in the proper element sample. Superimposed, we display the orbital location of asteroids of families in the CX-complex (plus signs) and S-complex (circles).

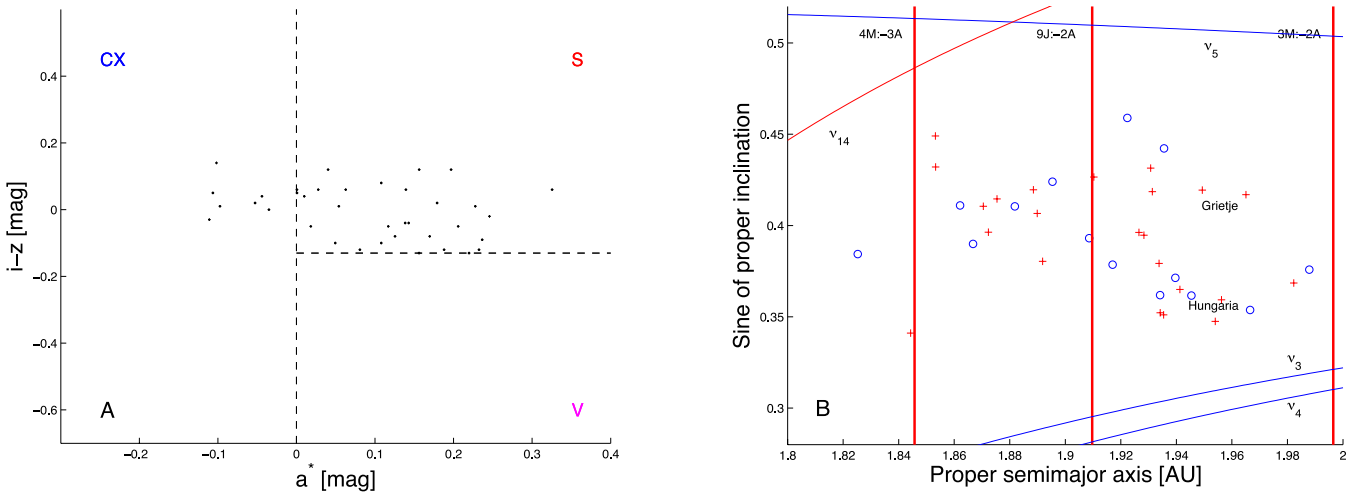

Figure 17. Panel A: an $(a^*, i - z)$ projection of Hungaria-region asteroids in our multidomain sample. Panel B: an $(a, \sin(i))$ projection of the same asteroids, where objects in the CX-complex are shown as blue circles and asteroids in the S-complex are identified as red plus signs.

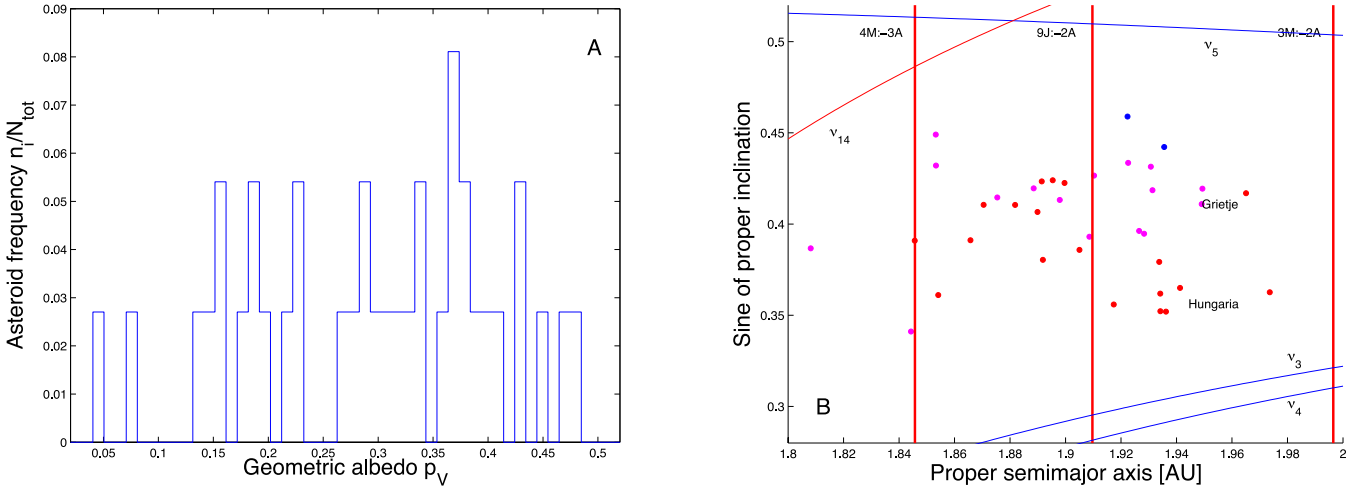

Figure 18. Panel A: a histogram of number frequency values $n_i/N_{\rm Tot}$ as a function of geometric albedo p_V for Hungaria-region asteroids in our multidomain sample. Panel B: an $(a, \sin(i))$ projection of the same asteroids, where blue full dots are associated with asteroids with $p_V < 0.1$, red full dots display asteroids with $0.1 < p_V < 0.3$, and magenta full dots show asteroids with $p_V > 0.3$.

9 CONCLUSIONS

In this work, we:

(i) Introduced a new method to obtain asteroid families and asteroid family haloes based on a distance metric in a multidomain composed of proper elements, SDSS-MOC4 $(a^*, i - z)$ colours and *WISE* geometrical albedo p_V.

(ii) Compared this new distance metric with other distance metrics in domain of proper elements, proper elements and SDSS-MOC4 colours, and proper elements and geometric albedo. The method is at best a factor of 2 more efficient in eliminating interlopers than other methods, and at worst it provides comparable results to groups found in domains of proper elements and SDSS-MOC4 colours only.

(iii) Applied this method to all the major known families in the asteroids' main belt, and in the Cybele and Hungaria orbital regions. Overall, we identified 62 asteroid families' haloes, of which 7 were in the inner main belt, 31 in the central main belt, 19 in the outer main belt, 3 in the Cybele group and 2 in the Hungaria region. We confirm the taxonomical analysis performed by Mothé-Diniz et al. (2005), Nesvorný et al. (2006), Carruba (2009a,b, 2010a,b) and other authors, with some small discrepancies for a few minor families in the central main belt.

Overall, apart from a few problematic cases such as the Eos family, our method appears to provide robust results in terms of asteroid family identification and in efficiency in eliminating interlopers from the clusters. While the sample of objects with data in all three domains is still limited, we believe that such an approach may be certainly more reliable than traditional HCM in identifying possible collisional groups. The possible future increase in the number of asteroids for which data in all three domains will be available, for instance because of the *GAIA* mission, may provide in the future data bases for asteroid family identification much larger than the one used in this work.

Many other applications of this new approach are possible with current data bases. An analysis of asteroid families in domains of proper frequencies such as $(n, g, g + s)$ (Carruba & Michtchenko 2007, 2009), where g is the precession frequency of the longitude of pericentre, and s the precession frequency of the longitude of the

node, SDSS-MOC4 colours and *WISE* albedo may provide useful insights on the secular evolution of asteroid families. Many exciting years of discoveries are still open, in our opinion, in the field of asteroid dynamics.

ACKNOWLEDGEMENTS

We are grateful to the reviewer of this article, Ricardo Gil-Hutton, for suggestions and comments that significantly increased the quality of this paper. We would also like to thank the São Paulo State Science Foundation (FAPESP) that supported this work via the grant 11/19863-3, and the Brazilian National Research Council (CNPq, grant 305453/2011-4). This publication makes use of data products from the *Wide-field Infrared Survey Explorer*, which is a joint project of the University of California, Los Angeles, and the Jet Propulsion Laboratory/California Institute of Technology, funded by the National Aeronautics and Space Administration. This publication also makes use of data products from NEOWISE, which is a project of the Jet Propulsion Laboratory/California Institute of Technology, funded by the Planetary Science Division of the National Aeronautics and Space Administration.

REFERENCES

Bendjoya P., Zappalà V., 2002, Asteroids III, University of Arizona Press, Tucson, p. 613
Bottke W. F., Vokrouhlický D., Rubincam D. P., Brož M., 2002, Asteroids III, University of Arizona Press, Tucson, p. 395
Brož M., Morbidelli A., 2013, Icarus, 223, 844
Bus J. S., 1999, PhD thesis, MIT
Bus J. S., Binzel R. P., 2002a, Icarus, 158, 106
Bus J. S., Binzel R. P., 2002b, Icarus, 158, 146
Carruba V., 2009a, MNRAS, 395, 358
Carruba V., 2009b, MNRAS, 398, 1512
Carruba V., 2010a, MNRAS, 403, 1834
Carruba V., 2010b, MNRAS, 408, 580
Carruba V., 2013, MNRAS, 431, 3557
Carruba V., Michtchenko T. A., 2007, A&A, 475, 1145
Carruba V., Michtchenko T., 2009, A&A, 493, 267
Carruba V., Morbidelli A., 2011, MNRAS, 412, 2040
Carruba V., Michtchenko T. A., Roig F., Ferraz-Mello S., Nesvorný D., 2005, A&A, 441, 819
Carruba V., Michtchenko T., Lazzaro D., 2007, A&A, 473, 967
Carruba V., Burns J. A., Bottke W., Nesvorný D., 2003, Icarus, 162, 308
Carruba V., Huaman M., Domingos R. C., Roig F., 2013, A&A, 550, A85
Gil-Hutton R., 2006, Icarus, 183, 93
Hergenrother C. W., Larson S. M., Spahr T. B., 1996, BAAS, 28, 1097
Ivezić Ž. et al., 2002, AJ, 122, 2749
Knežević Z., Milani A., 2003, A&A, 403, 1165
Machuca J. F., Carruba V., 2011, MNRAS, 420, 1779
Mainzer A. K. et al., 2011, ApJ, 731, 53
Masiero J. R. et al., 2011, ApJ, 741, 68
Michtchenko T. A., Lazzaro D., Carvano J. M., Ferraz-Mello S., 2010, MNRAS, 401, 2499
Migliorini F., Zappalà V., Vio R., Cellino A., 1995, Icarus, 118, 271
Milani A., Farinella P., 1994, Nat, 370, 40
Milani A., Knežević Z., 1994, Icarus, 107, 219
Milani A., Knezević Z., Novaković B., Cellino A., 2010, Icarus, 207, 769
Mothé-Diniz T., Roig F., Carvano J. M., 2005, Icarus, 174, 54
Nesvorný D., 2012, Nesvorny HCM Asteroid Families V2.0. EAR-A-VARGBDET-5-NESVORNYFAM-V2.0. NASA Planetary Data System
Nesvorný D., Bottke W. F., Dones L., Levison H. F., 2002, Nat, 417, 720
Nesvorný D., Jedicke R., Whiteley R., Ivezić Ž., 2005, Icarus, 173, 132
Nesvorný D., Bottke W. F., Vokrouhlický D., Morbidelli A., Jedicke R., 2006, in Lazzaro D., Ferraz-Mello S., Fernandes J. A., eds, Proc. IAU Symp. Vol. 229, Asteroids, Comets, Meteors. Cambridge Univ. Press, Cambridge, p. 289
Nesvorný D., Roig F., Gladman B., Lazzaro D., Carruba V., Mothé-Diniz T., 2008, Icarus, 183, 85
Novaković B., Tsiganis K., Knežević Z., 2010, Celest. Mech. Dyn. Astron., 107, 35
Novaković B., Cellino A., Knežević Z., 2011, Icarus, 216, 69
Parker A., Ivezić Ž., Jurić M., Lupton R., Sekora M. D., Kowalski A., 2008, Icarus, 198, 138
Roig F., Gil-Hutton R., 2006, Icarus, 183, 411
Russel C. T. et al., 2012, Sci, 336, 684
Tanga P., Cellino A., Michel P., Zappal V., Paolicchi P., dellOro A., 1999, Icarus, 141, 65
Tedesco E. F., Noah P. V., Noah M., Price S. D., 2002, AJ, 123, 1056
Tholen D. J., 1989, in Binzel R. P., Gehrels T., Matthews M. S., eds, Asteroid Taxonomic Classifications, University of Arizona Press, Tucson, p. 298
Vokrouhlický D., Brož M., Bottke W. F., Nesvorný D., Morbidelli A., 2006, Icarus, 183, 349
Vokrouhlický, Nesvorný D., Bottke W. F., Morbidelli A., 2010, AJ, 139, 2148
Warner B. D., Harris A. W., Vokrouhlický D., Nesvorný D., Bottke W. F., 2009, Icarus, 398, 1512
Williams J. G., 1992, Icarus, 96, 251
Wright E. L. et al., 2010, AJ, 140, 1868
Zappalà V., Cellino A., Farinella P., Knežević Z., 1990, AJ, 100, 2030
Zappalà V., Bendjoya Ph., Cellino A., Farinella P., Froeschlé C., 1995, Icarus, 116, 291
Zappalà V., Cellino A., di Martino M., Migliorini F., Paolicchi P., 1997, Icarus, 129, 1

This paper has been typeset from a TEX/LATEX file prepared by the author.

13

Considerações finais

Nesta dissertação foram revisados onze trabalhos que envolvem a evolução dinâmica, cronologia, propriedades físicas, rotacionais e colisionais de asteroides de alta inclinação. Novos métodos para determinação de famílias de asteroides em espaços de elementos próprios, frequência próprias, cores do SDSS-MOC4 e albedo do WISE foram discutidos nesta dissertação. Novas classes de famílias de asteroides, como os grupos identificáveis somente no espaço das frequências, ou os asteroides em configuração anti-alinhadas da ressonância ν_6, os asteroides de tipo Tina, foram identificados em alguns dos trabalhos apresentados.

Entender a presente distribuição orbital dos asteroides de alta inclinação, a origem destes objetos e sua possível evolução permanecem, na minha opinião, interessantes desafios para futuros projetos de pesquisa.